Yasuhiro Iwasawa · Kiyotaka Asakura
Mizuki Tada *Editors*

XAFS Techniques for Catalysts, Nanomaterials, and Surfaces

Springer

XAFS Techniques for Catalysts, Nanomaterials, and Surfaces

Yasuhiro Iwasawa • Kiyotaka Asakura
Mizuki Tada
Editors

XAFS Techniques for Catalysts, Nanomaterials, and Surfaces

Springer

Editors
Yasuhiro Iwasawa
The University of Electro-Communications
Innovation Research Center for Fuel Cells
Graduate School of Informatics and Engineering
Tokyo, Japan

Kiyotaka Asakura
Institute for Catalysis
Hokkaido University
Sapporo, Japan

Emeritus
The University of Tokyo
Tokyo, Japan

Mizuki Tada
Research Center for Materials Science
Nagoya University
Nagoya, Japan

ISBN 978-3-319-43864-1 ISBN 978-3-319-43866-5 (eBook)
DOI 10.1007/978-3-319-43866-5

Library of Congress Control Number: 2016952795

Printed on acid-free paper

This Springer imprint is published by Springer Nature
The registered company is Springer International Publishing AG Switzerland

Preface

This book contains 37 subjects and topics in 5 chapters based on recent developments in the XAFS approach to science and technology, describing the theories, calculation methods, computer programs, advanced methodologies and techniques, experiments, and applications to catalysts, nanoparticles, and surfaces. The book details advanced XAFS techniques and their applications, which enable high-quality research in various areas such as physics, chemistry, materials science, bioscience, engineering, energy science, environmental science, geoscience, metallurgy, and mineralogy. Fundamental characterization of catalysts, nanomaterials, and surfaces is an essential and important area of academic and industrial material development and important to addressing many of today's big global challenges.

The XAFS science and technology has significantly progressed in the past 50 years in association with developments of synchrotron radiation sources and storage rings with lower beam emittance and higher brilliance. In this book we concentrate on the distinct progress, advantage, and merit of the XAFS techniques in conducting fundamental and practical studies on a variety of advanced catalysts, nanomaterials, and surfaces with definite purposes and goals. We also describe recent important issues as examples and future prospects, while also providing the basic theory, principle, and analysis of XAFS and a systematic presentation of relevant data.

Powerful, unique, and versatile, XAFS techniques have provided in situ approaches under working/operando conditions for more realistic molecular-level understanding of catalysis mechanisms and dynamic functions of nanomaterials and surfaces. Recently, XAFS has developed by significant progress in real-time and spatially imaging XAFS measurements. These techniques have provided new pieces of information on real-time structural kinetics and dynamics by real-time characterization and on two- and three-dimensional mapping and visualization of catalyst layers, even a single nanoparticle, sensors, fuel cell electrode catalysts, batteries, biological assemblies, and so on. XAFS analysis methodology has also made progress in applications to more precise characterization of important

catalysts, nanomaterials, and surfaces, which cannot be obtained from other analysis techniques.

This book is written for not only students and academic researchers, but also for people involved in industrial research, in an effort to create synergy between academia, research institutions, and industry. This book is a comprehensive, theoretical, practical, and thorough guide to current XAFS spectroscopy and modern applications involving social needs research. Assuming only undergraduate-level physics, mathematics, and chemistry, the book is ideally suited for graduate students, young scientists, and senior scientists in any disciplines including XAFS-based research. The book also provides guidance to senior undergraduate students for their future research directions and interests.

We were happy to have excellent contributions of many world-class scientists from the USA, the UK, Germany, France, Japan, Italy, the Netherlands, Switzerland, Norway, Brazil, and Russia, reflecting the real international dimension of the book and broad interests and significance of XAFS-based researches. We are pleased to sincerely thank all of them. We thank all Springer staff for continuous encouragement, useful suggestions, and careful production throughout the XAFS book project. We believe that this book can contribute toward present and future fundamental and practical research of the related fields and will satisfy the widest range of researchers and students working in the domain or related topics.

Tokyo, Japan — Yasuhiro Iwasawa
Sapporo, Japan — Kiyotaka Asakura
Nagoya, Japan — Mizuki Tada

Contents

Part I
History and Progress of X-ray Absorption Fine Structure (XAFS)

Chapter 1
History and Progress of X-Ray Absorption Fine Structure (XAFS)

Yasuhiro Iwasawa

The history and progress of X-ray absorption fine structure (XAFS) since the discovery of X-rays (1896), the first theory of X-ray absorption near-edge structure (XANES) (1920), and the first observation and theory of extended X-ray absorption fine structure (EXAFS) (1931) are summarized in Table 1.1, showing principal achievements and landmarks for the theories, calculation methods, computer programs, methodologies and techniques, and applications to catalysts, nanoparticles, and surfaces. Developments of the XAFS approach to science and technology are associated with developments of synchrotron radiation sources and storage rings with increasing brilliance, combined with the production of soft X-rays and particularly hard X-rays, which enable high-quality researches in a variety of scientific fields such as physics, chemistry, bioscience, materials science and engineering, energy science, environmental science, geoscience, metallurgy, mineralogy, etc. Figure 1.1 illustrates the developments of XAFS analyses, measurement cells, frontier methodologies and techniques, spatially and time-resolved applications, and complex-molecular applications, exhibiting their representative examples. Now we find new XAFS paradigms of frontier sciences and technologies for catalysts, nanoparticles, and surfaces, including biomaterials, such as real-time analysis of in situ chemical states, short-lived dynamics, 2D and 3D in situ/operando imaging of real spaces, spatially resolved analysis of inhomogeneous materials, identification of diluted atoms/species, inelastic X-ray scattering analysis at the same chemical sites with different bonding and valence states, in situ analysis under extreme conditions, etc.

XAFS is an *element-specific*, *short-range*, *core-level* X-ray absorption spectroscopy (XAS) with *high sensitivity*. XAFS is divided into two regimes: XANES ($\lesssim$50 eV above around the absorption edge) and EXAFS (over several hundreds

Y. Iwasawa (✉)
Innovation Research Center for Fuel Cells, Graduate School of Informatics and Engineering, The University of Electro-Communications, Chofu, Tokyo 182-8585, Japan
e-mail: iwasawa@pc.uec.ac.jp

Y. Iwasawa et al. (eds.), *XAFS Techniques for Catalysts, Nanomaterials, and Surfaces*, DOI 10.1007/978-3-319-43866-5_1

Table 1.1 The history and progress of XAFS

Year	Theory, simulation, technique, application, etc.	Authors	Published journals
1896	Discovery of X-rays (Nov. 1895)	Röntgen	*Nature* , **53**, 274-277 (1896).
1913	Absorption edge measurement	Broglie	*Comptes Rendus* , **157**, 924-926 (1913).
1920	K-edge absorption	Fricke	*Phys. Rev.* , **16**, 202-215 (1920).
1920	First theory of XANES	Kossel	*Z. Phys.* , **1**, 119-134 (1920).
1931	XAFS for gases at different temperatures	Hanawalt	*Phys. Rev.* , **37**, 715-726 (1931).
1931	First theory of EXAFS	Kronig	*Z. Phys.* , **70**, 317-323 (1931).
1932	Curved crystal transmission spectrograph	Cauchois	*J. Phys. VIII* , **3**, 512-515 (1932).
1954	K-edge absorption	Johnston et al.	*Phys. Rev.* , **94**, 1585-1589 (1954).
1955	Amorphous/crystalline XAS	Sawada et al.	*J. Phys. Soc. Jpn.* , **10**, 464-468 (1955).
1960	K-edge absorption for solid catalysts	Van Nordstrand	*Adv. Catal.* , **12**, 149-187 (1960).
1970	XAFS point scattering theory	Sayers et al.	*Adv. X-ray Anal.* , **13**, 248-271 (1970).
1971	EXAFS Fourier analysis	Sayers et al.	*Phys. Rev. Lett.* , **27**, 1204-1208 (1971).
1972	Amorphou structure by EXAFS	Sayers et al.	*J. Non-Cryst. Solids* , **8-10**, 401-407 (1972).
1972	Total electron yield NEXAFS	Gudat et al.	*Phys. Rev. Lett.* , **29**, 169−172 (1972).
1974	EXAFS measurement at SPEAR	Lytle et al.	*Vacuum ultraviolet radiation physics* , 806-807 (1974).
1974	EXAFS theory	Stern	*Phys. Rev. B* , **10**, 3027-3037 (1974).
1974	Resonant inelastic X-ray scattering	Sparks, Jr.	*Phys. Rev. Lett.* , **33**, 262-265 (1974).
1975	Theory of EXAFS	Pendry et al.	*Phys. Rev. B* , **11**, 2795-2811 (1975).
1975	Total Reflection XRF	Wobrauschek et al.	*Anal. Chem.* , **47**, 852-855 (1975).
1975	XES of water	Nordgren et al.	*J. Phys. B* , **8**, L18-L20 (1975).
1976	Resonant X-ray Raman	Eisenberger et al.	*Phys. Rev. B* , **13**, 2377-2380 (1976).
1976	d band occupancy	Lytle	*J. Catal.* , **43**, 376-379 (1976).
1977	Auger electron yield NEXAFS	Bianconi et al.	*Solid State Commun.* , **24**, 539-542 (1977).
1978	Total electron yield EXAFS	Citrin et al.	*Phys. Rev. Lett.* , **41**, 309-312 (1978).
1978	Surface EXAFS	Stöhr et al.	*Phys. Rev. B* , **18**, 4132-4135 (1978).
1978	Surface EXAFS	Citrin et al.	*Phys. Rev. Lett* ., **41**, 309-312 (1978).
1978	EXAFS of supported Pt catalysts	Sinfelt et al.	*J. Chem. Phys.* , **68**, 2009-2010 (1978).
1979	White line peak intensity	Lytle et al.	*J. Chem. Phys.* , **70**, 4849-4855 (1979).
1980	One-electron XANES interpretation	Hodgson et al.	*J. Chem. Phys.* , **73**, 3274-3288 (1980).
1980	First-principle XANES calculation	Natoli et al.	*Phys. Rev. B* , **22**, 1104-1108 (1980).
1980	DXAFS	Matsushita et al.	*J. Appl. Cryst.* , **13**, 465-471 (1980).
1981	Reflectivity EXAFS	Martens et al.	*J. Phys. C* , **14**, 1523-1534 (1981).
1982	Molecular structure of a supported catalyst	Kuroda et al.	*Chem.Lett.* 1101-1104 (1982).
1982	Multiple scattering XAS calculation	Durham et al.	*Comput. Phys. Commun.* , **25**, 193-205 (1982).
1983	Multiple scattering NEXAFS	Natoli	*EXAFS and near edge structure* , 43-47 (1983).
1984	Multiple scattering XANES experiment	Stern et al.	*Phys. Rev. Lett.* , **52**, 1990-1993 (1984).
1985	In-situ XAFS of Mo_2/SiO_2 catalysis	Iwasawa et al.	*Z. Phys. Chem. N. F.* , **144**, 105-115 (1985).
1986	EXCURVE program	Gurman et al.	*J. Phys. C* , **19**, 1845-1861 (1986).
1986	CONTINUUM program	Natoli et al.	*Phys. Rev. A* , **34**, 4682-4694 (1986).
1986	Dispersive and total reflection XAS	Dartyge et al.	*Phys. Lett.* , **113A**, 384−388 (1986).
1987	X-ray magnetic circular dicroism	Schütz et al.	*Phys. Rev. Lett.* , **58**, 737-740 (1987).
1987	X-ray Raman scattering	Udagawa et al.	*Phys. Rev. B* **36**, 9410-9412 (1987).
1989	Time-resolved QXAFS	Frahm	*Rev. Sci. Instrum.* , **60**, 2515-2518 (1989).
1990	In-situ XAFS of Rh_2/SiO_2 catalysis	Iwasawa et al.	*J. Am. Chem. Soc.* , **112**, 3242-3244, 9096-9104 (1990).
1990	FEFF program	Rehr et al.	*Phys. Rev. B* **41**, 8139-8149 (1990).
1991	High-energy resolution fluorescence detected XANES	Hamalainen et al.	*Phys. Rev. Lett* ., **67**, 2850-2853 (1991).
1992	Polarized total reflection fluorescence EXAFS	Asakura et al.	*Catal. Lett.* , **15**, 247-254 (1992).
1992	Diffraction anomalous fine structure	Stragier et al.	*Phys. Rev. Lett.* , **21**, 3064-3067 (1992).
1993	Diffraction anomalous fine structure	Pickering et al.	*J. Am. Chem. Soc.* , **115**, 6302-6311 (1993).
1993	Laser pump X-ray probe	Thiel et al.	*Nature* , **362**, 40-43 (1993).
1995	Fluorescence μ-XANES	Sutton et al.	*Rev. Sci. Instrum.* , **66**, 1464-1467 (1995).
1995	GNXAS program	Cicco	*Physica B* , **208-209**, 125-128 (1995).
1995	FEFF program	Newville et al.	*Physica B* , **208-209**, 154-156 (1995).
1996	Molecular dynamics (MD)-EXAFS	Fulton et al.	*J. Phys. Chem.*, **100**, 13393-13398 (1996).
1995	EDA program	Kuzmin	*Physica B* , **208-209**, 175-176 (1995).
1997	FDMNES program	Joly	*J. Phys. IV* , **7**, C2-111-115 (1997).
1998	Real space multiple scattering XANES	Rehr et al.	*Phys. Rev. B* , **58**, 7565-7576 (1998).
1998	QXAFS-XRD combination	Clausen	*Catal. Today* , **39**, 293-300 (1998).
1999	Turbo-XAS	Pascarelli et al.	*J. Synchrotron Rad.* , **6**, 1044-1050 (1999).
1999	μ-XANES	Mosbah et al.	*Nucl. Instrum. Methods Phys. Res. Sect. B* , **158**, 214-220 (1999).
1999	Piezo-QEXAFS	Frahm et al.	*J. Synchrotron Rad.* , **6**, 591-593 (1999).
1999	Laser pump X-ray probe	Chen et al.	*J. Phys. Chem. B* , **103**, 3270-3274 (1999).

(continued)

Table 1.1 (continued)

2000	In-situ 1 s time-resolved DXAFS for Cu/ZSM-5 reduction	Yamaguchi et al.	*Catal. Lett.*, **68**, 139-145 (2000).
2000	In-situ 4.7 s time-resolved XAFS for Cu particle change	Böttger et al.	*Chem. Eur. J.*, **6**, 1870-1876 (2000).
2000	SPRKKR	Ebert	*Electr. Struct. & Phys. Prop. Solids*, Springer, 191-246 (2000)
2001	WIEN2k	Schwarz et al.	*Tech. Univ. Wien, Austria*, 2001. ISBN 3-9501031-1-2
2001	IFEFFIT	Newville	*J. Synchrotron Radiat.*, **8**, 322 (2001).
2001	Piezo-QEXAFS	Grunwaldt et al.	*J. Phys. Chem. B*, **105**, 5161-5168 (2001).
2001	Piezo-QEXAFS	Richwin et al.	*J. Synchrotron Rad.*, **8**, 354-356 (2001).
2002	PARATEC	Taillefumier et al.	*Phys. Rev. B*, **66**, 195107(1-8) (2002).
2002	In-situ 30 s time-resolved XANES for oxychlorination catalyst	Lamberti et al.	*Angew. Chem. Int. Ed.*, **41**, 4341-4344 (2002).
2002	15μm μ-XAFS	Fredrickson et al.	*Geochim. Cosmo. Acta*, **66**, 3247-3262 (2002).
2002	180 s time-resolved QXAFS and DXAFS	Dent	*Top. Catal.*, **18**, 2-35 (2003).
2002	μ-fluorescence/tomography	Sutton et al.	Rev. Mineral. & Geochem., **49**, 429-483 (2002).
2003	Reflectivity EXAFS	d'Acapito et al.	*X-ray and Inner-Shell Processes*, 388-394 (2003).
2003	In-situ XAFS for structural kinetics	Iwasawa	*J. Catal.*, **216**, 165-177 (2003).
2003	In-situ 100 ms time-resolved DXAFS for Rh/Al_2O_3 cluster disintegration	Iwasawa et al.	*Angew. Chem. Int. Ed.*, **42**, 4795-4799 (2003).
2003	operando XAFS	Weckhuysen	*Phys. Chem. Chem. Phys.*, **5**, 4351-4360 (2003).
2004	5 μm(KB mirror) μ-XAFS	Paktunc et al.	*Geochim. Cosmo. Acta*, **68**, 969-983 (2004).
2004	0.8 μm(Fresnel zone plate) μ-XAFS	Foriel et al.	*Geochim. Cosmo. Acta*, **68**, 1561-1569 (2004).
2005	ATHENA, ARTEMIS, HEPHAESTUS	Newville et al.	*J. Synchrotron Radiat.*, 12, 537-541 (2005).
2006	Combination of DXANES and XRF for micromapping	Muñoz et al.	*Geochem. Geophys. Geosyst.*, **7**, Q11020(1-10) (2006).
2006	Inelastic X-ray scattering	Fister et al.	*Rev. Sci. Instrum.*, **77**, 063901(1-7) (2006).
2007	In-situ time-resolved time-gating QEXAFS for fuel cells	Tada et al.	*Angew. Chem. Int. Ed.*, **46**, 4310-4315 (2007).
2007	In-situ 2 ms time-resolved DXAFS for oxygen storage/release	Iwasawa et al.	*Angew. Chem. Int. Ed.*, **46**, 9253-9256 (2007).
2007	Galvano QXAFS	Uruga et al.	*AIP Conf. Proc.*, **882**, 914-916 (2007).
2008	Scanning transmission X-ray microscopy	de Groot et al.	*Nature*, 456, 222-225 (2008).
2008	Real-time DFT-XAFS simulation	Vila et al.	*Phys. Rev. B* **78**, 121404(R) (2008).
2009	XANES tomography	Grunwaldt et al.	*Catal. Today*, **145**, 267-278 (2009).
2009	Free electron laser NEXAFS	Bernstein et al.	*Appl. Phys. Lett.*, **95**, 134102(1-3) (2009).
2010	Spatially-resolved QXAFS for CO oxidation	van Bokhoven et al.	*ChemCatChem*, **2**, 653-657 (2010).
2011	Single particle μ-XAFS for $NiO_x/Ce_2Zr_2O_{y\ y}$	Tada et al.	*Phys. Chem. Chem. Phys.*, **13**, 14910-14913 (2011).
2011	In-situ 500 ms time-resolved QXAFS for supported Pd catalyst	Reimann et al.	*J. Am. Chem. Soc.*, **133**, 3921-3930 (2011).
2011	Computed Tomographic XANES	Meirer et al.	*J. Synchrotron Rad.*, **18**, 773-781 (2011).
2011	VUV Fourier-transform spectroscopy	Oliveira et al.	*Nature Photonics*, **5**, 149-153 (2011).
2012	3D Laminography-XAFS for fuel cells	Tada et al. .	*Angew. Chem. Int. Ed.*, **51**, 10311-10314 (2012).
2012	DFT-MD-XAFS	Fulton et al.	*J. Phys. Chem. Lett.*, **3**, 2588-2593 (2012).
2013	Fast scanning microscopic XAFS	Tsuji et al.	*J. Phys.: Conf. Ser.*, **430**, 012019-1-6 (2013).
2014	Intra-nanoparticle nano-XAFS for $Pt/Ce_2Zr_2O_x$	Tada et al.	*ChemPhysChem.*, **15**, 1563-1568 (2014).
2014	Spatially/time-resolved XAFS for zeolite catalysts	Doronkin et al.	*J. Phys. Chem. C*, **118**, 10204–10212 (2014).
2014	Total reflection DXAFS	Abe et al.	*J. Phys.: Conf. Ser.*, **502**, 012035-1-4 (2014).
2014	In-situ 100 ms time-resolved QXAFS for bimetal fuel cells	Tada et al.	*J. Phys. Chem. C*, **118**, 15874-15883 (2014).
2014	2D nano-XAFS imaging for fuel cell degradation	Iwasawa et al.	*Angew. Chem. Int. Ed.* **53**, 14110-14114 (2014).
2014	Back illumination fluorescence XAFS	Asakura et al.	*Phys. Chem. Chem. Phys.*, **16**, 13748-13754 (2014).
2015	Same-view nano-XAFS/STEM-EDS for fuel cell degradation	Iwasawa et al.	*J. Phys. Chem. Lett.* **6**, 2121–2126 (2015).

Discovery and early study
Theories
Calculation methods
Computer programs
Methodologies and techniques
Applications to catalysts, nanoparticles and surfaces

eV after XANES) as shown in Fig. 1.2 (described in Chap. 2 in detail). XANES is associated with the excitation process of a core electron to bound and quasi-bound states, which is especially sensitive to oxidation state (valence) and coordination symmetry of the absorbing atom. EXAFS oscillations are approximately expressed by the sum of the sinusoidal functions of many shells on the basis of single scattering theory involving multiscattering effect by Eq. (1.1), which is usually used as a fitting function.

$$k^n\chi(k) = S_0^2 \sum_{R_i} \frac{k^n N_{R_i} F_{R_i}(k)}{kR_i^2} \sin\left(2kR_i + \Phi_{R_i}(k)\right) \exp\left(-\frac{2R_i}{\lambda_i(k)}\right) \exp\left(-2\sigma_{R_i}^2 k^2\right), \tag{1.1}$$

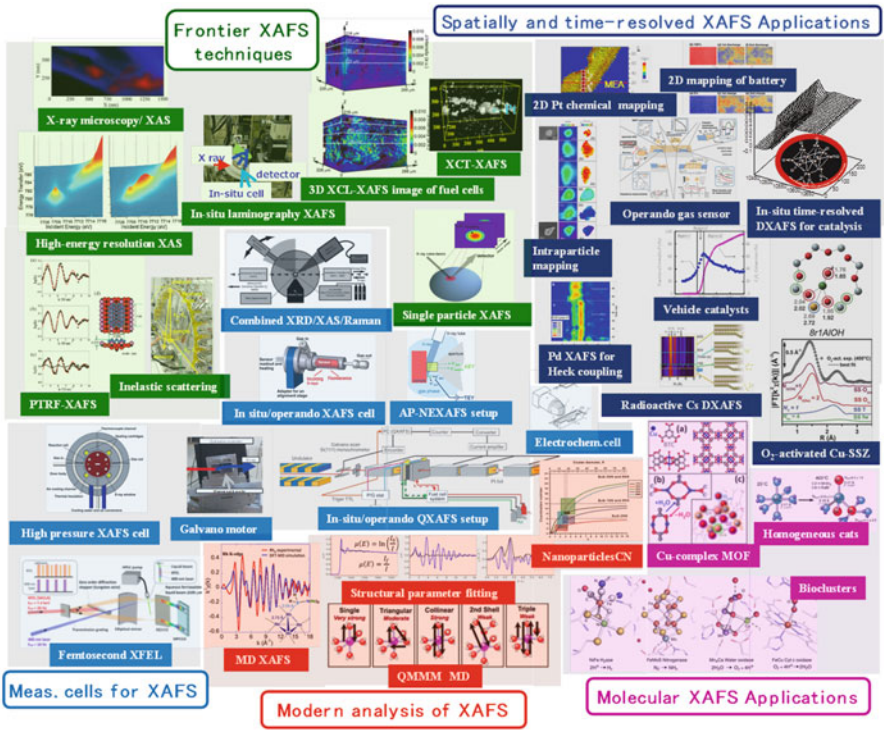

Fig. 1.1 Developments of XAFS: analyses, methods, techniques, and applications

where k, S_0^2, R_i, N, F, ϕ, λ, and σ represent photoelectron wave vector, reduction factor by multiple scattering effect, ith species at distance R, coordination number, back scattering amplitude function, phase shift function, mean free path of photoelectron, and Debye Waller factor, respectively. EXAFS can provide structural information on bond distance, coordination number, and atomic species of the neighbors of the absorbing atom. Thus, XAFS can determine the chemical state and local bonding structure for a selected atomic species. XAFS can be applied to *any sorts of functional materials* such as catalysts, sensors, biomaterials, fuel cells, secondary batteries, electronic devices, optical and magnetic devices, thin films, nano-medicines, etc. without requirement of long-range ordering in structures, *in any atmospheres* such as gas phases, liquids, solids, vacuum, reaction conditions, etc., at low-high temperatures, *for any mixtures and composites*. XAFS has great advantages in deciding molecular-level structures and electronic states of a variety of materials not only in a static state but also in a dynamic state (in situ/operando conditions), which are not possible by other techniques due to their theoretical and experimental analysis limitations.

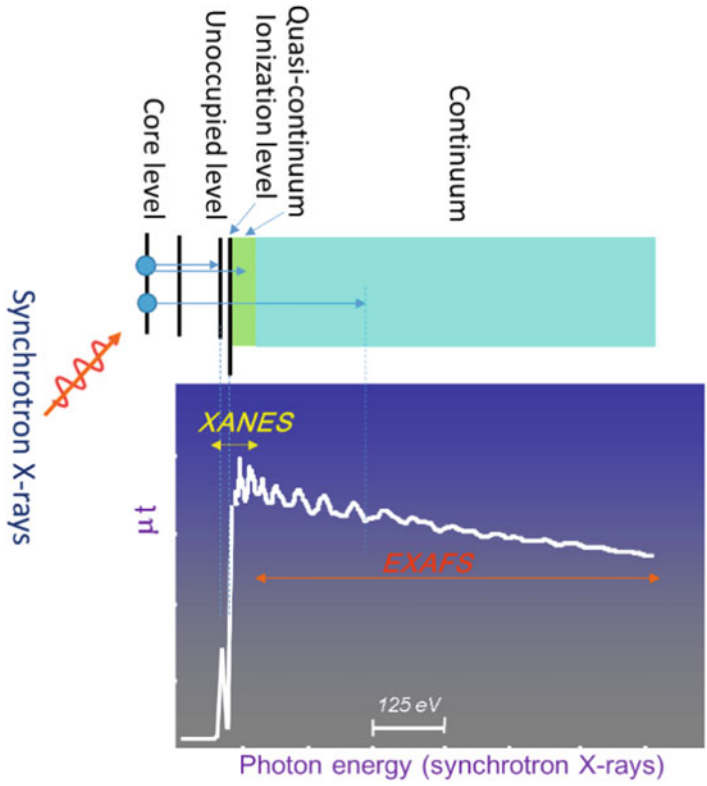

Fig. 1.2 The spectra and origin of XANES and EXAFS

With these advantages as base, the weak points of XAFS are also noted as follows. The XAFS information is one dimensional one averaged over all absorbing atoms with different local structures and environments involved in a sample. The XAFS curve-fitting analysis is not precise in contrast to XRD analysis; e.g., error ranges of bond distance and coordination number are at least ± 0.001 nm and $\pm 10\,\%$, respectively, for most samples of catalysts, nanoparticles, and surfaces. Although the XAFS curve-fitting results involve those error ranges, the XAFS techniques can provide significant structural parameters and electronic states for catalysts, nanoparticles, and surfaces in static and dynamic states, to which other modern physical techniques cannot be applied. Thus, the XAFS techniques have the unique and large advantages enough for scientific discussion on the physical and chemical properties of functional samples, but the XAFS analysis results may be further exactly discussed with the aid of other complementary experiments and theoretical calculations.

XAFS has had a great impact on catalyst research, identifying short-range structures and electronic states of many catalytic systems with nanocrystalline,

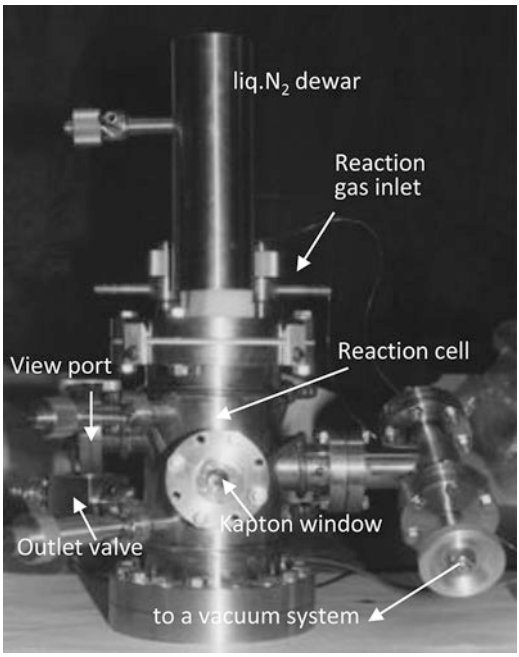

Fig. 1.3 An in-situ XAFS cell for XAFS measurements during catalyst fabrication and catalytic reaction processes

noncrystalline, or disordered phases [1–3]. The essence of catalytic functions and understanding of catalysis may be well characterized by advanced XAFS techniques, which have not been adequately addressed so much [4–6]. Pioneering XAFS works on supported metal catalysts were conducted by Lytle and his coworkers in 1970 years [7–10]. Typically, supported metal particles have usually particle sizes in the range of 1–2 nm diameter without long-range order and hence their structures cannot be targets with XRD. van't Blik et al. studied Rh clusters on Al_2O_3 by EXAFS before and after CO adsorption [11]. They found that the Rh clusters with a Rh-Rh distance of 0.265 nm were disrupted to monomeric Rh atoms bonded to the surface through oxygen after CO adsorption. Sato et al. reported the first molecular structure of a supported catalyst with Mo dimer, determining both metal-metal bonding and metal-light element bonding at the surface [12]. In 1985, Iwasawa et al. reported the first example of in situ characterization of a SiO_2-supported Mo dimer catalyst during the course of selective oxidation of ethanol to acetaldehyde with O_2 using an in situ XAFS cell as shown in Fig. 1.3 [13]. In the in situ XAFS observations the catalyst was treated under the ethanol reaction conditions and quenched by rapid cooling for the observation of key intermediate structures relevant to the catalytic reaction kinetics (see Chap. 21). XAFS has now become routinely used to elucidate the local structures and oxidation states of catalytic materials. XAFS techniques have developed and become essential tools in investigating chemical and physical states of practically real samples with higher

complexity. For example, the electrocatalysis of polymer electrolyte fuel cells (PEFC) for automobiles proceeds at surface layers of small Pt nanoparticles on carbon support in a wet multiphase reaction field under potential-operating PEFC conditions. Recently, the practically real PEFC catalysts were directly measured and visualized by in situ time-resolved XAFS and spatially resolved nano-XAFS imaging techniques to understand and improve the PEFC performance and degradation, whereas they cannot be characterized by other analysis methods, such as XRD, TEM/SEM, SPM, XPS, FT-IR, Raman, ultrafast laser spectroscopies, etc. [14–17].

Finally, science and technology is the wisdom and spirit obtained by humanity through the long history of evolution and is the biggest contributor to the optimization of society. Through the diligent construction of modern science and technology we can build a sustainable society. We have great expectations for advanced XAFS and related techniques for catalysts, nanomaterials, and surfaces in our life and future. The following chapters treat with fundamentals, recent applications, and future prospects of XAFS.

Acknowledgement I thank Dr. Oki Sekizawa at the University of Electro-Communications for his help in listing representative achievements on XAFS research.

References

1. Iwasawa Y (ed) (1996) X-ray absorption fine structure for catalysts and surfaces. World Scientific, Singapore
2. Koningsberger DC, Prins R (1988) X-ray absorption: principles, applications, techniques of EXAFS, SEXAFS and XANES. Wiley, New York
3. Iwasawa Y (1987) Chemical design surfaces for active solid catalysts. Adv Catal 35:187–264
4. Tada M, Zhang S, Malwadkar S, Ishiguro N, Soga J, Nagai Y, Tezuka K, Imoto H, Otsuka-Yao-Matsuo S, Ohkoshi S, Iwasawa Y (2012) The active phase of nickel/ordered $Ce_2Zr_2O_x$ catalysts with a discontinuity ($x = 7–8$) in methane steam reforming. Angew Chem Int Ed 51:9361–9365
5. Tada M, Uruga T, Iwasawa Y (2015) Key factors affecting the performance and durability of cathode electrocatalysts in polymer electrolyte fuel cells characterized by in-situ real time and spatially resolved XAFS techniques. Catal Lett (Silver Anniversary Special Issue) 145:58–70
6. Takao S, Sekizawa O, Samjeské G, Nagamatsu S, Kaneko T, Yamamoto T, Higashi K, Nagasawa K, Uruga T, Iwasawa Y (2015) Same-view nano-XAFS/STEM-EDS imagings of Pt chemical species in Pt/C cathode catalyst layers of a polymer electrolyte fuel cell. J Phys Chem Lett 6:2121–2126
7. Eisenberg P, Kincaid B, Hunter S, Sayers DE, Stern EA, Lytle FW (1974) EXAFS measurements at SPEAR. In: Proc. 4th int. conf. vacuum ultraviolet rad. phys. Pergamon, Oxford, p 806–807
8. Lytle FW (1976) Determination of d-band occupancy in pure metals and supported catalysts by measurement of the L_{III} X-ray absorption threshold. J Catal 43:376–379
9. Sinfelt JH, Via GH, Lytle FW (1978) Extended X-ray absorption fine structure (EXAFS) of supported platinum catalysts. J Chem Phys 68:2009

10. Lytle FW, Wei PSP, Greegor RB, Via GH, Sinfelt JH (1979) Effect of chemical environment on magnitude of x-ray absorption resonance at L_{III} edges. Studies on metallic elements, compounds, and catalysts. J Chem Phys 70:4849
11. van't Blik HFJ, van Zon JBAD, Huizinga T, Vis JC, Koningsberger DC, Prins R (1983) An extended X-ray absorption fine structure spectroscopy study of a highly dispersed. Rh/Al_2O_3 catalyst: the influence of CO chemisorption on the topology of rhodium. J Phys Chem 87:2264–2267
12. Sato Y, Iwasawa Y, Kuroda H (1982) EXAFS study of highly active Mo_2 catalyst. Chem Lett 7:1101–1104
13. Iwasawa Y, Asakura K, Ishii H, Kuroda H (1985) Dynamic behavior of active sites of a SiO_2-attached Mo(VI)-dimer catalyst during ethanol oxidation observed by means of EXAFS. Z Phys Chem N F 144:105–115
14. Tada M, Murata S, Asaoka T, Hiroshima K, Okumura K, Tanida H, Uruga T, Nakanishi H, Matsumoto S, Inada Y, Nomura M, Iwasawa Y (2007) In situ time-resolved dynamic surface events on the Pt/C cathode in a fuel cell under operando conditions. Angew Chem Int Ed 46:4310–4315
15. Saida T, Sekizawa O, Ishiguro N, Uesugi K, Hoshina M, Uruga T, Ohkoshi S, Yokoyama T, Tada M (2012) 4D visualization of a cathode catalyst layer in a polymer electrolyte fuel cell by 3D laminography–XAFS. Angew Chem Int Ed 51:10311–10314
16. Tada M et al (2014) Rate enhancements in structural transformations of Pt-Co and Pt-Ni bimetallic cathode catalysts in polymer electrolyte fuel cells studied by in situ time-resolved X-ray absorption fine structure. J Phys Chem C 118:15874–15883
17. Takao S, Iwasawa Y et al (2014) Mapping platinum species in polymer electrolyte fuel cells by spatially resolved XAFS techniques. Angew Chem Int Ed 53:14110–14114

Part II
Theory and Analysis of XAFS

Chapter 2
Theory and Analysis of XAFS

John J. Rehr, Joshua J. Kas, Fernando D. Vila, and Matthew Newville

2.1 Theory of EXAFS

2.1.1 Introduction

Owing to its element specific and short-range nature, core-level X-ray absorption spectroscopy (XAS) is now routinely used to elucidate the local structural, vibrational, and other physical properties of complex, aperiodic materials. XAS encompasses both extended X-ray absorption fine structure (EXAFS) and X-ray absorption near edge spectra (XANES) [1, 2], where the terms refer, respectively, to the structure in the X-ray absorption spectrum $\mu(\omega)$ at high and low energies relative to the absorption edge with the crossover typically at about 20–30 eV above the edge. The acronym XAFS refers to the fine structure at all energies. The extraordinary capabilities of these spectroscopies come at a price: they depend on comparisons with quantitative simulations of the spectra. Remarkably, however, theories of X-ray spectra have become increasingly accurate and sophisticated, generally overcoming this limitation [2–5].

J.J. Rehr (✉) • J.J. Kas • F.D. Vila
Department of Physics, University of Washington, Seatle, WA, USA
e-mail: jjr@u.washington.edu

M. Newville
University of Chicago, Consortium of Advanced Radiation Sciences, Advanced Photon Source, GSECARS, Argonne, IL, USA
e-mail: newville@cars.uchicago.edu

Y. Iwasawa et al. (eds.), *XAFS Techniques for Catalysts, Nanomaterials, and Surfaces*, DOI 10.1007/978-3-319-43866-5_2

Formally, the theory of XAS is based on Fermi's golden rule

$$\mu(\omega) \sim \sum_F |\langle 0|D|F\rangle|^2 \delta(\omega + E_0 - E_F), \tag{2.1}$$

which requires a summation over exact many-body final states $|F\rangle$, with energies E_F. However, practical calculations depend on the reduction of this relation to an effective, independent particle theory that takes into account several important many-body effects. The theoretical advances in recent years are the result of an improved understanding of these effects and accurate new approximations, in particular for inelastic losses and vibrational damping [6]. These developments rely on physics beyond the usual independent-particle approaches of quantum chemistry and condensed matter such as Hartree–Fock or density functional theory (DFT). Moreover, they involve different limits and time-scales, requiring a variety of approximations and computational methods like Green's function and Lanczos techniques. Besides XAS, these advances are applicable to a number of core-spectroscopies involving electronic excitations, including non-resonant inelastic X-ray scattering (NRIXS, also called X-ray Raman scattering or XRS) [7], and electron energy-loss spectroscopy (EELS) [8–11]. In this chapter we review these advances, focusing on the ideas behind the key approximations needed for a quantitative theory of EXAFS (Sect. 2.1) and XANES (Sect. 2.2). Section 2.3 contains a review of modern XAFS analysis methods, and Sect. 2.4 a number of illustrative structural modeling applications.

2.1.2 The EXAFS Equation

One of the key developments in the history of EXAFS was the famous equation of Sayers, Stern, and Lytle, which represents the normalized fine structure $\chi(\omega) = [\mu(\omega) - \mu_0]/\mu_0$ in XAS in terms of oscillatory contributions from near-neighbor atoms. Here μ_0 is the jump in the XAS at the edge. Although their model was heuristic, it included two key many-body effects, namely the mean free path of the photoelectron and vibrational damping [12]. This key observation demonstrates both the failure of any independent particle interpretation and the need to include both electronic and vibrational effects in quantitative theories. It also shows that XAS is a short-range order phenomenon, and cannot be described using conventional band-structure methods. Remarkably, an exact treatment based on the multiple-scattering (MS) path expansion can be cast in a similar form [1], namely

$$\chi(k) = S_0^2 \sum_R \frac{|f_{\text{eff}}(k)|}{kR^2} \sin(2kR + \Phi_k) e^{-2R/\lambda_k} e^{-2\sigma_R^2 k^2}, \tag{2.2}$$

except that all quantities are redefined to include curved-wave and many-body effects implicitly. In particular f_{eff} is the effective curved wave scattering amplitude

for a given photoelectron wave number k defined relative to the absorption threshold (or Fermi level μ) for X-ray absorption, i.e., with $k^2 = 2(E - \mu)$, λ_k the inelastic mean free path, and σ_R^2 the mean square relative vibrational amplitude of path R. The sum is over all multiple scattering paths, R being the half-path length, S_0^2 the many-body reduction factor which is typically about 0.8 as discussed below, and Φ_k a smoothly varying phase shift. Remarkably, the expansion generally converges rapidly away from the edge, with only of order 10^2 multiple-scattering paths in the EXAFS. This simplification is a consequence of the smallness of λ_k which is generally of order 5–20 Å. This representation also explains why the dominant peaks in the EXAFS Fourier transform $\chi(R) = \mathrm{FT}[\chi(k)]$ are close to the geometrical near-neighbor distances in a material, but shifted by system dependent phase shifts, $\delta R \approx \frac{1}{2} d\Phi_k/dk$. Moreover this MS path representation permits an analysis of experimental XAFS signals in terms of geometrical and vibrational properties of a material, provided one has a reasonable approximation of the phase shifts and λ_k.

2.1.3 Many-Body XAS Formula

Perhaps the easiest way to incorporate many-body effects is to follow the two-step approach derived by Campbell et al. [13]. The first step is the production of the photoelectron, by photoexcitation from a particular core-state, given by an effective one-body (i.e., quasi-particle) absorption $\mu^{(1)}(\omega)$. Second is the effect of inelastic losses and secondary excitations, e.g., plasmons and electron–hole pairs, that can be represented by an energy-dependent "spectral function" $A(\omega, \omega')$, which subsequently broadens and shifts the spectrum. This yields an exact representation of the many-body XAS in terms of a convolution

$$\mu(\omega) = \int d\omega' A(\omega, \omega')\, \mu^{(1)}(\omega - \omega'). \tag{2.3}$$

The shape of the spectral function $A(\omega, \omega')$ typically consists of a sharp "quasi-particle" peak of width related to the inverse mean free path, together with a broad satellite. Consequently the EXAFS problem can be factored into two parts: an effective quasi-particle XAS $\mu^{(1)}(\omega)$ and a part that accounts for inelastic losses. The quasi-particle XAS can be calculated using an independent-particle Fermi's golden rule, with the ΔSCF approximation, i.e., with the final single-particle states $|f\rangle$ calculated with the final state Hamiltonian in the presence of the core-hole

$$\mu^{(1)}(\omega) \sim \sum\nolimits_f |\langle i|d\, P|f\rangle|^2 \delta(\omega + E_i - E_f), \tag{2.4}$$

where $d = \vec{\epsilon} \cdot \vec{r}$ is the dipole operator and P the projection operator onto unoccupied states. Although this is a considerable simplification to Eq. (2.1), the

calculation and summation over final states in the golden rule is a serious computational bottleneck at high energies: the sum can only be carried out efficiently for highly symmetric systems such as atoms, small molecules, or periodic solids. On the other hand, many systems of interest lack symmetry. Reciprocal space (i.e., band structure) methods [14, 15] often ignore the effects of the core-hole and lattice vibrations, which spoil crystal translation symmetry, although the former can be treated approximately with super-cell approximation. Instead, different methods are needed. Remarkably, it is preferable computationally to re-express the XAS in terms of the photoelectron Green's function or propagator G in real space rather than explicitly calculating the final states. This formulation implicitly sums over all final states as can be seen by using the spectral representation of G for which $-\frac{1}{\pi}\mathrm{Im}\,G = \sum_f |f\rangle\,\delta(E-E_f)\,\langle f|$, so that the golden rule can be rewritten exactly as a single matrix element

$$\mu^{(1)}(\omega) = -\frac{1}{\pi}\ \mathrm{Im}\ \langle c|d\ G(r,r',E)\ d'|c\rangle. \tag{2.5}$$

This approach turns out to be advantageous for XAS calculations even in perfect crystals, since inelastic losses (i.e., the mean free path) limit the range probed by XAS experiment to clusters typically of order a few hundred atoms about a given absorption site.

2.1.4 Real-Space Multiple-Scattering Theory

We now briefly summarize the real-space multiple scattering (RSMS) theory used for practical calculations of EXAFS. The starting point of the theory is the separation of the potential into contributions from "scattering potentials" v_R localized on each atomic site R,

$$v_R(r) = v'_{\mathrm{coul}} + \Sigma(E) = \sum\nolimits_R v_R(r-R). \tag{2.6}$$

Here v'_{coul} is the Hartree potential calculated for the final state in the presence of a core hole, and $\Sigma(E)$ is the energy-dependent self-energy. With this separation and the approximation of local spherical symmetry at each site, the propagator is also separable

$$G(r,r',E) = \sum\nolimits_{L,L'} R_L(r) G_{LR,L'R'}\, R_{L'}(r'), \tag{2.7}$$

so that the expression for the XAS can be reduced to a calculation of atomic-like dipole-matrix elements $M_L = \langle c|\epsilon\cdot r|LR\rangle$ and matrix elements of $G(r,r',E)$.

$$\mu(E) = -4\pi e^2 \frac{\omega}{c} \sum_{LL'} M_L(E) G_{LL'} M_{L'}(E), \tag{2.8}$$

where $L = (l, m)$ denotes the angular momentum variables at each site R. Here and elsewhere we interchangeably use either the photoelectron energy E or the photon frequency ω to characterize the photoelectron energy. Interestingly, the relativistic generalization, which is needed for heavy atoms like Pt [16], is identical in form but with relativistic angular momentum variables (k, m). Relativistic corrections are essential for the treatment of spin-orbit effects, which are biggest in the atomic cores and hence crucially important for the transition matrix elements in heavy atoms. However, relativity has only weak effects on scattering of non-relativistic electrons in EXAFS. In FEFF, relativistic effects and spin-orbit corrections are treated to high accuracy using a relativistic Dirac–Fock prescription [17]. In addition the calculation of the scattering potentials at each site simplifies for electrons even of moderate energy (i.e., above about 10 eV of kinetic energy), where the scattering depends strongly on the density in the core of an atom, and hence spherical symmetry is an excellent approximation. Thus, self-consistency is not usually important in calculations of scattering in EXAFS. It is needed, however, to obtain an accurate estimate of the threshold (or Fermi energy E_F) and fractional occupations of the various valence states.

In RSMS, the propagator $G_{LL'}(E)$ naturally separates into intra-atomic contributions from the central atom G_c and multiple scattering contributions from the environment G^{sc}, so that $G = G_c + G^{sc}$. Consequently, the XAS μ naturally factors as

$$\mu(\omega) = \mu_0(\omega)[1 + \chi(\omega)], \tag{2.9}$$

where χ is the X-ray absorption fine structure (XAFS). Thus the net structure in the XAS μ depends both on the atomic background $\mu_0(\omega)$ and on the fine structure χ due to MS: $\chi = \mathrm{Im}\,\mathrm{Tr}_m G^{sc}_{LL'}$. Since $\mu_0(\omega)$ varies weakly with energy, these results are consistent with the experimental definition of the normalized XAFS $\chi = (\mu - \mu_0)/\Delta\mu_0$, where $\Delta\mu_0$ is the jump in the atomic background absorption at threshold. Formally, the matrix $G_{LL'}(E)$ can also be expressed as a sum over all MS paths that a photoelectron can take away from the absorbing atom and back [2], and thus gives rise to the multiple-scattering *path expansion*

$$G^{sc} = e^{i\delta'} \left[G^0 T G^0 + G^0 T G^0 T G^0 + \cdots \right] e^{i\delta}, \tag{2.10}$$

where the successive terms represent single, double, ... scattering processes and δ and δ' are partial-wave phase shifts. As noted above, this expansion converges rapidly for EXAFS with of order 10^2 paths. Remarkably, the sum sometimes converges adequately in XANES, particularly in cases with a short core-hole lifetime as in deep core levels in heavy elements. However, the path expansion is not always reliable near the edge, as discussed in Sect. 2.2. Due to the large dimension of $G_{LR,L'R'}(E)$, exact calculations with the path expansion can only be

carried out for very few low-order MS paths [18]. To overcome this computational bottleneck, an efficient approximation was devised based on the Rehr-Albers (RA) scattering matrix formalism [19]. The RA approach yields curved-wave calculations of the effective scattering amplitude $f_{\rm eff}$ (from which the FEFF code takes its name) in terms of a separable representation of the free propagator $G^0(E)$. With this representation the MS expansion can be re-expressed as a sum over MS paths R in a form essentially the same as the original EXAFS equation of Sayers, Stern, and Lytle [12], but with renormalized ingredients in all terms.

2.1.5 Mean Free Path

Two of the crucial differences between ground state electronic structure and excited states in core-level spectra are (1) the need for an energy dependent self-energy $\Sigma(E)$ instead of an exchange-correlation functional like DFT, and (2) the need for a screened core-hole. The self-energy is essentially a dynamically screened Hartree–Fock exchange interaction, and is the analog of the exchange-correlation potential $V_{\rm xc}$ of DFT. The real part of the self-energy varies by about 10 eV over XAS energies, slowly turning off in the classical limit, while the imaginary part is negative and varies by about 5 eV. The imaginary part accounts for (extrinsic) inelastic losses or final-state broadening, and can be expressed in terms of a mean free path and a core-hole lifetime Γ,

$$\lambda = k/[|\mathrm{Im}\,\Sigma| + \Gamma]. \tag{2.11}$$

The real part of $\Sigma(E)$ accounts for systematic shifts in peak positions compared to those calculated with DFT, leading to a stretching of the energy scale at low energies of about 10 %. One of the key developments in practical XAS codes is an efficient algorithm for calculations of $\Sigma(E)$ based on the GW approximation of Hedin [20]. For example, FEFF and several other XAS codes by default typically use a local density approximation for $\Sigma(E)$ based on the plasmon-pole dielectric constant. This approximation works well for EXAFS, and reduces to the ground state exchange-correlation potential near threshold. However, the plasmon-pole self-energy tends to overestimate losses in the XANES. This deficiency can be overcome by using a many-pole model, as discussed by Kas et al. [21] (see also Sect. 2.2).

2.1.6 Many-Body Amplitude Reduction Factor S_0^2

The effect of the convolution in the exact expression for the XAS in Eq. (2.3) is to average the one-electron XAS over the spectral function, so

$$\mu = \langle \mu_0 \rangle \left[1 + \sum\nolimits_R \langle \chi_R \rangle \right]. \tag{2.12}$$

Since the atomic absorption μ_0 is smoothly varying, the average $\langle \mu_0 \rangle \approx \mu_0$ has little effect. Here $\chi_R \sim \mathrm{Im}\left[\exp(2ikr)\right]$ is the XAFS contribution for a given path. Then, averaging χ_R over the quasi-particle peak gives rise to a damping factor $\exp\left(-2R/\lambda_k\right)$ from the mean free path, while the broad structure in the spectral function gives an additional factor denoted by S_0^2, which turns out to be only weakly dependent on R. Physically the mean free path term is dominated by the extrinsic losses, while S_0^2 is dominated by intrinsic losses. A more detailed analysis shows that this factorization is most appropriate at high energies in the EXAFS regime. Near the edge, one expects interference terms to suppress these effects and hence the energy dependence of these contributions to be important.

2.1.7 Thermal Vibrations and XAFS Debye–Waller Factors

The effects of thermal and structural disorder lead to strong exponential damping of the fine structure, and thus are of crucial importance in XAFS. This damping is dominated by an *XAFS Debye–Waller factor* $\exp\left(-2\sigma^2 k^2\right)$, where σ^2 is the mean square relative displacement (MSRD) of the near-neighbor bonds, and typically varies inversely with the local bond strength. Higher moments of the pair distribution function are sometimes important, especially in temperature dependent investigations of XAS. One of the key theoretical developments in the theory of vibrational damping in XAFS is the cumulant expansion, which yields an efficient parameterization of such thermal and configurational disorder [22, 23] in terms of a few moments or *cumulants* $\sigma^{(n)}$ of the pair distribution function. Formally this expansion yields a complex Debye–Waller factor $\exp\left[\sum_n (2ik)^n \sigma^{(n)}/n!\right]$ in G^{sc}, which contributes both to the amplitude and phase of the XAFS.

The thermal contributions to σ^2 often can be fit to a correlated Debye model [24]. The corrections to the dominant second cumulant depend on anharmonicity. The first cumulant $\sigma^{(1)}$ is the net thermal expansion, while the third $\sigma^{(3)}$ characterizes the asymmetry or skew of the pair distribution function. These odd order contributions can strongly affect the phase of the fine structure, especially at high energy, giving a contribution $2k\sigma^{(1)} - 4k^3\sigma^{(3)}/3 + \cdots$. Relations between the cumulants have been derived [25] which show, to leading order in the anharmonicity parameter, that $\sigma^{(1)} \propto \sigma^2(T)$ and $\sigma^{(3)}$ is related to $\sigma^2(T)$. The third cumulant is important in bond distance determinations and in interpretations of thermal expansion. If the third cumulant is neglected in the analysis, bond distances obtained from EXAFS typically appear unphysically short. Improved treatments of XAFS Debye–Waller factors have recently been developed which go beyond the correlated Debye approximation. They are described in more detail in Sect. 2.4.

2.2 Theory of XANES

2.2.1 Basic Interpretation of XANES

As discussed in the previous section, the formal theories of XANES and EXAFS are essentially the same, and are both given by Fermi's golden rule, i.e., $\mu(\omega) \sim \sum_F |\langle 0|D|F\rangle|^2 \delta(\omega + E_0 - E_F)$, where $|0\rangle$ and $|F\rangle$ are many-body initial and final electronic states. When an effective single-particle description of the spectrum is reasonable, this leads to

$$\mu(\omega) \sim \sum_f |\langle i|d|f\rangle|^2 \delta\big(\omega + \varepsilon_i - \varepsilon_f\big), \tag{2.13}$$

where $|i\rangle$ denotes the core orbital in question, $|f\rangle$ are unoccupied single-particle states, and $d = \vec{\epsilon} \cdot \vec{r}$ is the dipole operator. The basic interpretation of this equation is that the core-level electron is kicked out of the core-level by the photon (dipole transition operator) and into an unoccupied excited state of energy $\varepsilon_f = \varepsilon_c + \omega$, as required by energy conservation. The deep core electrons are very nearly angular momentum eigenstates, e.g., the K-edge is a transition from a 1s orbital. This fact, coupled with the dipole selection rule $l \to l \pm 1$, provides an interpretation of the spectrum in terms of the angular momentum projected density of states (LDOS) and smoothly varying transition matrix elements. For example, transitions from a 1s core-level are related to the p-DOS of the system, while transitions from a 2p core-level are related to the s-DOS and the d-DOS. In many cases the latter dominates and the spectrum can be interpreted in terms of the d-DOS alone. Although the dipole approximation is usually very good, there are some systems for which the pre-edge peaks are due to quadrupole transitions. In this case the selection rules are $\Delta l = 0, \pm 2$, e.g., transitions from the 1s state are related to the s- and d-DOS.

2.2.2 Differences Between XANES and EXAFS

Several of the approximations appropriate for the EXAFS regime (beyond about ~20—30 eV above the edge) are not valid in the near edge regime, with some of these related to the reduction of the many-body formulation to an effective single-particle description, as in Eq. (2.13). For example, in highly correlated systems such as transition metal oxides and f-electron systems, many-body effects can change the qualitative behavior of the near edge spectrum [26], while the main effect on the EXAFS region is simply an overall reduction in the amplitude of the fine structure, which is taken into account by the S_0^2 factor in the EXAFS equation, Eq. (2.2). Even in simpler systems, the approximations made to construct an effective single-particle Hamiltonian, i.e., quasiparticle self-energy models such as the plasmon

pole model, are most appropriate in the EXAFS regime. When calculating XANES they must be augmented, e.g., with the many-pole self-energy model [21]. Another approximation has to do with the description of vibrational and structural distortions. In particular, vibrational effects damp the EXAFS via the Debye–Waller factor $\exp(-2k^2\sigma^2)$. In the XANES, the effects of vibrations and disorder are sometimes more related to symmetry breaking, which allows transitions to states that were previously dipole forbidden, resulting in additional peaks in the near edge spectrum.

EXAFS is also less sensitive to the non-spherical details of the potentials, and a simple overlapped atomic muffin tin potential is adequate for most practical calculations. On the other hand, near-edge spectra can be quite sensitive to details of charge transfer and changes in Fermi level due to solid state effects. Thus the use of self-consistent potentials and often non-spherical symmetry are essential for accurate calculations of XANES. Finally, calculations of the single particle Fermi golden rule must be treated differently in the near edge region because the path expansion detailed in Eq. (2.10) often fails to converge (or converges very slowly) for low energy photoelectrons. This slow convergence is caused by two factors. First, the inelastic mean free path becomes large for low energy electrons so that very long paths must be included in the expansion. Second, large angle scattering amplitudes are not small at low energies, so that the XANES signal is not dominated by nearly linear scattering paths, and all multiple scattering paths must be taken into account.

2.2.3 *Full Multiple Scattering*

Although the path expansion method of calculation is not appropriate for the XANES, one can instead sum the expansion to all orders for any finite cluster of atoms via matrix inversion, so that instead of Eq. (2.10) we have

$$G = \left[1 - G^0 T\right]^{-1} G^0. \tag{2.14}$$

The matrices in this equation are represented in a site and angular momentum basis $|L, R\rangle$, so the rank of the matrix to be inverted is $N(l+1)^2$, where N is the number of atoms in the cluster, and l is the maximum angular momentum of an expansion in spherical harmonics. Matrix inversion can be expensive computationally for large matrices, since the time to invert scales like the cube of the rank of the matrix. Therefore, practical calculations must limit the cluster size and truncate the sum over angular momentum states. The cluster size cannot be too large, typically ~1000 atoms or less for most computations. Fortunately, one does not usually need such large clusters for XANES calculations since the finite core-hole lifetime keeps the inelastic mean free path from becoming too large. In addition, reasonable accuracy requires that $l_{\max}$ is of order $k_{\max}R_{\mathrm{mt}} + l_{\mathrm{occ}}$, where l_{occ} is the largest

angular momentum of the occupied states and $k^2_{\max} \sim E_{\max}$ in Rydberg units. Thus, in the XANES region one can safely set the maximum angular momentum to 4 at most, while at higher energies in the EXAFS matrix inversion becomes impractical. In the intermediate energy regime, Lanczos techniques can be used. In addition, the Green's function $G(E)$ is parameterized by the energy of the photoelectron, thus one inversion must be performed for each energy point in the spectrum. This makes the calculations parallelize naturally and can be done very efficiently on parallel computers [27].

2.2.4 Self-Consistent Potentials

The Green's function can also be used to calculate the total electron density, i.e.,

$$\rho(\vec{r}) = -\frac{1}{\pi}\int_{-\infty}^{\mu} \mathrm{Im}[G(\vec{r},\vec{r},E)]dE. \tag{2.15}$$

Thus the Green's function naturally replaces all the orbitals used in standard density functional theory codes, and the Kohn–Sham Hamiltonian can be solved self-consistently using the Green's function [1]. In the real-space multiple scattering code FEFF, this works as follows:

1. Atomic Dirac–Fock eigenfunctions and densities are calculated for each type of atom, and an overlapped atom approximation to the density is used as the initial guess in the self-consistency loop.
2. The density and exchange correlation functional is used to create a Kohn–Sham (LDA) potential.
3. The spherical muffin-tin approximation is applied.
4. The Green's function is calculated at each energy using a scattering state basis.
5. A new chemical potential μ is found by requiring that the total number of electrons N_e, is conserved, i.e., $N_e = -\frac{1}{\pi}\int_{-\infty}^{\mu}\int d^3r \mathrm{Im}[G(\vec{r},\vec{r},E)]dE$.
6. New densities are calculated from the new Green's function and chemical potential.
7. Steps 2–6 are repeated until the output density is sufficiently close to the input density.

Figure 2.1 shows the structure of the FEFF program, along with details of the self-consistency algorithm. Several other approximations made in FEFF are worth mentioning. First, FEFF allows the user to treat several atoms as identical, even if they are physically different, i.e., two oxygen atoms in different local environments can be constrained to have the same potentials. Second, the integral over space

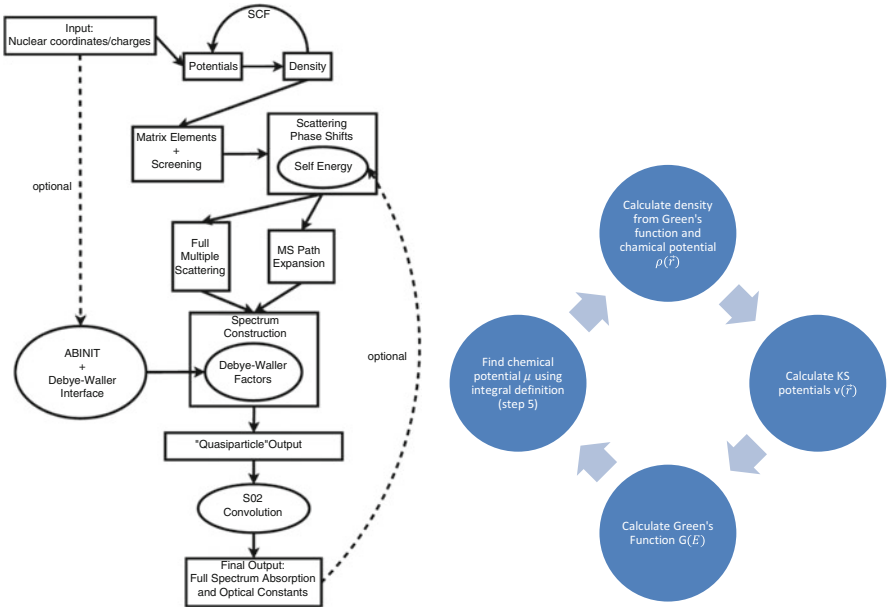

Fig. 2.1 Diagram showing the overall structure of calculations using the FEFF program (*left*) and an expanded view of the SCF procedure (*right*) detailed in the text

shown in step 5 above is approximated by a sum of integrals about each atom. Each of these integrals spans the volume of a sphere (the Norman sphere) defined such that the total overlapped atomic charge (including the nucleus) is zero.

Self-consistency of the densities and potentials can be very important for XANES calculations. For example, if an initial guess of the Fermi energy is too high, pre-edge peaks are missing. Self-consistency and the shift in the Fermi energy due to solid state effects also play a role in chemical shifts, and are very important in systems with multiple, physically unique absorbing sites, such as nanoparticles on a support.

2.2.5 Many-Body Effects: Quasiparticle Self-Energy Models

Many-body effects also play a large role in the XANES, and are responsible for energy dependent shifts and broadenings associated with the quasiparticle self-energy, as well as satellite peaks brought about by multi-electron excitations. While simple models such as the plasmon pole self-energy [28, 29] have been quite successful for calculations of EXAFS, more accurate models must be used near the edge. Most current calculations of these effects are based on the *GW* approximation of Hedin [30], i.e.,

$$\Sigma(E) = i\int \frac{d\omega}{2\pi}\, G(E-\omega)W(\omega)e^{-i\eta\omega}, \tag{2.16}$$

where G is the electron Green's function and $W = \epsilon^{-1}v$, is the screened Coulomb interaction. In the interest of retaining the efficiency of the plasmon pole model, we have developed a many-pole model self-energy which uses multiple poles to represent the loss function $L(\vec{q},\omega) = -\mathrm{Im}[\epsilon^{-1}(\vec{q},\omega)]$ [21], i.e.,

$$L(\vec{q},\omega) = \frac{\pi}{2}\sum_i g_i\omega_j\delta(\omega-\omega_i(\vec{q})). \tag{2.17}$$

The dispersion of the excitations is approximated by a polynomial $\omega_i(\vec{q})^2 = \omega_i^2 + v_F^2q^2 + \frac{q^4}{4}$ which retains the high momentum transfer limit [29]. The amplitudes g_i are fixed by matching to the loss function in the zero momentum transfer limit ($q \to 0$), giving $g_i = -[2\Delta\omega/\,\pi\omega_i]L(0,\omega_i)$. In this way the model is consistent with the inverse and first moments of the spectrum for any number of poles, and thus convergence with number of poles is relatively fast. Given this model of the dielectric function, the total self-energy can be expressed as a sum of single plasmon pole self-energies arising from interactions with "plasmons" at different frequencies, i.e., $\Sigma(E) = \Sigma_x + \sum_{(i)} g_i\Sigma_1(E,\omega_i)$. This model has been shown to produce reasonably accurate quasiparticle self-energies in comparison with more accurate, but much more time consuming calculations. The many pole model self-energy has been applied to a variety of systems and gives improved results for amplitudes and phases in XANES calculations using FEFF. The model can also be applied in a post processing step as a convolution of the spectrum with an energy dependent Lorentzian [31], as seen in Fig. 2.2, which shows a comparison of theoretical and experimental results for the Li K-edge XANES of LiF [4].

In addition to quasiparticle energies, we can also calculate the inelastic mean free path (IMFP) [34], which is related to the imaginary part of the self-energy, i.e., $\lambda_k(E) = k/|\mathrm{Im}[\Sigma(E)]|$. Figure 2.3 shows a comparison between calculated and experimental IMFP values for Cu, along with results from the plasmon pole model. These results show clear improvement in the agreement with experiment over the plasmon pole model, which is clearly inaccurate below $\sim 100\,\mathrm{eV}$.

Multi-electron excitations can also be calculated given the quasiparticle self-energy, via a convolution of the spectrum with an effective spectral function as in Eq. (2.3) [13, 21]. These calculations are based on a quasi-boson model, which also gives an estimate of the amplitude reduction factor S_0^2. In addition, the calculations yield the satellites on the spectrum which roughly show up as "replica" peaks in the spectrum, shifted by the energy of the main bosonic excitations of the system, and are reflected by peaks in the observed loss function.

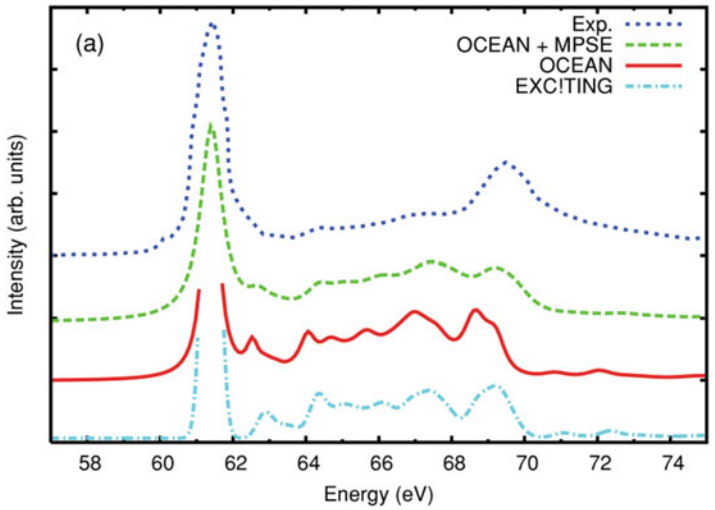

Fig. 2.2 Results for the Li K-edge XANES of LiF from the EXCITING BSE code (*cyan dot-dashed*) [32], the OCEAN BSE code (*red*), OCEAN plus the self-energy convolution (*green dashed*), and experiment (*blue dashed*) [33]. Figure taken from Ref. [4]

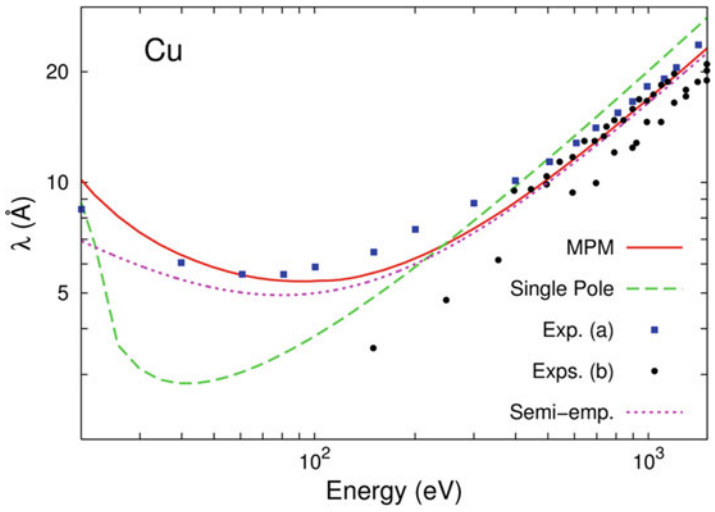

Fig. 2.3 Inelastic mean free path of Cu calculated using a single plasmon pole (*green dashes*), the many pole model (*solid red*), and a semi-empirical model (*pink dots*), compared to experimental data from (a) Ref. [35] (*blue squares*) and (b) Ref. [36] (*black circles*)

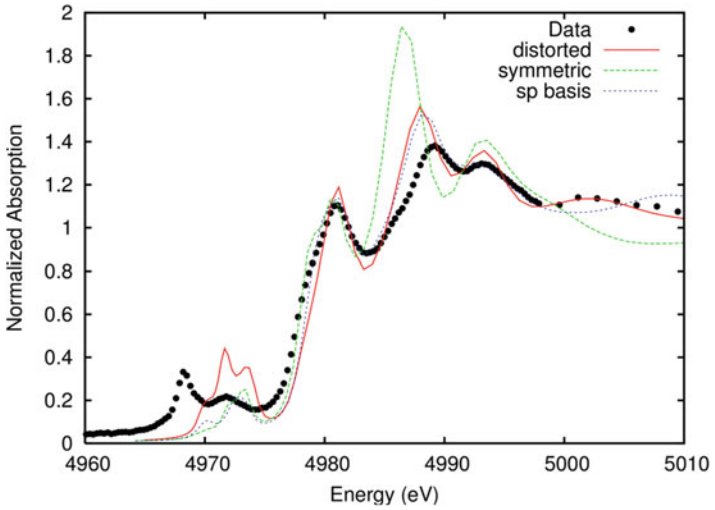

Fig. 2.4 Ti K-edge XANES of $PbTiO_3$ calculated using a distorted crystal structure (*solid red*), the same but with the basis limited to s- and p-states (*thin blue dots*), and using the ideal centro-symmetric crystal structure (*green dashes*), compared to experimental results (*black circles*)

2.2.6 *Information in XANES: Atomic and Electronic Structure*

XANES can be used to probe a variety of properties, including local electronic and chemical structure, atomic structure, and sometimes vibrational properties. For example, $L_{2,3}$-edges of transition metals can be related to the number of holes in the d-orbitals [37]. Shifts in the onset of the spectrum can also indicate charge transfer to and from a metallic particle, or changes in formal oxidation state. While EXAFS is extremely sensitive to the first shell distances and, to a lesser extent, to coordination numbers, XANES is complementary in the sense that it is more sensitive to the local symmetry around the absorbing atom [38]. For example, the spectrum of an atom with four nearest neighbors in tetrahedral symmetry changes appreciably when the symmetry is changed to square planar. Another effect of local symmetry is symmetry breaking due to vibrational effects [39]. An example of symmetry breaking is shown in Fig. 2.4, which displays the Ti K-edge spectrum of $PbTiO_3$ with and without distortions that break centro-symmetric symmetry.

2.2.7 *Use of Configurational Averaging for Vibrational and Static Disorder*

For complicated systems such as amorphous materials or systems at higher temperatures, the EXAFS can be calculated via Debye–Waller factors which damp each path at high k. The XANES is more difficult, since changes in symmetry can

allow previously forbidden transitions, resulting in new peaks in the spectrum. Thus a more accurate method for calculating XANES is to perform averaging over physically unique absorbing sites. This configurational averaging must be performed even when disorder is not present if the system in question has more than one physically unique absorber. For example, magnetite has both tetrahedrally and octahedrally coordinated iron atoms, thus one calculation should be performed for each of these sites, and the final signal obtained from weighted average of the calculated results, where the weighting depends on the site stoichiometry. Doped systems can also require this kind of configurational averaging if the doping concentration is high. Also, in nanoparticles there can be a large number of physically unique sites, based on the proximity to the surface of the particle, interaction with the support, and interaction with adsorbed molecules. All of these effects cause distortions, which ideally should be modeled along with the dynamic, temperature dependent effects. This can be done using, for example, ab initio molecular dynamics to obtain snapshots of the structure of the system [40–42]. The XANES can be calculated for each snapshot by averaging over unique sites, and an average over snapshots gives the final result. There are several approximation applied in the FEFF code that can affect the outcome of such calculations. First, core level shifts due to charge transfer can be important in the final averaged result, since these cause red or blue shifting of the absorption edge. Second, the chemical potential found by FEFF must be calculated carefully since this also causes shifting of the edge. For example, all calculations performed on a static nanoparticle should result in the same (or very nearly the same) chemical potential. This sometimes requires that a unique potential be defined for each type of atom, although atoms with similar chemical surroundings can in many cases be defined as the same type without much loss of accuracy in the results.

2.2.8 *Other Spectroscopies: EELS, XES, NRIXS, RIXS, Compton, etc.*

Many other spectroscopies are related to XAS as they involve similar physics and an analogous golden rule formalism. In particular, electron energy loss (EELS), X-ray emission (XES), and non-resonant inelastic X-ray scattering (NRIXS) are all similar to XAS, the main difference being that they probe different states, either because the transition operator is different, as in EELS and NRIXS, or because the initial and final states are different, as in XES. XES is particularly useful since it probes the occupied states of the system via the dipole operator, and is thus complementary to XAS [43]. EELS and NRIXS both obey a Fermi's golden rule with transition operators $e^{i\vec{q}\cdot\vec{r}}$ replacing the dipole operator, where $\vec{q}$ is the momentum transfer due to the scattering of the electron or photon [7, 44]. This momentum transfer can be controlled by adjusting the angle of detection, and thus the dipole limit can be reached in which case the signal is equivalent to XAS, with

$\widehat{q}$ replacing the polarization direction. The EELS amplitude contains a factor that damps the high momentum transfer signal, so that it is usually within the dipole limit, while NRIXS does not contain this factor, making it possible to probe the local unoccupied density of states for all angular momenta [45]. In addition, NRIXS is useful as a bulk probe of low energy edges, since the energy loss is required to match the edge energy, and high energy X-rays can still be used as the probe [46].

Resonant X-ray emission (RXES) is given by the Kramers–Heisenberg formula, which is similar to Fermi's golden rule, but includes a resonant energy denominator that focuses on a given transition. Although the formula is more complicated than XAS, the RXES spectrum can be approximated by the convolution of an effective XAS signal with the XES spectrum [47], i.e.,

$$\frac{d^2\sigma}{d\Omega d\omega} = \frac{\omega}{\Omega} \frac{\int d\omega_1 \mu_{\mathrm{XES}}(\omega_1)\overline{\mu}(\Omega, \Omega - \omega - \omega_1 + E_{\mathrm{b}})}{|\omega - \omega_1 + i\Gamma_{\mathrm{b}}|}, \tag{2.18}$$

where μ_{XES} is the XES spectrum, $\overline{\mu}$ is the effective XAS spectrum, and E_{b} and Γ_{b} are the core level energy and broadening corresponding to the initial (deep core) excitation, respectively. This formula can be used to estimate both core to core resonant inelastic X-ray scattering, core-valence RXES, and high energy resolution fluorescence detection (HERFD) XAS. Finally, Compton scattering can be calculated within the impulse approximation from the density matrix, $\rho(\vec{r}, \vec{r}\,') = -1/\pi \int_{-\infty}^{\mu} dE\, \mathrm{Im}[G(\vec{r}, \vec{r}\,', E)]$, making multiple scattering a natural formalism for these calculations [48].

2.3 Analysis of EXAFS and XANES

The analysis of EXAFS and XANES begins with a good quality experimental spectrum, and at least some understanding of the physical and chemical environment of the sample that gave that spectrum. Because EXAFS can be measured in a number of modes, and over a wide range of sample conditions and concentration of the absorbing element, care must be taken to ensure that the spectrum being analyzed has been corrected for systematic measurement errors such as over-absorption effects [49, 50] and detector saturation [51]. These topics are beyond the scope of the present chapter, but must be considered in order to get meaningful results from EXAFS and XANES analysis. Here, a good measurement of $\mu(E)$ is simply assumed. The key steps for reducing $\mu(E)$ to "the EXAFS" $\chi(k)$ are shown, the EXAFS Fourier transform presented, and the analysis of the EXAFS equation, Eq. (2.2), to extract coordination numbers, distances, and atomic species of the near-neighbors of the absorbing element is discussed. Finally, a simple approach to

analysis of experimental XANES spectra in terms of linear components of model spectra is outlined. Many treatments [52–56] give more complete and detailed discussions of EXAFS and XANES analysis.

2.3.1 Data Reduction

For all XAFS data, whether measured in transmission or emission mode, the data reduction and analysis are essentially the same. First, the measured intensity signals are converted to $\mu(E)$, normalized to unity edge jump, and then reduced to $\chi(k)$. Normalized $\mu(E)$ is suitable for XANES analysis, while EXAFS modeling using the EXAFS equation requires background-subtracted $\chi(k)$. In this section, we go through these steps of data reduction in some detail.

For transmission measurements, the Beer–Lambert law

$$I = I_0 e^{-\mu t}, \tag{2.19}$$

can be used to convert measured intensities to a quantity proportional to the absorption coefficient, $\mu(E)$. Here I_0 is the X-ray intensity incident on a sample, I is the X-ray intensity transmitted through the sample, and t is the sample thickness. This can be rearranged (and t ignored as a constant) to give

$$\mu(E) = \ln\left(\frac{I_0}{I}\right). \tag{2.20}$$

Usually neither I_0 nor I is an absolute intensity by itself, but signals from ion chambers, photodiodes, or other detectors that are proportional to these intensities. Thus, it is customary to see experimental values reported for "raw" $\mu(E)$ in the literature that do not have dimensions of inverse length, but rather are proportional to $\mu(E)$ in inverse length. Since the $\mu(E)$ will be re-scaled early in the data reduction, this not a problem. For measurements made by detecting emission of the excited atom (including X-ray fluorescence, Auger, and optical luminescence), $\mu(E)$ is given as

$$\mu(E) = \frac{I_\mathrm{f}}{I}, \tag{2.21}$$

where I_f is the emitted signal of interest. As with transmission measurements, there is no need to worry about getting absolute intensities, and one can use the ratio of measured intensities.

2.3.2 Pre-edge Subtraction and Normalization

The experimental $\mu(E)$ is reduced to a *normalized* $\mu(E)$, representing the absorption of one X-ray by the element and absorption edge of interest, for both XANES and EXAFS analysis. The resulting normalized $\mu(E)$ will have a value near 0 below the edge and be approximately 1 well above the edge. The first step in this process is to identify the edge or threshold energy, E_0. Since chemical differences can easily move the threshold by several eV, and because calibrations vary between monochromators and beamlines by similar amounts, the most important feature of the E_0 identified at this point is consistency. Though a crude approximation with little theoretical justification, the most common approach is to take the maximum of the first derivative of $\mu(E)$. This is easily reproduced, and readily applied to any spectrum, but may require refinement during fitting of the EXAFS.

Instrumental drifts from detectors and the expected E^{-3} dependence of $\mu(E)$ can be approximated by a polynomial dependence of $\mu(E)$. As a first approximation, a simple linear fit to the pre-edge range of the spectrum can be extrapolated and subtracted from the full spectrum. A slightly better approximation is to fit to the so-called Victoreen pre-edge function, $E^n\mu(E)$, where n is typically 1, 2 or 3. This is especially helpful for data measured in fluorescence with a solid-state detector for dilute species, where elastic and Compton-scattered X-ray intensity can leak into the energy window of the fluorescence peak of interest, and where this leakage decays as the incident energy increases.

Finally, the edge step $\Delta\mu$ is found, and the pre-edge subtracted $\mu(E)$ is divided by this value. Typically, a low-order polynomial is fit to $\mu(E)$ well above the edge (so as to avoid the XANES region), and the value of this polynomial is extrapolated to E_0 to give the edge step. It should be emphasized that this convention is fairly crude and can introduce systematic biases in the result for $\Delta\mu$.

These steps are illustrated in Fig. 2.5 for transmission XAFS data at the Fe K-edge of FeO. For XANES analysis, this amount of data reduction is generally sufficient. For both XANES and EXAFS analysis, the most important part of these steps is the normalization to the edge step. For XANES analysis, spectra are generally compared by amplitude, so an error in the edge step for any spectrum will directly affect the weight given to it. For EXAFS, the edge step is used to scale $\chi(k)$, and so is directly proportional to coordination number. Good normalization (such that $\mu(E)$ goes to 1 above the edge) is generally not hard, but requires some care, and it is important to assess how well and how consistently this normalization process actually works for a particular data set. Most analysis packages do these steps reasonably well, especially in making spectral normalization consistent for similar datasets, but it is not unusual for such automated estimates of the edge step to need an adjustment of 10 %.

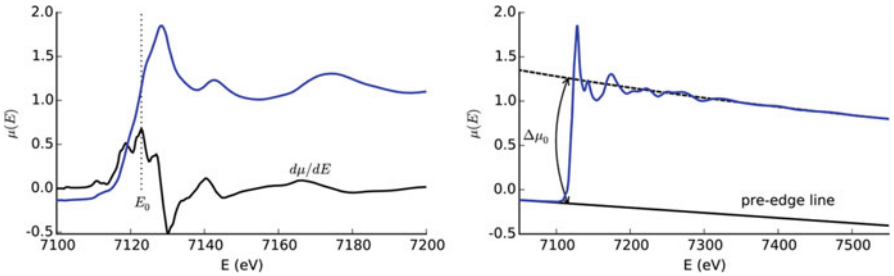

Fig. 2.5 *Left*: The XANES portion of the XAFS spectrum (*blue*), and the identification of E_0 from the maximum of the derivative $d\mu/dE$ (*black*). *Right*: XAFS pre-edge subtraction and normalization. A line or low-order polynomial is fit to the spectrum below the edge, and a separate low-order polynomial is fit to the spectrum well above the edge. The edge jump $\Delta\mu_0$ is taken as the difference between these two curves at E_0. Subtracting the pre-edge polynomial from the full spectrum and dividing by the edge jump gives the normalized XAFS

2.3.3 Background Subtraction

In order to model the EXAFS with equation Eq. (2.2), the EXAFS $\chi(k)$ must be separated from the absorption coefficient, using

$$\chi(E) = \frac{\mu(E) - \mu_0(E)}{\Delta\mu_0}. \tag{2.22}$$

Here, $\mu_0(E)$ represents the absorption coefficient of the absorbing atom without photoelectron scattering from the neighboring atoms, and $\Delta\mu_0$ is the edge step. Since $\mu_0(E)$ cannot be measured readily (if at all), it is approximated mathematically. Usually a piece-wise polynomial or *spline* is used for $\mu_0(E)$. While an ad hoc approach, and capable of being abused, this can be made robust with a small amount of care. The main challenge is to decide how flexible the spline should be, so as to ensure that it does not follow $\mu(E)$ closely enough to remove the EXAFS. That is, $\mu_0(E)$ should follow the slowly varying parts of $\mu(E)$ but not $\chi(E)$, which varies more quickly with E.

A simple approach that works well for most cases relies on the Fourier transform to mathematically express this idea that $\mu_0(E)$ should match the slowly varying parts of $\mu(E)$ but not the quickly varying parts of $\mu(E)$. The Fourier transform is critical to EXAFS analysis, and will be discussed in more detail shortly, but for now the most important point is that it gives a weight for each frequency making up a waveform. The EXAFS Fourier transform converts χ from wavenumber k to distance R.

For determining the background $\mu_0(E)$, the spline function should remove the low-R components of χ, while retaining the high-R components. Conveniently, distinguishing "low-R" from "high-R" can be made physically meaningful using the approximate distance to the nearest neighboring atom. As a realistic rule of thumb,

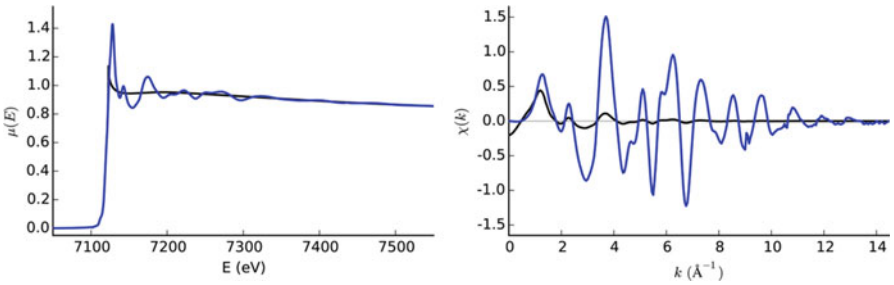

Fig. 2.6 *Left*: Background subtraction for Fe K-edge EXAFS of FeO. A smooth spline function (*black*) that matches the low-R components of $\mu(E)$ (*blue*), in this case using 1 Å for R_{bkg}, is used to approximate $\mu_0(E)$. *Right*: the EXAFS $\chi(k)$ (*black*) isolated after background subtraction. The EXAFS decays quickly with k, and weighting by k^2 (*blue*) amplifies the oscillations at high k

atoms are rarely closer together than about 1.5 Å—this is especially true for the heavier elements to which EXAFS is usually applied. Thus, a spline can be used for $\mu_0(E)$ that makes the resulting χ have as little weight as possible below some distance R_{bkg} (typically, 1 Å), while ignoring the higher R components of χ. While this approach [57] is not always perfect, it can be applied easily to any spectrum and has some physically meaningful basis. Figure 2.6 shows a typical background spline found for FeO, using a R_{bkg} of 1.0 Å, and the resulting $\chi(k)$.

2.3.4 EXAFS Fourier Transforms

The Fourier transform is central to the understanding and modeling of EXAFS data. While many resources describe Fourier transforms and their properties, a few important points about the use of Fourier transforms for EXAFS are made here. Figure 2.7 illustrates the EXAFS Fourier transform for the Fe K-edge data of FeO shown in Fig. 2.6. Two peaks are clearly visible below 3 Å, corresponding to the Fe–O and Fe–Fe distances in the rock-salt structure of FeO. Thus the Fourier transformed EXAFS separates different coordination spheres around the absorbing atom.

In Fig. 2.7, $|\chi(R)|$ almost looks like a radial distribution function, $g(R)$. While EXAFS does depend on the partial pair distribution—the probability of finding an atom at a distance R from an atom of the absorbing species—it must be emphasized that $|\chi(R)|$ is not a pair distribution function. This can be seen from the additional parts to the EXAFS equation, including the non-smooth k dependence of the scattering factor $f_{\mathrm{eff}}(k)$ and phase-shift $\Phi(k)$. An important feature of $\chi(R)$ is that the positions of the peaks are shifted to lower R from the interatomic distances of $g(R)$. For FeO, the first main peak occurs at 1.6 Å, while the FeO distance in FeO is ~2.1 Å. This is not an error, but is due to the scattering phase-shift—recall that the EXAFS goes as $\sin[2kR + \Phi(k)]$. For most systems involving single-scattering, $\Phi(k) \sim -k$ is a

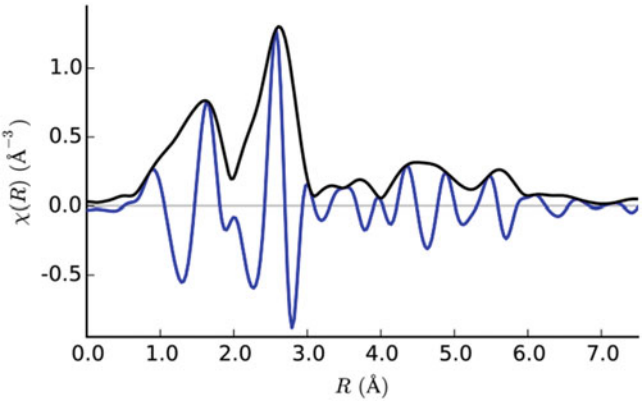

Fig. 2.7 The XAFS Fourier Transform, $\chi(R)$. The magnitude $|\chi(R)|$ (*black*) is the most common way to view the data, showing peaks corresponding to scattering from neighboring atoms. The Fourier transform $\chi(R)$ is a complex function, with both a real (*blue*) and imaginary parts

decent if crude approximation to the phase-shift, which gives a shift to the peaks in $\chi(R)$ of -0.5 Å or so relative to the actual interatomic distances.

The Fourier transform is inherently complex, and gives a complex function for $\chi(R)$ even though $\chi(k)$ is a strictly real function. It is common to display only the magnitude of $\chi(R)$ as shown in solid in Fig. 2.7, but the real (blue) and imaginary components contain important information that cannot be ignored when modeling EXAFS. In contrast to the standard form, the Fourier transform for EXAFS analysis uses conjugate variables of k and $2R$, reflecting the EXAFS equation. For numerical analysis, a discrete Fast Fourier transform is used. The data must be interpolated onto a uniformly spaced set of values in k. Typically, a spacing of $\delta k = 0.05$ Å^{-1} and an array size of $N = 2048$ k values are used. This gives a spacing of R points in the discrete $\chi(R)$ of $\delta R \approx 0.0307$ Å.

Prior to the transform, $\chi(k)$ is usually multiplied by a power of k, typically k^2 or k^3, as shown in Fig. 2.6. This weighting helps compensate for the strong decay with k of $\chi(k)$. In addition, $\chi(k)$ is multiplied by a window function $\Omega(k)$ which smooths the resulting $\chi(R)$ and removes ripples and ringing that would result from a sudden truncation of $\chi(k)$ at the ends of the data range. Since Fourier transforms are used in many fields, there is an extensive literature on such window functions and many choices available in most EXAFS analysis packages.

In many analyses, the inverse Fourier transform is used to select a particular R range and transform this back to k space, *filtering* out most of the spectrum and leaving only a narrow band of R values in the resulting filtered $\chi(k)$. This can isolate the EXAFS signal for a single shell of physical atoms around the absorbing atom, and was the basis of most early EXAFS analyses. This approach should be used with caution since, for all but the simplest of systems, it can be surprisingly difficult to effectively isolate the EXAFS contribution from an individual scattering atom

this way. It is almost never possible to isolate a second neighbor coordination sphere in this way. For this reason, many modern analyses of EXAFS will use a Fourier transform to convert $\chi(k)$ to $\chi(R)$, and use $\chi(R)$ for data modeling, without trying to isolate shells of atoms.

2.3.5 XAFS Data Modeling

The FeO data shown above is convenient to illustrate many aspects of EXAFS data modeling. FeO has a simple rock salt structure, with Fe surrounded by 6 O, with octahedral symmetry, and then 12 Fe atoms in the next shell. Starting with this simple structure, the scattering amplitudes $f_{\text{eff}}(k)$ and phase-shifts $\Phi(k)$ can be calculated theoretically using the FEFF formalism described above. These theoretical scattering factors (along with a calculation of the mean free path λ_k) can be used in the EXAFS equation to refine structural parameters R, N, and σ^2 to match a set of data. Typically, E_0 (the energy for which $k = 0$) is also adjusted to best match data, to compensate for the crude estimate made in the initial processing. While one can do the refinement with the measured $\chi(k)$, working with the complex $\chi(R)$ is generally preferred, as higher coordination shells can be selectively ignored. The examples shown here are done with the FEFF6 [2, 58] program to construct the theoretical factors, and the IFEFFIT [59–61] package to do the analysis. Some aspects of the analysis shown here may depend on details of these particular programs, but similar results can be obtained with any of several EXAFS analysis programs.

2.3.6 Running and Using FEFF for EXAFS Calculations

In order to calculate the $f_{\text{eff}}(k)$ and $\Phi(k)$ needed for the analysis, the FEFF program [58] uses a cluster of atoms, builds atomic potentials from this, and simulates a photoelectron with a particular energy being emitted by a particular absorbing atom and propagating along a set of scattering paths [62]. As detailed above, FEFF includes many subtle but quantitatively important effects. Because one starts with a cluster that represents the atomic structure, the FEFF fitting process is a *refinement* of the path lengths and coordination numbers for those paths. Conveniently, FEFF breaks up the results in a way that can be put into the standard form of the EXAFS equation, even for multiple-scattering paths. This allows analysis procedures to easily refine distances, apply multiplicative factors for coordination numbers and S_0^2, and apply disorder terms. Because the outputs have a uniform format, results from different runs of the programs can readily be mixed, which is important for modeling complex structures with multiple coordination environments for the absorbing atom.

2.3.7 First-Shell Fitting

To model the first shell EXAFS of FeO, a simulation of the EXAFS for the Fe–O scattering path is calculated by FEFF from a cluster derived from the known crystal parameters for FeO. Setting S_0^2 to 0.75, values for N, R, σ^2, and E_0 are refined until the model for χ best matches the complex $\chi(R)$ of the measured data. The results of this refinement are shown in Fig. 2.8, with best-fit values and estimated uncertainties for the refined parameters given in Table 2.1. These values are not perfect for crystalline FeO, especially in that the distance is contracted from the expected value of 2.14 Å, but they are reasonably close for a first analysis.

It is instructive to look at this refinement more closely and discuss a few details. The refinement was done on the $\chi(R)$ data, after a Fourier transform of $k^2\chi(k)\Omega(k)$ for both data and model, where $\Omega(k)$ represents a Hanning window with a range between $k = [2.5,\ 13.5]$ Å^{-1}, and with a dk parameter of 2 Å^{-1}. Both real and imaginary components of $\chi(R)$ between $R = [1.0,\ 2.0]$ Å were used. Figure 2.8 shows that the higher frequency components from the second shell of Fe–Fe dominate $k^2\chi(k)$. This is a useful reminder of the power of the Fourier transform in XAFS analysis: it allows one to ignore shells of higher frequency even if they have larger overall amplitude.

The refinement used a nonlinear least-squares fit to minimize a standard statistical definition for the chi-square statistic

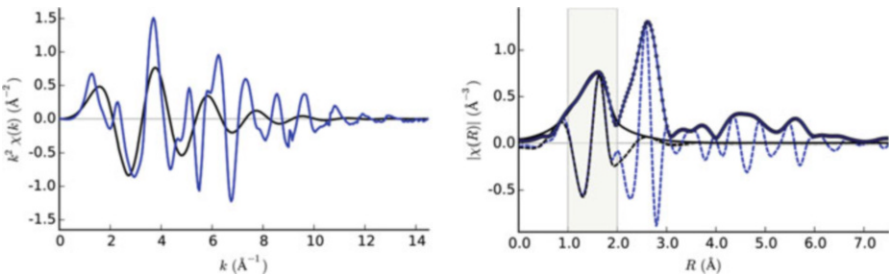

Fig. 2.8 First shell fit to EXAFS for FeO. *Left*: XAFS $k^2\chi(k)$ for data (*blue*) and best-fit model (*black*). *Right*, the real (*dashed*) and magnitude (*solid*) components of $\chi(R)$ for the data (*blue*) and best-fit model (*black*). The fitting range of $R = [1.0,\ 2.0]$Å is highlighted, showing that the model matches the data very well

Table 2.1 Best values and uncertainties (in parentheses) for the refined first shell parameters for FeO. The refinement fit the components of $\chi(R)$ between $R = [1.0, 2.0]$ Å after a Fourier transform using $k = [2.5, 13.5]$ Å^{-1}, a k-weight of 2, and a Hanning window function. S_0^2 was fixed to 0.75

Shell	N	R (Å)	σ^2 (Å^2)	ΔE_0 (eV)
Fe–O	5.5(0.6)	2.10(0.01)	0.015(.002)	−3.4(1.1)

$$\chi^2 = \sum_i^{N_{\text{data}}} \frac{[y_i^{\text{data}} - y_i^{\text{model}}(x)]^2}{\varepsilon^2}, \tag{2.23}$$

where y_i^{data} is the experimental data, $y_i^{\text{model}}(x)$ is the model constructed from the EXAFS equation and the variable fitting parameters x, ε is uncertainty in the data, and N_{data} is the number of points being fit. As mentioned above, the real and imaginary components of $\chi(R)$ were used as y for both data and model, though fitting to $k^2\chi(k)$ data is not uncommon. A crude estimate of ε can be made from the high frequency noise in $\chi(k)$ [63]. Historically, the problem of identifying N_{data} has been controversial. For any signal, the Nyquist–Shannon sampling theorem gives the resolution R (the smallest detectable difference in distances) based on $k_{\max}$, the maximum measured value of k, as $\delta R = \pi/2k_{\max}$. From this, it follows [64, 65] that the maximum number of independent measurements that can be extracted from an EXAFS spectrum is

$$N_{\text{ind}} \approx \frac{2\Delta k \Delta R}{\pi} + 1, \tag{2.24}$$

where Δk and ΔR are the range of useful data in k and R. For the first shell of FeO with $k = [2.5, 13.5]$ Å^{-1} and $R = [1.0, 2.0]$ Å, this gives $N_{\text{ind}} \approx 8$. The number of variables in a fit should not exceed this value.

2.3.8 Second-Shell Fitting

Including the second shell in the model for the FeO EXAFS involves adding the path for Fe–Fe scattering to the sum in the EXAFS equation. Variables for R, N, and σ^2 for the Fe–Fe shell will be included, while a single value for E_0 will be used for both the Fe–O and Fe–Fe paths. The fit range will be extended to $R = [1.0,\ 3.1]$ Å, increasing N_{ind} to ≈ 15.7, while the number of variables increases to 7. Results for this fit are shown Fig. 2.9 and Table 2.2. The structural values for distances and coordination number are consistent with the known crystal structure of FeO, though the Fe–O distance is a bit shorter than expected, and the Fe–Fe is a bit longer than expected, both suggesting that there may be some contamination of a ferric iron phase in the sample. Figure 2.9 shows the fit to be quite good, especially in the real part of $\chi(R)$, which is actually used in the fit. Figure 2.10 shows the individual contributions to the total best-fit spectrum. In k-space, the contribution from Fe–Fe is seen to have a shorter period than Fe–O due the longer interatomic distance. In addition, the Fe–Fe contribution persists to higher k due to the dependence of $f_{\text{eff}}(k)$ on Z of the scatterer. In R-space, substantial overlap can be seen between the two shells, even though there is a strong dip in $|\chi(R)|$ at 2 Å. Indeed, the inclusion of the Fe–Fe shell did subtly alter the best-fit results (though within the estimated uncertainty) for the Fe–O shell.

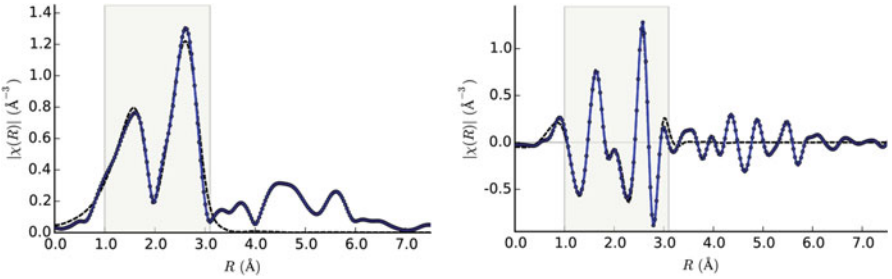

Fig. 2.9 EXAFS $|\chi(R)|$ (*left*) and $\mathrm{Re}[\chi(R)]$ (*right*) for FeO data (*blue*) and best-fit model (*black*) for the first two shells around Fe, including Fe–O and Fe–Fe scattering paths. The fitting range of $R = [1.0,\ 3.1]$Å is highlighted

Table 2.2 Best fit values and uncertainties (in parentheses) for the Fe–O and Fe–Fe shells for FeO. The refinement fit of $\chi(R)$ between $R = [1.0, 3.1]$ Å with all other parameters as in Table 2.1

Shell	N	R (Å)	σ^2 (Å^2)	ΔE_0 (eV)
Fe–O	5.4(0.7)	2.11(0.01)	0.013(.002)	−1.5(0.6)
Fe–Fe	12.6(1.4)	3.07(0.01)	0.015(.001)	−1.5(0.6)

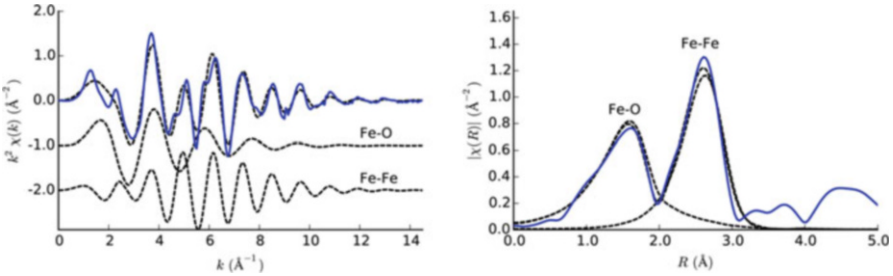

Fig. 2.10 Contributions of the first and second shell to the model for the FeO EXAFS. *Left*: the fit (*black*) matches the data (*blue*) in k-space much better than in Fig. 2.8. *Right*: the fit (*black*) and data (*blue*) for $|\chi(R)|$. In both, contributions from the Fe–O and Fe–Fe shells are shown in *dashed lines*

2.3.9 XANES Analysis

As discussed in Sect. 2.2.6, XANES is uniquely sensitive to oxidation state, coordination chemistry, and the partial density of unoccupied electronic states, and XANES spectra are much richer in spectral features than EXAFS, making it an excellent spectroscopic technique for almost every element [66]. Unfortunately, the EXAFS equation breaks down at low k, where λ_k diverges, so that a huge number of scattering paths contribute. With no readily parameterized XANES equation, quantitative XANES analysis has traditionally relied on fitting idealized

peak-shapes to spectral features or matching spectra to linear combinations of spectra from known systems. These approaches are reasonably well justified in many specific cases, but are not easy to generalize. Some work [67, 68] has been done to try adapt a suite of calculations to best-match experimental data using a reverse Monte-Carlo approach, which has the advantage of being able to use both the XANES and EXAFS portions of a spectrum, but is computationally slow. In the soft X-ray regime, and for certain 3d metal pre-edge peaks, quantitative analysis based on multiplet analysis is also robust and very useful for assigning electronic transitions [69].

Although the XANES cannot be numerically parameterized in terms of oxidation state or coordination chemistry, these can be determined using simpler spectroscopic analysis methods. For example, the pre-edge peaks in the K and L edges of 3d metal are very rich at identifying coordination chemistry and hybridization of electronic levels, even if the precise intensities of the different transitions is complicated to calculate accurately. To make analysis quantitative, fitted intensities of such peaks can be compared to calibration curves made from spectra of known materials. While such analysis is not ab initio, it can be robust and reliable with minimal effort. As an illustration of such XANES peak analysis, the left-hand side of Fig. 2.11 shows the pre-edge peaks of Fe_2O_3, and a fit to this edge structure using several peaks—in this case 3 separate Voigt functions and one error function. These peaks can be assigned as the atomic-like multiplet orbitals, and the 1s-4p transition. When applied over a range of experimental compounds, clear trends emerge and the XANES peak intensities can give excellent precision in oxidation state [70–72].

A second common approach to XANES analysis is to treat the spectra as a signature or fingerprint of a material, and determine the fractional composition of

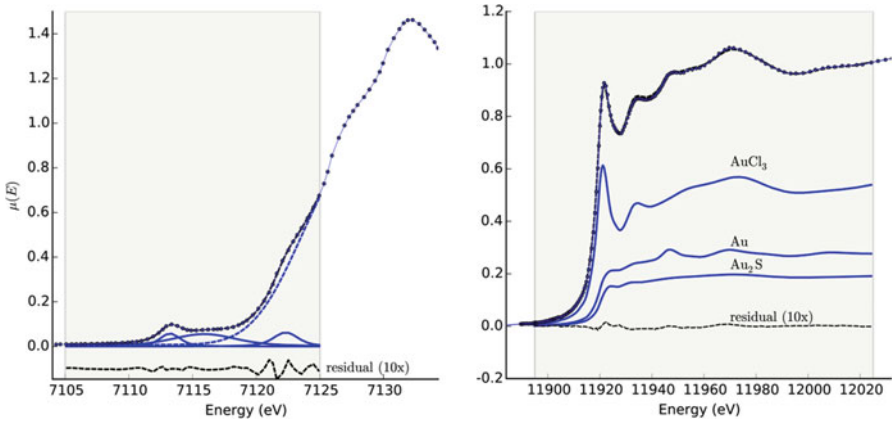

Fig. 2.11 *Left*: XANES pre-edge peak fit (*black*) for the Fe K edge data (*blue dots*) of Fe_2O_3, over the shaded fit range of $E = [7105, 7125]$eV. The fit used three Voigt peaks (*blue*, *solid*) and an error function (*blue*, *dashed*). The fit residual (*black*), has been multiplied by 10, and offset. *Right*: XANES fit of an unknown Au LIII-edge spectrum to a linear combination of spectra from model compounds (gold chloride, metal, and sulfide), with contributions of individual components (*blue*) and the fit residual. After Lengke et al. [76]

spectra from well-characterized materials. This approach uses simple linear statistical analysis, and so can build on a wide literature, including Principal Component Analysis [73] and related methods [74, 75]. As an illustration, the L_{III}-edge XANES spectrum of an experimental gold compound [76] is shown on the right-hand side of Fig. 2.11, along with the weighted components used to fit the spectrum. This approach relies heavily on the use of the correct components, and care must be taken to ensure that standard spectra are correctly calibrated in energy and normalized in intensity.

2.4 Theoretical Modeling of EXAFS and XANES

2.4.1 Introduction

The great success of EXAFS and XANES stems from the insights they provide into the atomic and electronic structure of complex materials. This has been especially important for catalytic systems, as discussed elsewhere in this volume. As shown in the previous sections, this success was aided in part by the development of robust theoretical methods to simulate a broad range of X-ray spectroscopies [1, 2, 19]. Although these methods have often been highly successful, a limitation is that the accuracy of the predicted spectra depends on the quality of the structural models used in the simulations. This is particularly important in XANES simulations. In the past, this drawback has been sidestepped by either the use of known crystallographic information, or by a combination of EXAFS modeling and chemical know-how of the nature of the material in order to build more complete structural models [77]. In recent decades, however, materials research has begun to focus on complex materials under *operando* or extreme conditions. Typical examples of these types of systems are supported nanocatalysts [40, 42, 78], solvated ions [41], and shocked materials. Reliable simulations under those conditions require more sophisticated models that capture the heterogeneous nature of the materials. Thus, the field of XAS modeling has recently progressed towards the interfacing of spectroscopy codes with existing software for calculations of structural and electronic properties [6]. In the following sections we present a few examples that highlight the power of this blend of spectroscopy, materials science, condensed matter physics and quantum chemistry methods.

2.4.2 Use of Modeling to Enhance EXAFS Analysis

While the fitting of EXAFS spectra using theoretical scattering amplitudes and phase-shifts is now a well-established methodology, the calculation of other parameters of the EXAFS equation, Eq. (2.2), such as path lengths, number of

near-neighbors N_R and mean-square relative displacements (MSRD) σ_R^2 have only recently become feasible on a routine basis. While many theoretical methods lack the accuracy needed to rival fitted EXAFS path lengths, they may be well suited to distinguish between alternative conformations, and provide good approximations to both the N_R and σ_R^2, thus making the fitting of the path lengths much more reliable in many complicated materials. In this section we discuss two ways in which theoretical modeling can enhance EXAFS fits: First, we focus on the calculation of ab initio Debye–Waller factors for systems where σ_R^2 can be described well using a combination of static and vibrational disorder. Second, we highlight the simulation of EXAFS spectra for systems with large dynamic disorder.

2.4.2.1 Ab Initio Debye-Waller Factors

The theory behind MSRDs or XAFS Debye–Waller factors and how to compute them ab initio is now fairly well established [79–82]. Briefly, the MSRD or σ_R^2 for a path R is defined by the thermal average:

$$\sigma_R^2 = \langle \left(R - \overline{R}\right)^2 \rangle, \tag{2.25}$$

where R and $\overline{R}$ are the instantaneous and mean path lengths, respectively. In the quasi-harmonic approximation, the average can be computed as a sum over vibrational or phonon eigenmodes [81] or, alternatively, in terms of the projected vibrational density of states $\rho_R(\omega)$ or VDOS, and the Debye integral

$$\sigma_R^2(T) = \frac{\hbar}{2\mu_R} \int_0^\infty \frac{1}{\omega} \coth\left(\frac{\beta\hbar\omega}{2}\right) \rho_R(\omega) d\omega, \tag{2.26}$$

where μ_R is the reduced mass for path R. Poiarkova and Rehr [79, 80] have shown that the VDOS can be calculated efficiently from the imaginary part of the lattice dynamical Green's function matrix element:

$$\rho_R(\omega) = -\frac{2\omega}{\pi} \mathrm{Im} \langle 0 | \frac{1}{\omega^2 - \mathbf{D} + i\varepsilon} | 0 \rangle \cong \sum_{\nu=1}^{N} w_\nu \delta(\omega - \omega_\nu). \tag{2.27}$$

Here $|0\rangle$ is a vector representing a normalized mass-weighted displacement of the atoms along the multiple-scattering path R. Efficient calculations of the lattice dynamical Green's function can be accomplished using a continued fraction representation obtained with the iterative Lanczos algorithm that yields an N-pole representation for the VDOS where ω_ν and w_ν are, respectively, the pole frequencies and weights of pole ν. $\mathbf{D}$, the dynamical matrix of force constants, or Hessian, is the main ingredient required for the calculation of theoretical MSRDs and is defined as:

$$D_{jl\alpha,j'l'\beta} = \left(M_j M_{j'}\right)^{-1/2} \frac{\partial^2 E}{\partial u_{jl\alpha} \partial u_{j'l'\beta}}, \tag{2.28}$$

where $u_{jl\alpha}$ and M_j are the $\alpha = \{x, y, z\}$ Cartesian displacement and mass of atom j in unit cell l, respectively, and E is the internal energy of the system. For molecular systems, **D** is routinely computed with quantum chemistry packages like Gaussian [83], NWChem [84], and ORCA [85], and the accuracy of different methods is well-established [86, 87]. For solids, the dynamical matrix can be computed, e.g., using ABINIT [88–90], VASP [91], and Quantum Espresso [92]. The MSRDs can be extracted from the output of these and other programs by using interface programs included in FEFF [6] and used directly to replace the values provided by phenomenological Einstein or Debye models. A typical example of the quality of the results that can be obtained for molecular ion complexes such as the one shown in Fig. 2.12 are presented in Table 2.3. The $Ru(bpy)_2(AP)(H_2O)^{++}$ complex was optimized and its Hessian calculated using the B3LYP exchange correlation functional, while using the SDD effective core potential and associated basis sets for all atoms. The agreement between the experimental [93] and theoretical coordination

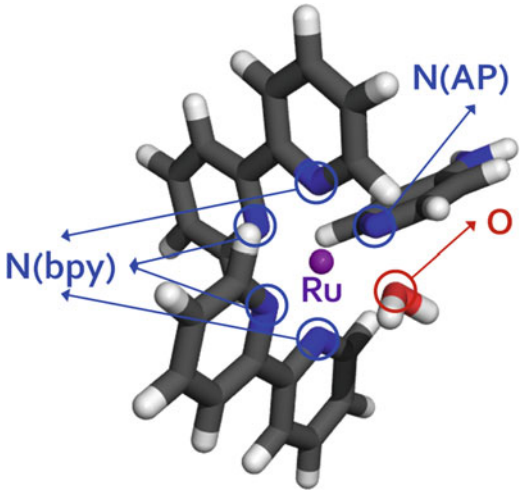

Fig. 2.12 Structure of $Ru(bpy)_2(AP)(H_2O)^{++}$ highlighting the near-neighbor sites used for computing the MSRDs shown in Table 2.3

Table 2.3 Comparison between the experimental [93] and theoretical near-neighbor distances and MSRDs (σ^2) for the $Ru(bpy)_2(AP)(H_2O)^{++}$ complex shown in n Fig. 2.12

	$R_{M\text{-}L}$ (in Å)		σ^2 (in 10^{-3} Å^2)	
Path	Theory	Expt.	Theory	Expt.
	2.08		2.49	
	2.04		2.32	
Ru-N (bpy)	2.10	2.05 ± 0.01	2.60	2.6 ± 0.9
	2.09		2.50	
Ru-N (AP)	2.14	2.10 ± 0.03	2.61	4 ± 3
Ru-O	2.22	2.06 ± 0.05	4.93	9 ± 7

distances for the tightly bound N near-neighbors is good, despite being slightly outside the EXAFS error bars. For the weakly bound water molecule, the theoretical distance is slightly overestimated, but still reasonable.

The agreement for the MSRDs (σ^2) is quite good and, given the error margins from the EXAFS fit, could be used "as is" in the EXAFS fit to replace the fitted values. In particular, the theoretical results provide a good alternative for the weaker bonds, where the EXAFS-fitted values have large uncertainties.

In practice, however, a better approach may be to set up a fitting model where the near-neighbor MSRDs are scaled by a single parameter. This approach is quite useful for systems with mixed coordination shells with different MSRDs where the number of EXAFS parameters becomes large and highly correlated.

2.4.2.2 Simulating EXAFS of Dynamic Systems

The standard approach to vibrational disorder in EXAFS assumes that the local environment surrounding the absorbing atom is relatively rigid, with small distortions that are harmonic, thus resulting in an approximately Gaussian pair distribution function [22]. Although broadly applicable, this approach can give poor results for systems like ions in solution or liquid materials, where the bonds between the absorber and its near-neighbors are continuously breaking and reforming. In such cases using an optimized structure plus vibrations is not sufficient, and an explicit sampling over the dynamical fluctuations is needed. A method of choice to obtain this sampling is molecular dynamics (MD) in conditions of temperature, pressure, and concentration that closely resemble those used in the experiments. MD simulations rely on the calculation of atomic forces that can be computed based on either model or ab initio potential energy surfaces [94, 95]. The former results in very efficient calculations, but have the drawback of requiring the parameterization of a model potential that might or might not be transferable to other systems and conditions. The latter, on the other hand, can be applied to a very broad range of conditions although at a very high computational cost. Both approaches has been applied successfully to the simulation of ions in solution [96, 97]. For example, Fulton et al. [41] have demonstrated near-quantitative prediction of EXAFS spectra for charged transition metal ions in solution. Figure 2.13 shows the module and imaginary parts of the real-space fine structure for Cr^{+3} in aqueous solution, compared to theory. The theoretical results were obtained from FEFF simulations using conformations sampled from a QM/MM MD simulation. Remarkably, these simulations do not include any type of experimental parameter and the thermal broadening of the distribution arises naturally from the averaging.

2.4.3 Use of Modeling to Enhance XANES Analysis

The theoretical modeling of XANES spectra poses bigger challenges than that of EXAFS due to two main reasons: (a) It demands more computationally intensive

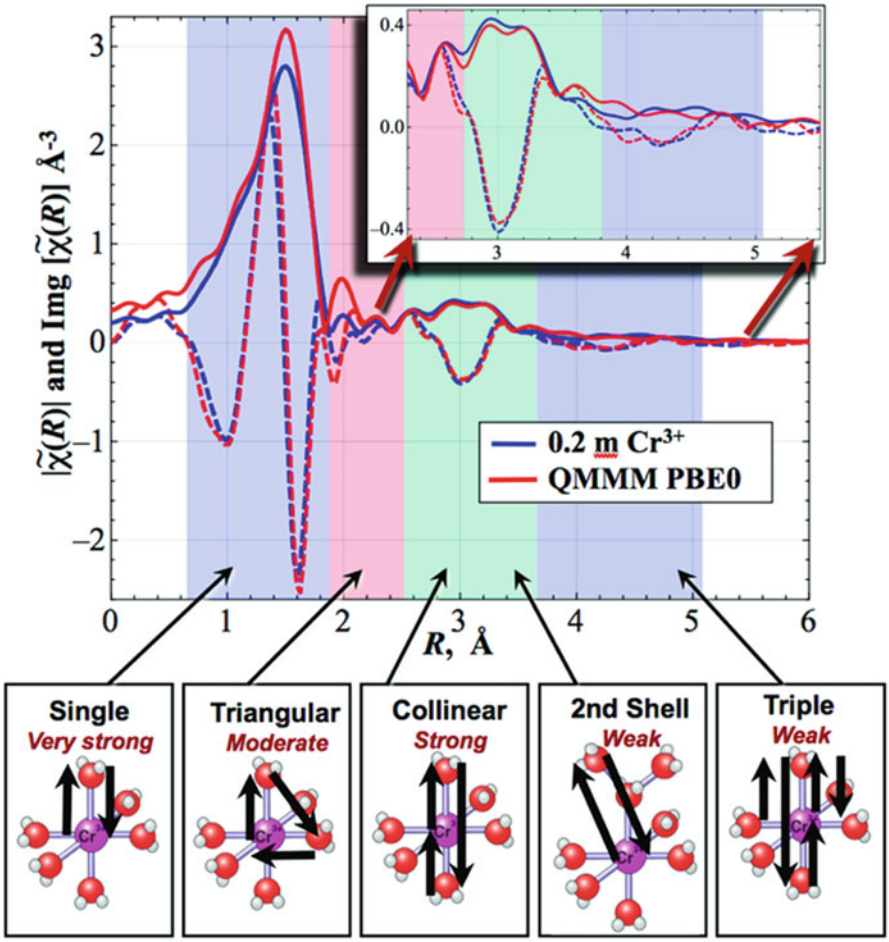

Fig. 2.13 k^2-weighted $|\tilde{\chi}(R)|$ (*solid lines*) and $\mathrm{Im}[\tilde{\chi}(R)]$ (*dashed lines*) for hydrated Cr^{+3}. The highlighting of different spectral regions shows the assignments to different types of single and multiple scattering events, as illustrated. The inset expands the view for the longer multiple scattering region (Reproduced with permission from Ref. 41)

simulations and, (b) generally there is incomplete information about the structure of the system under study. These two aspects result in the need for theoretical generation of structural models by means of optimizations or MD simulations. As in the case of EXAFS, the former are quite useful for quasi-rigid systems, while the latter are required for systems with dynamic fluctuations and bond-breaking. As opposed to EXAFS, XANES spectra are often less sensitive to the quality of the structural model, thus permitting the direct use of theoretical structures in the simulations. The advent of accurate and efficient DFT simulations has virtually eliminated the need to guess possible structures since one can now optimize accurate models based on simple external information such as composition

[98, 99]. Moreover, one can also take advantage of other information resulting from simulations such as thermodynamic properties, charge distribution (see below), and vibrational properties (see discussion on MSRDs above). In light of the current trend towards multi-spectroscopy, *operando* experimental approaches [100], this broad range of theoretical properties facilitates a more holistic interpretation of the experimental results. In the following sections we focus on two aspects of theoretical modeling of XANES. First, we discuss the importance of including dynamical disorder in XANES simulations to be able to reproduce experiment. Second, we focus on the enhanced understanding that emerges from the atomistic information provided by simulations.

2.4.3.1 Effects of Dynamical Disorder on XANES

As in the case of EXAFS, dynamic structural disorder plays a very important role in the accurate simulation of XANES [40, 78, 100]. For systems where the experiment naturally samples a large number of conformations, the XANES simulations must usually include similar sampling to be able to reproduce experiment. The most common way to do structural sampling theoretically is by means of molecular dynamics simulations over a suitable time-frame. These simulations can rely on model potential energy surfaces, as discussed for EXAFS above, or on ab initio DFT potentials (i.e., DFT/MD). In practice, the former is quite efficient and provides a good understanding of the structural properties for systems with a mixture of covalent and soft interactions. But, for other examples of dynamic systems with metallic bonds such as supported metal clusters, the use of DFT/MD is highly recommended. This approach also has the added bonus of providing very useful information about the electronic structure of the material. A classic example of this type of problem is the case of Pt and PtSn nanoclusters on γ-Al_2O_3 [40, 42], where modeling is needed to understand their intra-particle heterogeneity and their structural and electronic changes under realistic conditions. DFT/MD simulations reveal that the nanoscale structure and charge distribution are inhomogeneous and dynamically fluctuating over several time-scales, ranging from fast (200–400 fs) bond vibrations to slow fluxional bond breaking ($>$10 ps). To help visualize this fluctuating behavior, Fig. 2.14 shows an average of snapshots extracted from the MD simulations at two different temperatures. At low temperature (165 K), the cluster "rocks" over the surface. While mostly maintaining its shape, it is clearly less rigid than the surface. At high temperature (the catalyst *operando* temperature of 573 K), however, the cluster becomes highly fluxional due to the large number of bond-breaking events and is capable of diffusing over the surface.

The effects of the dynamic disorder on the XANES are very significant. Figure 2.15 shows a comparison between the experimental XANES spectra and those obtained from MD and Boltzmann sampling of the conformations. Despite the large fluctuations indicated by the standard deviation bars, the MD-sampled spectra are in very good agreement with experiment, capturing both the enhancement of the white line at high temperatures and the red shift of the edge. In contrast, the spectra

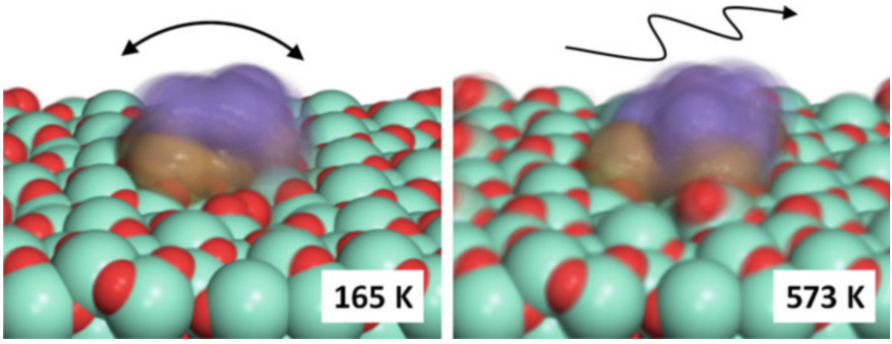

Fig. 2.14 Average image showing the dynamic behavior of Pt_{10} on γ-Al_2O_3 generated from snapshots of MD simulations at 165 and 573 K where the "blurriness" of the atoms indicate their mobility. The gold and purple spheres indicate Pt atoms that are oxidized ($+\delta$) or reduced ($-\delta$), while the red and teal ones represent the O and Al atoms, respectively. At 165 K, the cluster rocks on the same surface site while at 573 K it moves over the surface

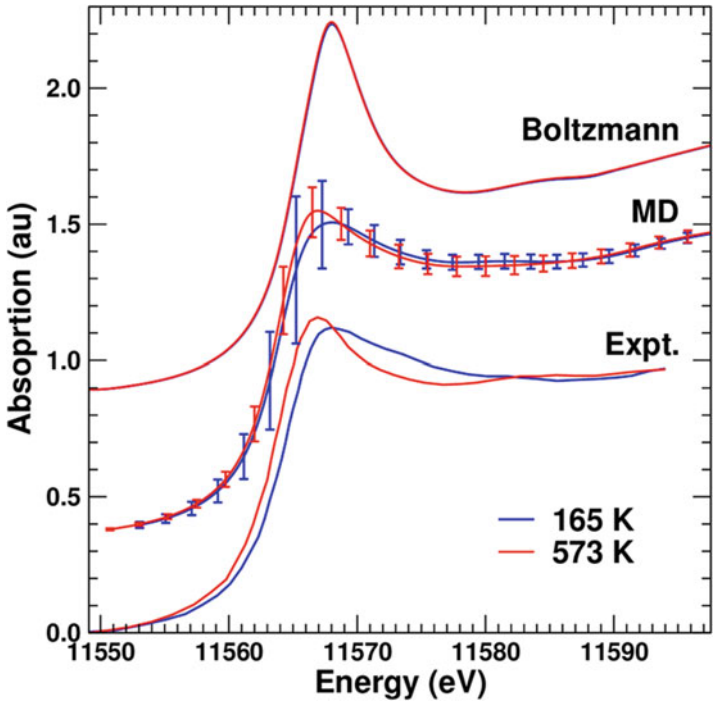

Fig. 2.15 Pt K edge XANES spectra for Pt_{10} on γ-Al_2O_3. The MD results were generated by averaging over conformations sampled from 6 ps runs and the error bars indicate the standard deviation of the spectrum. For comparison, results are also shown for a Boltzmann-average over conformations obtained by quenching the same MD samples

obtained from the Boltzmann-average of quenched conformations show little difference between both temperatures, and severely overestimate the intensity of the white line. The main difference between the MD and quenched conformation samplings stems mainly from the important role played by breaking and reforming bonds.

2.4.3.2 Understanding Electronic Structure Changes Through Modeling

Perhaps one of the most useful features of theoretical modeling is the possibility of directly visualizing atomistic changes in electron density distribution. This is particularly important since global probes such as EXAFS and XANES reveal the ensemble characteristics of materials while missing details of their internal structure. Moreover, changes in spectral features such as edge position and white line intensity that are commonly associated with charge density fluctuations in a qualitative way can be studied quantitatively and in detail. An excellent example of the atomistic understanding that is gained through modeling arises again in the case of Pt_{10} on γ-Al_2O_3 [40]. Figure 2.14 shows that the cluster is roughly separated into two layers, with one layer in contact with the surface (golden spheres) and another resting on top (purple spheres). The atoms in the contact layer become positively charge or "oxidized," while the others are neutral or slightly negatively charged ("reduced"). The MD simulations show that at high temperature, the number of contacts with the surface increases, thus removing more charge from the cluster which results in the expected red shift in the absorption edge position and increase in the white line intensity. Moreover, these charge fluctuations can be correlated with other observed trends such as negative thermal expansion in Pt clusters [40], and species segregation and differential reactivity in PtSn alloy clusters [42, 78]. This detailed atomistic understanding can only be achieved through the close integration of modeling and experiment.

References

1. Ankudinov AL, Ravel B, Rehr JJ, Conradson SD (1998) Real-space multiple-scattering calculation and interpretation of X-ray-absorption near-edge structure. Phys Rev B 58:7565
2. Rehr JJ, Albers RC (2000) Theoretical approaches to X-ray absorption fine structure. Rev Mod Phys 72:621
3. Onida G, Reining L, Rubio A (2002) Electronic excitations: density-functional versus many-body Green's-function approaches. Rev Mod Phys 74:601
4. Vinson J, Rehr JJ, Kas JJ, Shirley EL (2011) Bethe-Salpeter equation calculations of core excitation spectra. Phys Rev B 83:115106
5. Shirley E (1998) Ab initio inclusion of electron-hole attraction: application to X-ray absorption and resonant inelastic X-ray scattering. Phys Rev Lett 80:794
6. Rehr JJ et al (2009) Ab initio theory and calculations of X-ray spectra. C R Phys 10:548

7. Rehr JJ, Soininen JA, Shirley EL (2005) Final-state rule vs the Bethe-Salpeter equation for deep-core X-ray absorption spectra. Phys Scr T115:207
8. Moreno MS, Jorissen K, Rehr JJ (2007) Practical aspects of electron energy-loss spectroscopy (EELS) calculations using FEFF8. Micron 38:1
9. Sorini AP, Rehr JJ, Jorissen K (2008) In: Electron microscopy and multiscale modeling—EMMM-2007: an international conference, vol 999. AIP Publishing, pp 47–52
10. Jorissen K (2007) The ab initio calculation of relativistic electron energy loss spectra. Ph.D. thesis, University of Antwerp
11. Jorissen K, Rehr JJ, Verbeeck J (2010) Multiple scattering calculations of relativistic electron energy loss spectra. Phys Rev B 81:155108
12. Sayers DE, Stern EA, Lytle FW (1971) New technique for investigating noncrystalline structures: Fourier analysis of the extended X-ray-absorption fine structure. Phys Rev Lett 27:1204
13. Campbell LW, Hedin L, Rehr JJ, Bardyszewski W (2002) Calculations of inelastic losses and interference terms in X-ray absorption. Phys Rev B 65:064107
14. Muller JE, Jepsen O, Wilkins JW (1982) X-ray absorption-spectra—K-edges of 3d transition-metals, L-edges of 3d and 4d metals, and M-edges of Palladium. Solid State Commun 42:365
15. Blaha P, Schwarz K, Sorantin P, Trikey SB (1990) Full-potential, linearized augmented plane-wave programs for crystalline systems. Comput Phys Commun 59:399
16. Ebert H (1996) Magneto-optical effects in transition metal systems. Rep Prog Phys 59:1665
17. Ankudinov AL, Zabinsky SI, Rehr JJ (1996) Single configuration Dirac-Fock atom code. Comp Phys Commun 98:359
18. Gurman SJ, Binsted N, Ross I (1986) A rapid, exact, curved-wave theory for EXAFS calculations: II. The multiple-scattering contributions. J Phys C Solid State 19(1845)
19. Rehr JJ, Albers RC (1990) Scattering-matrix formulation of curved-wave multiple-scattering theory: application to X-ray-absorption fine structure. Phys Rev B 41:8139
20. Hedin L (1965) New method for calculating 1-particle Green's function with application to electron-gas problem. Phys Rev 139:A796
21. Kas JJ et al (2007) Many-pole model of inelastic losses in X-ray absorption spectra. Phys Rev B 76:195116
22. Crozier ED, Rehr JJ, Ingalls R (1988) In: Koningsberger DC, Prins R (eds) X-ray absorption: principles, applications, techniques of EXAFS, SEXAFS, and XANES. Wiley, New York, pp 373–442
23. Dalba G, Fornasini P (1997) EXAFS Debye-Waller factor and thermal vibrations of crystals. J Synchrotron Radiat 4:243
24. Beni G, Platzman PM (1976) Temperature and polarization dependence of extended X-ray absorption fine-structure spectra. Phys Rev B 14:1514
25. Frenkel AI, Rehr JJ (1993) Thermal expansion and X-ray-absorption fine-structure cumulants. Phys Rev B 48:585
26. Bianconi A et al (1987) Specific intermediate-valence state of insulating 4f compounds detected by L3 X-ray absorption. Phys Rev B 35:806
27. Ankudinov AL, Bouldin CE, Rehr JJ, Sims J, Hung H (2002) Parallel calculation of electron multiple scattering using Lanczos algorithms. Phys Rev B 65:104107
28. Lundqvist BI (1967) Single-particle spectrum of degenerate electron gas: 1. Structure of spectral weight function. Phys Konden Mater 6:193
29. Lundqvist BI (1967) Single-particle spectrum of degenerate electron gas: 2. Numerical results for electrons coupled to plasmons. Phys Konden Mater 6:206
30. Hedin L, Lundqvist S (1970) Effects of electron-electron and electron-phonon interactions on the one-electron states of solids. Solid State Phys 23:1
31. Kas JJ et al (2009) Many-pole model of inelastic losses applied to calculations of XANES. J Phys Conf Ser 190:012009
32. Gulans A et al (2014) Exciting: a full-potential all-electron package implementing density-functional theory and many-body perturbation theory. J Phys Condens Matter 26:363202

33. Hudson E et al (1994) Near-edge sodium and fluorine K-shell photoabsorption of alkali-halides. Phys Rev B 49:3701
34. Sorini AP, Kas JJ, Rehr JJ, Prange MP, Levine ZH (2006) Ab initio calculations of electron inelastic mean free paths and stopping powers. Phys Rev B 74:165111
35. Powell CJ, Jablonski A (1999) Evaluation of calculated and measured electron inelastic mean free paths near solid surfaces. J Phys Chem Ref Data 28:19
36. Werner WSM (2001) Electron transport in solids for quantitative surface analysis. Surf Interface Anal 31:141
37. Nesvizhskii AI, Ankudinov AL, Rehr JJ (2001) Normalization and convergence of X-ray absorption sum rules. Phys Rev B 63:094412
38. Farges F, Brown GE, Rehr JJ (1996) Coordination chemistry of Ti(IV) in silicate glasses and melts: 1. XAFS study of titanium coordination in oxide model compounds. Geochim Cosmochim Acta 60:3023
39. Ankudinov AL, Rehr JJ (2005) Nonspherical potential, vibronic and local field effects in X-ray absorption. Phys Scr T115:24
40. Vila FD, Rehr JJ, Kas JJ, Nuzzo RG, Frenkel AI (2008) Dynamic structure in supported Pt nanoclusters: real-time density functional theory and X-ray spectroscopy simulations. Phys Rev B 78:121404
41. Fulton JL et al (2012) Near-quantitative agreement of model-free DFT-MD predictions with XAFS observations of the hydration structure of highly charged transition-metal ions. J Phys Chem Lett 3:2588
42. Vila FD, Rehr JJ, Kelly SD, Bare SR (2013) Operando effects on the structure and dynamics of Pt_nSn_m/γ-Al_2O_3 from ab initio molecular dynamics and X-ray absorption spectra. J Phys Chem C 117:12446
43. Rehr JJ, Ankudinov AL (2004) Solid state effects on X-ray absorption, emission and scattering processes. Radiat Phys Chem 70:453
44. Jorissen K, Rehr JJ (2010) Calculations of electron energy loss and X-ray absorption spectra in periodic systems without a supercell. Phys Rev B 81:245124
45. Fister TT et al (2008) Local electronic structure of dicarba-closo-dodecarboranes $C_2B_{10}H_{12}$. J Am Chem Soc 130:925
46. Gordon RA, Seidler GT, Fister TT, Nagle KP (2011) Studying low-energy core-valence transitions with bulk sensitivity using q-dependent NIXS. J Electron Spectrosc Relat Phenom 184:220
47. Kas JJ, Rehr JJ, Soininen JA, Glatzel P (2011) Real-space Green's function approach to resonant inelastic X-ray scattering. Phys Rev B 83:235114
48. Mattern BA, Seidler GT, Kas JJ, Pacold JI, Rehr JJ (2012) Real-space Green's function calculations of Compton profiles. Phys Rev B 85:115135
49. Pfalzer P et al (1999) Elimination of self-absorption in fluorescence hard-X-ray absorption spectra. Phys Rev B 60:9335
50. Booth CH, Bridges F (2005) Improved self-absorption correction for fluorescence measurements of extended X-ray absorption fine-structure. Phys Scr T115:202
51. Knoll GF (2010) Radiation detection and measurement. John Wiley & Sons, New York
52. Stern EA, Heald SM (1983) In: Koch EE (ed) Handbook of synchrotron radiation. North-Holland, New York, pp 995–1014
53. Kelly SD, Hesterberg D, Ravel B (2008) In: Ulery AL, Drees LR (eds) Methods of soil analysis: Part 5—Mineralogical methods. Soil Science Society of America, Madison, WI, pp 387–463
54. Bunker G (2010) Introduction to XAFS: a practical guide to X-ray absorption fine structure spectroscopy. Cambridge University Press, Cambridge
55. Calvin S (2013) XAFS for everyone. CRC Press, Boca Raton, FL
56. Newville M (2014). In: Henderson GS, Neuville DR, Downs RT (eds) Spectroscopic methods in mineralology and materials sciences, vol 78. Reviews in mineralogy and geochemistry. Mineralogical Society of America, pp 33–74

57. Newville M, Livins P, Yacoby Y, Rehr JJ, Stern EA (1993) Near-edge X-ray-absorption fine structure of Pb: a comparison of theory and experiment. Phys Rev B 47:14126
58. Rehr JJ, Mustre de Leon J, Zabinsky SI, Albers RC (1991) Theoretical X-ray absorption fine structure standards. J Am Chem Soc 113:5135
59. Newville M (2001) IFEFFIT: interactive XAFS analysis and FEFF fitting. J Synchrotron Radiat 8:322
60. Ravel B, Newville M (2005) ATHENA, ARTEMIS, HEPHAESTUS: data analysis for X-ray absorption spectroscopy using IFEFFIT. J Synchrotron Radiat 12:537
61. Newville M (2013) Larch: an analysis package for XAFS and related spectroscopies. J Phys Conf Ser 430:012007
62. Newville M (2001) EXAFS analysis using FEFF and FEFFIT. J Synchrotron Radiat 8:96
63. Newville M, Boyanov B, Sayers DE (1999) Estimation of uncertainties in XAFS data. J Synchrotron Radiat 6:264
64. Lytle FW, Sayers DE, Stern EA (1989) Report on the international workshop on standards and criteria in X-ray absorption spectroscopies. Physica B 158:701
65. Stern EA (1993) Number of relevant independent points in X-ray-absorption fine-structure spectra. Phys Rev B 48:9825
66. Henderson GS, de Groot FMF, Moulton BJ, Neuville DR, Downs RT (2014). In: Spectroscopic methods in mineralogy and materials sciences, vol 78, pp 75–138
67. Benfatto M, Della Longa S (2001) Geometrical fitting of experimental XANES spectra by a full multiple-scattering procedure. J Synchrotron Radiat 8:1087
68. Smolentsev G, Soldatov A (2006) Quantitative local structure refinement from XANES: multi-dimensional interpolation approach. J Synchrotron Radiat 13:19
69. Stavitski E, de Groot FMF (2010) The CTM4XAS program for EELS and XAS spectral shape analysis of transition metal L edges. Micron 41:687
70. Wilke M, Farges F, Petit PE, Brown GE, Martin F (2001) Oxidation state and coordination of Fe in minerals: an FeK-XANES spectroscopic study. Am Mineral 86:714
71. Berry AJ, Danyushevsky LV, O'Neill HSC, Newville M, Sutton SR (2008) Oxidation state of iron in komatiitic melt inclusions indicates hot Archaean mantle. Nature 455:960
72. Cottrell E, Kelley KA, Lanzirotti T, Fischer RA (2009) Water and the oxidation state of subduction zone magmas (vol 325, p 605, 2009). Science 326:798
73. Wasserman SR, Allen PG, Shuh DK, Bucher JJ, Edelstein NM (1999) EXAFS and principal component analysis: a new shell game. J Synchrotron Radiat 6:284
74. Beauchemin S, Hesterberg D, Beauchemin M (2002) Principal component analysis approach for modeling sulfur K-XANES spectra of humic acids. Soil Sci Soc Am J 66:83
75. Lerotic M et al (2005) Cluster analysis in soft X-ray spectromicroscopy: finding the patterns in complex specimens. J Electron Spectrosc Relat Phenom 144:1137
76. Lengke MF et al (2006) Mechanisms of gold bioaccumulation by filamentous cyanobacteria from gold(III)—chloride complex. Environ Sci Technol 40:6304
77. Ankudinov AL, Rehr JJ, Low JJ, Bare SR (2002) Theoretical interpretation of XAFS and XANES in Pt clusters. Top Catal 18:3
78. Rehr JJ, Vila FD (2014) Dynamic structural disorder in supported nanoscale catalysts. J Chem Phys 140:134701
79. Poiarkova A, Rehr JJ (1999) Multiple-scattering X-ray-absorption fine-structure Debye-Waller factor calculations. Phys Rev B 59:948
80. Poiarkova A, Rehr JJ (1999) Recursion method for multiple-scattering XAFS Debye-Waller factors. J Synchrotron Radiat 8:313
81. Krappe HJ, Rossner HH (2002) Bayes-Turchin approach to X-ray absorption fine structure data analysis. Phys Rev B 66:184303
82. Vila FD, Rehr JJ, Rossner HH, Krappe HJ (2007) Theoretical X-ray absorption Debye-Waller factors. Phys Rev B 76:014301
83. Gaussian 09. Gaussian, Inc., Wallingford, CT, 2009

84. Valiev M et al (2010) NWChem: a comprehensive and scalable open-source solution for large scale molecular simulations. Comput Phys Commun 181:1477
85. Neese F (2012) The ORCA program system. Wiley Interdiscip Rev Comput Mol Sci 2:73
86. Irikura KK, Johnson RD, Kacker RN (2005) Uncertainties in scaling factors for ab initio vibrational frequencies. J Phys Chem A 109:8430
87. Alecu IM, Zheng J, Zhao Y, Truhlar DG (2010) Computational thermochemistry: scale factor databases and scale factors for vibrational frequencies obtained from electronic model chemistries. J Chem Theory Comput 6:2872
88. Gonze X, Lee C (1997) Dynamical matrices, Born effective charges, dielectric permittivity tensors, and interatomic force constants from density-functional perturbation theory. Phys Rev B 55:10355
89. Gonze X (1997) First-principles responses of solids to atomic displacements and homogeneous electric fields: implementation of a conjugate-gradient algorithm. Phys Rev B 55:10337
90. Gonze X et al (2009) ABINIT: first-principles approach to material and nanosystem properties. Comput Phys Commun 180:2582
91. Kresse G, Furthmüller J (1996) Efficient iterative schemes for ab initio total-energy calculations using a plane-wave basis set. Phys Rev B 54:11169
92. Giannozzi P et al (2009) QUANTUM ESPRESSO: a modular and open-source software project for quantum simulations of materials. J Phys Condens Matter 21:395502
93. Salassa L et al (2009) Structure of $[Ru(bpy)_n(AP)_{(6-2n)}]^{2+}$ homogeneous complexes: DFT calculation vs. EXAFS. J Phys Conf Ser 190:012141
94. Frenkel D, Smit B (2002) Understanding molecular simulation. Academic, San Diego
95. Car R, Parrinello M (1985) Unified approach for molecular-dynamics and density-functional theory. Phys Rev Lett 55:2471
96. Dang LX (1992) The nonadditive intermolecular potential for water revised. J Chem Phys 97:2659
97. Dang LX, Chang TM (1997) Molecular dynamics study of water clusters, liquid, and liquid-vapor interface of water with many-body potentials. J Chem Phys 106:8149
98. Kryachko ES, Ludeña EV (1990) Energy density functional theory of many-electron systems. Kluwer Academic Publishers, Dordrecht
99. Giustino F (2014) Materials modelling using density functional theory: properties and predictions. Oxford University Press, Oxford
100. Frenkel AI et al (2014) Critical review: Effects of complex interactions on structure and dynamics of supported metal catalysts. J Vac Sci Technol A 32:020801

Part III
Sources and Measurement Methods for XAFS

Chapter 3
Synchrotron-Radiation Sources, X-ray Optics and Beamlines

Tomoya Uruga

3.1 Synchrotron-Radiation Sources

A synchrotron radiation (SR) source is one of the best light sources for XAFS measurements, which need an intense energy-tunable X-ray source with a wide range. Two types of SR sources are available: a storage ring and a linear accelerator. Sects. 3.1–3.3 describe the storage-ring source and associated beamlines. Chapter 4 describes an X-ray free electron laser (XFEL) as an advanced linear-accelerator source.

3.1.1 Bending-Magnet Source

The main characteristics of SR light emitted from a storage ring are high brightness, a very wide and continuous spectral range, high directionality, variable polarity, and a pulsed time structure [1, 2]. The origins of these characteristics are described in the following.

A schematic drawing of a storage ring is shown in Fig. 3.1. Electrons are accelerated up to close to the speed of light by a linear or ring accelerator and injected to the storage ring. In the storage ring, the electrons are subjected to a Lorentz force in the direction perpendicular to their direction of motion in the magnetic field of the dipole bending magnet (BM); as a result, they emit an electromagnetic wave (i.e., SR light). The electric field of the SR light from the

T. Uruga (✉)
Japan Synchrotron Radiation Research Institute, Spring-8, Sayo, Hyogo 679-5148, Japan

Innovation Research Center for Fuel Cells, The University of Electro-Communications, Chofu, Tokyo 182-8585, Japan
e-mail: urugat@spring8.or.jp

Y. Iwasawa et al. (eds.), *XAFS Techniques for Catalysts, Nanomaterials, and Surfaces*, DOI 10.1007/978-3-319-43866-5_3

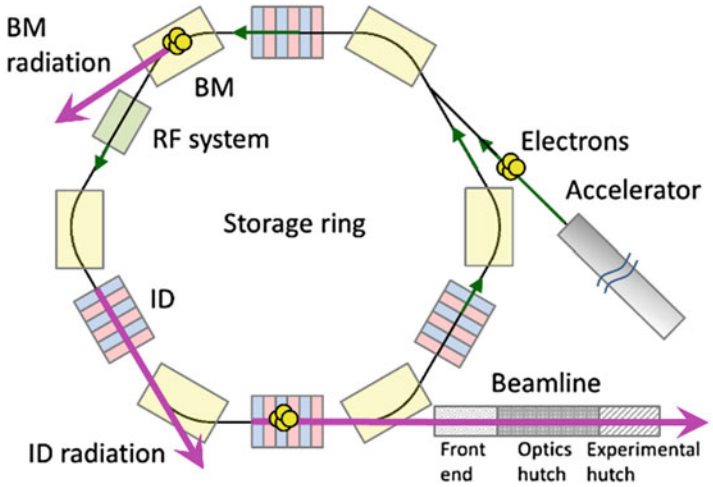

Fig. 3.1 Schematic drawing of a storage ring and beamline

Fig. 3.2 Schematic of BM radiation pattern

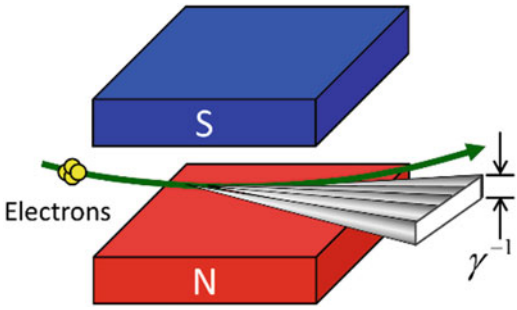

BM observed in the horizontal plane is polarized in the plane of acceleration, i.e., the horizontal plane. The SR pattern is compressed into a narrow cone in the direction tangential to the electron orbit due to a Lorentz compression of a relativistic effect (Fig. 3.2). The half-opening angle of the BM radiation in the vertical direction is γ^{-1}, which is called the "photon natural emission angle," and γ is a Lorentz factor given by

$$\gamma = \left[1 - (v/c)^2\right]^{-1/2} = E/m_0c^2 = 1957E \qquad [\text{GeV}], \tag{3.1}$$

where c is the speed of light, and v, m_0, and E are the speed, rest mass, and energy of the electron, respectively. In the case of $E = 8$ GeV, $\gamma^{-1} = 6.4 \times 10^{-5}$ rad, which indicates the BM radiation is highly directional in the vertical direction. On the other hand, the BM radiation is emitted along a curved electron obit, so its opening angle in the horizontal direction is determined by a slit opening installed in the downstream section and is typically in the order of milliradians (Fig. 3.2).

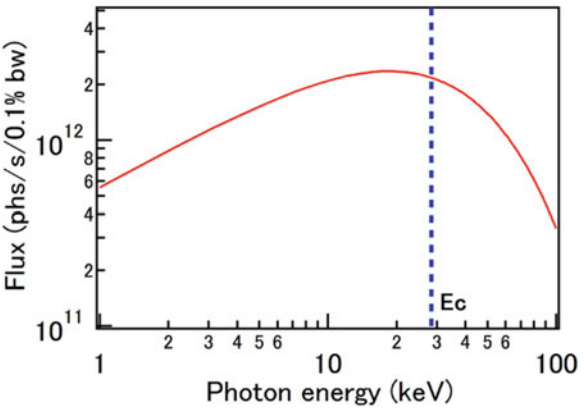

Fig. 3.3 X-ray flux of bending magnet BM1 at SPring-8 calculated using a synchrotron radiation calculation code SPECTRA [3]. Beam acceptance; 200 (h) and 100 (v) μrad

The SR light emitted from the electrons is observed as a pulse-like electromagnetic wave by an observer standing in the direction tangential to the electron orbit. The spectral distribution of SR light is calculated by a Fourier transform of the time structure of the electromagnetic wave, as shown in Fig. 3.3. The wavelength of radiation emitted from the moving electron is shifted to shorter values due to the Doppler effect. Thus, a storage ring with higher energy emits SR light with higher energy. The critical energy of BM radiation, E_c, which is defined as the energy that divides the emitted power into equal halves, is given by

$$E_c \ [\text{keV}] = 2.22E^3 \ [\text{GeV}]/R \ [\text{m}] = 0.665E^2 \ [\text{GeV}]B_0 \ [\text{T}], \tag{3.2}$$

where R is the radius of the electron orbit, and B_0 is the magnetic flux density of the BM. In the case of SPring-8 ($E = 8$ GeV, $B_0 = 0.679$ T), $E_c = 28.9$ keV. The maximum energy applicable to XAFS measurements is about three to four times E_c, which is higher than 100 keV at SPring-8.

3.1.2 *Insertion-Device Sources*

An insertion device (ID) consists of a linearly arranged periodic magnet array (Fig. 3.4) installed in the straight section between the BMs (Fig. 3.1). The electrons are made to wiggle by periodic accelerations due to the spatially periodic magnetic field. SR is generated at each acceleration point, and generated SRs are summed to generate an extremely intense light. In the case of the magnet array shown in Fig. 3.4, the electrons wiggle in a sinusoidal manner. The deflection angle of an electron, φ, is given by

$$\varphi = K\gamma^{-1} \cos(2\pi z/\lambda_u), \tag{3.3}$$

where λ_u is the period length of the magnet, and K is defined by

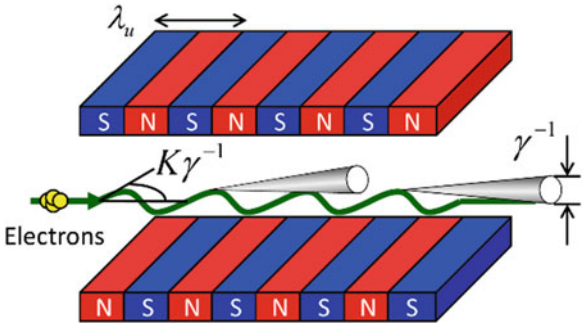

Fig. 3.4 Schematic of magnet array and ID radiation pattern

$$K \equiv 93.37 B_0 \ [\mathrm{T}] \lambda_u \ [\mathrm{m}]. \tag{3.4}$$

K is called the K-parameter (or deflection parameter) and determines the maximum deflection angle of the electron, $K\gamma^{-1}$. The characteristics of the radiation emitted by the ID strongly depend on the value of K, which can be controlled by the magnetic-field strength. Accordingly, two types of ID are available: wiggler ($K \gg 1$) and undulator ($K \lesssim 1$).

In the case of the undulator, the electron beam wiggles with a deflection angle close to or smaller than the photon natural emission angle, γ^{-1}. In the case of $K \ll 1$, the radiation emitted by the same electron beam at each period of the magnetic field interferes. The amplitude of the emitted radiation thus add up coherently, thereby increasing the radiation intensity N^2-fold (three to four orders) higher than the BM radiation (where N is the number of periods). The observed electromagnetic field of the radiation is close to a sinusoidal wave of the same period as that of the magnet; therefore, the spectrum obtained by its Fourier transform is monochromatic. In the case of $K \sim 1$, only the radiation emitted at a deflection angle smaller than γ^{-1} can be observed. Accordingly, the observed electromagnetic field is a modified sinusoidal wave, and the spectrum consists of harmonics as shown in Fig. 3.5. Energy of the nth harmonic, E_n, is given by

$$E_n = 4\pi hc\gamma^2 n\left(1 + K^2/2\right)^{-1} {\lambda_u}^{-1}, \tag{3.5}$$

E_n can be controlled by the magnet gap of the undulator. When narrowing the magnet gap, K increases in proportional to B_0 (Eq. 3.4), and then E_n decreases. The energy bandwidth of the undulator radiation, $\Delta E/E$ is usually 2–3 %. ΔE is a few-hundred electronvolts at 10 keV, which is adequate for XANES measurement but not for EXAFS measurement.

The Quick EXAFS and energy-dispersive EXAFS measurements presented in Sect. 10.1 and Chap. 11 need energy bandwidth wider than 1 keV. A tapered undulator was thus developed to adjust the energy bandwidth by tuning the taper of the gap of the magnet array (see Sect. 10.1). The coherency of the undulator radiation, however, decreases due to the disturbed magnetic-field periodicity.

In the wiggler, the electron beam wiggles with a large deviation angle, so only the radiation emitted at poles can be observed. The radiation intensities, not amplitudes, add up, thereby increasing the radiation intensity N-fold (a multi-pole

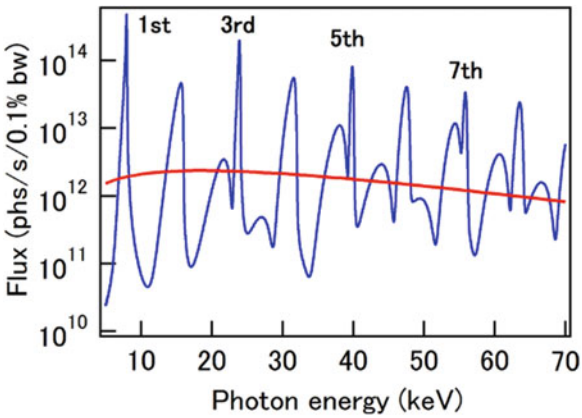

Fig. 3.5 X-ray flux of BM1 (*red*) and undulator (*blue*) at SPring-8. $K = 1.66$, $\lambda_u = 32$ mm, beam acceptance; 17 (h) and 17 (v) μrad

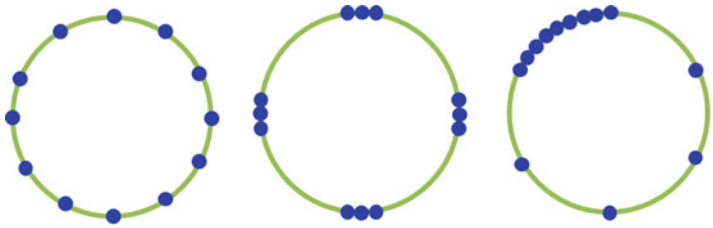

Fig. 3.6 Schematic of filling patterns of the electron bunches at SPring-8

wiggler). The observed electromagnetic field is a periodic positive-and-negative pulse train, so the spectrum is similar to that of BM (Fig. 3.3). As a result, bright and spectrally continuous light with short wavelengths is obtained. When increasing B_0 more than that of the BM by narrowing the magnet gap, E_n shifts to high (Eq. 3.2). Some compact or mid-class SR facilities have installed multi-pole wigglers in XAFS beamlines as an energy shifter.

The characteristics of the SR light mentioned above correspond to the case of an ideal electron beam in the ring. The actual electrons run in groups and have a finite spatial, angular, and energy spread, which influence the characteristics of the SR light. In the accumulation ring, a specific number of the electron population (bunch) runs at specific time intervals. A pulsed SR light is emitted at this time interval. Filling patterns of the electron bunch (Fig. 3.6) are designed for the specific time-resolved measurements described in Sect. 13.3.

3.2 X-Ray Optics

The XAFS measurement is conducted by measuring X-ray absorption accurately at X-ray energies around the absorption edge of the target element. The requirements for measuring high-quality XAFS spectra are narrow X-ray-energy bandwidth

(high energy resolution), low harmonic X-rays contaminant incident on the sample, adequate beam size for the measurement, a stable and low-noise measurement system, and a homogeneous sample. Most XAFS beamlines are constructed with the aim of satisfying the first four requirements. In many cases, the quality of the spectra is determined by sample preparation. The beamline design required for accurate XAFS measurement is described in the following sections.

SR beamlines consist of a light source, a front end section, an optics hutch, and experimental hutches (Fig. 3.1). The beam specifications, such as energy, size, and higher harmonics amounts, are adjusted to accommodate XAFS measurement using X-ray optics, such as a monochromator and a mirror.

3.2.1 Monochromator

The monochromator diffracts monochromatic X-rays of selected energy by adjusting the inclination angle of the net plane of the crystal (the angle of diffraction), θ_B, according to Bragg's low (Eq. 3.6) [2].

$$2d \ [\text{nm}] \sin\theta_B = 1.2398/E \ [\text{keV}], \tag{3.6}$$

where d is lattice spacing of the crystal (d-spacing). A single crystal silicon has been most widely used for the monochromator crystal, since it has excellent characteristics, such as good crystal perfection, good thermal property, and large crystal size. The energy bandwidth (energy resolution) of the diffracted beam is calculated from Eq. (3.6) and given by

$$\Delta E/E = \Delta\theta \cot\theta_B \tag{3.7}$$

$$\Delta\theta \approx \left[\Delta\theta_D{}^2 + \Delta\theta_I{}^2\right]^{1/2} \tag{3.8}$$

where $\Delta\theta_D$ is intrinsic diffraction width of the crystal, and $\Delta\theta_I$ is divergence angle of the incident beam. To achieve high energy resolution, both $\Delta\theta_D$ and $\Delta\theta_I$ have to be small. Higher-order net planes have smaller $\Delta\theta_D$ and realize higher energy resolution, but lower diffracted-beam intensity. Many XAFS beamlines operated in the hard-X-ray region use Si(1 1 1) crystal based on the diffracted-beam intensity with $\Delta E/E \lesssim 2 \times 10^{-4}$.

X-ay beam position must be kept fixed on the sample during XAFS scan. Accordingly, a conventional XAFS monochromator uses double crystals in parallel arrangement (double crystal monochromator, DCM) (Fig. 3.7). In the former, the position of the first or second crystal is adjusted to fix the exit beam height, h, during the energy scan according to Eq. (3.9) as

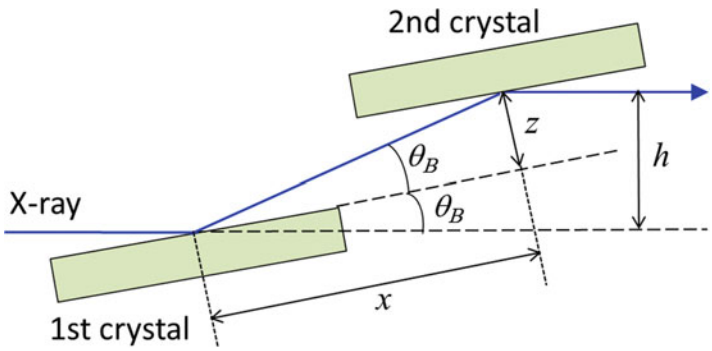

Fig. 3.7 Schematic layout of DCM crystals

$$x = h(2\sin\theta_B)^{-1}, \qquad z = h(2\cos\theta_B)^{-1} \tag{3.9}$$

To cover a wide energy range, switching mechanisms of multiple crystal pairs or net planes of the crystal are installed. The first crystal is usually mounted on a metal block cooled by water or liquid nitrogen to withstand the heat load of the SR.

3.2.2 Mirror

An X-ray mirror utilizes the total reflection by a material surface. At the interface of a vacuum and a material with refractive index n, the critical angle of total reflection, θ_c, is deduced by Snell's law, given by

$$\cos\theta_c = n = 1 - \delta + i\beta. \tag{3.10}$$

In the case of neglecting an absorption factor,

$$\theta_c \approx (2\delta)^{1/2} \approx 20\rho^{1/2}\mathrm{E}^{-1} \ \ (\mathrm{mrad}) \ \ \theta_c \ll 1 \tag{3.11}$$

where ρ is the weight density of the material (g/cm^3). In the hard X-ray region, δ is 10^{-4}–10^{-5}, so θ_c is 1–10 mrad. Thus, the mirror should be long to accept the SR light, such as 1 m. The critical energy of the mirror at the mirror glancing angle of θ_i is given by

$$E_{Mc} \approx 20\rho^{1/2}\theta_i{}^{-1} \tag{3.12}$$

The surface of the mirror substrate, such as SiO_2 and Si, is highly polished for high reflectivity and coated with high-weight-density materials, such as platinum ($\rho = 21.4$ g/cm^3) and rhodium ($\rho = 12.4$ g/cm^3). In the XAFS beamline, rhodium is usually used because platinum L-absorption edges disturb the XAFS spectra from

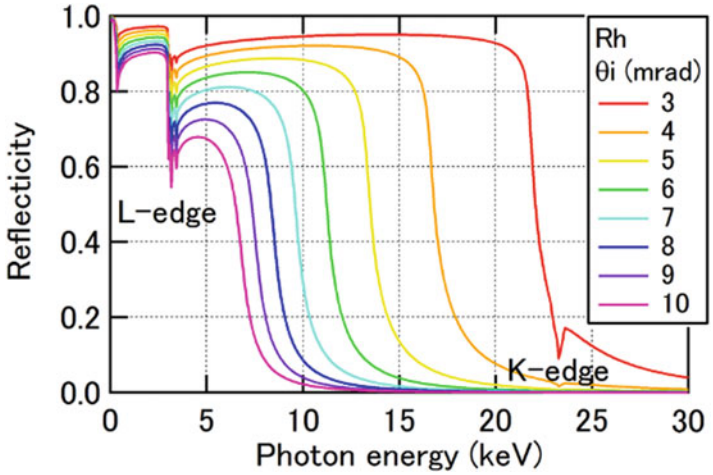

Fig. 3.8 Calculated reflectivity of Rh-coat mirror depending on glancing angle

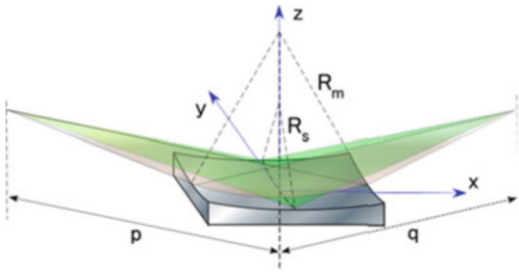

Fig. 3.9 Schematic of toroidal mirror

11.5 to 15 keV. The calculated reflectivity of the Rh-coat mirror vs. energy is shown in Fig. 3.8.

The mirror is used mainly for three purposes: focusing, collimation, and higher-energy rejection. The mirror surface for focusing and collimation is shaped as a one- or two-dimensional figured shape. A toroidal mirror for two-dimensional focusing is shown in Fig. 3.9. The toroidal shape is approximately realized by bending a sagittal cylinder mirror in the meridional direction (pseudo toroidal mirror). The radiuses of curvature in the meridional and sagittal directions are given by Eqs. (3.13) and (3.14), respectively,

$$R_{\mathrm{m}} = 2\sin\theta_{\mathrm{i}}{}^{-1}\left(p^{-1}+q^{-1}\right)^{-1}, \tag{3.13}$$

$$R_{\mathrm{s}} = 2\sin\theta_{\mathrm{i}}\left(p^{-1}+q^{-1}\right)^{-1}, \tag{3.14}$$

where p and q are distances from source to mirror and from mirror to focus, respectively. In the case of a collimation mirror, $q = \infty$. In the case of a hard-X-ray conventional mirror, $p = 15 - 50$ m, $q = 5 - 20$ m, and $\theta_{\mathrm{i}} = 1 - 10$ mad, so $R_{\mathrm{m}} = 0.1 - 10$ km and $R_{\mathrm{s}} = 30 - 100$ mm.

In the case of an XAFS beamline, rejection of the higher harmonics diffracted by the monochromator is the most important requirement. Two methods are applied to meet this requirement. One is to detune the parallelism of the double crystal of the monochromator so as to reduce the diffracted beam flux of higher harmonics due to the difference of intrinsic diffraction width. The other is to use the critical energy of the mirror. A double mirror effectively and stably reduces the higher harmonics to less than 10^{-4}. The beamline and its optics are described in the next sections.

3.3 Beamline

3.3.1 Bending Magnet and Wiggler Beamline

The designs of the BM and wiggler beamlines are similar, since their spectral shapes are almost the same. The schematic layout of the main optics in BM beamline BL01B1 at SPring-8, which is dedicated to conventional XAFS measurement in a wide energy range, is shown in Fig. 3.10 [4]. The DCM has a switching mechanism of the net plane of the crystal between Si(1 1 1), (3 1 1) and (5 1 1) to cover an energy range from 3.8 to 113 keV. BL01B1 has two mirrors installed upstream and downstream of the DCM. Both mirrors are meridional bent-flat types. The first mirror is used for beam collimation to achieve high energy resolution, and the second mirror is used for beam focusing at the sample in the vertical direction. Both mirrors are also used for the higher harmonic rejection. The glancing angle and bending radius of both mirrors are adjusted according to the critical energy of the X-rays. A change in the glancing angle of the first mirror necessitates a change in the height of the downstream components, sample and detectors.

In the BM beamline, the horizontal beam width at the mirror is more than several tens millimeters. Accordingly, a vertical reflecting (pseudo) toroidal mirror is often used for accepting a wide beam and conducting two-dimensional focusing at the sample.

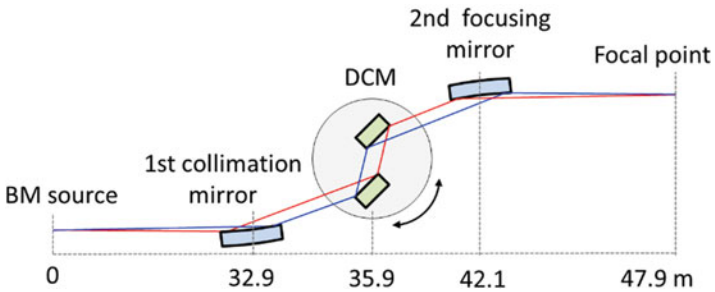

Fig. 3.10 Schematic layout of main optics in BM beamline BL01B1 at SPring-8

3.3.2 Undulator Beamline

An undulator XAFS beamline has the following features differing from those of a BM or wiggler beamline. First, the beam divergence, both in the vertical and horizontal directions, is quite small, enabling the monochromator and mirror to take both vertical and horizontal deflection geometries. The beam divergence in the vertical direction is close to the slope error of the mirror surface, so a collimation mirror is not needed. A stripe-coat mirror can be used to switch coating materials, such as platinum and rhodium. Second, the beam power density is quite high. In most cases, the first crystal of the DCM is cooled by liquid nitrogen. Third, the undulator gap is tuned at each measurement point in synchronization with the Bragg angle of the monochromator crystal, since the energy bandwidth of the undulator radiation is narrow. Fourth, the source size and divergence is small and useful for formation of a high-flux-density micro/nano X-ray beam by using focusing optics, such as a Kirkpatrick-Baez mirror and a Fresnel zone plate (described in Chap. 13).

The undulator beam has many advantages regarding beam quality (as mentioned above), which is indispensable for advanced XAFS measurements, such as fast time-resolved XAFS, micro/nano XAFS using a focused beam, polarized XAFS, and high energy resolution XAFS (described in Part 4). Most conventional XAFS measurements, however, do not need a high-quality undulator beam. In some cases, sample damage due to intense undulator X-ray beam irradiation is a serious problem.

References

1. Koch EE, Eastman DE, Farges Y (1983) Handbook of synchrotron radiation, vol 1a. North-Holland Publishing Company, Amsterdam, Chapter 1
2. Als-Nielsen J, McMorrow D (2011) Elements of modern X-ray physics, 2nd edn. John Wiley & Sons, England, Chapter 2
3. Tanaka T, Kitamura H (2001) SPECTRA: a synchrotron radiation calculation code. J Synchrotron Rad 8:1221
4. Uruga T, Tanida H, Yoneda Y, Takeshita K, Emura S, Takahashi M, Harada M, Nishihata Y, Kubozono Y, Tanaka T, Yamamoto T, Maeda H, Kamishima O, Takabayashi Y, Nakata Y, Kimura H, Goto S, Ishikawa T (1999) The XAFS beamline BL01B1 at SPring-8. J Synchrotron Rad 6:143

Chapter 4
XFEL

Makina Yabashi and Tetsuo Katayama

The twenty-first century saw the arrival of an exciting new light source, X-ray free electron lasers (XFELs). XFELs generate ultra-brilliant, coherent, and femtosecond X-ray pulses. X-ray spectroscopy is one of the most promising applications using XFEL, allowing one to directly probe ultrafast changes in electronic states and geometric structures during real chemical reactions at angstrom and femtosecond resolution using X-ray absorption and/or emission measurements.

In 2009, the Linac Coherent Light Source (LCLS) at the SLAC National Accelerator Laboratory in the USA generated the first FEL light in the hard X-ray region based on a self-amplified spontaneous emission (SASE) scheme [1]. In 2011, the SPring-8 Compact Angstrom free electron LAser (SACLA) at the SPring-8 complex in Japan produced the shortest wavelength XFEL light using a compact-scale facility [2–4]. Table 4.1 shows typical parameters for SACLA electron and photon beams. Every single pulse contains $>10^{11}$ X-ray photons within a sub-mm beam diameter at the sample point. The beam size can be further reduced to 1 μm or even smaller using state-of-the-art reflective focusing optics [5, 6]. The spectral width provided by the SASE scheme is typically ~50 eV in full width at half maximum (FWHM) at 10 keV. The temporal duration of an XFEL pulse can be as short as several femtoseconds, which enables one to conduct time-resolved measurements in the femtosecond regime by combining ultrafast optical lasers. Although possible arrival timing jitters between the XFEL and optical laser pulses can deteriorate the temporal resolution, recently developed techniques to measure the arrival jitter in every pulse can provide higher temporal resolution of the order of 10 fs for example [7, 8].

M. Yabashi (✉)
RIKEN SPring-8 Center, Sayo, Hyogo 679-5148, Japan
e-mail: yabashi@spring8.or.jp

T. Katayama
Japan Synchrotron Radiation Research Institute, Sayo, Hyogo 679-5198, Japan

Y. Iwasawa et al. (eds.), *XAFS Techniques for Catalysts, Nanomaterials, and Surfaces*, DOI 10.1007/978-3-319-43866-5_4

Table 4.1 Typical electron and photon beam parameters for SACLA BL3

Electron beam energy	5.1–8.5 GeV
Repetition rate	30 Hz (60 Hz max.)
Electron bunch duration	20 fs
Undulator period	18 mm
Undulator parameter	<2.2
Photon energy	4.0–20 keV
Saturation power	6–60 GW
FEL pulse energy	~0.5 mJ @ 10 keV (~3×10^{11} photons/pulse)
Photon pulse duration	2–10 fs

For performing X-ray absorption spectroscopy (XAS) experiments using an XFEL source, one can consider two complementary schemes: a wavelength scanning method and a dispersive method, similar to those used in synchrotron light sources. The former method, combined with fluorescence detection, provides a high sensitivity to small changes of X-ray absorbance in shallow volumes interacting with optical lasers [9, 10]. The latter method is useful for achieving an ultimate temporal resolution with simultaneous detection of the whole spectrum. Although the bandwidth of the SASE-XFEL light matches that required for the latter scheme, the random, stochastic spikes in the spectrum, which originate from the initial density modulations in the electron beam with typical widths from ~0.01 to ~1 eV [11], present considerable complications to data analysis, especially in the normalization processes. To overcome this difficulty, Katayama et al. developed a *dual-beam* dispersive XAS scheme [12], which combines a transmission-grating beam splitter and a dispersive spectrometer that consists of an elliptical mirror, a flat crystal analyzer, and an imaging detector [13]. Here, the positive first order diffraction of the grating was dedicated for measuring the XAS signal with samples, while the negative first order diffraction was used for normalization, as shown in Fig. 4.1. This scheme enabled sufficient sensitivity of the order of 10^{-3} for the absorbance change using pump laser excitation [14].

X-ray emission spectroscopy (XES) is also a powerful technique to understand the charge and spin dynamics in the femtosecond regime. For this purpose, a dispersive scheme in a von Hamos geometry is preferable for detecting the whole emission spectrum [15]. Since most XES measurements are time consuming, development of emission spectrometers with higher resolution and efficiency would contribute to enhanced data quality.

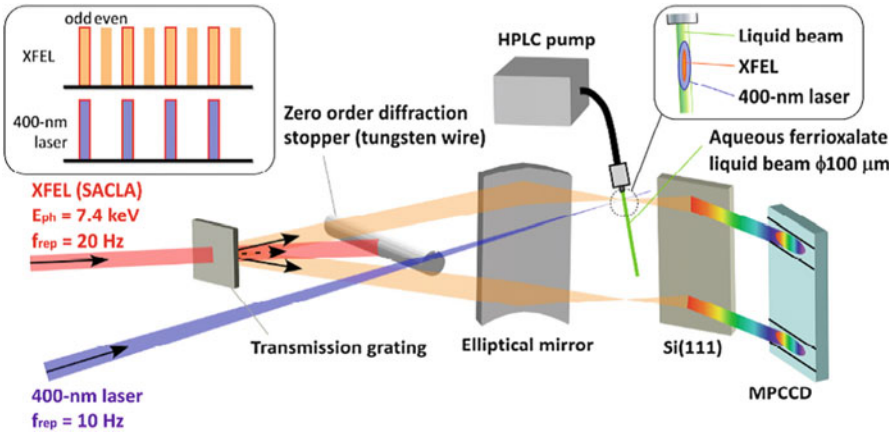

Fig. 4.1 Schematic of the dual-beam dispersive XAS method [reprinted with permission from the Optical Society, Optics Express, Vol. 22, 2014, pp. 1105–1113, Femtosecond time-resolved X-ray absorption spectroscopy of liquid using a hard X-ray free electron laser in a dual-beam dispersive detection method, Obara et al., Fig. 4.1, copyright]

References

1. Emma P et al (2010) First lasing and operation of an ångstrom-wavelength free-electron laser. Nat Photonics 4:641–647
2. Ishikawa T et al (2012) A compact X-ray free-electron laser emitting in the sub-ångström region. Nat Photonics 6:540–544
3. Tono K et al (2013) Beamline, experimental stations and photon beam diagnostics for the hard x-ray free electron laser of SACLA. New J Phys 12:083035
4. Yabashi M, Tanaka H, Ishikawa T (2015) Overview of the SACLA facility. J Synchrotron Radiat 22:477–484
5. Yumoto K et al (2013) Focusing of X-ray free-electron laser pulses with reflective optics. Nat Photonics 7:43–47
6. Mimura H et al (2014) Generation of 10^{20} W cm^{-2} hard X-ray laser pulses with two-stage reflective focusing system. Nat Commun 5:3539
7. Harmand M et al (2013) Achieving few-femtosecond time-sorting at hard X-ray free-electron lasers. Nat Photonics 7:215–218
8. Sato T et al (2015) Highly efficient arrival timing diagnostics for femtosecond X-ray and optical laser pulses. Appl Phys Express 8:012702
9. Lemke HT et al (2013) Femtosecond X-ray absorption spectroscopy at a hard X-ray free electron laser: application to spin crossover dynamics. J Phys Chem 117:735–740
10. Ogi Y et al (2015) Ultraviolet photochemical reaction of [Fe(III)(C2O4)3]3− in aqueous solutions studied by femtosecond time-resolved X-ray absorption spectroscopy using an X-ray free electron laser. Struct Dyn 2:034901
11. Saldin EL, Schneidmiller EA, Yurkov MV (1999) The physics of free electron lasers. Springer, Berlin
12. Katayama T et al (2013) Femtosecond x-ray absorption spectroscopy with hard x-ray free electron laser. Appl Phys Lett 103:131105
13. Inubushi Y et al (2012) Determination of the pulse duration of an X-Ray free electron laser using highly resolved single-shot spectra. Phys Rev Lett 109:144801

14. Obara Y et al (2014) Femtosecond time-resolved X-ray absorption spectroscopy of liquid using a hard X-ray free electron laser in a dual-beam dispersive detection method. Opt Express 22:1105–1113
15. Zhang W et al (2014) Tracking excited-state charge and spin dynamics in iron coordination complexes. Nature 509:345–348

Chapter 5
Measurements and Detectors

Masaharu Nomura

5.1 Transmission Measurement

XAFS spectra are measured in several modes such as transmission, fluorescence, and electron yield. Transmission mode is the basic of XAFS and is usually used to rather concentrated samples. The experimental setup is very simple as shown in Fig. 5.1. Two ionization chambers are put in a line and a sample is placed between them. The first ionization chamber is used to measure the intensity of the incoming X-rays (I_0) and the second one is used to measure that passed through the sample (I or I_1). The apparent absorbance is calculated as $\mu t = \ln(I_0/I)$. The detection efficiency for I_0 is 10–25 % and slightly lower than 100 % for I.[1] Length, composition, and pressure of the fill gas should be changed to meet these conditions. Sometimes the third ionization chamber (I_2) is used for the sake of energy calibration. In this case a reference sample is placed between I_1 and I_2 ionization chambers.[2] This technique is useful to discuss the small shift of absorption edge.

The structure of ionization chamber is simple, that is, two electrodes are aligned in parallel in a sealed box with two thin windows and the box is filled with a gas or a mixture of gases. X-rays are absorbed by atoms in the fill gas, ionizing them and forming electron–ion pairs. The emitted electrons ionize atoms in the fill gas. Typically 20–30 eV is required to produce an electron–ion pair in average.[3] By measuring the electron or ion current, we can know the X-ray intensity. Since the

[1] This is to maximize the detection efficiency for the X-rays of interest and minimize it for its higher orders.

[2] It is desirable to minimize the solid angle that the ion chambers see the sample so as to minimize the detected intensity of fluorescent X-rays from the reference sample.

[3] The value changes with the composition of the fill gas.

M. Nomura (✉)
High Energy Accelerator Research Organization, KEK, Tsukuba 305-0801, Japan
e-mail: masaharu.nomura@kek.jp

Y. Iwasawa et al. (eds.), *XAFS Techniques for Catalysts, Nanomaterials, and Surfaces*, DOI 10.1007/978-3-319-43866-5_5

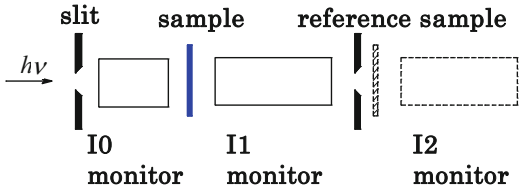

Fig. 5.1 Typical setup for transmission XAFS. Reference sample and I_2 monitor are optional

ion and electron recombine easily, electric field of ca. 1 kV/cm or more is applied between two electrodes to prevent recombination. If the electric field is not sufficient, nonnegligible part of electrons and ions recombines and the degree of recombination changes as functions of X-ray flux and energy, thus losing the linearity of the detection system. When the electric field is not sufficient, the output current increases with increasing the applied electric field. The output current becomes constant when enough high field is applied. The output current becomes fairly stable if twice high field is applied.

Ripples in high voltage power supply used to apply electric field become a source of noise, and thus very low noise power supply is required. The surface of insulators used in ionization chamber should be kept clean and dry since leakage current also becomes the origin of noise. Output current from an ionization chamber is sent to a fast current amplifier, the output voltage from it is converted to digital signal by using Analog-to-Digital converter (ADC) or a pair of Voltage-to-Frequency (V/F) converter and a scaler (pulse counter). The longer the time constant of the current amplifier, the smaller the noise. Thus, it should be carefully selected, especially when quick scanning XAFS is used.

Preparing uniform sample with appropriate absorbance is the most important point when measuring XAFS in transmission mode. X-rays pass through the thin part of sample is less absorbed thus gives incorrect μt in total [1]. It is recommended to prepare some samples of different thickness and compare their χ. If the amplitudes of χ are different, more careful sample preparation is required.

If the linearity of the detection system is good, μt signal becomes continuous even before and after beam injection. However, users cannot experience beam injections in recent synchrotron facilities since top-up injection is adopted. In such cases a simple performance test described below becomes useful. When a sample is placed before the entrance slit in place of the usual sample position, there should not appear any absorption edge in the XAFS spectrum. However, sometimes apparent "edge" is observed on the spectrum as shown in Fig. 5.2. If it is observed, one or some of the following reasons are suspected.

(a) nonlinearity of the detection system,
(b) improper offset adjustment of the detection system,
(c) significant higher order content in the incoming X-ray beam.

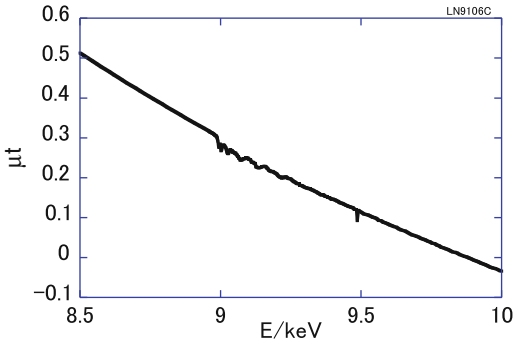

Fig. 5.2 Apparent edge and glitch observed when 18 μm thick copper foil is placed before the entrance slit

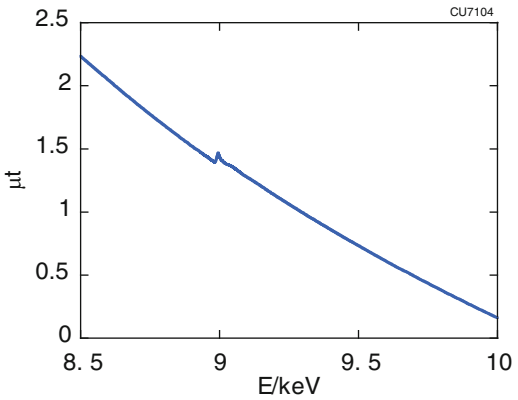

Fig. 5.3 XAFS spectrum of 10 mmol dm^{-3} Cu aq. Measured in transmission mode

5.2 Fluorescence

When the concentration of the element of interest becomes low (ex. 10 mmol dm^{-3} Cu aq.), it becomes hard to extract correct χ signal from transmission mode measurements (Fig. 5.3). In such cases, fluorescent mode XAFS that is to measure the intensity of fluorescent X-ray from the element of interest in place of transmitted X-ray becomes effective [2]. Fluorescence yield (FY) mode can be applied to a thin, concentrated sample and a dilute, thick sample. In these cases, the penetration depth of X-rays does not change significantly, and thus, observe the same sample depth within an XAFS spectrum. Thin metal layer on a substrate is a former example and dilute solutions, impurities in a sample are the latter example. Thus concentrated bulk samples should not be measured with fluorescent detection mode. The major source of noise (N) in fluorescence XAFS is statistical variation of detected photons, which includes the variation of both the fluorescence photons of interest (S) and background photons (B). The S/N ratio becomes $S/(S+B)^{1/2}$. In some cases such as biological samples, S/B becomes less than 0.01, and thus, it is very important to isolate the fluorescence signal.

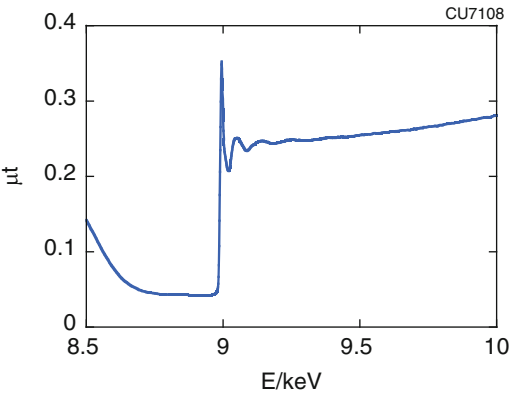

Fig. 5.4 XAFS spectrum of 10 mmol dm^{-3} Cu aq. Measured in fluorescent detection mode

A fluorescent ion chamber ($\phi 8.25$ cm $\times$ 3 cm)[4] is often used combined with filter and a slit assembly [3]. The principle of the fluorescent ion chamber is the same as that used in transmission mode but usually lower electric field is applied since the flux density of the fluorescent X-ray is much lower than that of incoming one. A filter is placed to absorb the scattered X-rays while passing the fluorescent X-ray from the sample. Z-1 filter (Z is the atomic number of the element of interest in the sample) is often used, but there are some possibilities for heavy elements and no appropriate one for light elements. When scattered X-ray is absorbed by the filter, fluorescent X-ray is emitted from it. A slit assembly is used to minimize it detected by the ion chamber. Figure 5.4 shows the XAFS spectrum of the same sample as shown in Fig. 5.3 taken with a fluorescent ion chamber with an Ni filter.

Combination of the filter and slit assembly is fairly powerful but cannot remove the scattered X-rays well when the scattered X-ray is much intense than the fluorescent one. In such cases, more powerful detection system is required. When a semiconductor absorbs an X-ray photon, electron–hole pairs are produced. The typical energy to produce it is ca. 3 eV in the case of Ge. Since the produced charge is one order larger than that in ionization chamber, each pulse signal produced by an X-ray photon can be handled separately. In this case, the pulse height of the signal reflects the energy of absorbed X-ray photon, and thus can distinguish the fluorescent signal and scattered one by using analog electronics or digital signal processor. Typical energy resolution (ΔE) is 130–300 eV for 5.9 keV X-ray photon (E) according to the size of the detector and shaping time of signal processing electronics. Pure Ge detector is usually used since it has high detection efficiency even for high energy X-rays and gives fairly good energy resolution [4]. Recently, silicon drift detector (SDD) is also used [5] since this is less expensive than Ge detector and easier to use. But its detection area is rather small, and the detection efficiency decreases to 50 % at 15 keV and 14 % at 25 keV because of low absorption constant and thin (ca. 0.3 mm) detection layer.

[4] It is sometimes called as "Lytle detector" according to the developer's name.

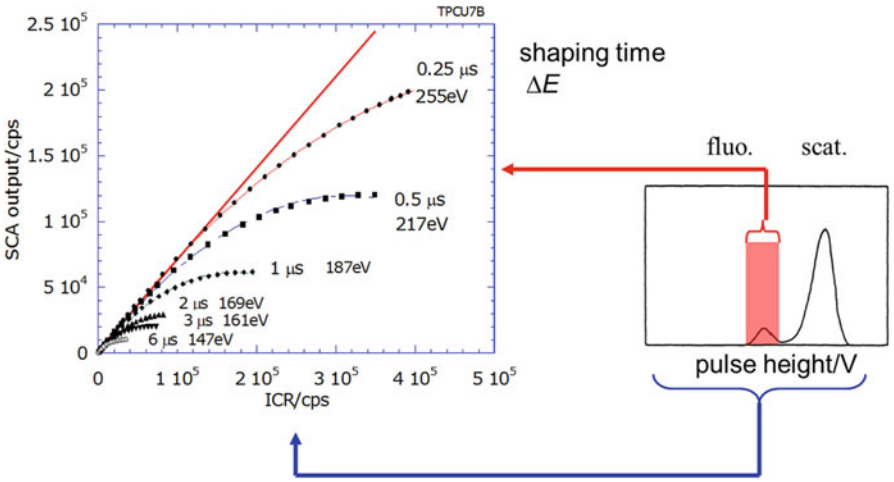

Fig. 5.5 Schematic pulse height distribution (*right*) and relative throughput curves as functions of the shaping time and ICR (*left*). ICR corresponds to the total signal in the right scheme and SCA output corresponds to the fluorescent signal

Figure 5.5 shows the schematic pulse height distribution (PHD) from Ge detector or SDD and the output signal rate of fluorescence as a function of incoming flux for various shaping times. PHD is a histogram of output pulses as a function of the pulse height. ICR (Incoming Count Rate)[5] corresponds to the total counting rate including the fluorescence and scattering signal, which corresponds to the integrated area of the right scheme. Output signal corresponds to the fluorescence signal intensity, which corresponds to the colored peak area. The output signal does not linearly respond to ICR; this is called as counting loss. This is due to that signal processing electronics cannot process the next signal for certain period after it processes a signal (dead time). The shorter shaping time (faster electronics) gives closer response to a linear line but gives worse energy resolution; the counting rate and the energy resolution are trade-off. The difference between the true counting rate and apparent one is called as counting loss. Since these curves reproduce well under certain condition, the original count rate can be calculated by using the ICR signal and output signal. Two fluorescent XAFS spectra are shown in Fig. 5.6a. One is the raw data which encountered beam injection while measuring a spectrum and gave rise to show discontinuity in the spectrum. When it is corrected for counting loss, the spectrum becomes continuous. Actually $k^3\chi$ signal continues as shown in Fig. 5.6b. As shown above, the correction for counting loss is inevitable except when the total counting rate is very low.

[5] It is also called as CRM (Count Rate Meter).

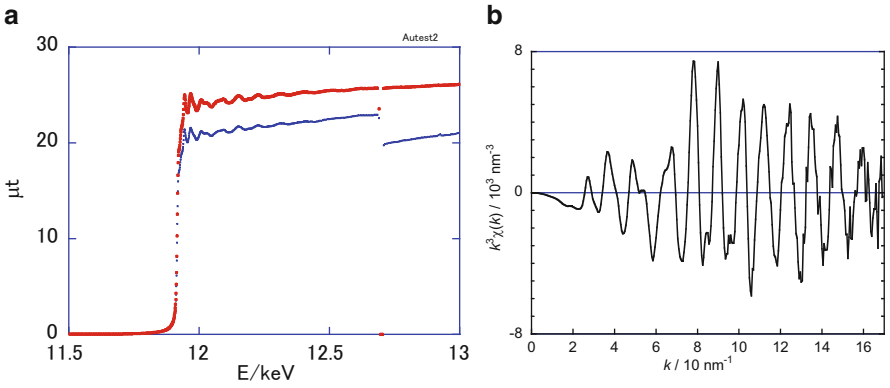

Fig. 5.6 (**a**) A fluorescent XAFS spectrum which encountered beam injection during a measurement (*thin line*) and that was corrected for counting loss (*thick line*). (**b**) Extracted EXAFS wiggle obtained from the spectrum corrected for counting loss

Although semiconductor detectors are powerful for fluorescent XAFS, their energy resolution sometimes becomes insufficient. That is neighboring peaks cannot be separated when the energy difference between them is smaller than the energy resolution of the detector. If the fluorescence peak cannot be separated, the S/N ratio becomes lower. In such cases, detection system with better energy resolution is required. One is a superconducting tunnel junction detector (STJ) [6]. The energy resolution is reported as 15 eV at 600 eV. STJ detector is suited for rather low energy X-rays. The other way is to use a crystal analyzer where the fluorescence X-ray is isolated by a crystal monochromator. Bent crystal Laue Analyzer (BCLA) [7] is often used. Small beam spot on the sample is used since the energy resolution of BCLA is limited by it.

5.3 Electron Yield

Total electron yield mode is often used in soft X-ray region since transmission mode is hard to use and fluorescence yield is rather low and the sample is placed under vacuum in general. The current from a high transmission (ca. 80 %) grid or thin metal foil is used as an I_0-monitor and that from the sample is used as I signal. Special care should be paid to the selection of materials used for grid or foil since fluorescent X-rays from impurities disturb measurements. When the current is too low, an electron multiplier is used in place of a direct current measurement.

Electron yield is also used in hard X-ray region in order to obtain the information from the surface layers (several tens nm). The principle is similar to that of ionization chamber and the ion or electron current emitted from the sample is measured; sample itself is an electrode. Sample cell is filled with He gas so as to

minimize the ionization of the fill gas by X-ray. This method is called as Conversion Electron Yield (CEY). If thin aluminized Mylar© is used as a counter electrode and put a fluorescence detector behind it, both FY and CEY XAFS spectra can be measured simultaneously.

5.4 Special Detection Modes

The above described three modes are usually used for XAFS measurements, but some special modes are reported and they may be useful in some special cases. One is to detect X-ray Excited Optical Luminescence (XEOL). In some cases XEOL can be used for site-selective measurements [8]. But XEOL gives curious spectra in some cases, and thus, it should be carefully examined if the obtained spectrum corresponds to true XAFS signal [9]. Another site-specific XAFS is Diffraction Anomalous Fine Structure (DAFS), which is a technique to measure the XAFS signal in diffraction spots [10]. Measurement of total reflected X-ray intensity is used to obtain surface sensitive information [11], but fluorescence XAFS under total reflection condition is more popular.

References

1. Lu K, Stern EA (1983) Size effect of powdered sample on EXAFS amplitude. Nucl Instrum Methods 212:475–478
2. Jaklevic J, Kirby JA, Klein MP, Robertson AS, Brown GS, Eisenberger P (1977) Fluorescence detection of EXAFS: sensitivity enhancement for dilute species and thin films. Solid State Commun 23:679–682
3. Lytle FW, Greegor RB, Sandstrom DR, Marques EC, Wong J, Spiro CL, Huffman GP, Huggins FE (1984) Measurement of soft X-ray absorption spectra with a fluorescent ion chamber detector. Nucl Instrum Methods Phys Res 226:542–548
4. Cramer SP, Tench O, Yocum M, George GN (1988) A 13-element Ge detector for fluorescence XAFS. Nucl Instrum Methods Phys Res A266:586–591
5. Kappen P, Tröger L, Materlik G, Reckleben C, Hansen K, Grundwaldt J, Clausen B (2002) Silicon drift detectors as tool for time-resolved fluorescence XAFS on low-concentrated samples in catalysis. J Synchrotron Rad 9:246–253
6. Ukibe M, Shiki S, Kitajima Y, Ohkubo M (2012) Soft X-ray detection performance of superconducting tunnel junction arrays with asymmetric tunnel junction layer structure. Jpn J Appl Phys 51:010115
7. Karanfil C, Bunker G, Newville M, Segre CU, Chapman D (2012) Quantitative performance measurements of bent crystal Laue analyzers for X-ray fluorescence spectroscopy. J Synchrotron Rad 19:375–380
8. Goulon J, Tola P, Lemonnier M, Dexpert-Ghys J (1983) On a site-selective EXAFS experiment using optical emission. Chem Phys 78:347–356

9. Emura S, Moriga T, Takizawa J, Nomura M, Baushspiess KR, Murata T, Harada K, Maeda H (1993) Optical-luminescence yield spectra produced by x-ray excitation. Phys Rev B Condens Matter 47:6918–6930
10. Stragier H, Cross JO, Rehr JJ, Sorensen LB, Bouldin CE, Woicik JC (1992) Diffraction anomalous fine structure: a new structural technique. Phys Rev Lett 69:3064–3067
11. Martens G, Rabe P (1980) The anomalous dispersion of the refractive index and the extended X-ray absorption fine structure at the K edge of Cu. J Phys C Solid State Phys 13:L913–918

Chapter 6
Cell Designs for In Situ and *Operando* Studies

Dmitry E. Doronkin, Henning Lichtenberg, and Jan-Dierk Grunwaldt

6.1 Introduction and Criteria for the Choice of an Appropriate Cell

The design of appropriate spectroscopic cells for in situ and *operando* XAFS studies of heterogeneous catalysts has been a very active field during the past decades as the investigation of catalysts at work has become a powerful approach to improve the activity and selectivity of catalysts in a rational manner [1–4]. The inherent advantage of X-rays is due to their penetrating power through solids, gases and liquids. The structural information can be gained under reaction conditions with reactors with similar geometry to those used in industrial catalysis. Various cells for in situ (e.g., in a gas atmosphere) or *operando* (i.e., while measuring the catalytic performance) spectroscopic studies have already been designed since the 1980s [5].

Still, during the past years a number of new in situ cells have been developed, e.g., to combine XAFS with complementary techniques [6], to optimize the geometry for XAS in fluorescence mode [7], to investigate heterogeneous catalysts in liquid phase [8] or to extend in situ XAS studies to high pressure reactions [9]. Hence, many different cell designs exist, which are mostly unique and tailored to a specific application. Only a few of them are commercially available [9, 10], and most of them are constructed by the research groups themselves. Recently, attempts to exchange experience and develop infrastructure for catalysis studies at synchrotrons emerged for example in the US (Synchrotron Catalysis Consortium, SCC) [11] as well as in Europe (e.g., SNBL [12, 13] and DUBBLE [14] beamlines at ESRF, SAMBA beamline [9] at SOLEIL and catalysis research at ANKA [15]).

D.E. Doronkin • H. Lichtenberg • J.-D. Grunwaldt (✉)
Institute for Chemical Technology and Polymer Chemistry (ITCP) and Institute of Catalysis Research and Technology (IKFT), Karlsruhe Institute of Technology, 76131 Karlsruhe, Germany
e-mail: grunwaldt@kit.edu

Y. Iwasawa et al. (eds.), *XAFS Techniques for Catalysts, Nanomaterials, and Surfaces*, DOI 10.1007/978-3-319-43866-5_6

Many of these organizations even provide infrastructure and support for the users without synchrotron experience; however, choosing an appropriate cell is a critical decision for a successful experiment.

The reasons for the wide variety of in situ cells are manifold. One of the main reasons is the high number of different applications. A spectroscopic cell for studying a catalyst while it is working (e.g., in a fast reaction) needs a completely different design than a cell for a catalyst that acts in a slow reaction which is not mass transfer limited, a reaction in liquid phase or an experiment where the catalyst is studied after reduction. Grunwaldt et al. [16] have described criteria to guide this development of in situ cells from the start of the construction to aim finally at the "best compromise"; many of those criteria are similar to those in the chemical engineering literature. An overview on different spectroscopic cells and the history of development of the in situ cells for XAFS studies of catalysts was furthermore given by Bare and Ressler [17]. The following considerations are important when choosing the appropriate cell:

- Are the data to be collected in transmission or in fluorescence mode? This depends on a number of factors including the nature of the sample (concentration of the element of interest and homogeneity of its distribution in the sample), the experimental design, and the necessity to combine XAFS with other spectroscopic techniques.
- The range of the photon energies to be covered. This is crucial for choosing the appropriate material and the thickness of X-ray windows.
- Operating temperatures and pressures as well as chemical compatibility of reactants with window, reactor and sealing materials. Maximum heating and cooling ramps, which are limited by the thermal mass of the cell.
- In case of catalytic reactions: Is the reaction fast or slow (internal mass transport limitations)? Does it occur in gas phase or liquid or even three-phase mixture (external mass transport limitations)?
- Are accurate measurements of catalyst activity, selectivity, and the temperature of the catalyst bed necessary? In particular, will the measurements be carried out under *operando* conditions?
- Are specific safety issues to be considered?
- Are spatially or time resolved studies (resolution) required?
- Should the XAS experiment be combined with other spectroscopic techniques?

Irrespective of the type of the cell an important decision has to be made concerning the X-ray transparent window material. The material has to absorb the minimum amount of incoming, transmitted and/or fluorescence X-rays and needs to be chemically, temperature, and mechanically stable for the desired application. The most commonly used X-ray window materials include beryllium, Kapton® (polyimide), quartz, glassy carbon, and boron nitride. For high pressure in situ cells and studies at higher photon energies (typically more than 10 keV) foils of light metals, e.g., Al or Ti can serve as X-ray windows. If a combination of techniques is required the window has to be transparent for all used photon energies, e.g., when combining XAS with simultaneous Raman measurements quartz reactors [13] or cells with mica windows [9] are used.

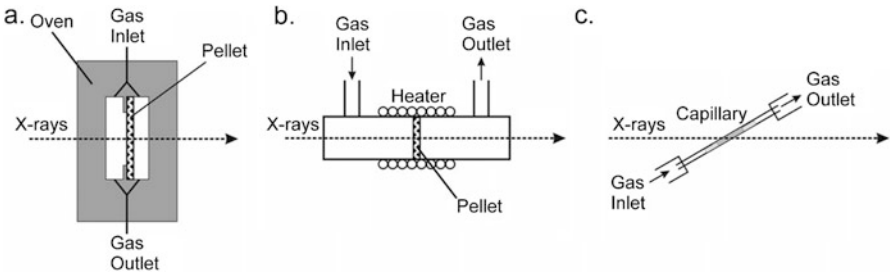

Fig. 6.1 Typical designs of in situ cells for studies of heterogeneous catalysts: (**a**) environmental cell with gas flowing around a pellet and (**b**) a cell with gas flowing through a pellet; (**c**) capillary microreactor cell with plug-flow reactor geometry for studying powder catalysts. Reproduced from ref. [16] with permission from the PCCP Owner Societies

In general, a cell design fulfilling all wishes of an experimentalist is rarely possible or available which results in compromises between the XAFS data quality and catalytic performance, easiness of operation, safety, and many more aspects. A comparison of in situ cells of principally different design concepts in terms of both spectral data quality and the relevance for the reaction kinetic (*operando*) measurements was reported by Grunwaldt et al. (Fig. 6.1) [16]. The more common design with a catalyst wafer (pressed pellet) placed in an environmental cell with gas flowing around the pellet (Fig. 6.1a) showed its suitability for obtaining good spectral quality data with homogeneous beam transmission. This makes this cell type suitable also for measurements with position-sensitive detectors, i.e., for energy dispersive EXAFS. An improved design of this cell, which is also used for infrared spectroscopy [18], involves gas flowing through a pellet (Fig. 6.1b). This design ensures gas diffusion through the entire cross section of a sample pellet; however, it requires preparation of pellets with sufficient porosity, e.g., using γ-alumina as a binder material which is not always possible without altering the catalytic properties of the sample material [16]. The other cell in the comparison was a capillary microreactor as example of plug-flow reactor geometry and catalyst in form of 80–120 μm particles (Fig. 6.1c), based on concepts by Clausen et al. [19] and Thomas et al. [20], and a powder sample in an enclosed cell reported by Bazin et al. [21]. While the pellet cell allowed higher quality XAFS data acquisition, the diffusion limitations through a catalyst wafer resulted in markedly different kinetics during temperature-programmed reduction of CuO/ZnO when compared to catalyst grains such as in a capillary cell. In the case of fast catalytic reactions (e.g., oxidation of methane over PdO_x/ZrO_2) gas bypass in the pellet cell and especially internal mass transport limitations were shown not only to significantly influence the measured catalytic data but also falsify conclusions on the structure since only the outer surface is really exposed to the reaction mixture [16].

The reason for different kinetics of Cu reduction is just due to internal mass transfer limitations as demonstrated in ref. [16]. For spherical particles the reaction time τ can be calculated using the shrinking core model:

$$\tau_{\text{internal}} \cong \frac{\rho_{\text{CuO}} \cdot R_{\text{p}}^2}{3D_{\text{e}} \cdot c_{\text{H2}}} \tag{6.1}$$

where ρ_{CuO} is the molar density of CuO in a particle, D_{e} is the effective diffusion coefficient, R_{p} is a particle radius (or pellet thickness), and C_{H2} is the hydrogen concentration. For an effective diffusion coefficient of 10^{-6}–10^{-8} m^2/s and a 100 μm particle τ amounts to 20 ms–2 s. This is already in the time range of time resolved studies using QEXAFS [22] and DEXAFS [23] and should be taken into account, i.e., a reaction faster than ≈1 ms may be hampered by internal diffusion or external mass transport, even in the ideal case of a sieved catalyst. Similar considerations apply to pressed catalyst wafers (pellets) where the total reduction time with the diffusion coefficients given above and 2 mm pellet thickness amounts to 33 s–56 min (depending on the porosity of the binder material) which makes it inapplicable for time-resolved experiments.

Internal mass transport may not only play a role during dynamic changes of temperature or concentration but also may even occur under stationary reaction conditions if the reaction rates are high such as for oxidation of methane. In heterogeneous catalysis, this is typically reflected by the "effectiveness factor" of the catalyst and estimated using the Thiele modulus [24]. Due to the high reaction rate the reactant (e.g., methane) is already consumed while diffusing into the porous solid catalyst and the inner part of the catalyst may thus not interact with the reactant at all. Since XAS experiments typically probe the whole catalyst and average the contributions from all atoms of a specific element, this will also strongly affect or even falsify the spectroscopic result.

Figure 6.2 shows an example of a methane concentration gradient calculated for the total oxidation of methane over Pd-based catalysts based on a reaction rate constant $k_{\text{r}} = 1.55 \cdot 10^3\ s^{-1}$ and an effective diffusion coefficient $D_{\text{e}} = 1.1 \cdot 10^{-6}\ m^2\ s^{-1}$ [16]. Whereas the concentration in an 80 μm large particle (sieved catalyst) only drops to 90 % of the surface concentration, the concentration of methane in a self-supporting disk drops to less than 10 % already at a penetration depth of 70 μm. This means that, in case of a net wafer thickness of 1 mm, transmission XAS will only to

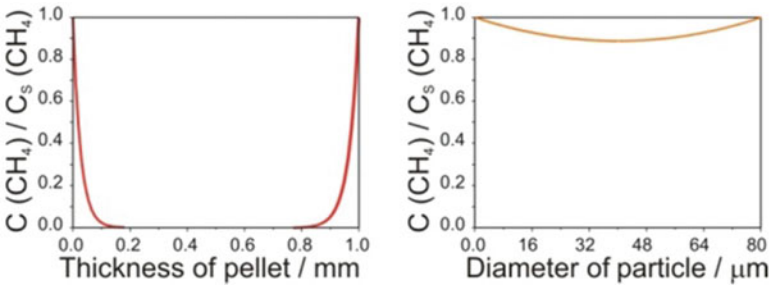

Fig. 6.2 Calculated profiles of the methane concentration (normalized by the surface concentration) during the total oxidation of methane for the cases of a 1 mm thick pellet and an 80 μm particle. Adapted from ref. [16] and ref. [25] with permission from the PCCP Owner Societies

a *minor* extent monitor the area within the catalyst where the reaction occurs. The effectiveness for a pressed wafer is with 3 % much lower than for a particle of 80 µm (88 %). For a Thiele modulus

$$\psi = L_c \sqrt{\frac{k_r}{D_e}} \leq 3 \tag{6.2}$$

the methane concentration drops to less than 10 % at the center of the catalyst particle (L_c is a characteristic length defined as half of the thickness for a disk and 1/6 of the particle diameter for round-shaped particles, cf. ref. [24]; k_r is the rate constant). Hence, the Thiele modulus is a very useful parameter which indicates whether internal mass transport is limiting and thus well suited for optimizing in situ and, especially, *operando* spectroscopic cells.

In conclusion, for fast reactions a finely sieved powder catalyst should preferentially be used. Similar considerations as for gas phase experiments can be made for liquids and higher pressure studies, where also external mass transport limitations at the fluid/solid interface may occur [16]. This compromise keeps the design of new in situ cells a very active field to fulfill the best spectroscopic conditions (depending on the photon energy, concentration of the element of interest as well as the required spatial resolution) and optimum catalytic conditions (gas phase, liquid phase, high pressure, temperature profiles, mass transfer limitations, continuous flow or batch-like). Therefore, there cannot be a universal solution. Instead, different applications require specific cell designs.

6.2 In Situ Cells for Studies of Catalysts in Form of Powders and Pellets

One of the first cells for the in situ XAFS studies of catalysts was designed by F. Lytle et al. [5]. The design (Fig. 6.3) has been adopted by many research groups and it is one of the few commercially available cells [26]. It allows transmission measurements on both self-supporting wafers and powders using a special boat-type inset. An additional ion chamber detector with a built-in amplifier is available for measurements in fluorescence mode. The gas atmosphere may be changed and the cell can be evacuated. The maximum pressure is rated up to 100 bar. It is possible to cool the sample holder with liquid nitrogen and to heat it up to approx. 1000 K using a built-in resistance heating unit. At the same time the outer shell of the cell is water-cooled to prevent heating the beamline components and the fluorescence detector. One downside of the design is the gas bypassing the sample which prevents obtaining quantitative catalytic data acquisition. The other drawback is that the temperature of the catalyst sample cannot be measured directly.

A significant improvement of the same general layout was reported by Hannemann et al. (Fig. 6.4) [7]. This cell allows measurements on (preferentially)

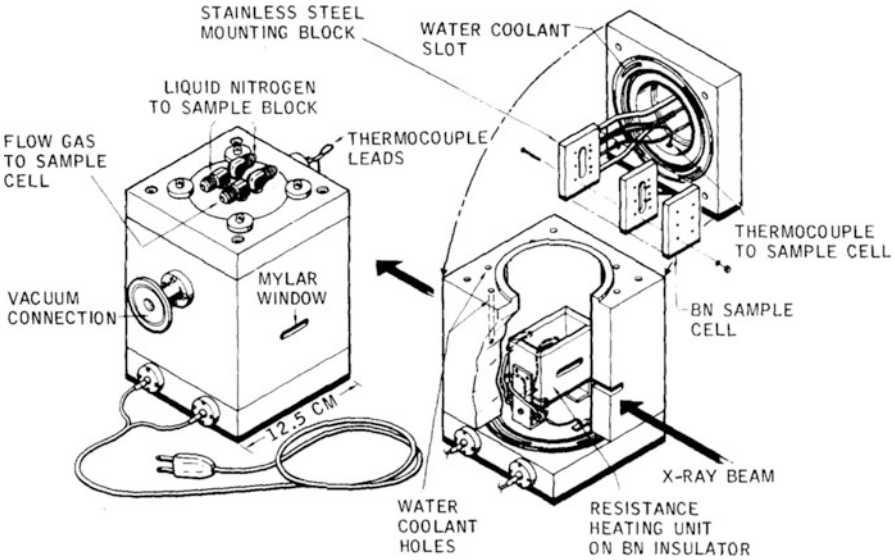

Fig. 6.3 Schematic view of the Lytle cell. Reprinted with permission from ref. [5]. Copyright 1979, AIP Publishing LLC

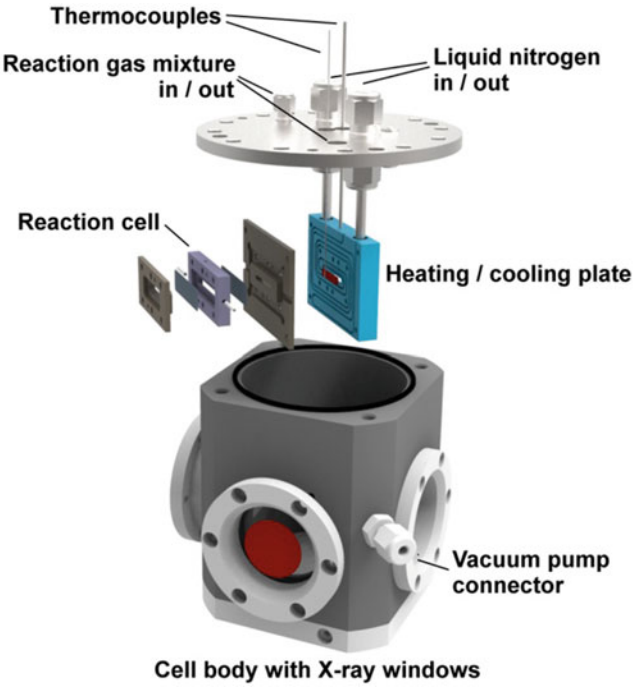

Fig. 6.4 Schematic view of the XAFS cell for transmission/fluorescence measurements and X-ray diffraction

powders (like the cell by Bazin et al. [21]) and self-supported wafers (pressed into the sample compartment). It mimics a plug flow reactor, is suitable for both gas and liquid environments and additionally allows online products analysis. The sample holder further allows cooling down to the temperature of liquid nitrogen and heating to 973 K. The heating is localized so that the temperature of the outer body does not exceed 423 K even without water cooling. The inner volume of the cell can be evacuated (e.g., to prevent ice formation on the X-ray windows during measurements at liquid nitrogen temperature) or filled with He for measurements at low energies. Different materials can be used for the sample holder depending on photon energy, pressure and the chemical nature of reactants/products. The thickness of the sample can be varied by using reaction cell insets of different thickness. A variable sample positioning angle relative to the beam, wide windows and funnel-shaped cutouts in the sample holder allow measurements of X-ray fluorescence and X-ray diffraction simultaneously with XAFS measurements in transmission mode. Notably, due to the windows on all four sides of the cell it can be used at many different beamlines with different detector arrangement.

A much simpler but not less versatile cell was originally suggested by Clausen et al. [19] and Thomas et al. [20], and further developed by Grunwaldt et al. (Fig. 6.5a) [16]. The concept is based on a thin quartz (or glass) capillary (0.5–3 mm o.d., 10–20 μm wall thickness, available from for example Hilgenberg GmbH, Hampton Research, and a number of other suppliers) connected to a gas dosing and a gas analysis units by means of graphite ferrules [16] or high-temperature epoxy glue for gas-tight sealing [27]. The catalyst, in form of small grains (grain size is typically within 50–150 μm range), is placed between two quartz wool plugs, and the overall assembly has a geometry of a regular plug-flow catalytic reactor with virtually no dead volume. The capillary can be cooled or heated by cold or hot nitrogen (air) blowers. Some of them are commercially available, e.g., a Cryojet from Oxford Instruments (85–500 K) [28] and a gas blower built by Cyberstar S.A. (now by FMB-Oxford, heating up to 1273 K) [29]. An alternative air blower LE Mini Sensor

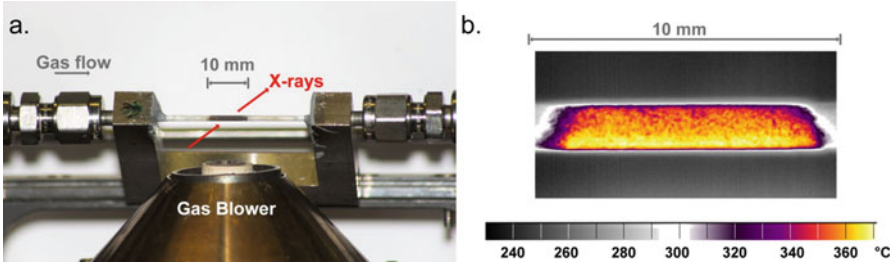

Fig. 6.5 (**a**) A photograph of the capillary cell used by Grunwaldt et al. [16], here mounted on top of a FMB Oxford Gas Blower (heater). The capillary microreactor is glued in the stainless steel holder by means of high-temperature epoxy-glue. (**b**) IR thermography image of the temperature distribution in a microreactor capillary filled with a Pt/Al_2O_3 catalyst at 400 °C Gas Blower setpoint in a flow of 50 ml/min He

from Leister Technologies AG originally designed for the plastic packaging industry can be used up to 900 K [26].

The remarkable versatility of this design allows simultaneous measurements of X-ray absorption, fluorescence, diffraction [6], and also optical spectroscopy such as Raman [6, 13] or UV–Vis [30]. The capillary microreactor cell is also suitable for studies of photocatalysts under working conditions [31]. Catalytic data can be measured and evaluated as for any conventional plug-flow reactor. There are certain drawbacks of the design, which should be taken into account when planning an experiment. First of all, precise measurement of the catalyst temperature is not possible, second, as for all plug-flow reactors, in case of fast reactions concentration gradients along the catalyst bed will occur [32]. Furthermore, although the cell was tested under pressures up to 50 bar [19], the actual maximum pressure depends on the particular capillary and cannot be defined a priori. Heating by a gas stream leads to temperature gradients (e.g., Fig. 6.5b) which may be critical and should be taken into account for certain catalytic reactions, e.g., total oxidation [33] with steep light-off curves. Some of the drawbacks can be negotiated with, i.e., heating of the catalyst by the intense X-ray beam can be estimated based on the change in the catalytic conversion [34], and in the case of concentration gradients spatially resolved XAS measurements are required [32, 35].

For high throughput X-ray absorption studies (to increase the number of measured catalysts) also a microreactor array was developed that allows to study the structural changes in six to ten solid samples with an independent gas supply to each reactor channel and also fast independent MS analysis [36, 37] and thereby real simultaneous *operando* acquisition of XANES spectra of working catalysts. The setup uses a fast CCD camera with X-ray absorption contrast as is schematically shown in Fig. 6.6.

Application of thin walled quartz capillaries limits the maximum pressure and requires several safety precautions against breaking the capillary. Other materials

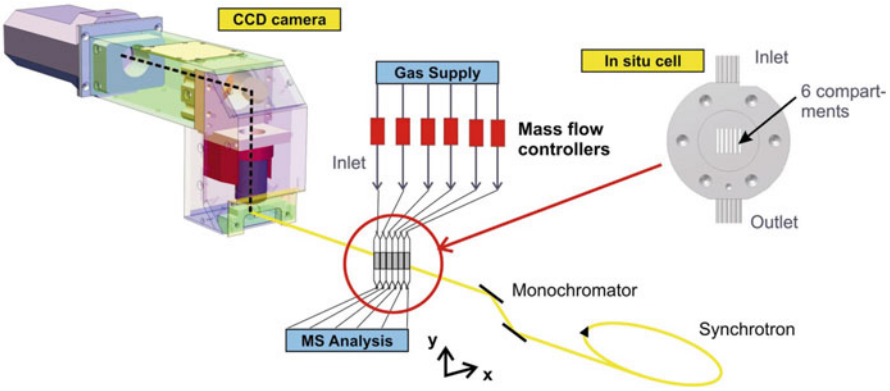

Fig. 6.6 Setup for parallel screening of the structure of heterogeneous catalysts at work using a CCD camera and a microreactor array. Reproduced from ref. [37] with permission.© IOP Publishing. All rights reserved

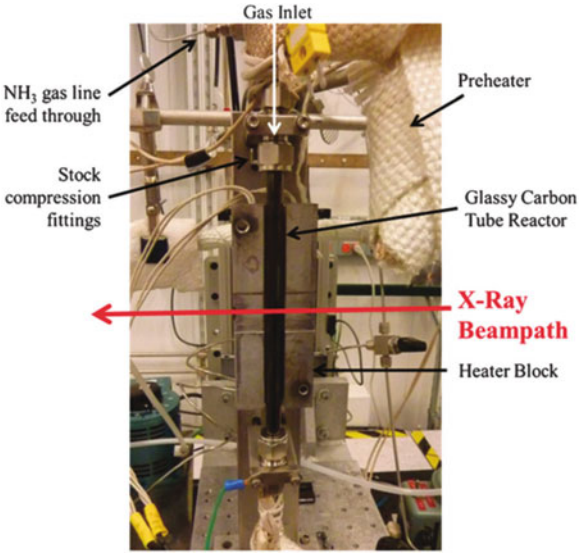

Fig. 6.7 A glassy carbon reactor installed in a heater block as reported by Kispersky et al. [40]. Reproduced from ref. [40] with permission of The Royal Society of Chemistry

with lower X-ray absorption than that of quartz were suggested for use as plug-flow microreactors. Bazin used carbon foil [21], Bare used Be tubes with 3 mm outer diameter and 0.5–0.75 mm wall thickness operated at temperatures up to 823 K and pressures up to 14 bar as an in situ plug flow reactors [38]. One advantage of the reported design is the possibility to directly measure the temperature of the catalyst bed since the reactor tube is thick enough to accommodate a thermocouple. The other advantage is that due to low X-ray absorption by the Be walls collection of XAFS data at photon energies below 5 keV is possible. The disadvantages lie in the chemical nature of the used beryllium (PF-60 grade Be contains up to 800 ppm Fe and other trace elements, which limits its application for certain catalytic reactions) and the toxicity of Be when oxidized which requires special care during handling [39]. To overcome the disadvantages of Be as reactor material Kispersky et al. reported the use of a vitreous carbon tube (glassy carbon, Fig. 6.7) as a robust relatively low-cost plug-flow in situ reactor [40]. With a 6 mm outer diameter and 4 mm inner diameter it is comparable to the reactors used in laboratory test rigs. The reactor was placed vertically for a down-flow operation which allowed spatially resolved XAFS measurements along the catalyst bed. The reactor can be heated to 823 K in oxidizing atmosphere and has been tested under pressures up to 25 bar. Both reactors of Bare [38] and Kispersky [40] were heated by means of an oven with openings for incoming and transmitted X-rays and as such can be used only for transmission XAS measurements.

High pressure studies (>20 bar) require special reactor designs as most of the X-ray window materials cannot withstand such pressure if made thin enough for low absorption of X-rays [41, 42]. Thus, the reactors and windows have to be reinforced. An example of a plug-flow reactor for transmission studies at high pressures (up to 150 bar) is shown in Fig. 6.8. The main body of the reactor is a

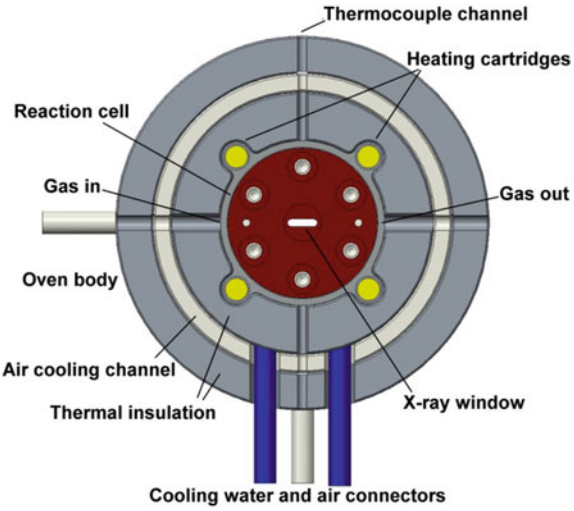

Fig. 6.8 Schematic view of a transmission cell for catalytic studies at high pressure (up to 150 bar)

solid stainless-steel block with bored holes for gas (or liquid) inlet and outlet. The catalyst is placed in the middle channel of the reactor body and covered by graphite sealings and Be windows. Several sets of reactor covers and spacers allow different thicknesses of the catalyst bed. The assembled reactor is heated by a specially designed oven composed of two parts (Fig. 6.8) with a water- or air-cooled outer shell to prevent heating of beamline components and to achieve fast cooling if necessary.

6.3 In Situ Cell for Studies in Liquid Phase and at Elevated Pressures

Not all catalytic processes are realized in flow-through reactors. Some liquid-phase reactions and reactions in supercritical fluids require high pressure batch reactors to run [41]. Also, hydrothermal synthesis of catalysts requires autoclaves [43]. An in situ batch autoclave-like reaction cell was reported by Grunwaldt et al. [8]. This cell (Fig. 6.9) mimics a conventional autoclave with a polyether–ether–ketone (PEEK) inset with two beam paths, one in the middle of the cell to probe the liquid phase and one at the bottom to probe the solid catalyst. The total volume of the cell is about 10 ml and it is rated for pressures up to 150 bar. It is equipped with a magnetic stirrer and can be heated up to 473 K. This cell allows monitoring solid species at the bottom and soluble species in the liquid, which may be relevant for sample preparation by hydrothermal or solvothermal synthesis [44], investigation of heterogeneized complexes or Pd-catalyzed Heck-reaction [45, 46].

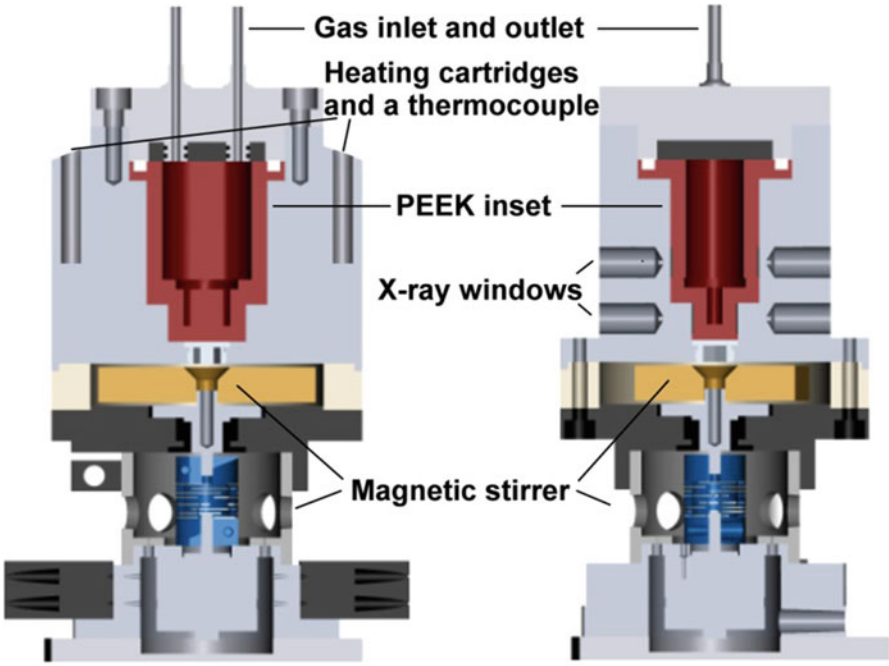

Fig. 6.9 Scheme of an in situ batch cell for studies of liquids and liquid/solid interfaces at high pressures

6.4 In Situ Cell for Studies of Chemical Sensors

Sensors are another type of nanomaterials closely related to catalysts in terms of structure and gas–solid interaction (cf. Chap. 25). Therefore, as in catalytic studies, characterization of sensing materials should be carried out in a realistic gas atmosphere and at realistic temperatures. For semiconducting sensors an important difference is for example the sandwich structure of sensors which is typically a sandwich consisting of a sensing material, electrodes, a substrate and heater layers [47]. In case of noble metal doped SnO_2-sensors the strongly absorbing SnO_2-matrix and especially the only 50 μm thick screen printed layer for chemical sensors makes transmission XAS measurements difficult or impossible, and therefore, in situ cells optimized for fluorescence measurements are required. In addition to the cell design, the sensor itself should be fabricated in a way to avoid interference of fluorescence from the element of interest and heaters or electrodes, e.g., for studies of Pt-containing sensor materials Au electrodes and Au/Pd heaters can be used [47]. An in situ cell suitable for studies of sensors is depicted in Fig. 6.10 [48]. It consists of a gas tight vessel, sensor heater and readout connectors, large Kapton® windows, a sensor holder and gas ports. Although primarily designed for fluorescence measurements, X-ray windows on both sides of the cell allow transmission XAS to be recorded as well.

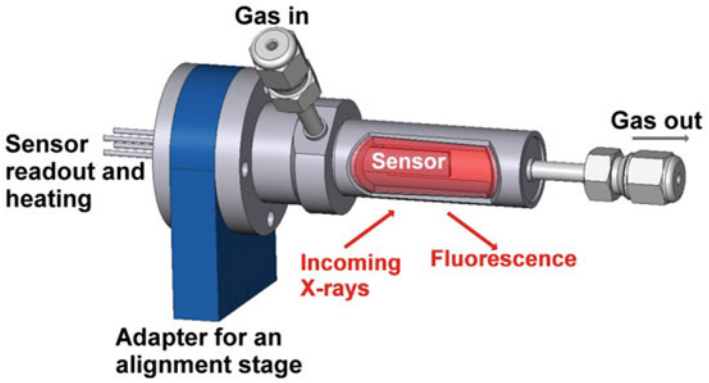

Fig. 6.10 3D drawing of an X-ray absorption/fluorescence cell for in situ and *operando* studies of sensors

6.5 In Situ Cells for Studies of Electrocatalysts

Unlike photocatalysts, electrocatalysts require specially developed cells for in situ and *operando* X-ray studies. The design concept of in situ electrochemical cells often reproduces real fuel cells and is based on a sandwich of electrodes. The anode and cathode are coated with the corresponding electrocatalysts and an ion (proton) conducting membrane. If the electrocatalysts to be studied are based on different metals, the only major modification required to adapt the fuel cell to in situ studies is to provide a thinning to serve as X-ray window [49, 50]. Some of the electrochemical cells do not require machining and can be built in the laboratory, e.g., an easy-to-build flexible electrochemical "coffee bag" type cell which is composed of a stack of metal and membrane foils in an aluminum bag with X-ray windows [51]. During the XAS experiment using the above mentioned cells, X-rays are transmitted through the whole fuel cell and in such a way anode and cathode materials are studied simultaneously. This works well when absorption edges of anode and cathode catalysts do not overlap, otherwise windows must be made in the anode and cathode layers to be able to study them separately as was done by C. Roth et al. who used a slightly modified commercial fuel cell as an in situ cell [52].

6.6 Conclusions and Outlook

The selected examples show that the combination of XAS and related photon-in/photon-out techniques with reaction cells operating close to realistic conditions provides a very powerful tool to establish structure–function relationships in catalysis and related areas. An appropriate design of spectroscopic cells is one of the keys to successful in situ and *operando* XAFS studies in gas and liquid phase or

even under challenging high pressure conditions. Criteria which are typically applied in chemical engineering are valuable for an optimization of in situ cells for time-resolved and for *operando* studies. Reaction cell design will remain a very active field in future as one can only aim for the "best compromise" and the criteria described in this chapter may give a hint how to achieve this goal most rapidly. This will significantly contribute to a better understanding of the dynamics of functional materials, in particular the catalyst structure while monitoring the catalytic performance or even the kinetics of catalytic processes.

References

1. Weckhuysen BM (2003) Determining the active site in a catalytic process: operando spectroscopy is more than a buzzword. Phys Chem Chem Phys 5:4351. doi:10.1039/b309650p
2. Topsøe H (2003) Developments in operando studies and in situ characterization of heterogeneous catalysts. J Catal 216:155–164. doi:10.1016/S0021-9517(02)00133-1
3. Grunwaldt J-D, Clausen BS (2002) Combining XRD and EXAFS with on-line catalytic studies for in situ characterization of catalysts. Top Catal 18:37–43. doi:10.1023/A:1013838428305
4. Bañares MA (2005) Operando methodology: combination of in situ spectroscopy and simultaneous activity measurements under catalytic reaction conditions. Catal Today 100:71–77. doi:10.1016/j.cattod.2004.12.017
5. Lytle FW, Wei PSP, Greegor RB et al (1979) Effect of chemical environment on magnitude of x-ray absorption resonance at L_{III} edges. Studies on metallic elements, compounds, and catalysts. J Chem Phys 70:4849–4855. doi:10.1063/1.437376
6. Grunwaldt J-D, van Vegten N, Baiker A, van Beek W (2009) Insight into the structure of Pd/ZrO_2 during the total oxidation of methane using combined in situ XRD, X-ray absorption and Raman spectroscopy. J Phys Conf Ser 190:012160. doi:10.1088/1742-6596/190/1/012160
7. Hannemann S, Casapu M, Grunwaldt J-D et al (2007) A versatile in situ spectroscopic cell for fluorescence/transmission EXAFS and X-ray diffraction of heterogeneous catalysts in gas and liquid phase. J Synchrotron Radiat 14:345–354. doi:10.1107/S0909049507024466
8. Grunwaldt J-D, Ramin M, Rohr M et al (2005) High pressure in situ x-ray absorption spectroscopy cell for studying simultaneously the liquid phase and the solid/liquid interface. Rev Sci Instrum 76:054104. doi:10.1063/1.1914787
9. La Fontaine C, Barthe L, Rochet A, Briois V (2013) X-ray absorption spectroscopy and heterogeneous catalysis: performances at the SOLEIL's SAMBA beamline. Catal Today 205:148–158. doi:10.1016/j.cattod.2012.09.032
10. The EXAFS Company. http://www.exafsco.com. Accessed 11 Aug 2016
11. Synchrotron Catalysis Consortium (SCC). http://www.yu.edu/scc. Accessed 11 Aug 2016
12. Abdala PM, Safonova OV, Wiker G et al (2012) Scientific opportunities for heterogeneous catalysis research at the SuperXAS and SNBL beam lines. Chimia 66:699–705. doi:10.2533/chimia.2012.699
13. van Beek W, Safonova OV, Wiker G, Emerich H (2011) SNBL, a dedicated beamline for combined in situ X-ray diffraction, X-ray absorption and Raman scattering experiments. Phase Transit 84:726–732. doi:10.1080/01411594.2010.549944
14. Martis V, Beale AM, Detollenaere D et al (2014) A high-pressure and controlled-flow gas system for catalysis research. J Synchrotron Radiat 21:462–463. doi:10.1107/S1600577513031937
15. Grunwaldt J-D, Hannemann S, Göttlicher J et al (2005) X-ray absorption spectroscopy on heterogeneous catalysts at the new XAS beamline at ANKA. Phys Scr 2005:769. doi:10.1238/Physica.Topical.115a00769

16. Grunwaldt J-D, Caravati M, Hannemann S, Baiker A (2004) X-ray absorption spectroscopy under reaction conditions: suitability of different reaction cells for combined catalyst characterization and time-resolved studies. Phys Chem Chem Phys 6:3037–3047. doi:10.1039/B403071K
17. Bare SR, Ressler T (2009) Chapter 6. Characterization of catalysts in reactive atmospheres by X-ray absorption spectroscopy. In: Gates BC, Knözinger H (eds) Advances in Catalysis, vol 52. Academic Press, San Diego, pp 339–465
18. Lesage T, Verrier C, Bazin P et al (2003) Studying the NOx-trap mechanism over a Pt-Rh/Ba/Al_2O_3 catalyst by operando FT-IR spectroscopy. Phys Chem Chem Phys 5:4435–4440. doi:10.1039/b305874n
19. Clausen BS, Topsøe H (1991) In situ high pressure, high temperature XAFS studies of Cu-based catalysts during methanol synthesis. Catal Today 9:189–196. doi:10.1016/0920-5861(91)85023-2
20. Sankar G, Wright PA, Natarajan S et al (1993) Combined QuEXAFS-XRD: a new technique in high-temperature materials chemistry; an illustrative in situ study of the zinc oxide-enhanced solid-state production of cordierite from a precursor zeolite. J Phys Chem 97:9550–9554. doi:10.1021/j100140a002
21. Bazin D, Triconnet A, Moureaux P (1995) An Exafs characterisation of the highly dispersed bimetallic platinum-palladium catalytic system. Nucl Instrum Methods Phys Res B 97:41–43. doi:10.1016/0168-583X(94)00713-6
22. Grunwaldt J-D, Lützenkirchen-Hecht D, Richwin M et al (2001) Piezo X-ray absorption spectroscopy for the investigation of solid-state transformations in the millisecond range. J Phys Chem B 105:5161–5168. doi:10.1021/jp010092u
23. Newton MA, Burnaby DG, Dent AJ et al (2001) Simultaneous determination of structural and kinetic parameters characterizing the interconversion of highly dispersed species: the interaction of NO with $Rh^{I}(CO)_2/\gamma$-Al_2O_3. J Phys Chem A 105:5965–5970. doi:10.1021/jp011621x
24. Levenspiel O (1972) Chemical reaction engineering. Wiley, New York
25. Grunwaldt J-D, Baiker A (2006) Time-resolved and operando XAS Studies on heterogeneous catalysts – from the gas phase towards reactions in supercritical fluids. In: Hedman B, Pianetta P (eds). AIP Conf. Proc. Stanford, California, p 597
26. Le Mini Sensor Kit. http://www.leister.com/en-gb/leister-technologies/process-heat/products/le-heaters/le-mini-sensor-kit. Accessed 11 Aug 2016
27. Tsakoumis NE, Voronov A, Rønning M et al (2012) Fischer–Tropsch synthesis: an XAS/XRPD combined in situ study from catalyst activation to deactivation. J Catal 291:138–148. doi:10.1016/j.jcat.2012.04.018
28. Oxford Instruments. http://www.oxford-instruments.com. Accessed 11 Aug 2016
29. FMB Oxford. http://www.fmb-oxford.com. Accessed 11 Aug 2016
30. Tinnemans SJ, Mesu JG, Kervinen K et al (2006) Combining operando techniques in one spectroscopic-reaction cell: new opportunities for elucidating the active site and related reaction mechanism in catalysis. Catal Today 113:3–15. doi:10.1016/j.cattod.2005.11.076
31. Chiarello GL, Dozzi MV, Scavini M et al (2014) One step flame-made fluorinated Pt/TiO_2 photocatalysts for hydrogen production. Appl Catal B 160–161:144–151. doi:10.1016/j.apcatb.2014.05.006
32. Grunwaldt J-D, Hannemann S, Schroer CG, Baiker A (2006) 2D-mapping of the catalyst structure inside a catalytic microreactor at work: partial oxidation of methane over Rh/Al_2O_3. J Phys Chem B 110:8674–8680. doi:10.1021/jp060371n
33. Gänzler AM, Casapu M, Boubnov A et al (2015) Operando spatially and time-resolved X-ray absorption spectroscopy and infrared thermography during oscillatory CO oxidation. J Catal 328:216–224. doi:10.1016/j.jcat.2015.01.002
34. Boubnov A, Carvalho HWP, Doronkin DE et al (2014) Selective catalytic reduction of NO over Fe-ZSM-5: mechanistic insights by operando HERFD-XANES and valence-to-core x-ray emission spectroscopy. J Am Chem Soc 136:13006–13015. doi:10.1021/ja5062505

35. Doronkin DE, Casapu M, Günter T et al (2014) Operando spatially- and time-resolved XAS study on zeolite catalysts for selective catalytic reduction of NOx by NH_3. J Phys Chem C 118:10204–10212. doi:10.1021/jp5028433
36. Grunwaldt J-D, Kimmerle B, Hannemann S et al (2007) Parallel structural screening of solid materials. J Mater Chem 17:2603. doi:10.1039/b705334g
37. Grunwaldt J-D (2009) Shining X-rays on catalysts at work. J Phys Conf Ser 190:012151. doi:10.1088/1742-6596/190/1/012151
38. Bare SR, Yang N, Kelly SD et al (2007) Design and operation of a high pressure reaction cell for in situ X-ray absorption spectroscopy. Catal Today 126:18–26. doi:10.1016/j.cattod.2006.10.007
39. Beryllium Products (Materion). http://materion.com/Products/Beryllium.aspx. Accessed 11 Aug 2016
40. Kispersky VF, Kropf AJ, Ribeiro FH, Miller JT (2012) Low absorption vitreous carbon reactors for operandoXAS: a case study on Cu/Zeolites for selective catalytic reduction of NOx by NH_3. Phys Chem Chem Phys 14:2229–2238. doi:10.1039/C1CP22992C
41. Grunwaldt J-D, Baiker A (2005) In situ spectroscopic investigation of heterogeneous catalysts and reaction media at high pressure. Phys Chem Chem Phys 7:3526–3539. doi:10.1039/B509667G
42. Grunwaldt J-D, Wandeler R, Baiker A (2003) Supercritical fluids in catalysis: opportunities of in situ spectroscopic studies and monitoring phase behavior. Catal Rev 45:1–96. doi:10.1081/CR-120015738
43. Michailovski A, Grunwaldt J-D, Baiker A et al (2005) Studying the solvothermal formation of MoO_3 fibers by complementary in situ EXAFS/EDXRD techniques. Angew Chem Int Ed 44:5643–5647. doi:10.1002/anie.200500514
44. Koziej D, Rossell MD, Ludi B et al (2011) Interplay between size and crystal structure of molybdenum dioxide nanoparticles-synthesis, growth mechanism, and electrochemical performance. Small 7:377–387. doi:10.1002/smll.201001606
45. Ramin M, Grunwaldt J-D, Baiker A (2005) Behavior of homogeneous and immobilized zinc-based catalysts in cycloaddition of CO_2 to propylene oxide. J Catal 234:256–267. doi:10.1016/j.jcat.2005.06.020
46. Reimann S, Stötzel J, Frahm R et al (2011) Identification of the active species generated from supported Pd catalysts in Heck reactions: an in situ quick scanning EXAFS investigation. J Am Chem Soc 133:3921–3930. doi:10.1021/ja108636u
47. Grunwaldt J-D, Hübner M, Koziej D et al (2013) The potential of operando XAFS for determining the role and structure of noble metal additives in metal oxide based gas sensors. J Phys Conf Ser 430:012078. doi:10.1088/1742-6596/430/1/012078
48. Koziej D, Hübner M, Barsan N et al (2009) Operando X-ray absorption spectroscopy studies on Pd-SnO_2 based sensors. Phys Chem Chem Phys 11:8620. doi:10.1039/b906829e
49. Tada M, Murata S, Asakoka T et al (2007) In situ time-resolved dynamic surface events on the Pt/C cathode in a fuel cell under operando conditions. Angew Chem Int Ed 46:4310–4315. doi:10.1002/anie.200604732
50. Principi E, Witkowska A, Dsoke S et al (2009) An XAS experimental approach to study low Pt content electrocatalysts operating in PEM fuel cells. Phys Chem Chem Phys 11:9987. doi:10.1039/b915086b
51. Villevieille C, Sasaki T, Novák P (2014) Novel electrochemical cell designed for operando techniques and impedance studies. RSC Adv 4:6782. doi:10.1039/c3ra46184j
52. Roth C, Martz N, Buhrmester T et al (2002) In-situ XAFS fuel cell measurements of a carbon-supported Pt–Ru anode electrocatalyst in hydrogen and direct methanol operation. Phys Chem Chem Phys 4:3555–3557. doi:10.1039/b204293b

Part IV
Advanced XAFS Techniques

Chapter 7
Quick XAFS

Tomoya Uruga

7.1 Introduction

Time-Resolved XAFS techniques are powerful tools for investigating the local structure and chemical state during physical and chemical reaction processes and have been used worldwide in synchrotron facilities. There are two major techniques: quick scan XAFS (QXAFS) and energy dispersive XAFS (DXAFS). In this section, the QXAFS techniques are described. The DXAFS techniques are described in Chap. 8.

The QXAFS technique was developed by Frahm et al. [1] in 1988 and has since been improved upon and used worldwide in synchrotron facilities as a standard XAFS measurement method. QXAFS is a relatively simple measurement method that speeds up conventional step scan XAFS by removing unnecessary operations. Conventionally, the step scan XAFS measurement is conducted by measuring the X-ray absorption of a sample at each energy point using a monochromatic X-ray selected by a double crystal monochromator (DCM) (see Chap. 3). The DCM moves to the target energy and stops, and the X-ray intensities and Bragg angle of the DCM crystal are then measured. This operation is repeated point by point at each XAFS measurement energy point for 100–500 points, which results in a time loss of more than several minutes per measurement in addition to the net X-ray exposure time.

Figure 7.1 shows a schematic of the arrangement and control system for transmission mode quick XAFS measurements. In the QXAFS method, the monochromator continuously moves from start to end position during XAFS spectrum measurement. The X-ray detector output signals and the Bragg angles of the

T. Uruga (✉)
Japan Synchrotron Radiation Research Institute, Spring-8, Sayo, Hyogo 679-5148, Japan

Innovation Research Center for Fuel Cells, The University of Electro-Communications, Chofu, Tokyo 182-8585, Japan
e-mail: urugat@spring8.or.jp

Y. Iwasawa et al. (eds.), *XAFS Techniques for Catalysts, Nanomaterials, and Surfaces*, DOI 10.1007/978-3-319-43866-5_7

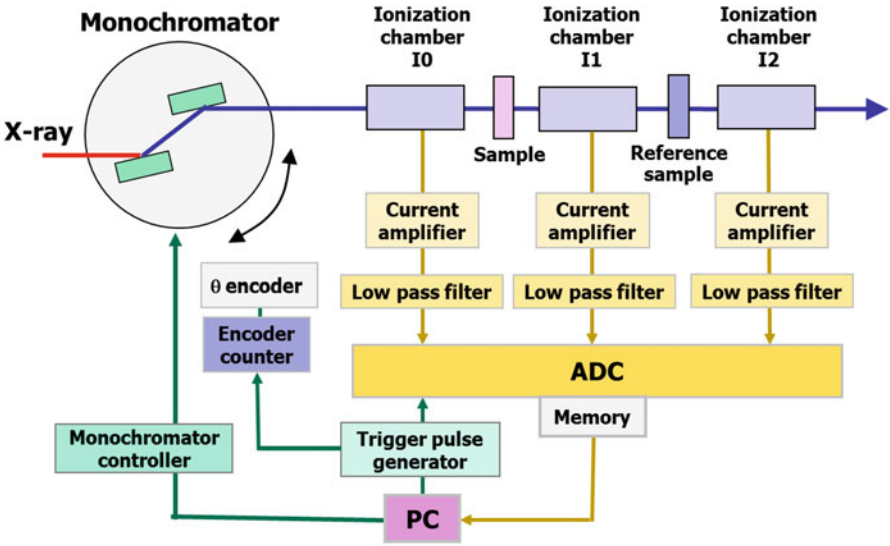

Fig. 7.1 Schematic of arrangement and control system for transmission mode QXAFS measurements

monochromator (i.e., the X-ray energy) are individually stored in a high-speed data storage system (such as memory) during continuous scanning. Thus there is no time loss other than the usual X-ray exposure time. QXAFS is also called time-on-the-fly scan mode XAFS. The beamline arrangement and optics of QXAFS can be basically the same as those of conventional step scan XAFS, so many conventional XAFS beamlines started using the QXAFS method with an adapted measurement system and control software, utilizing one DCM for both the step scan XAFS and QXAFS measurements. Most of the newly constructed XAFS beamlines come already installed with the QXAFS mode as a basic measurement method. The technical details of QXAFS and the methods it can be used with are discussed in the following sections. The applications are described in Part 5.

7.2 Measurement Method

As described above, in the QXAFS measurement, the X-ray intensities and angle of the monochromator crystal are simultaneously measured and temporarily stored in the memory of each measurement system during continuous monochromator scanning (see Fig. 7.1). The stored data set is transferred to the memory of the PC during or after the spectra measurement, depending on the system. Fast and/or direct data transfer from the measurement system to the memory of the PC during the measurement is required for sequential QXAFS measurement without dead time. The measurement timing is synchronized by trigger signals sent from the PC through a

pulse generation device. The trigger signal interval, i.e., the data sampling time, is usually constant.

The X-ray energy is calibrated by the Bragg angle of the monochromator measured with an encoder. In fast QXAFS measurement, the X-ray energy is further corrected with the simultaneously measured XAFS spectrum of a standard sample using the beam transmitted through the target sample (see Fig. 7.1).

When operating the QXAFS measurement system, a user can enter the measurement time for one XAFS spectrum, range, and step of the monochromator scan angle. The angle step is set to correspond to the energy step of the XANES region and transformed to the sampling time by the operation software.

The monochromator scan speed is in most systems constant, other than in the acceleration and deceleration periods. In most cases, the amplitude of the EXAFS oscillation is smaller in the higher k-region. Thus, the step scan XAFS measurements are usually conducted with a longer measurement time in the higher k-region to obtain spectra having a better signal to noise ratio. The raw QXAFS data is usually resampled at the points corresponding to constant interval of k, i.e., 0.5 nm^{-1}, by averaging the data between adjacent sampling points as shown in Fig. 7.2. The averaging data number, N_{ave}, depends on the k-range. From the relationship of $k = 0.51E_e^{1/2}$, where E_e is the photoelectron energy, N_{ave} is roughly estimated to be proportional to k, which indicates that the resampled data quality is higher in the higher k-range.

Further, a time-efficient QXAFS method was developed to measure higher quality spectra up to high-k regions in the shortest possible time [2]. This method involves sweeping the monochromator continuously at a variable angular speed depending on the k-region. Actually, users can divide an XAFS measurement region into several blocks and set a sweep speed for each block. Figure 7.2 shows the improved quality of the EXAFS spectra in the high k-region using the time-efficient QXAFS method.

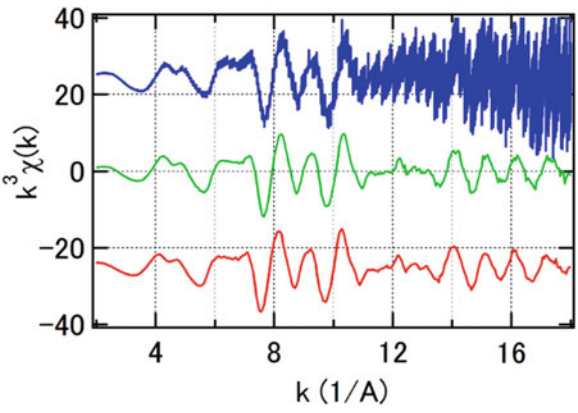

Fig. 7.2 Pd K-edge $k^3\chi(k)$ XAFS spectra of PdO. Raw (*blue*) and averaged data (*green*) measured at constant and variable (*red*) angular speeds. Measurements were under a transmission mode, and the measurement time was 1 min [2]

7.3 Characteristics of QXAFS

In this section, the main characteristics of QXAFS are described and compared with those of DXAFS. First, QXAFS can be conducted in the same mode as those available in step scan XAFS, e.g., transmission mode, fluorescence mode, total conversion electron yield mode, and reflection mode. Thus, QXAFS can be adapted for all samples measured by step scan XAFS, including dilute samples and thin films. Second, QXAFS can be adapted for spatially inhomogeneous samples and samples surrounded by highly scattering materials such as fuel cells as shown in Fig. 7.3 and batteries. Third, QXAFS can provide spectra having a higher energy resolution (Fig. 7.4), higher quality (especially in the EXAFS region), and higher *k*-region data in the low energy region than DXAFS spectra. Fourth, the temporal-spatial-resolved XAFS measurement can be conducted using two-dimensional imaging detectors or a micro- and nano-focused beam. Fifth, it is possible to combine XAFS measurement with SR X-ray-based techniques (XRD, SAXS, etc.) and measure the same part in a sample. These superior qualities of the

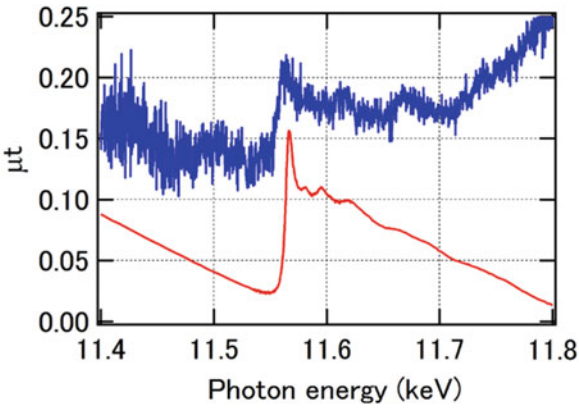

Fig. 7.3 Pt L_3-edge QXANES (*red*) and DXANES (*blue*) spectra of Pt catalyst in a membrane electrode assembly (MEA) of polymer electrode fuel cell (PEFC)

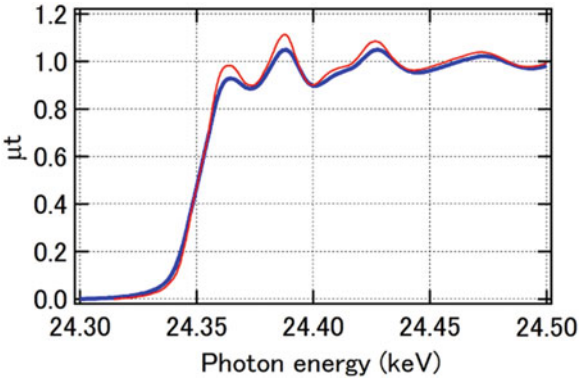

Fig. 7.4 Pd K-edge QXANES (*red*) and DXANES (*blue*) spectra of Pd foil

QXAFS method are advantageous in a practical sense for measuring actual samples under various operational conditions.

The time resolution of QXAFS is determined by factors related to hardware, such as scan speed of the monochromator and response time of the detectors and measurement systems, and factors related to the samples themselves, such as the time needed to measure spectra with a high enough quality for the XAFS analysis and to stimulate the reaction of the sample, such as gas diffusion.

However, QXAFS does have some disadvantages compared with DXAFS: specifically, a minimum time resolution and the absorbance at each energy point in one spectrum depending on the measurement time.

7.4 X-ray Optics at Bending Magnet and Wiggler Beamlines

At the bending magnet or wiggler beamlines, QXAFS measurements are conducted with the time resolution from seconds to minutes depending on the photon flux. In many beamlines, fixed-exit DCM is used for both the QXAFS and step scan XAFS measurements. The first crystal of the DCM is cooled with water or liquid nitrogen to withstand heat load. There are two types of DCM based on the control method. The first involves conducting a quick scan in keeping with a fixed-exit condition. To achieve a fixed-exit beam, the DCM needs to continuously control the rotation motion of both crystals and the translation motion of the first or second crystal. Mechanical link type DCMs have been developed to achieve this, where the rotation and translation motions are driven using a single motor. A technical challenge of the mechanical link DCM is how to keep the parallelism between both crystals during the translation motion of the first or second crystal. A number of different schemes have been developed to address this. These DCMs consist of a single rotational stage for mounting the double crystals and a translation stage for the first or second crystal.

In the other type of DCM method, a quick scan is performed without a fixed-exit condition. In this case, the QXAFS measurements are realized by rotating a pair of DCM crystals without translation motion of the first or second crystal, similar to a channel-cut crystal. The simply designed DCM for the step scan XAFS can be used here. Prior to the QXAFS measurement, the parallelism between both crystals is adjusted by measuring the rocking curve at the center energy of the QXAFS, which enables the stability of the beam flux. The height of the exit beam from the monochromator changes during the QXAFS scan. The downstream vertically focusing mirror, however, can keep the beam height at the sample (focal point) (see Fig. 7.5a). A simple cylindrically bent mirror can usually be used instead of the ideal parabolic mirror with good approximation due to the large radius of curvature. The length of the downstream focusing mirror has to be long enough to reflect the incident beam in spite of its height change. In the case of the standard DCM at

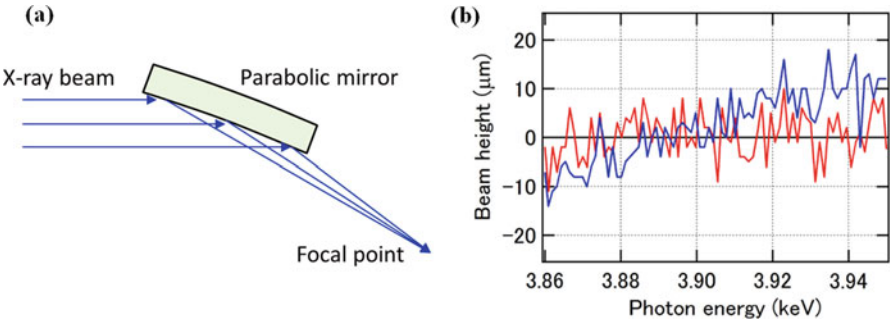

Fig. 7.5 (**a**) Schematic of vertical focusing mirror to keep beam height at focusing position. (**b**) Changes in beam height of sample during scanning with (*red*) and without translation of first crystal (*blue*) around 4 keV measured using position sensitive proportional counter [2]

SPring-8, offset between the incident and exit beam is 30 mm to stop high energy radiation from source by separating from monochromatized X-rays. The change of the exit beam is 2.2 mm during Ca K-edge XAFS scanning from 4 to 5.5 keV. Figure 7.5b shows that the beam height change at the sample is less than 20 μm with and without translation motion of the first crystal of the DCM [2]. Slightly larger beam height fluctuation during quick scanning was due to the slope error from the ideal surface at the off-center part of the downstream focusing mirror.

7.5 Undulator Beamline and Optics

The undulator source enables higher time resolution of the QXAFS due to a higher photon flux on the sample. The energy width of the first harmonic of the undulator is 2–3 %, which corresponds to about 200–300 eV at 10 keV. This is enough for the XANES measurements but unfortunately does not seem to be enough for the EXAFS measurements. There are two ways to conduct the QEXAFS measurement, depending on the undulator gap operation. One is synchronized continuous scans of the undulator gap and the DCM [3, 4]. This method ensures maximum photon flux from the undulator at each measurement energy point. However, the time resolution is limited by the scan speed of the undulator gap, which is more than several seconds for a QEXAFS scan over an energy range typically between −300 and 1500 eV above the absorption edge.

The other method is conducted with a fixed gap undulator that is either tapered or non-tapered (see Sects. 3.1–3.3). The tapered undulator increases the energy width of the harmonics by varying the taper ratio of the undulator gap. Figure 7.6 shows the spectral fluxes of the fundamental harmonic measured on the X-ray beam axis calculated using a synchrotron radiation calculation code SPECTRA [5] for two different taper ratios at the standard tapered undulator at SPring-8. The measured

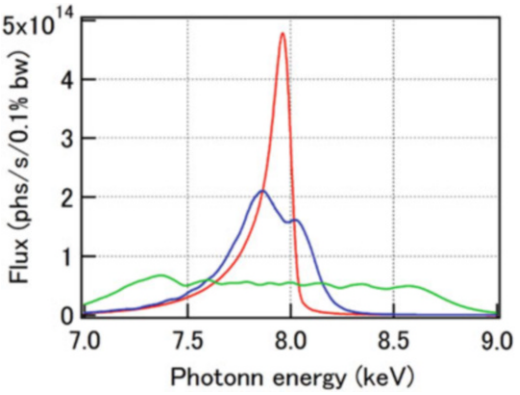

Fig. 7.6 Calculated spectral fluxes of fundamental harmonic for two different taper ratios at standard tapered undulator at SPring-8. Taper ratio; 0 (*red*), 0.5 mm/4.5 m (*blue*), and 2 mm/4.5 m (*green*)

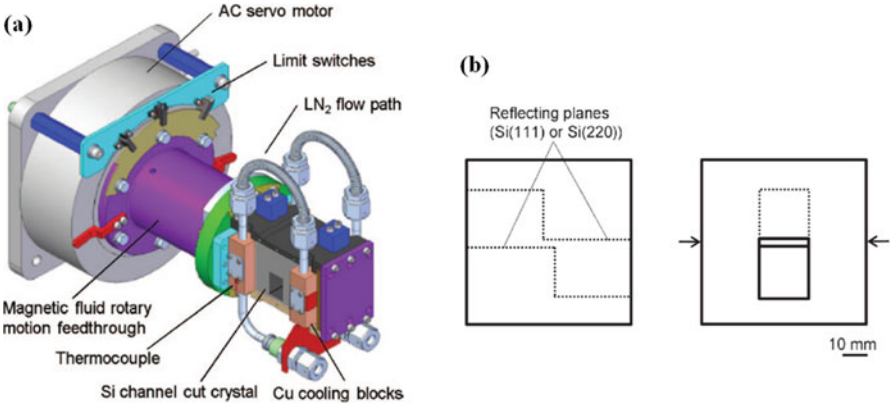

Fig. 7.7 Interior of QEXAFS monochromators using direct-drive servo motor (**a**) and schematic of crystal (**b**) [8]

energy widths were 600 and 1700 eV, which are suitable for the XANES and EXAFS measurements, respectively.

A faster QXAFS measurement system is realized by coupling the tapered undulator with a channel-cut monochromator system. Frahm et al. developed the QEXAFS monochromators based on a cam-driven tilt table for rapid angular oscillations between 0° and 3° mounted on a goniometer which defines the mean energy of the QXAFS spectrum [6, 7]. This monochromator uses a cryogenically cooled channel-cut monochromator system to withstand the high heat load and has achieved a time resolution of 12.5 ms. This type of monochromator is widely installed around the world, such as the SuperXAS beamline at SLS, SAMBA at SOLEIL, and X18B at NSLS.

The low divergent undulator radiation enables channel-cut crystal to be compact, which allows for faster angular oscillation. Figure 7.7a shows the interior of the QEXAFS monochromators using a direct-drive servo motor for angular oscillation

with the liquid-nitrogen cooled compact channel-cut crystal developed by Nonaka et al. at BL33XU in SPring-8 [8]. A schematic of the crystal is shown in Fig. 7.7b. The gap between the reflecting planes is 3 mm, which offsets the beam height by about 6 mm. This design enables the crystal to be downsized to $70 \times 70 \times 70$ mm^3. The crystal shape was designed to allow double-bounce Bragg reflection over an angular range of 4°–30°. This monochromator achieved a time resolution of 10 ms for the QEXAFS measurement. In this beamline, the double mirrors are placed apart at a distance of 10 m with a glancing angle of 1.5 mrad to separate reflected X-rays by 30 mm in the horizontal direction from high energy radiation. This configuration enables the rejection of the high energy components by a gamma-ray stopper. This type of monochromator and beamline arrangement has been installed at BL28XU and BL36XU at SPring-8.

QXAFS with a milliseconds time resolution was realized by using even faster monochromators. One is the piezo-driven double-crystal monochromator developed by Frahm et al. [9]. The monochromator crystals are mounted on piezo-driven tilt tables that can change the Bragg angle in an oscillatory manner with frequencies of more than 100 Hz within a narrow angular width, such as 0.13°. This system allows QXANES measurement with a time resolution of several ms.

The other monochromator consists of the channel-cut crystal having a very small inertia. This monochromator was first developed for the helical undulator in BL40XU at SPring-8 which has a non-tapered gap and gives a high flux but low power quasimonochromatic X-ray beam [10, 11]. This undulator generates on-axis fundamental radiation in the energy range from 8 to 17 keV. The total power was reduced to 7 to 15 W by eliminating off-axis higher harmonics in the front end without significant loss of the fundamental radiation. Low heat load radiation allowed the monochromator to be substantially downsized to $27 \times 13 \times 14$ mm^3 and the cooling devices to be removed [12]. The inertia of the monochromator crystal was about 10 gcm^2. This compact crystal can be repeatedly oscillated at a Bragg angle with a maximum 250 Hz in the EXAFS range at around 12 keV using a galvano scanner motor (Fig. 7.8). The helical undulator is not a tapered one and so the energy bandwidth of the fundamental radiation is 1.5–2.5 %, which is similar to that of the standard horizontal undulator. Such an incident beam profile of the helical undulator can be used for QEXAFS measurements by setting the peak of the

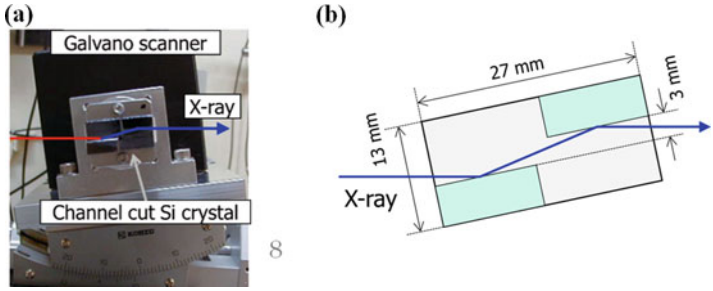

Fig. 7.8 Galvano scanner motor-driven monochromator (**a**) and schematic of channel-cut Si crystal (**b**) [12]

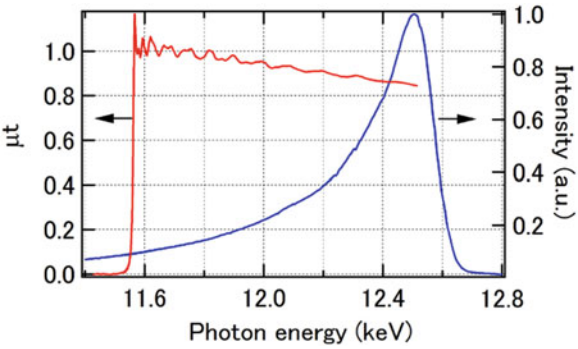

Fig. 7.9 QXAFS spectrum around Pt-L_3 edge of Pt foil in transmission mode (*red*) and incident beam intensity of helical undulator at BL40XU at SPring-8 (**blue**) [12]

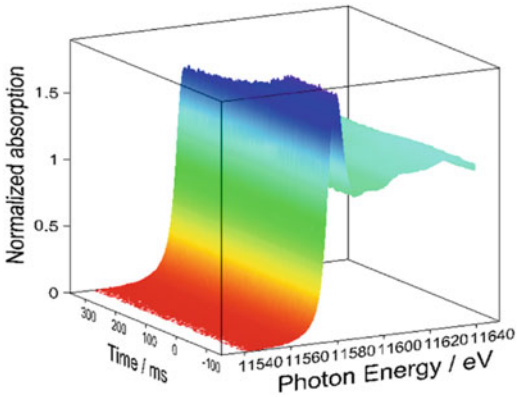

Fig. 7.10 QXAFS spectra around Pt-L_3 edge of Pt/C catalyst (Pt loading: 0.5 mg/cm^2) in PEFC in transmission mode measured using galvano scanner motor-driven monochromator [14]

fundamental radiation to the target energy region, such as the energy corresponding to around maximum k, because the EXAFS spectrum in the high k region requires a high incident photon flux. Figure 7.9 shows a QXAFS spectrum around the Pt-L_3 edge (11.6 keV) of Pt foil in the transmission mode together with the incident beam intensity. The first fundamental peak energy was set at 12.5 keV to measure data with a high S/N ratio up to $k = 150$ nm^{-1}. The intensity of the incident beam gently decreased toward the lower energy region but was still higher than that of the bending magnet source in SPring-8.

The galvano scanner motor driven monochromator with no cooling device can also be used for the tapered undulator radiation under certain conditions [13]. Calculation by the code SPECTRA [5] showed that the heat load of the undulator radiation on the monochromator crystal can be reduced to less than 5 W by rejecting higher harmonics and low energy parts using the mirrors and an absorber, respectively, and by limiting incident beam size using the front end slit. This heat load is acceptable for maintaining the Bragg condition of the crystal. This system results in fast quick XAFS measurements but causes a loss of beam flux—about 10 to 70 %, depending on the energy. Nonetheless, a photon flux of more than 10^{12} photons/s is available at the sample. Figure 7.10 shows the time-resolved QXANES spectra

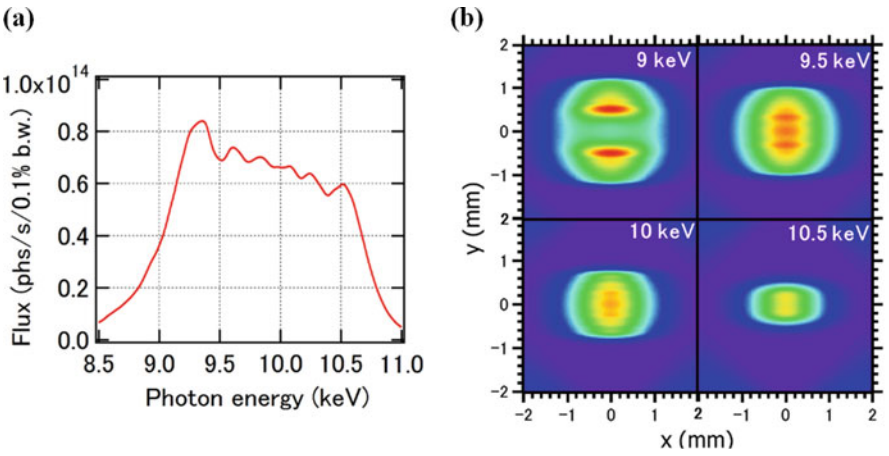

Fig. 7.11 Spectral fluxes of fundamental harmonic (**a**) and spatial distribution of standard tapered undulator radiation at SPring-8 depending on energy (**b**) at 30 m from source calculated using a code SPECTRA. Taper ratio; 2 mm/4.5 m

around the Pt-L_3 edge of the Pt/C catalyst in the PEFC for a voltage cycling process in the transmission mode with a time resolution of 2 ms [14].

It should be noted that the tapered undulator radiation has a spatial distribution that changes with the energy (Fig. 7.11). Some artifacts may occur in the XAFS spectrum in the case of measuring inhomogeneous samples using an unfocused beam, so in the QXAFS measurement using the tapered undulator radiation, the sample is required to have uniformity in an area larger than the X-ray beam size [15].

7.6 Detectors

Almost all X-ray measurement devices used in step scan XAFS can be applied for the QXAFS measurement, but some of them have been improved so as to achieve the faster response required from the high time resolution.

For the transmission mode fast QXAFS measurement with the time resolution of less than 1 s, fast response ionization chambers have been developed. One of these, a gridded ionization chamber, suppresses the slow ionic component of the ionization current by placing a metal grid between the electrodes and keeping it at an appropriate electric potential [16]. Only the fast electrons are able to pass the grid, which shortens the rise time of the chambers to less than 5.5 μs.

In fast fluorescence mode QXAFS measurements less than 1 s, a large area PIN-photodiode (PIN-PD) is used with an applied reverse bias voltage to achieve fast response on the order of micro seconds. It is noted in selecting the PIN-PD model that the larger area PIN-PD has a higher dark current and slower rise time. The Lytle-type detector (EXAFS Co.) is a large area fluorescence detector

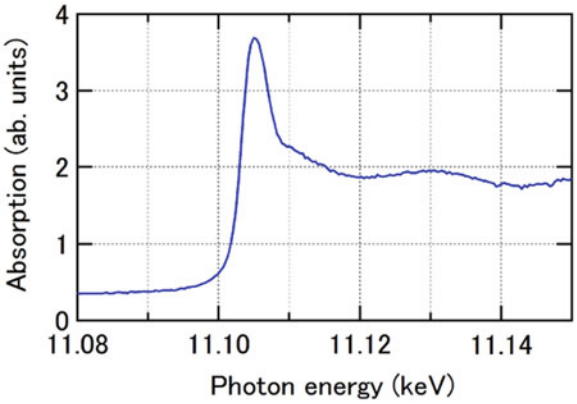

Fig. 7.12 Ge K-edge XANES spectra of $Ge_2Sb_2Te_5$ thin film measured over 45 s under fluorescence mode using 19-element Ge detector at BM beamline BL01B1 at SPring-8 [2]

conventionally used in step scan XAFS. As it has a response time of sub-seconds, it has been used for slow QXAFS measurements with a time resolution of more than minutes. Recently, two dimensional pixel array detectors (PADs) such as PILATUS, EIGER (DECTRIS Ltd.), and Merlin (Quantum Detector Ltd.) are starting to be applied. These are hybrid single photon-counting type detectors with a large area and a fast readout time of sub-ms to ms. These features are very useful in terms of application to a high quality fluorescence mode QXAFS detector. They can be used for QXAFS with a time resolution of more than sub-seconds.

For the measurement of ultra-dilute samples or thin films, energy dispersive detectors such as Ge detectors or silicon drift detectors (SDDs) are applied. Multi-element types are preferable for detection over a large area. The output voltage from the preamplifier of the detectors is amplified, digitalized, and stored in memory by a digital X-ray processor system. These measurement systems have a maximum photon count rate, such as 1 MHz (Ge detector) or 3 MHz (SDD) per element, which restricts time resolution to more than 1 s for the QEXAFS measurement. Figure 7.12 shows the Ge K-edge XANES spectra of $Ge_2Sb_2Te_5$ thin film measured over 45 s at the bending magnet beamline BL01B1 at SPring-8 [2].

7.7 Measurement Systems

Both an ionization chamber and PIN-PD are required to measure very small electric currents with a high speed and high accuracy, which makes such electric measurements quite difficult. The output current of these detectors is amplified to voltage by current amplifiers. The voltage signals are then digitalized and saved to a PC. Two types of system are used for digitalizing voltage signals. One is a set consisting of a voltage-to-frequency converter (VFC) and a frequency counter. This system sums the analog voltage signals measured over a time interval between start and stop trigger, which improves the spectral quality by increasing the statistical accuracy

and reducing random electrical noise. The other system is a set consisting of a low-pass filter (LPF) and analog-to-digital converter (ADC) (Fig. 7.1). The high-frequency electrical noise included in the output voltages is rejected by the front end LPF prior to the ADC. With the LPF, it is difficult to maintain high quality operation under a low-frequency (slow scan) measurement mode such as <0.1 Hz. The VFC counter system is superior to the LPF-ADC system in terms of the data quality in long time scale measurement such as >10 s. Thus, the VFC counter system is also conventionally used for the step scan XAFS measurement.

However, the VFC counter system has a limitation for highly time-resolved measurements due to the maximum frequency of the VFC. The counter rounds frequency output from the VFC to an integer, and the number of counts (not the number of photons) is require to be on the order of 10^3 and 10^6 for the quality analysis of XANES and EXAFS up to $k = 100\ \mathrm{nm}^{-1}$, respectively. The maximum frequency of the now commercially available VFC is 100 MHz. In the QEXAFS measurement, the number of data points is typically about 5000. In the case of QXAFS measurement with the time resolution of 1 s, the data sampling time is 200 μs, so the maximum number of counts at each sampling point is 20,000 using the 100 MHz VFC. After averaging the data process, the estimated maximum count number around $k = 100\ \mathrm{nm}^{-1}$ (typical N_{ave} is 10) is on the order of 10^5, which is not enough for EXAFS analysis. The VFC counter system is therefore not suitable for measurements with high time resolution (typically < 1 s).

Electrical noise is a critical issue in determining the spectral quality and should be reduced as much as possible. The grounding wires of measurement systems should be connected to a single point ground in the stabilized power supply. The outputs from devices other than detectors should be electrically separated from the ADC using an isolation module. The signal cables between the detector and current amplifier should be low noise type and as short as possible. It is important to use a low-noise high-resolution type ADC and a low-noise fast-response type current amplifier.

7.8 Spatiotemporally Resolved QXAFS

The spatiotemporally resolved QXAFS is a powerful tool for investigating the dynamic aspect of structures and electronic states of spatially heterogeneous samples during the chemical reaction. There are two types of two-dimensional (2D) spatiotemporally resolved QXAFS methods: microprobe QXAFS and a 2D full-field imaging QXAFS.

The microprobe QXAFS method uses micro- and nano-beams. Reflective focusing optics such as the Kirkpatrick-Baez (KB) mirror and capillary are commonly applied for QXAFS measurement since they have no chromatic aberration (see Sect. 10.1). The spatial resolution of the measurement is decided by the focused beam size, which can be less than 100 nm if using the KB mirror. In this method, the X-ray fluorescence mapping (XRF) is first measured to specify the distribution of

the element and frame structure. Then, the QXAFS measurements are conducted on specific positions in the sample. The microprobe QXAFS method is difficult to apply for the point-by-point measurement of the transient reaction, and the quality of the XAFS spectra is significantly affected by the shift in the position irradiated by X-ray beams due to vibration and/or thermal drift in the focusing devices and sample stages during XAFS measurements. This is more serious when carrying out measurements with smaller X-ray beams. Therefore, the microprobe QXAFS measurements at fixed points require high stability on the devices concerning the focused beam position.

Full-field QXAFS methods are generally more effective for site-dependent studies than point-by-point microprobe methods since the former can be conducted with almost no time lag when different sites are measured, which, however, can be used only for the transmission mode measurement. 2D full-field imaging QXAFS measurements are conducted using a 2D imaging detector such as PADs and indirect conversion method X-ray image detectors [17, 18]. The latter is composed of a visible light conversion unit, which converts the incident X-rays into visible light by a scintillator, and a CCD or CMOS camera. The spatial resolution is defined by that of the imaging detector. The detector is selected to suit the spatial resolution and field of view required in each experiment. The pixel size and detection area of the PADs, such as EIGER and PILATUS, are from 50×50 to 170×170 μm^2 and several of tens cm^2, which is suitable for measuring areas larger than several millimeters using the large profile beam of the bending magnet radiation. The maximum count rate of the PADs ranges from 10^5 to 10^6 photons/pixel/s. The X-ray flux incident to each pixel of the PAD is 10^7 to 10^8 photons/pixel/s in the case of bending magnet beamline BL01B1 at SPring-8. This means the photon flux rate needs to be reduced to 10^2 times in order to be adjusted to the maximum counting rate of the PAD using an attenuator. The maximum frame rate of the PADs is 100–1000 Hz, so the minimum time resolution of the QXANES and QEXAFS is about 1 s and 100 s, respectively.

The minimum spatial resolution and field of view of the indirect conversion method X-ray image detectors is a few μm and several-hundred μm, and the monochromatized undulator beam flux is detectable without attenuation. This enables the measurement of one XAFS spectrum less than 1 s using this detector coupled with a high-speed CMOS sensor camera with a frame rate of more than 10 kHz and the focused beam from the tapered undulator. The actual time resolution, however, is limited by the spectral quality required for the analysis.

The incident beam profile is usually approximated by the average of that measured before and after the QXAFS measurement at each energy point. Thus, this method requires high reproducibility on the incident beam profile by achieving high stabilities on the SR light source and X-ray optics, especially the monochromator.

Most of 2D spatial-resolved QXAFS techniques have been applied for the static experiments. 2D spatiotemporally resolved QXAFS studies have just begun.

7.9 Combined Methods of QXAFS

The simultaneous time-resolved method is a very useful and practical technique that enables probing the same part of the sample by complementary techniques and provides a detailed understanding of the dynamical chemical processes. This method gives more precise information than separately conducted measurements since the time-resolved experiments of the transient reactions might be generally difficult to reproduce exactly. So far, QXAFS has been combined with time-resolved SR X-ray-based methods such as X-ray diffraction [19], small angle X-ray scattering and wide angle X-ray scattering [20] and with non-X-ray-based methods such as IR, VIS, UV, and Raman. The combined method uses specially designed operand cells and setups of the sample cell and detectors. However, it is difficult to conduct fully simultaneous SR X-ray-based and QXAFS measurements since SR X-ray-based methods other than XAFS usually use a constant energy. The QXAFS and SR X-ray-based measurements are therefore conducted alternately by controlling the Bragg angle of the monochromator.

It is possible to conduct non-X-ray-based measurements at the same time as QXAFS measurements. However, there is a difference in probing depth between the X-ray and non-X-ray light.

7.10 Outlook

In this section, QXAFS and related techniques were described from the point of view of instrumentation.

The minimum time resolution of QXAFS is about one millisecond at present, which is limited by both monochromator scan speed and the response time of the ionization chamber. The performance of the present monochromator and ionization chamber seems to be close to the limit. To achieve higher time resolution, the development of a new technical principle for the monochromator and detector may be required. Also, a faster and more efficient fluorescence X-ray detector is expected to be developed for the measurement of dilute samples or thin films.

Not so much research has been conducted using fast QXAFS measurements with the time resolution of less than a hundred milliseconds so far. The reason for this is not only the poor spectral quality stemming mainly from the X-ray flux but also the fact that it is not easy to construct the reaction cell included in the stimulation system for the actual samples with this time scale. It is expected that QXAFS investigation of fast chemical reactions will be driven by the development of a dedicated reaction cell.

Time-resolved imaging techniques will be key for the investigation of the dynamic aspect of the actual heterogeneous chemical reaction. 2D spatiotemporally resolved QXAFS studies have just begun, and applications are expected to increase in various research fields. Recently, a 3D spatial-resolved XAFS method with a

resolution of several tens of nm has been applied under ex situ conditions. 3D spatiotemporally resolved XAFS is expected to be realized as a result of such technology developments.

The method combined with QXAFS is expected to further spread to SR X-ray-based techniques such as X-ray computed tomography, resonant inelastic X-ray scattering, and X-ray emission spectroscopy.

References

1. Frahm R (1988) Quick scanning exafs: first experiments. Nucl Instrum Methods A270:578
2. Uruga T, Tanida H, Kato K, Furukawa Y, Kudo T, Azumi N (2009) Improvement in XAFS beamline BL01B1 at SPring-8. J Phys Conf Ser 190:012041
3. Rogalev A, Gotte V, Goulon J, Gauthier C, Chavanne J, Elleaume P (1998) XAFS and X-MCD spectroscopies with undulator gap scan. J Synchrotron Radiat 5:989
4. Barrea ARA, Fischetti R, Stepanov S, Rosenbaum G, Kondrashkina E, Bunker GB, Black E, Zhang K, Gore D, Heurich R, Vukonich M, Karanfil C, Kropf AJ, Wang S, Irving TC (2005) Biological XAFS at the BioCAT undulator beamline 18ID at the APS. Phys Scr T115:867
5. Tanaka T, Kitamura H (2001) SPECTRA: a synchrotron radiation calculation code. J Synchrotron Radiat 8:1221
6. Frahm R, Richwin M, Lützenkirchen-Hecht D (2005) Recent advances and new applications of time-resolved X-ray absorption spectroscopy. Phys Scr T115:974
7. Stötzel J, Lützenkirchen-Hecht D, Frahm R (2010) A new flexible monochromator setup for quick scanning X-ray absorption spectroscopy. Rev Sci Instrum 81:073109
8. Nonaka T, Dohmae K, Araki T, Hayashi Y, Hirose Y, Uruga T, Yamazaki H, Mochizuki T, Tanida H, Goto S (2012) Quick-scanning X-ray absorption spectroscopy system with a servo-motor-driven channel-cut monochromator with a temporal resolution of 10 ms. Rev Sci Instrum 83:083112
9. Richwin M, Zaeper R, Lutzenkirchen-Hecht D, Frahm R (2001) Piezo-QEXAFS: advances in time-resolved X-ray absorption spectroscopy. J Synchrotron Radiat 8:354
10. Hara T, Tanaka T, Seike T, Bizen T, Marechal X, Kohda T, Inoue K, Oka T, Suzuki T, Yagi N, Kitamura H (2001) In-vacuum X-ray helical undulator for high flux beamline at SPring-8. Nucl Instrum Methods Phys Res A 467–468:165
11. Inoue K, Oka T, Suzuki T, Yagi N, Takeshita K, Goto S, Ishikawa T (2001) Present status of high flux beamline (BL40XU) at SPring-8. Nucl Instrum Methods Phys Res A 467–468(674)
12. Uruga T, Tanida H, Inoue K, Yamazaki H, Irie T (2007) Quick XAFS system using quasimonochromatic undulator radiation at SPring-8. AIP Conf Proc 882:914
13. Sekizawa O, Uruga T, Tada M, Nitta K, Kato K, Tanida H, Takeshita K, Takahashi S, Sano M, Aoyagi H, Watanabe A, Nariyama N, Ohashi H, Yumoto H, Koyama T, Senba Y, Takeuchi T, Furukawa Y, Ohata T, Matsushita T, Ishizawa Y, Kudo T, Kimura H, Yamazaki H, Tanaka T, Bizen T, Seike T, Goto S, Ohno H, Takata M, Kitamura H, Ishikawa T, Yokoyama T, Iwasawa Y (2013) New XAFS beamline for structural and electronic dynamics of nanoparticle catalysts in fuel cells under operating conditions. J Phys Conf Ser 430:012020-1
14. Uruga T et al, to be submitted
15. Tischer M (2013) Undulators at PETRA: experience and perspectives. In: 3-Way meeting, Argonne, http://aps.anl.gov/Users/3Way/presentations/Tischer.pdf
16. Müller O, Stötzel J, Lützenkirchen-Hecht D, Frahm R (2013) Gridded ionization chambers for time resolved X-ray absorption spectroscopy. J Phys Conf Ser 425:092010
17. Tanida H, Yamashige H, Orikasa Y, Oishi M, Takanashi Y, Fujimoto T, Sato K, Takamatsu D, Murayama H, Arai H, Matsubara E, Uchimoto Y, Ogumi Z (2011) In situ two-dimensional imaging quick-scanning XAFS with pixel array detector. J Synchrotron Radiat 18:919

18. Tanida H, Yamashige H, Orikasa Y, Fujimoto T, Oishi M, Murayama H, Arai H, Katayama M, Inada Y, Ohta T, Uchimoto Y, Ogumi Z (2013) In situ two-dimensional micro-imaging XAFS with CCD detector. J Phys Conf Ser 430:012021
19. Grunwaldt J-D, Clausen BS (2002) Combining XRD and EXAFS with on-line catalytic studies for in situ characterization of catalysts. Top Catal 18:37
20. Nikitenko S, Beale AM, van der Eerden AMJ, Jacques SDM, Leynaud O, O'Brien MG, Detollenaere D, Kaptein R, Weckhuysen BM, Bras W (2008) Implementation of a combined SAXS/WAXS/QEXAFS set-up for time-resolved in situ experiments. J Synchrotron Radiat 15:632

Chapter 8
Energy Dispersive XAS

Sakura Pascarelli and Olivier Mathon

8.1 Introduction

This chapter presents an overview of energy dispersive X-ray absorption spectroscopy (EDXAS), as developed and used at synchrotron radiation sources. It mainly covers time resolved studies, with emphasis on technical aspects.

In EDXAS, a curved crystal disperses and focuses a polychromatic X-ray beam onto the sample (Fig. 8.1). This crystal is named a polychromator, by analogy with the monochromators used on the energy scanning spectrometers. The Bragg angle of incidence varies continuously from one side of the crystal to the other.

Consequently, the energy of the X-ray beam diffracted by the crystal varies also continuously from one side of the crystal to the other, introducing a correlation between the X-ray beam propagation direction and its energy. The beam transmitted by the sample is then detected by a position sensitive detector, where the energy-direction correlation introduced by the polychromator is transformed into an energy-position correlation. To measure a XAS spectrum, the incident and transmitted intensities as a function of photon energy $I_0(E)$ and $I_1(E)$ are obtained from the spatial distribution of photons on the detector without and with the sample respectively. All energy points of the absorption spectrum are acquired in parallel. Due to the parallel acquisition scheme, an EDXAS spectrometer operates intrinsically in a time resolved manner. The time resolution is ultimately defined by the performance of the detector (minimum exposure time and maximum frame rate) and the characteristics of the X-ray source (number of photons per detector pixel).

Besides the acquisition speed, another major advantage of EDXAS is its intrinsic stability, because during acquisition there are no moving components. This leads to a reduction of systematic noise and to high stability of the energy scale and focal

S. Pascarelli (✉) • O. Mathon
European Synchrotron Radiation Facility, 38000 Grenoble, France
e-mail: sakura@esrf.fr

Y. Iwasawa et al. (eds.), *XAFS Techniques for Catalysts, Nanomaterials, and Surfaces*, DOI 10.1007/978-3-319-43866-5_8

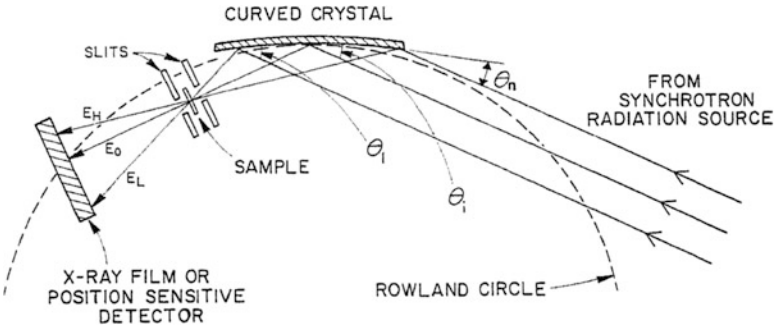

Fig. 8.1 Historical optical scheme of the energy dispersive X-ray absorption spectrometer (Ref. [1])

spot position. The combination of speed and stability has led to unprecedented sensitivity in the detection of atomic displacements through measurements in differential mode [2]. If a high brilliance source is utilized, focal spots of the order of a few microns can be achieved [3], and EDXAS becomes an ideal playground for high pressure investigations [4] or hyperspectral mapping on heterogeneous samples [5]. EDXAS has also been applied as a chemical and orbital selective probe of magnetism [6, 7].

This chapter focuses on the time-resolved applications of EDXAS. It is structured as follows. Section 8.2 outlines the historical development of this technique and gives an overview of the existing facilities worldwide. It then compares the dispersive vs the scanning spectrometer for time resolved XAS applications. Section 8.3 discusses the working principle of the energy dispersive XAS spectrometer, it introduces the equations for the evaluation of energy bandpass and resolution and discusses the limitations on the focal spot. Section 8.4 reports examples of applications of EDXAS in different time resolution domains, with emphasis on acquisition methods and detection systems. The fast and parallel acquisition of the full XAS, with short exposure time and short deadtime between consecutive exposures makes EDXAS very attractive for its ability to "film" the time evolution of a dynamic process. EDXAS was developed in the early 80s to track the evolution of the local and electronic structure of the absorber during a chemical reaction in real time (Sect. 8.4.1). In more recent years, this real-time capability has also shown great potential to probe matter in thermodynamical conditions that are so extreme that they can be produced only for short periods of time (Sect. 8.4.2). Finally, thanks to advances in detector technology, today exposure time has decreased to levels that enable the selection of a single X-ray pulse (from a single electron bunch in the ring), and EDXAS has recently been exploited to probe nanosecond-lived excited states of matter using a single shot acquisition (Sect. 8.4.3).

8.2 Energy Dispersive X-ray Absorption Spectroscopy

8.2.1 Historical Development of EDXAS and Overview of Existing Facilities

Synchrotrons all over the world have invested in EDXAS spectrometers in the past 40 years. Starting from the synchrotron pioneering work in the early 80s [1], this technique has spread to many other synchrotron sources worldwide. The first EDXAS beamlines were built in Japan [8], France [9], Germany [10] and UK [11, 12]. EDXAS beamlines are now operational in Brazil (LNLS), India (Indus II), France (ESRF and SOLEIL), Japan (PF-AR and SPring8), Thailand (SLRI), and soon in UK (DLS) and China (SSRF). Table 8.1 below presents an overview of the existing EDXAS facilities, together with source type and principal characteristics of the spectrometer. In order to obtain a polychromatic fan with a sufficient energy bandwidth to cover a full EXAFS spectrum, a source with a large horizontal divergence (bending magnet or wiggler) is generally chosen. This is the case for all existing EDXAS beamlines, except for the NW2A beamline at PF-AR and the EDXAS beamline of the European Synchrotron Radiation Facility (ESRF) ID24. The future D-line of SSRF, Shanghai Synchrotron Radiation Facility, is foreseen to be built also on an undulator source. The first EDXAS beamline built on a third generation undulator source [13] features an original optical scheme where the large divergence is created using a strongly focusing mirror. This mirror not only creates a sufficiently large divergence that undulator sources do not have, but also creates a secondary source allowing the production of a micron sized focal spot [14]. This scheme allows obtaining 10^{13}–10^{14} photons per second on the sample in the whole EDXAS bandwidth, leading to an ultimate time resolution in the order of 1 μs for a single measurement, together with a μm scale focal spot size.

8.2.2 Dispersive Versus Scanning Spectrometer for Time Resolved Experiments

The main advantages of EDXAS spectrometers with respect to energy scanning spectrometers are: (1) the speed of acquisition, since all energy points are acquired in parallel on the position sensitive detector, (2) a small focal spot size together with a high flux, and (3) the stability of the energy scale and focal spot position, since there are no moving components during acquisition. There are two main limitations that are intrinsic to EDXAS. The first one is related to the need to maintain the energy-direction correlation created by the polychromator throughout the whole path from the crystal to the detector. This poses severe constraints on the morphology and microstructure of the sample: systems which produce strong small angle scattering are not suited for EDXAS (see for example Ref. [24]). The second is due

Table 8.1 Overview of existing or planned EDXAS beamlines worldwide

Beamline	Synchrotron	Source	Energy (keV)	PLC	H. Spot size (μm)	Min. exposure time/rep rate	Ref.	Status
D06A	LNLS-Brazil	BM	4–14	B	250	1/120 ms	[15]	Oper.
D-line	SSRF-China	U	5–20	B-L			[16]	Construct.
BL08	Indus II-India	BM	4–24	B	200	10/300 ms	[17]	Oper.
ID24	ESRF-France	U	5–28	B-L	3–20	0.15 μs/ 2.8 μs	[18]	Oper.
ODE	SOLEIL-France	BM	3.5–25	B	25	10 μs/ 50 μs	[19]	Oper.
NW2A	PF-AR-Japan	U	5–40	B-L	500	0.5 μs/ 23 μs	[20]	Oper.
BL14B1	Spring8-Japan	BM	7–40	B-L	90–160	6 ms	[21]	Oper.
BL28B2	Spring8-Japan	BM	8–80	B-L	100	6 ms	[21]	Oper.
BL2.2	SLRI-Thailand	BM	2.4–8	B	1000	1 ms/25 ms	[22]	Oper.
I20	DLS-UK	W	6–26	B	50	0.5 μs/ 10 μs	[23]	Comm.

BM bending magnet, *U* undulator, *W* wiggler, *PLC* polychromator, *B* Bragg geometry, *L* Laue geometry

to the fact that detection using de-excitation processes (fluorescence, total electron yield, etc.) is not possible, since all energies impinge on the sample simultaneously.

In addition to these fundamental limitations, the EXAFS k-range is limited at low energies because the energy bandwidth of the polychromatic fan scales with the cotangent of the Bragg angle (see Eq. 8.1). Finally, the fact that in general the incident and transmitted intensity (I_0 and I_1) are not measured simultaneously may represent a drawback, especially in case of incident intensity fluctuations with time (X-ray beam instabilities). By giving up the parallel detection over the full energy range and using a sequential acquisition mode [24], the energy dispersive spectrometer has demonstrated its capacity for fast-time resolved XAS studies in fluorescence mode [25].

The limitations mentioned above have certainly played a role in the development of EDXAS, and although this technique has spread quite rapidly, the EDXAS user community remains a minor portion of the global XAS user community. In addition to these intrinsic limitations, the technical challenges to build and use an EDXAS spectrometer are important: for example dealing with stability issues, designing efficient polychromator crystals and benders, or developing dedicated detectors.

In the domain of dynamical studies, EDXAS beamlines have been historically used for applications dealing with homogeneous and heterogeneous catalysis [26]. The typical timescales of this kind of experiments ranges from minutes down to the ms. With the development of fast energy scanning spectrometers (QEXAFS) [27], the tens of ms timescale are now accessible to scanning spectrometers. In addition, these experiments often deal with small absorber concentrations (roughly $< 1\,\%$ wt) and can then benefit from the fluorescence detection mode on scanning spectrometers. Therefore, the interest of using EDXAS spectrometers on these timescales has decreased.

Dynamical processes on timescales faster than the 10 ms range can be investigated with scanning spectrometers by using pump and probe techniques, where the time evolution of the absorption at a single energy is recorded. But an EDXAS spectrometer can follow the process in “film” mode, i.e., with complete XAS spectra continuously recorded one after the other as the dynamical process evolves in time. If combined to a high flux source, an EDXAS spectrometer allows to obtain a sufficient signal to noise ratio in a single ”film”. This is particularly important for experiments that cannot be cycled indefinitely [28] or where the sample is destroyed after the run [29]. An EDXAS spectrometer can also operate in pump-and-probe mode. Again, the technique is particularly suited to single shot experiments where the sample is lost at the end of the run or/and when the dynamical process varies from shot to shot [30].

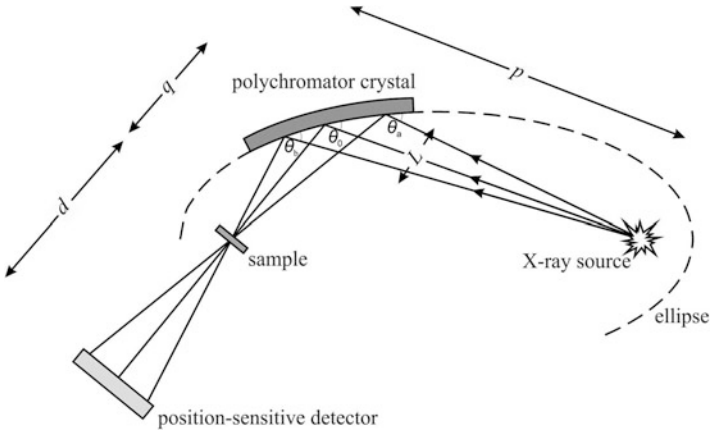

Fig. 8.2 Principle of operation of the energy-dispersive XAS spectrometer

8.3 The Energy Dispersive Spectrometer

The energy dispersive spectrometer employs a curved crystal to focus and disperse a polychromatic fan of X-rays onto the sample position, introducing a correlation between the photon energy and the direction of propagation (see Fig. 8.2). The beam transmitted by the sample is detected by a position sensitive detector positioned at the end of the 2θ spectrometer arm where energy is correlated to position. The crystal is curved to an elliptical shape. The radius R of the closest circle is given by:

$$1/p + 1/q = 2/R \sin\theta_0$$

where p, q, and θ_0 are respectively the source–crystal and crystal–sample distances and central Bragg angle. In Fig. 8.2, L is the horizontal dimensions of the beam intercepted by the polychromator, and $L/\sin\theta_0$ is the footprint of the beam on the crystal surface.

This Section introduces the basic equations for the evaluation of energy bandpass and energy resolution and discusses the limitations on the focal spot of an EDXAS spectrometer. Beamline ID24 at the ESRF is used as an illustrative example.

8.3.1 Energy Bandwidth

The full spectral range diffracted by the crystal ΔE is proportional to the variation of Bragg angle θ along the beam footprint on the crystal, $\Delta\theta$:

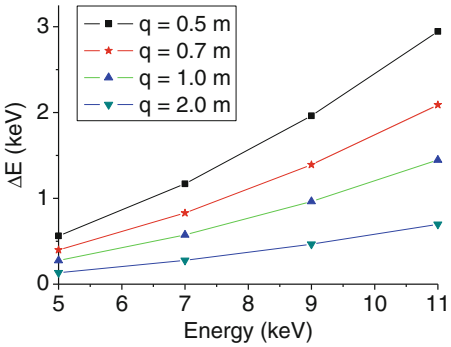

Fig. 8.3 Full spectral range ΔE diffracted by a Si(1 1 1) polychromator as a function of central energy E_0, from Eqs. (8.1) and (8.2), calculated for $L = 50$ mm and $p = 30$ m

$$\Delta E = E_0 \Delta\theta \cot\theta_0 \tag{8.1}$$

where E_0 is the central energy. $\Delta\theta$ can be calculated from p, q, and L as follows:

$$\Delta\theta = \frac{L}{\sin\theta} \frac{1}{2} \left(\frac{1}{q} - \frac{1}{p}\right) \tag{8.2}$$

Equation (8.2) is valid as long as $L/\sin\theta$ is smaller than the useful length of the polychromator crystal. In general, EDXAS spectrometers are installed on synchrotron sources having a large horizontal divergence, which easily provides a large beam footprint on the surface of the crystal to provide a sufficiently large energy bandwidth ΔE to cover a full EXAFS spectrum in a single shot.

Equation (8.1) highlights an additional important limitation of EDXAS: at low energies, the full spectral range diffracted by the polychromator ΔE is strongly reduced due to the $\cot\theta$ factor. This is illustrated in Fig. 8.3, which shows typical ΔE vs E_0 values for different q values obtained on ID24, using a Si(1 1 1) polychromator placed at $p = 30$ m from the source. For a fixed choice of E_0, ΔE strongly depends on the polychromator-sample distance q. At low energies ($E < 7$ keV), the k-range of the EXAFS is strongly reduced.

8.3.2 *Energy Resolution*

The energy resolution of an energy dispersive spectrometer depends on the central energy, E_0, the crystal diffracting planes (h, k, l), the focusing distance q and detector position d. A simple expression $\delta E/E$ for can be derived from Bragg's law:

$$\frac{\delta E}{E_0} = \delta\theta \cot\theta_0, \tag{8.3}$$

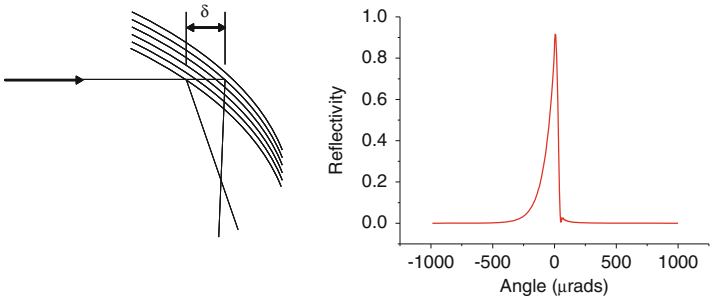

Fig. 8.4 (*Left*) Schematic effect of X-ray penetration in a curved crystal. (*Right*) Simulation of the diffraction profile deformation of Si(1 1 1) crystal at 15 keV due to a 3 m radius of curvature

where $\delta\theta$ is the overall "monochromatic" angular spread. For a polychromator in Bragg geometry (i.e., the incident and the diffracted beam propagate on the same side of the crystal), $\delta\theta$ includes contributions from several factors: the spatial resolution of the detector $\delta\theta_1$, the size of the X-ray source $\delta\theta_2$, and the Darwin width of the curved polychromator crystal $\delta\theta_3$:

$$\delta\theta^2 = \delta\theta_1^2 + \delta\theta_2^2 + \delta\theta_3^2 \tag{8.4}$$

The Darwin width spread due to the crystal curvature is included in $\delta\theta_3$.

The incident beam intercepts Bragg planes with a continuously different angle when it penetrates the crystal leading to an asymmetrical reflectivity profile of the highly curved Bragg-type crystal [31]. The effect can be simulated [32] and is illustrated in Fig. 8.4. This has severe consequences: a degradation of the energy resolution and an asymmetrical shape of the focal spot. This contribution increases with energy and with crystal curvature. It is small at 7 keV and becomes dominant at 18 keV for a Si(1 1 1) crystal. This is the fundamental limitation of the Bragg geometry in the achievement of small focal spots and high energy resolution at high energies ($E > 13$ keV). As an illustration, we report in Figs. 8.5 and 8.6 the angular contributions $\delta\theta_i$ and the energy resolution $\delta E/E$ respectively, calculated for ID24 in the case of a Bragg Si(1 1 1) crystal focusing at $q = 0.7$ m with a detector at $d = 3.3$ m.

These figures show that the main contributions derive from $\delta\theta_3$. In particular, Fig. 8.5 shows the increase of the spread of the Darwin width with energy, while Fig. 8.6 illustrates that for energies larger than 15 keV, the energy resolution of the bent Bragg crystal exceeds the K-edge core-hole lifetime contribution. This effect, together with the geometric reduction in horizontal acceptance of the crystal at low Bragg angles, limits the use of the Bragg geometry to the range 5–13 keV approximately. For this reason, polychromators in the Laue geometry (i.e., the incident and the diffracted beam propagate on opposite sides of the crystal) have been developed for high energy applications of EDXAS [31]. In the bent symmetric Laue case, the deformation induced by bending is orthogonal to the reciprocal lattice. The case can be treated as an unbent crystal and, contrary to the Bragg case, there is no

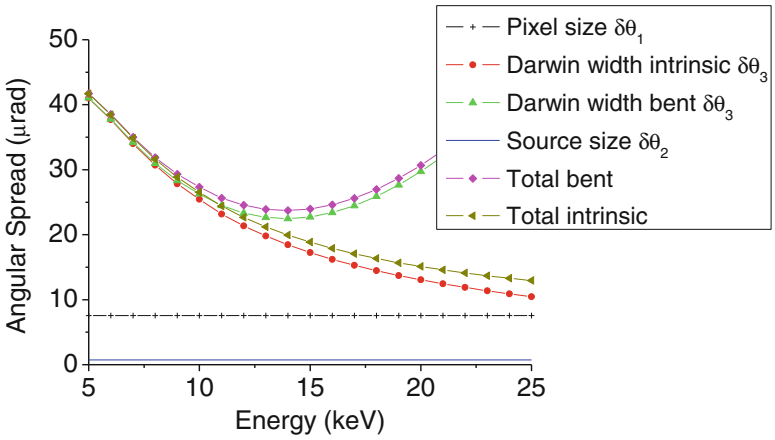

Fig. 8.5 Angular contribution to the energy resolution versus central energy E_0, $q = 0.7$ m, detector at $d = 3.3$ m for a Si(1 1 1) crystal

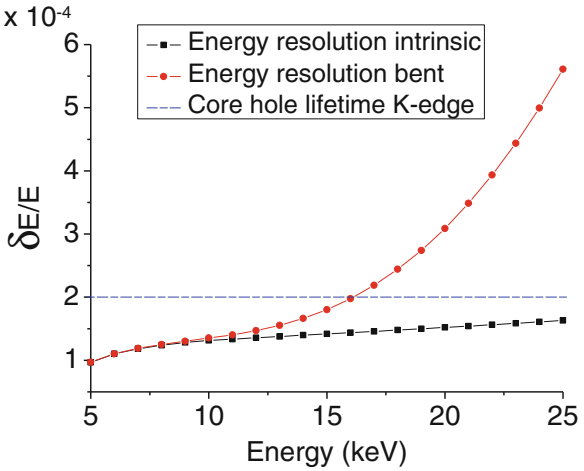

Fig. 8.6 Energy resolution versus central energy E_0, $q = 0.7$ m, detector at $d = 3.3$ m for a Si(1 1 1) crystal

broadening of the Darwin width whatever the bending radius is. Consequences are that there is no broadening of the focal spot size nor a loss in energy resolution at high energy, but an additional $\delta\theta$ term is required in Eq. (8.4) to take into account the spread of the monochromatic beam on the detector due to the Borrmann fan.

8.3.3 Focusing Properties

Focusing using bent Bragg planes cannot be described in the same way as focusing with total reflection optical elements. Due to X-ray beam penetration into the

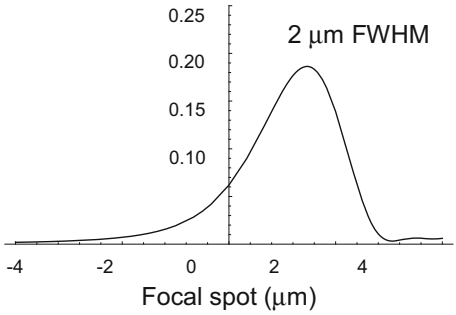

Fig. 8.7 Dynamical contribution to the focal spot size for a Si(1 1 1) crystal at 7 keV with $p = 30$ m and $q = 1$ m

crystal, there are two effects that affect focusing. The first one is due to the variation of Bragg angle as a function of penetration depth, due to the bent shape of the crystal (see Fig. 8.4). The second effect is due to Bragg diffraction. In Bragg diffraction conditions, a crystal (bent or flat), has a natural angular acceptance (Darwin width) ω_D when highlighted by a monochromatic divergent beam. This leads to a monochromatic diffracted beam with a natural divergence $\Delta\theta = 2\omega_D$. Due to the focusing diffraction limit, such a beam leads to an intrinsic transverse focal spot size Δx of:

$$\Delta x \cdot \Delta\theta = \Delta x \cdot 2\omega_D = 0.89\lambda$$

if the diffraction profile is approximated by a rectangle. At 7 keV for a Si(1 1 1) crystal the intrinsic dynamical contribution to the focal spot size is $\Delta x \sim 2$ µm. This result has been confirmed by dynamical theory simulations of the Bragg bender case [33] as shown in Fig. 8.7.

For a polychromatic incident beam, the final spot size is the result of the sum of all monochromatic contributions. Therefore focusing a polychromatic incident divergent beam with a bent crystal leads to an intrinsic spot size limit of the order of 2 µm FWHM in the Bragg geometry. Another limiting factor to the spot size is the slope error of the Bragg polychromator crystal. The difficulties here are related to the manufacture of large Si crystals, the thickness of which needs to remain constant to within a few microns along the full length. The protocol for the manufacture of such crystals is constantly being improved, but it is still very difficult to achieve the desired shape over the full footprint of the beam on the polychromator. The consequences are that focal spot sizes will in general be dependent on the portion of the polychromatic fan (or on the portion of the illuminated footprint on the crystal) that is selected. On ID24, at the Fe K-edge and at $q \sim 0.75$ m, the focal spot achieved is $\sim 4 \times 4$ µm^2 FWHM with an selected energy range of $\Delta E_{sel} \sim 500$ eV, although the full spectral range diffracted by the polychromator in this geometry is $\Delta E \sim 800$ eV (from Eq. 8.1). The accuracy of the crystal bending and therefore the bender and crystal preparation technology is a key point of the EDXAS spectrometer.

8.4 Time Resolved Applications

8.4.1 From the Minute Down to the ms

In the domain of time resolved studies, EDXAS spectrometers have been historically used for *operando* catalysis applications. The typical timescale of this kind of experiments spreads from minutes down to the ms. On this timescale, the limitation in data quality is, in many situations, not linked to the photon flux. The EDXAS spectrometer acts as a camera to record the time evolution of the XAS signal through the studied phenomena: the chemical reaction is filmed in situ. From a technical point of view, the time resolution is linked to the speed of the camera, i.e., the repetition rate and minimum exposure time of the pixel detector. On many EDXAS beamlines, detectors based on Charge Coupled Device (CCD) cameras optically coupled with a scintillator screen have been implemented. On ID24, a 1D CCD device is implemented, with a repetition rate of 4 kHz and minimum integration time of 200 µs [34]. One limiting factor of such a device is the decay time of the scintillator screen. A compromise needs to be found between the three main parameters characterizing a scintillator screen: X-ray conversion efficiency, the emission spectrum that should be coupled to the CCD characteristics and the luminescence decay time. On ID24, a P43 (Gd_2O_2S:Tb) screen is generally used with decay time of 1.5 ms (100–10 %) and 3.2 ms (100–1 %). For the fastest applications, a P47 (100 ns, 100–10 %) screen can be adopted at the price of efficiency.

The first papers reporting on XAS studies of kinetics down to the ms timescale appeared at the XAFS conference in 1986 [8, 35]. Since then, EDXAS has been applied in many fields of chemistry and catalysis to probe the evolution of local and electronic structure during kinetic processes, such as nanoparticle formation, catalytic processes and chemical reactions. A nice example of EDXAS in this field is reported in Ref. [36], where selective catalytic oxidation of benzene to phenol was investigated. Re L_3 EXAFS combined to Density Functional Theory (DFT) calculations probed the catalytically active structure and the structural transformation and dynamics of new zeolite-supported interstitial-N/Re-clusters which were found to have impressive selectivities (as high as 94 % at 553 K) for this reaction. There are also many examples of in situ *operando* investigations of catalytic processes exploiting synchronous combined measurements of EDXAS with UV-vis/Infrared/Raman/Mass spectrometry or X-ray diffraction [26]. The main difficulty of these experiments lies in the design of multi-technique compatible in situ cells that must reproduce the real catalytic *operando* conditions as closely as possible.

8.4.2 *Down to the μs*

Below the ms, fluorescent screen based CCD cameras start to be limited either by the maximum repetition rate of the detector or/and the decay time of the scintillator screen. To overcome these limitations, microstrip-based detector have been specifically developed for EDXAS ultra-fast X-ray spectroscopy studies. A first version based on a 1024 element Si microstrip chip combined with custom developed low noise, fast readout, electronics (XCHIP) [37] demonstrated minimum integration time down to the μs with 100 kHz repetition rate. At the same time, Si based devices have demonstrated a poor detection efficiency and a susceptibility to radiation damage under the high flux of third synchrotron generation sources, especially at high energy (above ~12 keV). This lead to the development of a second generation of microstrip detectors for high energies (XH) based on a 1024 element germanium microstrip [38]. The XH detector has been designed to provide almost 100 % detection efficiency over the working range of 5–40 keV and immunity to radiation damage. At the same time, readout electronics was upgraded to provide an excellent system linearity (better than 0.1 %), minimum exposure time below 100 ns and higher readout performance (355 kHz frame rate). These values correspond to the ESRF X-ray time structure.

When integration time decreases down to few tens of microseconds, the natural X-ray time structure of synchrotron based sources cannot be neglected and a synchronization of the detection to the electron bunch (in general with the RF cavity) is mandatory. Figure 8.8 presents the intensity variations along one ring circumference in the ESRF 7/8 + 1 filling mode [39], recorded with the XH detector using an integration time of 88 ns. As a consequence, the basic frequency to synchronize a detector, for the fastest applications, should be equal to one ring circumference, i.e., 2.8 μs at the ESRF (355 kHz).

In this range of timescales, between the ms and the μs, a dispersive spectrometer can be particularly suited to study matter under extreme conditions of pressure, temperature, and magnetic field. The interest is not directly linked to the dynamics

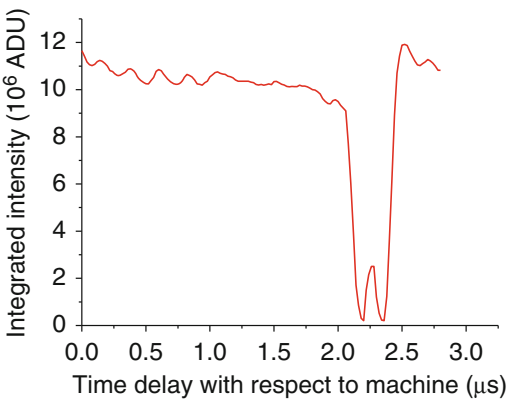

Fig. 8.8 Detector integrated intensity as a function of time over one single synchrotron circumference at ESRF in 7/8 + 1 filling mode

of the experiment but rather to the capacity to create thermodynamical states that are metastable, difficult or very expensive to produce for longer periods or completely unreachable in static mode.

The dispersive spectrometer is of particular interest when the experiment is non-reversible, for example when the sample in destroyed at the end of the run (single shot experiment). This is especially true when the dispersive spectrometer is coupled with a high flux source like an undulator or a wiggler. The flux on the sample can then reach 10^{14} photons per seconds in the energy bandwidth, leading to a flux of about 10^5 photons per pixel (per XAS point) and per μs. In theory, this flux is sufficient to obtain a good signal to noise ratio in the XAS spectrum in a single shot experiment. This possibility is illustrated by recent work on dynamic excitation of Fe towards the warm dense matter regime using ohmic ramps [29]. The dispersive spectrometer can play also an interesting role when the number of repetitions is limited due to the fatigue of one component, for example of a resistive coil in a pulsed high magnetic field experiment [28]. The lifetime of the coil (in number of shots before failure) decreases as field magnitude increases. Pulsed magnetic field experiments are possible on scanning spectrometers, but full XAS information at high fields is very expensive in terms of coil degradation due to the very large number of cycles required.

Figure 8.9 reports results from the investigation of a Mn spin-crossover compound, H3taa¼tris(1-(2-azolyl)-2- azabuten-4-yl)amine, [also named MnIII (taa)]. Such compounds have much potential for application in controllable magnetic devices. The figure shows magnetic field induced modifications of the Mn K-edge XANES recorded at $T = 29$ K as a function of magnetic field up to 37 T. The magnet could generate pulsed fields up to 37 T for a duration of 1 ms. For each discharge process, twenty discrete spectra were acquired with exposures of 100 μs and dead time of 14.4 μs between them.

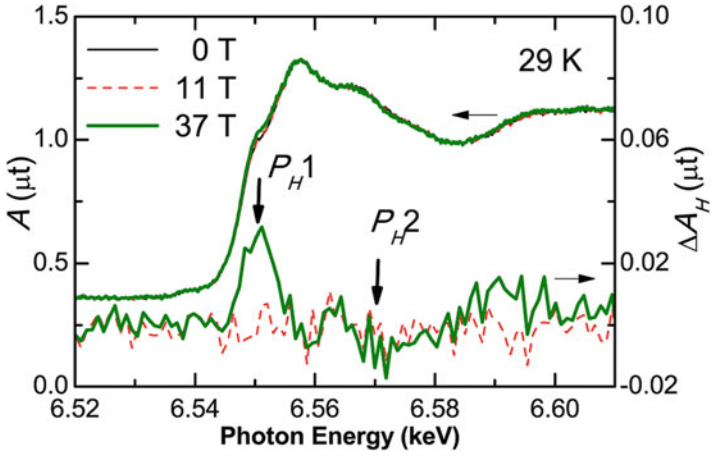

Fig. 8.9 Field-dependent Mn K-edge XANES spectra (*left axis*) and the difference spectra, ΔA_H (*right axis*), at 29 K in magnetic fields of 0, 11, and 37 T. From Ref. [28]

Finally, even if thermodynamical conditions can be reached in static mode, the unique combination of fast and parallel acquisition of the XAS spectrum together with a small focal spot is of high interest to probe samples subject to extreme conditions, and to check their stability in time. This is for example the case of investigations of matter at high pressures and temperatures, such as melts at conditions of Earth's interior [40].

8.4.3 Below the Microseconds

Below the μs it becomes necessary to work with a single X-ray bunch. The technique generally used is the pump-and-probe approach where the time resolution is defined by the delay between the pump (start) and the probe (stop). The time resolution is then limited either by the duration of the pump or by the duration of the probe. In practice, the time resolution is very often limited by the duration of the X-ray bunch, i.e., around 100 ps. The role of the detector in this mode is only to select the desired X-ray bunch and to reject the side bunches. The important parameter of the detector is consequently the minimum integration time. The XH, with a minimum integration time of about 80 ns, is perfectly suited for this kind of experiments. From a general point of view, the repetition rate of the experiment is limited by the repetition rate of the pump, for example, a laser operating at few tens of Hertz. Consequently, the request for the repetition rate of the detector is less demanding than in "film" mode. The principal disadvantage of the dispersive approach with respect to similar pump-probe applications using scanning spectrometers, is the restriction to a transmission geometry. However, this limitation is alleviated with highly stable X-ray sources, and thus the intrinsic gain by multiplexing the X-ray spectrum is still a very significant real-time gain in kinetic studies of structural changes. EDXAS in combination with a single 100 ps bunch has been used to take fast snapshots of the time evolution of photo-excited Cu based complexes [41], as illustrated in Fig. 8.10.

The additional value of using a dispersive spectrometer in such pump-and-probe method is highlighted again when the experiment is non-repeatable. For example, when the pump itself is not perfectly reproducible (i.e., the energy delivered by the laser is not constant shot to shot) or when the sample is damaged or destroyed at the end of each pump-and-probe cycle. It is then important to obtain a sufficiently good signal-to-noise ratio with a single X-ray bunch integration. At ESRF with the ID24 EDXAS spectrometer, in four bunch filling mode and coupled to four undulators, 20,000 ph./pixels/single X-ray bunch have been measured at 7 keV in the direct beam. This is sufficient to obtain clean XANES features in many cases. A recent experiment has shown that EXAFS measurements can be achieved on dynamically compressed Fe by means of a high power laser pulse (Fig. 8.11) [30].

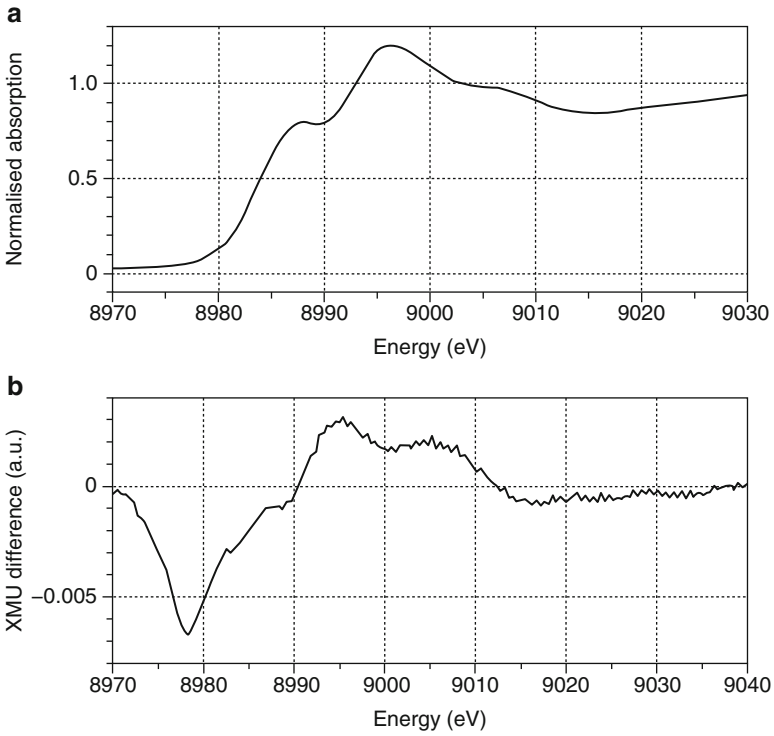

Fig. 8.10 (**a**) Cu K-edge XANES and (**b**) the difference between the excited and ground state XANES (*bottom*) in $[Cu^{I}(dmp)_2]PF_6$ in CH_3CN (20 mM). From Ref. [41]

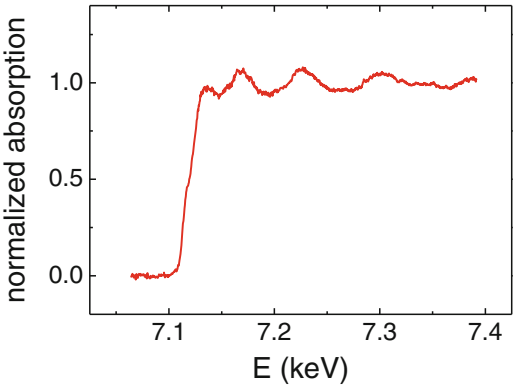

Fig. 8.11 Fe K-edge XANES using a unique 100 ps bunch on an Fe target dynamically compressed by a laser shock

References

1. Matsushita T, Phizackerley RP (1981) A fast X-ray absorption spectrometer for use with synchrotron radiation. Jpn J Appl Phys 20:2223–2228
2. Pettifer RF, Mathon O, Pascarelli S et al (2005) The measurement of tiny displacements using X-ray absorption spectroscopy. Nature 435:78–81
3. Pascarelli S, Mathon O (2010) Advances in high brilliance energy dispersive X-ray absorption spectroscopy. Phys Chem Chem Phys 12:5535–5546
4. Aquilanti G, Mathon O, Pascarelli S (2009) Achievements in high-pressure science at the high-brilliance energy-dispersive X-ray absorption spectrometer of ESRF, ID24. J Synchrotron Radiat 16:699–706
5. Munoz M, De Andrade V, Vidal O et al (2006) Redox and speciation micromapping using dispersive X-ray absorption spectroscopy: application to iron chlorite mineral of a metamorphic rock thin section. Geochem Geophys Geosyst 7:Q11020-1–Q11020-10
6. Baudelet F, Brouder E, Dartyge E et al (1990) Magnetic properties of $ReFe_2$, $CeFe_2$, $GdFe_2$, $LuFe_2$ compounds studied by magnetic X-ray dichroism. Europhys Lett 13:51–757
7. Torchio R et al (2014) Following chemical structures using synchrotron radiation. Coord Chem Rev 277–278:1–300
8. Saigo S, Oyanagi H, Matsushita T et al (1986) Stopped-flow X-ray absorption spectroscopy in dispersive mode. J Phys Colloques 47(C8):555–561
9. Dartyge E, Depautex C, Dubuisson JM et al (1986) X-ray absorption in dispersive mode: a new spectrometer and a data acquisition system for fast kinetics. Nucl Instrum Methods Phys Res A 246:452–460
10. Hagelstein M, Cunis S, Frahm R et al (1989) The energy dispersive X-ray absorption spectrometer DEXAFS at HASYLAB. Physica B 158:324–325
11. Allinson NM, Baker G, Greaves GN et al (1988) PDA system for energy dispersive EXAFS. Nucl Instrum Methods Phys Res A 266:592–597
12. Dent A, Evans J, Newton M et al (1999) High-quality energy-dispersive XAFS on the 1 s timescale applied to electrochemical and catalyst systems. J Synchrotron Radiat 6:381–383
13. Hagelstein M, San Miguel A, Fontaine A et al (1997) The beamline ID24 at ESRF for energy dispersive X-ray absorption spectroscopy. J Phys IV France 7(C2):303–308
14. Pascarelli S, Mathon O, Munoz M et al (2006) Energy dispersive absorption spectroscopy for hard X-ray micro-XAS applications. J Synchrot Radiat 13:351–358
15. Cezar JC, Souza-Neto NM, Piamonteze C et al (2010) Energy-dispersive X-ray absorption spectroscopy at LNLS: investigation on strongly correlated metal oxides. J Synchrotron Radiat 17:93–102
16. Wei X, personal communication
17. Bhattacharyya D, Poswal AK, Jha SN et al (2009) First results from a dispersive EXAFS beamline developed at INDUS-2 synchrotron source at RRCAT, Indore, India. Nucl Instrum Methods Phys Res A 609:286–293
18. Pascarelli S, Mathon O, Mairs T et al (2016) The Time-resolved and Extreme-conditions XAS (TEXAS) facility at the European Synchrotron Radiation Facility: the energy-dispersive X-ray absorption spectroscopy beamline ID24. J Synchrotron Radiation 23:353–368
19. Baudelet F, Kong Q, Nataf L et al (2011) ODE: a new beam line for high-pressure XAS and XMCD studies at SOLEIL. High Pressure Res 31:136–139
20. Ouyang ZW, Matsuda YH, Nojiri H et al (2009) Insulator-metal phase transition of Pr(0.6)Ca(0.4)MnO(3) studied by X-ray absorption spectroscopy in pulsed magnetic fields. J Phys Condens Matter 21:016006-1–016006-5
21. http://www.spring8.or.jp/en/facilities/bl/list/
22. Poo-arporn Y, Chirawatkul P, Saengsui W et al (2012) Time-resolved XAS (Bonn-SUT-SLRI) beamline at SLRI. J Synchrotron Radiat 19:937–943
23. http://www.diamond.ac.uk/Beamlines/Spectroscopy/I20/I20-1.html

24. Pascarelli S, Neisius T, De Panfilis S (1999) Turbo-XAS: dispersive XAS using sequential acquisition. J Synchrot Radiat 6:1044–1050
25. Nagai S, Dohmae K, Ikeda Y et al (2008) In situ redispersion of platinum autoexhaust catalysts: an on-line approach to increasing catalyst lifetimes? Angew Chem Int Ed 47:9303–9306
26. Newton MA, Dent AJ (2013) In: Rodriguez JA, Hanson JC, Chupas PJ (eds) Energy-dispersive EXAFS: principles and application in heterogeneous catalysis, in-situ characterization of heterogeneous catalysts. John Wiley & Sons, Ltd, Hoboken
27. Stötzel J, Lützenkirchen-Hecht D, Frahm R (2010) A new flexible monochromator setup for quick scanning X-ray absorption spectroscopy. Rev Sci Instrum 81:073109-1–073109-4
28. Her JL, Matsuda YH, Nakano M et al (2012) Magnetic field-induced spin-crossover transition in [Mn^{III}(taa)] studied by X-ray absorption spectroscopy. J Appl Phys 111:053921-1–053921-4
29. Marini C, Occelli F, Mathon O et al (2014) A microsecond time resolved X-ray absorption near edge structure synchrotron study of phase transitions in Fe undergoing ramp heating at high pressure. J Appl Phys 115:093513-1–093513-4
30. Torchio R, Occelli F, Mathon O et al (2016) Microscopic properties of shocked Fe studied by single pulse synchrotron XAS measurements to 500 GPa. Sci Rep 6:26402. doi:10.1038/srep26402
31. Hagelstein M, Ferrero C, Hatje U et al (1995) Curved crystal transmission optics for energy dispersive X-ray absorption spectroscopy. J Synchrotron Radiat 2:174–180
32. Sanchez del Rio M, Perez-Bocanegra N, Shi X et al (2015) Simulation of X-ray diffraction profiles for bent anisotropic crystals. J Appl Crystallogr 48:477–491. doi:10.1107/S1600576715002782
33. Mocella V, private communication
34. Kantor I, Labiche JC, Collet E et al (2014) A new detector for sub-millisecond EXAFS spectroscopy at the European Synchrotron Radiation Facility. J Synchrotron Radiat 21:1240–1246
35. Dartyge E, Fontaine A, Tourillon G et al (1986) EXAFS in dispersive mode, a new tool for studying *in situ* kinetics: example of electrochemical inclusion of copper species in an organic conductor. J Phys Colloques 47:607–614
36. Bal R, Tada M, Sasaki T et al (2006) Direct phenol synthesis by selective oxidation of benzene with molecular oxygen on an interstitial-N/Re cluster/zeolite catalyst. Angew Chem-Int Edit 45:448–452
37. Headspith J, Salvini G, Thomas SL et al (2003) XSTRIP—a silicon micro strip-based X-ray detector for ultra- fast X-ray spectroscopy studies. Nucl Instr Meth Phys Res A 512:239–244
38. Headspith J, Groves J, Luke PN et al (2007) First experimental data from XH, a fine pitch germanium microstrip detector for energy dispersive EXAFS (EDE). IEEE Nucl Sci Symposium Conf R 1–11
39. 868 electron bunches are homogeneously distributed over 7/8 of the circumference, and a single 2 mA bunch is placed in the middle of the remaining 1/8
40. Aquilanti G, Trapananti A, Karandikar A, et al (2015) Melting of iron determined by X-ray absorption spectroscopy to 100 GPa. www.pnas.org/cgi/doi/10.1073/pnas.1502363112
41. Tromp M, Dent AJ, Headspith J et al (2013) Energy dispersive XAFS: characterization of electronically excited states of copper(I) complexes. J Phys Chem B 117:7381–7387

Chapter 9
Pump Probe XAFS

Toshihiko Yokoyama and Yohei Uemura

9.1 Introduction

Changes of structure and chemical states of catalysts have been successfully observed with XAFS under reaction conditions. Nowadays, a XAFS spectrum can be obtained even within several milliseconds by using quick XAFS (QXAFS) and dispersive XAFS (DXAFS) techniques. However, much faster fundamental processes of catalysts should be also key phenomena to understanding catalytic reactions. For example, lifetimes of photocarriers, transfer processes and active sites of catalysis should govern the photocatalytic activity. In order to observe such fast events, the demanding time resolution of XAFS measurements is less than microseconds, which is much shorter than the time resolution of QXAFS and DXAFS techniques. *A pump-probe XAFS* technique is applicable if the processes can take place repeatedly. The pump-probe XAFS technique has been developed since 1980s [1]. Nowadays, the time range of phenomena observed by the pump-probe XAFS technique is from sub-picoseconds to several hundreds of microseconds.

9.2 A Typical Pump-Probe XAFS System

X-rays coming from synchrotrons are short pulses with 100-ps time duration (or less than 100 ps). A pulse laser is employed to excite electronic states of samples and is synchronized with the X-ray pulses so that XAFS spectra of the excited states

T. Yokoyama (✉) • Y. Uemura
Department of Materials Molecular Structure, Institute for Molecular Science,
Okazaki 444-8585, Japan
e-mail: yokoyama@ims.ac.jp

Y. Iwasawa et al. (eds.), *XAFS Techniques for Catalysts, Nanomaterials, and Surfaces*, DOI 10.1007/978-3-319-43866-5_9

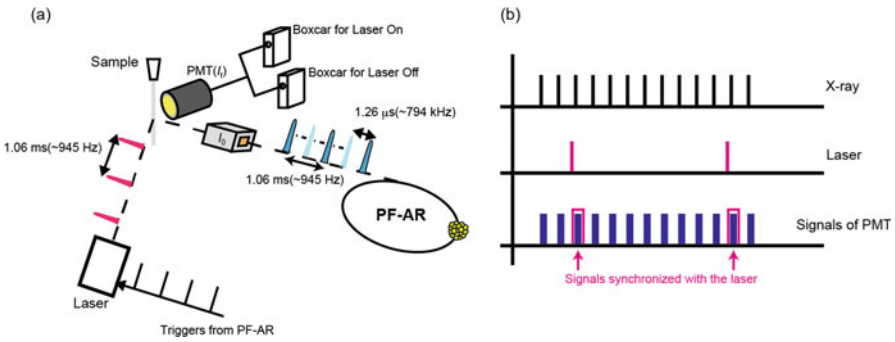

Fig. 9.1 (**a**) The pump-probe XAFS system at the beamline NW14A PF-AR. (**b**) A diagram of X-ray pulses, laser pulses and PMT signals

can be recorded with a 100-ps time resolution. As an example of the pump-probe XAFS system, a schematic setup at the beamline NW14A, Photon Factory Advanced Ring (PF-AR), Tsukuba, Japan is shown in Fig. 9.1a [2, 3]. PF-AR is always operated in a single-bunch mode, where only one electron bunch circulates and the frequency of X-ray pulses is about 794 kHz. In order to synchronize the excitation laser with the X-ray pulses, the laser frequency (F) should be equal to be 794/N kHz, where N is the integer. For example, the excitation laser is set to about 945 Hz (=794,000/840 Hz) in NW14A.

X-ray absorption signals just after the laser excitation need to be gathered selectively in order to measure XAFS spectra of the excited state. The samples are kept dilute since the ratio of the excited state to the ground state in the samples can increase as the sample concentration gets lower. XAFS spectra of dilute samples are usually measured in a fluorescence mode. A photomultiplier tube (PMT) with a scintillator is often employed as a detector in the NW14A system. The output signal from the PMT decays very fast (within 10 ns). Each output signal can be seen as an isolated pulse shown in Fig. 9.1b. The output pulses in the certain period of time after the laser excitation are collected electrically. The rate of the signal acquisition is about 945 Hz. Boxcar integrators are equipped with the pump-probe system in NW14A to obtain the PMT signals synchronized with the laser excitation.

Pump-probe XAFS systems in other synchrotron radiation facilities are similar as far as the laser frequency is much less than that of X-ray pulses. It is noted that the synchronization between X-ray pulses and the excitation laser should be taken into account on the measurements of incident X-ray intensity (I_0). Most of synchrotron radiation facilities are operated in a multi-bunch mode and each electron bunch gives a different X-ray intensity. The intensity of I_0 synchronized with the laser has to be also measured selectively in order to normalize X-ray absorption correctly. In such a case, fast detectors (PMT or an avalanche photodiode) and an electric gating system (boxcar integrator) should be employed for I_0 measurements.

In contrast, slow detectors such as ionization chambers are available to measure I_0 in the facilities operated in the single-bunch mode as PF-AR.

The pump-probe XAFS technique is a very useful and powerful technique to understand the structure and the chemical state of excited species. However, it was difficult to obtain the data with a good S/N ratio enough to analyze EXAFS. Normally the excitation lasers for the pump-probe XAFS experiments were operated at about 1 kHz in order to make the laser fluence as large as possible. The photon flux of X-rays was poor at such a low repetition rate (the repetition rate from synchrotrons is usually 1 MHz or much more). It took much longer time to obtain reliable data than normal XAFS measurements. Recently, new pump-probe XAFS systems have been established at Advanced Light Source (APS), Chicago, USA [4] and Swiss Light Source (SLS), Villigen, Switzerland [5]. A high power and high repetition rate laser are employed in both the systems. The pump-probe experiments at more than hundreds kHz can provide high-quality spectra in a reasonable time as several hours. For example, the time for EXAFS measurements required with the high repetition system at APS [4] was 1/10 of the measurement time with a conventional 1-kHz repetition system.

9.3 Applications of the Pump-Probe XAFS Technique

There have been studies on photoexcited species in solvents observed by the pump-probe XAFS technique and the recent results of the pump-probe XAFS experiments were reviewed [6, 7]. Chen et al. observed the bond breaking and recovery processes of a Ni-phenylporphyrin complex dissolved in piperizine (Fig. 9.2) [8].

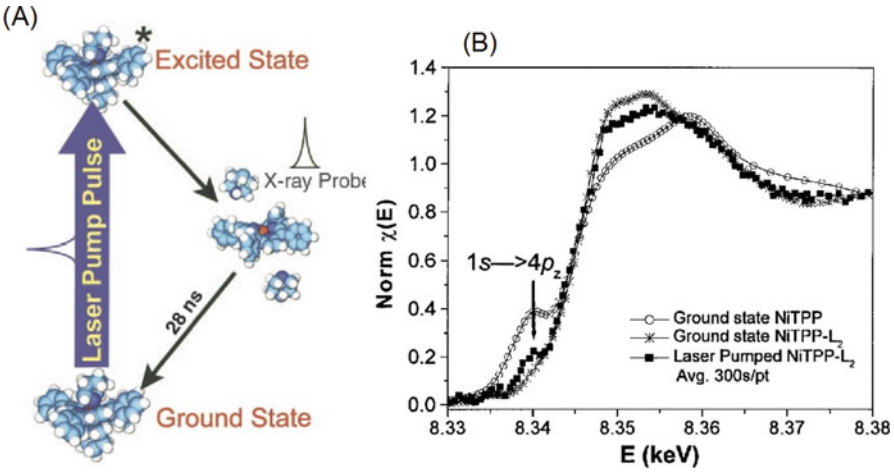

Fig. 9.2 (**a**) The schematic image of the ground and excited states and the intermediate of NiTPP dissolved in piperidine. (**b**) The XANES spectra of the ground state of NiTPP and NiTPP-L_2 and the excited state of NiTPP-L_2. From Ref. 8. Reprinted with permission from AAAS

In the ground state, two piperizine molecules are bonded to the Ni atom that has an octahedral-coordination structure, which is denoted by NiTTP-L_2 while the Ni-phenylporphyrin complex denoted by NiTTP has a square-planner coordination without solvent. After the excitation by the pulse laser, the piperizine molecules leave the Ni atom. The chemical bond between piperizine and Ni is recovered during the relaxation process. Their experiments discovered that the recovery of the chemical bond took 28 ns. There were two kinds of the chemical bonds between Ni and N after the laser excitation. One bond is at 2.09 Å attributed to the unexcited NiTTP-L_2 molecules in the solvent. The other is at 1.92 Å and this value is identical to the bond length of NiTPP. The XANES spectra after the excitation were reproduced by the linear combination of the XANES of NiTPP-L_2 and NiTPP. Considering these results, no other species but the square-planner species exist after the excitation.

Recently, Uemura et al. reported the photoexcitation states of WO_3 observed by the pump-probe XAFS technique [9]. WO_3 is a popular photocatalyst and is active for oxidation of water. WO_3 can be excited to absorb light whose wavelength is less than 480 nm. Understanding the photoexcitation mechanism of WO_3 is important to develop more active photocatalysts using visible light. The valence band of WO_3 is mainly composed by O 2*p* orbitals and the conduction band of WO_3 by W 5*d*. If WO_3 absorbs light, electrons in the valence band are excited to the conduction band. In W L_{III}-edge XANES the electron transition from W 2*p* to 5*d* appears as an intense dipole-allowed absorption often called a white line. The intensity of the white line is proportional to the vacancies of W 5*d* orbitals. It is expected that the intensity decreases while the excited electrons exist in the conduction band.

In Fig. 9.3, W L_{III} XANES spectra of WO_3 before and after the excitation are shown. Distinct changes of the XANES spectra are found around 10,216 eV. The

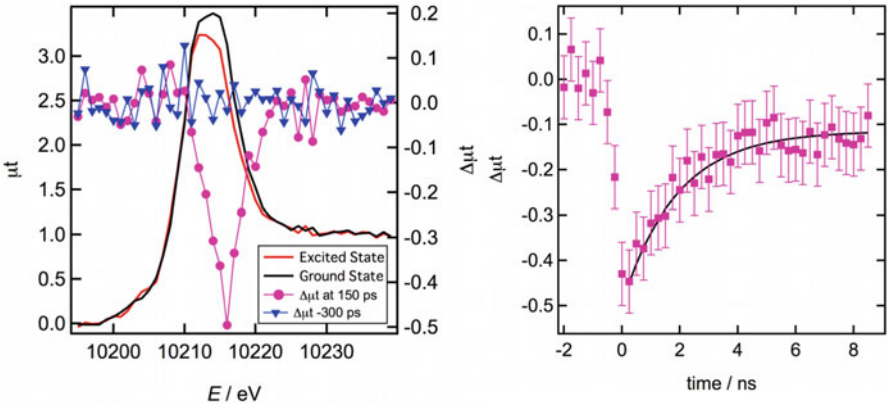

Fig. 9.3 (*Left*) W L_{III} XANES spectra of WO_3 at the ground and excited state. Difference spectra of the W L_{III} XANES at 150 ps after the excitation and at 300 ps before the excitation. (*Right*) Time evolution of the XAS intensity at 10,216 eV

change can be seen as a negative peak in the difference spectrum at 150 ps after the excitation. The lifetime of the excitation state was estimated as 0.5(1) ns^{-1} from the decay of the XAFS intensity at 10,216 eV.

9.4 X-Ray Free Electron Laser

The time resolution of the pump-probe XAFS technique is typically 100 ps which is the pulse duration of the X-ray pulses from storage rings. Today, much shorter X-ray pulses can be obtained in X-ray Free Electron Lasers (XFEL). XFEL provides intense and coherent X-ray pulses whose duration is less than 50 fs. The intense and short X-ray pulses can give opportunities to access the dynamics of structure and electronic states of photoexcited species in a femtosecond timescale. The photoexcited state of $Fe[bpy]^{2+}$ was reported in the XFEL in USA (LCLS) [10]. Obara et al. [11] successfully observed the photoexcitation state of Fe(III) oxalic acid in SACLA, the XFEL facility in Japan. The pump-probe XAFS system at SACLA is shown in Fig. 9.4a. SACLA is a SASE- (Self Amplification of Spontaneous Emission) XFEL where every X-ray pulses coming from SACLA has different energy profile and special distribution. It is necessary to measure the intensities of incident and transmitted X-rays simultaneously in order to perform spectral normalization. They employed a transmission grating to split X-ray into two beams. The one beam is used for incident X-ray and the other is for transmitted X-ray. An elliptical mirror was employed to focus X-rays at the sample position. Difference spectra of Fe K-edge XANES after the laser excitation are shown in Fig. 9.4b. The electron transfer from the ligands ($C_2O_4^{2-}$) to Fe(III) was

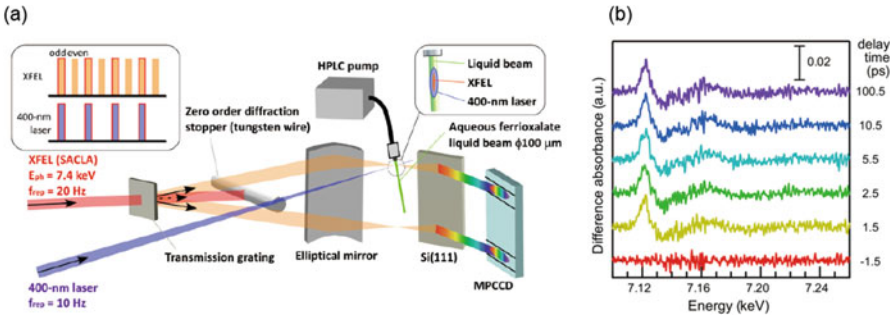

Fig. 9.4 (**a**) The pump probe XAFS system in SACLA. X-rays from SACLA are split into two beams in order to measure XAS since each X-ray pulse from XFEL has different energy profile. The lower beam is measured to use as incident X-ray intensity (I_0) and the upper beam penetrates through the sample. Photoecitation of Fe(III) oxalic acid was observed with the system. The time resolution was less than 300 fs. The pumped and umpumped spectra are measured by turns. (**b**) Difference spectra of Fe K-edge XAFS of 0.5 M $Fe(III)(C_2O_4)_3^{3-}$ solution. From Ref. 11. Reprint permitted from OSA

successfully observed by the pump-probe XAFS system in SACLA. The peak around 7.12 keV was attributed to the edge shift of Fe K-edge XAFS because Fe (III) was reduced to Fe(II) due to the electron transfer (The relaxation process of the excited state was not observed since the lifetime of Fe(II) species is very long which is more than several milliseconds [12].). The time resolution was less than 300 fs. The pump-probe XAFS technique in XFELs enables us to access dynamics of the structures and electronic states in a femtosecond timescale.

References

1. Mills DM, Lewis A, Harootunian A et al (1984) Time-resolved X-ray absorption spectroscopy of carbon monoxide-myoglobin recombination after laser photolysis. Science 223:811–813
2. Sato T, Nozawa S, Ichiyanagi K et al (2009) Capturing molecular structural dynamics by 100 ps time-resolved X-ray absorption spectroscopy. J Synchrotron Radiat 16:110–115
3. Nozawa S, Adachi S, Takahashi J et al (2007) Developing 100 ps-resolved X-ray structural analysis capabilities on beamline NW14A at the Photon Factory Advanced Ring. J Synchrotron Radiat 14:313–319
4. March AM, Stickrath A, Doumy G et al (2011) Development of high-repetition-rate laser pump/x-ray probe methodologies for synchrotron facilities. Rev Sci Instrum 82:073110
5. Lima FA, Milne CJ, Amarasinghe DCV et al (2011) A high-repetition rate scheme for synchrotron-based picosecond laser pump/x-ray probe experiments on chemical and biological systems in solution. Rev Sci Instrum 82:063111
6. Chen LX, Zhang X, Shelby ML (2014) Recent advances on ultrafast X-ray spectroscopy in the chemical sciences. Chem Sci 5:4136–4152
7. Chergui M (2010) Picosecond and femtosecond X-ray absorption spectroscopy of molecular systems. Acta Crystallogr A66:229–239
8. Chen LX, Jager WJH, Jennings G et al (2001) Capturing a photoexcited molecular structure through time-domain X-ray absorption fine structure. Science 292:262–264
9. Uemura Y, Uehara H, Niwa Y et al (2014) In situ picosecond XAFS study of an excited state of tungsten oxide. Chem Lett 43:977–979
10. Lemke HT, Bressler C, Chen LX et al (2013) Femtosecond X-ray absorption spectroscopy at a hard X-ray free electron laser: application to spin crossover dynamics. J Phys Chem A 117:735–740
11. Obara Y, Katayama T, Ogi Y et al (2014) Femtosecond time-resolved X-ray absorption spectroscopy of liquid using a hard X-ray free electron laser in a dual-beam dispersive detection method. Opt Express 22:1105–1113
12. Parker CA, Hachard CG (1959) Photodecomosition of complex oxalates. Some preliminary experiments by flash photolysis. J Phys Chem 63:22–26

Chapter 10
Spatially Resolved XAFS

Mizuki Tada and Nozomu Ishiguro

10.1 Micro-XAFS and Nano-XAFS

10.1.1 Introduction

The functions of solid materials are highly related to their structures, and the visualization of heterogeneous structures of solid materials is one of the interesting targets for XAFS analysis. Conventional XAFS measurement is performed by micron-size X-ray beams, and it can provide average structural information of a target sample in a beam spot. In the case of a powder sample, the information of local coordination is averaged for all powders with heterogeneous morphology, composition, surface structures, etc. in a beam spot of X-rays, and the local coordination of inhomogeneous assemblies cannot be separated by the conventional XAFS measurement.

Recently, the focusing techniques of X-ray beams are developing and micron to nanometer size X-ray beams can be prepared at synchrotron facilities. Kirkpatrick–Baez (KB) mirrors are practical optics to focus down X-ray beams, and the utilization of such focusing X-ray beams enables to visualize the heterogeneous properties of solid materials. Micro-XAFS and nano-XAFS have been developed as

M. Tada (✉)
Research Center for Materials Science, Nagoya University, Nagoya, Aichi 464-8602, Japan

Department of Chemistry, Graduate School of Science, Nagoya University, Nagoya, Aichi 464-8602, Japan

Element Visualization Team, Materials Visualization, Photon Science Group, RIKEN SPring-8 Center, Sayo, Hyogo 679-5148, Japan
e-mail: mtada@chem.nagoya-u.ac.jp

N. Ishiguro
Element Visualization Team, Materials Visualization, Photon Science Group, RIKEN SPring-8 Center, Sayo, Hyogo 679-5148, Japan

Y. Iwasawa et al. (eds.), *XAFS Techniques for Catalysts, Nanomaterials, and Surfaces*, DOI 10.1007/978-3-319-43866-5_10

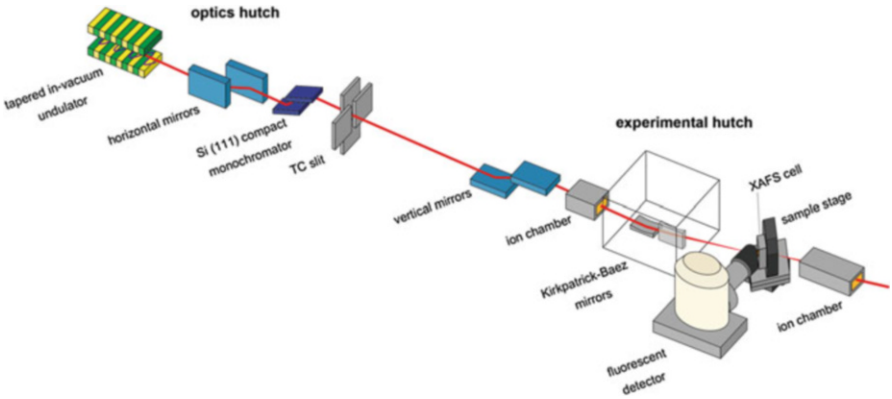

Fig. 10.1 A typical optical setup of nano-XAFS using KB mirrors

simple two-dimensional spatially resolved XAFS techniques and applied for solid samples such as heterogeneous catalysts.

10.1.2 Principle of Micro/Nano-XAFS

The optical setup of micro-XAFS or nano-XAFS is simple as illustrated in Fig. 10.1. An X-ray beam through a slit is focused down by a set of Kirkpatrick–Baez (KB) mirrors, which is composed of two elliptically bended mirrors. A sample is mounted on a piezo stage and set at the focusing point of the X-ray beam. Fluorescent X-rays from the sample is detected on an appropriate detector such as a Ge detector inclined to the sample.

Focusing size of X-ray beams depends on the accuracy of KB mirrors and beam line at a synchrotron facility. Recently, hard X-ray beams for XAFS measurements can be focused down to micron to nanometer size, and XAFS measurements using focused X-ray beams are called as micro-XAFS or nano-XAFS, depending on X-ray beam size. The space resolution of the XAFS measurements is decided by both X-ray beam size and the scanning distance of a piezo stage that a sample is mounted. 100 nm-order X-ray beams are processed in the hard X-ray region for nano-XAFS analysis at SPring-8 (Hyogo, Japan) [1–3].

Fluorescent X-rays from a sample irradiated focused X-rays are often so small that sufficient acquisition time is required for micro/nano-XAFS measurements. In particular, EXAFS data requires long acquisition time. The drifts of optics and a sample stage are serious to damage to the space resolution of nano-XAFS measurements with long acquisition time. The drift of temperature is often seriously affected to the drifts of the equipment, and a set of KB mirrors is used to be set in a closed chamber filled with inert helium gas (Fig. 10.2).

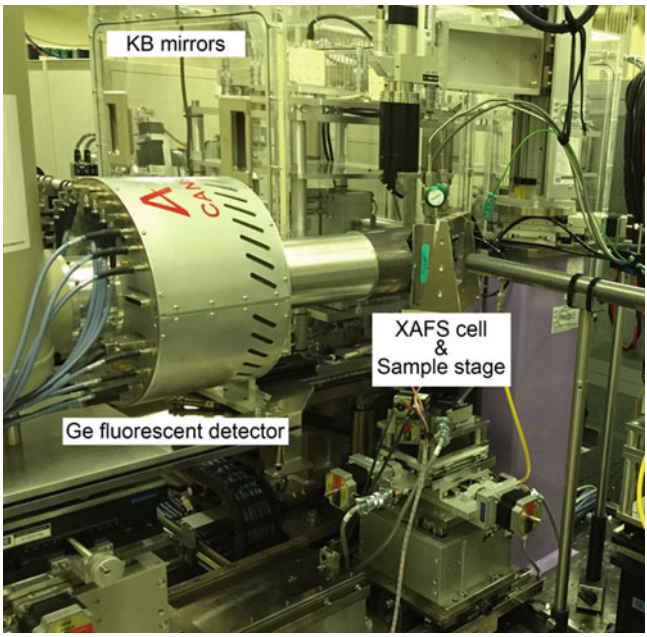

Fig. 10.2 A photo of the KB mirror system and sample stage at the BL36XU station at SPring-8

10.1.3 Imaging by Micro/Nano-XAFS

The visualization of heterogeneous structures of solid materials is one of the important targets in microanalysis. Microscope techniques such as STM and AFM suggest the atomic-scale information of solid surfaces, which are highly important for understanding heterogeneous catalysis. Electron microscopy such as TEM shows the morphologies and lattice parameters of solid materials at nano scale. However, the chemical information (oxidation state, symmetry, local coordination, etc.) cannot be obtained from these microscopy techniques.

Micro/nano-XAFS displays great ability to monitor the chemical information of heterogeneous solid materials at micro/nanometer scale. In the case of a powder sample, which is one of the typical forms of solid materials, the micro/nano-XAFS can separate structural information at particle level (Fig. 10.3). When the size of a focused X-ray beam is similar to that of an individual solid particle, the structural information in the individual particle, which corresponds to the average of all atoms of a target element in the particle, can be obtained by the micro/nano-XAFS. The utilization of a focused X-ray beam whose size is smaller than a sample particle provides the spatial information inside the single particle, and the two-dimensional reflection images of the distribution and chemical states of a target element can be provided.

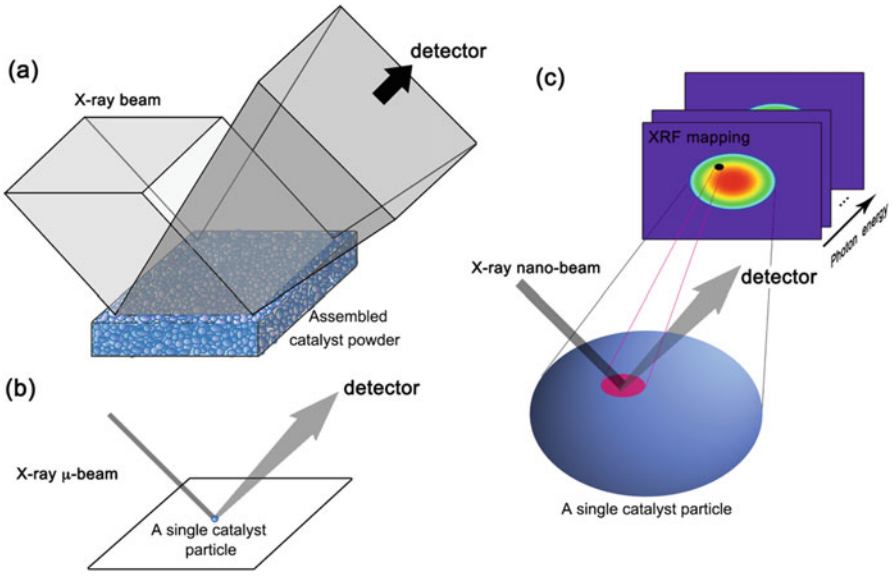

Fig. 10.3 A schematics of (**a**) conventional XAFS for assembled powder, (**b**) micro-XAFS for a single particle, and (**c**) nano-XAFS for a single particle

10.1.4 Applications of Micro-XAFS to Environmental Analysis

Microanalysis using X-ray beam started from environmental analysis application, which is one of the active fields for microanalysis. Various environmental matrices such as rocks, peats, soils, minerals, and sediments have been analyzed by micro-XAFS combining micro-XRF [4]. For examples, Ryser applied micro-XANES analysis to Se-bearing minerals from the Western US phosphate resource area [5]. They broke rock and shale samples to fine powders and measured micro-XAFS to determine Se speciation in the samples. Takahashi also reported the Se distribution in barite in marine sediments and their chemical states by micro-XRF and XAFS [6]. Denecke reported the mapping of Np in a rock with 300 μm size and succeeded in measuring XAFS spectra of the rock by micro-XAFS [7]. Less sample preparation, non-destructive analysis, and high spatial resolution are advantageous of micro-XRF/XAFS.

Langner et al. reported the As *K*-edge micro-XRF/XAFS analysis of As in peat to investigate its spatial distribution [8]. The toxicity of redox-sensitive arsenic highly depends on its oxidation state and speciation [9], and the separation of As (V) and As(III), which are common arsenate, is explored [10, 11]. The element-selective feature of micro-XRF showed the distribution of each element (e.g., As, Fe, and S) in the peat. High sensitivity of As *K*-edge micro-XANES spectra to As

oxidation state revealed differences in As oxidation states in the sample and micro-EXAFS enabled the identification of their chemical species.

Industrial waste, ash, and dust were also analyzed by micro-XRF and micro-XAFS techniques and the distribution of several elements in the samples were elucidated [12, 13]. Nakai et al. analysed radioactive species in microparticles after the Fukushima nuclear accident in Japan [14]. Various metal elements such as Cs, U, and Pb were observed in aerosol samples collected after the Fukushima nuclear accident. The combination of micro-XRD revealed the chemical states of these elements and the nature of the microparticles.

10.1.5 Applications of Micro/Nano-XAFS to Solid Catalysts

XAFS becomes one of the most typical characterization techniques of solid catalysts, in particular supported metal species on support surfaces because of its non-crystalline structures at the surfaces. Because of their limited loading on support surfaces, the utilization of synchrotron facility is necessary to record high quality data for EXAFS analysis. Micro/nano-XANES/EXAFS are applied to heterogeneous solid catalysts, showing the distribution of composing elements and their local structures.

10.1.5.1 Analysis of Active Species of $NiO_x/Ce_2Zr_2O_y$ Individual Catalyst Particles for CH_4 Reforming

Ce-Zr mixed oxides have been used as supports of automobile exhausting catalysts because of their oxygen storage/release properties [15–17]. Ce is the key metal for the oxygen storage/release property, and the bulk oxygen in the mixed oxides fluctuates accompanied with the redox reaction of Ce species (Ce^{3+}–Ce^{4+}). Crystalline $Ce_2Zr_2O_y$ solid solution, whose Ce and Zr atoms are regularly ordered in a pyrochlore structure, was reported to exhibit stoichiometric oxygen storage/release property [18–21]. The high oxygen storage/release property of the crystalline $Ce_2Zr_2O_y$, denoted as CZ-*y*, can be applied to other catalytic reactions by collaborating with other metal species.

Ni attached crystalline $Ce_2Zr_2O_y$, denoted as NiO_x/CZ-*y*, was reported to be active for methane steam reforming, which is the production of hydrogen from methane and water [22]. The NiO_x/CZ-*y* catalyst exhibited the better conversion of CH_4 compared to Ni/CeO_2, Ni/ZrO_2, and Ni/CeO_2-ZrO_2 at 923 K at the H_2O–CH_4 ratio of 1. The deactivation of carbon deposition is serious on Ni reforming catalysts, but the NiO_x/CZ-*y* catalyst exhibited more stable performance under the identical conditions.

The catalytic activity of methane steam reforming strongly depended on the oxygen content (*y*) in the NiO_x/CZ-*y* catalyst. The most reduced phase, Ni/CZ-7 prepared by reduction with H_2 was active under the steady-state reforming

conditions, while the most oxidized phase, NiO/CZ-8 prepared by oxidation with O_2 was inactive under the conditions. The activity drastically changed at $y = 7.5$, and the catalyst showed a remarkable discontinuous behaviour for the methane reforming activity [22].

The catalyst pretreatments (reduction and oxidation) bring about both changes in the attached Ni and the oxygen content (y) of the CZ-y support. The systematic characterization of the NiO_x/CZ-y catalyst by XRD, Ni K-edge XANES and EXAFS, and Ce L_{III}-edge XANES and EXAFS, suggested that metallic Ni was active species for the reforming reaction. It was found that the reforming activity was decided by not only the chemical state of Ni but also the oxygen content (y) in the CZ-y support. The reduction of NiO_x species at the surfaces strongly depended on the nature of the CZ-y support, and the transport of oxygen atoms at the interface of NiO_x and the CZ-y surface is suggested to be key issue to decide the reforming activity.

The average size of the CZ-y was 750 ± 370 nm, and a focused hard X-ray beam with a similar size (1000 nm (h) $\times$ 800 nm (v)) can be prepared at Ni K-edge (8332 eV) at the SPring-8 BL37XU station. The catalyst particles were dispersed on a thin SiO_2 membrane with the thickness of 30 μm and oxidized and reduced samples (NiO/CZ-8 and Ni/CZ-7, respectively) were independently prepared by the appropriate oxidation/reduction processes at 773 K. The fraction of aggregated particles on the SiO_2 membranes was estimated to be 0.7 % and 1.9 % for the NiO/CZ-8 and Ni/CZ-7 samples, respectively, by the analysis of SEM images, indicating the most of the catalyst particles were isolated on the substrates.

The X-ray beam focused by KB mirrors, whose energy was 8428 eV, was irradiated to the sample, and micro-XRF was recorded by two-dimensionally scanning of a sample stage mounting the sample (Fig. 10.4A). The catalyst particles contained Ni and Ce hence the mapping of Ni $K\alpha$ (7478 eV) and Ce $L\alpha$ (4840 eV) + $L\beta_1$ (5262 eV) fluorescent X-rays suggest the position of the catalyst particles on the

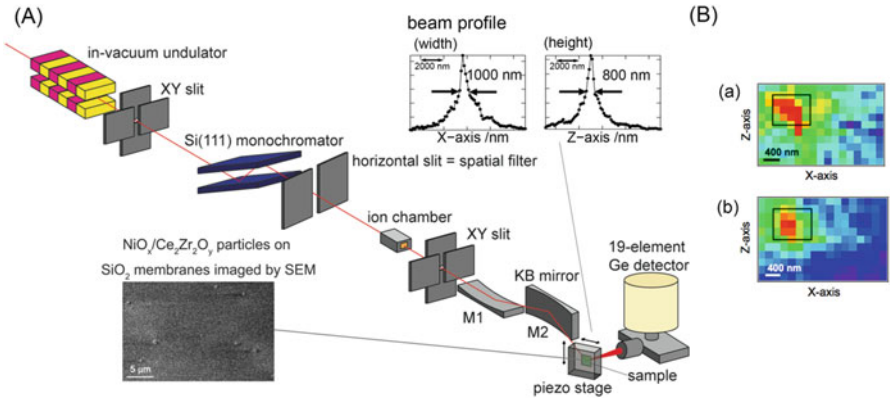

Fig. 10.4 (**A**) Setup of micro-XRF/XAFS for NiO_x/CZ-y and its beam profiles at the sample position (8 keV). (**B**) Two-dimensional mapping of (**a**) Ni $K\alpha$ (7478 eV) and (**b**) Ce $L\alpha$ (4840 eV) + $L\beta_1$ (5262 eV) fluorescent X-rays for a SiO_2 membrane with NiO/CZ-8 catalyst particles [23]

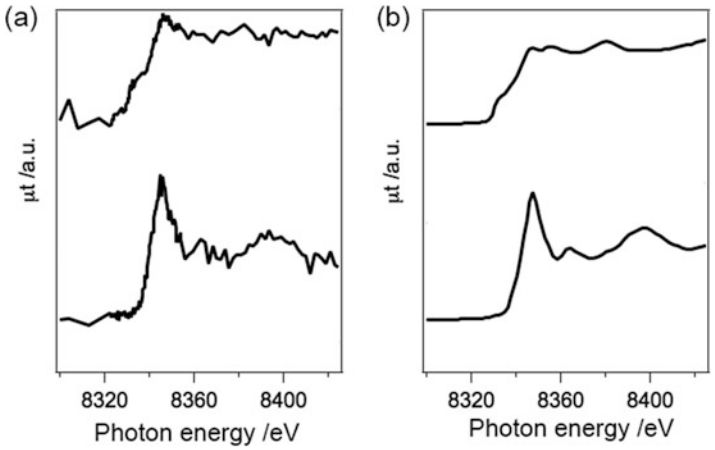

Fig. 10.5 (**a**) Ni *K*-edge micro-XANES spectra of the single particles of NiO_x/CZ-7 and NiO/CZ-8. (**b**) Ni *K*-edge XANES spectra of the assemblies of particles of Ni/CZ-7 and NiO/CZ-8 [23]

substrates. As shown in Fig. 10.4B, the significant contrasts of both fluorescent X-ray mappings of Ni $K\alpha$ and Ce $L\alpha + L\beta_1$ at the similar position on the SiO_2 substrate, suggesting the position of the catalyst particle. The acquisition time was 1 or 2 s at each point in Fig. 10.4 [23].

Then the micro-XANES and EXAFS spectra were measured at the center of the catalyst particle determined by the mapping of micro-XRF. Figure 10.5a shows the Ni *K*-edge micro-XANES spectra of Ni/CZ-7 and NiO/CZ-8. Compared to the reference data of their powder assemblies measured by conventional XAFS with mm-order X-ray beam (Fig. 10.5b), the quality of the micro-XANES spectra was low but the characteristics of the XANES spectra were observed. On the CZ-7 catalyst particle, the white line intensity of the micro-XANES spectrum was much lower than that of the Ni species on the CZ-8 particle, reflecting the oxidation states of the attached Ni species in the individual particles.

We also measured the micro-EXAFS spectrum of the NiO/CZ-8 particle, which was inactive phase for the methane reforming reaction. The Ni *K*-edge micro-EXAFS spectrum recorded for 3 h could be successfully curve-fitted as shown in Fig. 10.6. Synchrotron beam fluctuation at the observed center position was within 200 nm (1 pixel in Fig. 10.1) over 3 h. Similar oscillations were observed for NiO and the two shells assigned to Ni-O at 0.208 nm and Ni-Ni at 0.292 nm were contributed, where their coordination numbers were 5.4 ± 1.2 and 11.7 ± 0.9, respectively. This is the example of determining the local coordination of a single particle of a practical catalyst by micro-EXAFS.

On the NiO_x/CZ-*y* catalyst, small Ni particles attached on the surface of the CZ support, and the distribution and local coordination of each Ni particles cannot be visualized by micro-XAFS technique because of its spatial resolution much larger than the particle size. The reduction of focusing size of X-ray beams and mechanical drift during measurements should be improved to achieve higher spatial

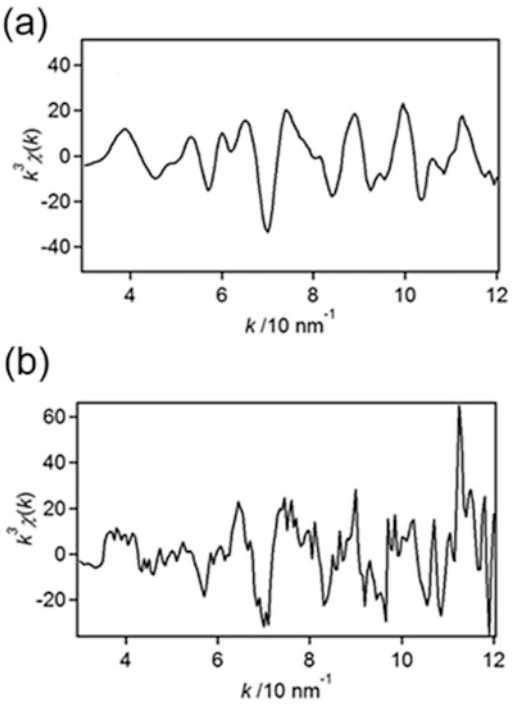

Fig. 10.6 The EXAFS oscillations and their curve-fitting results of NiO/CZ-8. (**a**) Conventional EXAFS for the assembly of the particles ($k = 30$–110 nm^{-1}, $R = 0.125$–0.315 nm, $R_f = 1.7$ %). (**b**) Micro-EXAFS for a single particle ($k = 30$–110 nm^{-1}, $R = 0.127$–0.325 nm, $R_f = 1.2$ %) [23]

resolution for the micro-analysis. It is significant that the obtained image is two-dimensional reflection of a sample and the resolution of depth direction is lost in the mapping [23].

10.1.5.2 Analysis of a Single Catalyst Particle by Nano-XAFS

Recently, focused X-ray nanobeam, whose size was 320 nm (h) × 250 nm (v) or 190 nm (h) × 290 nm (v), at Ce L_{III}-edge (5.7 keV) was processed at the BL39XU or BL36XU station at SPring-8 (Fig. 10.7) [24]. The beam size is smaller than that of the average particle size of CZ-*y*, thus two dimensional imaging of Ce oxidation states for Pt-supported CZ-*y* catalyst particles were recorded by using the focused X-ray beam.

Several Pt/CZ-*y* samples with different oxygen compositions (*y*) ranging between 7 and 8 were prepared on thin SiC membranes (300 nm thick). The appropriate treatments with hydrogen or oxygen brought about changing in their oxygen compositions, which were estimated by powder X-ray diffraction. Accompanied with decreasing oxygen compositions in the CZ-*y* support by the reduction with H_2, the down shifts of their diffraction peaks (e.g., (4 4 0) diffraction) were clearly observed, as reflected the expansion of its lattice parameters (Fig. 10.8a). The powder XRD patterns suggested the average oxygen compositions of the CZ-*y*

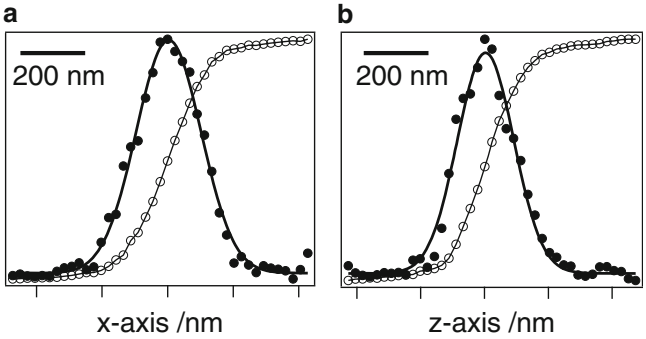

Fig. 10.7 Beam profile of focused X-ray beam (6 keV) at the BL36XU station, SPring-8. (**a**) Width and (**b**) height

particle assemblies on the SiC membranes, and their broad peaks showed the distribution of the oxygen composition in the particle assemblies.

In contrast, nano-XAFS provided the structural information of each particle, as shown in Fig. 10.8b. The 2D imaging at 5.7697 keV, which was an isosbestic point of Ce^{3+} and Ce^{4+}, showed similar shape of each catalyst particle, which was measured by SEM (Fig. 10.8c). It is well known that Ce L_{III}-edge XANES is highly sensitive to Ce oxidation states, and the intensity ratio ($R_{Ce3+/Ce4+}$) of the B_0 mode transition ($2p \rightarrow 4f^1 5d^1$) of Ce^{3+}, whose peak top was observed at 5.7302 keV, and the C mode ($2p \rightarrow 4f^0 5d^1$) transitions of Ce^{4+} (5.7410 keV) (Eq. 10.1) is regarded to be almost relative to the atomic ratio of Ce^{3+}/Ce^{4+} (Eq. 10.2) [25, 26]. Therefore, the mapping of $R_{Ce3+/Ce4+}$ provides the atomic ratio of Ce^{3+}/Ce^{4+} in the CZ-*y* particle.

$$R_{Ce3+/Ce4+} = [\mu t(E = 5730.2\,eV) - \mu t(E = 5680.0\,eV)/[\mu t(E = 5741.0\,eV) - \mu t(E = 5680.0\,eV)] \quad (10.1)$$

$$R_{Ce3+/Ce4+} = (11.5(\pm 0.4)) - (1.34(\pm 0.05)) \times x \quad (10.2)$$

We compared several particles with different oxygen compositions in Fig. 10.8. Significant contrasts of the intensity ratio ($R_{Ce3+/Ce4+}$) inside the catalyst particles were clearly observed, showing the oxygen composition at each position inside the particles. For examples, in the case of a Pt/CZ-7.6 catalyst particle prepared by the reduction of Pt/CZ-8 with H_2, whose particle size was 3.2 μm, the center of the particle projection was mainly yellow, whereas the outer region was presented in green. These results indicate that the surface of the particle was more reduced compared to the core of the particle. Other particles with intermediate oxygen compositions showed variation of oxygen components inside the particles, showing the heterogeneous chemical compositions in the single catalyst particles.

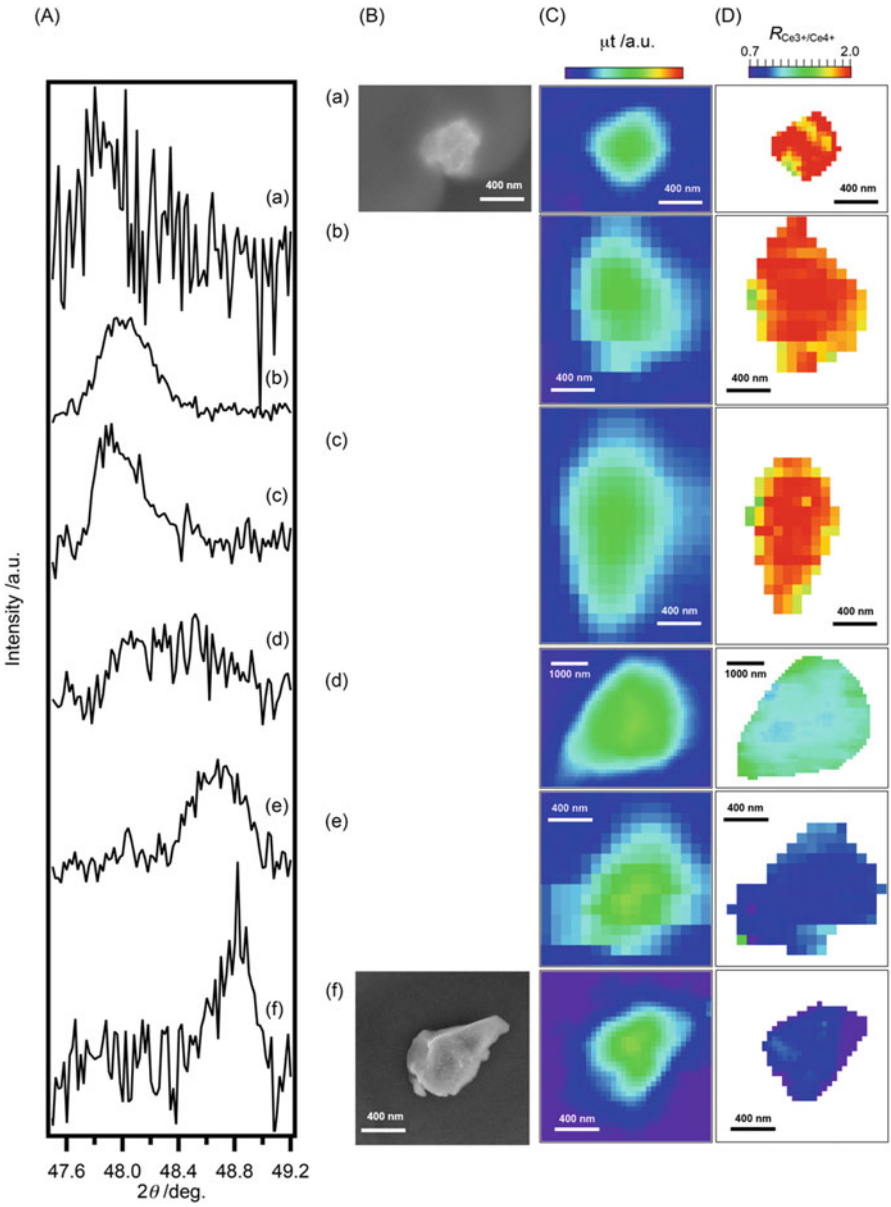

Fig. 10.8 (**a**) Powder X-ray diffraction patterns, (**b**) SEM, (**c**) imaging at the isosbestic point (5769.7 eV), and (**d**) $R_{Ce3+/Ce4+}$ for Pt/CZ-y particles dispersed on SiN membranes [20]

Ce L_{III}-edge nano-XANES spectra were successfully recorded at each position of the catalyst particles (Fig. 10.9). In the cases of the fully reduced catalyst, the uniform contrast inside the particle was observed, indicating uniform Ce valence states (Ce^{3+}) in the samples. On the other hand, there were significant differences in

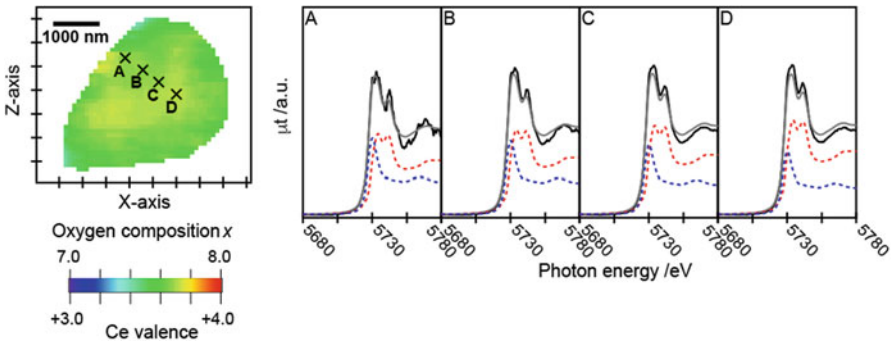

Fig. 10.9 Oxygen composition distribution 2D-mappings and space-resolved Ce L_{III}-edge nano-XANES spectra of Pt/CZ-x. (**a**) Pt/CZ-7.1, (**b**) Pt/CZ-7.5 prepared by the reduction with H_2. Measuring positions of each XANES spectrum correspond to black markers on the 2D-mapping [20]

the nano-XANES spectra for the particle of Pt/CZ-7.6, whose trend was agreed with the 2D nano-XRF mapping in Fig. 10.8. The nano-XAFS results implied the formation of domain structures of Ce oxidation states in the solid-solution particles.

The present scanning nano-XAFS analysis cannot reveal metal species supported on the surface of CZ support because of its limited spatial resolution. Local structure at the interface of supported metal species and the CZ support would be related to the bulk oxygen diffusion and reactivity of the supported catalysts. The further developments on the spatial resolution of nano-XAFS and the utilization of model catalyst systems would be promising to approach the domain structures of such heterogeneous materials.

10.1.5.3 Micro/Nano-XAFS Applications to Electrocatalysts and Fuel Cell Catalysts

The synthesis and utilization of electrocatalysts are one of the most important targets for micro/nano-XAFS analysis. In particular, the visualization of membrane electrode assembly (MEA), which is a thin membrane material coated with electrocatalyst layers for polymer electrolyte fuel cell (PEFC), is applied for space-resolved analysis [27]. The synthetic processes of electrocatalysts were also investigated by micro-XAFS analysis combining other micro-analysis techniques, and the compositional and chemical state distributions in metal oxide-polymer matrix systems were reported to improve material quality [28, 29].

Takao et al. have succeeded in mapping Pt chemical species in Pt/C cathode catalyst layers in PEFC by a scanning micro/nano-focused beam XAFS mapping method and by a micro/nano-QXAFS method, and provided new pieces of nano-spatial information on the site-preferential oxidation, leaching and detachment of Pt cathode nanoparticles in degraded PEFCs [27, 30, 31]. For the micro/nano-XAFS measurements by micro/nano-beams of 570 nm × 540 nm and 228 nm × 225 nm, sliced MEA samples were prepared by picking up the MEA from the PEFC stack,

slicing the MEA to a 1 μm thick piece by an ultra-microtome, putting the sliced piece on a SiN membrane, and arranging the sliced sample-membrane in a designed XAFS cell under humid N_2. The resultant ex situ micro/nano-XAFS spectra are regarded to be equivalent to in situ XAFS spectra for the degraded PEFC MEA because the MEA piece sample is always under humid N_2 atmosphere without exposing air and the MEA degradation is irreversible. The acquisition time for the scanning micro/nano-XAFS and micro/nano-QXAFS measurements was 1.6 s or 15 min for each spectrum, respectively, under which conditions the MEA samples were not damaged by the miciro/nano-beam irradiation.

Figure 10.10 shows the Pt L_{III}-edge jump mapping (a), normalized white line peak area (WLPA) mapping (b), and Pt valence mapping (c) around the Pt/C cathode layer with a micro-crack in a degraded MEA [27, 30]. It is to be noted that the Pt valence in most parts of the micro-crack region was calculated as 2+ by the linear relationship between the normalized WLPA and Pt valence, whereas Pt nanoparticles in the other cathode areas were metallic as shown in Fig. 10.10c [30]. Figure 10.10d are the line-scan profiles of the Pt L_{III}-edge jump (Pt quantity) and Pt valence in the scanning sub-micro-XAFS spectra along the red arrow of Fig. 10.10b. The Pt valence in the cathode electrocatalyst layer began to increase

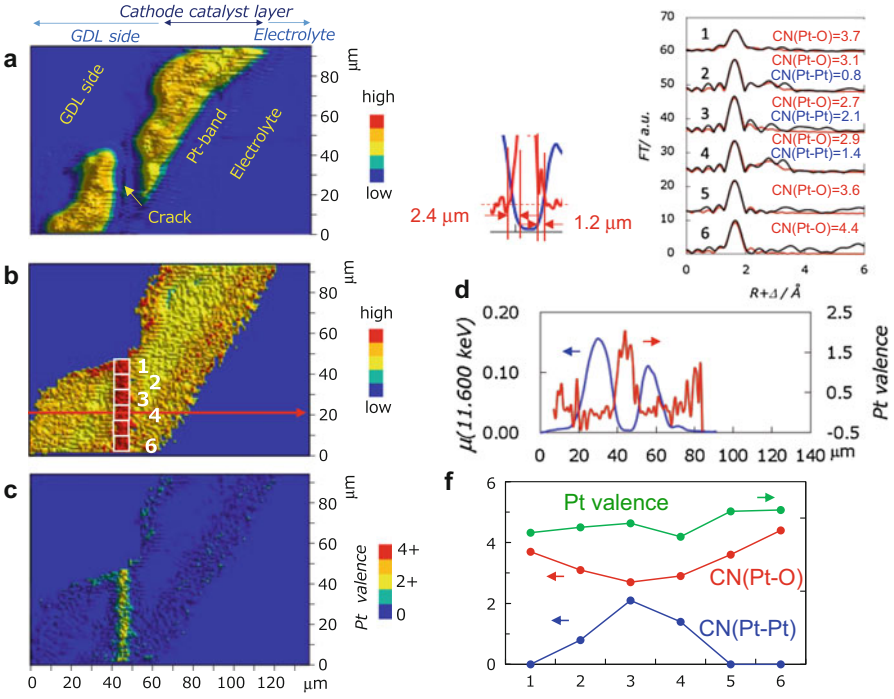

Fig. 10.10 Mapping of Pt chemical species in a degraded MEA by the scanning sub-micro XAFS mapping method and coordination parameters of Pt species by the sub-micro QXAFS method. The acquisition time for the scanning micro/nano-XAFS and micro/nano-QXAFS measurements was 1.6 s or 15 min for each spectrum, respectively [27, 30]

from the places at the distances of roughly 1.2 and 2.4 μm on both cathode sides of the micro-crack far from the boundary edge to show the maximum Pt valence (Pt^{2+}) in the micro-crack area. The micro-crack areas 1, 5, and 6 accommodated Pt^{2+} species and the coordination number (CN) of Pt-O at 0.200 nm was 4.0 (±0.4) but no Pt-Pt bonding was observed in Fig. 10.10e, which means that the Pt^{2+} species does not have any Pt-Pt bonds but have a four-coordinated Pt^{2+}-O_4 structure. There are Nafion ionomers with sulfonic group and water in the micro-crack region and the Pt^{2+} species may be stabilized by coordination with the sulfonic group (Nf-SO_3) as well as H_2O to form $[Pt(Nf\text{-}SO_3)_x(H_2O)_y]^{2+}$. It was suggested that Pt nanoparticles at the boundary of the Pt/C cathode layer toward the micro-crack are regarded to be first oxidized, then dissolved into the ionomers with moisture in the micro-crack region [30]. As for the other micro-crack areas 2–4 of Fig. 10.10b, the CNs of Pt-Pt and Pt-O were 1.0–1.8 and 2.7–3.1, respectively, where the Pt valences were estimated as 1.8–1.9. It is probable that both small Pt^0 clusters and Pt $^{2+}$-O_4 species coexist in the micro-crack areas 2–4. Thus, the micro-cracks larger than about 2 μm boundary may promote the MEA degradation by oxidizing and leaching Pt nanoparticles as Pt^{2+}-O_4 coordination species.

Takao et al. also reported non-destructive same-view nano (228 nm × 225 nm)-XAFS and TEM/STEM-EDS imagings for the PEFC MEA Pt/C cathode catalyst layers under humid N_2 atmosphere by using a new same-view stacking membrane cell [31]. The degraded MEA was prepared by anode-gas exchange cycles. The complementary nano-XAFS and STEM-EDS imagings allowed to find the formations of the leached Pt^{2+} oxidation species and detached metallic Pt nanoparticles/clusters in the Nafion ionomer-filled nano-hole areas of the degraded Pt/C cathode due to carbon corrosion. The two ways of either leaching or detaching of the Pt nanoparticles from the carbon support depended on the Pt/ionomer ratios in the nano-hole areas. These detailed degradation aspects could help to design MEA cathodes with better durability.

10.1.6 Perspective

The spatially resolved micro-XAFS and nano-XAFS techniques using X-ray focused beams can provide new insights into the two-dimensional spatial visualization and mapping of the morphology, composition, domain structure, coordination structure, oxidation states, corrosion, aggregation, fragmentation, etc. which are critical issues for property, functionality, and catalysis of micromaterials and nanomaterials such as catalysts, functional materials, fuel cells, batteries, devices, biomaterials, and marine resources. These in situ and ex situ XAFS techniques can also image depth profiles of thin membranes like PEFC MEAs. The techniques can be consorted with other techniques such as TEM/STEM-EDS and ambient-pressure HAXPES, which may address complementary analysis results from combined viewpoints. The element-selective nano-XAFS is a promising technique to visualize the inhomogeneous presence and distribution of chemical states in a single micro/nanoparticle as well as a variety of nanomaterials.

References

1. Terada Y, Tanida H, Uruga T, Takeuchi A, Suzuki Y, Goto S (2011) High-resolution X-ray microprobe using a spatial filter and its application to micro-XAFS measurements. AIP Conf Ser 1365:172–175
2. Suzuki M, Kawamura N, Mizumaki M, Terada Y, Uruga T, Fujiwara A, Yamazaki H, Yumoto H, Koyama T, Senba Y, Takeuchi T, Ohashi H, Nariyama N, Takeshita K, Kimura H, Matsushita T, Furukawa Y, Ohata T, Kondo Y, Ariake J, Richter J, Fons P, Sekizawa O, Ishiguro N, Tada M, Goto S, Yamamoto M, Takata M, Ishikawa T (2013) A hard X-ray nanospectroscopy station at SPring-8 BL39XU. J Phys Conf Ser 430:012017
3. Sekizawa O, Uruga T, Tada M, Nitta K, Kato K, Tanida H, Takeshita K, Takahashi S, Sano M, Aoyagi H, Watanabe A, Nariyama N, Ohashi H, Yumoto H, Koyama T, Senba Y, Takeuchi T, Furukawa Y, Ohata T, Matsushita T, Ishizawa Y, Kudo T, Kimura H, Yamazaki H, Tanaka T, Bizen T, Seike T, Goto S, Ohno H, Tanaka M, Kitamura H, Ishikawa T, Yokoyama T, Iwasawa Y (2013) New XAFS beamline for structural and electronic dynamics of nanoparticle catalysts in fuel cells under operating conditions. J Phys Conf Ser 430:012020
4. Majumdar S, Peralta-Videa JR, Castillo-Michel H, Hong J, Rico CM, Gardea-Torresdey JL (2012) Applications of synchrotron μ-XRF to study the distribution of biologically important elements in different environmental matrices: a review. Anal Chem Acta 755:1–16
5. Ryser AL, Strawn DG, Marcus MA, Johnson-Maynard JL, Gunter ME, Moller G (2005) Micro-spectroscopic investigation of selenium-bearing minerals from the Western US Phosphate Resource Area. Geochem Trans 6:1–11
6. Tokunaga K, Yokoyama Y, Kawagucci S, Sakaguchi A, Terada Y, Takahashi Y (2013) Selenium coprecipitated with barite in marine sediments as a possible redox indicator. Chem Lett 42:1068–1069
7. Denecke MA, Brendebach B, de Nolf W, Falkenberg G, Janssens K, Simon R (2009) Spatially resolved micro-X-ray fluorescence and micro-X-ray absorption fine structure study of a fractured granite bore core following a radiotracer experiment. Spectrochim Acta Part B 64:791–795
8. Langner P, Mikutta C, Suess E, Marcus MA, Kretzschmar R (2013) Spatial distribution and speciation of arsenic in peat studied with microfocused X-ray fluorescence spectrometry and X-ray absorption spectroscopy. Environ Sci Technol 47:9706–9714
9. Smedley PL, Kinniburgh DG (2002) A review of the source, behaviour and distribution of arsenic in natural waters. Appl Geochem 17:517–568
10. Anawar HM, Akai J, Komaki K, Terao H, Yoshioka T, Ishizuka T, Safiullah S, Kato K (2003) Geochemical occurrence of arsenic in groundwater of Bangladesh: sources and mobilization processes. J Geochem Explor 77:109–131
11. Masscheleyn PH, Delaune RD, PatrickJr WH (1991) Effect of redox potential and pH on arsenic speciation and solubility in a contaminated soil. Environ Sci Technol 25:1414–1419
12. Pinakidou F, Katsikini M, Paloura EC, Kavouras P, Komninou P, Karakostas T, Erko A (2006) Application of μ-XAFS for the determination of the crystallization ratio in a series of vitroceramic materials containing industrial waste. Nucl Instrum Methods Phys Res Sec B 246:238–243
13. Pinakidou F, Katsikini M, Paloura EC, Kavouras P, Kehagias T, Komninou P, Karakostas T, Erko A (2007) On the distribution and bonding environment of Zn and Fe in glasses containing electric arc furnace dust: a μ-XAFS and μ-XRF study. J Hazard Mater 142:297–304
14. Abe Y, Iizawa Y, Terada Y, Adachi K, Igarashi Y, Nakai I (2014) Detection of uranium and chemical state analysis of individual radioactive microparticles emitted from the Fukushima nuclear accident using multiple synchrotron radiation X-ray analyses. Anal Chem 86:8521–8525
15. Gandhi HS, Piken AG, Shelef M, Delosh RG (1976) Laboratory evaluation of three-way catalysts. SAE Paper, 760201

16. Sugiura M (2003) Oxygen storage materials for automotive catalysts: ceria-zirconia solid solutions. Catal Surv Asia 7:77–87
17. Matsumoto SI (2004) Recent advances in automobile exhaust catalysts. Catal Today 90:183–190
18. Suda A, Ukyo Y, Sobukawa H, Sugiura M (2002) Improvement of oxygen storage capacity of CeO_2-ZrO_2 solid solution by heat treatment in reducing atmosphere. J Ceram Soc Jpn 110:126–130
19. Nagai Y, Yamamoto T, Tanaka T, Yoshida S, Nonaka T, Okamoto T, Suda A, Sugiura M (2002) X-ray absorption fine structure analysis of local structure of CeO_2–ZrO_2 mixed oxides with the same composition ratio (Ce/Zr=1). Catal Today 74:225–234
20. Sasaki T, Ukyo Y, Kuroda K, Arai S, Muto S, Saka H (2004) Crystal structure of $Ce_2Zr_2O_7$ and β-$Ce_2Zr_2O_{7.5}$. J Ceram Soc Jpn 112:440–444
21. Sakamoto Y, Kizaki K, Motohiro T, Yokota Y, Sobukawa H, Uenishi M, Tanaka H, Sugiura M (2002) New method of measuring the amount of oxygen storage/release on millisecond time scale on planar catalyst. J Catal 211:157–164
22. Tada M, Zhang S, Malwadkar S, Ishiguro N, Soga J, Nagai Y, Tezuka K, Imoto H, Otsuka-Yao-Matsuo S, Ohkoshi S, Iwasawa Y (2012) The active phase of nickel/ordered Ce2Zr2O (x) catalysts with a discontinuity (x = 7–8) in methane steam reforming. Angew Chem Int Ed 51:9361–9365
23. Tada M, Ishiguro N, Uruga T, Tanida H, Terada Y, Nagamatsu S, Iwasawa Y, Ohkoshi S (2011) μ-XAFS of a single particle of a practical $NiO_x/Ce_2Zr_2O_y$ catalyst. Phys Chem Chem Phys 13:14910–14913
24. Ishiguro N, Uruga T, Sekizawa O, Tsuji T, Suzuki M, Kawamura N, Mizumaki M, Nitta K, Yokoyama T, Tada M (2014) Visualization of the heterogeneity of cerium oxidation states in single Pt/$Ce_2Zr_2O_x$ catalyst particles by nano-XAFS. ChemPhysChem 15:1563–1568
25. El Fallah J, Boujana S, Dexpert H, Kiennemann A, Majerus J, Touret O, Villain F, Le Normand F (1994) Redox processes on pure ceria and on Rh/CeO2 catalyst monitored by X-ray absorption (fast acquisition mode). J Phys Chem 98:5522–5533
26. Modeshia DR, Wright CS, Payne JL, Sankar G, Fiddy SG, Walton RI (2007) Low-temperature redox properties of nanocrystalline cerium (IV) oxides revealed by in situ XANES. J Phys Chem C 111:14035–14039
27. Tada M, Uruga T, Iwasawa Y (2015) Key factors affecting the performance and durability of cathode electrocatalysts in polymer electrolyte fuel cells characterized by in situ real time and spatially resolved XAFS techniques. Catal Lett 145:58–70
28. Bocchetta P, Gianoncelli A, Abyaneh MK, Kiskinova M, Amati M, Gregoratti L, Jezersek D, Mele C, Bozzini B (2014) Electrosynthesis of Co/PPy nanocomposites for ORR electrocatalysis: a study based on quasi-in situ X-ray absorption, fluorescence and in situ Raman spectroscopy. Electrochim Acta 137:535–545
29. Bozzini B, Bocchetta P, Gianoncelli A (2015) Coelectrodeposition of ternary Mn-oxide/polypyrrole composites for ORR electrocatalysts: a study based on micro-X-ray absorption spectroscopy and X-ray fluorescence mapping. Energies 8:8145–8164
30. Takao S, Sekizawa O, Nagamatsu S, Kaneko T, Yamamoto T, Samjeske G, Higashi K, Nagasawa K, Tsuji T, Suzuki M, Kawamura N, Mizumaki M, Uruga T, Iwasawa Y (2014) Mapping platinum species in polymer electrolyte fuel cells by spatially resolved XAFS techniques. Angew Chem Int Ed 53:14110–14114
31. Takao S, Sekizawa O, Samjeské G, Namagatsu S, Kaneko T, Yamamoto TI, Higashi K, Nagasawa K, Uruga T, Iwasawa Y (2015) Same-view nano-XAFS/STEM-EDS imagings of Pt chemical species in Pt/C cathode catalyst layers of a polymer electrolyte fuel cell. J Phys Chem Lett 6:2121–2126

Chapter 11
Computed Laminography XAFS

Mizuki Tada and Hirosuke Matsui

Three-dimensional imaging of a solid sample is attractive for high-throughput and non-destructive characterization methods, and computed tomography (CT) is well developed and widely used for several analytical methods such as electron microscopy. X-ray computed tomography (XCT) can obtain three-dimensional structural data of a solid sample, in particular morphology and elemental information.

At the measurements of XCT, a sample is perpendicularly rotated to an incident X-rays, and transmission image at each rotating angle is recorded with a two-dimensional detector. A series of transmission images at different rotation angles are computationally reconstructed and a three-dimensional image of the sample is obtained [1, 2]. XCT has been applied to functional materials such as heterogeneous catalysts [3, 4], lithium batteries [5, 6], and PEFC components [7, 8].

The conventional reconstruction of XCT requires XCT projected images at all rotating angles to obtain absolute three-dimensional image of a sample (Fig. 11.1). In the case of a flat sample, the cross section of a sample at the rotating angle around 90° is beyond observation field area. To image a flat sample, limited-angle CT, which is a reconstruction method by using projected images at limited rotating angles, and X-ray computed laminography (XCL) have been developed [9].

M. Tada (✉)
Research Center for Materials Science, Nagoya University, Nagoya, Aichi 464-8602, Japan

Department of Chemistry, Graduate School of Science, Nagoya University, Nagoya, Aichi 464-8602, Japan

Element Visualization Team, Materials Visualization, Photon Science Group, RIKEN SPring-8 Center, Hyogo 679-5148, Japan
e-mail: mtada@chem.nagoya-u.ac.jp

H. Matsui
Department of Chemistry, Graduate School of Science, Nagoya University, Nagoya, Aichi 464-8602, Japan

Y. Iwasawa et al. (eds.), *XAFS Techniques for Catalysts, Nanomaterials, and Surfaces*, DOI 10.1007/978-3-319-43866-5_11

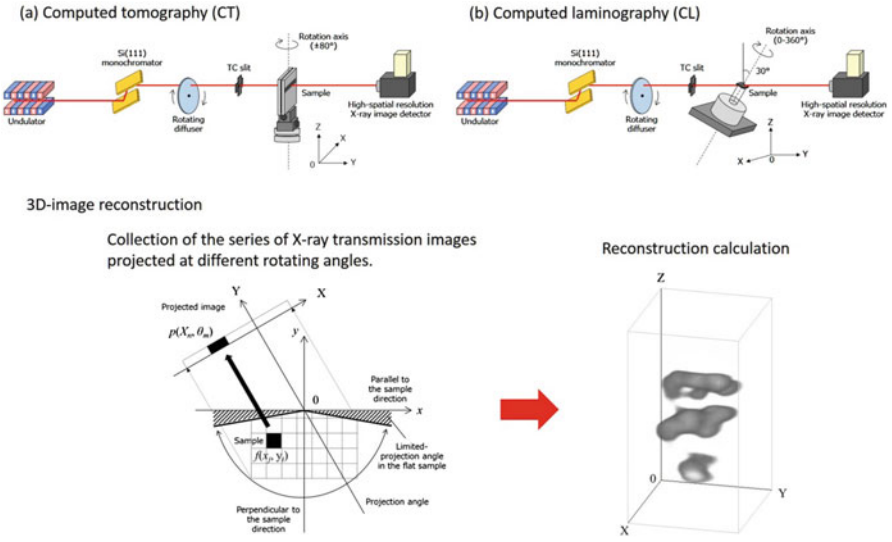

Fig. 11.1 Setup of (**a**) X-ray computed tomography (XCT) and (**b**) X-ray computed laminography (XCL) and an example of 3D-image reconstruction

In XCL, the rotating axis of a sample is not fixed at 90° to incident X-ray beam as shown in Fig. 11.1. The inclined sample stage mounting a sample is rotated and transmitted images are recorded. For examples, Hoshino et al. succeeded in obtaining three-dimensional images of Cu grids with sub-μm spatial resolution by the XCL techniques [9]. On the other hand, limited-angle CT is mainly applied to medical imaging such as mammography/tomography breast imaging [10, 11] and dental imaging [12]. The assessment of glued timber integrity was also investigated by limited-angle microfocus XCT [13].

A reconstructed XCT or XCL image at an X-ray energy corresponds to be X-ray absorbance mapping at the energy, as a result, the three-dimensional structural image (morphology) of a sample is visualized. When the X-ray energy of XCT or XCL measurements is changed, a three-dimensional X-ray absorbance mapping at the different X-ray energy is obtained. From XCT or XCL images at particular X-ray energies, spectroscopic information at each position of a sample can be discussed. The method combining XCT/XCL and XAFS spectroscopy is called XCT-XAFS/XCL-XAFS [14], and the integrated analysis of XCT/XCL and XAFS or XRD has been applied to find three-dimensional structural/chemical information to functional materials [15–17].

We applied the XCL-XAFS technique to a membrane electrode assembly (MEA) of polymer electrolyte fuel cell (PEFC), which is a flat membrane sample with layered structures. In a PEFC MEA, there are two catalyst layers at cathode and anode, and they are stacked on the surface of a Nafion membrane. The dissolution and degradation of Pt cathode electrocatalysts are still serious problems

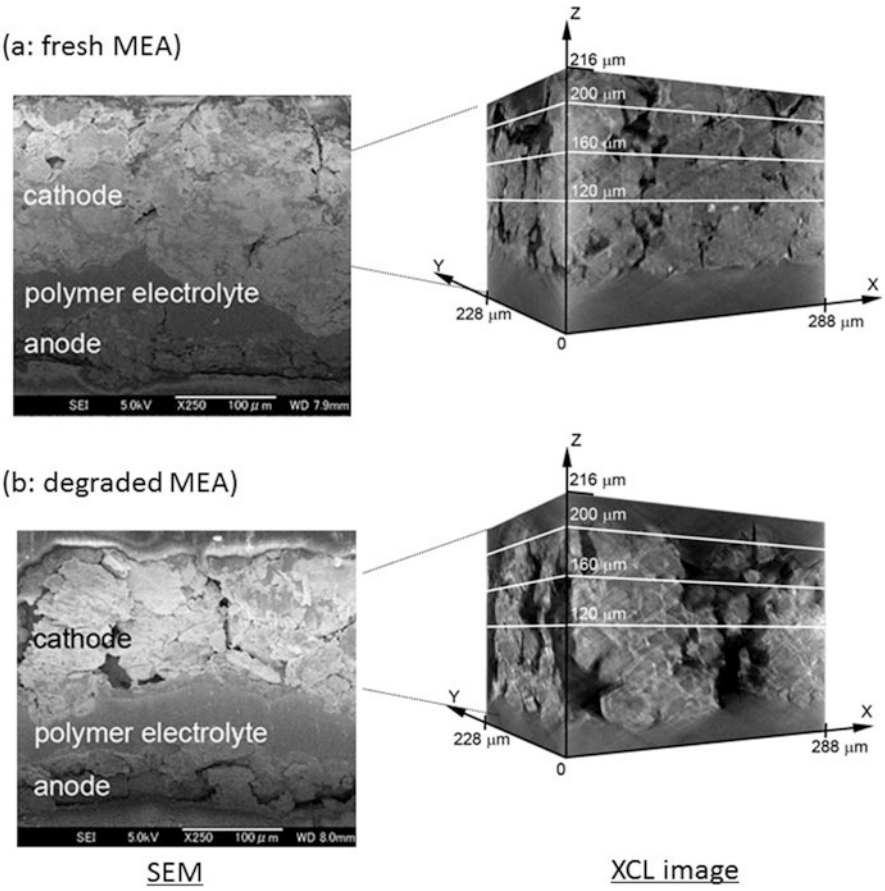

Fig. 11.2 Cross-sectional SEM images (*left*) and three-dimensional reconstructed XCL images at 11.496 keV before Pt L_{III}-edge (*right*) of a fresh (**a**) and degraded (**b**) MEAs [16]

for practical operation of PEFC, and the XCL-XAFS showed the heterogeneous distribution of Pt cathode electrocatalysts in the MEA in a non-destructive manner [16, 17].

MEAs commercially prepared (5×5 cm^2) with 50 wt% Pt/C cathode electrocatalysts were conducted to typical voltage-cycling steps. A degraded MEA was prepared by the additional aging and accelerated degradation testing (200 cycles). Both samples were cut into 1 cm $\times$ 1 cm pieces and set on SiC membrane holders. The thickness of the cathode catalyst layer of the fresh MEA was observed to be about 140–210 μm by cross-sectional SEM analysis (Fig. 11.2).

Ex situ XCL-XAFS of the PEFC MEAs was measured at the BL47XU beamline at SPring-8, Japan. X-rays from the BL47XU undulator were monochromatized by Si(1 1 1) crystals. A rotating beam diffuser composed of a sheet of a paper was installed at the upstream part of the experimental hutch to reduce speckle noises

coming from optical components in the X-ray beam path (Fig. 11.1). The rotational axis of the sample was inclined 30° from the vertical direction, which was perpendicular to the optical axis, toward the downstream direction for the XCL measurements.

XCL images at 11.496 keV, which is the energy before Pt L_{III}-edge, showed the morphology of the MEA samples as shown in Fig. 11.2. The XCL images clearly showed the structures of the MEAs with many cracks in a random pattern. In the degraded MEA after the accelerated degradation testing, the thickness of the cathode catalyst layer was about 115–210 μm and conspicuous expansion of the crack structures was observed throughout the whole area of the cathode catalyst layer.

We recorded XCL images at a different X-ray energy of 11.572 keV after Pt L_{III} edge, which corresponds to be the isosbestic point of Pt and PtO_2. Difference in X-ray absorption intensity at 11.572 keV to that at 11.496 keV can be calculated by the XCL images at these energies, showing the spatio-distribution of Pt species in the samples. Figure 11.3 shows three-dimensional spatio-distribution of Pt atoms in the fresh and degraded MEAs visualized by XCL images. In the fresh MEA, Pt catalysts distributed the whole parts of the cathode catalyst layer although original crack structures existed in the MEA. On the other hand, serious heterogenization of the Pt electrocatalysts was clearly observed in the degraded MEA as shown in Fig. 11.3b. The significant aggregation of Pt cathode electrocatalysts was observed at many parts in the cathode catalyst layer. The XCL images clearly revealed the spatio-differences in the degradation of the Pt catalysts in the MEAs.

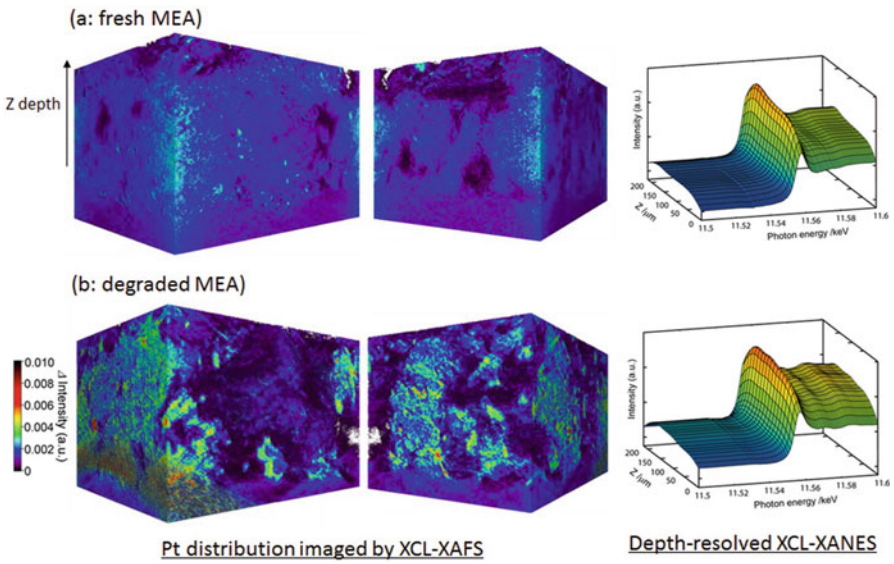

Fig. 11.3 The three-dimensional spatio-distribution of Pt atoms in the cathode catalyst layers imaged by Pt L_{III}-edge XCL-XAFS (*left* and *middle*) and depth-resolved XCL-XANES spectra (*right*) of the fresh (**a**) and degraded (**b**) MEAs [16]

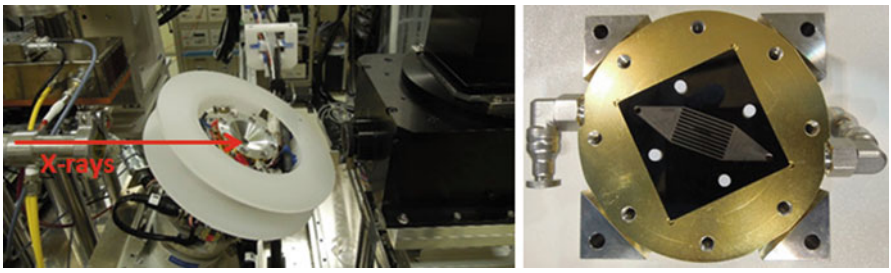

Fig. 11.4 An in situ PEFC cell for in situ XCL-XAFS measurements

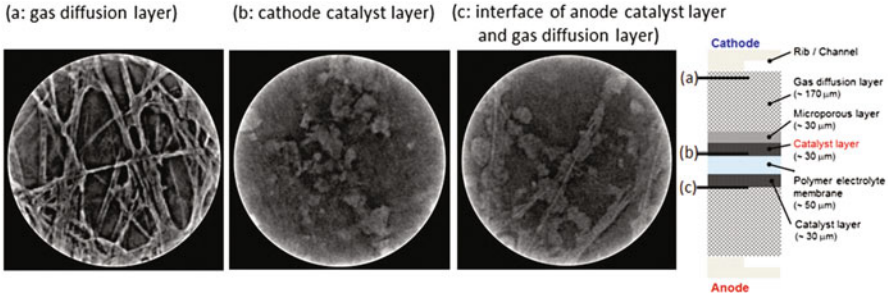

Fig. 11.5 Examples of reconstructed in situ XCL images at 0.4 V (anode: H_2 flow, cathode: air flow, and cell temperature: 305 K) for the MEA after the 15,000 cycles of ADT. X-ray energy was 11.525 keV. Thickness of each layer was 0.3125 μm. (**a**) A cross-sectional image of its cathode gas diffusion layer, (**b**) that of its cathode catalyst layer, and (**c**) that of the interface of its anode catalyst layer and anode gas diffusion layer

Large differences were also found on depth-resolved Pt L_{III}-edge XCL-XANES spectra of the fresh and degraded MEAs in Fig. 11.3. In the fresh MEA, the Pt quantity gradually increased with depth of the cathode catalyst layer and reached a maximum at about 170 μm deep. In contrast, more heterogeneous wavy was observed to the depth of the degraded MEA. It is suggested that the degradation process highly affected to the distribution of the Pt electrocatalysts in μm level.

An in situ PEFC cell was developed for in situ XCL-XAFS measurements as presented in Fig. 11.4, and in situ XCL measurements of an MEA for PEFC were investigated under PEFC operating conditions. Figure 11.5 shows the cross-sectional XCL images at 11.525 keV of a PEFC MEA with Pt/C cathode electrocatalyst after the 15,000 cycles of ADT. The XCL measurements were performed with the flow of H_2 at anode and that of air at cathode, and the cell was heated at 305 K. The cell voltage was maintained at 0.4 V during the XCL measurements. Total imaging depth of XCL images was about 500 μm, and the thickness of each layer was 0.3125 μm.

At the depth of a gas diffusion layer at cathode, the morphology of carbon fiber was clearly visualized in the cross-sectional XCL image (Fig. 11.5a). At its cathode catalyst layer, the cross-sectional XCL image widely changed and deposited Pt/C

cathode electrocatalyst was imaged (Fig. 11.5b). At anode, similar contrasts were observed for its anode catalyst layer and its gas diffusion layer (Fig. 11.5c). The in situ XCL measurements clearly showed the morphology of each layers in the MEA.

In the cases of Pt cathode electrocatalysts in PEFC, the structural differences in the Pt electrocatalysts are not so large and the surfaces of Pt nanoparticles oxidized or reduced in the operating cycles. Expected differences in the Pt L_{III}-edge XANES and EXAFS spectra are so small to clearly detect by in situ XCL-XAFS and it was difficult to obtain significant imaging data of Pt L_{III}-edge XCL-XAFS for the sample under in situ conditions with lots of water. The application of limited-angle XCT-XAFS would be promising to approach in situ three-dimensional imaging of PEFC MEAs.

References

1. Sakdinawat A, Attwood D (2010) Nanoscale X-ray imaging. Nature Photon 4:840
2. Grunwaldt J-D, Schoer CG (2010) Hard and soft X-ray microscopy and tomography in catalysis: bridging the different time and length scales. Chem Soc Rev 39:4741
3. Perea DE, Arslan I, Liu J, Ristanovic Z, Kovarik L, Arey BW, Lercher JA, Bare SR, Weckhuysen BM (2015) Determining the location and nearest neighbors of aluminum in zeolites with atom probe tomography. Nat Commun 6:7589
4. Meirer F, Kalirai S, Weker JN, Liu Y, Andrews JC, Weckhuysen BM (2015) Agglutination of single catalyst particles during fluid catalytic cracking as observed by X-ray nanotomography. Chem Commun 51:8097–8100
5. Meirer F, Cabana J, Liu Y, Mehta A, Andrews JC, Pianetta P (2011) Three-dimensional imaging of chemical phase transformations at the nanoscale with full-field transmission X-ray microscopy. J Synchrotron Radiat 18:773
6. Nelson J, Misra S, Yang Y, Jackson A, Liu Y, Wang H, Dai H, Andrews JC, Cui Y, Toney MF (2012) In operando X-ray diffraction and transmission X-ray microscopy of lithium sulfur batteries. J Am Chem Soc 134:6337
7. Mukaide T, Mogi S, Yamamoto J, Morita A, Koji S, Takada K, Uesugi K, Kajiwara K, Noma T (2008) In situ observation of water distribution and behavior in a polymer electrolyte fuel cell by synchrotron X-ray imaging. J Synchrotron Radiat 15:329
8. Sasabe T, Deevanhxay P, Tsushima S, Hirai S (2011) Soft X-ray visualization of the liquid water transport within the cracks of micro porous layer in PEFC. Electrochem Commun 13:638
9. Hoshino M, Uesugi K, Takeuchi A, Suzuki Y, Yagi N (2011) Development of an X-ray micro-laminography system at Spring-8. AIP Conf Proc 1365:250
10. Raylman RR, Majewski S, Smith MF, Proffitt J, Hammond W, Srinivasan A, McKisson J, Popov V, Weisenberger A, Judy CO (2008) The positron emission mammography/tomography breast imaging and biopsy system (PEM/PET): design, construction and phantom-based measurements. Phys Med Biol 53:637–653
11. Qian X, Rajaram R, Calderon-Colon X, Yang G, Phan T, Lalush DS, Lu J, Zhou O (2009) Design and characterization of a spatially distributed multibeam field emission X-ray source for stationary digital breast tomosynthesis. Med Phys 36:4389–4399
12. Je U, Cho H, Lee M, Oh J, Park Y, Hong D, Park C, Cho H, Choi S, Koo Y, Kor J (2014) Dental cone-beam CT reconstruction from limited-angle view data based on compressed-sensing (CS) theory for fast, low-dose X-ray imaging. Phys Soc 64:1907–1911

13. Sanabria SJ, Wyss P, Neuenschwander J, Niemz P, Sennhauser U (2011) Assessment of glued timber integrity by limited-angle microfocus X-ray computed tomography. Eur J Wood Wood Prod 69:605–617
14. Ham K, Butler LG (2007) Algorithms for three-dimensional chemical analysis via multi-energy synchrotron X-ray tomography. Nuclear Instr Methods Phys Res B 262:117–127
15. Bealea AM, Gibson EK, O'Briena MG, Jacquesc SDM, Cernikd RJ, Michiele MD, Cobdenf PD, Pirgon-Galinf Ö, Waterg L, Watsong MJ, Weckhuysen BM (2014) Chemical imaging of the sulfur-induced deactivation of Cu/ZnO catalyst. J Catal 314:94–100
16. Saida T, Sekizawa O, Ishiguro N, Hoshino M, Uesugi K, Uruga T, Ohkoshi S, Yokoyama T, Tada M (2012) 4D visualization of a cathode catalyst layer in a polymer electrolyte fuel cell by 3D laminography-XAFS. Angew Chem Int Ed 51:10311–10314
17. Tada M, Uruga T, Iwasawa Y (2015) Key factors affecting the performance and durability of cathode electrocatalysts in polymer electrolyte fuel cells characterized by in situ real time and spatially resolved XAFS techniques. Catal Lett 145:58–70

Chapter 12
X-Ray Absorption with Transmission X-Ray Microscopes

Frank de Groot

12.1 Introduction

In this section we focus on the use of transmission X-ray microscopy (TXM) to measure the XAS spectra. In the last decade a range of soft X-ray and hard X-ray TXM microscopes have been developed, allowing the measurement of XAS spectra with 10–100 nm resolution. In the hard X-ray range the TXM experiments pose the same restrictions on in situ experiments as bulk XAS experiments, allowing experiments with capillaries to study catalysts under working conditions. In the soft X-ray range, dedicated transmission nanoreactors are needed. Considering catalysts the main result the in situ TXM experiments are the determination of nanometer range variations of catalysts under working conditions. An important property of X-rays is their short wavelength below 1 nm. This allows direct imaging of catalysts in scanning mode or full field mode. In contrast, visible light with an energy of 1 eV has a diffraction limited resolution of approximately 500 nm and VUV light with an energy of 10 eV has a diffraction limit of ~50 nm.

We will compare TXM microscopes in detail with transmission electron microscopes (TEM) that allow a similar combination with spectroscopy using electron energy loss spectroscopy (EELS). We will omit scanning probe near field microscopes as they are limited to surfaces and do not directly look at the interior of catalyst materials, including the non-exposed internal surfaces. Catalytic activity very often takes place within micro and/or mesoporous structures implying that not only the external surface of a catalyst is of importance. Examples include the active sites within zeolites and enzymes. The catalytic active sites in these systems cannot be studied with probes that only map the outside of the system. TEM and TXM

F. de Groot (✉)
Inorganic Chemistry and Catalysis, Utrecht University, 3584 CG Utrecht, The Netherlands
e-mail: f.m.f.degroot@uu.nl

Y. Iwasawa et al. (eds.), *XAFS Techniques for Catalysts, Nanomaterials, and Surfaces*, DOI 10.1007/978-3-319-43866-5_12

detect a column of material through the system of study. As such they provide information on both the surface structure and the internal structure of a material.

12.2 Soft X-Ray TXM Microscopes

In a scanning TXM microscope, a synchrotron X-ray absorption beamline is used to illuminate a Fresnel zone plate. The zone plate characteristics determine the spot size to which the X-ray beam is focused, typically between 10 and 50 nm. The focal length is in the order of a few millimeters, which is a design limitation for in situ reactor cells. Full-field TXMs use two zone plates, allowing the synchronous detection of an image plane [1]. Soft X-ray TXM microscopes cover the energy range between 200 and 2000 eV. This includes the 1s core states or K edges of the elements from carbon (280 eV) to phosphorus (2150 eV) [2]. A range of soft ray TXM microscopes exist, including beamlines at NSLS Brookhaven [3]; BESSY Berlin [4]; SLS Villingen (Pollux) [5]; CLS Saskatoon [6], and ALS Berkeley [7, 8]. The soft X-ray range included C, N, O and also Mg, Al, Si, and P. The soft X-ray 2p core states ($L_{2,3}$ edges) range from potassium (290 eV) to Sr (2000 eV). In particular the 3d transition metal ions are important for catalysis and are often studied, also because they provide very rich $L_{2,3}$ edge spectral shapes. A range of other edges are available for heavier elements. Using the specific absorption of a core level one can obtain quantitative elemental maps in a TXM microscope, for example by determining the ratio between a recorded map just before and after the edge.

Soft X-ray K edges can be interpreted as mapping the empty states of the element under study. The variation in the empty states implies variation in the XAS spectral shape, which can be used for chemical contrast. The spectral shapes of carbon, nitrogen and oxygen containing systems reveal a large variation in spectral shapes and, as such, are ideal for chemical contrast [9]. The transition metal L edges cannot be interpreted with a density of states concept, as their spectral shape is dominated by multiplet effects induced by the core hole in the final state [10]. One observes a rich spectral fine structure allowing detailed chemical analysis. Transition metal L edges are split by the 2p spin-orbit coupling splits the L edge into its L_3 and L_2 components. Intra-atomic correlations (multiplet effects), crystal field effects and the effects of charge fluctuations dominate the spectral shape analysis [11]. Charge transfer multiplet analysis yields information on the metal valence, spin state, the site symmetry, and the crystal field strength [12, 13].

Soft X-rays have a strong interaction with matter. This implies that transmission experiments are only possible for solid samples of limited thickness. In addition, the transmission through gas atmospheres is also affected by significant soft X-ray absorption, limiting the X-ray path through the gas phase to several 100 μm. The windows should ideally have thickness below 50 nm of a light material. The sample thickness for soft X-rays must ideally be in the (sub)micron range, dependent also

on concentration and elemental composition. Note that the experiments are transmission experiments implying that the edge energy and concentration of the probed element determines the ideal thickness of the sample.

Because of the X-ray transmission induced sample limitations, traditionally soft XAS spectra have been measured with electron yield detection or fluorescence yield (FY) detection. Yield methods use the core hole decay, which gives rise to electrons and X-rays escaping from the surface of the substrate. Detection of these decay products, allows the measurement of samples with arbitrary thickness. With total electron yield (TEY), one detects all electrons that emerge from the sample surface and due to the electron escape depth of a few nm this turns the TXM into a surface technique. For dilute systems, transmission might not yield a measurable signal and FY is an option. A complication is that the optical component of a TXM microscope is usually very close to the sample, which makes it difficult to use TEY and FY detectors. Soft X-ray TXM is ideally suited to study, in addition to the organic phase (by their C, N, O K edges) also the inorganic phase via their metal edges.

In Fig. 12.1 we compare the spatial resolution and the maximal sample thickness of a TXM experiment with transmission electron microscopy (TEM) combined with Electron Energy Loss Spectroscopy (EELS). TEM-EELS can be considered as

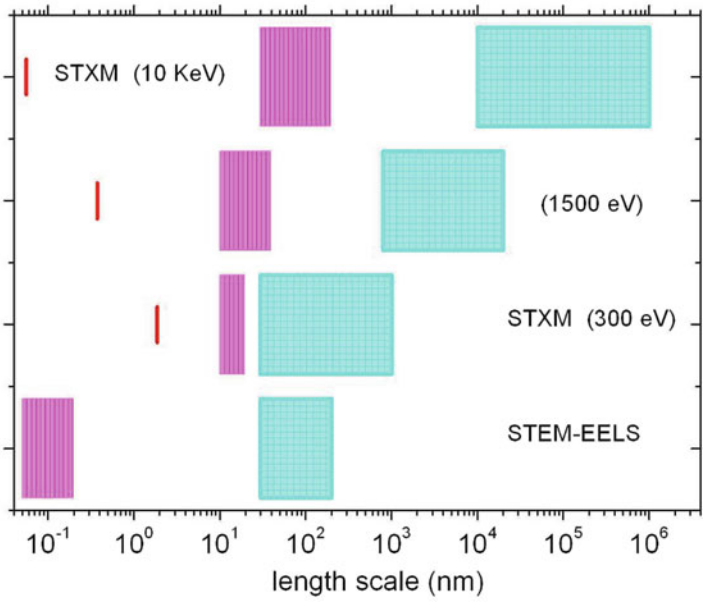

Fig. 12.1 The range of experimental, spatial resolutions (*pink*) and maximal sample thicknesses (*blue*) are indicated on a logarithmic scale for, from *bottom* to *top*, TEM-EELS, TXM at 300 eV, TXM at 1.5 keV and TXM at 10 keV. The sample thicknesses is limited by attenuation but also by spectral deformations due to saturation effects. The *red vertical lines* indicate the diffraction limited resolution of the X-rays

the electron analogue of TXM-XAS. The data for TEM-EELS assumes a 100 keV electron beam. The resolution of TEM-EELS is between 0.1 and 0.5 nm, with some possible improvements to less than 0.1 nm [14–16]. The maximal sample thickness for chemical contrast imaging is dependent on the material. TXM experiments have resolution of approximately 10 nm [17], larger than the diffraction limited resolution. The maximal sample thickness of TXM is dependent on energy. In case of edge absorption in the soft X-ray range the sample thickness for which the signal is not distorted can be as low as 50 nm. This does not mean that thicker samples cannot be measured, but the signal will be distorted. For hard X-rays, for example at 10 keV one needs different, thicker, zone plates. Recently hard X-ray zone plates have also reached resolution of 10 nm. The reduced X-ray absorption strength and scattering of hard X-rays increase the possible sample thickness towards the mm range. Hard X-ray microscopy experiments in the micron range are very interesting for catalysis as the hard X-rays allow realistic catalytic conditions.

12.3 In Situ Soft X-Ray TXM of Catalytic Solids

The first in situ TXM-XAS experiments on a working catalyst have been published in 2008 by de Smit et al. [18]. They measured an iron-based Fischer–Tropsch catalyst under working conditions. The Fischer–Tropsch reaction enables the production of high-purity chemicals and transportation fuels from sources other than conventional crude oil, most notably natural gas, coal, and biomass.

Figure 12.2 shows an example of an Fe_2O_3 nanoparticle that was reduced under 1 bar hydrogen pressure. After initial reduction on the outside the reduction is first complete in the interior of the nanoparticle. For the Fischer-Tropsch catalyst the Fe 2p XAS was used to map the iron valence and the oxygen K edge to distinguish between different oxygen-containing species (SiO_2 and iron oxides; cf. Fig. 12.3). The carbon K edge was measured to image the type and location of carbon species

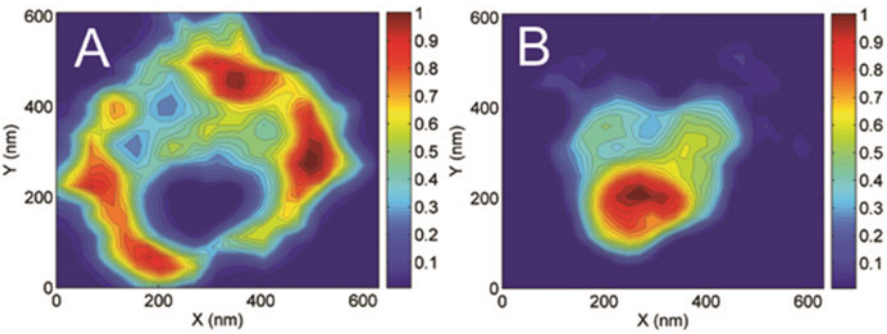

Fig. 12.2 Elemental map of (**a**) iron-oxide and (**b**) iron metal in an Fe_2O_3 nanoparticle after reduction at 250 °C, using the iron L edge STXM XAS spectra. The spatial variation of the reduction is shown

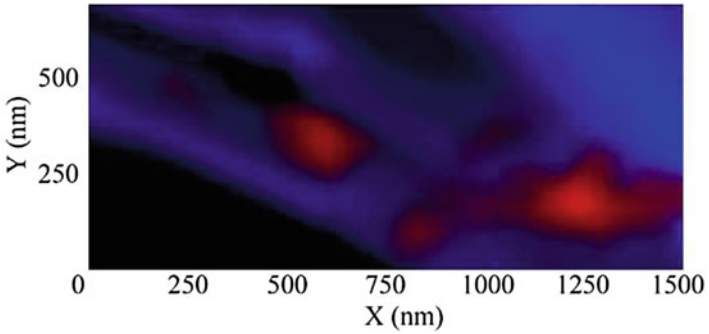

Fig. 12.3 Elemental map of SiO_2 (*blue*) and Fe_2O_3 (*red*) of an iron-based Fischer-Tropsch catalyst, using the oxygen K edge and iron L edge STXM XAS spectra

present in the catalyst during reaction. For further details, we refer to the original publications [19]. As such, this nanoscale chemical imaging technique provides insights into the local particle morphology and chemical reduction behavior of a complex Fischer-Tropsch catalyst system.

12.4 Nanoreactors

One common goal in the design of nanoreactors is the minimization of the path length that X-rays have to travel through the gas and/or liquid reactant phase. This will minimize X-ray attenuation and yield higher signal intensities. One possibility is to use nanoreactors that are designed for in situ TEM studies [20]. The current design of the cell allows for experiments up to ~2 bar and 500 °C (Fig. 12.4).

12.5 Comparison of STXM-XAS with STEM-EELS

The main difference between STXM-XAS and STEM-EELS is the significantly stronger interaction with matter of electrons compared with X-rays [21]. Table 12.1 gives a brief overview and in the subsequent paragraphs we briefly discuss these aspects, including energy resolution, energy range, time resolution, spatial resolution, detection modes, detection limits, sample thickness, sample conditions, sample damage, and tomography options.

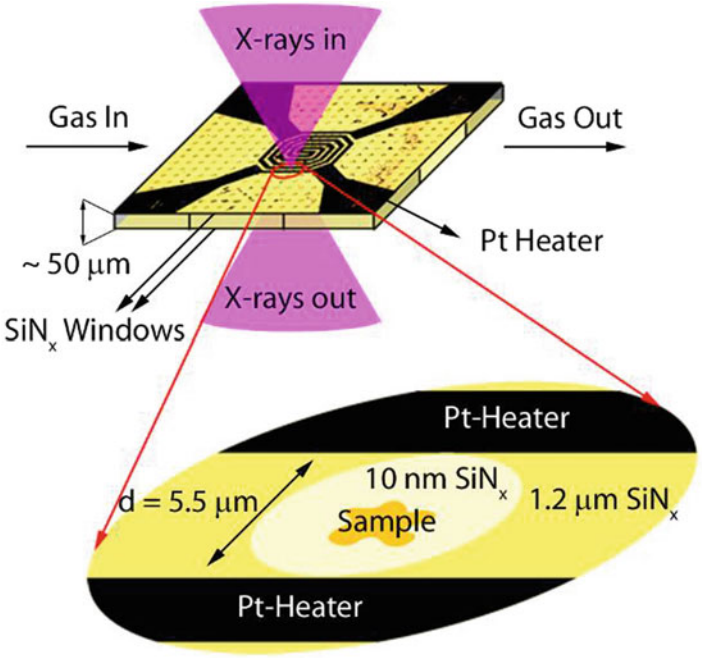

Fig. 12.4 Sketch of the nanoreactor windows indicating the spiral heater and the ~5 × 5 µm^2 windows used to investigate the material of interest

Table 12.1 Overview of the comparisons between STXM-XAS and STEM-EELS

	STXM-XAS	STEM-EELS
Spatial resolution	10 nm	0.1 nm
Energy resolution	0.2–0.6 eV	0.2 eV
Energy range	200–2500 eV	1–1500 eV
Data collection	Single energy	All energies
Detection modes	Transmission (T) Fluorescence Yield (FY) Electron Yield (EY)	Transmission (T)
Sample thickness	200–20,000 nm	<500 nm
Element sensitivity	1000 ppm (T) 10 ppm (FY)	1000 ppm (T)
In situ pressure	1 bar	Vacuum (*1 bar in TEM*)
Beam damage	High	Very high

12.5.1 Spatial and Energy Resolution

The spatial resolution can be below 0.1 nm for STEM-EELS microscopes [22, 23], which is a factor 100 better than the spatial resolution in STXM-XAS. The energy resolution of soft X-rays on a STXM beamline is typically $E/\Delta E = 5000$ and implying better than 0.2 eV resolution at the carbon K edge. De facto this implies that for solids the experimental resolution is mainly determined by the lifetime broadening of the core holes. The energy resolution of EELS varies significantly from microscope to microscope. Most EELS-dedicated microscopes have a core level energy resolution of 0.2–0.5 eV.

12.5.2 Detection Modes and Limits

In STEM-EELS all core levels are measured simultaneously. In STXM-XAS, the X-ray energy is set to one particular value and only at that energy the X-ray absorption is measured. STXM-XAS can be measured with EY and turned into a surface probe, or it can be measured with FY for dilute species. STEM-EELS and STXM-XAS are transmission experiments and the required contrast for a core level signal implies that spectral shapes of dilute species cannot be measured. As a rule, concentrations above 5000 ppm are required for good spectra.

12.5.3 In Situ Conditions and Sample Thickness

Soft X-ray STXM can be measured up to 2 bar and up to 550 °C. Hard X-ray experiments can be performed under extreme conditions, including high-pressure diamond anvil cells. STEM-EELS requires a sample less than ~200 nm thin. STXM-XAS can handle samples with thicknesses up to 20 μm at 1.5 keV and in the millimeter range for hard X-rays. The much thicker specimen that can be handled with STXM-XAS offers a wider and more flexible range of materials that can be studied, including objects such as intact biological cells.

12.5.4 Sample Damage

STEM-EELS requires a high radiation dose in comparison with normal TEM, which implies that sample damage is potentially high, including knock-on damage, carbon deposition, sputtering, and electrostatic charging. In STXM-XAS a highly focused X-ray beam is used, which, especially at resonance, generates large amount

of electrons, yielding damage from electrostatic charging and carbon deposition. Combining all beam damage effects and the required doses for imaging, as a rule it is found that STXM-XAS causes less damage than STEM-EELS [24, 25].

In conclusion, it can be stated that STEM-EELS offers better spatial resolution and the simultaneous detection of all core levels. STXM-XAS can handle large samples and a wider range of sample conditions including catalysis under working conditions.

12.6 Future Developments

The temperature and pressure range of STXM will increase to 1000 °C and 10 bar, thereby extending the range of feasible materials science and catalysis experiments. An important future development is the performance of in situ STXM tomographic experiments. STXM of ultra-dilute samples with concentrations down to 100 ppm are not straightforward in transmission mode, implying that fluorescence yield detection must be used. Such fluorescence yield based experiments would allow the mapping of impurities/promoters in heterogeneous catalyst and in materials science in general.

STXM will likely not reach the 0.1 nm spatial resolution as obtained by electron microscopy. STEM-EELS experiments on the other hand will be unfeasible for many samples and for many sample conditions.

References

1. Rehbein S, Heim S, Guttmann P, Werner S, Schneider G (2009) Ultrahigh-resolution soft-X-ray microscopy with zone plates in high orders of diffraction. Phys Rev Lett 103:110801
2. de Groot FMF, de Smit E, van Schooneveld MM, Aramburo LR, Weckhuysen BM (2010) In-situ scanning transmission X-ray microscopy of catalytic solids and related nanomaterials. ChemPhysChem 11:951
3. Ade H, Smith AP, Zhang H, Zhuang GR, Kirz J, Rightor E, Hitchcock A (1997) X-ray spectromicroscopy of polymers and tribological surfaces at beamline X1A at the NSLS. J Electron Spectrosc Relat Phenom 84:53
4. Wiesemann U, Thieme J, Guttmann P, Früke R, Rehbein S, Niemann B, Rudolph D, Schmahl G (2003) First results of the new scanning transmission X-ray microscope at BESSY-II. J Phys IV 104:95
5. Raabe J, Tzvetkov G, Flechsig U, Boge M, Jaggi A, Sarafimov B, Vernooij MGC, Huthwelker T, Ade H, Kilcoyne D, Tyliszczak T, Fink RH, Quitmann C (2008) PolLux: a new facility for soft X-ray spectromicroscopy at the Swiss Light Source. Rev Sci Instrum 79:113704
6. Kaznatcheev KV, Karunakaran C, Lanke UD, Urquhart SG, Obst M, Hitchcock AP (2007) Soft X-ray spectromicroscopy beamline at the CLS: commissioning results. Nucl Inst Meth A 582:96–99

7. Warwick T, Ade H, Cerasari S, Denlinger J, Franck K, Garcia A, Hayakawa S, Hitchcock A, Kikuma J, Klingler S, Kortright J, Morisson G, Moronne M, Rightor E, Rotenberg E, Seal S, Shin HJ, Steele WF, Tonner BP (1998) Development of scanning X-ray microscopes for materials science spectromicroscopy at the Advanced Light Source. J Synchrotron Radiat 5:1090–1092
8. Warwick T, Ade H, Kilcoyne D, Kritscher M, Tylisczcak T, Fakra S, Hitchcock A, Hitchcock P, Padmore H (2002) A new bend-magnet beamline for scanning transmission X-ray microscopy at the Advanced Light Source. J Synchrotron Radiat 9:254–257
9. Chen JG (1997) NEXAFS investigations of transition metal oxides, nitrides, carbides, sulfides and other interstitial compounds. Surf Sci Rep 30:1–152
10. Ade H, Zhang X, Cameron S, Costello C, Kirz J, Williams S (1992) Chemical contrast in X-ray microscopy and spatially resolved XANES spectroscopy of organic specimens. Science 258:972–975
11. de Groot F, Kotani A (2008) Core level spectroscopy of solids. Taylor & Francis, New York, p 3
12. Cramer SP, de Groot FMF, Ma Y, Chen CT, Sette F, Kipke CA, Eichhorn DM, Chan MK, Armstrong WH, Libby E, Christou G, Brooker S, McKee V, Mullins OC, Fuggle JC (1991) Ligand field strengths and oxidation states from manganese L edge spectroscopy. J Am Chem Soc 113:7937–7940
13. de Groot F (2005) Multiplet effects in X-ray spectroscopy. Coord Chem Rev 249:31–63
14. Batson PE, Dellby N, Krivanek OL (2002) Sub-angstrom resolution using aberration corrected electron optics. Nature 418:617–620
15. Muller DA (2009) Structure and bonding at the atomic scale by scanning transmission electron microscopy. Nat Mater 8:263–270
16. Muller DA, Kourkoutis LF, Murfitt M, Song JH, Hwang HY, Silcox J, Delby N, Krivanek OL (2008) Atomic-scale chemical imaging of composition and bonding by aberration-corrected microscopy. Science 319:1073–1076
17. Chao W, Kim J, Rekawa S, Fischer P, Anderson EH (2009) Demonstration of 12 nm resolution Fresnel zone plate lens based soft X-ray microscopy. Opt Express 17:17669–17677
18. de Smit E, Swart I, Creemer JF, Hoveling GH, Gilles MK, Tyliszczak T, Kooyman PJ, Zandbergen HW, Morin C, Weckhuysen BM, de Groot FMF (2008) Nanoscale chemical imaging of a working catalyst by scanning transmission X-ray microscopy. Nature 456:222
19. de Smit E, Swart I, Creemer JF, Karunakaran C, Bertwistle D, Zandbergen HW, de Groot FMF, Weckhuysen BM (2009) Nanoscale chemical imaging of the reduction behavior of a single catalyst particle. Angew Chem Int Ed 48:3632–3636
20. Creemer JF, Helveg S, Hoveling GH, Ullmann S, Molenbroek AM, Sarro PM, Zandbergen HW (2008) Atomic-scale electron microscopy at ambient pressure. Ultramicroscopy 108:993–998
21. Thomas JM, Hernandez-Garrido JC (2009) Probing solid catalysts under operating conditions: electrons or X-rays? Angew Chem Int Ed 48:3904–3907
22. Egerton RF, Li P, Malac M (2004) Radiation damage in the TEM and SEM. Micron 35:399–409
23. Bosman M, Keast VJ, Garcia-Munoz JL, D'Alfonso AJ, Findlay SD, Allen LJ (2007) Two-dimensional mapping of chemical information at atomic resolution. Phys Rev Lett 99:086102
24. Rightor EG, Hitchcock AP, Ade H, Leapman RD, Urquhart SG, Smith AP, Mitchell G, Fischer D, Shin HJ, Warwick T (1997) Spectromicroscopy of poly(ethylene terephthalate). J Phys Chem B 101:1950–1960
25. Howells MR, Hitchcock AP, Jacobsen CJ (2009) Introduction: special issue on radiation damage. J Electron Spectrosc Relat Phenom 170:1–3

Chapter 13
Operando EXAFS and XANES of Catalytic Solids and Related Materials

Gareth T. Whiting, Florian Meirer, and Bert M. Weckhuysen

13.1 Introduction

The continuous improvement of X-ray sources, optics, and detectors since the start of the twenty first century has paved the way for unprecedented studies of functional materials at work. Studying these typically highly complex materials while they are working requires a sophisticated combination of analysis techniques that can provide chemical information about the ongoing processes at multiple time- and/or length scales. This makes X-rays an excellent probe for such studies, as they are (usually) non-destructive, can be used for relatively fast processes (0.01–2 s), and can operate in harsh environments, for example under high pressure or temperature. In order to link the (spatio-)temporal chemical information obtained by X-ray absorption spectroscopy (XAS) to the task performed by the functional material, it is necessary to collect additional complementary information about the running process (performance). It is this simultaneous measurement together with a combined data analysis that defines "*operando*" studies.

We therefore want to start by defining the term "*operando*," in the context of XAS and how it differs from the term "in situ." Taking the topic of catalysis as an example, "*operando*" (latin for *working*/*operating*) XAS analysis (oxidation state, local coordination, etc.) involves studying the catalyst in its working place, under true reaction conditions. Whereas "in situ" (latin for *on site*), has been reported for both true and model catalytic reaction conditions. Moreover, in order for a system to be termed "*operando*," the simultaneous online analysis of activity and/or selectivity (performance) with for example, mass spectrometry (MS) or gas chromatography (GC), must take place [1, 2]. Therefore by combining XAS with online

G.T. Whiting • F. Meirer • B.M. Weckhuysen (✉)
Inorganic Chemistry and Catalysis group, Debye Institute for Nanomaterials Science, Utrecht University, 3584 CG Utrecht, The Netherlands
e-mail: B.M.Weckhuysen@uu.nl

Y. Iwasawa et al. (eds.), *XAFS Techniques for Catalysts, Nanomaterials, and Surfaces*, DOI 10.1007/978-3-319-43866-5_13

performance analysis, molecular-level structure–activity relationships are formed, such as linking the redox properties of catalytic active sites with changes in catalyst activity/selectivity. In line with this aspect, *operando* is also in turn used to verify the validity of the measurements under the environment of the X-ray beam (compared to a standard reactor). Factors such as local heating, or chemical and/or structural damage by the X-ray beam are potential problems which can lead to influences on the performance of the material [3].

Although this description of *operando* XAS may appear simplistic, the combination of both structural/chemical characterization (XANES/EXAFS) and performance analysis under true reaction conditions poses a considerable challenge. Depending on the heterogeneous catalytic process (solid/liquid or solid/gas interface), true reaction conditions often refer to "harsh" conditions, such as high pressures, high temperatures and in some cases potentially harmful reactants/products (among others), which requires the use of specially designed reactors/cells. Moreover, correlating XAS data with performance data in a spatially and temporally resolved manner is considerably difficult, given the bulk nature of "standard" XANES/EXAFS analysis and the fast kinetics of most catalytic reactions, respectively. Therefore, advanced XAS techniques are required (i.e., Quick-XAS, transmission X-ray microscopy), which make it possible to measure spectra on the sub-second time-scale and in a spatially resolved manner.

The origin of the term "*operando*" in relation to spectroscopy was first proposed during a discussion between Eric Gaigneaux, Gerhard Mestl, Miguel Bañares, and Bert Weckhuysen in 2000 during the 220th ACS National Meeting in Washington, DC (USA) [4]. This has since led to a succession of international conferences on the topic of *operando* spectroscopy, with the first in Lunteren (The Netherlands), in March 2003. The first time the term "*operando*" spectroscopy was used in a publication was by Miguel Bañares and coworkers in 2002, whereby a combination of Raman spectroscopy and online gas chromatography (GC) were applied, to develop structure–activity relationships of supported vanadium oxide catalysts under working propane selective oxidation (and ammoxidation) conditions [5]. Here, it was discovered that both surface mono-oxo vanadium oxide species and $SbVO_4$ phases are necessary for efficient propane ammoxidation. This gives a very early example of the type of information that can be acquired under *operando* conditions, with more detailed examples to be discussed later on in this Chapter. However, it is fair to state here, that there already exists several earlier literature examples, which combined spectroscopy of the working catalyst with online activity measurements, but did not use the term "*operando*" (represented by the fading empty squares in Fig. 13.1).

When looking to the *operando* X-ray absorption spectroscopy (XAS) literature (Fig. 13.1), it is clear that the introduction of this term into the scientific community in 2000 received great interest, with many publications produced thereafter, increasing year by year. Although only a limited number of publications exist in the *operando* XAS literature (139 compared to 3534 in situ studies), it is important to note that not all authors employ the term "*operando*" when performing simultaneous online performance analysis, and still use the term "in situ". In this chapter,

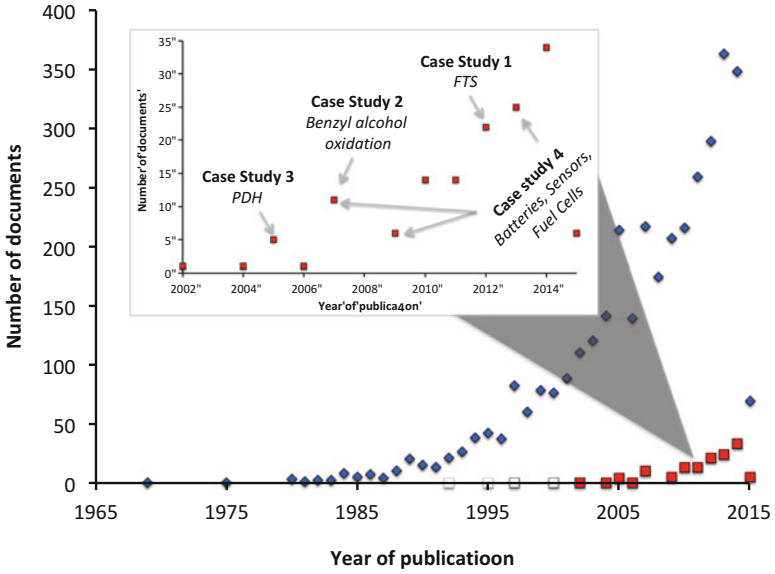

Fig. 13.1 Open literature search of both terms: "in situ XAS" (*diamonds*) and "*operando* XAS" (*squares*) using the Scopus database (*), highlighting the first time the term *operando* was used in a publication (2002). (Note: additional "*operando*" studies were previously published without the use of the term (*clear squares*)). The inlay presents the limited number of "*operando* XAS" publications to date, with the topics of case studies to be discussed in this chapter (Fischer–Tropsch Synthesis (FTS); Benzyl alcohol oxidation; Propane dehydrogenation (PDH); Batteries, sensors, and fuel cells), highlighted according to their year of publication. (*): The literature search was performed on March 2nd 2015

we discuss, making use of relevant case studies (Fig. 13.2), some of the fields that employ *operando* XAS, including catalysis, batteries, sensors, and fuel cells. Our main focus is on the topic of heterogeneous catalysis, discussing the use of *operando* XAS for several important processes and its influence on our further understanding of these systems. We refer the interested reader to several recent review articles, which are relevant to this topic, and which describe in more detail some of the developments taking place in this exciting field of research [6–13].

13.2 *Operando* XAS in Catalysis and Related Materials

13.2.1 Case Study 1: Fischer–Tropsch Synthesis

The Fischer–Tropsch Synthesis (FTS) process, invented by Franz Fischer and Hans Tropsch in 1926, involves the conversion of synthesis gas (mixture of H_2 and CO), into long-chain hydrocarbons [14]. The process is carried out industrially using an iron- or cobalt-based supported catalyst, with cobalt favored due to its high activity

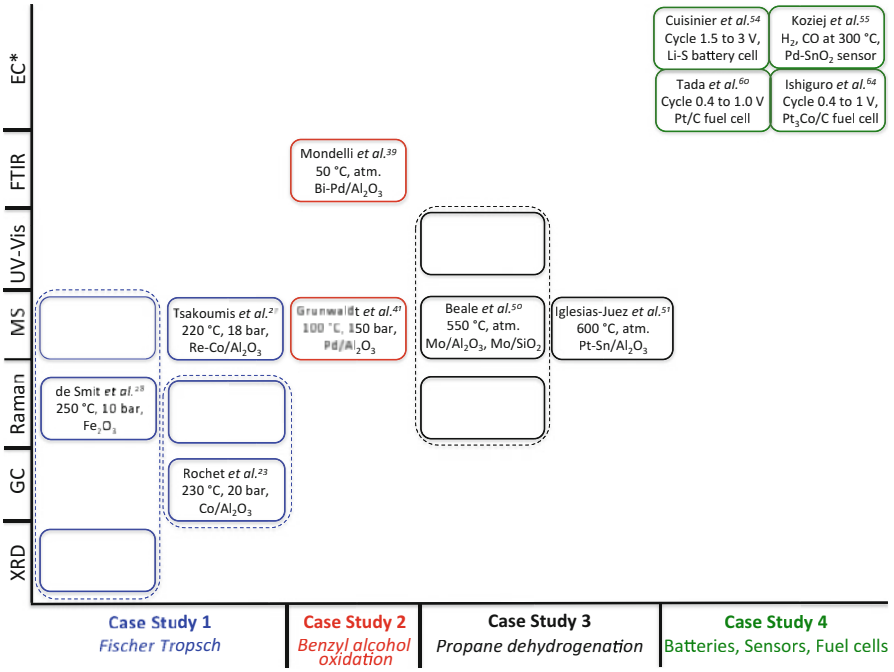

Fig. 13.2 Schematic which provides an overview of the selected case studies discussed in this Chapter and the combined techniques used within, on both solid catalyst systems and related materials in the field of *operando* XAS. *Electrochemical techniques refer to simultaneous online potentiostat and DC resistance measurements

and selectivity to linear paraffins, while iron is relatively cheap with respect to cobalt, and is now also explored for lower olefin synthesis. For example, in Qatar, gas-to-liquid (GTL) plants such as "Oryx" (Qatar Petroleum/Sasol) and "Pearl" (Shell), are based on Co-based catalysts [15]. Catalytic performance is of great value to industrial companies, with catalyst deactivation currently a substantial problem, fueling significant research interest [16–20]. Given that the catalyst in question undergoes many stages such as activation, induction, reaction, and recycling during FTS, accompanied by a range of deactivation mechanisms, a better understanding of the working catalyst behavior is vital. Sintering, reoxidation of the metal active site, and mixed metal–support compound formation are some of the possible causes for deactivation [21, 22], which require catalyst characterization under realistic FTS working conditions. The most common method of characterization is on spent catalysts, but is hampered by wax coverage on the catalyst, as well as problems with air sensitivity of the active metal [21]. Therefore, in situ or *operando* characterization methods are necessary in order to unravel the complex bulk/surface deactivation mechanisms taking place. Realistic FTS conditions are in the range of 210–250 °C, 15–30 bar and a H_2/CO ratio of ~2. Therefore, in situ cell design is one crucial and often limiting factor when considering the choice of characterization technique. XAS offers an excellent means to obtain structural

and chemical information of the active metal (as well as other elements) during these conditions, provided that the cell used allows meeting the relevant conditions. By coupling X-ray absorption spectroscopy (XAS) of the working catalyst with online catalytic performance monitoring and relating it with catalyst deactivation on a molecular-level scale, *operando* studies offer the best solution to improve cycle length, catalytic activity and selectivity. Given that very few XAS studies in the literature actually operate under true *operando* conditions, we will provide a brief outline here of these experiments on supported Co-based catalysts.

As discussed previously, cell design is of vital importance in determining the possibility of performing time-resolved experiments with conditions that mimic "real/working" catalytic reaction conditions. Rochet et al. [23] describe the use of an XAS cell (based on the design of Kawai et al. [24]) to study the structure and behavior of cobalt nanoparticles on a supported FTS catalyst. The catalyst under investigation consists of 7 wt% Co on alumina, prepared via incipient wetness impregnation and activated under a reducing atmosphere. The in situ cell is designed around its low-volume, with mica windows [25] that are X-ray-transparent and structurally, chemically, and thermally stable (Fig. 13.3a). Given that *operando* experiments require the potential to work under robust reaction conditions, the XAS cell is in line with this and can reach temperatures as high as 600 °C, with up to 50 bar pressure and under a range of oxidizing or reducing gas mixtures.

Unlike standard extended X-ray absorption fine structure (EXAFS) measurements which can take up to 20 min–1 h to acquire an X-ray absorption spectrum, Quick-EXAFS (QEXAFS) measurements allow the acquisition of the EXAFS in just a few seconds using a continuous-scan mode of the monochromator and maintains a high signal-to-noise ratio. QEXAFS experiments were performed in transmission mode at the SAMBA beamline at SOLEIL (Source Optimisée de Lumière d'Energie Intermédiaire de LURE), France, with the outlet of the reactor cell connected to an AirHead™ probe for online Raman spectroscopy monitoring of hydrocarbons produced. The conversion rate of CO was determined using a known CO partial pressure at the inlet and measuring it again at the outlet of the cell. Also, by applying a multivariate analysis approach to the C-H vibration bands that formed, information regarding product (alkane) selectivity was obtained, in order to relate performance with structural alterations on the catalyst (QEXAFS). During the activation treatment (under reducing atmosphere), the X-ray absorption near edge structure (XANES) of the recorded spectra revealed that the Co_3O_4 spinel structure in CoO was reduced as expected, to metallic cobalt. However, 23 % of the catalyst was still present as CoO, showing an insufficient reduction. When switching to a syngas atmosphere (270 °C, H_2/CO ratio of 2 at 20 bar), 76 % CO conversion was achieved and a significant intensity of Raman bands attributed to alkanes (69 % methane) and water were produced, with a slight reoxidation of the Co metallic nanoparticles. This was observed to be nanoparticle size-dependent using EXAFS analysis, with 2–4 nm nanoparticles being thermodynamically susceptible to oxidation. As methane selectivity and water production is drastically reduced upon decreasing the reaction temperature to 230 °C (accompanied by an increase in selectivity towards higher alkanes), the cobalt species are further

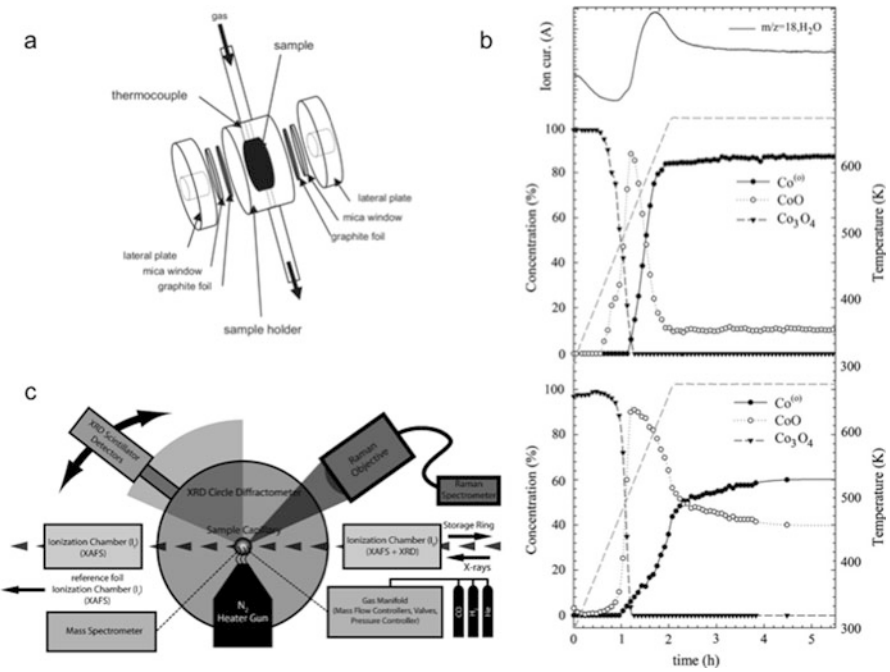

Fig. 13.3 (**a**) Schematic drawing of the in situ XAS cell to study the local order of cobalt atoms in a supported FT catalyst (Adapted from Ref. [23]). (**b**) Monitoring of cobalt phases evolving during reduction of Re-promoted (*top right*) and unpromoted Co/γ-Al_2O_3 (*bottom right*) catalysts by quantitative XANES, accompanied by MS signal of water production ($m/z = 18$) (Adapted from Ref. [26]). (**c**) Schematic representation of the combined XRD/XAS/Raman spectroscopic experimental setup with online mass spectrometry employed by de Smit et al. to investigate Fe-based catalysts during FTS (Adapted from Ref. [27])

reduced. This is associated with the increasing partial pressure of water, with a metal core-thin oxide layer-like structure thought to form. However, it is inherently difficult to interpret such structures from a mixture of "totally reduced Co nanoparticles... mixed with irreducible small CoO nanoparticles" [23].

Rochet et al. [28] in another case use a similar catalyst and the same XAS cell with the outlet attached to a Gas Chromatograph (GC), in order to measure catalytic performance simultaneously. However, the actual catalytic testing was performed prior to XAS measurements at SOLEIL and therefore does not fall under our definition of *operando*. Nonetheless, this shows the potential difficulties, (such as transport of equipment to synchrotron facilities), posed when performing *operando* experiments at synchrotron facilities.

Coupling a mass spectrometer to the outlet of the in situ cell provides another means of measuring catalytic performance simultaneously during XAS analysis. Tsakoumis et al. [26] display an excellent example of this combined XAS/high-resolution-X-ray powder diffraction (HR-XRPD) *operando* experiment, on both

1 wt% Re promoted and unpromoted 20 wt% Co/γ-Al_2O_3 for FTS (220 °C, 18 bar, $H_2/CO = 2.1$). The combination of techniques allowed information to be gathered on both short- (EXAFS) and long-range order (XRD), with the catalyst studied throughout all stages of FTS. Experiments were performed at the Swiss-Norwegian Beamlines (SNBL) at the European Synchrotron Radiation Facility (ESRF) (station BM01B), using a quartz capillary in situ cell. Its diameter of 980 μm is significantly smaller than that of the cell employed by Rochet et al. [23] (13 mm). However, results were in good agreement with those of a lab-scale fixed-bed reactor. During the activation period, XANES analysis with online mass spectrometry (MS) showed that both the unpromoted and promoted catalysts are reduced at different rates from spinel Co_3O_4 to metallic cobalt, accompanied by an increase in the amount of water produced, as evidenced by Rochet et al. [23]. During the induction period, divalent cobalt was detected in the promoted catalyst, with the unpromoted catalyst subject to further reduction. With no change in the XAS signal observed during deactivation (displayed by MS), any bulk transformations were disregarded. Therefore, a surface-related deactivation mechanism explained this phenomenon; however, it shows that the bulk nature of XAS analysis is one limitation when probing catalyst reactor beds.

Cats et al. have applied a means to overcome this limitation, using Transmission X-ray Microscopy (TXM), to gain spatial resolution (better than 30 nm in 2D) on a single working 15 wt% Co/TiO_2 FTS catalyst particle [29]. Again, this research is not strictly *operando* in our definition, as the catalytic performance data was collected (using MS) prior to the XANES analysis in the same in situ capillary cell (used at the synchrotron) with the same reaction conditions (10 bar, 250 °C, $CO:H_2 = 1:2$). The reduction to metallic Co is evident during the reduction step, with only a small contribution of oxidized Co ($CoTiO_3$ and CoO). During FTS, there was no change in chemical state of Co under these reaction conditions, even on a local scale.

As stated previously, Fe-based catalysts are also important in the FTS process and are on par with Co-based catalysts in terms of the number of *operando* XAS investigations. One of the more standout case studies is on the stability and reactivity of ε, χ, and θ iron-carbide phases during realistic FTS conditions (10 bar, 250 °C, CO/H_2: 5:5 mL/min) by de Smit et al. [27]. Using a combination of XAS/X-ray diffraction (XRD)/Raman spectroscopy, coupled with an online MS (connected to the outlet of the capillary reactor), (Fig. 13.3c) *operando* studies were performed at the SNBL, ESRF, France. It is known that a number of phases (ε-Fe_2C, ε′-$Fe_{2.2}C$, Fe_7C, χ-Fe_5C_2, and θ-Fe_3C) form during high-pressure/temperature FTS, but the exact role on the catalytic performance is unclear. Unfortunately, the small crystallite size, accompanied by the sensitive nature of the catalyst (oxidized upon exposure to air), do not allow for correct ex situ studies and therefore the application of *operando XAS* is vital. It was shown that a catalyst consisting of mainly crystalline χ-Fe_5C_2 was vulnerable to oxidation during FTS, while a separate catalyst containing θ-Fe_3C and amorphous carbide phases obtained a lower activity and selectivity. This was associated with the successive formation of carbonaceous species (studied by Raman spectroscopy) on the surface of the

catalyst. Therefore, we can now say that such amorphous phases (and the resulting textural properties of the catalyst) have a major influence on the determination of the catalyst performance.

The lack of spatial resolution in the field of *operando* XAS is one current limitation that needs to be addressed in the future. Previous to the work of Cats et al. [29] who employed in situ TXM to investigate Co-based catalysts, Gonzalez-Jimenez et al. used the same technique to investigate the reduction degree and distribution of Fe in a 20 μm Fe-based catalyst particle (mixture of $Fe_2O_3/TiO_2/ZnO/K_2O$) during realistic FTS conditions (10 bar, 350 °C, $Co/H_2 = 1$) [30]. Again, it is important to note that this is not an *operando* study in our definition, due to the off-line analysis of the catalytic performance, but is an excellent example of the possibilities available to us regarding spatial resolution (~30 nm). Initially it was observed that the fresh particle was present in a trivalent oxidized phase of Fe_2O_3 and Fe_2TiO_5. The introduction of FTS conditions first led to the reduction of Fe_2O_3 to Fe_3O_4 and then to Fe_2TiO_5 (still present up to 7 h of reaction). The Fe_2TiO_5 phase was nearly fully converted to reduced iron species (Fe_3O_4 and FeC_x) after 7 h (Fig. 13.4). Catalytic performance analysis was measured separately under similar

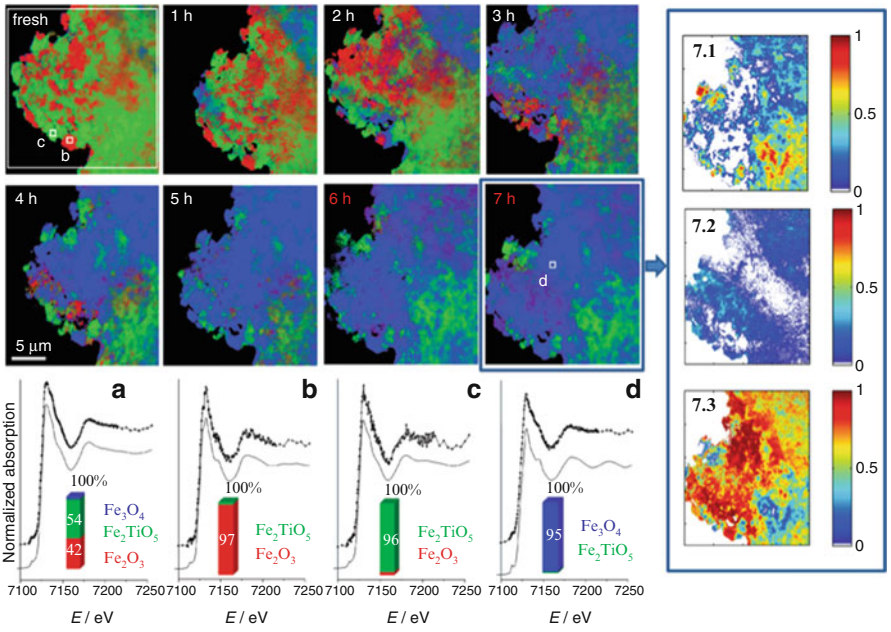

Fig. 13.4 2-D chemical maps displaying the distribution of different iron species in a 21 × 21 μm^2 particle in He and post FTS reaction (after 7 h) as a function of time on stream. Key: *green* for Fe_2TiO_5; *red* for Fe_2O_3; *blue* for Fe_3O_4 (For the maps after 6 and 7 h reaction, *red* corresponds with FeC_x). (**a**) Fe K-edge bulk XANES spectra of whole particle; (**b–d**) Fe K-edge on a 28 × 28 nm^2 single pixel of three different regions. Experimental data is indicated by (*dotted line*) and fitted data by (*dashed line*), respectively. Phase map distributions of Fe_2TiO_5 (7.1), FeC_x (7.2), and Fe_3O_4 (7.3) over the catalyst particle after 7 h on stream (Adapted from Ref. [30])

conditions and compared with TXM data. It was shown that with increasing time on stream, FeC_x crystallites enlarge or increase in number, which is linked with an increasing selectivity to methane (and decrease in selectivity to CO).

It is clear that these few *operando* studies are paving the way to a better understanding of the structure–performance relationships in FTS processes. The combination of XAS analysis with online catalytic performance allows for a better understanding of the mechanistic aspects during the reaction, which cannot be realized with model systems or under idealistic conditions (in situ/ex situ). Usually these methods provide information on catalysts that are exposed to environments other than the true working conditions, or on catalysts, which contain an unrealistic loading of active metal. Given the numerous deactivation mechanisms proposed from such studies, these recent *operando* studies help resolve these postulations. We have now obtained a relation of Co oxidation/reduction with water partial pressure produced in the reactor, together with monitoring of the Co local structure during all stages of the FTS process. Although vast improvements have been made on these initial *operando* studies, more focus is needed on the enhancement of spatial resolution (i.e., TXM), as XAS is a bulk technique and catalyst surface-gas phase information is needed to further the development of the catalytic FTS process.

13.2.2 Case Study 2: Benzyl Alcohol Oxidation

The partial oxidation of alcohols to aldehydes and ketones plays a major role in the fine chemicals industry. An example of which is the selective oxidation of benzyl alcohol to benzaldehyde, used in processes such as the production of perfumes and pharmaceuticals, to name but a few. Benzaldehyde is commonly produced using environmentally undesirable solvents, such as chlorinated hydrocarbons [31]. The use of oxidants such as O_2, H_2O_2, and *t*-butylhydroperoxide (TBHP) are now increasingly reported in the presence of solid catalysts, due to their benign impact on the environment and their cheap cost [32, 33]. Examples of catalysts commonly employed are transition metal compounds (e.g., Mo, Mg) [34, 35] or supported monometallic/bimetallic precious metal catalysts (e.g., Au, Pd) [36, 37]. Promoter metals are often added to enhance activity, product selectivity and prevent catalyst deactivation. However, the exact role of the promoter and how it affects the catalytic process is complex and still under debate [38]. Some possible explanations could be the geometric blocking or protection of the active metal center, or even alloy formation [39]. Taking Pd as an example, the aerobic oxidation of benzyl alcohol follows a two-step dehydrogenation mechanism, whereby the alkoxide is adsorbed, before β-H elimination to produce benzaldehyde. The reaction takes place on reduced Pd sites, with the role of oxygen to shift the equilibrium towards the aldehyde product (by oxidizing the co-product hydrogen) with complex side reactions [38–40]. As this reaction proceeds in the liquid-phase environment, characterization techniques are required which can study the catalyst during

realistic reaction conditions. Spectroscopic techniques are an obvious choice, particularly Attenuated Total Reflection Infrared (ATR-IR) to follow surface species evolving, due to its "enhanced selectivity towards the solid–liquid interface" [39], but also XAS to follow the oxidation state and local structure of the metals present on the catalyst. Moreover, in order to form an understanding of the structure–performance relationship of the working catalyst, *operando* investigations are vital.

One of the earliest examples of *operando* XAS analysis on supported catalysts dates back as early as 2003, with Grunwaldt et al. using a 0.5 wt% Pd/Al_2O_3 supported catalyst and "supercritical" CO_2 ($scCO_2$) as the solvent for benzyl alcohol oxidation [41]. The use of quotation marks for supercritical is because the CO_2 is present as "a dense fluid phase at temperatures exceeding its mixture critical point." In order to establish the realistic high-pressure reaction conditions required for such a reaction (150 bar, flow of 0.11 mol/min), and given the spectroscopic and safety issues at play, a specially designed in situ cell was employed. An important aspect of the cell was that its volume was drastically smaller (0.5 mL) than a conventional fixed-bed reactor (38 mL), however, results obtained with both were remarkably comparable. Whilst the sieved catalyst was held in place by two quartz wool plugs inside the compartment (attached to an oven), the outlet of the reactor was connected to a MS for simultaneous online catalytic performance analysis. QEXAFS experiments were performed in the continuous scanning mode at the Hamburger Synchrotron Labor (HASYLAB at DESY, Germany), with the aim to gain structural information of the catalyst (oxidation state of Pd) under a reducing atmosphere and during reaction conditions. The XAS time-resolved reduction of the PdO_x/Al_2O_3 catalyst by benzyl alcohol (150 bar, 80 °C, alcohol feed rate of 0.002 mol/min) showed a decrease in the white line at 24.362 eV (Fig. 13.5a) associated with palladium oxide. Following reduction, liquid CO_2 was introduced, with the temperature raised to 80 °C and benzyl alcohol and oxygen added. Almost immediately, the catalyst was slightly oxidized (displayed by a change in the near-edge structure of the Pd K-edge), most probably due to residual oxygen in the solvent. One limitation of performing XAS analysis at such high pressure is the higher degree of noise in the spectra, which could be "due to slight fluctuations in pressure induced by the compressor causing a change in density." The oxygen concentration in the feed was varied in order to observe the effect on the oxidation state of Pd during the reaction (Fig. 13.5a). By increasing the oxygen concentration in the feed, the rate of alcohol conversion went through a maximum. This was clearly due to the higher surface coverage of oxygen on Pd particles (observed in XAS spectra), favoring the oxidation reaction. However, increasing the oxygen concentration further lead to over-oxidized Pd (creating PdO_x species), producing a decrease in activity with fewer reduced Pd sites available for alcohol adsorption/oxidation (Fig. 13.5b).

The more common approach to aerobic benzyl alcohol oxidation involves a liquid phase catalytic reaction. Mondelli et al. studied a 0.75 wt% Bi promoted 5 wt % Pd/Al_2O_3 catalyst during the reaction [39]. Using a combined approach of ATR-IR and XAS analysis, coupled to a Fourier Transform Infrared (FT-IR)

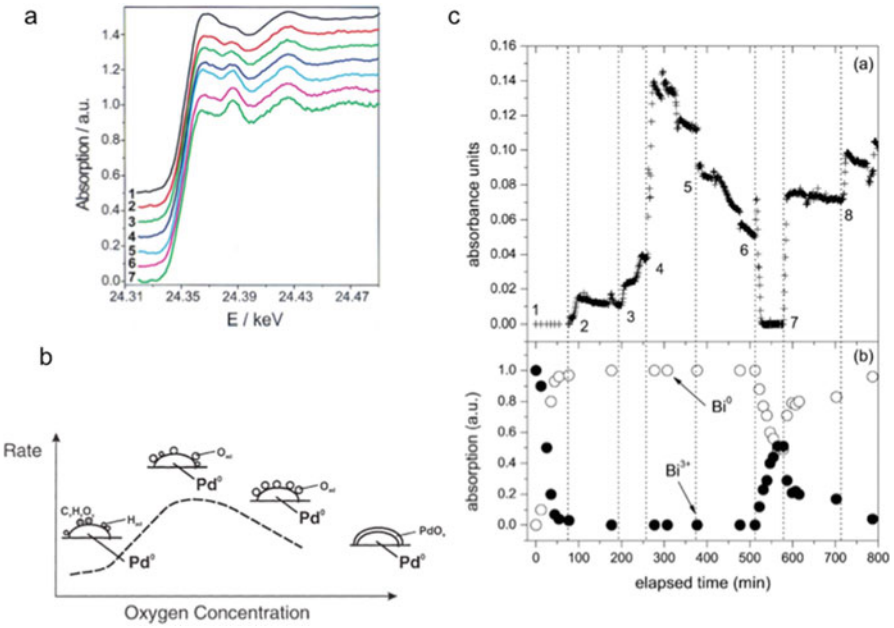

Fig. 13.5 (**a**) Time-resolved X-ray absorption spectra of PdO_x/Al_2O_3 during reduction by benzyl alcohol (150 bar, 80 °C, alcohol feed rate 0.002 mol/min, 0.3 g catalyst): (*1*) fresh catalyst in $scCO_2$ without benzyl alcohol; (*2*) alcohol introduced in $scCO_2$; (*3*) after 6 min; (*4*) 12 min; (*5*) 24 min, 100 °C; (*6*) 30 min, 100 °C; (*7*) 48 min, 100 °C (Adapted from Ref. [41]). (**b**) A simplified model of the structure–activity relationships formed during Pd/Al_2O_3 catalytic oxidation of benzyl alcohol in $scCO_2$ (Adapted from Ref. [41]). (**c**) Combining XANES and online FT-IR to form structure–performance relationships of Pd-Bi/Al_2O_3 during benzyl alcohol oxidation (*a*) Time-resolved intensity of the 1713 cm^{-1} band (benzaldehyde) and (*b*) change in the oxidation state of Bi, recorded at the Bi L_3-edge. Conditions: cyclohexane solvent, $C_{alcohol} = 0.02$ M, 50 °C. Changes in experimental conditions: "(*1*) before H_2-saturated cyclohexane; (*2*) before benzyl alcohol in Ar-saturated cyclohexane; (*3*) before benzyl alcohol in air-saturated cyclohexane; (*4*) before benzyl alcohol in O_2-saturated cyclohexane; (*5*) temperature lowered to 30 °C; (*6*) before O_2-saturated cyclohexane; (*7*) before benzyl alcohol in O_2-saturated cyclohexane at 50 °C; (*8*) before increasing temperature to 60 °C." (Adapted from Ref. [39])

spectrometer , *operando* studies allow the simultaneous relation between the surface species evolved, the metals oxidation state and the catalytic performance. The core of the setup is based around the interchangeable cells used for ATR-IR and XAS measurements (analogous conditions). However, stringent comparison of data obtained by both techniques is only meaningful to a limited extent due to the different cell designs, which can affect mass transport properties. A continuous flow cell reactor (0.12 mL volume) was employed at ANKA Synchrotron Laboratory (Forschungszentrum, Karlsruhe, Germany) for studying the Bi L_3-edge and also at HASYLAB, DESY (Beamline X1, Hamburg, Germany) for investigation of the Pd K-edge. The amount of benzaldehyde in the effluent of the in situ cell was calibrated using the Beer–Lambert law and solutions of known concentrations.

When dehydrogenation conditions were employed (Ar atmosphere), low activity was observed for both Bi-promoted and unpromoted catalysts, with both metals in a reduced state. ATR-IR showed a significantly higher amount of CO was present on the surface of the unpromoted catalyst in contrast to the promoted catalyst. It appears that Bi prevents side reactions, in particular, the decarbonylation and further oxidation of benzaldehyde. Although a large increase in activity was observed immediately after aerobic conditions were introduced, the Pd and Bi oxidation states remained stable (EXAFS) for the Bi-Pd/Al_2O_3 catalysts (Fig. 13.5c). The suggested "geometric blocking of Pd by Bi" as well as Bi controlling the oxygen supply to the active metallic center, appears to inhibit Pd-reoxidation, maintaining high catalytic activity and selectivity.

These studies show that *operando* XAS can be used even under the harshest of reaction conditions in "supercritical" and liquid-phase processes. One of the main reasons that *operando* conditions can be applied for this process is the cell design, which unlike previous in situ experiments, allows the capture of surface species formed (using spectroscopic techniques) leading to catalytic performance evaluation, with simultaneous structural/oxidation state analysis. As stated previously, these structure–performance relationships are vital, with an understanding of the role of the promoter in the complex reaction mechanisms potentially leading to better process efficiency, due to enhanced catalyst development. Previously obtained knowledge on the liquid-phase oxidation of alcohols mainly focused on the use of spectro-electrochemical methods, with model catalysts and electrolytic solutions [42–44]. However, these *operando* XAS case studies finally provide a means to observe the link between species evolving on the catalyst surface and the role of the promoter, which can lead to better catalyst design.

13.2.3 Case Study 3: Propane Dehydrogenation

The significant interest in the catalytic dehydrogenation of light alkanes, in particular propane, is due to the high demand for propene (also commonly referred to as propylene), as an important intermediate for a range of chemical applications, i.e., polypropylene production [45]. Supported Cr-based catalysts are typically used in the industrial process, with alternatives such as Pt and Mo also offering high activity [46–48]. Conventionally, propane dehydrogenation runs under cyclic operation, with successive reaction and regeneration steps (at around 500–650 °C, atmospheric pressure). However, a major problem is associated with fast catalyst deactivation, known to occur via coking or cracking, influencing both stability and selectivity, respectively [49]. This therefore ensures a large expense for the operator, but also a diminishing selectivity towards propene each regeneration cycle. To tackle this problem, a better understanding of how the catalyst operates and deactivates under realistic reaction conditions (many cycles) is needed, with many reports only focusing on characterization of the catalyst before and after one cycle. In particular, it is vital to obtain a correlation between the oxidation state/

local structure of the active metal with catalytic performance (i.e., the decline in propene selectivity). In situ XAS provides an excellent means to obtain this information, but given that coke formation is one of the main contributors to catalyst deactivation, other spectroscopic techniques are also required in order to observe its extent. Therefore, the need for a combination of several techniques at once under realistic reaction conditions to study the complex reaction mechanism, whilst simultaneously obtaining online catalytic performance, poses a real challenge. Here we briefly discuss how this is achieved, with up to three simultaneous characterization techniques in an *operando* setup.

In order to develop an understanding of the catalyst behavior during dehydrogenation and regeneration during typical propane dehydrogenation conditions, Beale et al. proposed a unique combination of ultraviolet–visible (UV–Vis)/Raman/XAS in one setup [50]. Performed a decade ago, this was the first reported use of more than two spectroscopic techniques simultaneously to study heterogeneous catalysts at work. Using either a 13 wt% Mo–Al_2O_3 or –SiO_2 supported catalyst, the aim was to discover the active site and deactivation mechanisms which take place during successive propane dehydrogenation cycles at 550 °C. Figure 13.6 depicts the setup in a simplistic manner, with the focal point based around the specially designed quartz reactor tube (6 mm o.d. and 1 mm i.d.) "ground down on three sides to approximately 200 μm to ensure sufficient X-ray transmission" [50]. Energy dispersive (ED)-EXAFS allows the collection of the whole X-ray absorption spectrum during fast processes (using a poly-chromator crystal) and was applied in transmission mode, with UV–Vis and Raman spectra obtained with detectors placed orthogonal to the X-ray beam, and opposite to each other. Experiments were performed on beamline ID24 at the ESRF (Grenoble, France) with an

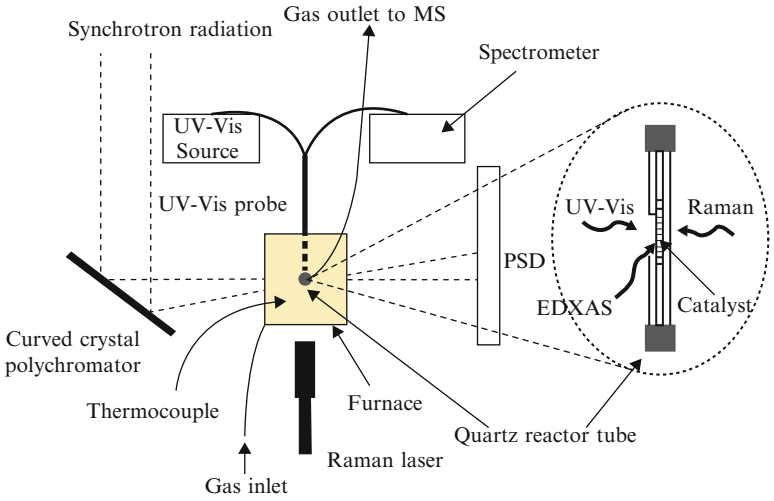

Fig. 13.6 Schematic of the combined all-in-one *operando* UV–Vis/Raman/ED-XAFS/MS setup used to study the active sites and deactivation mechanism of SiO_2- and Al_2O_3-supported MoO_x catalysts during propane dehydrogenation–regeneration cycles (Adapted from Ref. [50])

ED-XAFS spot size of 300 μm and the reactor outlet connected to a MS for online catalytic performance analysis. Taking the first propane dehydrogenation cycle (PD1) using Mo/SiO_2 as an example, the combination of UV–Vis (band at 350 nm), Raman (Mo species on the surface) and ED-EXAFS (1s-4d pre-edge feature at 20,002 eV), Beale et al. were able to determine that "Mo^{6+} species were present as a mixture of distorted tetrahedral and octahedral environments." These features soon decreased during the subsequent PD step. This was accompanied with a darkening of the catalyst evidenced by UV–Vis (overall decrease in the diffuse reflectance), suggesting coke formation. A decrease in the pre-edge peak intensity and a corresponding increase in the 1s-5p transition (20,022 eV), were consistent with some reduction of Mo^{6+} to Mo^{4+}. As this was an *operando* study, these features were linked with online catalytic activity, whereby a decline in propene production confirmed the initial deactivation of the catalyst. Upon regeneration (5 % O_2/He), the changes witnessed were reversed to some extent, but with an increase in the size of the MoO_3 clusters (combined with CO_2 formation due to coke burning or propane combustion), noted to lead to irreversible catalyst deactivation in subsequent cycles. In comparison with Mo/Al_2O_3, the initial coke formation occurred at a higher rate than in Mo/SiO_2. Finally, the dispersed MoO_3 species present on the surface Mo/Al_2O_3 were found to be harder to reduce than the MoO_3 clusters on Mo/SiO_2.

Almost 5 years later, Iglesias-Juez et al. used a combination of UV–Vis/Raman together with *operando* high-energy resolution fluorescence detected (HERFD) XANES measurements, in order to observe the effect multiple reaction-regeneration cycles have on catalytic behavior [51]. HERFD-XANES offers an enhanced signal-to-noise ratio, by tuning the emitted energy to a fluorescence line and recording the intensity variation of the fluorescence line as a function of the incident energy. In particular, they sought to understand the "structural and electronic properties of supported Pt and Pt-Sn nanoparticles" of both supported Pt/Al_2O_3 and promoted $Sn\text{-}Pt/Al_2O_3$ catalysts. As the UV–Vis/Raman measurements were recorded separately from the XAS data, we will focus mainly on the latter, together with its online monitoring of catalytic performance using a MS. Beamline ID26 at the ESRF was used in combination with an in situ cell (max. temperature of 1000 °C) provided by the Sample Environment Support Service (SESS) of the ESRF. Each cycle consisted of a reduction at 600 °C (20 % H_2/He) and a subsequent propane dehydrogenation step (10 % C_3H_8/He, 600 °C), followed by regeneration (O_2) and re-reduction (H_2). A total of ten cycles were investigated. In terms of catalytic activity, the Sn promoted Pt/Al_2O_3 catalyst achieved a higher propene turnover and higher stability. This was discovered to be associated with the formation of an Sn-Pt alloy, which "modifies the Pt electronic properties leading to more electron-poor, active particles" [51]. The lower propane conversion obtained by the Pt/Al_2O_3 catalyst was due to the stronger interaction of propane with Pt, revealed by the Pt L_3 μXANES data (changes in the white line intensity and shift of the edge position, after pre-edge background removal). This was also used to explain the higher coke formation on the catalyst, with blocking of potential active sites (with species such as doubly bonded propyl molecules). For the Pt/Al_2O_3 catalyst, no noticeable changes were observed in the HERFD-XANES spectra (Fig. 13.7a) during the first reaction. The following O_2

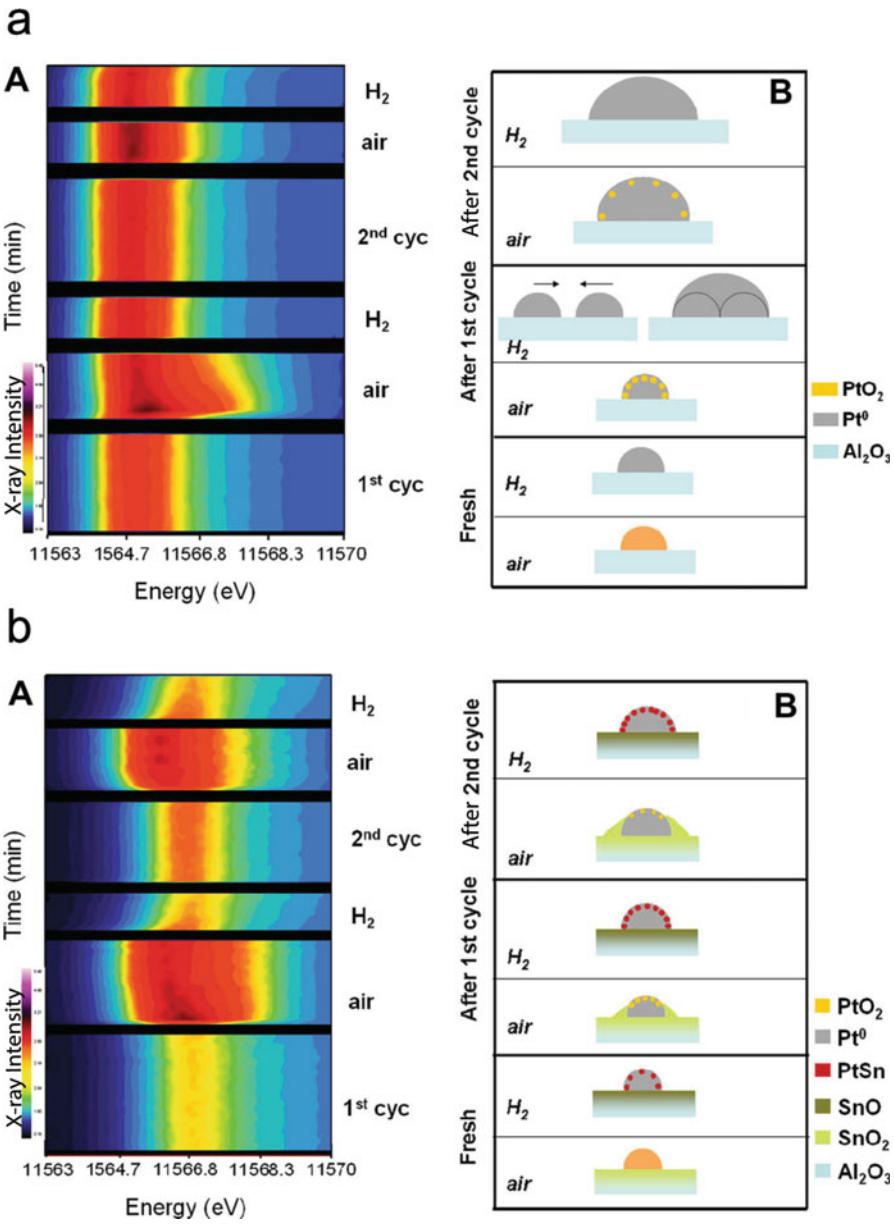

Fig. 13.7 (**a** and **b**) correspond to catalysts Pt/Al_2O_3 and $Sn\text{-}Pt/Al_2O_3$, respectively, with (*A*) the intensity contour map of *operando* HERFD XANES spectra acquired during the first two propane dehydrogenation–regeneration cycles and (*B*) the corresponding schematic model of the metal species present during the different treatment steps (Adapted from Ref. [51])

treatment removed the coke and partially reoxidized Pt on the surface. These were fully reduced to metallic Pt upon further reduction in H_2, however, a more intense white line suggested the sintering of Pt nanoparticles. Successive reaction-regeneration cycles were found to result in bigger Pt nanoparticles (confirmed by EXAFS). This growth occurred to a lesser extent on the Sn promoted Pt/Al_2O_3 catalyst with the Sn thought to prevent the sintering process (Fig. 13.7b). However, it was also noticeable that Sn enrichment of the alloy occurs over multiple cycles, leading to a diminishing dehydrogenation activity overall.

Given the nature of the propane dehydrogenation reaction, whereby varying cycles are required to remove coke and reactivate the catalyst, an *operando* study is vital to securing information on the behavior of the catalyst under true conditions, which can aid in process efficiency, i.e., by adjusting the length time of each cycle. Concerning the case studies discussed here, we now have an understanding of how coking is linked with the promoting metal and active metal oxidation state (i.e., Mo) and subsequently the catalytic activity. Furthermore, by maintaining the *operando* method upon regeneration cycles, we now know that the local structure of the active metal varies and also affects the catalytic activity in sequential propane dehydrogenation steps. Not only does the combination of three techniques in one *operando* XAS setup emphasize the range of possibilities in this system, but it also provides a means to study similar catalytic systems.

13.2.4 Case Study 4: Related Materials

13.2.4.1 Batteries

Cells, which use chemical transformations as the basis for electrochemical energy storage, are of great interest currently in the rechargeable battery market. Of particular importance is the Li-S battery, which offers up to five times higher energy density than Li-ion batteries. Li-S batteries operate on the basis of lithium dissolution at the anode forming polysulfide salt species (i.e., Li_2S, Li_2S_2, and Li_2S_3) during discharge and plating out on charging [52, 53]. However, their poor capacity retention, due to incomplete electrochemical redox, is a major drawback of Li-S batteries. Understanding the nature of polysulfide species formed and their role on affecting the cell capacity is paramount to the further development of Li-S batteries and can only be achieved using real-time *operando* conditions. XAS offers a powerful spatiotemporal method of studying charge transfer and structural features, both of which are key in electrochemical cycling of electrode materials. Cuisinier et al. [54] report the use of a cathode consisting of "sulfur impregnated in porous hollow-carbon spheres paired with a non-sulfurous electrolyte incorporated in a cell designed to prevent dead zones." Experiments were performed at sector 9-BM-B at the Advanced Photon Source (Argonne National Laboratory, USA) in fluorescence mode. Using *operando* XANES at the S K-edge, the mechanisms of sulfur redox chemistry during cycling (charge/discharge) were probed. During the

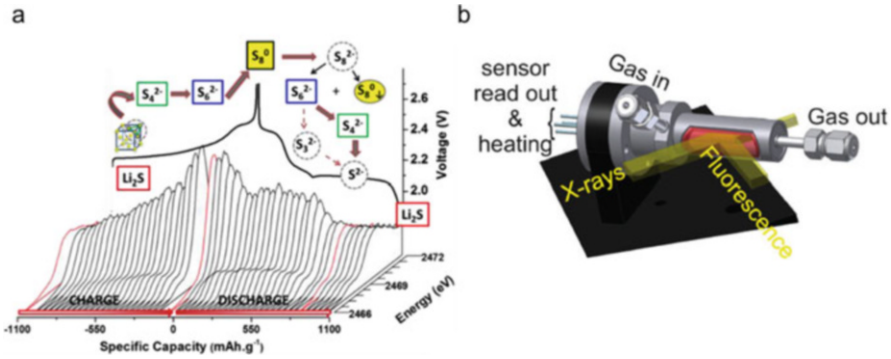

Fig. 13.8 (**a**) Evolution of X-ray absorption as a function of electrochemical charge and discharge cycling (V), linking the specific capacity of the cell with the Li and S species formed in an *operando* XAS setup (Adapted from Ref. [54]). (**b**) Schematic of fluorescence XAS cell used to monitor the change of the sensors' resistance during exposure to reducing gases as high temperatures (Adapted from Ref. [55])

charge cycle, S_6^{2-} is produced at the expense of S_4^{2-}, propagating "the oxidation of Li_2S into more stable Li_2S_6"(Fig. 13.8a). This coincided with a voltage rise and the final oxidation of S_6^{2-} to α-S_8. A noticeable feature of this *operando* charge cycle is the significant rise in the white line of the S K-edge spectra, accompanied with a disappearance of the low-energy peak associated with the complete conversion of the cathode to sulfur. The discharge cycle leads to many sequential steps (Fig. 13.8a), with the first plateau attributed to disproportionation of S_8^{2-}. In the second step, elemental sulfur is converted to poly-sulfides (i.e., S_4^{6-}). The final reduction step corresponds with a sudden increase in Li_2S formation, with the total conversion of poly-sulfides resulting in a voltage drop (preventing reduction of remaining sulfur).

It is clear that *operando* XAS is an excellent method to study and relate what actually happens inside the electrochemical cell and how it performs. Given the varying species formed during each charge and discharge cycle, XAS is one of the best techniques available to observe their oxidation state and local structure. Cell design is of course vital in this case, because in order to obtain true performance analysis, the cell must be as close as possible to a real working system, whilst allowing the simultaneous penetration of X-rays. These results briefly described here, now show the in depth mechanisms of sulfur redox chemistry during cycling, and how these affect the batteries' capacity. Not only can these results be used to enhance the efficiency of Li-S batteries, but *operando* XAS can be applied to understand and draw links with similar systems, such as cobalt-based batteries.

13.2.4.2 Sensors

Gas sensors applied to reducing gases are traditionally based on porous SnO_2, with noble metals such as Au, Pd, and Pt added to enhance the sensitivity/stability and decrease the operation temperature [56–59]. However, the role of the additive in

lowering the operation temperature for instance is not well understood. Theories such as "spill-over" ("enriching surface of support with reactive species") or "Fermi-level control" ("change in stoichiometry/chemical state of the noble metal/metal oxide") mechanisms are put forward, assuming the additive is in its metallic or oxidized form at the surface of the porous matrix [55]. A major flaw in these postulations is that nearly all studies are performed on "model" samples (higher weight loading of additive than realistically used) and in "idealized" conditions (realistic conditions are: 30–200 ppm H_2; 10–50 ppm CO/air, 200 or 300 °C). *Operando* XAS with simultaneous monitoring of the sensor response (by DC resistance measurements), offers a valuable method to explore the structure and oxidation state of the noble metal additive. Although the porous SnO_2 matrix is heavily absorbing, and the content of the metal in question is extremely low, Koziej et al. presented the use of a specially designed in situ cell (Fig. 13.8b) at ID26 beamline, ESRF [55]. The sensitive layer inside the cell is 50 μm thick, 3.5 mm wide and 7 mm long, with a Pt heater contributing to controlled temperatures of 50–400 °C. Samples containing 0.2 wt% (realistic), 2 and 3 wt% (model) Pd-SnO_2 powders were employed under the following conditions: "30–125 ppm H_2 in dry and humid air; 10–50 ppm CO in air; 1000 ppm H_2 in He and 50 ppm O_2" [55]. Both XANES and EXAFS indicated the presence of fully oxidized Pd in an atomic distribution included in the SnO_2 lattice in the 0.2 wt% Pd-SnO_2 powder, with palladium oxide particles present in the 2 wt% Pd-SnO_2 sample. During exposure to CO and H_2, high sensor readings were recorded for 0.2 wt% Pd-SnO_2, with no change in the Pd oxidation state. However, slightly reduced Pd-particles were found to form in the 3 wt% Pd-SnO_2 sensor. These results ruled the previous "spill-over" and "Fermi-level" mechanisms invalid, as these are based on metallic or oxidized Pd at the surface of SnO_2, with the role of Pd more likely to be due to binding to the surface lattice oxygen, "providing sites for oxygen adsorption" and "reaction with reducing gases mostly taking place on the surface of SnO_2" [55].

Given that previous studies were focused on samples under idealistic conditions and/or on model catalysts, the information provided by *operando* XAS here is evidently valuable to enhancing our understanding of the mechanistic aspects of gas sensors. We are now able to observe the oxidation state of the noble metal as well as the metal oxide during true sensing conditions. Understanding the gas sensing mechanism has important advantages in the development of future sensing materials.

13.2.4.3 Fuel Cells

Fuel cells in the form of proton-exchange-membranes (PEMs) are widely thought as replacements to current environmentally damaging automobile systems [60–62]. However, at the moment, they are not realizing their potential due to their inadequate durability. Traditional PEMs consist of a membrane electrode assembly (MEA) which has a "stacked structure consisting of an anode catalyst layer, a proton-conducting membrane electrolyte, and a cathode catalyst layer" [63]. Here

protons and electrons are formed from the conversion of hydrogen on a metal catalyst at the anode catalyst surface. Each proton moves via the proton-conducting membrane to the surface of the cathode catalyst. Protons and molecular oxygen react to produce water on a supported Pt-based catalyst. A major drawback of such a system however is in the dissolution (deactivation) of Pt under realistic operating conditions. This occurs during "power-on-off" processes (voltage change of 1.0–0.4 V), forming rapid (few seconds) electrochemical reactions on the electrode surfaces. Therefore, a thorough investigation into the chemistry at the electrode surface, during real operation conditions (sequential voltage changes), is needed to improve their durability. Combining XAS with an online potentiostat, structure–performance relationships can be obtained on a MEA fuel cell under real operating conditions. Tada et al. measured such a system at the BL01 station at Spring-8 (JASRI) on a Pt/C cathode catalyst and Pt-free Pd/C anode catalyst stacked between two current collectors [64]. In order to record information of such rapid changes in voltage, a novel Time-Gating Quick XAFS (TG-QXAFS) technique was employed (1 s time resolution), with typical XAFS being too slow (15 s due to rotation of the monochromator). In other words, QXAFS measured over a 15 s period are recorded, divided into 15 parts of 1 s intervals, and combined into one interval. During the Pt reduction (voltage stepping: 1.0 to >0.4 V) and oxidation (0.4 to >1.0 V) processes under a N_2 atmosphere, it was discovered that a "hysteresis loop for the structural changes in the Pt cathode particles" exist (Fig. 13.9) [64]. During oxidation of Pt, Pt–OH covalent bonds form on the surface of the Pt particles, due to several electron transfer processes, which each have significant time lags between one another. The reduction process also experienced a similar time lag, but with a different reaction mechanism involving two intermediate phases (Pt–O dissociation and coordinated OH ions accumulation of electric charge of the Pt particles). Finally, increasing the voltage to 1.4 V and performing repeated voltage-stepping, did not lead to Pt ions dissolving in the electrolyte under a N_2 atmosphere. However, in air, Pt–Pt bonds immediately break and dissolution of Pt ions gradually occurs when electric potential accumulates on the electrode surface.

In 2012, the group of Tada et al. made another breakthrough in the field of *operando* XAS on MEA-based polymer electrolyte fuel cells (PEFCs) [63]. Using similar operation conditions to their previous work (voltage cycling of 0.4–1.0 V) [64], Ishiguro et al. employed a Pt_3Co/C cathode catalyst to observe the structural kinetics of surface events taking place [63]. *Operando* time-resolved QXAFS at the Pt L_{III}-edge and Co K-edge were analyzed at 500 ms intervals, revealing "ten rate constants of the dynamic surface events," which were significantly higher for the Pt_3Co/C catalyst compared to those of the Pt/C catalyst, providing an enhanced fuel-cell performance and durability. This was associated with a greater increase in the rate constants attributed to "reduction processes of Pt-O bond breaking, Pt-Pt bond reformation, and change in the charge density of Pt," with the addition of Co to Pt.

The determination of the origin of surface adsorbates and even their coverage during the operation of a fuel cell has provided new insights into the kinetic and mechanistic aspects during working conditions. Using an *operando* XAS technique,

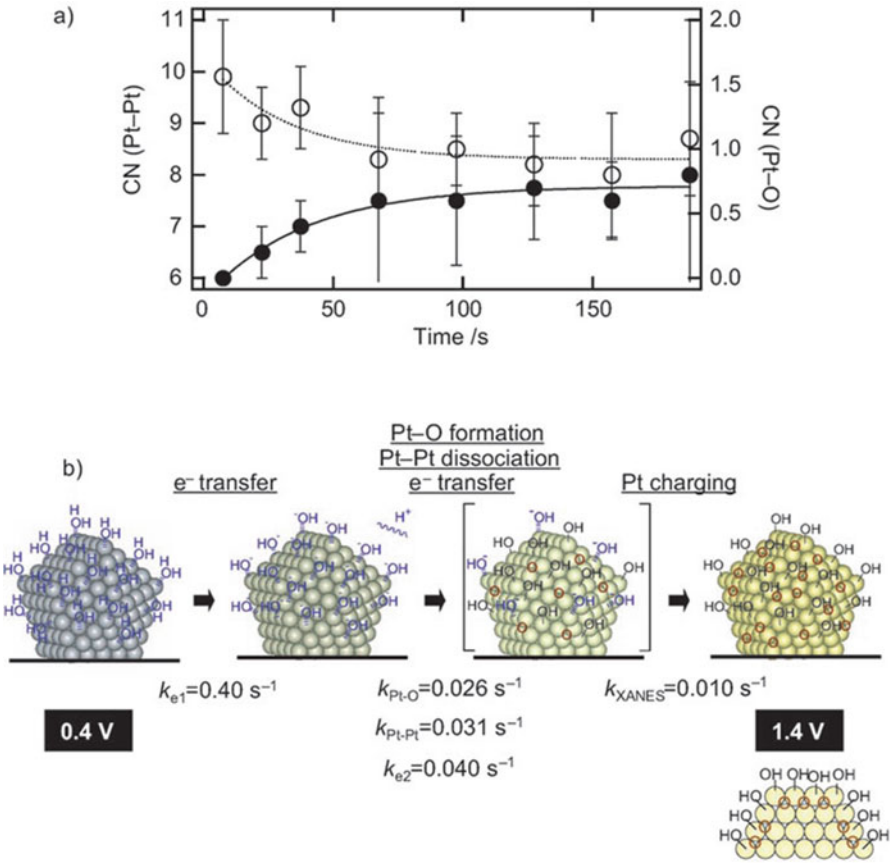

Fig. 13.9 (**a**) "Coordination numbers of the Pt–Pt (*empty circles*) and Pt–O (*filled circles*) bonds measured every 15 s by the usual QXAFS for the oxidation process jumping from 0.4 to 1.4 V. (**b**) The structural model of the Pt nanoparticles suggested by in situ time resolved QXAFS. Anode: H_2; cathode:N_2, 333 K (Adapted from Ref. [64])

we are able to observe the detailed change in particle structure/coordination with simultaneous monitoring of the cells performance during voltage-cycling. Due to the rapid nature of the chemical reactions taking place, faster acquisition of XAS is required in order to observe those short-lived intermediate adsorbate species. The work of Tada et al. provides a new insight into these species, using TG-QEXAFS [64]. This advanced technique is only the beginning of understanding the fast kinetic mechanisms taking place in operating fuel cells, with more spatial information needed in the future, to understand where and how such intermediate adsorbate species are distributed.

13.3 Conclusions and Future Perspectives

The significant interest in *operando* XAS studies since the start of the twenty first century, together with the continuing development of proper spectroscopic-reaction cells and advancements in synchrotron facilities able to perform such experiments, has paved the way to enhancing our understanding of important reaction systems. Under our definition of *operando* XAS, whereby the simultaneous online analysis of performance is coupled with chemical/physical information obtained using XAS, we have provided a glance at several current systems available in the field of heterogeneous catalysis, as well as in batteries, sensors, and fuel cells (Fig. 13.2), and how they are furthering our knowledge in these important areas of research.

Given the topic of heterogeneous catalysis as an example, ex situ and in situ XAS studies do not provide sufficient detailed insight into the molecular-level structure–activity (performance) relationships during true working conditions. This is due to a number of factors, but is mainly due to the absence of the relevant reaction environment that the catalyst actually operates under, when in a real reactor. *Operando* XAS provides a means to form such experiments and conclusions, but is considered highly complex, due to the multiple time and/or length scales that have to be monitored.

The case studies we describe in this chapter show that such obstacles can be overcome to a large extent, and provide new information that is furthering our understanding of how these functional materials operate, which can lead to better process efficiency for example. Although online analysis of the performance is necessary for *operando* XAS experiments, it is clear that a combination of multiple techniques (not only XAS), such as UV–Vis, Raman and FT-IR spectroscopy are also required to form the complete picture of the chemical and physical processes taking place. One of the focal points of each case study in this chapter (in terms of obtaining such *operando* XAS systems) is in the design of the spectroscopic-reaction cell. Depending on the true reaction conditions required, together with the information desired, the reactor cell plays a pivotal role in allowing for instance harsh reaction conditions (i.e., high pressure/temperature) accompanied by X-ray and spectroscopic working parameters.

The crucial information obtained in each case study points towards the vast advantage *operando* XAS has over ex situ and in situ studies. However, we are still only at the beginning of our development of *operando* XAS systems. Further enhancements in obtaining spatiotemporal information is desperately required in order to gather greater insight into intermediate species formed on for example the catalyst surface during operating conditions. The studies of Gonzalez-Jimenez et al. [30], Cats et al. [29], and Tada et al. [64] already give us a glimpse of the possibilities available in improving space and time scales, respectively. The use of techniques such as X-ray microscopy and Time-Gating Quick XAFS (TG-QXAFS) can provide remarkable information on the scale of ~30 nm and 1 s time-resolution, respectively.

These recent developments in collecting spatiotemporal spectroscopic information are also game changing in terms of data analysis methods. While traditional XAS evaluation methods focused on the detailed analysis of individual absorption spectra, such an approach becomes unfeasible in the case of, for example, spectroscopic TXM data consisting of several millions of XANES. Therefore, future evaluation procedures in both *operando* and in situ spectroscopy will, even more than today, have to include advanced statistical evaluation methods like multivariate analysis of the whole, multidimensional data matrix. While multivariate analysis is an established, versatile tool for the analysis of spectroscopic data collected with a single technique, it holds the promise of applying it to multi-technique data, i.e., evaluating simultaneously recorded spectroscopic data as one hyperdimensional data set. This approach would complete *operando* spectroscopy in the true sense of the definition given in the introduction—from data collection to data evaluation—and provide an unbiased basis for interpreting correlations between the many, varying parameters of interest in an *operando* experiment.

Therefore, the continued development of reactor cell design, enhanced data-analysis, coupled with the development of advanced techniques to improve spatiotemporal resolution, is vital in order to form an arsenal to apply *operando* XAS on a wider scale to more interesting and complex systems.

References

1. Weckhuysen BM (2003) Determining the active site in a catalytic process: *operando* spectroscopy is more than a buzzword. Phys Chem Chem Phys 5:4351–4360
2. Bañares MA (2005) *Operando* methodology: combination of in situ spectroscopy and simultaneous activity measurements under catalytic reaction conditions. Catal Today 100:71–77
3. Mesu JG, Beale AM, de Groot FMF, Weckhuysen BM (2006) Probing the influence of X-rays on aqueous copper solutions using time-resolved in situ combined video/X-ray absorption near-edge/ultraviolet-visible spectroscopy. J Phys Chem B 110:17671–17677
4. Weckhuysen BM (2002) Snapshots of a working catalyst: possibilities and limitations of in situ spectroscopy in the field of heterogeneous catalysis. Chem Commun 97–110
5. Bañares MA, Guerrero-Pérez MO, Fierro JLG, Cortez GG (2002) Raman spectroscopy during catalytic operations with on-line activity measurement (*operando* spectroscopy): a method for understanding the active centres of cations supported on porous. J Mater Chem 12:3337–3342
6. Weckhuysen BM (2009) Chemical imaging of spatial heterogeneities in catalytic solids at different length and time scales. Angew Chem Int Ed 48:4910–4943
7. Buurmans ILC, Weckhuysen BM (2012) Heterogeneities of individual catalyst particles in space and time as monitored by spectroscopy. Nat Chem 4:873–886
8. Beale AM, Jacques SDM, Weckhuysen BM (2010) Chemical imaging of catalytic solids with synchrotron radiation. Chem Soc Rev 39:4656–4672
9. Grunwaldt J-D, Schroer CG (2010) Hard and soft X-ray microscopy and tomography in catalysis: bridging the different time and length scales. Chem Soc Rev 39:4741–4753
10. Singh J, Lamberti C, van Bokhoven JA (2010) Advanced X-ray absorption and emission spectroscopy: in situ catalytic studies. Chem Soc Rev 39:4754–4766
11. Newton MA, van Beek W (2010) Combining synchrotron-based X-ray techniques with vibrational spectroscopies for the in situ study of heterogeneous catalysts: a view from a bridge. Chem Soc Rev 39:4845–4863

12. Bordiga S, Groppo E, Agostini G, van Bokhoven JA, Lamberti C (2013) Reactivity of surface species in heterogeneous catalysts probed by in situ X-ray absorption techniques. Chem Rev 113:1736–1850
13. Andrews JC, Weckhuysen BM (2013) Hard X-ray spectroscopic nano-imaging of hierarchical functional materials at work. Chemphyschem 14:3655–3666
14. Davis BH, Occelli ML (eds) (2007) Fischer-tropsch synthesis, catalysts and catalysis, Studies in Surface Science and Catalysis, 163, Elsevier, Oxford
15. Remans TJ, Jenzer G, Hoek A (2008) Gas-to-Liquids. In: Ertl G, Knozinger H, Schuth F, Weitkamp J (eds) Handbook of heterogeneous catalysis. Wiley, Weinheim
16. Moodley DJ, van de Loosdrecht J, Saib AM, Overett MJ, Datye AK, Niemantsverdriet JW (2009) Carbon deposition as a deactivation mechanism of cobalt-based Fischer–Tropsch synthesis catalysts under realistic conditions. Appl Catal A Gen 354:102–110
17. Sirijaruphan A, Horváth A, Goodwin JG Jr, Oukaci R (2003) Cobalt aluminate formation in alumina-supported cobalt catalysts: effects of cobalt reduction state and water vapor. Catal Lett 91:89–94
18. Bertole C, Mims CA, Kiss G (2002) The effect of water on the cobalt-catalyzed Fischer–Tropsch synthesis. J Catal 210:84–96
19. Jacobs G, Das TK, Zhang Y, Li J, Racoillet G, Davis BH (2002) Fischer–Tropsch synthesis: support, loading, and promoter effects on the reducibility of cobalt catalysts. Appl Catal A Gen 233:263–281
20. Tavasoli A, Abbaslou RMM, Trepanier M, Dalai AK (2008) Fischer–Tropsch synthesis over cobalt catalyst supported on carbon nanotubes in a slurry reactor. Appl Catal A Gen 345:134–142
21. Tsakoumis NE, Rønning M, Borg Ø, Rytter E, Holmen A (2010) Deactivation of cobalt based Fischer–Tropsch catalysts: a review. Catal Today 154:162–182
22. Saib AM, Moodley DJ, Ciobîcă IM, Hauman MM, Sigwebela BH, Weststrate CJ, Niemantsverdriet JW, van de Loosdrecht J (2010) Fundamental understanding of deactivation and regeneration of cobalt Fischer–Tropsch synthesis catalysts. Catal Today 154:271–282
23. Rochet A, Moizan V, Diehl F, Pichon C, Briois V (2013) Quick-XAS and Raman operando characterisation of a cobalt alumina-supported catalyst under realistic Fischer–Tropsch reaction conditions. Catal Today 205:94–100
24. Kawai T, Chun W-J, Asakura K, Koike Y, Nomura M, Bando KK, Oyama ST, Sumiya H (2008) Design of a high-temperature and high-pressure liquid flow cell for x-ray absorption fine structure measurements under catalytic reaction conditions. Rev Sci Instrum 79:014101
25. Rochet A, Moizan V, Briois V, Pichon C (2011) Design of a high-pressure and high-temperature cell for operando X-ray absorption spectroscopy in heterogeneous catalysis. Diam Light Source Proc 1:e130
26. Tsakoumis NE, Voronov A, Rønning M, van Beek W, Borg Ø, Rytter E, Holmen A (2012) Fischer–Tropsch synthesis: an XAS/XRPD combined in situ study from catalyst activation to deactivation. J Catal 291:138–148
27. De Smit E, Cinquini F, Beale AM, Safonova OV, van Beek W, Sautet P, Weckhuysen BM (2010) Stability and reactivity of $\epsilon - \chi - \theta$ iron carbide catalyst phases in Fischer – Tropsch synthesis: controlling μ C. J Am Chem Soc 132:14928–14941
28. Rochet A, Moizan V, Pichon C, Diehl F, Berliet A, Briois V (2011) *In situ* and *operando* structural characterisation of a Fischer–Tropsch supported cobalt catalyst. Catal Today 171:186–191
29. Cats KH, Gonzalez-Jimenez ID, Liu Y, Nelson J, van Campen D, Meirer F, van der Eerden AMJ, de Groot FMF, Andrews JC, Weckhuysen BM (2013) X-ray nanoscopy of cobalt Fischer-Tropsch catalysts at work. Chem Commun 49:4622–4624
30. Gonzalez-Jimenez ID, Cats K, Davidian T, Ruitenbeek M, Meirer F, Liu Y, Nelson J, Andrews JC, Pianetta P, de Groot FMF, Weckhuysen BM (2012) Hard X-ray nanotomography of catalytic solids at work. Angew Chem Int Ed 51:11986–11990

31. Choudhary VR, Dumbre DK, Bhargava SK (2009) Oxidation of benzyl alcohol to benzaldehyde by tert -butyl hydroperoxide over nanogold supported on TiO_2 and other transition and rare-earth metal oxides. Ind Eng Chem Res 48:9471–9478
32. Liotta L, Venezia A, Deganello G, Longo A, Martorana A, Schay Z, Guczi L (2001) Liquid phase selective oxidation of benzyl alcohol over Pd–Ag catalysts supported on pumice. Catal Today 66:271–276
33. Schultz MJ, Park CC, Sigman MS (2002) A convenient palladium-catalyzed aerobic oxidation of alcohols at room temperature. Chem Commun 24:3034–3035
34. Ming-Lin G, Hui-Zhen L (2007) Selective oxidation of benzyl alcohol to benzaldehyde with hydrogen peroxide over tetra-alkylpyridinium octamolybdate catalysts. Green Chem 9:421–423
35. Su Y, Wang L-C, Liu Y-M, Cao Y, He H-Y, Fan K-N (2007) Microwave-accelerated solvent-free aerobic oxidation of benzyl alcohol over efficient and reusable manganese oxides. Catal Commun 8:2181–2185
36. Choudhary VR, Dhar A, Jana P, Jha R, Uphade BS (2005) A green process for chlorine-free benzaldehyde from the solvent-free oxidation of benzyl alcohol with molecular oxygen over a supported nano-size gold catalyst. Green Chem 7:768–770
37. Caravati M, Grunwaldt J-D, Baiker A (2007) Comparative in situ XAS investigations during aerobic oxidation of alcohols over ruthenium, platinum and palladium catalysts in supercritical CO_2. Catal Today 126:27–36
38. Mällat T, Baiker A (2004) Oxidation of alcohols with molecular oxygen on solid catalysts. Chem Rev 104:3037–3058
39. Mondelli C, Ferri D, Grunwaldt J-D, Krumeich F, Mangold S, Psaro R, Baiker A (2007) Combined liquid-phase ATR-IR and XAS study of the Bi-promotion in the aerobic oxidation of benzyl alcohol over Pd/Al_2O_3. J Catal 252:77–87
40. Besson M, Gallezot P (2000) Selective oxidation of alcohols and aldehydes on metal catalysts. Catal Today 57:127–141
41. Grunwaldt J-D, Caravati M, Ramin M, Baiker A (2003) Probing active sites during palladium-catalyzed alcohol oxidation in "supercritical" carbon dioxide. Catal Lett 90:221–229
42. Souto RM, Rodríguez JL, Pastor E, Iwasita T (2000) Spectroscopic investigation of the adsorbates of benzyl alcohol on palladium. Langmuir 16:8456–8462
43. Markusse A, Kuster BF, Schouten JC (2001) Platinum catalysed aqueous methyl α-d-glucopyranoside oxidation in a multiphase redox-cycle reactor. Catal Today 66:191–197
44. Gangwal VR, van Wachem BGM, Kuster BFM, Schouten JC (2002) Platinum catalysed aqueous alcohol oxidation: model-based investigation of reaction conditions and catalyst design. Chem Eng Sci 57:5051–5063
45. Sanfilippo D (2000) Dehydrogenation of paraffins; key technology for petrochemicals and fuels. CatTech 4:56–73
46. Vajda S, Pellin MJ, Greeley JP, Marshall CL, Curtiss LA, Ballentine GA, Elam JW, Catillon-Mucherie S, Redfern PC, Mehmood F, Zapol P (2009) Subnanometre platinum clusters as highly active and selective catalysts for the oxidative dehydrogenation of propane. Nat Mater 8:213–216
47. Mitchell PC, Wass S (2002) Propane dehydrogenation over molybdenum hydrotalcite catalysts. Appl Catal A Gen 225:153–165
48. Sattler JJHB, Ruiz-Martinez J, Santillan-Jimenez E, Weckhuysen BM (2014) Catalytic dehydrogenation of light alkanes on metals and metal oxides. Chem Rev 114:10613–10653
49. Santhosh KM, Hammer N, Rønning M, Holmen A, Chen D, Walmsley JC, Oye G (2009) The nature of active chromium species in Cr-catalysts for dehydrogenation of propane: new insights by a comprehensive spectroscopic study. J Catal 261:116–128
50. Beale AM, van der Eerden AMJ, Kervinen K, Newton MA, Weckhuysen BM (2005) Adding a third dimension to operando spectroscopy: a combined UV-Vis, Raman and XAFS setup to study heterogeneous catalysts under working conditions. Chem Commun 3015–3017

51. Iglesias-Juez A, Beale AM, Maaijen K, Weng TC, Glatzel P, Weckhuysen BM (2010) A combined in situ time-resolved UV–Vis, Raman and high-energy resolution X-ray absorption spectroscopy study on the deactivation behavior of Pt and PtSn propane dehydrogenation catalysts under industrial reaction conditions. J Catal 276:268–279
52. Barchasz C, Molton F, Duboc C, Leprêtre J-C, Patoux S, Alloin F (2012) Lithium/sulfur cell discharge mechanism: an original approach for intermediate species identification. Anal Chem 84:3973–3980
53. Yamin H, Gorenshtein A, Penciner J, Sternberg Y, Peled E (1988) Lithium sulfur battery: oxidation/reduction mechanisms of polysulfides in THF solutions. J Electrochem Soc 135:1045–1048
54. Cuisinier M, Cabelguen P-E, Evers S, He G, Kolbeck M, Garsuch A, Bolin T, Balasubramanian M, Nazar LF (2013) Sulfur speciation in Li–S batteries determined by *operando* X-ray absorption spectroscopy. J Phys Chem Lett 4:3227–3232
55. Koziej D, Hübner M, Barsan N, Weimar U, Sikora M, Grunwaldt J-D (2009) *Operando* X-ray absorption spectroscopy studies on Pd-SnO_2 based sensors. Phys Chem Chem Phys 11:8620–8625
56. Bârsan N, Weimar U (2003) Understanding the fundamental principles of metal oxide based gas sensors; the example of CO sensing with SnO_2 sensors in the presence of humidity. J Phys Condens Matter 15:R813–R839
57. Tsud N, Johánek V, Stará I, Veltruská K, Matolın V (2001) XPS, ISS and TPD study of Pd–Sn interactions on Pd–SnO_x systems. Thin Solid Films 391:204–208
58. Capone S, Siciliano P, Quaranta F, Rella R, Epifani M, Vasanelli L (2001) Moisture influence and geometry effect of Au and Pt electrodes on CO sensing response of SnO_2 microsensors based on sol–gel thin film. Sens Actuators B Chem 77:503–511
59. Mädler L, Sahm T, Gurlo A, Grunwaldt J-D, Barsan N, Weimar U, Pratsinis SE (2006) Sensing low concentrations of CO using flame-spray-made Pt/SnO_2 nanoparticles. J Nanopart Res 8:783–796
60. Weber AZ, Newman J (2004) Modeling transport in polymer-electrolyte fuel cells. Chem Rev 104:4679–4726
61. Jacobson MZ, Colella WG, Golden DM (2005) Cleaning the air and improving health with hydrogen fuel-cell vehicles. Science 308:1901–1905
62. Steele BC, Heinzel A (2001) Materials for fuel-cell technologies. Nature 414:345–352
63. Ishiguro N, Saida T, Uruga T, Nagamatsu S, Sekizawa O, Nitta K, Yamamoto T, Ohkoshi S, Iwasawa Y, Yokoyama T, Tada M (2012) *Operando* time-resolved X-ray absorption fine structure study for surface events on a Pt_3Co/C cathode catalyst in a polymer electrolyte fuel cell during voltage-operating processes. ACS Catal 2:1319–1330
64. Tada M, Murata S, Asakoka T, Hiroshima K, Okumura K, Tanida H, Uruga T, Nakanishi H, Matsumoto S, Inada Y, Nomura M, Iwasawa Y (2007) *In situ* time-resolved dynamic surface events on the Pt/C cathode in a fuel cell under *operando* conditions. Angew Chem Int Ed 46:4310–4315

Chapter 14
XAFS for Ultra Dilute Systems

Kiyotaka Asakura

14.1 Introduction: Fluorescence Method and Dilute Systems

X-ray absorption fine structure (XAFS) is usually measured in a transmission mode to measure the transmitted beam intensity, I, normalized by the incident X-ray intensity, I_0, and the absorbance can be calculated as follows:

$$\mu t = \ln\left(\frac{I}{I_0}\right). \tag{14.1}$$

To obtain XAFS data with a good signal-to-noise ratio (S/N), we should use an edge height ($\Delta\mu t$) of nearly 1 and a total absorbance ($\mu_t t$) of less than 3–4. The total absorbance is the sum of the absorbance of the target X-ray absorption edge $\mu_a t$ and the background absorbance ($\mu_b t$) arising from other elements and the other edges, and is given as $\mu_t t = (\mu_b + \mu_a)t$. For a dilute sample, $\mu_t t$ may exceed 5 if one tries to keep the edge height approximately 1, owing to the large $\mu_b t$. This results in a decreased transmitted beam and a much poorer S/N spectrum. In such a case, the edge height may be reduced even if the thickness increases, owing to higher harmonics and/or stray light preventing the reliable acquisition of data. It should be noted that one has to reduce the thickness to keep the total absorbance less than 3–4 even if $\Delta\mu t$ is less than 1 to obtain a better XAFS. With the bright beam source, we can achieve a good S/N ratio XAFS spectra even if the edge jump is 0.1. For more dilute systems, the fluorescence detection method is often applied.

The sample is irradiated with higher energy X-rays than the energy of the X-ray absorption edge. The photoabsorption yields emission of a photoelectron and the

K. Asakura (✉)
Institute for Catalysis, Hokkaido University, Sapporo 001-0021, Japan
e-mail: askr@cat.hokudai.ac.jp

Y. Iwasawa et al. (eds.), *XAFS Techniques for Catalysts, Nanomaterials, and Surfaces*, DOI 10.1007/978-3-319-43866-5_14

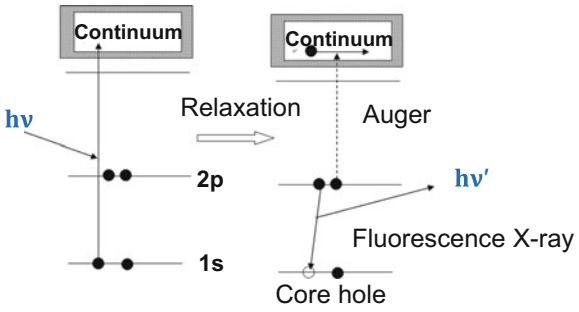

Fig. 14.1 Photoabsorption and relaxation processes of the core hole

creation of the core hole left at the target atom. The created core hole is usually relaxed by the transition of an electron from the outer shell accompanied by Auger electron emission or by fluorescence X-ray radiation to liberate the extra energy between the outer shell electron and core electron, as shown in Fig. 14.1.

The fluorescence intensity is proportional to the number of core holes, which is then proportional to the absorption coefficient of the target element. When the target element is randomly distributed in the sample, the intensity of the fluorescence signal can be expressed as:

$$I_{\mathrm{f}} = \int dI_{\mathrm{f}} \propto \int \mu_{\mathrm{a}} I(x) dx = \int_0^L \mu_{\mathrm{a}} I(0) e^{-\mu_{\mathrm{t}} x} dx = \frac{\mu_{\mathrm{a}}}{\mu_{\mathrm{t}}} I(0)(1 - e^{-\mu_{\mathrm{t}} L}), \tag{14.2}$$

where, I_{f}, $I(x)$, and $I(0)$ are the intensities of the fluorescence X-ray with the incident X-rays at positions x and 0, respectively. As mentioned above μ_{t} can be divided into two parts, μ_{a} and the background μ_{b}, and L is the sample thickness. When the target element is present in a thin film, the equation can be written as (thin film case):

$$I_{\mathrm{f}} \propto \mu_{\mathrm{a}} I(0) L. \tag{14.3}$$

If L is sufficiently thick and the target element is very dilute (extremely dilute case) then:

$$\mu_{\mathrm{t}} \approx \mu_{\mathrm{b}} \tag{14.4}$$

$$I_{\mathrm{f}} = \frac{\mu_{\mathrm{a}}}{\mu_{\mathrm{b}}} I(0). \tag{14.5}$$

In only the thin film or extremely dilute cases, the I_{f} is proportional to μ_{a}, the absorption coefficient of the target edge. Otherwise, I_{f} is not proportional to μ_{a} because μ changes with μ_{a} as it contains EXAFS oscillations. Consequently, fluorescence EXAFS is distorted especially in its amplitude. This is termed the "self-absorption effect" and the fluorescence method cannot be applied. Hence, a dilute sample is suitable for the fluorescence method.

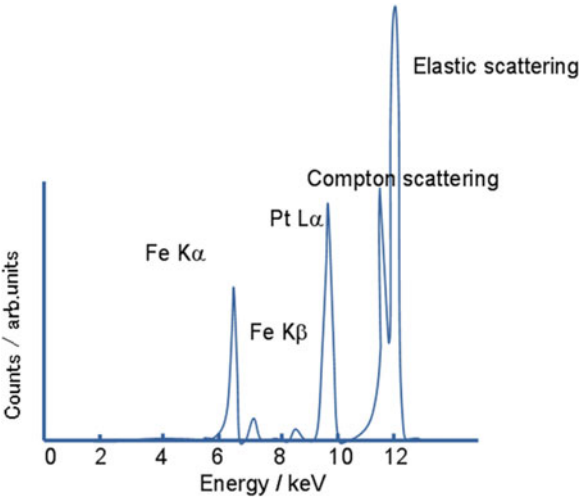

Fig. 14.2 Pt-Fe sample in solution after the Pt L_3-edge

14.2 What Is the Detection Limit of Fluorescence XAFS?

Figure 14.2 shows the energy distribution of the X-ray emission and scattering spectra over a wide range from PtFe system dissolved in solution.

Pt fluorescence appears when the incidence X-ray energy is more than the energy of the Pt L_3-edge. There are peaks at higher energies corresponding to the elastic scattering of incoming X-rays and Compton scattering. At lower energies than the Pt fluorescence, fluorescence peaks arising from other coexisting element (Fe) are observed.

The detection limit is determined by these background X-rays even if one uses a strong X-ray source. Since EXAFS exhibits a 1 % modulation in absorbance for the absorption edge height, a fluorescence of at least more than 10^4 counts is needed to obtain a S/N >1 when only the fluorescence signal is detected (or no background X-ray is present; the signal is $100 = 10^4 \times 1\,\%$ and noise $= \sqrt{10^4} = 100$). If the fluorescence intensity is 10^4 cps, 1 s of accumulation will enable a signal with S/N = 1 and 100 s (10^6 counts) is necessary for a sufficient S/N ratio (10^3) to obtain a reliable XAFS oscillation.

However, the situation changes when the fluorescence intensity is the same but background components are present. If the background intensity is 10^5 cps, the fluorescence is 10^4 cps, and we want to measure the EXAFS with a S/N = 1, at least 10 s is required because EXAFS oscillation $= 10^4$ (cps) $\times$ 10 (s) $\times$ 1 % = 1000 while the noise $= \sqrt{\left(10^5 + 10^4\right)(\text{cps}) \times 10(\text{s})} \approx 1000$. If a S/N ratio of 10^3 is necessary, a collection time of 10^7 s (7 years) is required. This means that when the background level is high, the EXAFS measurement is not possible even though the fluorescence signal is enough. Importantly, the noise is proportional to the square root of the total intensity and not to that of signal. To reduce the measuring time, the

background has to be removed and the signal should be detected more effectively so that an energy selective fluorescence measurement is required.

14.3 Lytle Detector [1]

The strongest background contribution is from elastic scattering X-rays which have the same photon energy as the incident X-rays, while the fluorescence X-rays have a lower photon energy than the elastic signal, as shown in Fig. 14.2. Amount of detected elastic scattering X-rays can be easily reduced by the combination of a low pass filter and a Soller slit. As the low-pass filter, the Z-1 element is used, where Z is the atomic number of the target element. The Z-1 filter usually has an absorption edge between the fluorescence signal and the absorption edge, as shown in Fig. 14.3. For example, Ni fluorescence appears around 7460 eV while its K-absorption edge is observed at 8333 eV. The Z-1 element for Ni is Co, whose K-edge is 7709 eV. Thus, Co strongly absorbs the elastic scattering X-rays but weakly absorbs the fluorescence signal from the target element (Ni). However, the elastic scattering X-ray excites the Z-1 filter to result in the fluorescence of the Z-1 element, which may reach the detector to increase the background signal. Since the emission positions from the Z-1 filter and sample are different, the fluorescence from the Z-1 filter can effectively be removed by the Soller slit which has a focus on the sample, as shown in Fig. 14.4. A previous report explains how to make the Z-1 filter [2]. The Z-1 material, with appropriate thickness (edge jump normally 3 or 6), is hardened by glue and is made flat. In a moderately dilute sample (more than a few hundred ppm), the large area ionization chamber enables a large solid angle whilst the ionization chamber itself has no energy resolution. The combination of the Z-1 filter and the Soller slit is mandatory to achieve a good S/N ratio in the Lytle detector. The detector system is called a Lytle detector [1]. Figure 14.5 shows the Pt L_3-edge XAFS with a 200 ppm solution. In the L edge, the low-pass filter is not the Z-1, but instead, K-edge elements is chosen whose absorption edge is located

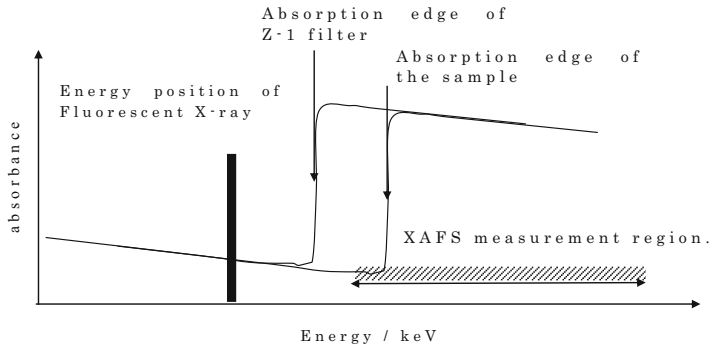

Fig. 14.3 Energy relation of the fluorescence signal and Z-1 filter

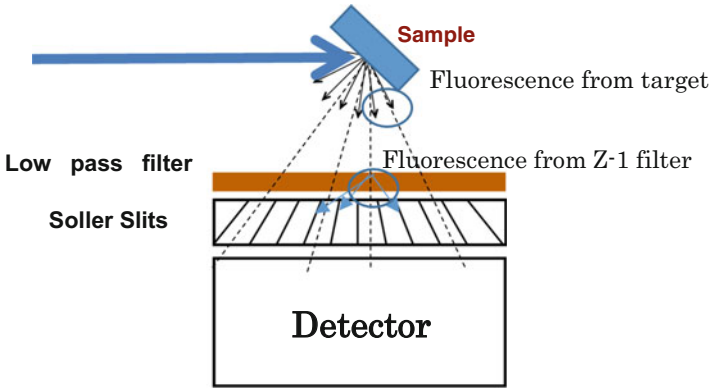

Fig. 14.4 Experimental setup of the Lytle detector

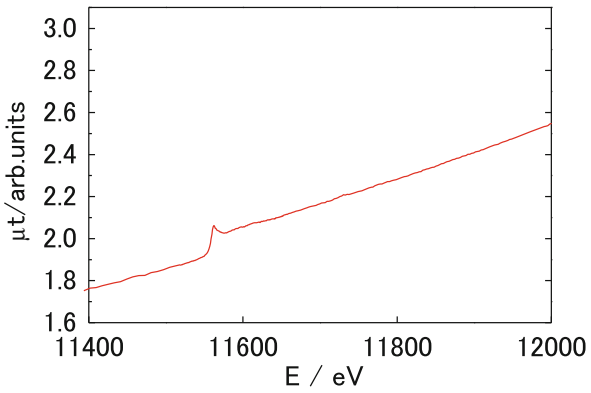

Fig. 14.5 Pt L_3-edge XAFS with a 200 ppm solution. Ga was used as the low-pass filter

between the absorption edge for the target element and its fluorescence. In the case of Pt, three K-edge elements are available, Ge, Ga, and Zn. In Fig. 14.5, Ga was used as the low-pass filter.

14.4 Pulse Counting Detectors

For more dilute systems, the background signal becomes larger and energy resolved fluorescence detection is required. There are several energy-resolved detectors, such as solid state detectors (SSDs), silicon drift detectors (SDDs), gas proportional detectors (GPDs), or scintillation detectors (SDs), as shown in Table 14.1.

The energy resolution can be achieved by the pulse counting and the pulse height analysis (PHA). When the photon enters the counter, the electron and hole pairs are both created in the semiconductor detectors (SSDs and SDDs). The valence electrons are excited to the conduction bands. The band gap is 1.1 eV for Si and 0.7 eV

Table 14.1 Detectors for fluorescence XAFS

Detectors	Detection method	Energy resolution ($E/\Delta E$)	Cost	Solid angle	Maximum counting rate	Remarks
Ionization chambers	Current	None	Low	Large		Lytle detector
Proportional counter	Pulse	10	Low	Large	10^6–10^7	
Scintillation counter	Pulse	2–10	Middle	Middle	10^5–10^6	Miniaturization Multielement
Silicon drift detector	Pulse	10–100	High	Small	10^5–10^6	Peltier cooling Multielement
Solid state detector	Pulse	20–100	Very high	Small	10^4–10^5	Liquid N_2 Multielement

for Ge; hence, many electrons are excited by one X-ray photon. The number of excited electrons is proportional to the X-ray photon energy. These electrons accumulate to the electrodes to create one electric pulse from one X-ray photon. Consequently, the electric pulse height is proportional to the incoming X-ray energy. In the GPDs, gases are ionized to create electron and ion pair. The ionization energy of Ar is 30 eV giving a lot of electron and ion pairs, which are converted to an electric current pulse at the electrode. In the SDs, X-rays are converted to visible light where the number of photons is proportional to the X-ray energies and the photons are converted to electrons and finally one electric pulse. The important point is that the final electric pulse height is proportional to the X-ray photon energy. The PHA of each electric pulse created from the detector provides the photon energy information. Since the number of electric pulses for each energy is proportional to the number of X-ray photons, the X-ray intensity (number of X-ray photons) is determined by counting the electric pulses. This method is called the pulse counting method, which is in contrast to the Lytle detector with an ionization chamber, where the pulses are integrated to be a direct current (DC).

The merit of the pulse counting method is the energy resolution, which enables us to distinguish between the fluorescence and the elastic scattering. Its drawback is the counting loss when too many pulses enter the detector. Since each pulse has a finite pulse width, two X-ray photons cannot be distinguished when the two X-ray photons arrive at almost the same time. When two pulses simultaneously enter the detector, one signal pulse will be created with its height being the sum of the energy of two photons. Thus, the PHA is not able to identify the pulse as the fluorescence signal and the two pulses cannot be counted. The time that the detector is unable to distinguish between two pulses is called the dead time. If the counting rate is too high, the detector becomes saturated, so the detector should be placed far away from the sample to reduce the total number of pulses and to prevent the saturation of the detector. Note that the counting loss depends not only on the fluorescence but also on the total number of pulses. This means that the intensity of background

X-rays (mainly elastic scattering X-rays) has to be small. The pulse counting system is often used with the combination of the low-pass filter and the Soller slit to remove the elastic scattering X-rays.

When the counting rate is not too high, the counting rate loss can be corrected. The counting rate loss equation is given as follows [3],

$$m_0 = m(1 + n\tau_1)/(1 - n\tau_2), \tag{14.6}$$

where m_0, m are the true and observed photon counts of the fluorescence X-rays (selected signal). The n, τ_1, and τ_2 are total number of X-rays (termed as the ICR (input count rate) or CRM (count rate meter)), and the dead times for the fluorescence X-rays and total X-rays, respectively.

τ_1 and τ_2 are determined by a fitting using the following equations:

$$\begin{aligned} n &= I_0(1 - I_0\tau_1) \\ m &= \beta n(1 - n\tau_2), \end{aligned} \tag{14.7}$$

where β is another fitting parameter.

Table 14.1 summarizes the maximum measurable counting rate, energy resolution, and solid angle for each detector [4, 5]. SSDs have the highest energy resolution although the maximum counting rate is small and its dead time loss is large. Figure 14.6 shows the EXAFS spectra of 50 ppm Pt dissolved in CCl_4 using the SSD and low pass (Ge)filter + Soller slit. The dead time correction has been applied. The multi-element SSD is usually used to increase the solid angle and to overcome the dead time loss problem [6]. Cramer et al. measured the XAFS using 13 Ge detectors clustered in a 1:3:5:3:1 pattern [6]. The counting rate reached 75.000 cps. Oyanagi et al. developed a 100 elements SSD detector (Ge pixel array detector) and obtained counting rates of up to 10^7 cps [7].

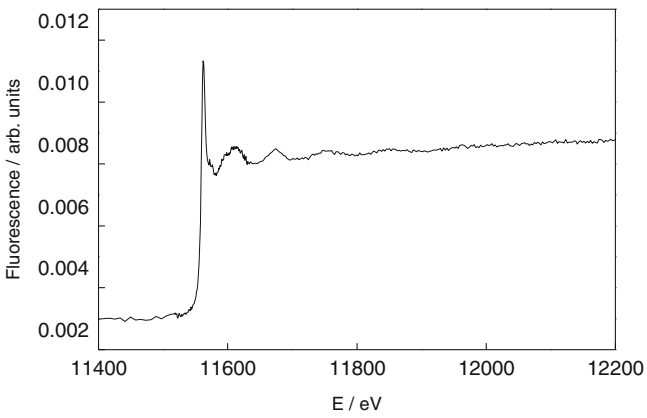

Fig. 14.6 50 ppm Pt in CCl_4 solution using SSD

Another problem for SSDs is that the SSDs require liquid N_2 for operation. Recently, a SDD has been used for the fluorescence XAFS measurements and exhibited a high energy resolution with smaller dead time losses [8]. In addition, this detector does not require liquid N_2 cooling, but can be operated using Peltier cooling. A CdTe detector also has a high counting rate and does not require liquid N_2, but the energy resolution is poor. However the miniaturization of the CdTe detector is possible and it can be positioned close to the sample [9].

When the sample is more dilute or contains other elements and impurities, higher energy resolution is needed. The superconducting tunnel junction detector provides a high energy resolution detector with 10–15 eV and can be applied to the fluorescence XAFS measurements for low Z elements [10, 11]. However, the counting rate is not so high.

14.5 Fluorescence Spectroscopy [12]

Another method for detection in an ultra-dilute system is to use a monochromator to separate the fluorescence of the target element from the other signals. The flat crystal requires a parallel beam to select the fluorescence beam. The Soller slit is used to collimate the X-ray beam, but this results in the loss of many X-rays. Recently, a half-focus polycapillary tube has been used for collecting and collimating the X-rays from the sample, as shown in Fig. 14.7 [13]. The polycapillary is an optical device composed of curved glass tubes in which the X-rays are totally reflected by the glass walls and guided along the tube, as shown in Fig. 14.7. Because the tubes are curved (Fig. 14.7b), the dispersed X-rays are collected in parallel beams through the bundle of the glass capillary tubes (Fig. 14.7c). The collecting angle from the sample was reported as 20° with an angle divergence of

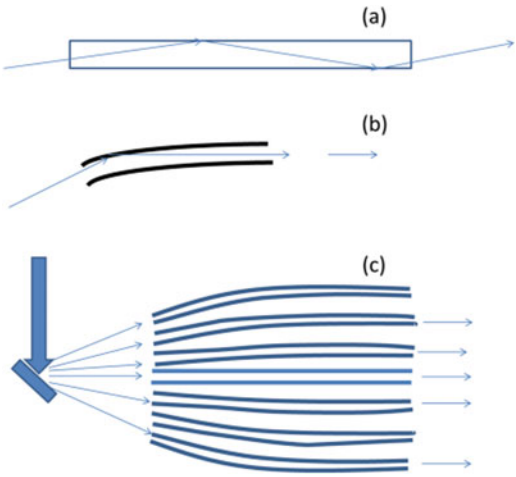

Fig. 14.7 Principle of the polycapillary. (**a**) Hollow glass capillary tube where the X-ray is transmitted through the tube with total reflection occurring on the wall. (**b**) Curved glass tube to change the X-ray propagation direction. (**c**) Bundle of the multitube (polycapillary) which makes the disperse X-ray parallel

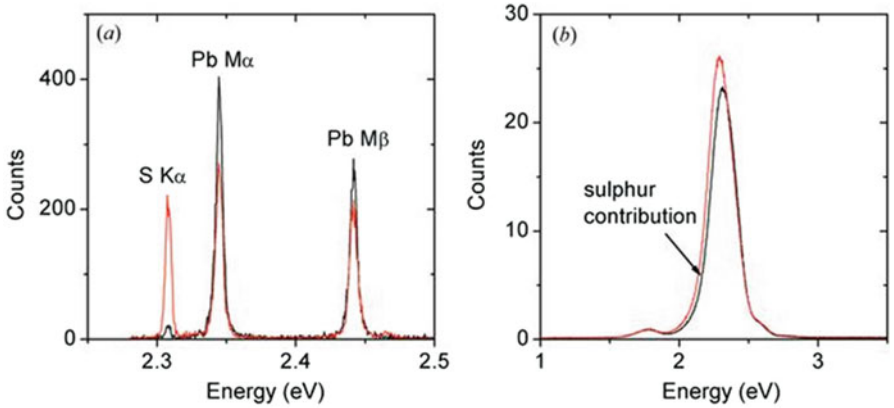

Fig. 14.8 Emission spectra of a pigment (**a**) obtained using a polycapillary and a flat monochromator with emission arising from different areas (*red* and *black*), (**b**) SDD (IUCr's copyright permission; Fig. 10 in Ref. 13, http://dx.doi.org/10.1107/S0909049510010691)

3.4 mrad [13]. Thus, the energy resolution for Si(111) as a monochromator was 40 eV at 7.1 keV and 10 eV at 3.5 keV. The detection limit was reported to be tens of ppm [13]. Figure 14.8 shows the X-ray emissions from the submicrometer order pigments of the old painting [13]. The main ingredient is Pb. A small amount of sulfur was included. Pb Mα (2345.5 eV) and S Kα (2308 eV) fluorescence peaks had the similar energies. Figure 14.8a shows the emission spectrum analyzed by the capillary tube and flat monochromator where S and Pb fluorescence were well separated, while the SDD is unable to separate the fluorescence, as shown in Fig. 14.8b.

When the curved monochromator is used, the X-ray can be collected and refocused on the detector side using a Johan- or Johansson-type crystal, details of which will be in the section of this book discussing the high energy resolution. Sokaras et al. used 40 Johan-type spherically bent Si(1 1 0) crystals to achieve 0.019 of 4π sr rad [14, 15]. To increase the solid angle, a barrel-type monochromator was developed, as shown in Fig. 14.9 [16].

In a Johan- or Johansson-type monochromator, the monochromator surface is on or approximately on the Rowland circle. The other configuration of the monochromator is a log spiral where the angle between the line from one point to the surface and surface normal is a constant [17]. Thus, a log spirally curved monochromator in both Bragg or Laue cases can be used as a crystal analyzer.

The log spiral curve is a curve written as:

$$r = ae^{b\phi}, \tag{14.8}$$

where r, ϕ are the distance and the angle in the polar coordinates, respectively, as shown in Fig. 14.10. The log spiral curve has a feature that the angle, θ, between the radial direction, $\vec{r}$, and surface normal, $\vec{n}$, is constant.

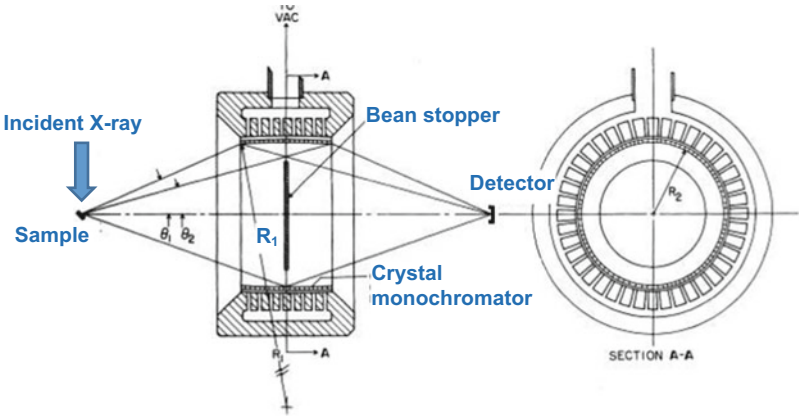

Fig. 14.9 The barrel-type fluorescence monochromator. R_1 is the Rowland radius. Permission for reuse from American Physical Society (Copyright 1979, License No. 3654981239295; Fig. 1 of Ref. 16)

$$\cos\theta = \frac{\vec{r}\cdot\vec{n}}{|\vec{r}|\,|\vec{n}|} = \frac{(x,y)\cdot\left(\frac{dy}{dx},-1\right)}{\sqrt{x^2+y^2}\cdot\sqrt{\left(\frac{dy}{dx}\right)^2+1}} = \frac{1}{\sqrt{b^2+1}} \tag{14.9}$$

$$b = \pm\tan\theta$$

When $b = 0$, the log spiral is a circle. If θ is the Bragg angle, the diffraction occurs at all points on the curve. Therefore, the X-ray coming from the one spot satisfies the Bragg condition for all points on the log spiral surface, as shown in Fig. 14.10a [17]. From Eq. (14.9), b should be $\pm\tan\theta$. The curve is energy dependent and the dynamic control of its curvature is necessary to change the energy [18]. In this case, 4 eV energy resolution at 10 keV was reported [18].

Figure 14.10b shows the Laue type log spiral analyzer [19, 20]. The X-ray from the point source is diffracted to the other side of the crystal. To increase the acceptance angle, an asymmetrically cut crystal monochromator is usually used. The log spiral shape is written as:

$$r(\phi) = \rho\cos(\chi-\theta_B)\exp[\tan(\chi-\theta_B)\phi] \tag{14.10}$$

where θ_B and χ are the Bragg angle and an asymmetrical angle, respectively. The asymmetrical angle is an angle between the crystal surface normal and the crystal plane. The incident X-ray angle against the surface normal, θ, is written as follows, which is constant for all log spiral surfaces:

$$\theta = \chi - \theta_B \quad \text{or} \quad \theta_B = \chi - \theta \tag{14.11}$$

The X-rays are dispersed from the imaginary focal point on the sample side. The Soller slit parallel to the monochromatized X-ray direction can select the certain

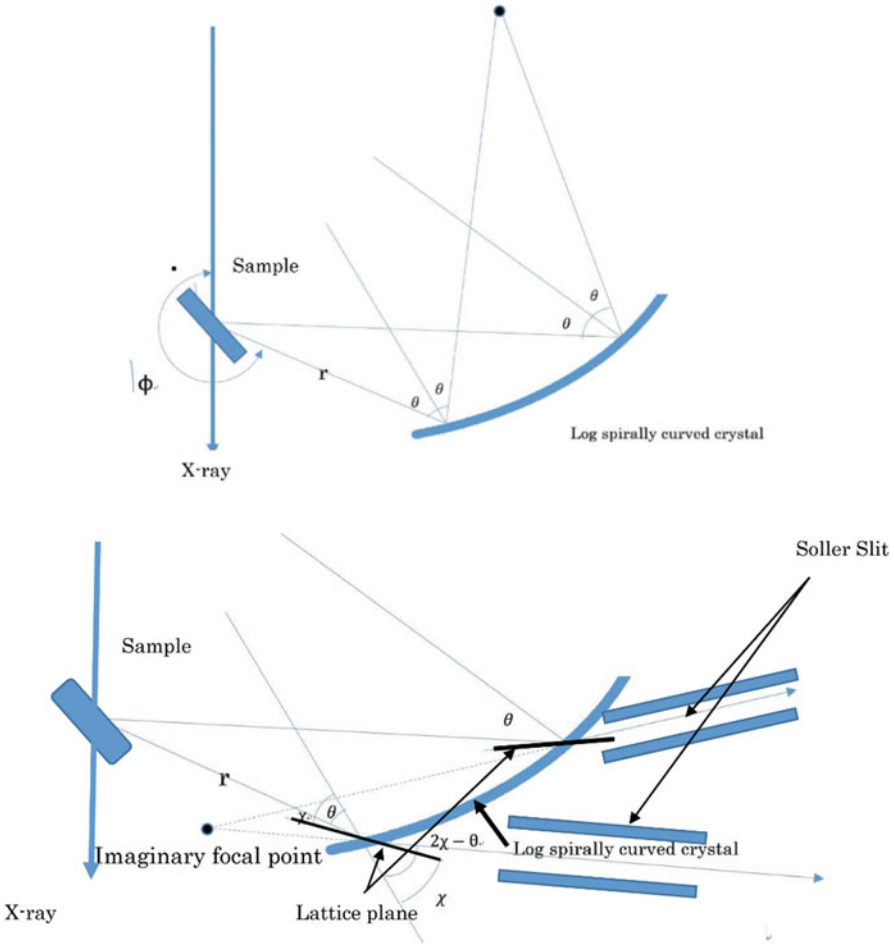

Fig. 14.10 Bent crystal with log spiral curve in a Brag case (**a**) and a Laue case (**b**)

energy to satisfy the Bragg conditions. The Laue type log spiral analyzer is now commercially available, and is known as the bent crystal Laue analyzer (BCLA) [19]. In principle, it can collect fluorescence X-rays of about 0.1 sr from the sample. An energy resolution of approximately 14 eV was reported in the 8 keV region [21]. Takahashi et al. used the BCLA for the analysis of minerals [22–25]. Natural minerals are composed of several elements with different concentrations which may interrupt and hinder the fluorescence signal of the target element existing in a low concentration. They measured XAFS spectra of about 10 ppm Os in molybdenite by using the BCLA where the Zn impurity hinders the Os L_3-edge measurement when an SSD was used [24].

The lower limit of the surface XAFS is determined by the bulk X-ray background. The total reflection is one way to increase the surface sensitivity. However,

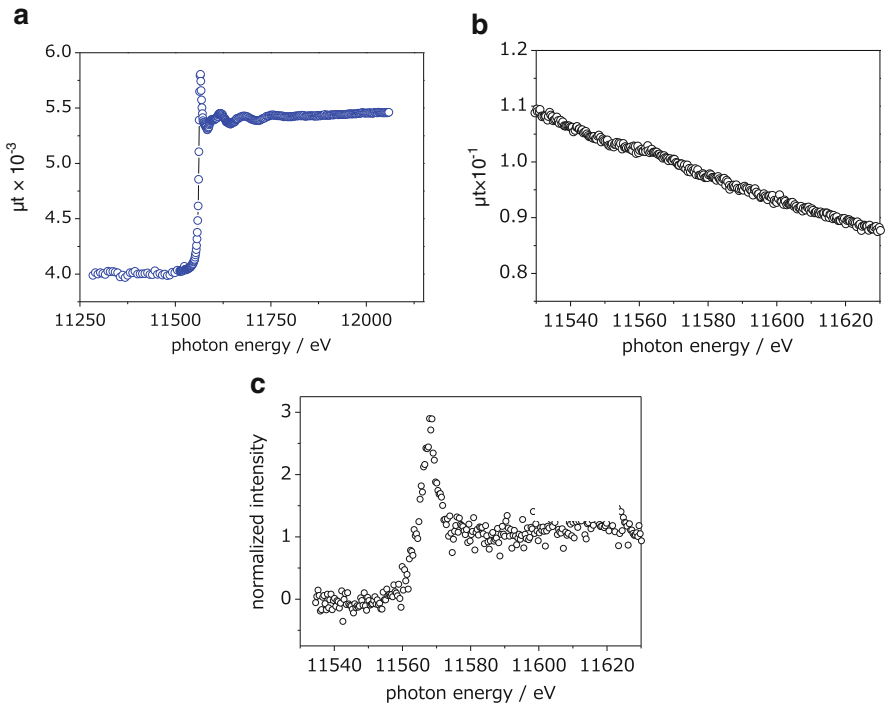

Fig. 14.11 The fluorescence EXAFS of Pt on HOPG (**a**) in air, (**b**) contacting solution, and (**c**) contacting solution with BCLA [15]

it requires a large flat surface area as discussed in the other section. A crystal analyzer may be another possible choice to increase the lower limit. We have applied the BCLA to Pt on highly oriented pyrolytic graphite(HOPG). The Pt density on HOPG was 10^{15} cm^{-2}. Figure 14.11 shows XAFS spectra of Pt on one side of a very thin HOPG surface used as a model electrode for the fuel cell. HOPG was used as an X-ray window and electrode for the model fuel cell which allowed us to carry out in situ spectroscopy. The sample was illuminated through the HOPG and the fluorescence signal from Pt was measured again through the HOPG. We named the measurement system back-illuminated fluorescence X-ray absorption fine structure (BI-FXAFS) [15]. One can measure the XAFS signal by using a low-pass filter (usually a Z-1 filter) and an SSD in air, as shown in Fig. 14.11, where the scattering from the thin HOPG and air are negligible. However, when the electrolyte solution present was in contact with the Pt particle to carry out in-situ measurements under the electrochemical conditions, the signal was hardly observed because of the strong scattering coming from the solution. The large background arising from scattering X-rays masked the fluorescence signal even if the low-pass filter and SSD were used, as shown in Fig. 14.11. We rarely observed an edge jump. However, Figure 14.11c shows the spectrum of the same sample with the BCLA set

between the sample and the SSD detector. The clear edge jump was observed so that the crystal analyzer could improve the detection limit to allow us to investigate the monolayer (10^{14} cm^{-2}) sample on the surface. High brilliant focused beam will provide much better XAFS signal.

14.6 Summary

To investigate a small amount of a sample, one may use the fluorescence XAFS method which improves the S/N ratio. The detection limit is determined by the background X-rays, such as elastic scattering X-ray, Compton scattering, and fluorescence X-rays from other elements. Exploiting the energy difference of the fluorescence X-rays, one can selectively separate the fluorescence X-rays from other background X-rays. The fluorescence X-rays of the target element can be elucidated by a low-pass filter, the energy resolved detectors (SSDs, SDDs, GPDs, and SCs), and a crystal monochromator. The crystal monochromator has the merit of high resolution. The development of high brilliant photon sources to provide a small spot size will enable the fluorescence method with a crystal monochromator to be used on a practical level for low concentration samples.

References

1. Lytle FW, Greegor RB, Sandstrom DR, Marques EC, Wong J, Spiro CL, Huffman GP, Huggins FE (1984) Measurement of soft X-ray absorption spectra with a fluorescent ion chamber detector. Nucl Instrum Methods Phys Res A 226(2–3):542–548. doi:10.1016/0168-9002(84)90077-9
2. Wong J (1984) Method for fabricating large-area X-ray filters. Nucl Instrum Methods Phys Res 224(1–2):303–307. doi:10.1016/0167-5087(84)90479-4
3. Nomura M (1998) Dead-time correction of a multi-element SSD for fluorescent XAFS. J Synchrotron Radiat 5(3):851–853. doi:10.1107/S090904959800003X
4. Kohra K, Kikuta S (1979) X-ray diffraction technique. University of Tokyo Press, Tokyo
5. Kikuta S (2011) X-ray scattering and synchrotron radiation. University of Tokyo Press, Tokyo
6. Cramer S, Tench O, Yocum M, George G (1988) A 13-element Ge detector for fluorescence EXAFS. Nucl Instrum Methods Phys Res A 266(1):586–591
7. Oyanagi H, Fonne C, Gutknecht D, Dressler P, Henck R, Lampert MO, Ogawa S, Kasai K, Mohamed SB (2003) Ge pixel array detector for high throughput X-ray spectroscopy. Nucl Instrum Methods Phys Res A 513(1–2):340–344. doi:10.1016/j.nima.2003.08.059
8. Gauthier C, Goulon J, Moguiline E, Rogalev A, Lechner P, Strüder L, Fiorini C, Longoni A, Sampietro M, Besch H, Pfitzner R, Schenk H, Tafelmeier U, Walenta A, Misiakos K, Kavadias S, Loukas D (1996) A high resolution, 6 channels, silicon drift detector array with integrated JFET's designed for XAFS spectroscopy: first X-ray fluorescence excitation spectra recorded at the ESRF. Nucl Instrum Methods Phys Res A 382(3):524–532. doi:10.1016/S0168-9002(96)00814-5
9. Chun WJ, Asakura K, Iwasawa Y (1996) Application of a Cdte solid-state detector to polarization-dependent total-reflection fluorescence Xafs measurements. J Synchrotron Radiat 3(Part 4):160–162

10. Friedrich S (2006) Cryogenic X-ray detectors for synchrotron science. J Synchrotron Radiat 13 (2):159–171. doi:10.1107/S090904950504197X
11. Ohkubo M, Shiki S, Ukibe M, Matsubayashi N, Kitajima Y, Nagamachi S (2012) X-ray absorption near edge spectroscopy with a superconducting detector for nitrogen dopants in SiC. Sci Rep 2. doi:http://www.nature.com/srep/2012/121114/srep00831/abs/srep00831.html#supplementary-information
12. Sa J (ed) (2014) High resolution XAS/XES analyzing electronic structures of catalysts. CRC Press, Boka Raton, FL
13. Szlachetko J, Cotte M, Morse J, Salomé M, Jagodzinski P, Dousse JC, Hoszowska J, Kayser Y, Susini J (2010) Wavelength-dispersive spectrometer for X-ray microfluorescence analysis at the X-ray microscopy beamline ID21 (ESRF). J Synchrotron Radiat 17(3):400–408. doi:10.1107/s0909049510010691
14. Sokaras D, Nordlund D, Weng T-C, Mori RA, Velikov P, Wenger D, Garachtchenko A, George M, Borzenets V, Johnson B, Qian Q, Rabedeau T, Bergmann U (2012) A high resolution and large solid angle x-ray Raman spectroscopy end-station at the Stanford Synchrotron Radiation Lightsource. Rev Sci Instrum 83(4):043112. doi:10.1063/1.4704458
15. Uehara H, Uemura Y, Ogawa T, Kono K, Ueno R, Niwa Y, Nitani H, Abe H, Takakusagi S, Nomura M, Iwasawa Y, Asakura K (2014) In situ back-side illumination fluorescence XAFS (BI-FXAFS) studies on platinum nanoparticles deposited on a HOPG surface as a model fuel cell: a new approach to the Pt-HOPG electrode/electrolyte interface. Phys Chem Chem Phys 16(27):13748–13754. doi:10.1039/c4cp00265b
16. Hastings JB, Eisenberger P, Lengeler B, Perlman ML (1979) Local-structure determination at high dilution: internal oxidation of 75-ppm Fe in Cu. Phys Rev Lett 43:1807–1810
17. Sakayanagi Y (1982) Bragg optics of a logarithmic spiral surface. Jpn J Appl Phys 21:L225–L226
18. Adams BW, Attenkofer K (2008) An active-optic X-ray fluorescence analyzer with high energy resolution, large solid angle coverage, and a large tuning range. Rev Sci Instrum 79 (2):23102. doi:10.1063/1.2823527
19. Zhong Z, Chapman LD, Bunker BA, Bunker GB, Fischetti R, Segre CU (1999) A bent Laue analyzer for fluorescence EXAFS detection. J Synchrotron Radiat 6(3):212–214. doi:10.1107/s0909049599002022
20. Kropf A, Finch RJ, Fortner JA, Aase S, Karanfil C, Segre CU, Terry J, Bunker G, Chapman LD (2003) Bent silicon crystal in the Laue geometry to resolve X-ray fluorescence for X-ray absorption spectroscopy. Rev Sci Instrum 74:4696
21. Kujala NG, Karanfil C, Barrea RA (2011) High resolution short focal distance Bent Crystal Laue Analyzer for copper K edge x-ray absorption spectroscopy. Rev Sci Instrum 82 (6):063106. doi:10.1063/1.3595675
22. Takahashi Y, Uruga T, Tanida H, Terada Y, Nakai S, Shimizu H (2006) Application of X-ray absorption near-edge structure (XANES) using bent crystal analyzer to speciation of trace Os in iron meteorites. Anal Chim Acta 558(1):332–336
23. Yamamoto Y, Takahashi Y, Kanai Y, Watanabe Y, Uruga T, Tanida H, Terada Y, Shimizu H (2008) High-sensitive measurement of uranium LIII-edge X-ray absorption near-edge structure (XANES) for the determination of the oxidation states of uranium in crustal materials. Appl Geochem 23(8):2452–2461. doi:10.1016/j.apgeochem.2008.02.005
24. Kashiwabara T, Takahashi Y, Uruga T, Tanida H, Terada Y, Niwa Y, Nomura M (2010) Speciation of tungsten in natural ferromanganese oxides using wavelength dispersive XAFS. Chem Lett 39(8):870–871. doi:10.1246/cl.2010.870
25. Kashiwabara T, Takahashi Y, Marcus MA, Uruga T, Tanida H, Terada Y, Usui A (2013) Tungsten species in natural ferromanganese oxides related to its different behavior from molybdenum in oxic ocean. Geochim Cosmochim Acta 106:364–378. doi:10.1016/j.gca.2012.12.026

Chapter 15
Reflection XAFS

Francesco d'Acapito

15.1 Introduction

"Reflection XAFS" or "ReflEXAFS" is a particular collection mode of X-ray absorption spectroscopy (XAS) data with the probe beam impinging on the sample in total external reflection conditions. The main advantage of total reflection XAS is that the extinction length of the probe beam is greatly reduced respect to the normal incidence as shown in Fig.15.1:

This makes ReflEXAFS a surface-sensitive technique in the range of a few nm with the considerable advantage that it does not need ultrahigh vacuum conditions like electron-based techniques. Then, this method can be applied to a variety of interfaces (gas–solid, liquid–solid, liquid–liquid, and solid–solid) realizing "*in operando*" conditions for the materials under study. The toll to pay is the size of the sample that needs to be quite long in the beam direction in order to intercept a sufficient portion of the beam when placed in total reflection condition.

In this contribution the basic theoretical aspects of this technique are reviewed and then a list of remarkable experimental apparatuses is presented. Successively, some examples of experiments using total reflection XAS are described, and in the final section some perspectives of development of this technique are given.

F. d'Acapito (✉)
CNR-IOM OGG, ESRF, LISA-ORG, 38000 Grenoble, France
e-mail: dacapito@esrf.fr

Y. Iwasawa et al. (eds.), *XAFS Techniques for Catalysts, Nanomaterials, and Surfaces*, DOI 10.1007/978-3-319-43866-5_15

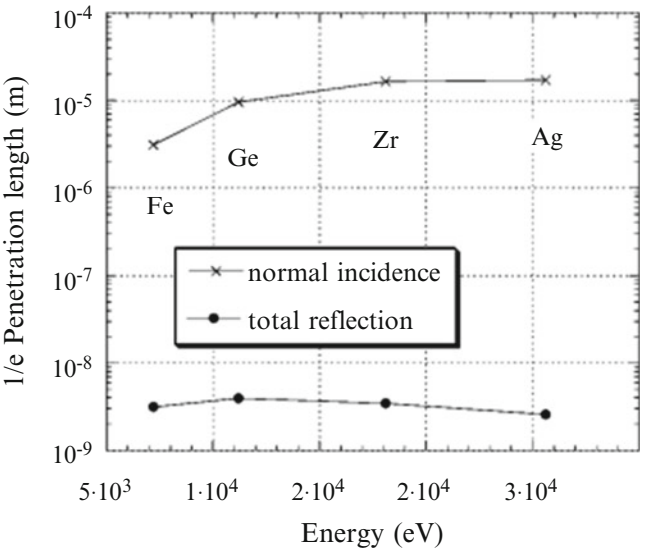

Fig. 15.1 Extinction length of a probe beam just above the K absorption edge in a set of relevant elements in their metallic state. The comparison is done between normal incidence (*upper curve*) and total reflection (*lower curve*) and a reduction of about four orders of magnitude of the extinction length is evidenced in total reflection. From Ref. [44]

15.2 Principles of Reflection XAFS

Reflection XAS (also called GIXAFS or ReflEXAFS) is based on the total external reflection of X-rays at the interface between two media where the deeper one possesses the highest electronic density. If the impinging (probe) beam shines the material below a given angle (the critical angle, ϕ_c) it is completely reflected and enters in the medium only for an extremely thin layer. This is an optical phenomenon widely observed also in the visible range; the difference here is that, in the case of an interface vacuum-material, the former plays the role of the "*high-density*" medium. The phenomenon can be understood by considering the refraction index of an idealized system consisting in electrons (mass m_e charge q_e) bound to the nuclei via a harmonic potential (spring constant k_i). Neglecting dissipation, the equation of motion of electrons i responding to an external field E_0 at angular frequency ω is $m_e\ddot{x} + \kappa_i x = q_e E_0 e^{i\omega t}$ [1], and it can be demonstrated that such a system generates the following refraction index: [2] $n = \sqrt{1 + \frac{N\alpha}{\varepsilon_0}} \approx 1 + \frac{Nq_e^2}{2\varepsilon_0 m_e} \sum \frac{1}{\omega_{0i}^2 - \omega^2}$ where i is the sum over all the electrons and N the atomic volume density and α the polarizability. When the energy of the X-rays is sufficiently high that most of electrons are above their resonance frequencies they will respond in antiphase respect to the field (and similarly will do the α) and the resulting refraction index will exhibit a real part slightly *less* than 1. This

means that the phase velocity in the medium is higher than the speed of light in the vacuum and the medium acts as if it had a lower electronic density than vacuum. In a more complete treatment [3] the refraction index can be written as $n = 1 - \delta - i\beta$ where β and δ come from the scattering factors (in particular it holds that $\beta = \frac{\lambda\mu}{4\pi}$, being λ the X-ray wavelength and μ the absorption coefficient) and they are linked by the Kramers–Kronig (KK) relation $\delta(E) = \int_0^\infty \beta(E) \frac{\varepsilon^2}{E^2 - \varepsilon^2}\, d\varepsilon$. Using the Fresnel formulas for modeling of refraction at an interface a complete description of the reflection can be given in homogeneous as well as on stratified media. Defining $X = \frac{\phi}{\phi_c}$, $Y = \frac{\beta}{\delta}$ and $h = X^2 + \sqrt{\left(X^2 - 1\right)^2 + Y^2}$ the reflectivity R expressed as the ratio between the moduli of the impinging and reflected electric fields is $R = \frac{h - X\sqrt{2(h-1)}}{h + X\sqrt{2(h-1)}}$. For sake of simplicity, it is recalled here just some basic simple formulas as the expression of the critical angle as $\phi_c = \sqrt{2\delta}$ and the extinction length $z_{1/e}$ of the refracted beam in case of small incidence angle and negligible absorption $z_{1/e} = \frac{\lambda}{4\pi\phi_c}$. Being δ is a quantity of about 10^{-5}, ϕ_c is in the order of a few mrad and $z_{1/e}$ around a few nm.

When considering β and δ functions in a condensed system it is clear that the former quantity contains both an atomic background β_0 plus the features coming from the photo-electron interference in the expression of the absorption coefficient (XAS effect) Δβ. Similarly happens for δ in virtue of the KK relation with β. Thus, the reflectivity R as a function of the photon energy E will contain the XAS features, making possible an investigation of surfaces within a range of a few nm under the surface. On the other hand, the analysis of the data appears to be extremely complex due to the nontrivial relationship between R(E) and the quantities β and δ (also known under the name of "anomalous dispersion effects").

15.3 Data Analysis Methods

The first observation of XAS features in a reflectivity spectrum was carried out by Barchewitz et al. [4] and soon after Martens and Rabe [5–7] pointed out the presence of both β and δ contributions in R and that for data collection below the critical angle the β-XAS dominated in R whereas well above f_c the δ-XAS dominates. They also defined a method for extracting the pure β contribution from a spectrum collected at any angle by considering the atomic and oscillating parts $\beta = \beta_0 + \Delta\beta$ and $\delta = \delta_0 + \Delta\delta$ plus a relationship $f = \left[\frac{\Delta\beta}{\Delta\delta}\right]$ linking the two. Considering, however, that the more interesting applications of ReflEXAFS are taken well below the critical angle ($\phi \ll \phi_c$) Bosio et al. [8] and Poumellec et al. [9] proposed an approximated method for the treatment of data collected in that condition valid for the case of the semi-infinite solid. In the case of small incidence angle the

following relation between β and R holds: $\beta = \delta * \left[\frac{\sqrt{(1-X^2)}}{X}\right] \frac{1-R}{1+R}$ where X has the same definition as above. Starting with an initial value for δ° a first approximation of β° is derived, Then, with a Kramers–Kronig transformation KK{β°} a second function δ°° is found that generates β°°. Carrying out this procedure several times a self-consistent solution is rapidly found.

Following the way traced in Ref. [5–7], Borthen and Strehblow (BS) [10, 11] defined a further method based on the expression of the oscillating part of the reflectivity χ_R(E) as a linear combination $\chi_R(E) = a\Delta\delta(E) + b\Delta\beta(E)$ with the a and b coefficients to be calculated on a model system. All these methods were applicable to semi-infinite solids whereas it was recognized the necessity of treating also the more general case of layered systems. The first formulation of a method permitting the analysis of this class of samples was presented by Heald et al. [12–14] and was based on the expression of the total (i.e., including possible additional layers) R(E) (or even the fluorescence, F(E)) as a sum of two contributions one β-dependent and the other δ-dependent. This latter part was estimated from a partial derivative $\Delta R/\Delta\beta \times \Delta\beta/\Delta\delta$ where this last factor was identified as bearing a phase factor of about 75–80° (compared with 90° previously estimated by Martens and Rabe). Based on similar principles is also the method proposed by Tani et al. [15] where the function $\Delta\beta/\Delta\delta$ is determined via an iterative cycle. An extension of this method applied to layered systems has been recently proposed by Lopez-Flores et al. [16] where the R(E) quantity is obtained in a matrix form involving the partial derivatives of R respect to β and δ relative to each layer of the sample.

In the years 2000 together with the interest to layered systems the problem of correctly including the surface roughness become the subject of investigations [17]. Already Martens and Rabe [vi–vii] have underlined the importance of this parameter in the ReflEXAFS data analysis and a series of papers [18–20] have addressed in detail this aspect also considering the Distorted Wave Born Approximation (DWBA) [21], as a possible alternative theory respect to Fresnel's. In these papers it was recognized the importance of considering the surface roughness mainly for possible artifacts affecting the signal amplitude [22] and that a treatment using Parratt's (Fresnel) formulas corrected by a Névot–Croce (NC) [22] roughness parameter gave the same results as the more complex DWBA model in the case of specular reflection. However, the use of DWBA permitted the elaboration of a variant of the ReflEXAFS technique based on the off-specular reflected beam, i.e., collecting the data on the so-called Yoneda peak [23]. Non specular effects, are not included in the Parratt's formalism, but can be obtained from DWBA and this opens the opportunity of a new experimental technique with increased sensitivity to the interfaces in the sample presenting the higher degree of lateral heterogeneities [24]. In these papers the quantitative XAS analysis was carried out with a (BS) method.

Benzi et al. [25] (as also suggested in Ref. [26]) have proposed a code (CARD) [27] that works in an opposite way respect to the previously mentioned methods.

Instead of converting R(E) in a b(E) for successive analysis with conventional tools they proposed the use of modified XAS theoretical paths for modeling the oscillating part of R(E). In practice, the relevant reflectivity parameters (layers thickness, roughness, composition) of the sample are determined by fitting one or more reflectivity spectra at fixed energy (and variable angle ϕ) of the sample. With these parameters, the reflectivity R(E) of the sample is simulated including one at a time the theoretical EXAFS paths generated by a suitable code (Feff in the present version of the code). From this reflectivity function a new theoretical EXAFS signal is extracted and can be used for the data analysis. In this case the full Fresnel (with NC corrections for roughness) formulas are used with no additional approximations also in the case of layered systems. [28]

Up to here it has been treated the case where the optical constants of the absorbing species contribute significantly to the refraction index of the probed layer (*concentrated sample* case). In the case of very thin film this is no longer the case: the optical constant of the probed layer is dominated by the matrix and do not exhibit edge jump nor XAS oscillations in the region investigated (*diluted sample* case). In this case the reflectivity signal does not possess any XAS modulation and fluorescence detection must be used. (Actually, fluorescence could be used also in the analysis of thick samples but it was long ago pointed out [29] that reflectivity has a greater surface sensitivity in case of rough samples) The great advantage in this case is that it can be demonstrated that no corrections are necessary and the collected data can be treated in the conventional way [30, 31].

15.4 Data Collection Methods and Instrumentation

ReflEXAFS is an ideal technique in the study of surface systems especially when real conditions for the surface are required. Coupled with the highly polarized beams coming from synchrotrons, this technique provides a detailed description of well oriented samples. This, because the polarization vector can be oriented either parallel or perpendicular to the surface (linear dichroism) so enhancing the sensitivity to bonds placed along that vector. This effect is different if {K, $L_{(I)}$} or {$L_{(II)}$, $L_{(III)}$} edges are considered. In the former case the relation between the amplitude N_{Kedge} of a single bond making an angle δ with the polarization vector is $N_{\mathrm{Kedge}} = 3\cos^2\delta$ whereas in the latter case it is $N_{\mathrm{Ledge}} = 0.7 + 0.9 * \cos^2\delta$ [32]. This technique has been called polarization dependent total reflection XAFS (PTRF-XAFS) [33] and has been largely exploited by the catalysis community to describe adsorbate on model surfaces. Another aspect that can be exploited using total reflection is the large variation of the extinction length of the probe X-ray beam as a function of the incidence angle. This value passes from a few nm to a few mm so giving the possibility of studying the surface and the bulk of the sample just by changing the incidence angle from below to above the critical value. An example of these surface-bulk studies can be found in Ref. [34] and others are presented later.

Several experimental apparatuses for ReflEXAFS data collection have been presented in the past. A noticeable instrument is that presented in Ref. [33, 35, 36] describing a measurement chamber coupled with a preparation chamber for in situ studies and installed at the BL-7 beamline at KEK dedicated to studies in the fields of chemistry and catalysis. The samples could be kept at a pressure variable form ultrahigh vacuum (10^{-9} mbar) to ambient pressure and at a temperature from 100 to 800 K. The sample was conditioned in the preparation chamber and successively transferred in the measurement chamber. Here, it could be oriented with the surface either parallel or perpendicular to the beam polarization vector so permitting the collection of PTRF-XAFS data on systems like Pt particles on Al_2O_3 (0001) or V on ZrO_2 (100) surfaces (see following sections). Be windows permitted to collect the reflected and fluorescence beams with ion chamber or NaI detectors. Successively, an evolution of that instrument was presented by the same group [37] with more a better performing multielement solid state energy resolving detector and a more complete set of ancillary surface characterization techniques (Auger, RHEED). A measure chamber with similar capabilities of data collection with different sample orientation was presented in Ref. [38, 39] and installed at the BL13B beamline at the Photon Factory. The chamber was more conceived for experiments in the surface science field and permitted to collect data in multiple sample orientations in ultrahigh vacuum and temperatures between 15 and 300 K. Also in this case particular care was used in the choice of the fluorescence detector as both Si(Li) and HP-Ge multielement devices were used to reach sensitivity of about 0.1 Monolayer. Further data collection apparatuses have been presented in literature some of which keeping the sample kept in the ambient environment or with the sample stage mounted on a multiaxis diffractometer [40–42] whereas in others the sample manipulator is entirely confined in a vacuum chamber to limit the effects of air absorption or scattering [43, 44].

A particular challenging topic was constituted by ReflEXAFS on liquid surfaces. In this case indeed, the need of keeping a well stable surface free from ripples and other mechanical instabilities lead to the realization of peculiar experimental apparatuses. The first aspect is that the impinging beam needs to be tilted instead of the sample so the sample stage is preceded by a flat mirror that bends the beam at the desired angular value. Angle variable reflectivity is measured changing at the same time the angle of the mirror and the height of the sample to keep the beam at its center. The issue of ripples at the liquid surfaces is solved by using vibration damping solutions like a floating sample boat placed in a pool filled with a damping liquid [45, 46]. A further apparatus for liquid surfaces is reported in Ref. [47] operative at the DELTA storage ring and equipped with a Langmuir trough for the formation in situ of Langmuir–Blodgett (LB) films.

An activity that has been growing in importance in the last years has been that coupling time resolved XAS techniques like Quick-XAS or dispersive XAS with total reflection studies with the aim of describing in time the evolution of surfaces. Using Quick-XAS [48, 49] it has been reported the capability of collecting data below 1 s in a widely extended k space, whereas dispersive XAS opens the way to

much shorter collection time (4–10 ms) although paid with a more limited extension of the spectrum [50].

A final remark is to be done on methods based on the standing waves generated in multilayer systems. In this case it was demonstrated the feasibility of data collection keeping the standing wave in the same position respect to the layers during the whole energy scan [51] so opening the possibility of data collection enhancing either the interfaces or the central portions of the layers. Also from the modulations of the position of a multilayer Bragg peak as a function of the energy (coming from the d-XAS part of the sample refraction index) it was demonstrated to be possible to extract EXAFS oscillations [52] similarly to what is done with the diffraction anomalous fine structure (DAFS) technique.

15.5 Experimental Examples

15.5.1 Surface Adsorbates

One of the major investigation fields where XAS in total reflection mode has been applied is the study of crystalline oxide surfaces of interest in catalysis like TiO_2 and Al_2O_3. In particular, the adsorption site of different metals on these surfaces has been studied. In this class of experiments total reflection XAS reveals to be unavoidable due to the extremely low metal coverage (of the order of 10^{-2} Mono-Layers or 10^{13} at/cm^2) so needing to limit at maximum the penetration of the probe beam into the substrate and minimize in this way the deleterious effects of coherent diffraction. The availability of instruments with full 6 axes goniometers in ultrahigh vacuum for sample orientation has permitted the development of PTRF-XAS [53]. The procedure consists in collecting XAS data on surfaces in total reflection condition and orienting the surface in several different positions to place the polarization vector along a set of relevant crystallographic directions and enhance in this way selected atomic bonds (Fig. 15.2)

With this technique it has been demonstrated the possibility of defining full three-dimensional (3D) models of adsorption sites of metals on surfaces. Indeed, data are collected in three different orientations and then for any proposed structural model the relative polarized XAS spectra are calculated and compared with experimental data. This comparison permits the selection of the structural model best reproducing at the same time all three spectra so recovering a 3D information that is usually lost in the (spherical averaged) XAS spectra (see Fig.15.3). Examples of use of this technique are given in a series of papers about the location of Mo ions on oxide surfaces [54–58]. Various atomic arrangements were found that were put in relationship with the acidity of the host surface [58]. When Mo was deposited on TiO_2 (rutile) (110) it formed Mo–Mo dimers oriented along the [110] direction whereas on Al_2O_3 the metal sits in the center of a square base pyramid of oxygen atoms. Copper on TiO_2(110) showed a marked tendency to aggregate in trimers or

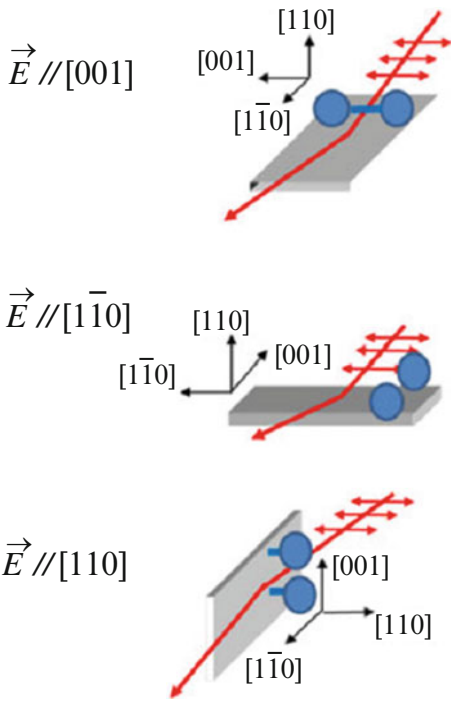

Fig. 15.2 Working principle of the PTRF-XAFS technique. By orienting the crystal surface in different ways respect to the beam polarization vector various bonds can be enhanced either parallel (*upper* and *middle panel*) or perpendicular (lower panel) to the surface. From Ref. [53]

hexamers well oriented respect to the surface and depending on the calcination temperature after deposition [59]. The pretreatment of the surface with organic compounds [60, 61] permitted to obtain dispersed metal ions in the +1 valence state. Also in the case of Ni it revealed to be extremely difficult to obtain dispersed ions on the rutile (110) surface. Koike et al. [62] reports on the determination of the Ni site for an unprecedented low coverage of 10^{13} Ni/cm^2 that fully demonstrates the effectiveness of total reflection technique in treating highly diluted systems. Ni forms chemical bonds with the bridging oxygen atoms in the surface and occupies the site that would be taken by Ti if a further layer were grown on the clean surface. A similar behavior of dispersion only at very low coverage and "cation site occupation" is reported for Ni on Al_2O_3 [63]. The metal–substrate interaction drives also the formation of metal island on the surface [64] for coverage levels of about 10^{14} Ni/cm^2 whereas for denser deposition values Ni forms three-dimensional metallic clusters.

Ni on different Al_2O_3 surfaces has also been studied upon aqueous phase deposition [65]. It was found that Ni deposits in the form α-Ni(OH)$_2$ appear on the (1–102) face whereas no deposit appears on the (0001) surface. This was a clear example on how different surfaces can lead to different reaction behavior and further examples are given in the following sections. On the subject of non-crystalline surfaces the site of Cr ions at extremely low coverage (2×10^{14} Cr/cm^2) on glassy SiO_2 has been investigated, showing that the metal acts as a

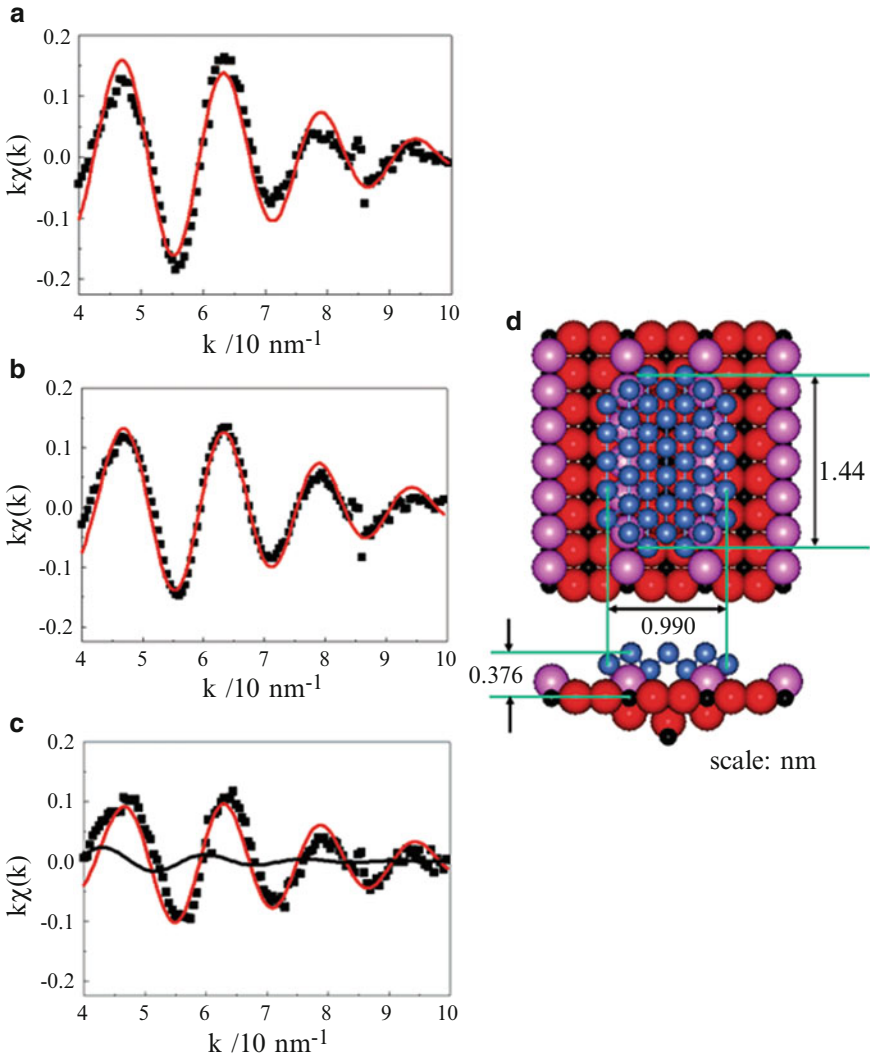

Fig. 15.3 Example of data analysis for PTRF-XAFS data. Comparison between the experimental XAS data for three independent orientations of the sample (**a**, **b**, **c**) and the theoretical XAS (*red lines*) relative to the structure shown in (**d**). Carrying out this procedure allows the determination of the structure formed on the surface using a three-dimensional information. Figure from Ref. [64]

bridge between two available O atoms on the surface and it can cycle between $^{2+}$ and $^{6+}$ valence states following exposure to O_2 or CO. [66]

This particular data collection mode has found applications not only in catalysis but also in environmental science. Indeed, the possibility of studying the interaction of single mineral surfaces with polluting species has revealed to provide a more

complete description of the binding site then the analysis of powdered samples. The interaction of arsenate with hematite (0001) and (10–12) faces was studied with polarized grazing incidence XAS [67]. The study evidenced that the rearrangement of the surfaces under the effect of moisture leads to the availability of edges of FeO_6 octahedra where arsenate species bond forming a bidentate complex. On the other hand arsenate in the case of alumina (0001) and (11–20) faces [68] and rutile (110) and (001) faces [69] was reported forms both monodentate and bidentate complexes.

15.5.2 Liquid Surfaces

A further application of polarized total reflection XAS is the analysis of liquid surfaces. In this case, being not possible to change the sample orientation respect to the beam polarization, it was this vector to be moved via a quarter wave plate. It is worth noticing that coupling measurements at low incidence angle (about 1 mrad) on a liquid surface while varying the beam polarization via a quarter wave plate represents a considerable experimental challenge. Studies have been conducted on Zn and Cu porphyrins on air/water and heptane/water interfaces. A marked dichroic behavior was observed for the 1s–$4p_z$ resonance peak appearing in the pre-edge region of both metals and that was used to determine the angle of the molecule plane respect to the interface. In the case of Zn [70, 71] Zn-TPP molecule orients parallel to the surface (and a similar behavior is reported for Zn–TPPC at the heptane–water interface) [72] whereas Zn-PP molecules appear to be tilted by an angle comprised between 57° and 43° depending on its surface concentration. For Cu porphirins CuPP and CuChl the orientation angle was found to be constant with concentration at respective values of 29° and 34° [73]. The different behavior of the orientation of these molecules was put in relation with the capability of hydration behavior of the metal and the intermolecular lateral interactions. Other studies on the hydration of Br^- ions in ionic liquids [74, 75] permitted to distinguish two sites for Br one "free" surrounded by water molecules and the other "bound" partially linked to its counter-ion. For what concerns LB films it has been shown that a considerable experimental simplification can be obtained by depositing the layers on glassy substrates and then use them in a conventional sample manipulator, so avoiding the orientation constraints posed by the liquid surface. The interaction of Zn with phospholipids (DMPA and DMPC) has been studied in Ref. [76] finding the metal coordinated with oxygen about 0.2 nm, with no particular evidence of further coordination shells whereas in the cases of Cd and Pb [77] the metals have respectively an uni-dentate and bi-dentate coordination with the stearate molecules (DSPA) of the LB film.

15.5.3 Surface Reactions

One of the peculiar aspects of ReflEXAFS is that it can provide a probe for the topmost few nm of a surface thanks to the limited extinction length of the probe beam. This has been exploited in a variety of experiments studying the reaction of the surface of a bulk sample with an external environment. Frahm and his coworkers report about a rutile TiO_2 surface intercalated with Li [78]. This is a model system for Li-ion batteries and the aim of the study was to investigate the valence state of Ti only in the surface layer where Li is inserted during the intercalation process. A specially conceived cell permitted the collection of ReflEXAFS data at different moments of the voltammetric cycle. The result is that on the surface there is a shift at lower energies of the Ti-K absorption edge meaning a reduction of the metal. The Ti valence was estimated to change from +4 to +3.6 upon Li loading. The analysis of the EXAFS region permitted moreover to identify the intercalated phase as the anatase-like $Li_{0.6}TiO_2$. The surface reduction of Ti has been successively evidenced also for Li intercalation of the Anatase form of TiO_2 and for the same process was reported on Mo on Li:MoO_3 electrodes [79, 80]. Another topic in electrochemistry studied by ReflEXAFS has been the anodic oxidation of Ag electrodes. An Ag-K edge ReflEXAFS study of was conducted with Ag electrodes immersed in 1 M NaOH aqueous solution with data collected again at different points of the voltammogram cycle [81]. It was demonstrated that the Ag oxidation of the outermost layer starts at potential values lower than the Nernst potential. The same authors in a successive paper [82] showed that for potential values less than +0.75 V the phase formed at the surface is Ag_2O whereas above that value oxygen-deficient structures are formed with Ag in a double valence Ag^+ and Ag^{3+}. Ag was also studied during dissolution in a weakly acid solution [83]. The surface layer resulted to be an Ag^+ oxide with a geometry different from that of crystalline Ag_2O, most probably an amorphous form. Surface oxidation of metal layer has also been studied by the Yoneda-XAS technique. [84] This last technique has been demonstrated to be particularly sensitive to all phases exhibiting lateral inhomogeneities as it is the case for highly disordered oxide layers (Fig. 15.4).

Air exposed Cu thin films were analyzed with a specially developed quantitative data analysis procedure. The oxide develops in two layers: an outer CuO fraction and an inner Cu_2O fraction with a thickness increasing with the exposure time. ReflEXAFS ha been applied to the study of oxidation upon annealing on Nb layers buried under Al [85]. It was shown that the buried Nb surface is stable up to 200 °C and only at 600 °C the oxide fraction is increased. A further study on surface oxidation was carried out on stainless steel samples where it was evidenced that annealing the specimens in inert gas (Ar, N_2) adding silane together with H_2 dropped considerably the amount of residual oxide at the surface [86].

Together with gas–solid and liquid–solid reactions also solid–solid reactions have been the object of ReflEXAFS studies, in particular the reaction between Al_2O_3 and NiO giving rise to the $NiAl_2O_4$ spinel. Thin films of NiO were grown on

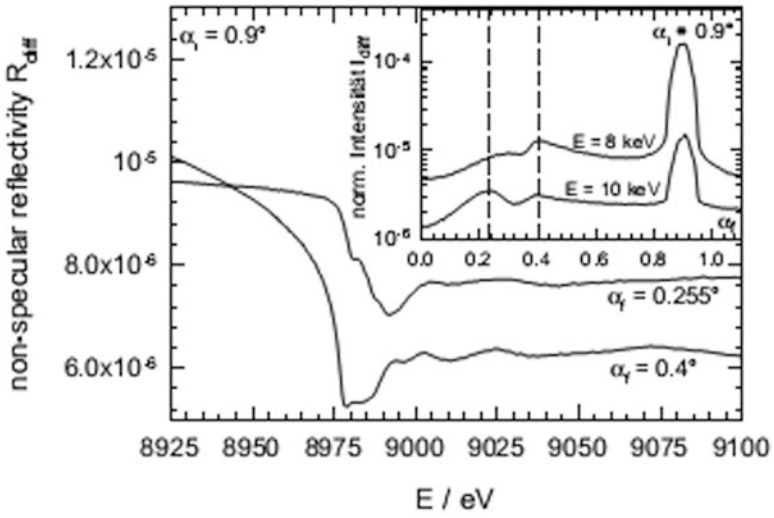

Fig. 15.4 Raw Yoneda-XAS (i.e., off specular) spectra of a Cu thin film exposed to air. The incidence angle of the probe beam was set at 0.9° whereas the exit angle was set at 0.255 or 0.4° as shown in the *inset* [84].

different surfaces of Al_2O_3 and were annealed in vacuum to trigger the reaction. In the case of the Al_2O_3(1–211) face it was shown that a treatment above 1000 °C leads to the formation of the spinel whereas at 930 °C this phase is not yet formed but a precursor phase is visible, presumably $Ni_xAl_{2-x}O_3$ [87, 88]. The reactivity depends on the face considered for Al_2O_3: the (0001) face barely reacts at 1000 °C whereas the (1–102) exhibits a good reactivity as the (1–211) face [28, 88]. A depth-resolved study was carried out by collecting data below and above the critical angle as shown in Fig. 15.5. By using the CARD code and considering a multilayer model for the sample it was evidenced an unreacted oxide phase remaining on the surface and a reacted (spinel) phase as well as an intermediate one (i.e., not simply obtainable as linear combination oxide-spinel) in depth [25, 27]. The balance of these phases is different for the two faces with the (0001) face markedly less reactive than the other.

15.5.4 Thin Films

As already pointed out in the case of adsorbates, ReflEXAFS reveals its strength in the study of deposited thin films. In this case it helps in minimizing the spurious signal from the substrate (incoherent scattering, Bragg peaks from crystalline matrices) enhancing the contribution of the layer to the total signal. An example in electrochemistry reports on Cu and Cd deposited from aqueous solution on Pt(533) surfaces studied by ReflEXAFS in situ using a specially developed

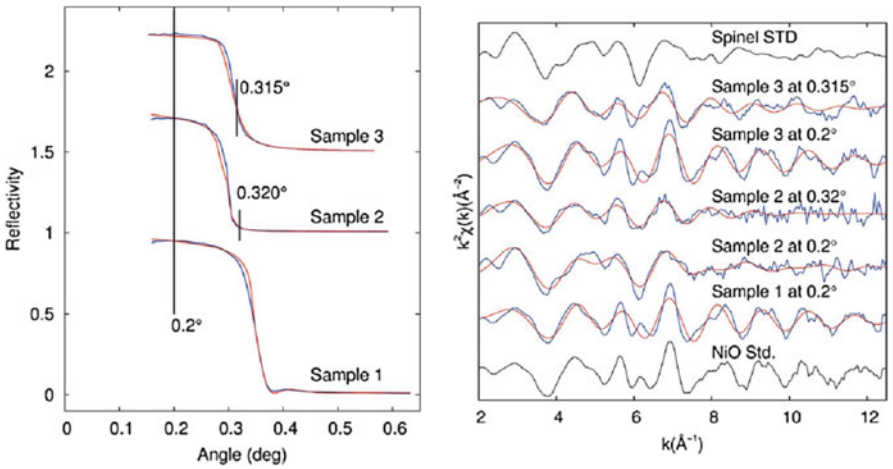

Fig. 15.5 *Right*: ReflEXAFS data (*black*) and best fit (*red*) on the surface reaction NiO-Al_2O_3. three different cases are shown here: Sample1 = pure unreacted NiO on face (1–102), Sample2 = NiO as 1) treated at 1000 °C, Sample3 = NiO on face (0001) and treated at 1000 °C. *Left*: Reflectivities at 8100 eV showing the data collection angles above and below the critical value. The differences of the ReflEXAFS spectra are due to different content of the various phases involved. Figure from Ref. [28]

deposition cell [89]. For potential values above the Nernst potential Cu forms linear aggregates at the surface terraces steps and then, for lower potentials, 2-dimensional clusters are formed that eventually merge in a complete mono-layer with a 1×1 structure. Cd has a similar behavior with the difference that the final mono-layer is not in register with the surface. Also thin films deposited in situ by radio-frequency sputtering have been extensively studied by XAS. In the case of Bi thin (6 nm) films quench-deposited at 20 K on float-glass substrates it was possible to establish a link between the irreversible increase of the resistivity that appears at about 45 K and the structure [90]. In particular it was evidenced that the film is initially amorphous and that crystallization takes place upon annealing and this structure is stable upon successive cooling. The deposition of thicker (18 nm) films leads directly to a crystalline rhombohedral phase and these films do not exhibit the irreversible resistivity soaring observed for the thinner layers [91]. In the case of Ag and Au [17] and SnN [92] thin films deposited by sputtering the fcc structures typical of the bulk form are found whereas for Ta oxide films [17, 93], the structure of the film is markedly disordered. RefleXAFS has also permitted the determination of the structure of thin films for sensors applications as in the case of Pd-diethylbiphenyl [94], Pt-diethylbiphenyl [95], and other organo-metallic Pd (II) thiol complexes [96].

A particular case of deposited thin films can be considered also the deposits of atmospheric aerosols or dusts in environmental science studies. The fact of reducing the spurious signal from the substrate by depositing the sample on a clean surface permits the collection of better quality data in cases where the amount of

sample is particularly reduced, as reported in the following studies about speciation of Fe in atmospheric dust. Urban aerosols only after 1 h of collection were analyzed, minimizing in this way the time during which possible Fe^{2+} phases could undergo reduction [97]. Fe^{3+} species were found to dominate the signal showing that the reduction takes place in a very short time. Instead, to enhance the signal from atmospheric aerosols extracted from Antarctica deep ice cores the total reflection technique was used and Fe was also found in a predominantly Fe^{3+} state [98].

15.5.5 Materials for Electronics and Optics

Materials for electronics and optics are frequently prepared as surface or subsurface (some hundreds of Å below the surface) systems. Electronic devices are realized on Silicons by doping with various techniques (ion implantation, vapor phase) whereas surface waveguides are realized on glass in the case of devices for optics. Applying ReflEXAFS to these systems permits to concentrate the beam to the layer containing the absorbing atoms and limiting the propagation of the probe beam in the substrate.

Indium doping of Silicon represents a particularly challenging topic as In has a very low solubility in this matrix. The ReflEXAFS at the In-K edge revealed that In implanted at 183 keV and 5×10^{13} at/cm^2 (i.e., at the solubility limit) is substitutional with a structure in agreement with the structural simulations, whereas the addition of C leads to the formation of In/C complexes in the matrix [99]. Raising the implantation dose at 5×10^{14} at/cm^2 leads to the formation of In clusters [100]. Adding Carbon lead to the formation of In/C complexes also at high concentration opening the route to a possible exploitation of this element as p-dopant of Si [101]. Another considerable dopant (n type) for Si is As and in recent year it has attracted the attention of the community for the realization of ultrashallow junctions. In this case As is introduced in Si by implantation at very low energy (1–3 keV) and high fluence (10^{15} at/cm^2) to realize highly doped layers (peak conc. 10^{21} at/cm^3). By using depth resolved analysis realized by collecting the data above and below the critical angle it was evidences as Arsenic partially migrates in the surface oxide of the Si substrates forming inactive oxides and As clusters [34], whereas deep in the matrix it is substitutional and linked to vacancies. As clusters are also reported in some cases also inside the Si matrix [102] and suitable thermal processes are needed to maximize the total electrically active As [103]. Always in the field of microelectronics ReflEXAFS has been used for the study of thin layers of lanthanide oxides (Yb_2O_3, Lu_2O_3, Y_2O_3) on Si as hi dielectric constant substitutes for native SiO_2. In the former two cases the structure of the epitaxial layer is close to the bulk oxide [104], whereas the Y_2O_3 case revealed a mixed Y/Si phase for the first few layers before the formation of the bulk phase [105]. In the field of materials for optics ReflEXAFS permitted the analysis of surface layers like Na-Tl ion-exchanged glasses [106] and Erbium-doped Silica-Titania-Hafnia thin films deposited by sol gel [107].

15.6 Conclusion and Perspectives

ReflEXAFS has revealed to be a powerful technique in a variety of research fields from surface chemistry to materials science. The perspectives of this experimental technique will depend critically on the evolution of the experimental apparatuses (X-ray sources and detectors) and on the improvements in data analysis.

On the first topic the advent of new rings with low horizontal emittance (see namely the design of the new ring for the European Synchrotron Radiation Facility) [108] will provide beams with a low horizontal size that will improve the quality of data collected with the samples surface perpendicular to the orbit plane. It is worth to stress here that the source brightness is a key point in the development of a ReflEXAFS instrument as the X-ray optics must provide a beam with at the same time low dimension and low divergence[1]. Also for XAS experiments on X-ray free electron lasers (X-FEL) the total reflection geometry could be exploited to minimize the local dose on flat samples. Care should be used in the design of time-resolved experiments: given that a typical FEL pulse is of the order of 100 fs this corresponds to a length of 3 mm and the beam footprint on the sample should not exceed this value, as instead it is frequently the case at synchrotron sources. A further possible field of evolution could be the use of X-ray emission spectroscopy (XES) in total reflection conditions. Here, a serious problem is posed by the geometry of the emitting portion of the sample that has the form of a long rectangle whereas a point emitter is preferred for the currently used spectrometers. Apart using a wavelength dispersive analyzer based on a cylindrical optics another interesting possible solution could be represented by solid state detectors with high energy resolution, namely superconducting transition edge sensors (TES) of superconducting tunnel junction (STJ) devices. If their use was already suggested several years ago [109], recently arrays of TES have been presented that could represent an interesting solution for XES in total reflection conditions [110].

For what concerns data analysis it has been shown that at present there are codes for a rigorous analysis of data both in fluorescence and reflectivity modes so data analysis is no longer to be considered as a critical issue. A major improvement could come from an increased quality of XAS signal simulation based on structural modeling as described in the examples above. The wide availability of codes for structural simulation based on density functional theory will help in the interpretation of the experimental data by comparison with fully relaxed bulk or surface structures. But an even more powerful could become the simulation of the XAS

[1] The low dimensions are trivially required to limit the length of the sample whereas the low divergence is required in order to keep the total reflection condition of all the portions of the beam. This is different from what realized in microfocusing beamlines where the small dimensions of the beam are realized at the expense of a considerably increased beam divergence.

spectrum using molecular dynamics [111, 112] about supported Pt nanoclusters or Zn, Fe impurities in Lead antimonate [113]. In this way the different candidate structures could be simulated with a realistic evaluation of the thermal/configurational disorder and compared in a more incisive way to the experimental results.

References

1. Feynman RP, Leighton RB, Sands M (1977) The Feynman lectures on physics. Addison Wesley, Boston
2. d'Acapito F (2003) Introduction to the ReflEXAFS technique in synchrotron radiation: fundamentals, methodologies and applications, vol 82, Conference Proceedings of the Italian Physics Society. SIF, Bologna, p 191. ISBN 88-7438-008-9
3. Parratt LG (1954) Surface studies of solids by total reflection of X-rays. Phys Rev 95:359
4. Barchewitz R, Cremonese-Visicato M, Onori G (1978) X-ray photoabsorption of solids by specular reflection. J Phys C 11:4439
5. Martens G, Rabe P (1980) EXAFS studies on superficial regions by means of total reflection. Phys Stat Solidi A58:415
6. Martens G, Rabe P (1980) EXAFS of a thin film of Cu measured by total reflection. Phys Stat Solidi A57:K31
7. Martens G, Rabe P (1981) The extended X-ray absorption fine structure in the reflectivity at the K edge of Cu. J Phys C 14:1523
8. Bosio L, Cortes R, Defrain A, Froment M (1984) Exafs from measurements of X-ray reflectivity on passivated electrodes. J Electroanal Chem 180:265
9. Poumellec B, Cortes R, Lagnel F, Tourillon G (1989) A new method to extract the X-ray absorption fine structures from the reflectivity spectra: application to the study of (Ti, Nb)O2 amorphous solid solutions. Physica B 158:282
10. Borthen P, Strehblow HH (1995) X-ray-reflectivity fine structure and EXAFS. Phys Rev B 52:3017
11. Borthen P, Strehblow HH (1995) X-ray reflectivity fine structure from homogeneous materials in the hard-energy range. J Phys Condens Matter 7:3779
12. Heald SM, Chen H, Tranquada JM (1988) Glancing-angle extended X-ray-absorption fine structure and reflectivity studies of interfacial regions. Phys Rev B 38:1016
13. Chen H (1989) Chen studies of Cu-Al interfaces using glancing angle X-ray reflectivity and XAS. Ph.D. Thesis, City University of New York
14. Heald S (1992) EXAFS at grazing incidence: data collection and analysis. Rev Sci Instrum 63:873
15. Tani K, Iwata N, Mitsueda T, Ueha M, Saisho H, Iwasaki H (2004) X-ray absorption near edge spectroscopy from reflection X-ray absorption fine structure under the grazing incidence conditions. Spectrochim Acta B 59:1221
16. Lopez-Flores V, Ansell S, Ramos S, Bowron DT, Diaz-Moreno S, Munoz-Paez A (2009) Development of ReflEXAFS data analysis for deeper surface structure studies. JPCS 190:012110
17. Lutzenkirchen-Hecht D, Frahm R (2000) Structural investigations of sputter deposited thin fims: reflection mode EXAFS, specular and non specular X-ray scattering. Physica B 283:108
18. Keil P, Lutzenkirchen-Hecht D, Frahm R (2005) Selective study of atoms in rough surfaces by means of off-specular grazing incidence XAFS. Europhys Lett 71:77
19. Keil P, Lutzenkirchen-Hecht D, Frahm R (2005) Calculation of grazing incidence EXAFS: Fresnel theory versus DWBA. Phys Scr T115:246

20. Keil P, Lutzenkirchen-Hecht D (2009) Surface-sensitive reflection-mode EXAFS from layered sample systems: the influence of surface and interface roughness. J Synchrotron Radiat 16:443
21. Sinha SK, Sirota EB, Garoff S, Stanley HB (1988) X-ray and neutron scattering from rough surfaces. Phys Rev B 38:2297
22. Nevot L, Croce P (1980) Caracterisation des surfaces par reflexion rasante de rayons X. Application a l'etude du polissage de quelques verres silicates. Revue de Physique Appliquee 15(3):761
23. Yoneda Y (1963) Anomalous surface reflection of X rays. Phys Rev 131:2010
24. Lutzenkirchen-Hecht D, Keil P, Frahm R (2007) Combining non-specular X-ray scattering and X-ray absorption spectroscopy for the investigation of buried layers. Surf Sci 601:4232
25. Benzi F, Davoli I, Rovezzi M, D'Acapito F (2008) A new procedure for the quantitative analysis of extended X-ray absorption fine structure data in total reflection geometry. Rev Sci Instrum 790:103902
26. Lutzenkirchen-Hecht D, Frahm R (2006) Time-resolved in situ investigations of reactive sputtering processes by grazing incidence X-ray absorption spectroscopy. Surf Sci 600:4380
27. The code is freely available at the address: http://www.esrf.eu/computing/scientific/CARD/CARD.html
28. Costanzo T, Ghigna P, Pin S, Spinolo G, d'Acapito F (2014) Studying the surface reaction between NiO and Al_2O_3 via total reflection EXAFS (ReflEXAFS). J Synchrotron Radiat 21:395
29. Affrossman S, Doyle S, Lamble GM, Morris MA, Roberts KJ, Sheen DB, Sherwood JN, Oldman RJ, Hall D, Davey RJ, Greaves GN (1986) The surface sensitivity of fluorescence EXAFS at reflection conditions. J Phys Colloq C8:C8–C167
30. Jiang DT, Crozier ED, Hienrich B (1991) Structure determination of metastable epitaxial Cu layers on Ag(001) by glancing-incidence X-ray-absorption fine structure. Phys Rev B 44:6401
31. Jiang DT, Crozier ED (1997) Glancing angle EXAFS of ultra thin films: negligible anomalous dispersion effects. J Phys IV France 7 Coll C2 (1997): C2–247
32. Iwasawa Y (1997) Recent progress in surface scientific approaches to oxide catalysis. Catal Surv Jpn 1:3
33. Shirai M, Nomura M, Asakura K, Iwasawa Y (1995) Development of a chamber for in situ polarized total-reflection fluorescence X-ray absorption fine structure spectroscopy. Rev Sci Instrum 66:5493
34. d'Acapito F, Milita S, Satta A, Colombo L (2007) Depth resolved study of impurity sites in low energy ion implanted As in Si. J Appl Phys 102:043524
35. Chun WJ, Shirai M, Tomishige K, Asakura K, Iwasawa Y (1996) PTRF X-ray absorption fine structure as a new technique for catalyst characterization. J Mol Catal A 107:55–65
36. Asakura K, Chun WJ, Iwasawa Y (2000) Polarization-dependent total-reflection fluorescence EXAFS study about active structures on single crystal oxides as model catalyst surfaces. Top Catal 10:209
37. Chun WJ, Tanizawa Y, Shido T, Iwasawa Y, Nomura M, Asakura K (2001) Development of an in-situ polarization dependent total-reflection fluorescence XAFS measurement system. J Synchrotron Radiat 8:168
38. Oyanagi H, Owen I, Grimshaw M, Head P, Martini M, Saito M (1995) A new apparatus for surface X-ray absorption and diffraction studies using synchrotron radiation. Rev Sci Instrum 66:5477
39. Oyanagi H (1998) A new apparatus for polarized X-ray absorption fine structure using grazing-incidence fluorescence excitation. J Synchrotron Radiat 5:48
40. Pizzini S, Roberts KJ, Greaves GN, Harris N, Moore P, Pantos E, Oldman RJ (1989) Instrumentation for glancing angle X-ray absorption spectroscopy on the synchrotron radiation source. Rev Sci Instrum 60:2525

41. Lutzenkirchen-Hecht D, Wagner R, Watenpuhl A, Frahm R (2009) The materials science X-ray beamline BL8 at the DELTA storage ring. J Synchrotron Radiat 16:264
42. Lopez-Flores V, Ansell S, Bowron DT, Diaz-Moreno S, Ramos S, Munoz-Paez A (2007) Optimized end station and operating protocols for reflection extended X-ray absorption fine structure (ReflEXAFS) investigations of surface structure at the European Synchrotron Radiation Facility beamline BM29. Rev Sci Instrum 78:013109
43. Smith AD, Roper MD, Padmore HA (1995) A ReflEXAFS apparatus for use with soft X-rays in the sub-4-keV energy range. Nucl Instrum Meth Phys Res B 97:579
44. d'Acapito F, Davoli I, Ghigna P, Mobilio S (2003) The ReflEXAFS station at the GILDA beamline (BM08) of ESRF. J Synchtrotron Rad 10:260
45. Watanabe I, Tanida H, Kawauchi S, Harada M, Nomura M (1997) X-ray absorption spectroscopy of liquid surface. Rev Sci Instrum 68:3307
46. Tanida H (2004) Total-reflection X-ray absorption fine structure on liquid surface. Spectrochim Acta B 59:1071
47. Lutzenkirchen-Hecht D, Wagner R, Bieder S, Frahm R (2013) Grazing incidence X-ray absorption spectroscopy under non-ambient conditions: Investigations of liquid surfaces at DELTA beamline 8. J Phys Conf 425:132006
48. Lutzenkirchen-Hecht D, Stotzel J, Muller O, Frahm R (2013) Surface science in sub-seconds by a combination of grazing incidence geometry and QEXAFS. J Phys Conf 425:092001
49. Lutzenkirchen-Hecht D, Stotzel J, Muller O, Frahm R (2013) Quick-Scanning QEXAFS in grazing incidence: surface science in sub-seconds. J Phys Conf 430:012124
50. Abe H, Niwa Y, Nitani H, Nomura M (2014) Development of surface sensitive DXAFS measurement method by applying Kramers-Kronig relations to total reflection spectra. J Phys Conf 502:012035
51. Rovezzi M, d'Acapito F, Patelli A, Rigato V, Salmaso G, Bontempi E, Davoli I (2006) Characterization of thermally treated Mo/Si multilayer mirrors with standing wave-assisted EXAFS. Nucl Instrum Meth Phys Res B 246:127
52. Staub U, Zaharko O, Grimmer H, Horisberger M, d'Acapito F (2001) Real-part EXAFS from multilayer Bragg reflections: a promising new EXAFS technique. Europhys Lett 56:241
53. Takakusagi S, Chun WJ, Uehara H, Asakura K, Iwasawa Y (2013) Polarization-dependent total-reflection fluorescence X-ray absorption fine structure for 3D structural determination and surface fine tuning. Top Catal 56:1477
54. Chun WJ, Asakura K, Iwasawa Y (1998) Polarization-dependent total-reflection fluorescence XAFS study of Mo oxides on a rutile TiO2(110) single crystal surface. J Phys Chem B 102:9006
55. Chun WJ, Asakura K, Iwasawa Y (1998) Anisotropic structure analysis for Mo oxides on TiO2(110) single crystal surface by polarization-dependent total-reflection fluorescence EXAFS. Chem Phys Lett 288:868
56. Chun WJ, Asakura K, Iwasawa Y (1998) The structure analysis of MoOx/TiO2 (110) by polarization-dependent totalreflection fluorescence X-ray absorption fine structure. Catal Today 44:309
57. Chun WJ, Asakura K, Iwasawa Y (2001) Anisotropic ordering of Mo species deposited on TiO2(110) characterized by polarization-dependent total reflection fluorescence EXAFS (PTRF-EXAFS). Catal Today 66:97
58. Asakura K, Ijima K (2001) Polarization-dependent EXAFS studies on the structures of Mo oxides dispersed on single crystals. J Electron Spectros Relat Phenom 119:185
59. Tanizawa Y, Shido T, Chun WJ, Asakura K, Nomura M, Iwasawa Y (2003) Three-dimensional structure analyses of Cu species dispersed on TiO2(110) surfaces studied by polarization-dependent total-reflection fluorescence X-ray absorption fine structure (PTRF-XAFS). J Phys Chem B 107:12917
60. Chun WJ, Koike Y, Ijima K, Fujikawa K, Ashima H, Nomura M, Iwasawa Y, Asakura K (2007) Preparation of atomically dispersed Cu species on a TiO2(110) surface premodified with an organic compound. Chem Phys Lett 433:345

61. Chun WJ, Koike Y, Ashima H, Kinoshita K, Ijima K, Fujikawa K, Suzuki S, Nomura M, Iwasawa Y, Asakura K (2009) Atomically dispersed Cu species on a TiO2(110) surface precovered with acetic anhydride. Chem Phys Lett 470:99
62. Koike Y, Ijima K, Chun WJ, Ashima H, Yamamoto T, Fujikawa K, Suzuki S, Iwasawa Y, Nomura M, Asakura K (2006) Structure of low coverage Ni atoms on the TiO2 (110) surface – polarization dependent total-reflection fluorescence EXAFS study. Chem Phys Lett 421:27
63. Ijima K, Koike Y, Chun WJ, Saito Y, Tanizawa Y, Shido T, Iwasawa Y, Nomura M, Asakura K (2004) A local structure of low coverage Ni species on the a-Al2O3 (0001) surface – a polarization dependent EXAFS study. Chem Phys Lett 384:134
64. Koike Y, Fujikawa K, Suzuki S, Chun WJ, Ijima K, Nomura M, Iwasawa Y, Asakura K (2008) Origin of self-regulated cluster growth on the TiO2(110) surface studied using polarization-dependent total reflection fluorescence XAFS. J Phys Chem C112:4667
65. Tougerti A, Llorens I, d'Acapito F, Fonda E, Hazemann J-L, Joly Y, Thiaudiere D, Che M, Carrier X (2012) Surface science approach to the solid–liquid interface: surface-dependent precipitation of Ni(OH)2 on a-Al2O3 surfaces. Angew Chem 51:7697
66. Agostini G, Groppo E, Bordiga S, Zecchina A, Prestipino C, d'Acapito F, van Kimmenade E, Thulne PC, Niemantsverdriet JW, Lamberti C (2007) Reactivity of Cr species grafted on SiO2/Si(100) surface: a reflection extended X-ray absorption fine structure study down to the submonolayer regime. J Phys Chem C 111:16437
67. Waychunas G, Trainor T, Eng P, Catalano J, Brown G, Davis J, Rogers J, Bargar J (2005) Surface complexation studied via combined grazing-incidence EXAFS and surface diffraction: arsenate on hematite (0001) and (10–12). Anal Bioanal Chem 383:12
68. Zhang M, He G, Pan G (2014) Structure and stability of arsenate adsorbed onα-Al2O3 single-crystal surfaces investigated using grazing-incidence EXAFS measurement and DFT calculation. Chem Geol 389:104
69. Zhang M, He G, Pan G (2015) Binding mechanism of arsenate on rutile (110) and (001) planes studied using grazingincidence EXAFS measurement and DFT calculation. Chemosphere 122:199
70. Tanida H, Nagatani H, Watanabe I (2003) Polarized total-reflection X-ray absorption fine structure for self-assembled monolayer of zinc porphyrin at air–water interface. J Chem Phys 118:10369
71. Nagatani H, Tanida IH, Ozeki T, Watanabe J (2006) Zinc(II) porphyrins at the air-water interface as studied by polarized total-reflection X-ray absorption fine structure. Langmuir 22:209
72. Nagatani H, Tanida H, Harada M, Asada M, Sagara T (2010) Polarized total-reflection X-ray absorption fine structure of zinc(II) porphyrin at the heptane-water interface. J Phys Chem C 114:18583
73. Nagatani H, Tanida H, Watanabe I, Sagara T (2009) Extended X-ray absorption fine structure of copper(ii) complexes at the air–water interface by a polarized total-reflection X-ray absorption technique. Analyt Sci 25:475
74. Imai Y, Li HH, Takumi H, Tanida H, Watanabe I, Takiue T, Matsubara H, Aratono M (2012) Study on the distribution of binary mixed counterions in surfactant adsorbed films by total reflection XAFS measurements. J Colloid Interface Sci 388:219
75. Nagatani H, Harada M, Tanida H, Sakae H, Imura H (2014) Coordination structure of bromide ions associated with hexyltrimethylammonium cations at liquid–liquid interfaces under potentiostatic control as studied by totalreflection X-ray absorption fine structure. J Chem Phys 140:101101
76. d'Acapito F, Emelianov I, Relini A, Cavatorta P, Gliozzi A, Minicozzi V, Morante S, Solari PL, Rolandi R (2002) Total external reflection X-ray absorption spectroscopy reveals a zinc coordination shell in phospholipid Langmuir-Blodgett films. Langmuir 18:5277
77. Bergamino M, Relini A, Rispoli P, Giachini L, d'Acapito F, Rolandi R (2013) An EXAFS study of the binding of Cd and Pb ions to lipid films. Eur Phys J E 36:102

78. Lutzenkirchen-Hecht D, Wagemaker M, Keil P, van Well AA, Frahm R (2003) Ex situ reflection mode EXAFS at the Ti Kedge of lithium intercalated TiO2 rutile. Surf Sci 538:10–22
79. Wagemaker M, Lutzenkirchen-Hecht D, Keil P, van Well AA, Frahm R (2003) Quasi-in-situ reflection mode XANES at the Ti K-edge of lithium intercalated TiO2 rutile and anatase. Physica B 336:118
80. Haake U, Lutzenkirchen-Hecht D, Frahm R (2006) In situ electrochemical lithium intercalation into amorphous oxide thin films. Surf Interface Anal 38:330
81. Lutzenkirchen-Hecht D, Strehblow H-H (2006) The anodic oxidation of silver in 1M NaOH: electrochemistry, ex situ XPS and in situ X-ray absorption spectroscopy. Surf Interface Anal 38:686
82. Lutzenkirchen-Hecht D, Strehblow H-H (2009) Anodic silver (II) oxides investigated by combined electrochemistry, ex situ XPS and in situ X-ray absorption spectroscopy. Surf Interface Anal 41:820
83. Lutzenkirchen-Hecht D, Frahm R (2005) Reflection mode X-ray absorption spectroscopy: new applications in surface science research. Physica B 357:213
84. Keil P, Frahm R, Lutzenkirchen-Hecht D (2010) Native oxidation of sputter deposited polycrystalline copper thin films during short and long exposure times: comparative investigation by specular and non-specular grazing incidence X-ray absorption spectroscopy. Corros Sci 52:1305
85. d'Acapito F, Mobilio S, Cikmacs P, Merlo V, Davoli I (2000) Temperature modification of the Nb oxidation at the Nb/Al interface studied by reflEXAFS. Surf Sci 468:77
86. Lutzenkirchen-Hecht D, Wulff D, Wagner R, Frahm R, Hollander U, Maier HJ (2014) Thermal anti-oxidation treatment of CrNi-steels as studied by EXAFS in reflection mode: the influence of monosilane additions in the gas atmosphere of a continuous annealing furnace. J Mater Sci 49:5454
87. d'Acapito F, Ghigna P, Alessandri I, Cardelli A, Davoli I (2003) Probing the initial stages of solid-state reactions by total reflection EXAFS (reflEXAFS). Nucl Instrum Meth Phys Res B 200:421
88. Ghigna P, Spinolo G, Alessandri I, Davoli I, d'Acapito F (2003) Do we have a probe for the initial stages of solid state reactions? Phys Chem Chem Phys 5:2244
89. Prinz H, Strehblow HH (2002) The structure of Cu- and Cd-UPD-layers on a stepped Pt(533) single crystal surface studied by grazing incidence XAFS, XRD and XPS. Electrochim Acta 47:3093
90. Markert C, Lutzenkirchen-Hecht D, Wagnerand R, Frahm R (2009) In situ surface-sensitive X-ray investigations of thin quench condensed bismuth films. Eur Phys Lett 86:46007
91. Lutzenkirchen-Hecht D, Markert C, Wagner R, Frahm R (2009) In-situ investigation of Bi thin film condensation by surface sensitive X-ray absorption spectroscopy at cryogenic temperatures. J Phys Conf 190:012114
92. Lutzenkirchen-Hecht D, Frahm R (2005) Structure of reactively sputter deposited tin-nitride thin films: a combined X-ray photoelectron spectroscopy, in situ X-ray reflectivity and X-ray absorption spectroscopy study. Thin Solid Films 493:67
93. Bruder K, Keil P, Lutzenkirchen-Hecht D, Frahm R (2005) In situ investigations of thin film formation by reactive sputtering. Phys Scr T115:963
94. d'Acapito F, Fratoddi I, d'Amato R, Russo MV, Contini G, Davoli I, Mobilio S, Polzonetti G (2004) Structure of a monolayer of Pd-diethynylbiphenyl deposited on chromium studied by total reflection EXAFS. Sensors Actuators B 100:131
95. Battocchio C, d'Acapito F, Smolentsev G, Soldatov AV, Fratoddi I, Contini G, Davoli I, Polzonetti G, Mobilio S (2006) XAS study of a Pt-containing rod-like organometallic polymer. Chem Phys 325:422
96. Battocchio C, Fratoddi I, Venditti I, Yarzhemsky VG, Norov YV, Russo MV, Polzonetti G (2011) EXAFS in total reflection (reflEXAFS) for the study of organometallic Pd(II) thiol complexes based self-assembled monolayers on gold. Chem Phys 379:92

97. Fittschen UEA, Meirer F, Streli C, Wobrauschek P, Thiele J, Falkenberg G, Pepponi G (2008) Characterization of atmospheric aerosols using synchrotron radiation total reflection X-ray fluorescence and Fe K-edge total reflection X-ray fluorescence-X-ray absorption near-edge structure. Spectrochim Acta B 63:1489
98. Cibin G, Marcelli A, Maggi V, Sala M, Marino F, Delmonte B, Albani S, Pignotti S (2008) First combined total reflection X-ray fluorescence and grazing incidence X-ray absorption spectroscopy characterization of aeolian dust archived in Antarctica and Alpine deep ice cores. Spectrochim Acta B 63:1503
99. d'Acapito F, Shimizu Y, Scalese S, Italia M, Alippi P, Grasso S (2006) Experimental determination of the local geometry around In and In–C complexes in Si. Appl Phys Lett 88:212102
100. d'Acapito F, Golosio B, Shimizu Y, Scalese S, Italia M, Alippi P, Grasso S (2007) The site of in dopants. In: Si, AIP Conference Proceedings, CP882, X-ray Absorption Fine Structure—XAFS13, vol 375
101. d'Acapito F, Shimizu Y, Scalese S, Italia M, Alippi P, Grasso S (2006) The effect of thermal treatments on the local geometry around indium in In and In + C high dose implanted Si. Nucl Instrum Meth Phys Res B 253:59
102. d'Acapito F, Maurizio C, Malvestuto M (2004) The atomic site of As implanted in Si at ultra-low energies. Mat Sci Eng B 114–115:386
103. Giubertoni D, Pepponi G, Bersani M, Gennaro S, d'Acapito F, Doherty R, Foad MA (2006) An EXAFS investigation of arsenic shallow implant activation in silicon after laser sub-melt annealing. Nucl Instrum Meth Phys Res B 253:9
104. Malvestuto M, Scarel G, Wiemer C, Fanciulli M, d'Acapito F, Boscherini F (2006) X-ray absorption spectroscopy study of Yb2O3 and Lu2O3 thin films deposited on Si(100) by atomic layer deposition. Nucl Instrum Meth Phys Res B 246:90
105. Malvestuto M, Carboni R, Boscherini F, d'Acapito F, Spiga S, Fanciulli M, Dimoulas A, Vellianitis G, Mavrou G (2005) X-ray absorption study of the growth of Y_2O_3 on Si(001). Phys Rev B 71:075318
106. Maurizio C, d'Acapito F, Ghibaudo E, Broquin JE (2008) Tl ion-exchange borosilicate glass: investigation of the Tl site by X-ray absorption spectroscopy. J Non-Cryst Solids 354:124
107. d'Acapito F, Marques AC, Santos LF, Almeida RM (2008) EXAFS study of the Er3+ ion coordination in SiO_2–TiO_2–HfO_2 sol–gel films. J Non Cryst Solids 354:4940
108. ESRF upgrade programme phase II (2015–2022) technical design study. Available at http://www.esrf.eu/home/orange-book.html
109. d'Acapito F, Maurizio C (2004) Applications of low-temperature detectors to synchrotron radiation. Nucl Instrum Meth Phys Res A 520:602
110. Uhlig J, Doriese WB, Fowler JW, Swetz DS, Jaye C, Fischer DA, Reintsema CD, Bennett DA, Vale LR, Mandal U, O'Neil GC, Miaja-Avila L, Joe YI, El Nahhas A, Fullagar W, Parnefjord Gustafsson F, Sundstroem V, Kurunthu D, Hilton GC, Schmidt DR, Ullom JN (2015) High-resolution X-ray emission spectroscopy with transition-edge sensors: present performance and future potential. J Synchrotron Radiat 22:766
111. d'Acapito F (2011) Advanced methods for the analysis of X-ray absorption spectroscopy data applied to semiconductors. Semicond Sci Technol 26:064004
112. Vila F, Rehr JJ, Kas J, Nuzzo RG, Frenkel AI (2008) Dynamic structure in supported Pt nanoclusters: real-time density functional theory and X-ray spectroscopy simulations. Phys Rev B 78:121404 (R)
113. Cartechini L, Rosi F, Miliani C, d'Acapito F, Brunetti BG, Sgamellotti A (2011) Modified Naples yellow in Renaissance majolica: study of Pb–Sb–Zn and Pb–Sb–Fe ternary pyroantimonates by X-ray absorption spectroscopy. J Anal At Spectrom 26:2500

Chapter 16
High-Energy Resolution XAS

Frank de Groot

16.1 Introduction

High-energy resolution X-ray absorption refers to the measurement of XANES spectra with the use of a detector signal that is measured coherently with the XANES measurement. The detector signal can be fluorescence, which is known under the name High-Energy Resolution Fluorescence Detected (HERFD) XANES. Similarly one can define High-Energy Resolution Auger Detection (HERAD) XANES.

The first HERFD experiments have been performed by Hamalainen and coworkers [1]. They recorded the dysprosium L_3 edge by detecting the 2p3d fluorescence with an energy resolution better than the core hole lifetime broadening. They indeed observed a much more structured spectral shape with respect to the conventional XANES spectrum. A similar experiment was performed on the Mn K pre-edge [2]. The first spectra using nonradiative decay channels have been published by the groups of Sham [3] and Drube [4, 5].

16.2 Principle of High-Resolution XANES

In a HERFD experiment, a XANES spectrum is measured with a resolution that appears sharper than the lifetime broadening of the core hole. HERFD spectra are popular for the K edges of 3d transition metals and also for the $L_{2,3}$ edges of rare

F. de Groot (✉)
Inorganic Chemistry and Catalysis, Utrecht University, 3584 CG Utrecht, The Netherlands
e-mail: f.m.f.degroot@uu.nl

Y. Iwasawa et al. (eds.), *XAFS Techniques for Catalysts, Nanomaterials, and Surfaces*, DOI 10.1007/978-3-319-43866-5_16

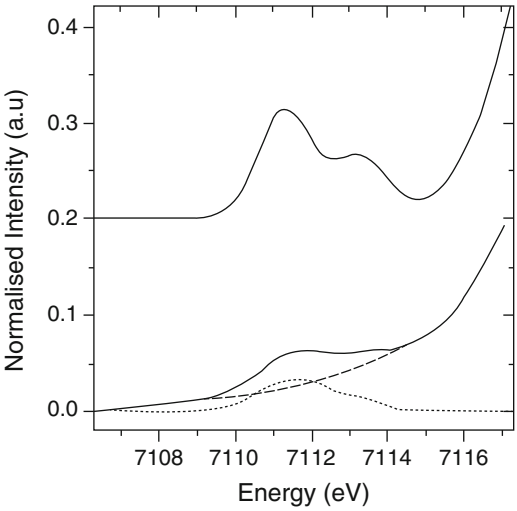

Fig. 16.1 HERFD XANES (*top*) and normal XANES (*bottom*) at the iron K edge of Fe_2SiO_4 [6]

earths and actinides. The quadrupole pre-edge structures in these edges appear much sharper in the HERFD spectra, see for example the iron pre-edge of Fe_2SiO_4 in Fig. 16.1 [6]. The sharper features allow for a much more detailed analysis.

The main principle of HERFD XANES can best be described assuming a single 1s resonance state at the edge that is linked to a single 1s2p X-ray emission decay final state [7]. By tuning the incident photon energy close to the 1s absorption state, the X-ray absorption and X-ray emission processes occur coherently and the overall 1s2p process is described by the Kramers–Heisenberg formula:

$$F(\Omega,\omega)=\sum_j\left|\sum_i\frac{\langle j|T_2|i\rangle\langle i|T_1|g\rangle}{E_\mathrm{g}+\hbar\Omega-E_i+i\Gamma_i}\right|^2\delta\left(E_\mathrm{g}+\hbar\Omega-E_j-\hbar\omega\right)$$

This formula forms the basis of all resonant X-ray processes. The scattering cross section F is given as a function of the excitation energy (Ω) and the emission energy (ω). The ground state (g) is excited to an intermediate state (i), characterized by a 1s core hole via the dipole operator (T_1). The second dipole operator (T_2) describes the X-ray emission decay to the final state (j) with a 2p core hole. The denominator contains the binding energy of the core hole state and its lifetime broadening. A resonance occurs if the excitation energy is equal to the 1s edge. The general spectral landscape can be viewed as a two-dimensional space with axis Ω and ω.

Figure 16.2 shows a contour-plot of the resonant inelastic X-ray scattering (RIXS) plane indicating a single core hole resonance coupled to a single final state [8]. The gray area is the peak maximum, which is set at 100. The first contour-line is set at 64 and each following line represents respectively 32, 16, 8, etc., as indicated in the figure. The horizontal axis shows the X-ray excitation energy. The X-ray absorption spectrum consists of a single resonance with an

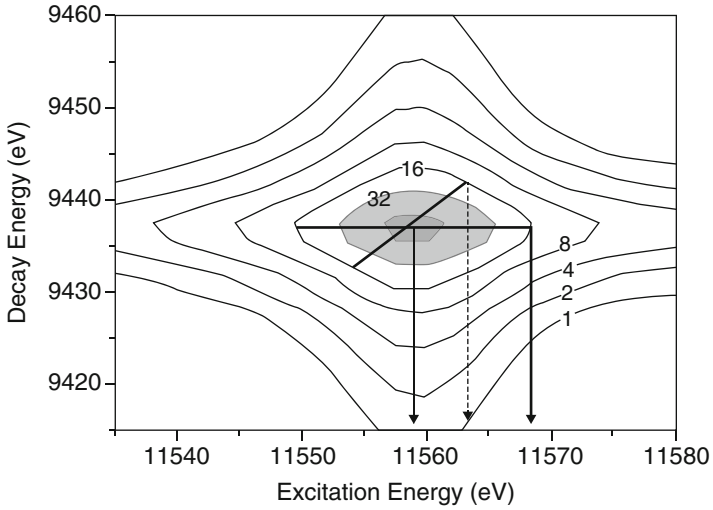

Fig. 16.2 Two-dimensional contour plot of the RIXS plane of a single resonance and a single final state [8]

energy of approximately 11,560 eV. The vertical axis shows the final state energies with a maximum of the X-ray emission decay at 2123 eV.

Instead of normal X-ray absorption, one can measure the X-ray absorption spectrum at a fixed emission energy. This relates to the diagonal line in Fig. 16.2. The effective lifetime related broadening can be derived from the figure, and is given by

$$\Gamma = 1/\sqrt{\Gamma_i^{-2} + \Gamma_j^{-2}}$$

If the intermediate state lifetime broadening is much large than the final state lifetime broadening the total HERFD lifetime is approximately equal to the final state lifetime broadening. The Lorentzian broadening thus decreases in comparing normal X-ray absorption and selective X-ray absorption. In case of a single resonance this is a real effect that can be exploited in HERFD experiments.

In the case of a series of resonances with, in particular a series of different final state energies, the situation becomes more complex. Figure 16.3 shows the experimental data of 2p4f quadrupole pre-edge of LaF_3 at 460 eV [9]. The vertical X-ray emission axis shows the 2p5d decay channel centered at 0 eV. Detecting the HERFD XANES with such RIXS plane yields a number of pre-edge peaks related to the multiple X-ray emission channels, as indicated in the panel on the right. Note that this HERFD XANES spectrum is NOT the same as the XANES spectrum itself. The XANES spectrum consists of only a single peak at 460 eV; all the other

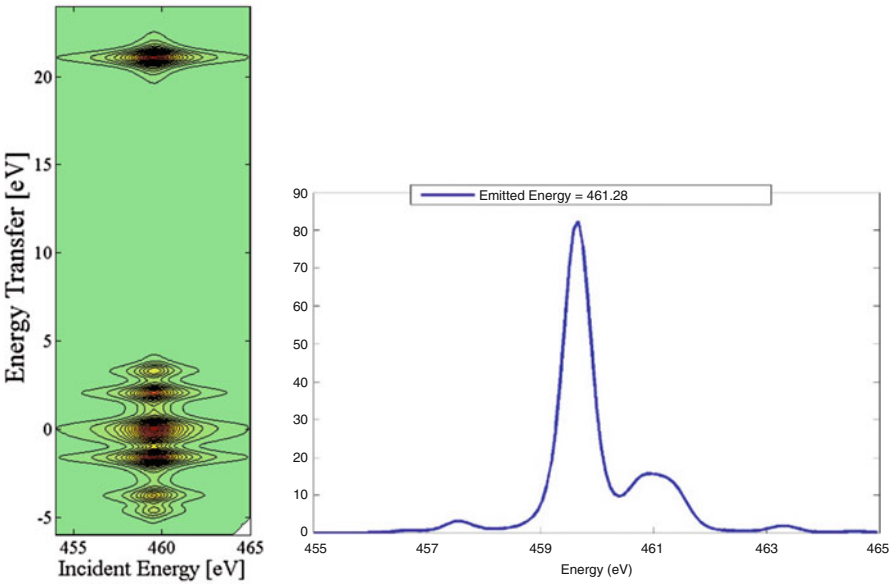

Fig. 16.3 Two-dimensional contour plot of the 2p5d RIXS plane of a single XANES excitation at 460 eV coupled to multiple X-ray emission final states. The HERFD cross section yields a spectrum with many peaks, which in this example is not the same as the XANES spectrum [9]

structures are tails from different X-ray emission channels. This is an important warning that HERFD spectra should always be treated carefully in their approximation as pure XANES spectra.

16.3 Resonant Inelastic X-ray Scattering

A general way to present RIXS is by showing 2D plots that provide a comprehensive picture of the 1s X-ray absorption and the 1s2p X-ray emission processes. For quantitative purposes it is, however, more convenient to compare 1D spectral shapes. There are a number of ways one can create spectral shapes out of the 2D images [10]. In Fig. 16.4, three cross sections are shown, respectively:

- The constant incident energy (CIE) spectrum, a vertical cross section at fixed excitation energy (7112 eV in the figure). This relates to resonant X-ray emission spectra.
- The constant transferred energy (CTE) spectra, a horizontal cross section at a constant transferred energy in Fig. 16.4a. In Fig. 16.4b, the CTE scan is a diagonal cross section. A constant transferred energy implies that for all excitation energies the same final states are probed. This could also be called constant final state (CFS) spectra.

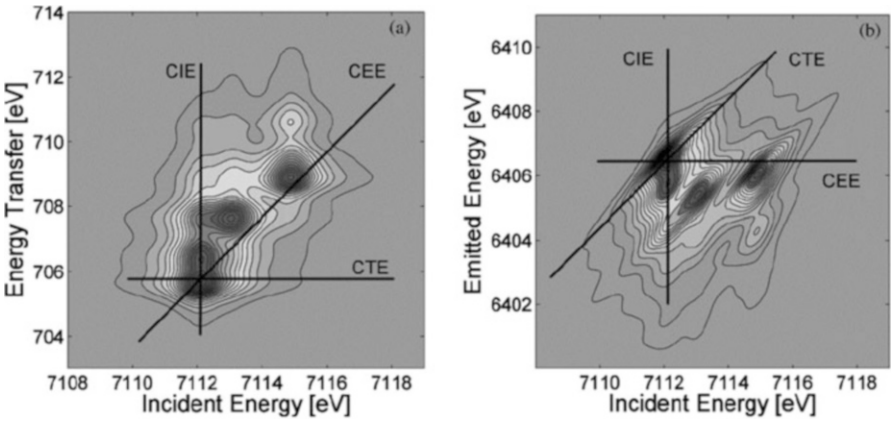

Fig. 16.4 Two-dimensional contour plot of the 1s2p RIXS plane of an iron compound. RIXS planes can be given with two different choices for the axes, where the vertical axis can be used for the energy transfer (*left*) or for the emitted energy (*right*). Three cross sections can be made, respectively the constant emission energy (CEE) that identifies with the HERFD spectrum, the constant incident energy (CIE) spectrum and the constant transfer energy (CTE) spectrum [10]

- The constant emission energy (CEE) spectra: a diagonal cross section at a constant emission energy in Fig. 16.4a. In Fig. 16.4b, the CEE scan is a horizontal cross section at fixed emission energy. This relates to the HERFD spectrum the so-called "lifetime."

16.4 Using the Chemical Options of the RIXS Plane

There are a number of ways in which one can use the RIXS planes to derive detailed information. We will briefly mention these options:

16.4.1 Valence Selective X-ray Absorption

If there is a valence shift in the X-ray emission energies of for example Fe^{2+} and Fe^{3+}, one can use the separate resonances to selective detect the XANES spectra of Fe^{2+} and Fe^{3+} in the same material. This has been demonstrated for the case of Prussian blue that contains a combination of Fe^{2+} and Fe^{3+} sites [11]. In case of an active catalyst one can track both signals and as such follow the time-evolution of the valence selective XANES spectra. In principle this also applies for the EXAFS spectra as has been shown in Ref. 11.

16.4.2 Spin Selective X-ray Absorption

Using the 1s3p X-ray emission channel, the main peak and the satellite are correlated with the spin state of the metal ion. As such one can distinguish different spin states in the X-ray absorption spectrum. It can be shown that spin selective X-ray absorption relates to the local spin moment and is essentially the same for a paramagnet and a ferromagnet [12].

16.5 Analysis of HERFD Spectra of the Pre-edge Peaks of Transition Metal K Edges

Over the last years, the use of HERFD XANES has greatly improved our knowledge of the 3d transition metal K pre-edge structures. In short the pre-edges can be understood as follows. For all systems there is the 1s3d quadrupole transition directly into the empty 3d states. This is essentially an atomic transition that has the same strength for any 3d valence hole. The pre-edge fine structure can be calculated with crystal field multiplet models. At higher energy there is the 1s4p dipole transition that defines the main K edge. The main K edge structure can be calculated with, for example, DFT based models such as band structure and multiple scattering [13].

Next there are a few options:

(a) If the system is divalent, has a metal ion with inversion symmetry, and has isolated transition metal ions, no additional features are present.
(b) If the metal ion has no inversion symmetry, the metal 3d states mix with the metal 4p states. This implies that there are dipole transitions to the pre-edge and the pre-edge intensity will strongly increase in intensity.
(c) If the metal ion has a trivalent or tetravalent nature, contains ligand bridged metal sites, and has inversion symmetry, non-local peaks will appear in the pre-edge region. The non-local peaks typically appear at 2.5 eV higher energy, and this energy difference is related to the additional core hole potential of the 3d excitonic states.

Figure 16.5 shows the RIXS planes of two low-spin Co(III) systems. The system that contains isolated Co ions only shows the quadrupole peak. The solid state oxide system that contain close Co-O-Co bonds show an additional peak at 2.5 eV higher excitation energy, related to a non-local excitation: The 1s core hole is dipole excited to a 4p state that hybridizes with the 3d-band of a cobalt ion that is close by. The energy of this non-local peak has higher excitation energy because the local 1s3d quadrupole peak is pulled down by the core hole potential [14].

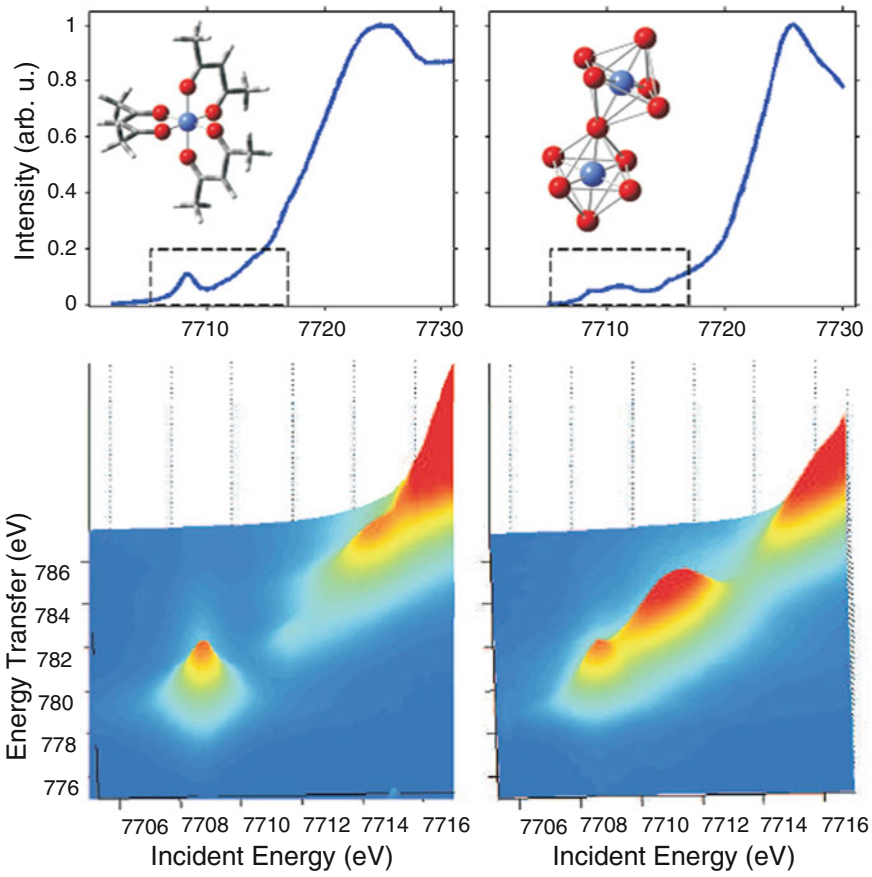

Fig. 16.5 Two-dimensional contour plot of the 1s2p RIXS plane of two low-spin Co(III) systems, an isolated molecular system (*left*) and a solid state oxide system (*right*). The solid state spectrum has an additional peak related to the non-local transition [14]

References

1. Hamalainen K, Siddons DP, Hastings JB, Berman LE (1991) Elimination of the inner-shell lifetime broadening in X-ray-absorption spectroscopy. Phys Rev Lett 67:2850
2. Hamalainen K, Kao CC, Hastings JB, Siddons DP, Berman LE, Stojanoff V, Cramer SP (1992) Spin-dependent X-ray absorption of MnO and MnF2. Phys Rev B 46:14274
3. Sham TK, Ohta T, Yokoyama J, Takada Y, Kitajima Y, Funabashi M, Kuroda H (1990) Ru *L*-edge X-ray absorption near edge structures (XANES) from Ru $LM_{4,5}M_{4,5}$ and $M_{4,5}N_{4,5}N_{4,5}$ auger yields. J Electron Spectrosc Relat Phenom 53:177
4. Drube W, Treusch R, Materlik G (1995) Nonradiative X-ray resonant Raman scattering from solids. Rev Sci Instrum 66:1616
5. Drube W, Treusch R, Sham TK, Bzowski A, Soldatov AV (1998) Sublifetime-resolution Ag L3-edge XANES studies of Ag-Au alloys. Phys Rev B 58:6871

6. Heijboer WM, Glatzel P, Sawant KR, Lobo RF, Bergmann U, Barrea RA, Koningsberger DC, Weckhuysen BM, de Groot FMF (2004) Kβ-detected XANES of framework-substituted FeZSM-5 zeolites. J Phys Chem B 108:10002
7. de Groot F, Kotani A (2008) Core level spectroscopy of solids. Taylor and Francis CRC Press, Boca Raton, FL
8. de Groot FMF, Krisch MH, Vogel J (2002) Spectral sharpening of the Pt *L* edges by high-resolution X-ray emission. Phys Rev B 66:195112
9. Suljoti E, de Groot FMF, Nagasono M, Glatzel P, Hennies F, Deppe M, Pietzsch A, Sonntag B, Fohlisch A, Wurth W (2009) Spin-orbit mediated interference in the radiative and nonradiative channels of the La 4d core resonances. Phys Rev Lett 103:137401, E. Suljoti et al. (unpublished)
10. de Groot FMF, Glatzel P, Bergmann U, van Aken PA, Barrea RA, Klemme S, Havecker M, Knop-Gericke A, Heijboer WM, Weckhuysen BM (2005) 1s2p resonant inelastic X-ray scattering of iron oxides. J Phys Chem B 109:20751
11. Glatzel P, Jacquamet L, Bergmann U, de Groot FMF, Cramer SP (2002) Site-selective EXAFS in mixed-valent compounds using HERFD. Inorg Chem 41:3121
12. de Groot FMF, Pizzini S, Fontaine A, Hämäläinen K, Kao CC, Hastings JB (1995) Local-spin-selective X-ray absorption and X-ray MCD of MnP. Phys Rev B 51:1045
13. de Groot F, Vankó G, Glatzel P (2009) The 1s X-ray absorption pre-edge structures in transition metal oxides. J Phys Condens Matter 21:104207
14. Vankó G, de Groot FMF, Huotari S, Cava RJ, Lorenz T, Reuther M (2008) Intersite 4p-3d hybridization in cobalt oxides: a resonant X-ray emission spectroscopy study. Preprint arXiv:0802.2744

Chapter 17
Nonresonant Inelastic X-ray Scattering and X-ray Raman Scattering

Timothy T. Fister

17.1 Introduction

In analogy to the connections between Raman scattering and absorption in the optical regime, X-ray Raman scattering (XRS) is an alternative to X-ray absorption spectroscopy, particularly for sub-keV excitations. XRS is the nonresonant inelastic X-ray scattering (NIXS, or NRIXS) from core or semi-core electrons and has a similar energy-dependence as X-ray absorption, albeit with a much smaller overall cross section. However, as a high-energy photon-in/photon-out approach, XRS has found widespread use for samples at extreme conditions, such as high pressure experiments in diamond anvil cells, as well as samples incompatible with vacuum conditions, like many liquids. Compared to absorption spectroscopy, XRS has key technical advantages beyond bulk sensitivity, including lack of self-absorption and the ability to access dipole-forbidden final states in certain cases. It also shares many of the same components as hard X-ray absorption/emission spectroscopy and has found a niche as a complementary technique available at multiple synchrotron facilities worldwide [1–9].

17.2 Physics of X-ray Raman scattering

NIXS has been used to measure a wide range of phenomena, ranging from acoustic excitations at meV losses to Compton scattering typically measured at keV energy scales. In general, NIXS measures the fraction of X-rays scattered into a solid angle, $d\Omega$, within a range of energy loss, $d(E_f - E_i) = d(\hbar\omega)$. This double differential

T.T. Fister (✉)
Chemical Sciences and Engineering Division, Argonne National Laboratory, Argonne, IL, USA
e-mail: fister@anl.gov

Y. Iwasawa et al. (eds.), *XAFS Techniques for Catalysts, Nanomaterials, and Surfaces*, DOI 10.1007/978-3-319-43866-5_17

cross section is equal to a static contribution from Thomson scattering modulated by the dynamic structure factor $S(\vec{q},\omega)$, i.e.,

$$\frac{d^2\sigma}{d\Omega d\omega} = \left(\frac{d\sigma}{d\Omega}\right)_{\text{Th}} S(\vec{q},\omega), \tag{17.1}$$

where $\vec{q}$ is the X-ray momentum transfer and ω is the energy loss term. Using Fermi's Golden Rule, the dynamic structure factor can be written in terms of the electron's matrix element, with a delta function enforcing energy conservation:

$$S(\vec{q},\omega) = \sum_f \left|\langle f|e^{i\vec{q}\cdot\vec{r}}|i\rangle\right|^2 \delta(E_\text{f} - E_\text{i} - \hbar\omega). \tag{17.2}$$

When q^{-1} is smaller than the size of the initial (or final) state, Eq. (17.2) can be approximated by the leading term in the expansion of $e^{i\vec{q}\cdot\vec{r}}$. In this so-called dipole approximation, dynamic structure factor is proportional to the absorption coefficient, μ, with the direction of $\vec{q}$ playing the role of X-ray polarization in XAS.

$$\begin{aligned} S(\vec{q},\omega) &= \sum_f \left|\langle f|1 + i\vec{q}\cdot\vec{r} - (\vec{q}\cdot\vec{r})^2 + \cdots|i\rangle\right|^2 \delta(E_\text{f} - E_\text{i} - \hbar\omega) \\ &\times \underset{qa\ll 1}{\rightarrow} \sum_f \left|\langle f|\vec{q}\cdot\vec{r}|i\rangle\right|^2 \delta(E_\text{f} - E_\text{i} - \hbar\omega) \propto \mu(\omega) \\ &= \sum_f \left|\langle f|\hat{\varepsilon}\cdot\vec{r}|i\rangle\right|^2 \delta(E_\text{f} - E_\text{i} - \hbar\omega) \end{aligned} \tag{17.3}$$

Higher-order multipole terms in the matrix element give rise to dipole-forbidden transitions that are inaccessible to XAS. This unique feature is discussed in Sect. 17.3.

The physical process for XRS is intuitively similar to XAS and is illustrated in Fig. 17.1a. Rather than being absorbed, a photon loses a fraction of its energy during scattering with a bound electron. When that energy transferred exceeds that electron's binding energy, it is excited to some final state, modulated by matrix element shown in Eqs. (17.2) and (17.3), leading to a similar step-edge as XAFS. That same photon could scatter from any of the other electrons with lower binding energies though, so the XRS signal typically coincides with a smoothly varying Compton background as seen in Fig. 17.1.

Near-edge structure can be easily extracted by fitting this background or by calculating the Compton profile using the impulse approximation. Extended fine structure can even be extracted [10–15], in analogy to EXAFS, i.e.,

$$S(q,\omega) = S_0(q,\omega)[1 + \chi(q,\omega)] \sim \mu(\omega) = \mu_0[1 + \chi(\omega)] \tag{17.4}$$

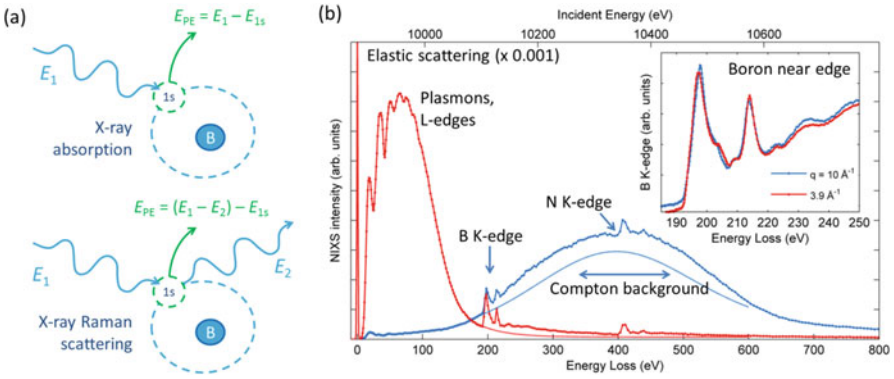

Fig. 17.1 (**a**) Illustration comparing XAS and XRS. (**b**) Inelastic scattering from hexagonal BN. The core-level edges and the Compton background are labeled for reference. The *inset* shows fine structure near the B K-edge. The scattered energy was fixed at 9890 eV (near backscatter for the Si 555 analyzer reflection) and the incident energy is shown at the top axis

Both the fine structure and atomic background (S_0) can be calculated using a Greens function approach analogous to XAFS methods [16, 17] or using DFT-based approaches. The contributions to the atomic background S_0 include valence and core electrons, requiring careful modeling and background subtraction. Methods for modeling and fitting the Compton background to extract the XRS signal has been described previously by Sternemann [18], Huotari [11], and Sahl [19].

17.3 Measuring XRS

Even when integrated over all q, the cross section for NIXS is vastly smaller than photoelectric processes for most materials at typical scattering conditions ~10 keV. When factoring in the small amount of solid angle that's typically measured and the Compton background from all other electrons in the sample and its surrounding environment, it's no surprise that XRS was not heavily studied until the advent of third generation synchrotron sources and is still primarily used for experiments where its bulk sensitivity or q-dependence is required. That said, recent advances in the source, optics, and detector technology have dramatically expanded the scope of XRS beyond first-row K-edges, opening up the technique to classes of materials ranging from gaseous samples [20, 21] to actinides [22, 23].

XRS, and NIXS in general, requires diffractive optics to resolve the energy of incident and scattered X-rays. As illustrated in Fig. 17.2, the incident energy is typically tuned by a monochromator and a cone of scattered X-rays are integrated using analyzers that are bent or diced to a spherical curvature that approximates the Rowland circle condition. The scattered X-rays are typically kept at a fixed energy defined by its Bragg angle and a momentum transfer set by its angle from incident

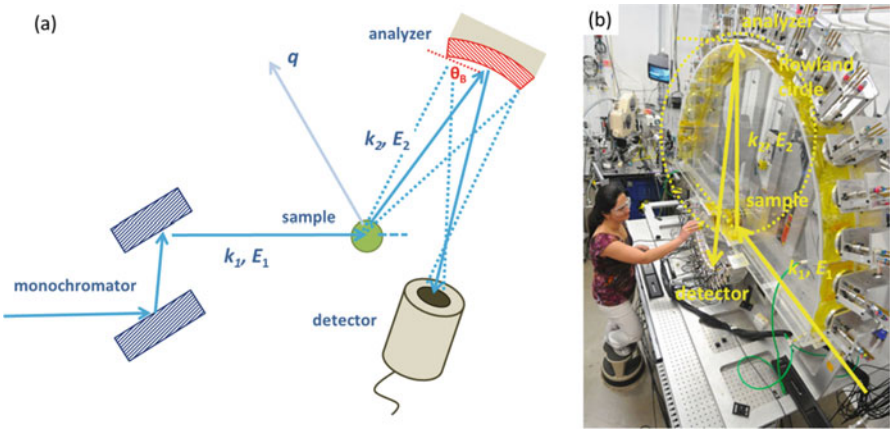

Fig. 17.2 (**a**) Illustration of the major components required to measure inelastic X-ray scattering. (**b**) Photo of the LERIX detector at the Advanced Photon Source, sector 20ID. Ray tracing of the components in (**a**) overlay the photograph. Note that LERIX, like many multielement setups, uses multiple sets of analyzers and detectors to simultaneously measure spectra at multiple values of q. The 1m Rowland circle defining diffraction from the silicon analyzer crystal is also shown for reference

beam, as seen in Fig. 17.2. Since the analyzers are typically positioned near backscatter with respect to the sample and detector, the energy resolution is largely defined by the upstream monochromator. Resolution of 0.2–1.0 eV is ideal for XRS due to core-hole lifetime broadening making XRS compatible with typical XAFS beamlines. In fact, coarser analyzer resolution actually increases count-rates, which is often the limiting factor in the measurement.

To increase the overall NIXS and XRS signal, setups incorporating arrays of analyzers at fixed [24] or variable [2] q have been developed in the last decade. The energy resolution and throughput of NIXS has also improved by incorporating area detectors with pixels small enough to resolve the energy spread of the scattered X-rays [25, 26]. Similarly, area detectors can be used to resolve the spatial extent of the sample using the point-to-point focusing of the analyzer. This is particularly relevant for samples embedded in a diamond anvil cell or capillary, as shown in Fig. 17.3.

While current multielement setups have certainly increased the solid angle measured by XRS, there is still plenty of room for growth. Analyzers capable of reaching lower radius of curvature would greatly increase solid angle. XRS could also benefit from working at higher energies, where a greater sample volume can be accessed and the shifting weight of the Compton background could make higher energy loss spectra become more feasible. Recent developments using bent Laue analyzers at recently demonstrated the feasibility of XRS at 20 keV [15].

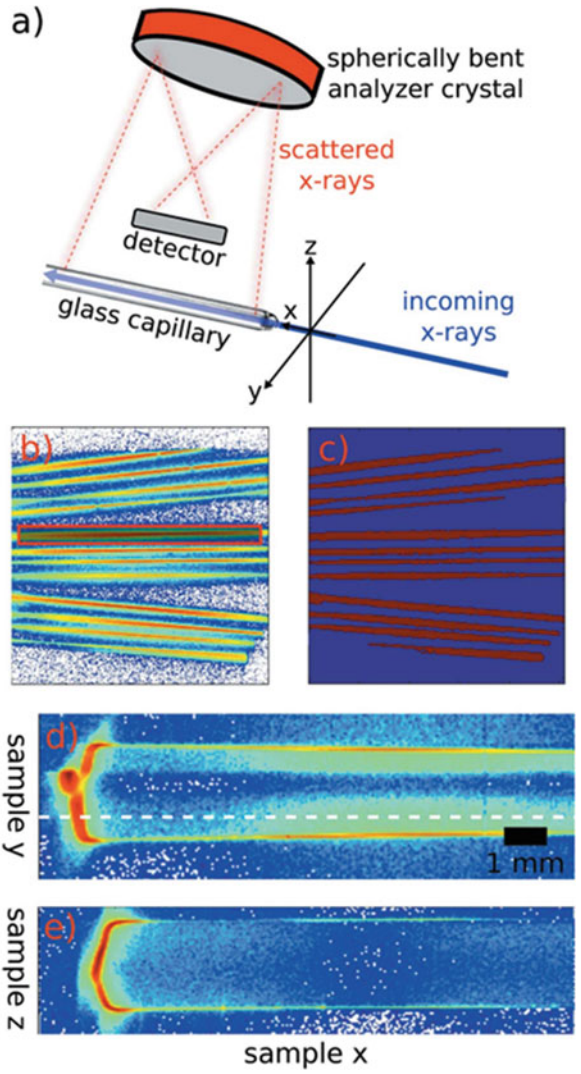

Fig. 17.3 Many samples cannot be approximated as point-sources. The point-to-point focusing from a spherically bent crystal actually provides an image of the sample and its environment which can be resolved on an area detector. In the work by Sahle et al. [19], NIXS from a liquid sample in a glass capillary was imaged in this manner so that the weaker signal from the liquid could be extracted from the strong quartz background

17.4 XRS in Extreme Environments

XAS below 1 keV has been largely limited to vacuum conditions and often only probes the surface or near-surface phenomena [27, 28]. This surface-sensitivity has been invaluable for studying catalysts and thin films [29], but often prevents the study of materials in situ or samples with high vapor pressure (like many liquids) [14, 30–32]. With few exceptions [33], XRS is a bulk sensitive technique, which can be advantageous for studying volatile samples [34, 35], like battery components [36], or materials at extreme conditions [37–39]. Despite its low cross section, XRS

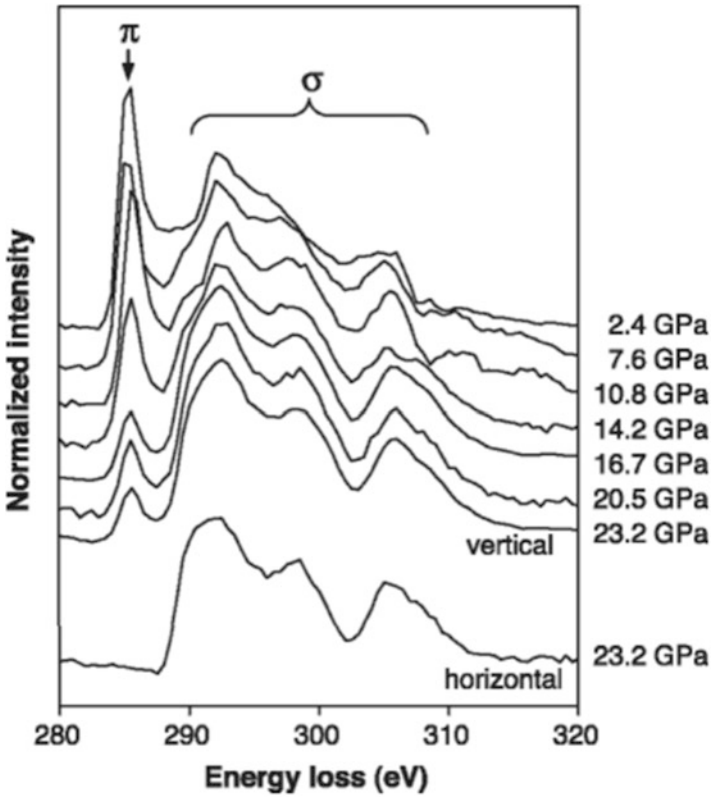

Fig. 17.4 Graphite undergoes the well-known transition to a diamond structure under extreme pressures. The transition from sp^2 to sp^3 hybridization can be easily seen by the reduction of the pre-edge π* resonance in the C K-edge [39]

is insensitive to sampling depth, which often complicates the analysis of soft X-ray measurements that rely on electron yield (variable photoelectron escape depth) or fluorescence (self-absorption).

One area previously inaccessible to soft X-rays has been the study of materials at high pressure [38–46]. These experiments involve diamond anvil cell, where the sample is embedded in a pressure medium that's sealed by a beryllium gasket. A classic early example of high pressure XRS was the transition of graphitic carbon to diamond at ultrahigh pressures [39]. As seen in Fig. 17.4, the signature of sp^2 hybridized graphite, a strong π* resonance corresponding to unoccupied out-of-plane p orbitals, is gradually reduced and converted to diamond's sp^3 spectrum. This study incorporates not only the bulk sensitivity of XRS, but its ability to measure natural dichroism via the direction of the X-ray momentum transfer (see Eq. 17.3).

The ability to probe low-Z K-edges with bulk sensitivity was recognized as a unique opportunity for catalysts early in the development of XRS [7, 47, 48]. As sources and detectors matured, the technique has started to be used for

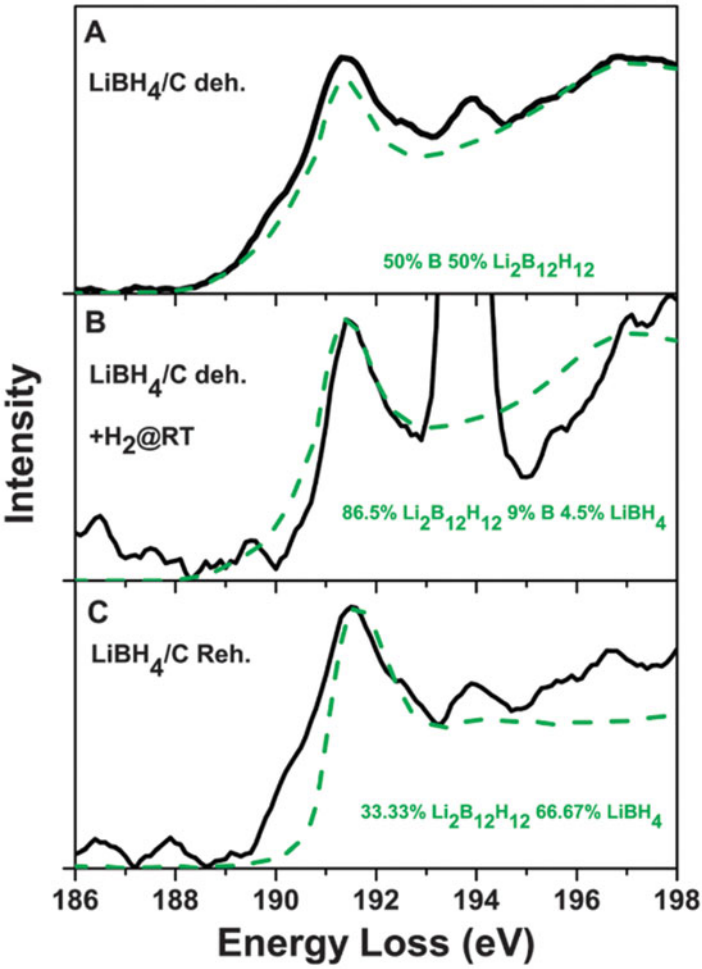

Fig. 17.5 B K-edge XRS from (**a**) dehydrated $LiBH_4$ carbon nanocomposites, (**b**) in the presence of H_2 and (**c**) rehydrated $LiBH_4$ [50]

accessing changes in the spectroscopy of catalysts at relevant working conditions, i.e., at atmospheric pressure in a variable gas environment [49, 50]. Borohydrides have long been seen as key material for hydrogen storage and fuel cell applications. These attributes can be seen directly in Fig. 17.5, where scattering from boron in $LiBH_4$ is strongly affected by changes in the gas environment. In the presence of H_2 gas, a nanocomposite of carbon and an active borohydration species shows a strong change in the B K-edge due to dehydration to $Li_2B_{12}H_{12}$ and rehydration to $LiBH_4$. The results were corroborated by the Li K-edge as well.

17.5 XRS Beyond the Dipole Limit

Using high energy X-ray scattering to probe low energy excitations provides an additional benefit over soft X-ray absorption: the ability to measure dipole-forbidden final states. XAFS at, say, a K-edge is limited to transitions to *p*-type final states due to the dipole selection rule (i.e., $\Delta l = \pm 1$). Final states with *s*-, or *d*-type symmetry are typically identified by hybridization or via weakly allowed pre-edge resonances. In XRS, these states emerge at higher q, corresponding to selection rules associated with higher order terms in the expansion of the matrix element in Eq. (17.3). One of the first studies exploiting this q-dependence was the work of Hamalainen's group [51], which used the increase of a pre-edge peak in LiF's F K-edge to identify its core-exciton as *s*-type. This analysis was followed up by Seidler's group who studied core excitons in B_4C [52], NaF, and NaCl [53]. In particular the symmetry of the exciton in B_4C helped identify its origin at the one crystallographic site exhibiting inversion symmetry (Fig. 17.6).

Furthermore, the different symmetry states can be physically separated by measuring the q-dependence of the XRS spectrum. This method was formalized by Soininen and coworkers, who recast the dynamic structure factor in an angular momentum (l) basis [54]. For a powder, this simplified to

$$S(q,\omega) = \sum_{l=0} |M_l(q,\omega)|^2 \rho_l(\omega), \tag{17.5}$$

where terms in the angular momentum projected density of states are weighted by factors that depend only on the initial state's atomic properties. Using Eq. (17.4), XRS can be used to quantitatively extract the hybridization of the density of states itself [52].

As an example, this method was used on $C_2B_{10}H_{12}$, an icosahedral molecule that is the most well-known member of the carboranes [55]. As seen in Fig. 17.7, the dipole forbidden $s \rightarrow s$ transitions found at high q helped pinpoint radially hybridized s-p states that are related to the molecules 3D aromaticity. Similar analysis has been performed to understand bonding in superionic Li_3N [56], battery interphases [34], and the superconductor MgB_2 [57].

While XRS has been largely used for first row K-edges, it has been increasingly used for excitations from semicore levels from higher Z edges. This was pioneered for L-edges in semiconductors [58–61] and metals [10, 62, 63], and more recently has been extended to lanthanides [64–66] and actinides [22, 67]. This was initially surprising since the micron-scale penetration lengths in high-Z materials severely limits the scattering volume for inelastic processes. For open band *f* and *d*-electron materials, the ability to bypass dipole excitations opens up remarkably strong transitions at high q to unoccupied atomic orbitals that would otherwise be inaccessible by absorption. As seen in Fig. 17.8, these orbitals provide a clear ability to probe *f*-electron occupation which is crucial for understanding the exotic chemical properties of actinides. The strong q-dependence from the uranium $O_{4,5}$ edge,

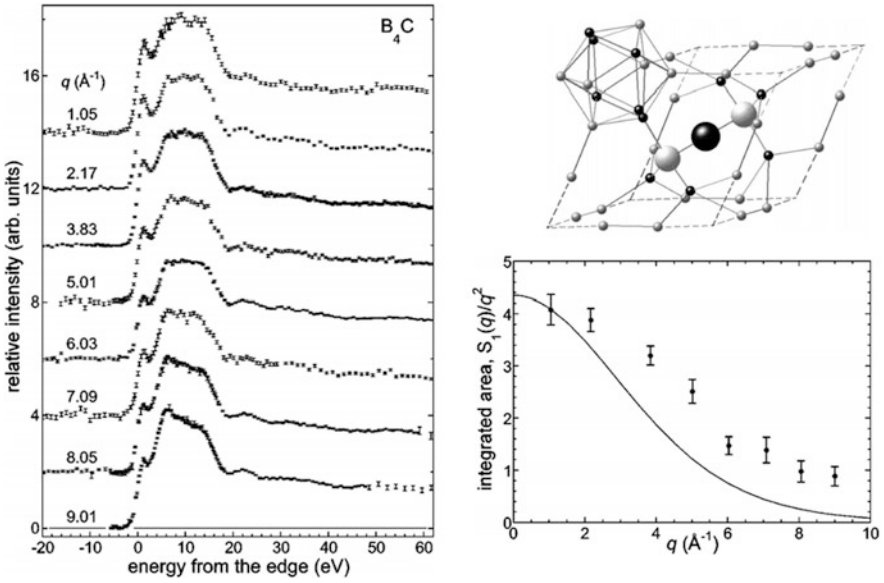

Fig. 17.6 (*Left*) The most marked changes in the B K-edge of B_4C can be seen in the excitonic feature just below the conduction band (0 eV in the plot), due to the extended nature of the exciton. (*Right*) This decrease in the integrated intensity of the feature with q confirms its p-type symmetry. This analysis confirmed that the exciton is associated with the one boron site that has inversion symmetry, denoted by the large black atom in the upper right model [52]

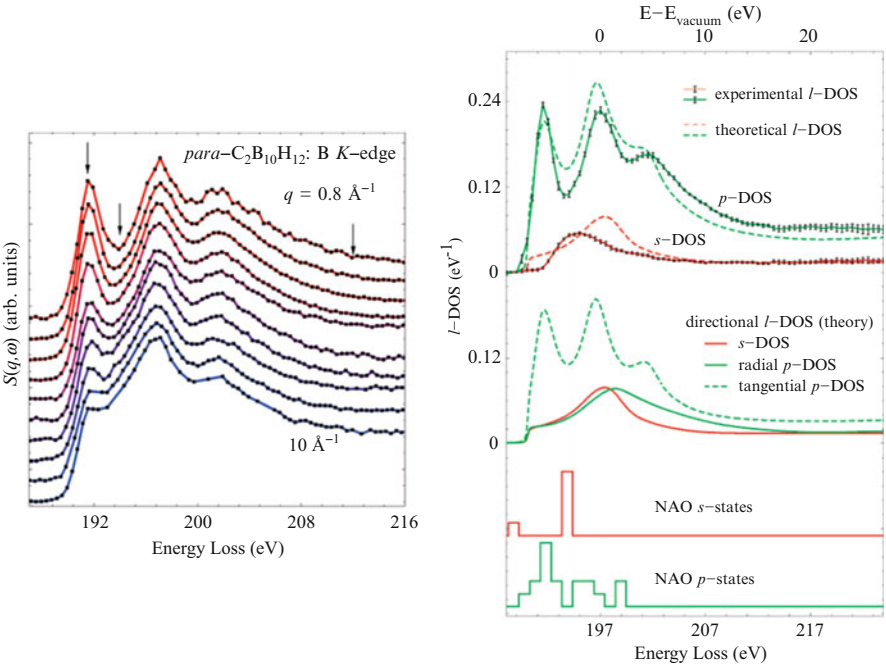

Fig. 17.7 (*Left*) XRS taken at the B K-edge from $C_2B_{10}H_{12}$ as a function of momentum transfer from 0.8–10 $Å^{-1}$. (*Right*) Using Eq. (17.4), the s- and p-DOS were extracted from the data and compared to theory

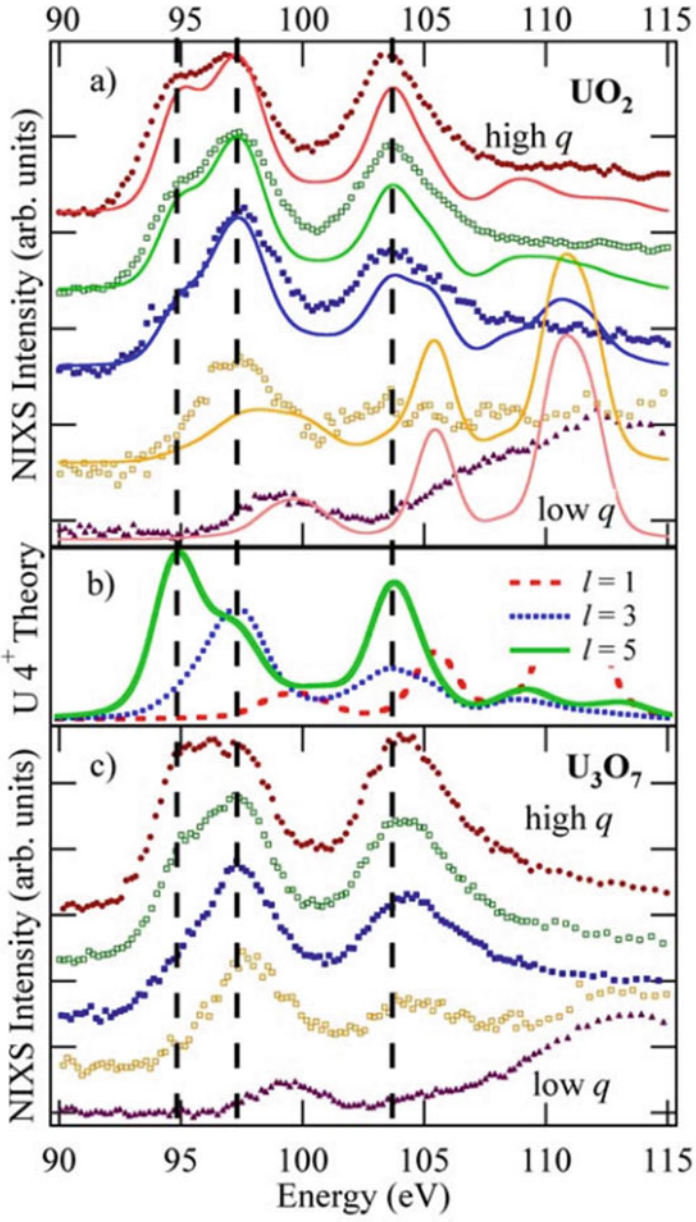

Fig. 17.8 Near valence shells, like the U $O_{4,5}$ edges from Bradley et al. [67] often have extremely strong q-dependence arising from dipole-forbidden transitions to open f orbitals. Single-atom multiplet calculations provide an elegant comparison between UO_2 and mixed-valence U_3O_7

where the previously observed giant dipole resonance gives way to sharp multiplet lines arising from octupole ($\Delta l = 3$) and triakontadipole ($\Delta l = 5$) transitions from the combined angular momentum transfer of the hybridized 5d-5f states (combined

angular momentum up to $l = 7$). In the case of UO_2 (pure $5f^2$) and mixed-valent U_3O_7, the *f*-character can be identified from these high order multipole transitions using a single-atom calculation. This study also incorporates the bulk sensitivity of XRS, which is necessary to penetrate through multiple layers of shielding typically required for radioactive samples.

These studies represent just a small fraction of the growing body of work using X-ray Raman scattering. They show that XRS provides alternative capabilities to XAS or electron energy loss spectroscopy for materials requiring non-vacuum conditions or reaching final states inaccessible to traditional spectroscopies. Continuing advances in optics and detector technology are helping to stimulate this technique to more challenging edges from materials across the periodic table.

References

1. Tohji K, Udagawa Y (1987) Novel approach for structure analysis by X-ray Raman scattering. Phys Rev B 36(17):9410–9412
2. Fister TT, Seidler GT, Wharton L, Battle AR, Ellis TB, Cross JO, Macrander AT, Elam WT, Tyson TA, Qian Q (2006) Multielement spectrometer for efficient measurement of the momentum transfer dependence of inelastic X-ray scattering. Rev Sci Instrum 77(6):063901
3. Hamalainen K, Krisch M, Kao CC, Caliebe W, Hastings JB (1995) High-resolution X-ray spectrometer based on a cylindrically bent crystal in nondispersive geometry. Rev Sci Instrum 66(2):1525–1527
4. Kao CC, Hamalainen K, Krisch M, Siddons DP, Oversluizen T, Hastings JB (1995) Optical design and performance of the inelastic scattering beamline at the National Synchrotron Light Source. Rev Sci Instrum 66(2):1699–1702
5. Seidler GT, Feng YJ (2001) A filter based analyzer for studies of X-ray Raman scattering. Nucl Instrum Methods Phys Res A 469(1):127–132
6. Alonso-Mori R, Kern J, Sokaras D, Weng TC, Nordlund D, Tran R, Montanez P, Delor J, Yachandra VK, Yano J, Bergmann U (2012) A multi-crystal wavelength dispersive X-ray spectrometer. Rev Sci Instrum 83(7):073114
7. Bergmann U, Groenzin H, Mullins OC, Glatzel P, Fetzer J, Cramer SP (2004) X-ray Raman spectroscopy—a new tool to study local structure of aromatic hydrocarbons and asphaltenes. Petrol Sci Technol 22(7–8):863–875
8. Verbeni R, Pylkkanen T, Huotari S, Simonelli L, Vanko G, Martel K, Henriquet C, Monaco G (2009) Multiple-element spectrometer for non-resonant inelastic X-ray spectroscopy of electronic excitations. J Synchrotron Radiat 16:469–476
9. Tirao G, Stutz G, Cusatis C (2004) An inelastic X-ray scattering spectrometer at LNLS. J Synchrotron Radiat 11:335–342
10. Fister TT, Seidler GT, Hamner C, Cross JO, Soininen JA, Rehr JJ (2006) Background proportional enhancement of the extended fine structure in nonresonant inelastic X-ray scattering. Phys Rev B 74(21):214117
11. Huotari S, Pylkkanen T, Soininen JA, Kas JJ, Hamalainen K, Monaco G (2012) X-ray-Raman-scattering-based EXAFS beyond the dipole limit. J Synchrotron Radiat 19:106–113
12. Comelli G, Stohr J, Jark W, Pate BB (1988) Extended X-ray-absorption fine-structure studies of diamond and graphite. Phys Rev B 37(9):4383–4389
13. Tohji K, Udagaw Y (1989) X-ray Raman scattering as a substitute for soft-X-ray extended X-ray-absorption fine structure. Phys Rev B 39(11):7590–7594

14. Bowron DT, Krisch MH, Barnes AC, Finney JL, Kaprolat A, Lorenzen M (2000) X-ray-Raman scattering from the oxygen K edge in liquid and solid H_2O. Phys Rev B 62(14):R9223–R9227
15. Hiraoka N, Fukui H, Tanida H, Toyokawa H, Cai YQ, Tsuei KD (2013) An X-ray Raman spectrometer for EXAFS studies on minerals: bent Laue spectrometer with 20 keV X-rays. J Synchrotron Radiat 20:266–271
16. Soininen JA, Ankudinov AL, Rehr JJ (2005) Inelastic scattering from core electrons: a multiple scattering approach. Phys Rev B 72(4):045136
17. Mattern BA, Seidler GT, Kas JJ, Pacold JI, Rehr JJ (2012) Real-space Green's function calculations of Compton profiles. Phys Rev B 85(11):115135
18. Sternemann H, Sternemann C, Seidler GT, Fister TT, Sakko A, Tolan M (2008) An extraction algorithm for core-level excitations in non-resonant inelastic X-ray scattering spectra. J Synchrotron Radiat 15:162–169
19. Sahle CJ, Mirone A, Niskanen J, Inkinen J, Krisch M, Huotari S (2015) Planning, performing and analyzing X-ray Raman scattering experiments. J Synchrotron Radiat 22:400–409
20. Bradley JA, Seidler GT, Cooper G, Vos M, Hitchcock AP, Sorini AP, Schlimmer C, Nagle KP (2010) Comparative study of the valence electronic excitations of N-2 by inelastic X-ray and electron scattering. Phys Rev Lett 105(5):053202
21. Sakko A, Galambosi S, Inkinen J, Pylkkanen T, Hakala M, Huotari S, Hamalainen K (2011) Inelastic X-ray scattering and vibrational effects at the K-edges of gaseous N_2, N_2O, and CO_2. Phys Chem Chem Phys 13(24):11678–11685
22. Caciuffo R, van der Laan G, Simonelli L, Vitova T, Mazzoli C, Denecke MA, Lander GH (2010) Uranium 5d-5f electric-multipole transitions probed by nonresonant inelastic X-ray scattering. Phys Rev B 81(19):195104
23. Bradley JA, Sen Gupta S, Seidler GT, Moore KT, Haverkort MW, Sawatzky GA, Conradson SD, Clark DL, Kozimor SA, Boland KS (2010) Probing electronic correlations in actinide materials using multipolar transitions. Phys Rev B 81(19):193104
24. Sokaras D, Nordlund D, Weng TC, Mori RA, Velikov P, Wenger D, Garachtchenko A, George M, Borzenets V, Johnson B, Qian Q, Rabedeau T, Bergmann U (2012) Proton induced quasi-monochromatic X-ray beams for soft X-ray spectroscopy studies and selective X-ray fluorescence analysis. Rev Sci Instrum 83(4):043112
25. Huotari S, Vanko G, Albergamo F, Ponchut C, Graafsma H, Henriquet C, Verbeni R, Monaco G (2005) Improving the performance of high-resolution X-ray spectrometers with position-sensitive pixel detectors. J Synchrotron Radiat 12:467–472
26. Huotari S, Pylkkanen T, Verbeni R, Monaco G, Hamalainen K (2011) Direct tomography with chemical-bond contrast. Nat Mater 10(7):489–493
27. Stohr J (1992) NEXAFS spectroscopy. Springer, Berlin
28. Chen JG (1997) NEXAFS investigations of transition metal oxides, nitrides, carbides, sulfides and other interstitial compounds. Surf Sci Rep 30(1–3):1–152
29. Chakhalian J, Freeland JW, Habermeier HU, Cristiani G, Khaliullin G, van Veenendaal M, Keimer B (2007) Orbital reconstruction and covalent bonding at an oxide interface. Science 318(5853):1114–1117
30. Wernet P, Nordlund D, Bergmann U, Cavalleri M, Odelius M, Ogasawara H, Naslund LA, Hirsch TK, Ojamae L, Glatzel P, Pettersson LGM, Nilsson A (2004) The structure of the first coordination shell in liquid water. Science 304(5673):995–999
31. Bergmann U, Di Cicco A, Wernet P, Principi E, Glatzel P, Nilsson A (2007) Nearest-neighbor oxygen distances in liquid water and ice observed by X-ray Raman based extended X-ray absorption fine structure. J Chem Phys 127(17):174504
32. Lehmkuhler F, Sakko A, Steinke I, Sternemann C, Hakala M, Sahle CJ, Buslaps T, Simonelli L, Galambosi S, Paulus M, Pylkkanen T, Tolan M, Hamalainen K (2011) Temperature-induced structural changes of tetrahydrofuran clathrate and of the liquid water/tetrahydrofuran mixture. J Phys Chem C 115(43):21009–21015

33. Fister TT, Fong DD, Eastman JA, Iddir H, Zapol P, Fuoss PH, Balasubramanian M, Gordon RA, Balasubramaniam KR, Salvador PA (2011) Total-reflection inelastic X-ray scattering from a 10-nm thick $La_{0.6}Sr_{0.4}CoO_3$ thin film. Phys Rev Lett 106(3):037401
34. Fister TT, Schmidt M, Fenter P, Johnson CS, Slater MD, Chan MKY, Shirley EL (2011) Electronic structure of lithium battery interphase compounds: comparison between inelastic X-ray scattering measurements and theory. J Chem Phys 135(22):224513
35. Chan MKY, Shirley EL, Karan NK, Balasubramanian M, Ren Y, Greeley JP, Fister TT (2011) Structure of lithium peroxide. J Phys Chem Lett 2(19):2483–2486
36. Balasubramanian M, Johnson CS, Cross JO, Seidler GT, Fister TT, Stern EA, Hamner C, Mariager SO (2007) Fine structure and chemical shifts in nonresonant inelastic X-ray scattering from Li-intercalated graphite. Appl Phys Lett 91(3):031904
37. Tse JS, Shaw DM, Klug DD, Patchkovskii S, Vanko G, Monaco G, Krisch M (2008) X-ray Raman spectroscopic study of water in the condensed phases. Phys Rev Lett 100(9):095502
38. Lee SK, Eng PJ, Mao HK, Meng Y, Newville M, Hu MY, Shu JF (2005) Probing of bonding changes in B_2O_3 glasses at high pressure with inelastic X-ray scattering. Nat Mater 4 (11):851–854
39. Mao WL, Mao HK, Eng PJ, Trainor TP, Newville M, Kao CC, Heinz DL, Shu JF, Meng Y, Hemley RJ (2003) Bonding changes in compressed superhard graphite. Science 302 (5644):425–427
40. Mao WL, Mao H-k, Meng Y, Eng PJ, Hu MY, Chow P, Cai YQ, Shu J, Hemley RJ (2006) X-ray-induced dissociation of H_2O and formation of an O-2-H-2 alloy at high pressure. Science 314(5799):636–638
41. Lee SK, Eng PJ, Mao HK, Meng Y, Shu J (2007) Structure of alkali borate glasses at high pressure: B and Li *K* -edge inelastic X-ray scattering study. Phys Rev Lett 98(10)
42. Kumar RS, Dandekar D, Leithe-Jasper A, Tanaka T, Xiao YM, Chow P, Nicol MF, Cornelius AL (2010) Inelastic X-ray scattering experiments on B4C under high static pressures. Diamond Relat Mater 19(5–6):530–532
43. Yi YS, Lee SK (2012) Pressure-induced changes in local electronic structures of SiO_2 and $MgSiO_3$ polymorphs: insights from ab initio calculations of O K-edge energy-loss near-edge structure spectroscopy. Am Mineral 97(5–6):897–909
44. Inkinen J, Sakko A, Ruotsalainen KO, Pylkkanen T, Niskanen J, Galambosi S, Hakala M, Monaco G, Huotari S, Hamalainen K (2013) Temperature dependence of CO_2 and N_2 core-electron excitation spectra at high pressure. Phys Chem Chem Phys 15(23):9231–9238
45. Lee SK, Eng PJ, Mao HK (2014) Probing of pressure-induced bonding transitions in crystalline and amorphous earth materials: insights from X-ray Raman scattering at high pressure. In: Henderson GS, Neuville DR, Downs RT (eds) Spectroscopic methods in mineralogy and materials sciences, GeoScienceWorld, vol 78, pp 139–174
46. Nyrow A, Sternemann C, Wilke M, Gordon RA, Mende K, Yavas H, Simonelli L, Hiraoka N, Sahle CJ, Huotari S, Andreozzi GB, Woodland AB, Tolan M, Tse JS (2014) Iron speciation in minerals and glasses probed by M-2/3-edge X-ray Raman scattering spectroscopy. Contrib Mineral Petrol 167(5):1–13
47. Bergmann U, Glatzel P, Cramer SP (2002) Bulk-sensitive XAS characterization of light elements: from X-ray Raman scattering to X-ray Raman spectroscopy. Microchem J 71 (2–3):221–230
48. Gordon ML, Tulumello D, Cooper G, Hitchcock AP, Glatzel P, Mullins OC, Cramer SP, Bergmann U (2003) Inner-shell excitation spectroscopy of fused-ring aromatic molecules by electron energy loss and X-ray Raman techniques. J Phys Chem A 107(41):8512–8520
49. Miedema PS, Ngene P, van der Eerden AMJ, Weng T-C, Nordlund D, Sokaras D, Alonso-Mori R, Juhin A, de Jongh PE, de Groot FMF (2012) In situ X-ray Raman spectroscopy of $LiBH_4$. Phys Chem Chem Phys 14(16):5581–5587
50. Miedema PS, Ngene P, van der Eerden AMJ, Sokaras D, Weng TC, Nordlund D, Au YS, de Groot FMF (2014) In situ X-ray Raman spectroscopy study of the hydrogen sorption properties of lithium borohydride nanocomposites. Phys Chem Chem Phys 16(41):22651–22658

51. Hamalainen K, Galambosi S, Soininen JA, Shirley EL, Rueff JP, Shukla A (2002) Momentum dependence of fluorine K-edge core exciton in LiF. Phys Rev B 65(15)
52. Feng YJ, Seidler GT, Cross JO, Macrander AT, Rehr JJ (2004) Role of inversion symmetry and multipole effects in nonresonant X-ray Raman scattering from icosahedral B_4C. Phys Rev B 69(12):125402
53. Nagle KP, Seidler GT, Shirley EL, Fister TT, Bradley JA, Brown FC (2009) Final-state symmetry of Na 1s core-shell excitons in NaCl and NaF. Phys Rev B 80(4)
54. Soininen JA, Mattila A, Rehr JJ, Galambosi S, Hamalainen K (2006) Experimental determination of the core-excited electron density of states. J Phys Condens Matter 18(31):7327–7336
55. Fister TT, Vila FD, Seidler GT, Svec L, Linehan JC, Cross JO (2008) Experimental determination of the core-excited electron density of states. J Am Chem Soc 130(3):925–932
56. Fister TT, Seidler GT, Shirley EL, Vila FD, Rehr JJ, Nagle KP, Linehan JC, Cross JO (2008) The local electronic structure of alpha-Li3N. J Chem Phys 129(4):044702
57. Mattila A, Soininen JA, Galambosi S, Huotari S, Vanko G, Zhigadlo ND, Karpinski J, Hamalainen K (2005) Local electronic structure of MgB2 by X-ray Raman scattering at the boron K edge. Phys Rev Lett 94(24)
58. Sternemann C, Soininen JA, Volmer M, Hohl A, Vanko G, Streit S, Tolan M (2005) X-ray Raman scattering at the Si L-II,(III)-edge of bulk amorphous SiO. J Phys Chem Solid 66 (12):2277–2280
59. Sternemann C, Soininen JA, Huotari S, Vanko G, Volmer M, Secco RA, Tse JS, Tolan M (2005) X-ray Raman scattering at the L edges of elemental Na, Si, and the N edge of Ba in Ba8Si46. Phys Rev B 72(3)
60. Sakko A, Sternemann C, Sahle CJ, Sternemann H, Feroughi OM, Conrad H, Djurabekova F, Hohl A, Seidler GT, Tolan M, Hamalainen K (2010) Suboxide interface in disproportionating a-SiO studied by X-ray Raman scattering. Phys Rev B 81(20)
61. Feroughi OM, Sternemann C, Sahle CJ, Schroer MA, Sternemann H, Conrad H, Hohl A, Seidler GT, Bradley J, Fister TT, Balasubramanian M, Sakko A, Pirkkalainen K, Hamalainen K, Tolan M (2010) Phase separation and Si nanocrystal formation in bulk SiO studied by X-ray scattering. Appl Phys Lett 96(8)
62. Sternemann C, Sternemann H, Huotari S, Lehmkuhler F, Tolan M, Tse JS (2008) The barium giant dipole resonance in barite: a study of soft X-ray absorption edges using hard X-rays. J Anal Atom Spectrom 23(6):807–813
63. Sahle CJ, Sternemann C, Sternemann H, Tse JS, Gordon RA, Desgreniers S, Maekawa S, Yamanaka S, Lehmkuhler F, Wieland DCF, Mende K, Huotari S, Tolan M (2014) The Ba 4d-4f giant dipole resonance in complex Ba/Si compounds. J Phys B Atom Mol Opt Phys 47 (4):045102
64. Gordon RA, Seidler GT, Fister TT, Haverkort MW, Sawatzky GA, Tanaka A, Sham TK (2008) High multipole transitions in NIXS: valence and hybridization in 4f systems. Epl 81(2)
65. Gordon RA, Haverkort MW, Sen Gupta S, Sawatzky GA (2009) Orientation-dependent X-ray Raman scattering from cubic crystals: natural linear dichroism in MnO and CeO_2. In: 14th international conference on X-ray absorption fine structure (Xafs14), proceedings 190
66. Gordon RA, Seidler GT, Fister TT, Nagle KP (2011) Studying low-energy core-valence transitions with bulk sensitivity using q-dependent NIXS. J Electron Spectrosc Relat Phenom 184(3–6):220–223
67. Bradley JA, Moore KT, van der Laan G, Bradley JP, Gordon RA (2011) Core and shallow-core d- to f-shell excitations in rare-earth metals. Phys Rev B 84(20)

Chapter 18
Molecular Dynamics Simulations and XAFS (MD-XAFS)

Gregory K. Schenter and John L. Fulton

18.1 Introduction

18.1.1 Quantifying Structure with MD-XAFS

A quantitative method of interpreting structure in XAFS spectra is available through a first-principles comparison to molecular dynamics simulations (MD-XAFS). The synergy of these two methods can provide important insights into a variety of different chemical systems far beyond what is available from each individual technique. Molecular dynamics (MD) is used to generate a relevant equilibrium ensemble based upon an accurate description of molecular interactions. These interactions are predicted using either empirical potentials or electronic structure in terms of efficient density functional theory, or in principle, from more comprehensive electronic structure techniques that systematically account for electron correlation and weak interaction. The underlying basis for both XAFS and MD is the molecular structure. In XAFS, the positions of atoms about the central absorbing atom of interest are probed by photoelectron backscattering of the ejected core electron. A similar representation of the local atom structure is one of the central entities from a molecular dynamics simulation that is given by the radial pair distribution function, $g_{ab}(r)$. The $g_{ab}(r)$'s represent the probability of finding an atom "b" at some distance from a central atom "a" of interest. Historically, peaks in the $g_{ab}(r)$ from the MD are compared in a qualitative way to features in the radial structure plot, $|\widetilde{\chi}(R)|$, derived from the XAFS spectrum. However, the MD-XAFS method is a fully quantitative, first-principles method to directly compute the full XAFS spectra using the millions of atomic positions that are part of a typical molecular dynamics trajectory and that

G.K. Schenter • J.L. Fulton (✉)
Physical Sciences Division, Pacific Northwest National Laboratory, P.O. Box 999, Richland, WA 99354, USA
e-mail: john.fulton@pnnl.gov

Y. Iwasawa et al. (eds.), *XAFS Techniques for Catalysts, Nanomaterials, and Surfaces*, DOI 10.1007/978-3-319-43866-5_18

represent a thermodynamic ensemble. The point to stress is that this XAFS spectrum, which is generated using first-principles methods (or MD-XAF spectrum), includes contributions from all of the possible photoelectron single- and multiple-scattering events that are a consequence of the arrangement of atoms about the absorber. The resulting MD-XAFS spectrum captures the correlations in positions, angular structure, and geometry. There are several ways in which the MD-XAFS method can be used including (1) gaining insights into the chemistry of the experimental system, (2) evaluating and assigning specific structural features in the experimental XAFS spectrum to atom types or their positions, and (3) validating or benchmarking the simulated MD structure against the measurement. The combined methods of XAFS and MD provide a powerful probe of the structure. Ultimately, these methods improve the understanding of the relationship between structure, fluctuations, energy, forces, and the motions that control the chemical properties of the system.

Using the classical method of XAFS data analysis, which is now some 40 years old, the scientist makes logical choices about atom positions for the first- and second-shell atom types based upon an understanding of the expected chemistry of the system. Next, a theoretical standard (e.g., FEFF [1–3]) is generated to model the scattering contribution from each of the expected paths. Least squares fitting is then used to refine atom-atom distances and determine the disorder parameters (Debye-Waller factors). This classical method becomes increasingly intractable as distances increase beyond the first shell since the number of different possible scattering paths increases geometrically with the distance from the absorber. The problem is also compounded by the contribution of the photoelectron multiple-scattering paths that add another layer of complexity to the analysis. For instance, certain angular orientations of sets of atoms (especially collinear arrangements) lead to dramatically enhanced photoelectron scattering through a focusing effect. Such an analysis quickly becomes complex, requiring an expert for analysis. MD-XAFS greatly simplifies this process because the entire set of single and multiple-scattering paths out to approximately four and five shells from the absorber, is treated exactly, thus fully accounting for the atom disorder (static and dynamic) as well as the asymmetry or anharmonicity of the distribution for all atoms in the simulation.

In many condensed phase systems, the structures of interest often do not exist in a single state but exist in equilibrium with two or more species. This is especially true in reacting systems where the catalyst can exist as a resting state in equilibrium with various excited states along the reaction pathway. Using classical XAFS methods, the ability to deconvolute these structural contributions in XAFS becomes difficult for equilibria involving more than a couple of different species. On the other hand, when the MD simulation accurately represents the overall equilibrium speciation, then generation of an MD-XAFS spectrum that exactly replicates the experimental spectrum helps verify the fidelity of the simulation and helps in the understanding of the overall chemical speciation.

Another factor that has led to the dramatic rise and adoption of the MD-XAFS method is the high structural fidelity of density functional theory electronic

structure (DFT)-based molecular dynamics for probing diverse chemical systems at modest size length scales. Historically, the interaction between atoms and molecules was represented using empirical functions such as the Lennard-Jones function modified in various ways to treat atomic charge and longer range electrostatic interactions. The structural parameters in the Lennard-Jones representation are optimized through a process of fitting to various micro- and macroscopic experimental properties. In this way, it is possible to achieve a reasonable representation of pairs of molecular interactions. The DFT-based MD methods advance this process in two major ways. First, the interatomic interactions are a response to the electronic structures of the individual atoms in the simulation. Equally important, for systems that contain a multitude of different chemical components, DFT-MD methods properly treat all the possible pair interactions without a need of developing a new empirical potential for each atom-atom type. This fact enables studies of systems with great chemically complexity or systems that are undergoing chemical reactions. Even within the last 5 years the fidelity of DFT-MD methods has experienced a dramatic improvement that in many instances achieves a nearly quantitative representation of the structural features in the experimental system.

The XAFS region is commonly split into x-ray absorption near edge spectroscopy (XANES) and the extended x-ray absorption fine structure (EXAFS) regions. For both of these spectral regions the overall process of converting an MD ensemble into an XAFS spectrum using that appropriate x-ray absorption theory is nearly identical. In this chapter, the focus is solely upon generation of EXAFS spectra from the MD ensemble; however, there are many equally interesting opportunities for XANES analysis that will not be covered in this discussion.

18.1.2 Recent Literature Highlights

Early studies using molecular dynamics directly coupled to an electron multiple-scattering calculation (MD-XAFS) to better understand the XAFS signal, involved the analysis of the complex solvation of ionic species such as Sr^{2+}, Br^{-}, Ni^{2+}, Cu^{+}, and Cu^{2+} [4–8]. Around the same time, colocated research groups influenced each other and it was found that such an analysis could unravel the complexities associated with the aqueous ion/surface interface [9]. Due to simulation efficiency at the time, these studies were limited by an empirical description of molecular interaction. Soon to follow, MD-XAFS techniques were used routinely to benchmark empirical potentials and the solvation of a variety of ions including Cr^{3+}, Ca^{2+}, Sr^{2+}, K^{+}, Cl^{-} [10–13].

These approaches found limited success. It was a challenge for the empirical potentials to both recover the measured ion-water bond distance as well as the Debye-Waller factor. With the development of density functional theory (DFT) electronic structure driven sampling, more complex molecules such as UO_2^{2+} and metals Ag^{+}, Zn^{2+}, Ce^{3+}, U, Ca^{2+} have become routine [14–19].

Other studies of ion solvation using MD-XAFS include testing of nonempirical cation-water potentials for aqueous Cr^{3+} and of Ir^{3+} [20, 21]. There are studies of the use of empirical potentials for modeling Br^- hydration and the formation of Ag chloride complexes in water at temperature up to 450 °C [22, 23]. In related areas the solvation of K^+ in solid polymer electrolytes was modeled using empirical force fields that are derived from ab initio methods [24, 25]. In solid phase studies, MD-XAFS has been used to evaluate empirical force-field models in a wide band-gap semiconductor, ZnO [26], and in probing vacancies in NiO nanoparticles [27, 28]. It is also important to note, in the context of aqueous ion, the recent extensive studies of halides [29] and lanthanoids [30] ions using an analysis method in which the XAFS spectra are generated from MD g(r)'s.

For MD-XAFS, the balance between the bond distance and the Debye-Waller factor appeared to be resolved with the use of DFT sampling. This was demonstrated for a series of transition-metal ions [31]. Other examples of unprecedented detail regarding the balance between forces resolved by DFT electronic structure, include the improved understanding of the iodide anion and its propensity to be at a vapor/liquid interface [32]. Improved descriptions of short-range interaction supplied by DFT have proven to be essential to describe the solvation of complex ions such as iodate (IO_3^-) [33], as well as the balance associated with ion pairing in hydrochloric acid ($Cl^- \bullet H_3O^+$) [34]. Such consistency between molecular interaction and measure XAFS signal has impacted the analysis of catalytic systems [35, 36].

18.2 Theory: Calculating an XAFS Spectra from MD Simulation

18.2.1 The Process of Generating an MD-XAFS Spectrum

The method used to generate an XAFS spectrum from a molecular dynamics simulation is shown conceptually in Fig. 18.1. The first step is to generate a trajectory of the fully equilibrated chemical system representing the statistic ensemble of the system. Such a trajectory typically contains several thousand individual snapshots. These collective snapshots represent a configuration in a statistical mechanical ensemble corresponding to a certain density (or pressure) and temperature of the measured system. For each snapshot, all of the atom positions (x, y, z coordinates) about the absorber(s) of interest are used as input to the XAFS ab initio scattering code (e.g., FEFF) [3]. This process is repeated for each snapshot to create an ensemble average spectrum that contains the contributions from all of the structural information in the full trajectory.

This process of generating an MD-XAFS spectrum is formally represented by Eq. 18.1,

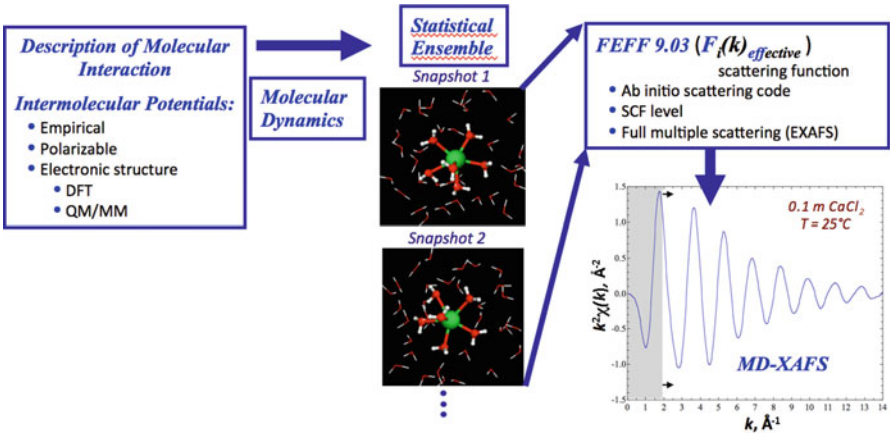

Fig. 18.1 A schematic of the flow path used for the calculation of an MD-XAFS spectrum

$$\chi(k) = \frac{1}{\text{frames}} \sum_{i}^{\text{frames}} \sum_{j}^{\text{paths}} S_0^2 \frac{F_{ij}(k)}{kR_{ij}^2} e^{-2R_{ij}/\lambda_{ij}} sin\left(2kR_{ij} + \varphi_{ij}(k)\right) \tag{18.1}$$

wherein $F(k)$, $\varphi(k)$, and λ are the scattering amplitudes, the photoelectron phase shifts, and the photoelectron mean free paths, respectively, as calculated by FEFF9 [1]. S_0^2 is the core hole lifetime amplitude factor. Treatment of the disorder, (Debye-Waller factor), the third and fourth cumulants of the distribution are included implicitly in the simulation and thus are treated exactly in the generation of the MD-XAFS spectrum.

For each individual snapshot, approximately 10^3 relevant scattering paths (SS and MS) are included. The trajectories typically contain several thousand frames or snapshots and thus an ensemble average of greater than approximately 10^6 scattering events is accumulated in the resultant MD-XAFS spectrum. It is important to emphasize that the MD-XAFS method [4, 9] represents all the relevant photoelectron scattering events (~10^6) including single *and multiple-scattering* processes that uniquely define the static and dynamic structures about the absorber [15, 16]. By implicitly including all relevant multiple-scattering signals we are able to go beyond the traditional route of comparing individual g (r)'s from MD trajectories to the single-scattering contributions of the XAFS spectra. The method also makes no assumptions about the shape (disorder) of the pair distribution functions from the simulation. This MD-XAFS approach was originally implemented using MD simulation based upon empirical interaction potentials [4, 12]. More recently, DFT-based simulations have been used such as those for evaluating hydration of cations or anions in water [16, 32, 33]. In many cases, as we will illustrate later, the agreement between the calculated XAFS spectrum from DFT-base MD simulation and the experimental spectra is nearly quantitative.

The comparison of the calculated and the measured $\chi(k)$ spectra requires one preprocessing step. The theoretical and experimental absorption edge energies or E_0's must coincide. The required accuracy of less than ± 1.0 eV for the predicted E_0 is presently not possible with current efficient electron multiple-scattering theories. For this reason, E_0 is a single adjustable parameter that is required to properly align the experimental and theoretical spectra. It is important to match the absorption edge energy, E_0, between theory and experiment to properly compare their $\chi(k)$ plots. The main criterion is that the primary oscillations in $\chi(k)$ plots of the experiment and simulation must converge to the same values as k approaches zero. More importantly, the E_0 shift for the multiple-scattering and the longer range scattering paths must also be properly aligned. Without a proper E_0 alignment, the longer range structure beyond the first peak of the Fourier-transformed $\mathrm{Im}[\widetilde{\chi}(R)]$ plots will be distorted. For example, one method to assure an overall E_0 match in the multiple-scattering region is to first window a certain region in the higher R-space and then inverse transform to generate a "q plot." The phase of the oscillations should converge as q approaches zero so that a further minor correction to the initial E_0 estimate is sometimes required. Typically, a single E_0 value is used for all single and multiple-scattering paths. The inclusion of automated self-consistent potential calculations (SCF) within FEFF9 [1] provides the best possible initial estimate of edge energies for all single and multiple-scattering paths.

In the sections that follow several aspects of MD-XAFS that are useful in the interpretation of various structural feature are described. In this way, the MD-XAFS spectrum can be used as a diagnostic tool to interpret features in the experimental spectrum. There are multiple ways in which MD-XAFS can be applied. Four of these methods are presented later.

18.2.2 Incremental or Partial Structural Contributions to the Total MD-XAFS Spectrum

When the atomic structure in local regions about the absorber includes atoms that are at slightly different distances (static disorder), or the atoms contain significant amount of dynamic disorder, or when there is more than one type of atom, it is often difficult to assign a particular feature in the radial structure function, $|\widetilde{\chi}(R)|$, to a certain atom configuration. In XAFS analysis this problem is compounded by the fact that the photoelectron phase shift function ($\varphi(k)$ in Eq. 18.1) causes broadening of the Fourier transform and displacement of the apparent atom positions even though the true spatial resolution is often equal to that obtained from the best XRD or ND spectra. The use of MD-XAFS offers that ability to dissect the contribution from various atom groups to the measured XAFS spectrum. Figure 18.2a shows an example of this process for the ordering of water molecules about the iodide ion whose structure is shown schematically in the insert [32]. The I-O pair distribution functions from DFT-MD are decomposed into their incremental Nth-neighbor

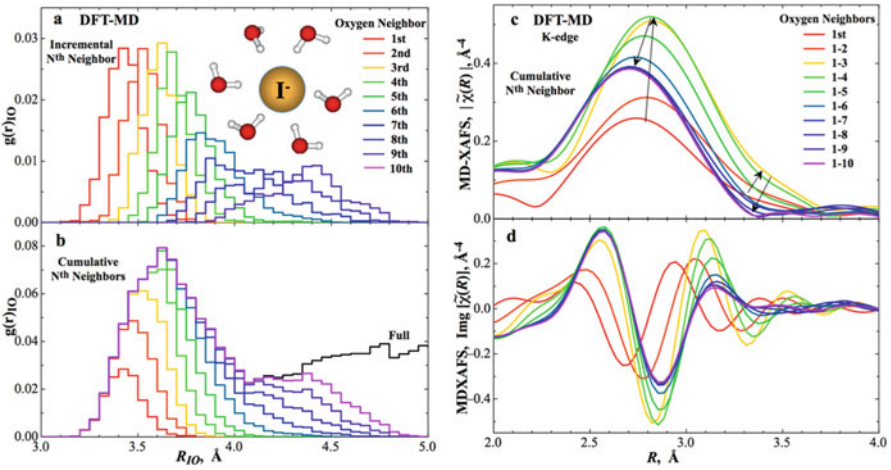

Fig. 18.2 The incremental and cumulative radial distribution functions (**a** and **b**) are used to calculate the corresponding partial cumulative XAFS radial structure plots (**c** and **d**) for a series of water molecules that hydrate the first shell and part of the second shell for an iodide ion in bulk water. Reprinted with permission from ref. [32]. Copyright 2010 American Chemical Society

contributions shown in Fig. 18.2a. These incremental contributions of water populations were constructed as follows. For each representative configuration the water molecules are sorted with respect to the iodide-oxygen distance to identify successive water molecule neighbors. In Fig. 18.2b, the cumulative Nth-neighbor populations show how the distribution of water molecules evolves as the number of water molecules increases up to the full I-O g(r). These cumulative subsets are used to calculate the cumulative MD-XAFS spectra in Fig. 18.2c, d. It is clear to see the complex way in which the XAFS spectrum evolves with each successive shell. This method helps to delineate which regions of the spectrum can be assigned to which hydration shells of the incremental plot in Fig. 18.2a [32].

Whereas the information in the g(r) plot of Fig. 18.2b is only relevant to the single-scattering paths about the absorber, the information in the cumulative XAFS plots in Fig. 18.2c, d contains all the possible single- and multiple-scattering paths that are within the selected set of atoms. In Fig. 18.2c, d, we show the convergence of the amplitude and imaginary part of the XAFS signal, respectively. The arrows indicate the progression with increasing inclusion of nearest neighbors. We find that the signal becomes converged by the inclusion of the seventh nearest neighbor. Beyond this the distribution of position becomes broad and the effective Debye Waller factor reduces its contribution to the XAFS signal. The consistency of the prediction of the XAFS signal [32] with the measured signal gives us confidence that the density functional theory description of the molecular interaction between iodide and water can be predictive in describing the local solvation structure of such species.

18.2.3 *Differentiating Single and Multiple-Scattering Contributions at Coincident Distances*

Figure 18.3b shows portions of the calculated MD-XAFS spectra for hydrated Cr^{3+} ions that are schematically illustrated in Fig. 18.3a. This example illustrates how the scattering contributions from features in the longer range structure in the region from about 2 to 6 Å can be evaluated. This small, trivalent cation is hydrated by six waters in the first shell and they are ordered in a nearly pure octahedral symmetry [31]. This octahedral symmetry leads to a set of strong, collinear multiple-scattering paths (MS) whose position in the radial structure plot (k^2-weighted $|\widetilde{\chi}(R)|$) overlies the region for the single-scattering (SS) from a well-ordered second hydration shell (see Fig. 18.3b). The question arises then about whether these two spatially coincident contributions can be independently resolved in the XAFS spectrum. MD-XAFS is used to isolate these features to compare their relative contributions, as illustrated in Fig. 18.3b. The result shows that the contributions from SS and MS structures each have a unique pattern that allows these two scattering feature to be readily resolved. In this system, many paths contribute to both the SS and MS signals making it difficult to assign parameters to all of the paths and manually fit the signal, resulting in an underdetermined system. The MD generation of the ensemble provides the additional constraints provided by molecular interaction and statistical thermodynamics, allowing a consistent characterization of the system, maximizing the impact of the experimental measurement. These results are similar to an earlier report of this system [20].

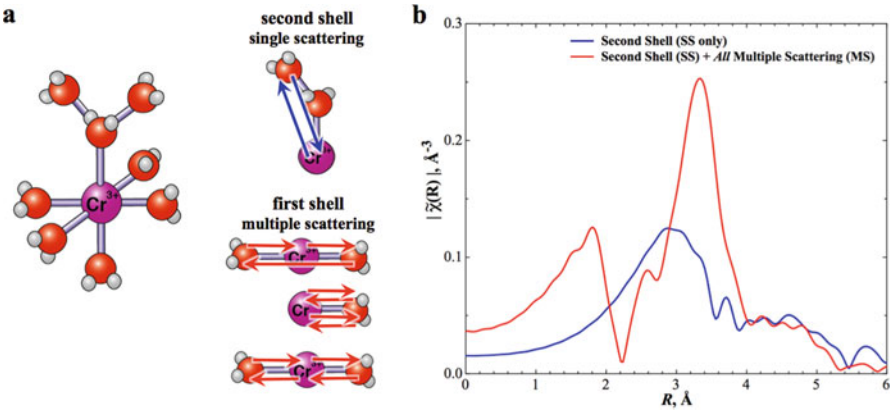

Fig. 18.3 Example of using MD-XAFS to calculate specific structural contributions to the overall spectrum. In (**a**), the single-scattering path for the second shell water and the multiple-scattering paths of the first shell are schematically illustrated. In (**b**), there is a comparison of the scattering contribution from the second shell single-scattering paths with the multiple-scattering contributions from the first shell. Reprinted with permission from ref. [31]. Copyright 2012 American Chemical Society

18.2.4 *Predicting Long-Range XAFS Structure with MD-XAFS*

The same approach may be applied to features at even longer distances, especially for those materials that have lower degrees of static or dynamic disorder where scattering features up to as far as 8 Å from the absorber might be expected. Such features can have contributions from accumulation of 100's or even 1000's of different types of scattering paths. In this case, the relative contributions of these scattering paths can only be evaluated using a method that takes advantage of the information from the full molecular ensemble.

An example of this long-range structure is provided in Fig. 18.4 for aqueous Zn^{2+}, which like Cr^{3+} also has an octahedral first hydration shell. In Fig. 18.4, results from both a GGA functional (PBE96) and a hybrid functional (PBE0) DFT simulation are shown in comparison to the experimental results [16, 31]. This example illustrates how features at such long distances are predicted by MD-XAFS. In Fig. 18.4a, specific regions of the R-space spectra are windowed and then they are back-transformed to the q-space plots shown in Fig. 18.4b, c. This procedure can be used to determine if the structure that arises in the simulated spectrum coincides

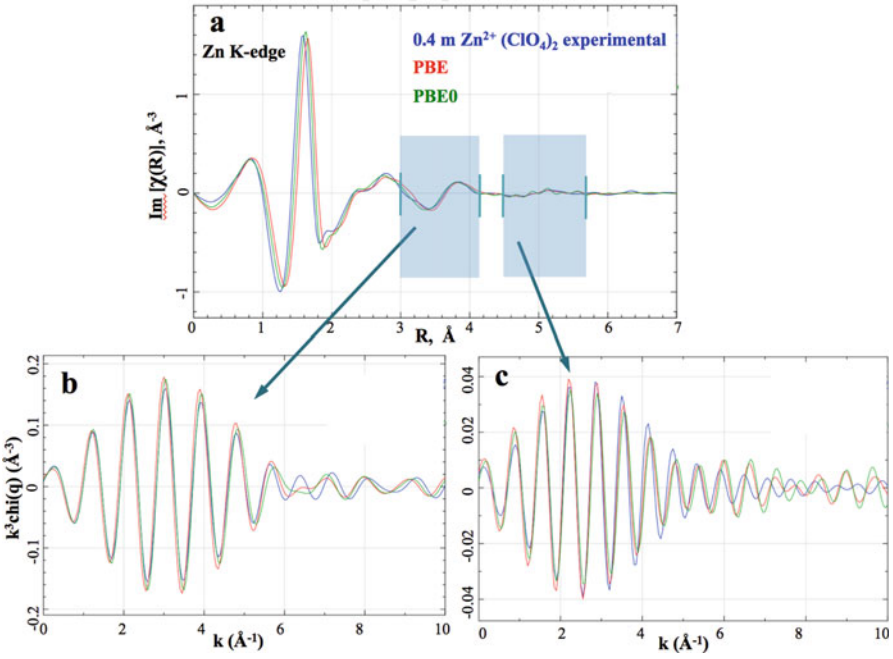

Fig. 18.4 Specific regions of the R-space spectra are windowed and then they are back-transformed to q-space for 0.4 m Zn^{2+} in water. Two different DFT protocols (PBE and PBE0) are compared to the experimental spectrum. Reprinted with permission from ref. [31]. Copyright 2012 American Chemical Society

with the amplitude envelope and the frequency of the oscillations in $\chi(k)$ of the experimental spectrum. In Fig. 18.4a, two different regions, between $3 < R < 4$ Å and $4.5 < R < 5.6$ Å, have been windowed and the resulting inverse transform to q-space is shown in Fig. 18.4b, c, respectively.

As might be expected, for the multiple-scattering region in the shorter range region from 3 to 4.1 Å, the inverse-transform q-space spectrum (Fig. 18.4b) is quantitatively reproduced by the simulations. However, the expectation for the region between 4.5 and 5.6 Å (in Fig. 18.4c) is different. The origin of these features is not completely known because there are 100's of contributing scattering paths that contribute to this region. In part, there are significant contributions from collinear O-Zn-O triple-scattering processes. Both of the DFT simulations accurately capture all of these higher order scattering processes. The ability of the simulation to calculate the long-range structure provides a stringent test of the fidelity of the simulation since even small amounts of structural error would alter the "fingerprint" in this long-range structure.

18.2.5 Multi-edge XAFS Evaluation of Multiple Scattering Using MD-XAFS

There are often limits in the ability of XAFS to discriminate small differences in structure or symmetry. The analysis of XAFS taken at two different edges (e.g., K- and L-edges) can be used in some cases to dramatically improve the structural resolution. For instance, *multiple-scattering* oscillations at the L_2 and L_3-edges have distinctly different phase and amplitude functions than at the K-edge [15]. These phase and amplitude functions depend not only on the symmetry of the multiple-scattering paths but also on the nature of the final state electronic wave function probed by the dipole-allowed transition. Hence, the multiple-scattering portions of K-edge spectra acquired with L_2- or L_3-edge spectra provide independent measurements of the local symmetry not a redundant measurement as is commonly believed. Figure 18.5 illustrates this concept using theory calculations (FEFF) [3] for clusters of water molecules having two different idealized symmetries about an Ag^+ ion. In one case, there are 5 waters in a bipyramidal arrangement and in the other case 4 waters are in a tetrahedral arrangement. For all of the single-scattering paths, there is a simple π-phase shift in the $\chi(k)$ oscillations for these s- versus p- initial states. However for the multiple-scattering portion of the spectrum, the ligand symmetry also strongly defines the phase shift for s- and p-states. The resultant $\mathrm{Im}[\widetilde{\chi}(R)]$ plots that are compared in Fig. 18.5a, b show that the symmetry uniquely controls the multiple-scattering features.

This multiedge analysis method is demonstrated by the use of MD-XAFS to resolve the hydration structure about the iodate anion in water [32]. Initial DFT molecular dynamics simulations predict a very unusual hydration structure about iodate. As shown in the schematic of Fig. 18.6, the region near the O's of the iodate

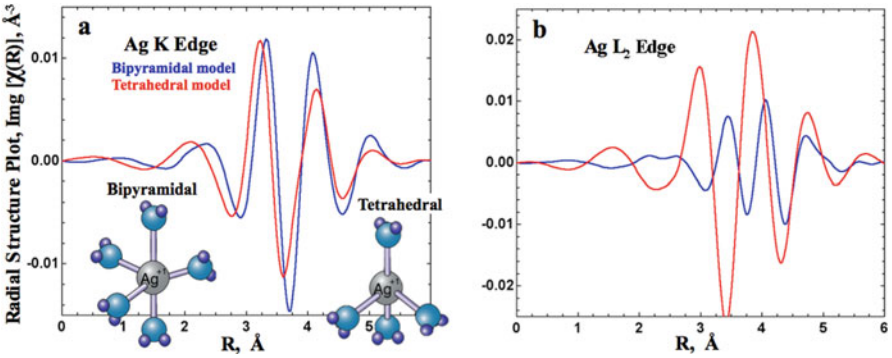

Fig. 18.5 A simple representation (from FEFF9 [1]) of how the local symmetry, in this case bipyramidal versus tetrahedral, about the absorber (Ag^+) affects the structure of the multiple-scattering paths measured at the K- versus the L_2- edges of Ag. Reprinted with permission from ref. [15]. Copyright 2009 American Chemical Society

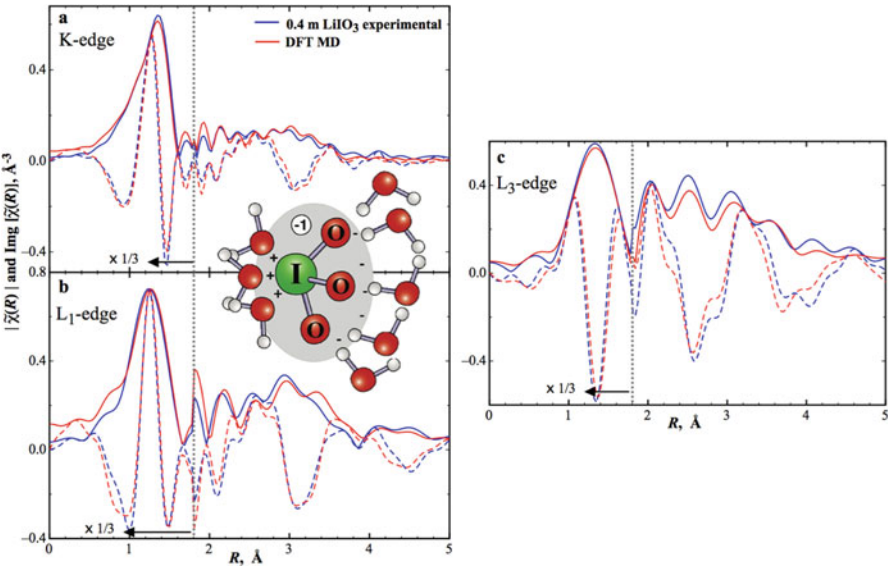

Fig. 18.6 Comparison of the (**a**) K-edge, (**b**) L_1-edge, and (**c**) L_3-edge XAFS spectra for the 0.4 m $LiIO_3$ in water. Both k^2-weighted $|\widetilde{\chi}(R)|$ (*solid*) and $\mathrm{Im}[\widetilde{\chi}(R)]$ (*dashed*) plots are shown for the experiment and the DFT-MD simulation. The region below1.8 Å has been rescaled by 1/3 for better emphasis of the high-R structure. Reprinted with permission from ref. [33]. Copyright 2011 American Chemical Society

is hydrated by waters that are oriented with their H's pointed toward the anion. In the region about the iodine atom, the waters are rotated approximately 180° such that the O's are interacting with the I atom. This leads to the remarkable conclusion that one region of iodate behaves like a cation while the other region behaves like an

anion. Multiedge analysis offers the opportunity to clearly resolve this structure experimentally. In Fig. 18.6, the K-, L_1-, and L_3-edge experimental spectra are compared to those calculated from DFT-MD simulations. Across the entire R-range there is near-quantitative agreement for all three edges, thus confirming the structural features of the simulation.

18.3 Molecular Dynamics XAFS for Diverse Chemical Systems

Perhaps the most important role of MD-XAFS, when combined with experimental spectra, is to derive a deeper understanding of the chemistry and structure in condensed phase systems. In particular, density functional theory-based MD can accommodate the extreme chemical diversity of many systems by treating the dozens of different intermolecular interactions and their chemical reactions using first-principle methods. DFT represents a powerful representation of molecular interaction that contains an explicit representation of electron charge density and takes into account electronic structure, allowing for an effective treatment of bonding. It is a technique that contains a balance between efficiency and accuracy that enables effective sampling of configurations of systems of sufficient size to be predictive.

The sections below provide brief examples of several different types of chemical systems in which DFT-MD simulations quantitatively replicate the average structure in the experimental system. The examples include (1) the hydration structure about aqueous divalent and trivalent transition metal ions in water, (2) the structure of a Rh_4 catalyst cluster while it is active in a dehydrogenation reaction, (3) the structure about an Al atom in two different crystalline solids, and (4) the ion-pair structure of Cl^- with hydronium ion (H_3O^+) in water.

18.3.1 Transition Metal Ions in Water

The hydration of transition metal ions is important in catalysis, biochemical reactions especially those involving enzymes and in broad areas of geochemistry. Figure 18.7 compares the structure for a series of cations [31] including Cr^{3+}, Fe^{3+}, Mn^{2+}, Co^{2+}, Ni^{2+}, Zn^{2+}, and Ca^{2+}. These divalent and trivalent cations generally have 6 coordinating waters in the first shell in an octahedral symmetry. The cations that have smaller ion radii or high ionic charge (3+) will also have a well-defined second hydration shell containing approximately 12 water molecules. The XAFS signal for all of these systems is dominated by single scattering from the waters in the first shell. Equally important with respect to the structural information are the photoelectron multiple-scattering paths originating from the first shell waters. The

multiple-scattering paths lead to a unique XAFS signature or fingerprint that is different for each ion due to small differences in the distances and disorder. Finally, there are the single-scattering paths from the second hydration shell that also contribute significantly to the total photoelectron scattering.

Figure 18.7 compares the experimental $\mathrm{Im}|\widetilde{\chi}(R)|$ spectra with the predicted spectra from two different types of DFT-MD simulations [31]. One of the simulations (AIMD) uses a GGA functional (PBE96) wherein all molecules in the

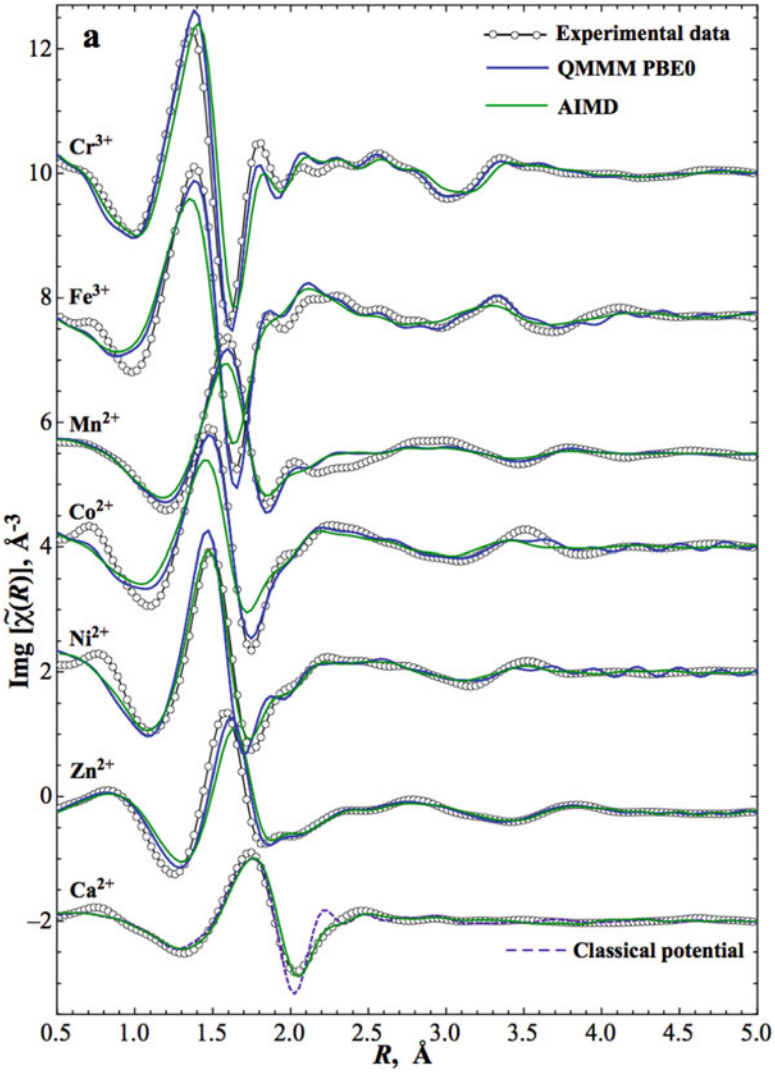

Fig. 18.7 MD-XAFS spectra from two different DFT-MD simulations for a series of transition metal cations. Reprinted with permission from ref. [31]. Copyright 2012 American Chemical Society

simulation are treated at the same DFT level. The other type of the simulation (QM/MM) uses a more computationally expensive hybrid functional that includes exchange (PBE0) to describe the first-shell water, whereas the higher water shells are treated using classical empirical potentials (MM). As shown in Fig. 18.7, both levels of theory provide near-quantitative agreement with the experimental spectra for most ions including the single-scattering peak at about 1.5–2 Å as well as the more challenging multiple-scattering features at 3–4.5 Å. This level of agreement is difficult to achieve with classical potentials without development of, and careful optimization of the ion-water interaction potentials. This example exemplifies the quality and ease of implementation of DFT-MD simulations. This example also shows the ease in which various simulation approaches can be benchmarked against a range of different chemical systems.

Only through comparison with a comprehensive series of ions having different interaction strengths is it possible to identify systematic errors that are part of the DFT theory. A large improvement in agreement of the theory was obtained by increasing the accuracy of the pseudopotential from the common default setting. By including the 3 s and 3p functions in the description of the pseudopotential, thereby better describing polarization, there is a large improvement in the predicted first shell bond distance by approximately 0.1 Å. The second factor affecting the DFT accuracy is the level of exchange in the theory. Inclusion of exchange (PBE0) further improved the metal-water distance by about 0.03 Å and also results in significant improvement in the predicted Debye Waller factor for the first shell [31].

18.3.2 Reacting System of Rh_4 Clusters During the Dehydrogenation of Amine Borane

Another example of MD-XAFS analysis involves tracking the structure of a transition-metal catalyst during (operando) a chemical reaction [35]. The reaction of interest involves the dehydrogenation of amine boranes (Fig. 18.8b) representing a possible starting point for hydrogen storage [35, 37, 38]. This dehydrogenation reaction is readily catalyzed by a homogeneous Rh species. As illustrated in the schematic of Fig. 18.8a, the catalyst involves a Rh_4 cluster that is capped on each Rh atom by two ligands of methyl ammonium borane that are binding through the B atom.

Figure 18.8c shows three examples of different snapshots from the DFT trajectory for his reaction [35]. The Rh_4 cluster undergoes significant alteration during the cycle of the amine borane dehydrogenation reaction. Some of observed intermediate species are shown in the schematics of Fig. 18.8d that illustrate not only the alteration of the ligand bonding but also alteration of the Rh-Rh bonding.

The XAFS spectrum for many of these predicted intermediates is quite different from those of the dominant species. The simulation shows that the catalyst is highly fluxional in nature and that the reacting Rh_4 cluster progresses through a broad

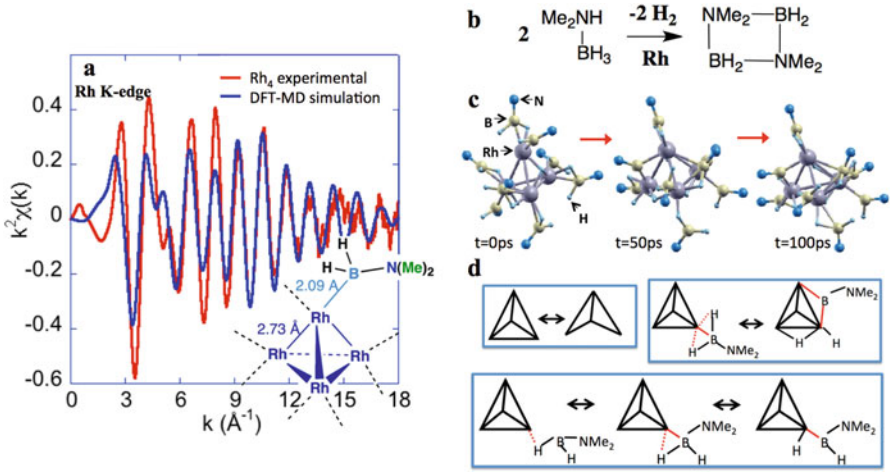

Fig. 18.8 In (**a**), MD-XAFS results for the time-average Rh_4 cluster in a $k^2\chi(k)$plot are shown. The other panels show the overall reaction (**b**), three representative simulation snapshots (**c**), and a few representative structures for the various fluxional species (**d**). Reprinted with permission from ref. [35]. Copyright 2009 American Chemical Society

range of transition states. The DFT simulations thus confirm findings from XAFS measurements that (1) the time-average structure is a Rh_4 cluster, (2) the Rh-B and Rh-Rh bond distances are in agreement with the experimental values, and (3) the primary ligand on the Rh binds through a B and not N (of amine borane). In summary, the DFT molecular dynamics sampling of the statistical ensemble of configurations provides remarkable agreement with the XAFS spectrum measured under reaction conditions. The combination of XAFS spectroscopy and simulation provides key insights into the active site and catalytic reaction pathways.

18.3.3 Alumina and Zeolite Structure at the Al Atomic Site

All of the previous examples have involved solution-phase or homogeneous systems. The MD-XAFS method is equally useful for solid phase samples (crystalline or amorphous). As an example, the Al K-edge XAFS spectra for two different crystalline materials are shown in Fig. 18.9 [36]. In Fig. 18.9a, the Al K-edge spectra of pure α-Al_2O_3 (corundum) are shown. Figure 18.9b shows the spectrum for the Al tetrahedral sites (T-site) within an aluminosilicate zeolite (HBEA) that has an overall Al:Si ratio of 1:75. For these crystalline materials, the method of generating the MD trajectory is somewhat different than for solution phase spectra. The initial configuration for the MD simulation starts with the established crystal XRD structure. Further, in these examples, the density is fixed to the measured density. Finally, the MD trajectory at 300 K is generated to establish an ensemble of

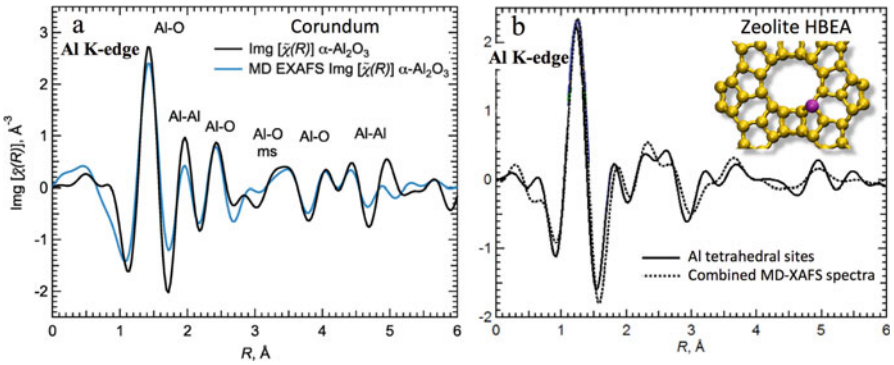

Fig. 18.9 Experimental and calculated MD-XAFS spectra for (**a**) pure α-Al_2O_3 (corundum) and (**b**) an aluminosilicate zeolite (HBEA, with Al:Si ratio of 1:75). Reprinted with permission from ref. [36]. Copyright 2014 American Chemical Society

atom positions about the photo-absorber. As shown in Fig. 18.9a, b, the features of the experimental $\mathrm{Im}|\widetilde{\chi}(R)|$ spectra up to at least 5 Å are well reproduced by the DFT-MD simulation in both cases. There are large differences in the positions and amplitudes of the peaks in these two spectra reflecting the very different structure. For α-Al_2O_3, the Al occurs in a distorted octahedral position whereas the Al atoms in the zeolite reside in tetrahedral sites.

In the case of zeolite HBEA, there are nine crystallographically different T-sites. Each T-site has significant variations in the bond angles and distances that give rise to XAFS spectra that can be used to help differentiate the distribution of Al among the various T-site positions. The substitution of Al into these nine different T-sites is not random since during the synthesis process there are preferential locations of Al in certain sites. To discriminate Al atoms at certain T-sites, MD-XAFS spectra were first generated for each of the nine different Al T-sites. Through comparison with the experimental spectra the Al distribution into three classes of T-sites could be demonstrated [36].

18.3.4 Chemistry of Aqueous HCl

The chemical equilibrium between different states can be probed with XAFS under special circumstances when there are a limited number of structurally independent species. MD-XAFS has been used to explore the structure of concentrated aqueous HCl solutions [34]. The classical understanding of this solution is that the acid is fully dissociated into two noninteracting species, the hydrated anion (Cl^-) and the hydronium cation (H_3O^+). However, an earlier XAFS study [39] proposed that at moderate to high concentrations of HCl, the chloride and hydronium may exist as a contact ion pair species ($Cl^- - H_3O^+$).

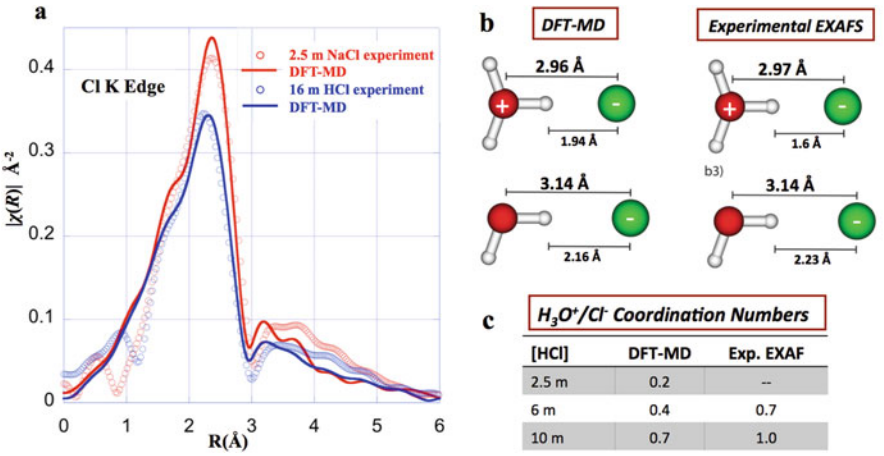

Fig. 18.10 (**a**) Comparison of the experimental Cl K-edge XAFS (*open symbols*) and with MD-XAFS (*solid lines*) spectra for 2.5 m NaCl and 16 m HCl. (**b**) Cl-O bond distances for water and hydrondium and (**c**) the chloride-hydronium coordination numbers. Reprinted with permission from ref. [34]. Copyright 2014 American Chemical Society

Figure 18.10 compares the experimental and calculated Cl K-edge spectra for 2.5 m NaCl and 16 m HCl solutions. In the case of 2.5 m NaCl, it is well established that the first-shell hydration structure contains the fully solvated Cl^- having approximately 6–7 water at a Cl-O distance of 3.14 Å. In Fig. 18.10a, for the concentrated HCl (6 m), there is a shortening of the distance for the main Cl-O peak and a reduction in the amplitude. This is the result of the formation of a new first-shell Cl^- species due to the contact-ion pairing with H_3O^+ that resides at a Cl-O distance that is about 0.2 Å shorter. There is excellent agreement between the experimental and the MD-XAFS spectra. In addition, as shown in Fig. 18.10b, c, the structural parameters of the ion pair bond distances and coordination numbers are in excellent agreement. The overall MD-XAFS analysis creates a new picture where there is extensive ion pairing in acid solutions even at moderate concentrations [34]. This demonstrates that, instead of being a neutral noninteracting species, Cl^- is an active participant in the chemistry that defines the pH scale through its ion pairing with H_3O^+.

18.4 Summary

MD-XAFS is such a powerful technique and simulation capabilities have advanced to the point where it is practical to make it a common practice in the analysis of complex systems. It is an analytical probe of structure, competing with other x-ray as well as neutron diffraction techniques. Similar quality information that

significantly complements other techniques can be obtained. Furthermore, the complexity of the analysis is reduced by embracing a technique that focuses on an element or region of interest, allowing spatial resolution that competes with other techniques.

Acknowledgement This development could not be achieved without the support from our colleagues including John Rehr, Maureen McCarthy, Bruce Palmer, Mali Balasubramanian, Chris Mundy, Marcel Baer, Liem Dang, Shawn Kathmann, Eric Bylaska, Roger Rousseau, Vanda Glezakou. This work was supported by the U.S. Department of Energy (DOE) Office of Science, Office of Basic Energy Sciences (BES), Division of Chemical Sciences, Geosciences & Biosciences. Pacific Northwest National Laboratory (PNNL) is operated for the U.S. DOE by Battelle.

References

1. Rehr JJ, Kas JJ, Vila FD, Prange MP, Jorissen K (2010) Parameter-free calculations of X-ray spectra with FEFF9. Phys Chem Chem Phys 12(21):5503–5513
2. Rehr JJ, Kas JJ, Prange MP, Sorini AP, Takimoto Y, Vila F (2009) Ab initio theory and calculations of X-ray spectra. C R Phys 10(6):548–559
3. Rehr JJ, Albers RC (2000) Theoretical approaches to x-ray absorption fine structure. Rev Mod Phys 72(3):621–654
4. Palmer BJ, Pfund DM, Fulton JL (1996) Direct modeling of EXAFS spectra from molecular dynamics simulations. J Phys Chem 100(32):13393–13398
5. Wallen SL, Palmer BJ, Pfund DM, Fulton JL, Newville M, Ma YJ, Stern EA (1997) Hydration of bromide ion in supercritical water: an X-ray absorption fine structure and molecular dynamics study. J Phys Chem A 101(50):9632–9640
6. Wallen SL, Palmer BJ, Fulton JL (1998) The ion pairing and hydration structure of Ni^{2+} in supercritical water at 425 degrees C determined by x-ray absorption fine structure and molecular dynamics studies. J Chem Phys 108(10):4039–4046
7. Fulton JL, Hoffmann MM, Darab JG, Palmer BJ, Stern EA (2000) Copper(I) and copper (II) coordination structure under hydrothermal conditions at 325 degrees C: an X-ray absorption fine structure and molecular dynamics study. J Phys Chem A 104(49):11651–11663
8. Hoffmann MM, Darab JG, Palmer BJ, Fulton JL (1999) A transition in the Ni^{2+} complex structure from six- to four-coordinate upon formation of ion pair species in supercritical water: an X-ray absorption fine structure, near-infrared, and molecular dynamics study. J Phys Chem A 103(42):8471–8482
9. McCarthy MI, Schenter GK, ChaconTaylor MR, Rehr JJ, Brown GE (1997) Prediction of extended x-ray-absorption fine-structure spectra from molecular interaction models: $Na^{+}(H_2O)_{(n)}$-MgO (100) interface. Phys Rev B 56(15):9925–9936
10. Campbell L, Rehr JJ, Schenter GK, McCarthy MI, Dixon D (1999) XAFS Debye-Waller factors in aqueous Cr^{+3} from molecular dynamics. J Synchrotron Radiat 6:310–312
11. Dang LX, Schenter GK, Fulton JL (2003) EXAFS spectra of the dilute solutions of Ca^{2+} and Sr^{2+} in water and methanol. J Phys Chem B 107(50):14119–14123
12. Dang LX, Schenter GK, Glezakou VA, Fulton JL (2006) Molecular simulation analysis and X-ray absorption measurement of Ca^{2+}, K^{+} and Cl^{-} ions in solution. J Phys Chem B 110 (47):23644–23654
13. Glezakou V-A, Chen YS, Fulton JL, Schenter GK, Dang LX (2006) Electronic structure, statistical mechanical simulations and EXAFS spectroscopy of aqueous potassium. Theor Chem Acc 115:86–99

14. Nichols P, Bylaska EJ, Schenter GK, de Jong W (2008) Equatorial and apical solvent shells of the UO(2)(2+) ion. J Chem Phys 128(12):124507
15. Fulton JL, Kathmann SM, Schenter GK, Balasubramanian M (2009) Hydrated structure of Ag (I) ion from symmetry-dependent, K- and L-edge XAFS multiple scattering and molecular dynamics simulations. J Phys Chem A 113(50):13976–13984
16. Cauet E, Bogatko S, Weare JH, Fulton JL, Schenter GK, Bylaska EJ (2010) Structure and dynamics of the hydration shells of the Zn^{2+} ion from ab initio molecular dynamics and combined ab initio and classical molecular dynamics simulations. J Chem Phys 132(1):194502
17. Atta-Fynn R, Bylaska EJ, Schenter GK, de Jong WA (2011) Hydration shell structure and dynamics of curium(III) in aqueous solution: first principles and empirical studies. J Phys Chem A 115(18):4665–4677
18. Atta-Fynn R, Johnson DF, Bylaska EJ, Ilton ES, Schenter GK, de Jong WA (2012) Structure and hydrolysis of the U(IV), U(V), and U(VI) aqua ions from ab initio molecular simulations. Inorg Chem 51(5):3016–3024
19. Bogatko S, Cauet E, Bylaska E, Schenter G, Fulton J, Weare J (2013) The aqueous Ca^{2+} system, in comparison with Zn^{2+}, Fe^{3+}, and Al^{3+}: an ab initio molecular dynamics study. Chem A Eur J 19(9):3047–3060
20. Merkling PJ, Munoz-Paez A, Martinez JM, Pappalardo RR, Marcos ES (2001) Molecular-dynamics-based investigation of scattering path contributions to the EXAFS spectrum: the Cr^{3+} aqueous solution case. Phys Rev B 6401(1):2201
21. Carrera F, Torrico F, Richens DT, Munoz-Paez A, Martinez JM, Pappalardo RR, Sanchez Marcos E (2007) Combined experimental and theoretical approach to the study of structure and dynamics of the most inert aqua ion $Ir(H_2O)(6)$ (3+) in aqueous solution. J Phys Chem B 111(28):8223–8233
22. Ferlat G, Soetens JC, San Miguel A, Bopp PA (2005) Combining extended x-ray absorption fine structure with numerical simulations for disordered systems. J Phys Condens Matter 17(5): S145–S157
23. Pokrovski GS, Roux J, Ferlat G, Jonchiere R, Seitsonen AP, Vuilleumier R, Hazemann J-L (2013) Silver in geological fluids from in situ X-ray absorption spectroscopy and first-principles molecular dynamics. Geochim Cosmochim Acta 106:501–523
24. Chaodamrongsakul J, Klysubun W, Vao-soongnern V (2014) Application of X-ray absorption spectroscopy and molecular dynamics simulation to study the atomistic solvation structure of tetraglyme:KSCN electrolytes. Mater Chem Phys 143(3):1508–1516
25. Chaodamrongsakul J, Merat K, Klysubun W, Vao-soongnern V (2013) A combined molecular dynamic simulation and X-ray absorption spectroscopy to investigate the atomistic solvation structure of cation in poly(vinyl alcohol):potassium thiocyanate (KSCN) solid electrolytes. J Non-Cryst Solids 379:21–26
26. Timoshenko J, Anspoks A, Kalinko A, Kuzmin A (2014) Local structure and dynamics of wurtzite-type ZnO from simulation-based EXAFS analysis. Phys Status Solidi C 11 (9–10):1472–1475
27. Anspoks A, Kalinko A, Kalendarev R, Kuzmin A (2013) Probing vacancies in NiO nanoparticles by EXAFS and molecular dynamics simulations. 15th international conference on x-ray absorption fine structure (Xafs15) 2013, 430
28. Anspoks A, Kalinko A, Kalendarev R, Kuzmin A (2012) Atomic structure relaxation in nanocrystalline NiO studied by EXAFS spectroscopy: role of nickel vacancies. Phys Rev B 86(17):174114
29. Migliorati V, Sessa F, Aquilanti G, D'Angelo P (2014) Unraveling halide hydration: a high dilution approach. J Chem Phys 141(4):044509
30. D'Angelo P, Zitolo A, Migliorati V, Chillemi G, Duvail M, Vitorge P, Abadie S, Spezia R (2011) Revised ionic radii of lanthanoid(III) ions in aqueous solution. Inorg Chem 50 (10):4572–4579
31. Fulton JL, Bylaska EJ, Bogatko S, Balasubramanian M, Cauet E, Schenter GK, Weare JH (2012) Near-quantitative agreement of model-free DFT-MD predictions with XAFS

observations of the hydration structure of highly charged transition-metal ions. J Phys Chem Lett 3(18):2588–2593
32. Fulton JL, Schenter GK, Baer MD, Mundy CJ, Dang LX, Balasubramanian M (2010) Probing the hydration structure of polarizable halides: a multiedge XAFS and molecular dynamics study of the iodide anion. J Phys Chem B 114(40):12926–12937
33. Baer MD, Pham VT, Fulton JL, Schenter GK, Balasubramanian M, Mundy CJ (2011) Is iodate a strongly hydrated cation? J Phys Chem Lett 2(20):2650–2654
34. Baer MD, Fulton JL, Balasubramanian M, Schenter GK, Mundy CJ (2014) Persistent ion pairing in aqueous hydrochloric acid. J Phys Chem B 118(26):7211–7220
35. Rousseau R, Schenter GK, Fulton JL, Linehan JC, Engelhard MH, Autrey T (2009) Defining active catalyst structure and reaction pathways from ab initio molecular dynamics and operando XAFS: dehydrogenation of dimethylaminoborane by rhodium clusters. J Am Chem Soc 131(30):10516–10524
36. Vjunov A, Fulton JL, Huthwelker T, Pin S, Mei D, Schenter GK, Govind N, Camaioni DM, Hu JZ, Lercher JA (2014) Quantitatively probing the Al distribution in zeolites. J Am Chem Soc 136(23):8296–8306
37. Chen YS, Fulton JL, Linehan JC, Autrey T (2005) In situ XAFS and NMR study of rhodium-catalyzed dehydrogenation of dimethylamine borane. J Am Chem Soc 127(10):3254–3255
38. Fulton JL, Linehan JC, Autrey T, Balasubramanian M, Chen Y, Szymczak NK (2007) When is a nanoparticle a cluster? An operando EXAFS study of amine borane dehydrocoupling by Rh_{4-6} clusters. J Am Chem Soc 129(39):11936–11949
39. Fulton JL, Balasubramanian M (2010) Structure of hydronium (H_3O^+)/chloride (Cl^-) contact ion pairs in aqueous hydrochloric acid solution: a zundel-like local configuration. J Am Chem Soc 132(36):12597–12604

Part V
XAFS Applications

Chapter 19
Metal Nanocatalysts

Yuanyuan Li and Anatoly I. Frenkel

19.1 Introduction

Metal nanoparticles (NPs) under several tens of nanometers in size have unique mechanical, optical, electronic, and catalytic properties that are different from their bulk counterparts [1–5]. Structural characterization of NPs is a key to answering many questions related to their catalytic properties, for example, what is the nature of catalytically active sites, or what are the reasons for their catalytic activity, selectivity, and stability. Various structural, geometric, and electronic characteristics were named "descriptors" of catalytic properties in transition metal catalysts, such as the number of under-coordinated sites [6, 7], or perimeter sites [7, 8], or number of (111) crystalline facets [9], or surface strain [10], or the position of the D-states relative to the Fermi level (a "D-band center" model) [11–15]. The main challenge preventing direct measurements of those characteristics is the small size of nanoparticles. Indeed, in size range of several nanometers, there are very few techniques capable of characterizing structure and electronic properties with sufficient spatial and energy resolutions. A challenge specific to catalysts is the need to monitor their structure and electronic properties in situ, during their work, also known as "in *operando* conditions." That latter requirement is particularly challenging to electron microscopy and other imaging techniques that are severely limited in use by requirements of high pressure and temperature, typical for many catalytic reactions. Other structural characterization techniques such as X-ray diffraction are limited by the small size of the nanoparticles that is responsible for broadening Bragg peaks used for structural refinement. XAFS analysis methods are excellent alternatives to imaging and scattering methods due to the excellent spatial, temporal, and energy resolutions of XAFS, and due to the relative ease of its

Y. Li • A.I. Frenkel (✉)
Department of Physics, Yeshiva University, New York, NY 10016, USA
e-mail: anatoly.frenkel@yu.edu

Y. Iwasawa et al. (eds.), *XAFS Techniques for Catalysts, Nanomaterials, and Surfaces*, DOI 10.1007/978-3-319-43866-5_19

application to real-time processes in *operando* conditions. In recent years, it became progressively more appreciated that supported NPs are complex systems whose catalytic properties are influenced not only by the structure of the particle but also in not a small degree by its interaction with support and adsorbates. In this chapter, we review the main attributes of supported NPs that affect their catalytic activities, recent solutions to the structural characterization of NPs and describe recent advances in solving three-dimensional structure, degree of alloying, and their changes under conditions of model and real catalytic reactions.

19.2 Size, Shape, Strain, Support, and Composition Effects on Catalytic Properties

With the decrease of particle size, the surface to volume ratio increases, shifting the balance between the surface and the bulk energies in favor of the former. Enhanced surface energy is responsible for generating substantial surface strain [16, 17], that can be relieved by some adsorbates, e.g., hydrogen [5, 18, 19]. The enhanced surface stress causes contraction of surface metal–metal bond length [16, 20, 21]. The surface energy and surface stress thus have important influence on the elastic properties of NPs.

In nanocatalysts strain is a ubiquitous attribute of their structure. It dominates the surface and support interface regions, and, in the case of bimetallics, is also present throughout the bulk, due to the size mismatch of two types of metals [10, 16, 22–25]. The increased surface strain results in the shift of D-band center [10, 26–28] which tunes the binding energy between surface atoms and adsorbed molecules [10–12], and changes cohesive energy of surface atoms which alters the thermodynamic properties and stiffness of NPs [17, 29].

Electronic structure of NPs could also be modified through the change of particle size. Lowering the coordination number of NPs causes the tendency towards localization of the valence electrons and gap formation, hence, the transition from metallic (at large sizes) to nonmetallic (in small sizes) properties. Another consequence of decreasing particle size is thus the reduction of the width of valence band and the shift of its center of gravity towards Fermi level which leads to an increase of the adsorption energy of adsorbate and a decrease of the dissociation barriers of adsorbed molecules [13, 14, 30]. For transition metals catalysts, their properties could thus be tailored through the D-band center position relative to the Fermi energy by changing the composition (adding different metal atoms) [13, 15, 31], surface strain, support material [32–35], or adsorbate coverage [12].

NPs with various shapes expose different facets, which may have different properties with respect to catalysis in the course of the same reaction [36, 37]. In addition, different surface types contain different fractions of under-coordinated atoms (on edge and vertex), which are considered to be the active sites in many reactions [6–9]. Shapes of NPs are shown to change with size [38], however, when

particles are extremely small, and they could adopt various geometries with comparable energies. The fluctuation of geometries and structures could lower the reaction barrier [39, 40]. Finally, the nanoparticles can coexist in the ordered and disordered states in the same size range, and their fractions can change in reaction condition, further hampering efforts in their characterization and thus understanding catalytic mechanisms [18].

Most heterogeneous nanocatalysts are deposited on supports, which distort the atomic structure of the interfacial layer in contact with the substrate, creating defects, strain at interface and may even change the shape of NPs [22, 32, 33]. On the other side, supports with different reducibility have different influences on the electronic structure of NPs. These structural and electronic factors control the metal/support adhesion energy, which affects chemical potentials of surface atoms and their binding ability to small adsorbates [35].

The addition of the second metal to monometallic systems was found to be an effective way to tune the properties and structures of nanocatalysts. The possible mixing patterns of bimetallic systems reported in literature vary from random alloys, core–shell, cluster-by-cluster, and other architectures, depending on the elements, their compositions and synthesis conditions [41, 42]. The introduction of the second metal could introduce strain, alter the electronic structure and, hence, the d-band center position, which greatly affects the interaction between the surface atoms and adsorbates. Many bimetallic systems were reported to change their structure and/or compositional motifs in response to the changes in the environmental conditions or in the process of catalytic reactions [43–45]. Tracking the structural changes of bimetallic systems *in operando* mode, that is, during real reaction conditions, while monitoring the reaction in real time, is thus quite important for revealing their working mechanisms.

19.3 Experimental Characterization of Nanoparticle Structure and Electronic Properties: The Uniqueness of XANES and EXAFS

X-ray diffraction (XRD), X-ray photoelectron spectroscopy (XPS), and electron microscopy are commonly used techniques for bulk or surface structure characterization. When particle size is in nanometer range, XRD is not very helpful due to the Bragg peak broadening. Electron microscopy, on the other hand, has very high resolving power, which helps reveal the atomic and surface structure of NPs [46]. However, if used in situ, only part of the ensemble of catalytic species can be reliably detected (above the resolution limit) and reports of applications of TEM to *operando* studies are still scarce. X-ray absorption spectroscopy (XAS), on the other hand, can be done in a number of sample conditions (liquid or gas, low or high temperatures and pressures) [47–52], and a number of reactor cells are available to date [53–57]. Its sensitivity to local structure and elemental specificity make it

uniquely fitting for studying nanomaterials. With the development of the analytical methods for XANES and EXAFS interpretation, a lot of information related to the physical properties of nanomaterials, such as stress-induced bond length change and disorder [19, 22, 58], three-dimensional geometry of small clusters [59, 60], electronic structure modification driven by support/environment [61], and mixing pattern of bimetallic systems [45, 62, 63], could be obtained. In recent years, with the proliferation of in situ and *operando* methods of catalyst characterization, combination of XAFS with other techniques (IR, Raman, XRD, NMR, UV–Vis, etc.) helped illuminate cooperative phenomena at the interfaces between nanoparticle, surface species, and support under realistic working conditions [43, 50, 56, 74–88].

In the following sections, we review recent progress in structural characterization of nanocatalysts by EXAFS methods.

19.4 Size and Geometry of Nanocatalysts by Coordination Number Analysis

Historically, the importance of EXAFS for catalysis studies [89] was realized almost immediately after XAFS was recognized as a new method of studying local structure in 1970s [90–94]. First works used it for measuring coordination numbers of supported monometallic and heterometallic NPs to obtain their average size (only first shell/single scattering analysis was possible) [95–98]. Then, with the development of multiple scattering (in the 1990s) [99] more advanced analysis methods were developed for determination of cluster size, shape, morphology, and mixing pattern in bimetallic systems. Information about the atomic architecture (three-dimensional packing of atoms) in a representative NP can be most directly gleaned from the coordination number of first nearest neighboring metal–metal bonds. The coordination number ($n_{AA(i)}$) of the ith shell with the radius R_i around the absorbing atom in a monometallic cluster is defined as the average number, per absorber, of nearest neighbors within a given shell:

$$n_{AA(i)} = \frac{2N_{\mathrm{AA(i)}}}{N_A}. \tag{19.1}$$

Here $N_{AA(i)}$ is the total number of the A–A nearest neighbors within the same coordination shell, and N_A is the total number of A-type atoms in the cluster. The factor of two in Eq. (19.1) is due to the fact that each atom of the A–A pair is an absorber and thus the number of these pairs should be doubled in calculating the A–A coordination numbers. Coordination numbers are obtained model-independently from data analysis of experimental EXAFS spectra. The most important information that is available via the coordination number analysis is the average particle

size, and several methods are available for its determination from the EXAFS coordination numbers [100].

One such method, developed by Calvin et al. [101], assumes homogeneous spherical shape of clusters with the radius R. For atoms in the *i*th shell around the absorbing atom, the coordination number of the *i*th shell ($N_{nano(i)}$) can be expressed as follows:

$$N_{nano(i)} = \left[1 - \frac{3}{4}\left(\frac{r_i}{R}\right) + \frac{1}{16}\left(\frac{r_i}{R}\right)^3\right] N_{bulk(i)}. \tag{19.2}$$

In Eq. (19.2), r_i is the distance between the absorbing atom and neighboring atoms in the *i*th shell, and $N_{bulk(i)}$ is the *i*th shell coordination number of bulk structure. This method allows the calculation of coordination number of an arbitrary coordination shell as a function of the cluster size, which in principle, can be used to discriminate between symmetric (quasi-spherical) and asymmetric clusters if the coordination numbers of the higher-order shells are measured by EXAFS. One disadvantage of this method is that it is limited to sufficiently large clusters (with number of atoms much larger than 100) [60].

Another useful method for estimating cluster size is comparing the first nearest coordination number (N_1) obtained from EXAFS analysis against model structures with known geometrical characteristics. For regular polyhedra (e.g., a cuboctahedron or an icosahedron), N_1 is a function of cluster order L, which is defined as the number of spacing between adjacent atoms along the edge (see example of $L = 2$ in Fig. 19.1) [102]. This method developed by Montejano-Carrizales et al. [102, 103], is easy to expand to other morphologies and cluster families [59]. For example, the truncated cuboctahedral model with the (111) plane parallel to the support is most close to the morphology found in many supported metal clusters (Fig. 19.1). The relationship between N_1 and L in a truncated cuboctahedron is: [104]

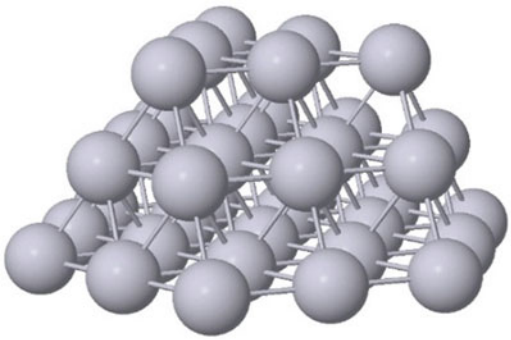

Fig. 19.1 Schematic of a truncated cuboctahedral cluster with 37 atoms ($L = 2$)

$$N_1 = \frac{3\left(20L^3 + 21L^2 + 7L\right)}{5L^3 + 12L^2 + 10L + 3}. \tag{19.3}$$

For truncated cuboctahedron with atom numbers of 10 ($L = 1$), 37 ($L = 2$), 92 ($L = 3$), and 185 ($L = 4$), the first nearest coordination numbers are 4.8, 7.0, 8.2, and 8.9, respectively.

Another method that is useful in the case when there is no particular symmetry known in advance, and/or nearest neighboring shells cannot be easily identified but the coordinates of atoms in the cluster are available from, e.g., first principle simulations, is the radial distribution function (RDF) method [59, 105]. This approach, proposed by Frenkel and Glasner [59], employs computer-generated cluster coordinates. The cluster-average pair radial distribution function $\rho(r)$ is computed for a cluster of N atoms:

$$\rho(r) = \frac{1}{N}\sum_{i=1}^{N}\rho_i(r),\ \rho_i(r) = \frac{dN_i}{dR_i}, \tag{19.4}$$

where $\rho_i(r)$ is the partial RDF for an atom i, and dN_i is the number of its neighbors within the spherical shell of thickness dR_i. The subsequent calculation of coordination numbers for an arbitrary coordination shell (between R_1 and R_2) is achieved by integrating the ρ(r):

$$n_i = \int_{R_1}^{R_2}\rho(r)dr. \tag{19.5}$$

Compared to the two methods described above, the RDF method enables rapid calculation of coordination numbers of clusters with arbitrary sizes and shapes. By combining electron microscopy with multiple-scattering EXAFS analysis and data modeling, several geometries with the same sequence of coordination numbers of the nearest-neighbor shells can be discriminated [106, 107]. The authors can be contacted for sharing their software program that performs RDF calculations for arbitrary cluster geometries.

The methods listed above for size estimation are strongly dependent on the knowledge of the first nearest coordination numbers that are, in turn, obtained reliably by EXAFS analysis if the bond length distribution is relatively symmetric [91, 108]. For supported nanocatalysts under working conditions, the substrate and adsorbates may induce stress, causing the bond length distribution to deviate strongly from the Gaussian shape by for example relaxing the surface atoms stronger compared to the core [16]. The asymmetric disorder in bond lengths results in an artifact of the data analysis where, if ignored, it leads to the underestimate of the coordination numbers [109]. Therefore, anharmonic corrections should be taken into account for systems with large disorders. Several methods have been proposed recently that take into account the asymmetric disorder and use structural analysis of EXAFS data to validate different theoretical models [110–112]. They are described in greater detail below.

Including multiple-scattering effects to EXAFS data analysis is another way to improve the accuracy for size determination and is also crucial for extending structural refinement of nanocatlysts beyond first nearest bond distance. From the geometrical characteristics of regular polyhedral clusters, the sequence of coordination numbers of the 1st, 2nd, 3rd, 4th, etc. nearest neighboring pairs of atoms for different types of polyhedra is unique. That uniqueness is used for comparison with EXAFS results, obtained model-independently, for the same coordination numbers (and for degeneracies of multiple-scattering paths) to determine the size, shape, structure, and, in some cases, surface orientation of NPs [59, 106, 113]. One example of such analysis is the characterization of supported Pt clusters [60, 106, 114, 115], which have been extensively studied by EXAFS to establish the relationship between cluster size, shape, and catalytic properties. The structural characteristics depend strongly on the preparation conditions and on the nature of support [6, 22, 107, 116, 117]. The demonstrations of the sensitivity of the cluster shape to the support and treatment conditions are shown in the following examples. The fully reduced γ-Al_2O_3 supported Pt NPs have a spherical structure through a preparative method of deposition precipitation [118] while PVP capped Pt NPs changed from spherical to flat structure after the particles were deposit on SiO_2 support [119]. In another example, the 1 wt% Pt/γ-Al_2O_3 catalyst containing 11 Pt atoms was three-dimensional after low temperature reduction (300 °C) and changed to the raft shape with the structure similar to Pt (100) after high temperature reduction (450 °C) [120]. Interestingly, for Pt/zeolite, the three-dimensional structure was retained after high temperature treatment [121].

As an example of the multiple scattering EXAFS analysis of the cluster shape, we use the structural modeling of carbon supported Pt NPs up to the 4th/5th Pt-Pt shell [106, 114]. Figure 19.2 illustrates such analysis

for size and shape determination and shows that the (111)-truncated hemispherical cuboctahedron provides good approximation for the 10 wt% Pt/C sample, with a particles size of about 1.7 nm [106]. To find connections between particle shape and catalytic properties, γ-Al_2O_3 supported Pt NPs with various shapes but analogous average size (~1 nm) were prepared and characterized by multiple-scattering analysis (up to 4th shell) of EXAFS data in combination with microscopic tools [107]. The shape having higher percentage of undercoordinated atoms (at edge or corner sites) on the surface was found effective for lowering the onset temperature for two-propanol oxidation [6].

A more approximate method that also relies on the coordination numbers of higher shells for determining the size and shape of NPs was proposed by A. Jentys [122]. This method modeled the first five coordination numbers as a function of particle size with a hyperbolic function for particles with shapes of spheres, cubes, and distorted cubes. The coordination number of the first (n_1) or second shell (n_2) was found independent with shape and thus used to estimate the average particle size. The curves of n_1/n_3 versus particle size were found to be different for different shapes. The shape can therefore be determined by comparing the curve of experimentally determined n_1/n_3 ratio with the model n_1/n_3 graph. Such analysis was expanded by Beale and Weckhuysen to larger number of shapes [123].

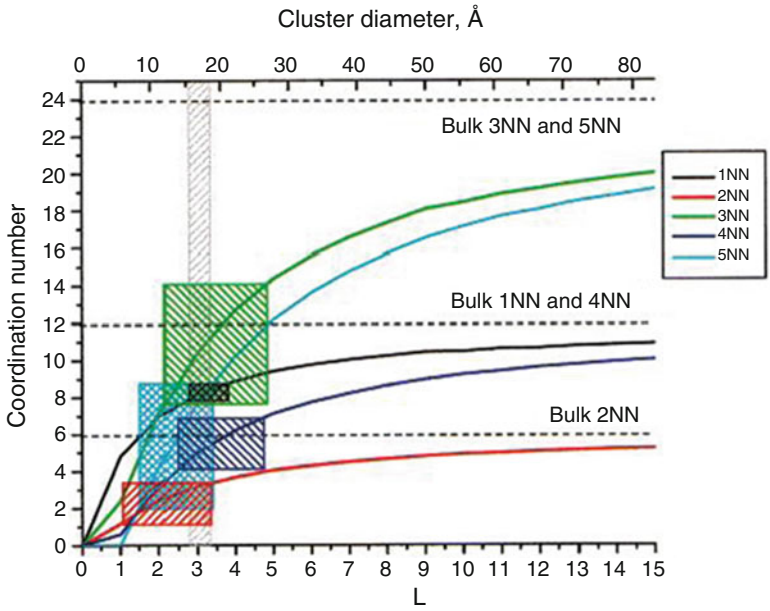

Fig. 19.2 Comparison of the average distances (up to 5NN), together with their error bars (shown as shaded rectangles), measured by EXAFS for the 10 wt% Pt/C sample and the calculated from a truncated (by (111) plane) cuboctahedron for cluster orders L up to 15. Reproduced with permission from ref. [106]. Copyright 2001 American Chemical Society

19.5 Using EXAFS to Characterize Bimetallic Nanocatalysts

Methods of high precision synthesis of bimetallic NPs for catalysis and electrocatalysis are actively sought, due to the increased demand to minimize the use of noble metals and for rational design of catalysts with desired activity and selectivity, and increased stability [42, 124–131]. Analogously to the definition of the coordination number for a homo-metallic pair, for heterometallic bonds, the coordination number is defined as:

$$n_{AB} = \frac{N_{AB}}{N_A}. \tag{19.6}$$

The information on the homo- and hetero-metallic coordination numbers n_{AA}, n_{AB}, n_{BA}, and n_{BB} is available from EXAFS measurements on the absorption edges of both A and B central atoms [25]. The analysis should be done for both edges concurrently, with constraints imposed on the heterometallic bonds during the fits:

$$n_{AB} = \frac{x_B}{x_A} n_{BA},\ R_{AB} = R_{BA},\ \sigma^2_{AB} = \sigma^2_{BA}. \tag{19.7}$$

Just as in the case of monometallic catalysts, multiple-scattering analysis of bimetallic catalysts allows for measurements of coordination numbers within the first few shells [114, 132]. These parameters elucidate the intra-particle composition, such as the extent of segregation or alloying of atoms, e.g., random distribution, as opposed to the positive or negative tendency to clustering [60, 132–140]. Once the above parameters are known, the total coordination number of metal–metal (M-M) neighbors per absorbing atom can be found from: [60]

$$n_{MM} = x_A n_{AM} + x_B n_{BM}. \tag{19.8}$$

The total coordination number can be employed to determine the size and shape using the same methods applied to monometallic particles described above.

For heterogeneouse distributions, the main question in the EXAFS analysis of bimetallic NPs is to detect a certain architectrual motif, e.g., a core–shell or cluster-to-cluster [41, 42, 45]. When atoms of the type A will segregate to the surface of the nanoparticle and B—to the core, then $n_{AM} < n_{BM}$ [60]. For *random* alloys, the average coordination numbers n_{AA} and n_{AB} are in the same proportion as the bulk concentrations of these elements in the sample: [60]

$$\frac{n_{AA}}{n_{AB}} = \frac{x_A}{x_B}. \tag{19.9}$$

For alloys with *positive* tendency to clustering of like atoms, e.g., when either the intraparticle or interparticle segregation is present, the left hand side should be *larger* than the right hand side:

$$\frac{n_{AA}}{n_{AB}} > \frac{x_A}{x_B}. \tag{19.10}$$

For homogeneous alloys (Fig. 19.3, center) in which the atoms A and B occur with equal probability within the particle or on the surface: $n_{AM} = n_{BM}$ [60].

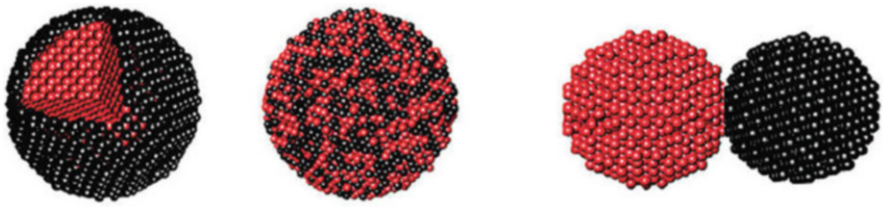

Fig. 19.3 Three main types of bimetallic configuration: left: core–shell; center: alloy; right: segregated monometallic clusters. Reproduced with permission from ref. [45]. Copyright 2009 American Chemical Society

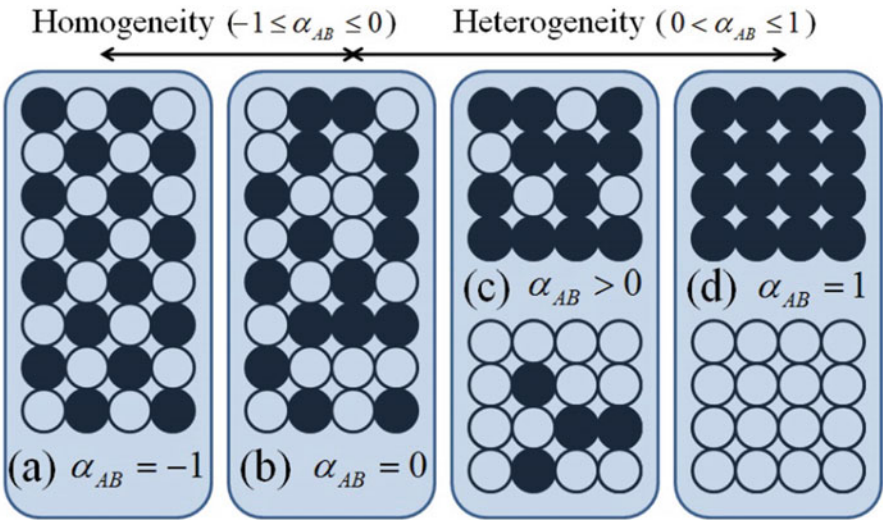

Fig. 19.4 (**a**, **b**) shows homogeneous configurations for the same 50–50 composition, characterized by a unique, non-positive values of the short range order parameter α. Different heterogeneous configurations, characterized by positive values of α, are shown in schemes (**c**, **d**). Reproduced with permission from ref. [62]. Copyright 2013, AIP Publishing LLC

Interpretation of the coordination numbers in heterogeneous systems in terms of a "representative cluster" can be misleading. We will discuss two commonly encountered systems that require particular care. One example is when two different NP systems differ in homogeneity of their atomic distributions, and the other—in the degree of their randomness. First, we consider a homogeneous system where all atoms have similar local environments within each NP. Two cartoons depicting two dimensional "nanoparticles" with this type of structure are shown in the Fig. 19.4a, b. Although the lattices are differently ordered, both types of atoms contain a similar number of neighbors for each element throughout the "cluster." The similarity becomes nearly perfect when the surface to volume ratio becomes negligible, i.e., for particles larger than 4–5 nm in diameter. Such atomic arrangements are homogeneous, as there is an equal probability to find any given atom type (A or B) anywhere within the NP. An example showing the other extreme is presented in the two cartoons in the Fig. 19.4d where the atoms of each type (A or B) are segregated within different part of the NP.

The second case we briefly discuss is when the two NP systems differ in the randomness of their atomic distributions. This characteristic will only apply to the homogeneous systems such as two NPs shown in Fig. 19.4a, b, because the two NPs shown in Fig. 19.4c, d are heterogeneous, i.e., inherently nonrandom. The cluster on the Fig. 19.4a has perfect order: both atomic types have equivalent surroundings. The cluster in Fig. 19.4b is random: for either atom (of type A or B), the probabilities of neighboring atoms being either type A or B are equal. One important consequence apparent from this simple example is the difference between the

short range order and homogeneity. For example, an alloy can be homogeneous but have a "negative tendency to clustering" (i.e., short range order) and is a phenomenon frequently encountered in metallurgy [141, 142].

These two examples illustrate the importance of understanding the short range order and homogeneity of bimetallic NPs when attempting to characterize their structure. It turns out that both of these can be quantitatively expressed using J. Cowley's short range order parameter introduced recently for bimetallic NP analysis by Frenkel, et al.: [143–145]

$$\alpha = 1 - \frac{N_{AB}/N_{AM}}{x_B}, \tag{19.11}$$

where x_B is the molar concentration of B-type atoms in the sample. As we show below, the Cowley parameter (α can vary in the interval between −1 and 1) can be used to investigate the degree of alloying or clustering within bimetallic NPs based on how positive/negative it is. In many cases, it can be used also as a "litmus test" demonstrating that atomic segregation, of either intra-cluster or inter-cluster type, occurred. We note that this equation has been previously employed in EXAFS studies of bulk bimetallic alloys [24] but its potential in NP studies remains unexplored.

For alloys that favor (disfavor) clustering of like atoms, α will be positive (negative). This parameter is therefore essential for studies of alloy—or core–shell, or cluster-on-cluster—NPs that can be characterized by different levels of ordering. Only after the short range order parameter is evaluated, can different models of segregation be compared. In either case, additional experimental information is needed to determine the fine detail of segregation, i.e., whether for example element A is predominantly at the surface or in the core. The analogue of the effect of compositional heterogeneity on the interpretation of the short range order within a "representative" NP is the interpretation of the size of the "representative" NP from EXAFS coordination numbers. In each case, an independent technique is needed, and in the latter case, the average particle size can be measured by electron microscopy.

We emphasize that the role of measuring and evaluating α extends beyond merely determining whether it is positive or negative. Even large negative values of α may signal segregation as there is only a finite range $\alpha_{\min} \le \alpha \le 0$ in which homogeneous systems can exist [143]. For example, $\alpha_{\min} = -1$ for two dimensional AB alloys shown in Fig. 19.4a, for β-brass CuZn of bcc structure [143], but it can also be fractional, e.g., $\alpha_{\min} = -1/3$ for fcc $Cu_{0.75}Au_{0.25}$ alloys [143]. Hence, if the measured value of α falls within either $-1 \le \alpha \le \alpha_{\min}$ or $0 < \alpha \le 1$ interval, the system is heterogeneous and the segregation of atoms is evident. Finally, we note that these conclusions were obtained assuming an idealized case where all particles are equivalent and the segregation may occur only within the NP. If the bimetallic composition varies from one NP to another, even random compositional distribution may generate positive values of α, a point which is discussed in greater detail below.

19.6 Pitfalls and Artifacts of the Analysis

In studies of the structure of NPs, coordination numbers are the most important structural parameters that can be obtained from EXAFS analysis. Coordination numbers of the first nearest neighbors (1NN) of X-ray absorbing atoms are obtained by EXAFS analysis very reliably, and are often employed for characterizing nanoclusters in terms of their structure, size, shape, and morphology [100, 106, 114, 146]. Coordination numbers of atomic pairs in bimetallic NPs are often used to discriminate between different types of short range order in the NPs, and/or ascertain the degree of compositional homogeneity in the sample [60, 100, 147]. In this section we emphasize the pitfalls in such interpretation when nanoparticle ensembles display a broad range of sizes and compositions. We show the implications of these effects on EXAFS results and describe corrective strategies.

The values of partial coordination numbers are important for analyzing composition habits of heterometallic clusters. For example, depending on the relationship between the partial 1NN numbers and the bulk composition of the nanoalloy, the latter is characterized as either homogeneous (when average environment around each atom is approximately the same) or heterogeneous (when different regions within the sample have different compositional trends, e.g., A- rich and B-rich, or when such segregation occurs within each cluster, e.g., A-rich core and B-rich shell) [147]. For homogeneous alloys, relationships (19.9) and (19.10) can be used to describe the short range order [60]. In this section we focus on random nanoalloys (that have zero short range order) and highlight challenges in their detection by EXAFS.

We now introduce the *total* coordination number of metal–metal pair, or n_{MM} which is equal to n_1 for monometallic clusters. For bulk alloys, when atoms of type A and B are distributed *randomly*, their partial coordination numbers are found from the overall compositions:

$$n_{AA} = n_{BA} = x_A n_{MM},\ n_{AB} = n_{BB} = (1 - x_A)\, n_{MM}, \tag{19.12}$$

where the composition is defined as: $x_{\mathrm{A}} = N_{\mathrm{A}}/N$. Note that in random bulk alloys, $n_{\mathrm{AA}} + n_{\mathrm{BB}} = n_{\mathrm{AA}} + n_{\mathrm{AB}} = n_{\mathrm{BB}} + n_{\mathrm{BA}} = n_{\mathrm{MM}}$. In a nanocluster with random compositional distribution, more accurate relationships should be used: [100]

$$\begin{aligned} n_{AA} &= \frac{N_A - 1}{N - 1} n_{MM} = \frac{N x_A - 1}{N - 1} n_{MM},\ n_{AB} = \frac{N - N_A}{N - 1} n_{MM} \\ &= \frac{N}{N - 1}(1 - x_A) n_{MM}, \quad n_{BA} = \frac{N_A}{N - 1} n_{MM} = \frac{N}{N - 1} x_A n_{MM}, \\ n_{BB} &= \frac{N_B - 1}{N - 1} n_{MM} = \left(1 - \frac{N x_A}{N - 1}\right) n_{MM}. \end{aligned} \tag{19.13}$$

We note that in random nanoalloys, same as in the bulk random alloys, $n_{\mathrm{AA}} + n_{\mathrm{AB}} = n_{\mathrm{BB}} + n_{\mathrm{BA}} = n_{\mathrm{MM}}$ but in the nanoalloys the sum of n_{AA} and n_{BB} is smaller than n_{MM}:

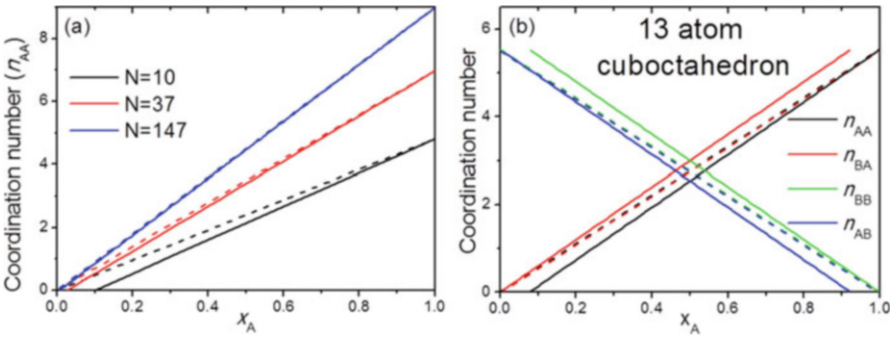

Fig. 19.5 (**a**) Exact (*solid lines*, Eq. 19.13) and approximate (*dashed lines*, Eq. 19.12) behaviors of the coordination numbers of A–A pairs for different cluster sizes. (**b**) Coordination numbers of different atomic pairs in random, 13-atom, cuboctahedral alloys. *Solid lines* correspond to exact calculations using Eq. 19.13 and *dashed lines* correspond to approximate calculations using Eq. 19.12. Reproduced from ref. [149] by permission of The Royal Society of Chemistry

$$n_{AA} + n_{BB} = \frac{N-2}{N-1} n_{MM}. \tag{19.14}$$

Equations (19.13 and 19.14) are exact, and they are equivalent to Eqs. (19.1, 19.6, 19.9, and 19.12) in the limit of large total number of atoms (N) and large concentrations (x_A), as demonstrated in Fig. 19.5a. Furthermore, in the random nanoalloys, the n_{AA} and n_{BB} are different from n_{BA} and n_{AB}, respectively, while in the random bulk alloys they are the same (Eqs. 19.12, 19.13 and Fig. 19.5b).

We have recently shown [100] that alloys with broad compositional distributions are expected to have positive values for the ensemble-average short range order despite having random intra-particle distribution of atoms. Hence, a random nanoalloy may be mistaken as a system with a core–shell motif if the NPs are not all stoichiometrically uniform. This prediction can be illustrated by the following simple example. Assume that the sample consists of two groups of bimetallic NPs. The first group consists of N particles where 30 % of all atoms are A-type and 70 %—B-type in each. The second group consists of N particles of 70 % and 30 % of A and B-type atoms, respectively. The average composition over the entire sample is then 50 % of A and 50 % of B atoms. Assume also that the distribution of atoms in each particle is random, i.e., the value of α calculated over each population is zero. Finally, assume that the geometry of all particles is the same and atoms occupy regular lattice sites. Ensemble-average calculation of the coordination numbers of AB type yields the following result: $N_{AB} = 0.3 \times 0.7 N_{AM} + 0.7 \times 0.3 N_{AM} = 0.42 N_{AM}$. Hence, the ensemble-average value of α measured by EXAFS will be equal to 0.16 (Eq. 19.11), in apparent contradiction to the local randomness ($\alpha = 0$) of each population. What follows is the more general demonstration of this effect [100, 148].

We assume that within each cluster, atoms of type A and B are distributed randomly, but x_A is different for each nanoparticle. For simplicity, we consider a

system that contains particles of the same structure and geometry. Effects of cluster size distribution [100] and asymmetric bond length disorder [109] on the apparent coordination numbers have been described separately. We distinguish between the particle-specific coordination number n_{AA} (calculated with Eq. (19.13)) in the cluster with the concentration x_A of A atoms, and the *apparent* (measured) coordination number $\widetilde{n}_{AA}$, which, in EXAFS measurement, averages the number of A nearest neighbors over all the A-type atoms in all clusters in the sample. We let the interparticle compositional distribution of x_A (denoted below as simply x) be a Gaussian with standard deviation σ_c and mean $\bar{x}$:

$$\rho(x) \propto \exp\left(-\frac{(x-\bar{x})^2}{2\sigma_c^2}\right). \tag{19.15}$$

In EXAFS signal, clusters with a greater number of A atoms are weighted more than the clusters with fewer A atoms. We thus write the apparent partial coordination numbers as:

$$\widetilde{n}_{AA} = \frac{\int_0^1 \rho(x) n_{AA}(x) x dx}{\int_0^1 \rho(x) x dx}. \tag{19.16}$$

Figure 19.6 shows the values of $\widetilde{n}_{AA}$ and $\widetilde{n}_{AA}$ for various values of $\bar{x}$ and σ_c calculated for a cluster containing $N = 100$ atoms. Cluster cartoons are added for clarity. A single cluster (the cuboctahedral shape was chosen for illustration purpose

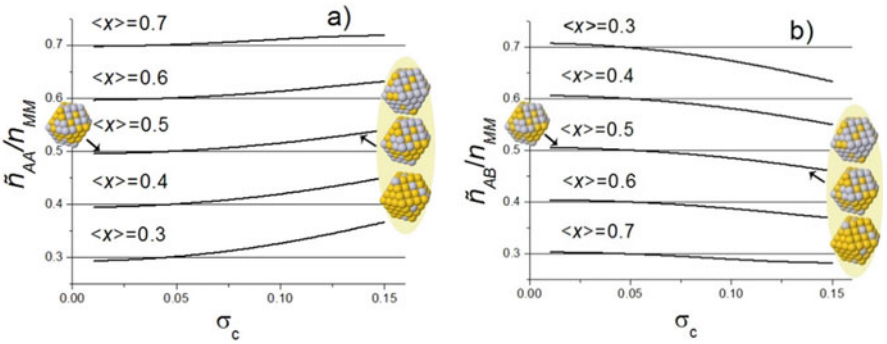

Fig. 19.6 Normalized partial coordination numbers of (**a**) *AA* and (**b**) *AB* pairs as functions of the standard deviation σ_c around the average cluster composition $<x>$ for clusters of $N = 100$ atoms, calculated assuming a Gaussian compositional distribution. In both figures, cartoons next to the $< x >= 0.5$ curve illustrate the difference between the narrow (one cluster on the left) and broad (three different clusters on the right) compositional distributions. Reproduced from ref. [148] by permission of The Royal Society of Chemistry

only) on the left corresponds to narrow inter-cluster compositional distribution (i.e., small σ_c). Three clusters on the right illustrate the change in composition from cluster to cluster (large σ_c). In all cases, the intra-cluster distributions are random.

These results indicate that the ensemble-average coordination numbers $\widetilde{n}_{AA}$ can be smaller for narrow compositional distributions or larger for broad distributions than the coordination numbers predicted by the equation $n_{\mathrm{AA}} = xn_{\mathrm{MM}}$. The reason they are smaller for narrow distributions than the nominal coordination numbers was demonstrated above (Eq. 19.13 and Fig. 19.5b). For broad distributions, the effect is due to the ensemble-averaging that favors A-rich clusters over the B-rich clusters (relative to $\bar{x}_{\mathrm{A}}$). Similar conclusions can be extended to the other partial coordination numbers. The two sets of values, $\widetilde{n}_{AA}$ and n_{AA}, as well as $\widetilde{n}_{AB}$ and n_{AB}, agree for $\sigma_c = \sqrt{x(1-x)/N}$, for which the normal distribution coincides with binomial distribution.

In summary, partial coordination numbers in heterometallic NPs can be employed to accurately quantify the intra-particle homogeneity and short-range order for arbitrary cluster sizes and a wide range of component fractions, provided that all the clusters possess nearly identical compositions. If the intra-cluster distribution is completely random but the elemental composition varies widely from cluster to cluster, the coordination numbers measured by EXAFS will point toward either negative ($\widetilde{n}_{AA} < n_{AA}$) or positive ($\widetilde{n}_{AA} > n_{AA}$) short range order, which, in the latter case, can be mistaken for a core–shell motif, among other segregation scenarios, even though all clusters are completely random. The only exception when the apparent coordination numbers coincide with those in the "mean" cluster is when the compositional distribution is binomial. With the knowledge of actual compositional distribution (e.g., using energy dispersive X-ray analysis done in electron microscopy experiment) it is possible to correct apparent coordination numbers for the compositional distribution effects (Fig. 19.6).

19.7 Overlapping Absorption Edges

Heterometallic systems containing two or more elements with overlapping absorption edges cannot be simply analyzed by EXAFS since the EXAFS at the higher energy edge overlaps with the EXAFS extending from the lower energy edge. This is a particularly significant problem for metals that neighbor each other in the periodic table such as Re, Ir, Pt, and Au, whose L_3, L_2, and L_1 absorption edges overlap. Unless these overlapping contributions are disentangled, extracting structural information from the data via traditional data analysis strategies is either not possible [149, 150] or difficult and/or insufficiently accurate [151].

The problem of overlapping edges in EXAFS analysis is not limited to heterometallic catalysts, of course. $BaTiO_3$ is among the most extensively studied perovskites, yet its EXAFS studies are complicated due to the overlap of Ti K-edge and Ba L_3 edge. B. Ravel et al. proposed a very original use of diffraction

anomalous fine structure (DAFS) technique to deconvolute the EXAFS signals from Ti and Ba [152, 153]. Other methods have appeared recently, based on the use of the high energy resolution fluorescence detection (HERFD) that enabled separation of emission lines from different elements [85, 154–156].

Menard et al. reported a new method for deconvolution of overlapping absorption edges that is based on the use of concurrent, multiple edge analysis of EXAFS data from each edge [63]. The analysis strategy is demonstrated here for an arbitrary bimetallic composition even though, for illustration purpose only, they used notation Ir and Pt for its constituent elements. Data analysis is done by a simultaneous fit of both Ir L_3 and Pt L_3 edges, which involve three contributions: (1) the Ir EXAFS in the Ir L_3 edge before the Pt L_3 edge; (2) the Ir EXAFS in the Pt L_3 edge; and (3) the Pt EXAFS in the Pt L_3 edge. Because (1) and (2) describe the same coordination environments they should be constrained analytically, in the process of fitting each contribution to the experimental data. The analysis is done in r-space and is limited to nearest neighbor scattering paths, which are usually well isolated from longer scattering paths in the Fourier transforms of the EXAFS signal $\chi(k)$. In this case, the EXAFS equations that are simultaneously fit are:

$$\chi_{\text{Ir edge}}(k_{\text{Ir}}) = \frac{S_{0,\text{Ir}}^2 N_{\text{Ir}}}{k_{\text{Ir}} R_{\text{Ir}}^2} \left| f_{\text{Ir}}^{eff}(k_{\text{Ir}}) \right| \sin\left[2k_{\text{Ir}} R_{\text{Ir}} - \frac{4}{3}\sigma_{\text{Ir}}^{(3)} k_{\text{Ir}}^3 + \delta_{\text{Ir}}(k_{\text{Ir}}) \right] e^{-2\sigma_{\text{Ir}}^2 k_{\text{Ir}}^2} e^{-2R_{\text{Ir}}/\lambda_{\text{Ir}}(k_{\text{Ir}})}, \tag{19.17}$$

and

$$\begin{aligned} \chi_{\text{Pt edge}}(k_{\text{Pt}}, k_{\text{Ir}}) = {} & \frac{S_{0,\text{Pt}}^2 N_{\text{Pt}}}{k_{\text{Pt}} R_{\text{Pt}}^2} \left| f_{\text{Pt}}^{eff}(k_{\text{Pt}}) \right| \sin\left[2k_{\text{Pt}} R_{\text{Pt}} - \frac{4}{3}\sigma_{\text{Pt}}^{(3)} k_{\text{Pt}}^3 + \delta_{\text{Pt}}(k_{\text{Pt}}) \right] \\ & \times e^{-2\sigma_{\text{Pt}}^2 k_{\text{Pt}}^2} e^{-2R_{\text{Pt}}/\lambda_{\text{Pt}}(k_{\text{Pt}})} + \frac{A S_{0,\text{Ir}}^2 N_{\text{Ir}}}{k_{\text{Ir}} R_{\text{Ir}}^2} \left| f_{\text{Ir}}^{eff}(k_{\text{Ir}}) \right| \sin \\ & \times \left[2k_{\text{Ir}} R_{\text{Ir}} - \frac{4}{3}\sigma_{\text{Ir}}^{(3)} k_{\text{Ir}}^3 + \delta_{\text{Ir}}(k_{\text{Ir}}) \right] e^{-2\sigma_{\text{Ir}}^2 k_{\text{Ir}}^2} e^{-2R_{\text{Ir}}/\lambda_{\text{Ir}}(k_{\text{Ir}})}. \end{aligned} \tag{19.18}$$

The factor $A = \Delta\mu_{0,\text{Ir}}/\Delta\mu_{0,\text{Pt}}$, where $\Delta\mu_{0,\text{Ir}}$ and $\Delta\mu_{0,\text{Pt}}$ are the changes in the absorption at the edge steps, is necessary because the extraction of $\chi(k)$ includes a normalization to these edge steps. The nonlinear least squares fitting of experimental data to Eqs. (19.17 and 19.18) should be done concurrently to the overlapping L_3 edges and can be achieved using available EXAFS analysis tools. In ref. [63], the interface programs Athena and Artemis were used. In practice, correction of the energy grid in k-space for the Ir EXAFS in the Pt L_3 edge should be made. The correction to the threshold energy (in eV) for the Ir EXAFS in the Pt L_3 edge is defined as $\Delta E_{0,\text{Ir}} - (349 + \Delta E_{0,\text{Pt}})$, where 349 eV is the difference between the empirical threshold energies. Such a large energy origin shift is necessary in this method since it accounts for a unique $k = 0$ reference point for the Ir EXAFS extending beyond the Pt edge when the Pt edge EXAFS is transformed to k-

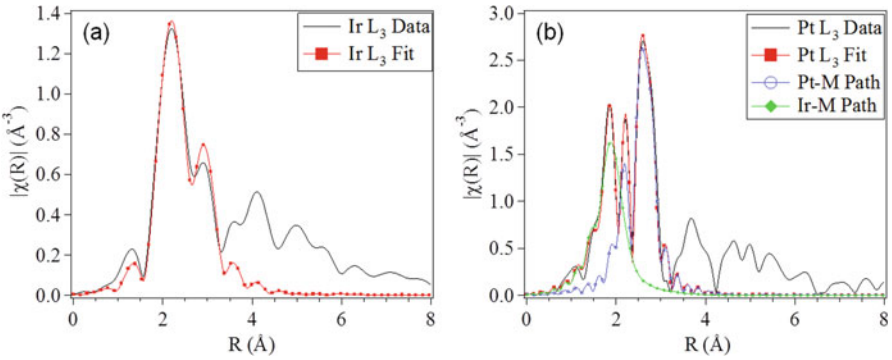

Fig. 19.7 Comparison of the data and fit of the Ir-Pt NPs on γ-Al_2O_3 under a H_2 atm measured at 215 K at the Ir L_3 and Pt L_3 absorption edges. Fourier transform magnitude of (**a**) the Ir L_3 data and fit, and (**b**) the Pt L_3 data and fit with the contributions of the individual paths represented. Reproduced with permission from ref. [63]

space. The exact value to use (here 349 eV) will depend on the E_0 values that are used in the edge subtraction of the EXAFS spectra. The representative data and fits in r-space are shown in Fig. 19.7. The signature of the Ir L_3 EXAFS "leaking" into the Pt L_3 EXAFS is a low r feature in Fig. 19.7b.

19.8 Outlook and Future Developments

With the ongoing development of X-ray absorption spectroscopy techniques, the opportunities for investigation of mechanisms of catalytic reactions employing nanoscale metal catalysts are growing and new challenges, previously ignored or overlooked, come to the surface. One such important challenge is the heterogeneity of the NP ensembles that is evident even in samples with narrow size and compositional distributions and is a common property of real catalysts with large compositional gradients. That heterogeneity, when ignored, causes artifacts in data analysis, as demonstrated above in the case of the compositional heterogeneity, and is also shown by Yevick and Frenkel [109] for the case of the structural heterogeneity due to surface relaxation in nm-scale clusters.

One possible solution is the single nanoparticle spectroscopy studies by XAS methods [157]. Current and future capabilities of X-ray spectromicroscopy based on coherence-limited imaging methods including nano-probe methods were discussed by Hitchcock and Toney [158]. These methods will benefit from the dramatic increase in brightness expected from a diffraction-limited storage ring. The applicability of nano-probe methods for spectroscopy studies of single NPs was illustrated by Y. Chu's group. They studied the oxidation process of individual PtNi NPs by a scanning multilayer Laue lens X-ray microscope and discovered the transformation of alloyed PtNi (140 to 320 nm) to Pt/NiO core–shell and the further

coalescence under thermal oxidation [159]. The scanning was performed using 10 nm step size and 30 nm focal spot size at beamline 26ID of the Advanced Photon Source at Argonne National Laboratory. This method is being developed for to the hard X-ray nanoprobe (HXN) beamline of the National Synchrotron Light Source II at BNL. Alternatively, photoemission electron microscopy was used for studying of individual Co NPs with the size of 8 nm. Significant variations in the shapes of the Co $L_{2,3}$ edges of the X-ray absorption spectra between different cobalt NPs were detected and attributed to different cobalt–oxygen interactions on a particle-by-particle basis [160]. For these spectromicroscopic methods on the basis of nanoprobe, the main challenge is to keep high flux while reducing the spot size. More details on challenges and limitations of nano-probe methods for catalytic investigations were addressed recently by Frenkel and van Bokhoven [157].

Studying nanocatalysts at the single-nanoparticle level and in *operando* mode adds more challenges. For spectroscopic methods, the key is to increase particle sensitivity and for electron microscopic methods it's to enable realistic working conditions. In most electron microscopy studies of catalysis, they were either investigated in an ex-situ mode, i.e., catalysts were pretreated elsewhere under controlled conditions of atmosphere, pressure and temperature, while measured under high vacuum at low temperatures, or under simulated working conditions with lower temperature and pressure compared to the real ones [46, 161, 162]. To bridge this "pressure gap", a new mode of operation is needed, where relevant (for structural analysis) techniques can probe catalysts in the same reaction conditions. Recently, Stach and Frenkel demonstrated the advantage of using such a micro-reactor, for nanocatalysis studies at ambient temperature and pressure [104]. Basing on the idea of combining electron microscopy with spectroscopic techniques by sharing the same reactor to make sure samples/conditions under study are the same for all types of techniques [163, 164], the group discovered the complex structural dynamics of Pt/SiO_2 under ethylene hydrogenation conditions that occurs at broad length scale [104].

In conclusion, with the development of XAFS instrumentation and analysis methods, the understanding of structure of nanoparticle catalysts is advanced from qualitative pictures of the mid-70s to much more quantitative ones that are capable to capture fine architectural and compositional details, and account for interparticle and intraparticle heterogeneities. More achievements are expected in the coming years, owing to the reduced beam sizes, improved energy and time resolutions, and new developments in the combinations of XAFS with complementary imaging and scattering methods in *operando* conditions.

References

1. Gilbert B, Huang F, Zhang H et al (2004) Nanoparticles: strained and stiff. Science 305:651–654
2. Zobel M, Neder RB, Kimber SAJ (2015) Universal solvent restructuring induced by colloidal nanoparticles. Science 347:292–294
3. Dreaden EC, Alkilany AM, Huang X et al (2012) The golden age: gold nanoparticles for biomedicine. Chem Soc Rev 41:2740–2779

4. Xu B, Zhang ZC, Wang X (2014) Engineering nanointerfaces for nanocatalysis. Chem Soc Rev 43:7870–7886
5. Sanchez SI, Menard LD, Bram A et al (2009) The emergence of nonbulk properties in supported metal clusters: negative thermal expansion and atomic disorder in Pt nanoclusters supported on γ-Al_2O_3. J Am Chem Soc 131:7040–7054
6. Mostafa S, Behafarid F, Croy JR et al (2010) Shape-dependent catalytic properties of Pt nanoparticles. J Am Chem Soc 132:15714–15719
7. Crespo-Quesada M, Yarulin A, Jin M et al (2011) Structure sensitivity of alkynol hydrogenation on shape- and size-controlled palladium nanocrystals: which sites are most active and selective? J Am Chem Soc 133:12787–12794
8. Jaramillo TF, Jørgensen KP, Bonde J et al (2007) Identification of active edge sites for electrochemical H_2 evolution from MoS_2 nanocatalysts. Science 317:100–102
9. Yudanov IV, Sahnoun R, Neyman KM et al (2002) CO adsorption on Pd nanoparticles: density functional and vibrational spectroscopy studies. J Phys Chem B 107:255–264
10. Walsh MJ, Yoshida K, Kuwabara A et al (2012) On the structural origin of the catalytic properties of inherently strained ultrasmall decahedral gold nanoparticles. Nano Lett 12:2027–2031
11. Ruban A, Hammer B, Stoltze P et al (1997) Surface electronic structure and reactivity of transition and noble metals. J Mol Catal A: Chem 115:421–429
12. Small MW, Kas JJ, Kvashnina KO et al (2014) Effects of adsorbate coverage and bond-length disorder on the d-band center of carbon-supported Pt catalysts. ChemPhysChem 15:1569–1572
13. Norskov JK, Bligaard T, Rossmeisl J et al (2009) Towards the computational design of solid catalysts. Nat Chem 1:37–46
14. Nørskov JK, Abild-Pedersen F, Studt F et al (2011) Density functional theory in surface chemistry and catalysis. Proc Natl Acad Sci U S A 108:937–943
15. Stamenkovic VR, Mun BS, Arenz M et al (2007) Trends in electrocatalysis on extended and nanoscale Pt-bimetallic alloy surfaces. Nat Mater 6:241–247
16. Huang WJ, Sun R, Tao J et al (2008) Coordination-dependent surface atomic contraction in nanocrystals revealed by coherent diffraction. Nat Mater 7:308–313
17. Ouyang G, Zhu WG, Sun CQ et al (2010) Atomistic origin of lattice strain on stiffness of nanoparticles. Phys Chem Chem Phys 12:1543–1549
18. Li L, Wang L-L, Johnson DD et al (2013) Noncrystalline-to-crystalline transformations in Pt nanoparticles. J Am Chem Soc 135:13062–13072
19. Frenkel AI, Small MW, Smith JG et al (2013) An in situ study of bond strains in 1 nm Pt catalysts and their sensitivities to cluster–support and cluster–adsorbate interactions. J Phys Chem C 117:23286–23294
20. Vermaak JS, Mays CW, Kuhlmann D (1968) On surface stress and surface tension.I. Theoretical considerations. Surf Sci 12:128–133
21. Frenkel AI, Nemzer S, Pister I et al (2005) Size-controlled synthesis and characterization of thiol-stabilized gold nanoparticles. J Chem Phys 123:184701–184706
22. Roldan Cuenya B, Frenkel AI, Mostafa S et al (2010) Anomalous lattice dynamics and thermal properties of supported size- and shape-selected Pt nanoparticles. Phys Rev B 82:155450
23. Sanchez SI, Small MW, J-M Z et al (2009) Structural characterization of Pt − Pd and Pd − Pt core − shell nanoclusters at atomic resolution. J Am Chem Soc 131:8683–8689
24. Frenkel AI, Machavariani VS, Rubshtein A et al (2000) Local structure of disordered Au-Cu and Au-Ag alloys. Phys Rev B 62:9364–9371
25. Frenkel AI, Stern EA, Voronel A et al (1996) Lattice strains in disordered mixed salts. Solid State Commun 99:67–71
26. Kibler LA, El-Aziz AM, Hoyer R et al (2005) Tuning reaction rates by lateral strain in a palladium monolayer. Angew Chem Int Ed 44:2080–2084

27. Kitchin JR, Nørskov JK, Barteau MA et al (2004) Role of strain and ligand effects in the modification of the electronic and chemical properties of bimetallic surfaces. Phys Rev Lett 93:156801
28. Mavrikakis M, Hammer B, Nørskov JK (1998) Effect of strain on the reactivity of metal surfaces. Phys Rev Lett 81:2819–2822
29. Sun CQ (2007) Size dependence of nanostructures: impact of bond order deficiency. Prog Solid State Chem 35:1–159
30. Hammer B, Nørskov JK (2000) Theoretical surface science and catalysis—calculations and concepts. In: Knozinger H, Gates BC (eds) Advances in catalysis. Academic, New York, pp 71–129
31. Kitchin JR, Nørskov JK, Barteau MA et al (2004) Modification of the surface electronic and chemical properties of Pt(111) by subsurface 3d transition metals. J Chem Phys 120:10240–10246
32. Comotti M, Li W-C, Spliethoff B et al (2005) Support effect in high activity gold catalysts for CO oxidation. J Am Chem Soc 128:917–924
33. Graoui H, Giorgio S, Enry CR (2001) Effect of the interface structure on the high-temperature morphology of supported metal clusters. Philos Mag B 81:1649–1658
34. Campbell CT, Sharp JC, Yao YX et al (2011) Insights into catalysis by gold nanoparticles and their support effects through surface science studies of model catalysts. Faraday Discuss 152:227–239
35. Campbell CT, Sellers JRV (2013) Anchored metal nanoparticles: effects of support and size on their energy, sintering resistance and reactivity. Faraday Discuss 162:9–30
36. Xu R, Wang D, Zhang J et al (2006) Shape-dependent catalytic activity of silver nanoparticles for the oxidation of styrene. Chem Asian J 1:888–893
37. Tian N, Zhou Z-Y, Sun S-G et al (2007) Synthesis of tetrahexahedral platinum nanocrystals with high-index facets and high electro-oxidation activity. Science 316:732–735
38. Karim AM, Prasad V, Mpourmpakis G et al (2009) Correlating particle size and shape of supported Ru/γ-Al_2O_3 catalysts with NH_3 decomposition activity. J Am Chem Soc 131:12230–12239
39. Häkkinen H, Abbet S, Sanchez A et al (2003) Structural, electronic, and impurity-doping effects in nanoscale chemistry: supported gold nanoclusters. Angew Chem Int Ed 42:1297–1300
40. Kacprzak KA, Akola J, Hakkinen H (2009) First-principles simulations of hydrogen peroxide formation catalyzed by small neutral gold clusters. Phys Chem Chem Phys 11:6359–6364
41. Ferrando R, Jellinek J, Johnston RL (2008) Nanoalloys: from theory to applications of alloy clusters and nanoparticles. Chem Rev 108:845–910
42. Ghosh Chaudhuri R, Paria S (2012) Core/shell nanoparticles: classes, properties, synthesis mechanisms, characterization, and applications. Chem Rev 112:2373–2433
43. Tupy SA, Karim AM, Bagia C et al (2012) Correlating ethylene glycol reforming activity with in situ EXAFS detection of Ni segregation in supported NiPt bimetallic catalysts. ACS Catal 2:2290–2296
44. Alayoglu S, Tao F, Altoe V et al (2011) Surface composition and catalytic evolution of $Au_x Pd_{1-x}$ ($x = 0.25$, 0.50 and 0.75) nanoparticles under CO/O_2 reaction in Torr pressure regime and at 200 °C. Catal Lett 141:633–640
45. Alayoglu S, Zavalij P, Eichhorn B et al (2009) Structural and architectural evaluation of bimetallic nanoparticles: a case study of Pt − Ru core − shell and alloy nanoparticles. ACS Nano 3:3127–3137
46. Yoshida H, Kuwauchi Y, Jinschek JR et al (2012) Visualizing gas molecules interacting with supported nanoparticulate catalysts at reaction conditions. Science 335:317–319
47. Adriano F (2001) EXAFS for liquids. J Phys Condens Matter 13:R23
48. Sharpe LR, Heineman WR, Elder RC (1990) EXAFS spectroelectrochemistry. Chem Rev 90:705–722

49. Russell AE, Rose A (2004) X-ray absorption spectroscopy of low temperature fuel cell catalysts. Chem Rev 104:4613–4636
50. Bentrup U (2010) Combining in situ characterization methods in one set-up: looking with more eyes into the intricate chemistry of the synthesis and working of heterogeneous catalysts. Chem Soc Rev 39:4718–4730
51. Comez L, Di Cicco A, Itié JP et al (2001) High-pressure and high-temperature X-ray absorption study of liquid and solid gallium. Phys Rev B 65:014114
52. Vankó G, Rueff J-P, Mattila A et al (2006) Temperature- and pressure-induced spin-state transitions in $LaCoO_3$. Phys Rev B 73:024424
53. Meunier FC (2010) The design and testing of kinetically-appropriate operando spectroscopic cells for investigating heterogeneous catalytic reactions. Chem Soc Rev 39:4602–4614
54. Bare SR, Yang N, Kelly SD et al (2007) Design and operation of a high pressure reaction cell for in situ X-ray absorption spectroscopy. Catal Today 126:18–26
55. Bare SR, Mickelson GE, Modica FS et al (2006) Simple flow through reaction cells for in situ transmission and fluorescence X-ray-absorption spectroscopy of heterogeneous catalysts. Rev Sci Instrum 77:023105
56. Grunwaldt JD, Caravati M, Hannemann S et al (2004) X-ray absorption spectroscopy under reaction conditions: suitability of different reaction cells for combined catalyst characterization and time-resolved studies. Phys Chem Chem Phys 6:3037–3047
57. Grunwaldt J-D, Ramin M, Rohr M et al (2005) High pressure in situ X-ray absorption spectroscopy cell for studying simultaneously the liquid phase and the solid/liquid interface. Rev Sci Instrum 76:054104
58. Erickson EM, Oruc ME, Wetzel DJ et al (2014) A comparison of atomistic and continuum approaches to the study of bonding dynamics in electrocatalysis: microcantilever stress and in situ EXAFS observations of platinum bond expansion due to oxygen adsorption during the oxygen reduction reaction. Anal Chem 86:8368–8375
59. Glasner D, Frenkel AI (2007) Geometrical characteristics of regular polyhedra: application to EXAFS studies of nanoclusters. AIP Conf Proc 882:746–748
60. Frenkel AI (2007) Solving the 3D structure of metal nanoparticles. Z Kristallogr 222:605–611
61. Small MW, Sanchez SI, Marinkovic NS et al (2012) Influence of adsorbates on the electronic structure, bond strain, and thermal properties of an alumina-supported Pt catalyst. ACS Nano 6:5583–5595
62. Frenkel AI, Wang Q, Sanchez SI et al (2013) Short range order in bimetallic nanoalloys: an extended X-ray absorption fine structure study. J Chem Phys 138:064202
63. Menard LD, Wang Q, Kang JH et al (2009) Structural characterization of bimetallic nanomaterials with overlapping X-ray absorption edges. Phys Rev B 80:064111
64. Funke H, Scheinost AC, Chukalina M (2005) Wavelet analysis of extended X-ray absorption fine structure data. Phys Rev B 71:094110
65. Chukalina MV, Dubrovskii YV, Funke H (2004) Wavelet analysis and its application in tunneling and X-ray spectroscopy. Low Temp Phys 30:930–936
66. Filez M, Redekop EA, Poelman H et al (2015) Advanced elemental characterization during Pt–In catalyst formation by wavelet transformed X-ray absorption spectroscopy. Anal Chem 87:3520–3526
67. Filez M, Redekop EA, Poelman H et al (2014) Unravelling the formation of Pt–Ga alloyed nanoparticles on calcined Ga-modified hydrotalcites by in situ XAS. Chem Mater 26:5936–5949
68. Antoniak C (2011) Extended X-ray absorption fine structure of bimetallic nanoparticles. Beilstein J Nanotechnol 2:237–251
69. Ferri D, Kumar MS, Wirz R et al (2010) First steps in combining modulation excitation spectroscopy with synchronous dispersive EXAFS/DRIFTS/mass spectrometry for in situ time resolved study of heterogeneous catalysts. Phys Chem Chem Phys 12:5634–5646

70. Eyssler A, Kleymenov E, Kupferschmid A et al (2011) Improvement of catalytic activity of $LaFe_{0.95}Pd_{0.05}O_3$ for methane oxidation under transient conditions. J Phys Chem C 115:1231–1239
71. Ferri D, Newton MA, Di Michiel M et al (2013) Synchrotron high energy X-ray methods coupled to phase sensitive analysis to characterize aging of solid catalysts with enhanced sensitivity. Phys Chem Chem Phys 15:8629–8639
72. König CFJ, van Bokhoven JA, Schildhauer TJ et al (2012) Quantitative analysis of modulated excitation X-ray absorption spectra: enhanced precision of EXAFS fitting. J Phys Chem C 116:19857–19866
73. König CFJ, Schildhauer TJ, Nachtegaal M (2013) Methane synthesis and sulfur removal over a Ru catalyst probed in situ with high sensitivity X-ray absorption spectroscopy. J Catal 305:92–100
74. Patlolla A, Baumann P, Xu W et al (2013) Characterization of metal-oxide catalysts in operando conditions by combining X-ray absorption and raman spectroscopies in the same experiment. Top Catal 56:896–904
75. Frenkel AI, Wang Q, Marinkovic N et al (2011) Combining X-ray absorption and X-ray diffraction techniques for in situ studies of chemical transformations in heterogeneous catalysis: advantages and limitations. J Phys Chem C 115:17884–17890
76. Patlolla A, Carino EV, Ehrlich SN et al (2012) Application of operando XAS, XRD, and Raman spectroscopy for phase speciation in water gas shift reaction catalysts. ACS Catal 2:2216–2223
77. Chen Y, Fulton JL, Linehan JC et al (2005) In situ XAFS and NMR study of rhodium-catalyzed dehydrogenation of dimethylamine borane. J Am Chem Soc 127:3254–3255
78. Beale AM, van der Eerden AMJ, Kervinen K et al (2005) Adding a third dimension to operando spectroscopy: a combined UV-Vis, Raman and XAFS setup to study heterogeneous catalysts under working conditions. Chem Commun 3015–3017
79. Newton MA, Jyoti B, Dent AJ et al (2004) Synchronous, time resolved, diffuse reflectance FT-IR, energy dispersive EXAFS (EDE) and mass spectrometric investigation of the behaviour of Rh catalysts during NO reduction by CO. Chem Commun 2382–2383
80. Bordiga S, Groppo E, Agostini G et al (2013) Reactivity of surface species in heterogeneous catalysts probed by in situ X-ray absorption techniques. Chem Rev 113:1736–1850
81. Singh J, Lamberti C, van Bokhoven JA (2010) Advanced X-ray absorption and emission spectroscopy: in situ catalytic studies. Chem Soc Rev 39:4754–4766
82. van Bokhoven JA, Louis C, Miller JT et al (2006) Activation of oxygen on gold/alumina catalysts: in situ high-energy-resolution fluorescence and time-resolved X-ray spectroscopy. Angew Chem 118:4767–4770
83. Tromp M, van Bokhoven JA, Safonova OV et al (2007) High energy resolution fluorescence detection X-ray absorption spectroscopy: detection of adsorption sites in supported metal catalysts. AIP Conf Proc 882:651–653
84. Glatzel P, Singh J, Kvashnina KO et al (2010) In situ characterization of the 5d density of states of Pt nanoparticles upon adsorption of CO. J Am Chem Soc 132:2555–2557
85. Hübner M, Koziej D, Bauer M et al (2011) The structure and behavior of platinum in SnO_2-based sensors under working conditions. Angew Chem Int Ed 50:2841–2844
86. Oudenhuijzen MK, van Bokhoven JA, Miller JT et al (2005) Three-site model for hydrogen adsorption on supported platinum particles: influence of support ionicity and particle size on the hydrogen coverage. J Am Chem Soc 127:1530–1540
87. Tromp M, Slagt MQ, Klein Gebbink RJM et al (2004) Atomic XAFS as a probe of electron transfer within organometallic complexes: data analysis and theoretical calculations. Phys Chem Chem Phys 6:4397–4406
88. Porosoff MD, Yu W, Chen JG (2013) Challenges and opportunities in correlating bimetallic model surfaces and supported catalysts. J Catal 308:2–10
89. Evans J (1989) EXAFS in the study of catalysts. In: Bond GC, Webb G (ed) Catalysis: volume 8, The Royal Society of Chemistry, p 1–41

90. Sayers DE, Stern EA, Lytle FW (1971) New technique for investigating noncrystalline structures: Fourier analysis of the extended X-ray-absorption fine structure. Phys Rev Lett 27:1204–1207
91. Stern EA (1974) Theory of the extended X-ray-absorption fine structure. Phys Rev B 10:3027–3037
92. Lytle FW, Sayers DE, Stern EA (1975) Extended X-ray-absorption fine-structure technique. II. Experimental practice and selected results. Phys Rev B 11:4825–4835
93. Stern EA, Sayers DE, Lytle FW (1975) Extended X-ray-absorption fine-structure technique. III. Determination of physical parameters. Phys Rev B 11:4836–4846
94. Lee PA, Pendry JB (1975) Theory of the extended X-ray absorption fine structure. Phys Rev B 11:2795–2811
95. Sinfelt JH, Via GH, Lytle FW (1978) Extended X-ray absorption fine structure (EXAFS) of supported platinum catalysts. J Chem Phys 68:2009–2010
96. Via GH, Sinfelt JH, Lytle FW (1979) Extended X-ray absorption fine structure (EXAFS) of dispersed metal catalysts. J Chem Phys 71:690–699
97. Sinfelt JH, Via GH, Lytle FW (1980) Structure of bimetallic clusters. Extended X-ray absorption fine structure (EXAFS) studies of Ru–Cu clusters. J Chem Phys 72:4832–4844
98. Via GH, Sinfelt JH, Lytle FW (1981) EXAFS studies of supported metal catalysts. In: Joy DC, Teo BK (eds) EXAFS spectroscopy. Springer, New York, pp 159–162
99. Mustre J, Yacoby Y, Stern EA et al (1990) Analysis of experimental extended X-ray-absorption fine-structure (EXAFS) data using calculated curved-wave, multiple-scattering EXAFS spectra. Phys Rev B 42:10843–10851
100. Frenkel AI, Yevick A, Cooper C et al (2011) Modeling the structure and composition of nanoparticles by extended X-ray absorption fine-structure spectroscopy. Annu Rev Anal Chem 4:23–39
101. Calvin S, Miller MM, Goswami R et al (2003) Determination of crystallite size in a magnetic nanocomposite using extended X-ray absorption fine structure. J Appl Phys 94:778–783
102. Montejano-Carrizales JM, Aguilera-Granja F, Morán-López JL (1997) Direct enumeration of the geometrical characteristics of clusters. Nanostruct Mater 8:269–287
103. Montejano-Carrizales JM, Morán-López JL (1992) Geometrical characteristics of compact nanoclusters. Nanostruct Mater 1:397–409
104. Li Y, Zakharov D, Zhao S et al (2015) Complex structural dynamics of nanocatalysts revealed in operando conditions by correlated imaging and spectroscopy probes. Nat Commun
105. Frenkel AI, Frankel SC, Liu T (2005) Structural stability of giant polyoxomolybdate molecules as probed by EXAFS. Phys Sci 2005:721
106. Frenkel AI, Hills CW, Nuzzo RG (2001) A view from the inside: complexity in the atomic scale ordering of supported metal nanoparticles. J Phys Chem B 105:12689–12703
107. Roldan Cuenya B, Croy JR, Mostafa S et al (2010) Solving the structure of size-selected Pt nanocatalysts synthesized by inverse micelle encapsulation. J Am Chem Soc 132:8747–8756
108. Stern EA (1988) Theory of EXAFS. In: Koningsberger DC, Prins R (eds) X-ray absorption: principles, applications, techniques of EXAFS, SEXAFS, and XANES. John Wiley & Sons, New York
109. Yevick A, Frenkel AI (2010) Effects of surface disorder on EXAFS modeling of metallic clusters. Phys Rev B 81:115451
110. Chill ST, Anderson RM, Yancey DF et al (2015) Probing the limits of conventional extended X-ray absorption fine structure analysis using thiolated gold nanoparticles. ACS Nano 9:4036–4042
111. Roscioni OM, Zonias N, Price SWT et al (2011) Computational prediction of L_3 EXAFS spectra of gold nanoparticles from classical molecular dynamics simulations. Phys Rev B 83:115409
112. Vila F, Rehr JJ, Kas J et al (2008) Dynamic structure in supported Pt nanoclusters: real-time density functional theory and X-ray spectroscopy simulations. Phys Rev B 78:121404

113. Frenkel A, Yang J, Johnson D et al (2009) Nanoscale atomic clusters, complexity of. In: Meyers RA (ed) Encyclopedia of complexity and systems science. Springer, New York, pp 5889–5912
114. Frenkel AI (1999) Solving the structure of nanoparticles by multiple-scattering EXAFS analysis. J Synchrotron Radiat 6:293–295
115. Frenkel AI, Cason MW, Elsen A et al (2014) Critical review: effects of complex interactions on structure and dynamics of supported metal catalysts. J Vac Sci Technol A 32:020801
116. Matos J, Ono LK, Behafarid F et al (2012) In situ coarsening study of inverse micelle-prepared Pt nanoparticles supported on γ-Al_2O_3: pretreatment and environmental effects. Phys Chem Chem Phys 14:11457–11467
117. Paredis K, Ono LK, Mostafa S et al (2011) Structure, chemical composition, and reactivity correlations during the in situ oxidation of 2-Propanol. J Am Chem Soc 133:6728–6735
118. Munoz-Paez A, Koningsberger DC (1995) Decomposition of the precursor $[Pt(NH_3)_4](OH)_2$, genesis and structure of the metal-support interface of alumina supported platinum particles: a structural study using TPR, MS, and XAFS spectroscopy. J Phys Chem 99:4193–4204
119. Giovanetti LJ, Ramallo-López JM, Foxe M et al (2012) Shape changes of Pt nanoparticles induced by deposition on mesoporous silica. Small 8:468–473
120. Vaarkamp M, Miller JT, Modica FS et al (1996) On the relation between particle morphology, structure of the metal-support interface, and catalytic properties of Pt/γ-Al_2O_3. J Catal 163:294–305
121. Vaarkamp M, Modica FS, Miller JT et al (1993) Influence of hydrogen pretreatment on the structure of the metal-support interface in Pt/zeolite catalysts. J Catal 144:611–626
122. Jentys A (1999) Estimation of mean size and shape of small metal particles by EXAFS. Phys Chem Chem Phys 1:4059–4063
123. Beale AM, Weckhuysen BM (2010) EXAFS as a tool to interrogate the size and shape of mono and bimetallic catalyst nanoparticles. Phys Chem Chem Phys 12:5562–5574
124. Long NV, Asaka T, Matsubara T et al (2011) Shape-controlled synthesis of Pt–Pd core–shell nanoparticles exhibiting polyhedral morphologies by modified polyol method. Acta Mater 59:2901–2907
125. Long NV, Duy Hien T, Asaka T et al (2011) Synthesis and characterization of Pt–Pd alloy and core-shell bimetallic nanoparticles for direct methanol fuel cells (DMFCs): Enhanced electrocatalytic properties of well-shaped core-shell morphologies and nanostructures. Int J Hydr Energ 36:8478–8491
126. Anderson JA, Garcia MF (eds) (2005) Supported metals in catalysis. Imperial College Press, London
127. Guczi L (2005) Bimetallic nano-particles: featuring structure and reactivity. Catal Today 101:53–64
128. Bukhtiyarov VG, Slin'ko M (2001) Metallic nanosystems in catalysis. Russ Chem Rev 70:147–159
129. Bazin D, Mottet C, Tréglia G (2000) New opportunities to understand heterogeneous catalysis processes on nanoscale bimetallic particles through synchrotron radiation and theoretical studies. Appl Catal A: Gen 200:47–54
130. Rase HF (2000) Handbook of commercial catalysts: heterogeneous catalysts. CRC Press, Boca Raton
131. Yang OB, Woo SI, Kim YG (1994) Comparison of platinum-iridium bimetallic catalysts supported on γ-alumina and HY-zeolite in n-hexane reforming reaction. Appl Catal A: Gen 115:229–241
132. Nashner MS, Frenkel AI, Adler DL et al (1997) Structural characterization of carbon-supported platinum – ruthenium nanoparticles from the molecular cluster precursor $PtRu_5C(CO)_{16}$. J Am Chem Soc 119:7760–7771
133. Nashner MS, Frenkel AI, Somerville D et al (1998) Core shell inversion during nucleation and growth of bimetallic Pt/Ru nanoparticles. J Am Chem Soc 120:8093–8101

134. Hills CW, Nashner MS, Frenkel AI et al (1999) Carbon support effects on bimetallic Pt – Ru nanoparticles formed from molecular precursors. Langmuir 15:690–700
135. Knecht MR, Weir MG, Frenkel AI et al (2007) Structural rearrangement of bimetallic alloy PdAu nanoparticles within dendrimer templates to yield core/shell configurations. Chem Mater 20:1019–1028
136. Weir MG, Knecht MR, Frenkel AI et al (2009) Structural analysis of PdAu dendrimer-encapsulated bimetallic nanoparticles. Langmuir 26:1137–1146
137. Toshima N, Harada M, Yonezawa T et al (1991) Structural analysis of polymer-protected palladium/platinum bimetallic clusters as dispersed catalysts by using extended X-ray absorption fine structure spectroscopy. J Phys Chem 95:7448–7453
138. Toshima N, Yonezawa T (1998) Bimetallic nanoparticles-novel materials for chemical and physical applications. New J Chem 22:1179–1201
139. Asakura K, Bian CR, Suzuki S et al (2005) An XAFS study on the polymer protected CuPd bimetallic nanoparticles – a novel heterobond-philic structure. Phys Sci T115:781
140. Harada M, Asakura K, Toshima N (1994) Structural analysis of polymer-protected platinum/rhodium bimetallic clusters using extended X-ray absorption fine structure spectroscopy. Importance of microclusters for the formation of bimetallic clusters. J Phys Chem 98:2653–2662
141. Kulkarni UD, Banerjee S, Krishnan RV (1985) On clustering and ordering instabilities in FCC solid solutions. Mater Sci Forum 3:111–121
142. Ma E (2005) Alloys created between immiscible elements. Prog Mater Sci 50:413–509
143. Cowley JM (1950) An approximate theory of order in alloys. Phys Rev 77:669–675
144. Cowley JM (1960) Short- and long-range order parameters in disordered solid solutions. Phys Rev 120:1648–1657
145. Cowley JM (1965) Short-range order and long-range order parameters. Phys Rev 138: A1384–A1389
146. Agostini G, Pellegrini R, Leofanti G et al (2009) Determination of the particle size, available surface area, and nature of exposed sites for silica-alumina-supported Pd nanoparticles: a multitechnical approach. J Phys Chem C 113:10485–10492
147. Hwang B-J, Sarma LS, Chen J-M et al (2005) Structural models and atomic distribution of bimetallic nanoparticles as investigated by X-ray absorption spectroscopy. J Am Chem Soc 127:11140–11145
148. Frenkel AI (2012) Applications of extended X-ray absorption fine-structure spectroscopy to studies of bimetallic nanoparticle catalysts. Chem Soc Rev 41:8163–8178
149. Flavell WR, Mian M, Roberts AJ et al (1997) EXAFS studies of $SrSn_{1-x}Sb_xO_3$ and $BaPb_{1-x}Bi_xO_3$. J Mater Chem 7:357–364
150. Michel CG, Bambrick WE, Ebel RH et al (1995) Reducibility of rhenium in Pt-Re/Al_2O_3 reforming catalysts: a temperature programmed reduction-X-ray-absorption near-edge structure study. J Catal 154:222–229
151. Rønning M, Gjervan T, Prestvik R et al (2001) Influence of pretreatment temperature on the bimetallic interactions in Pt-Re/Al_2O_3 reforming catalysts studied by X-ray absorption spectroscopy. J Catal 204:292–304
152. Ravel B, Bouldin CE, Renevier H et al (1999) Edge separation using diffraction anomalous fine structure. J Synchrotron Radiat 6:338–340
153. Ravel B, Bouldin CE, Renevier H et al (1999) X-ray-absorption edge separation using diffraction anomalous fine structure. Phys Rev B 60:778–785
154. Glatzel P, de Groot FMF, Manoilova O et al (2005) Range-extended EXAFS at the *L* edge of rare earths using high-energy-resolution fluorescence detection: A study of La in LaOCl. Phys Rev B 72:014117
155. Yano J, Pushkar Y, Glatzel P et al (2005) High-resolution Mn EXAFS of the oxygen-evolving complex in photosystem II: structural implications for the Mn4Ca cluster. J Am Chem Soc 127:14974–14975

156. Pushkar Y, Yano J, Glatzel P et al (2007) Structure and orientation of the Mn_4Ca cluster in plant photosystem II membranes studied by polarized range-extended X-ray absorption spectroscopy. J Biol Chem 282:7198–7208
157. Frenkel AI, van Bokhoven JA (2014) X-ray spectroscopy for chemical and energy sciences: the case of heterogeneous catalysis. J Synchrotron Radiat 21:1084–1089
158. Hitchcock AP, Toney MF (2014) Spectromicroscopy and coherent diffraction imaging: focus on energy materials applications. J Synchrotron Radiat 21:1019–1030
159. Kang HC, Yan H, Chu YS et al (2013) Oxidation of PtNi nanoparticles studied by a scanning X-ray fluorescence microscope with multi-layer Laue lenses. Nanoscale 5:7184–7187
160. Fraile Rodríguez A, Nolting F, Bansmann J et al (2007) X-ray imaging and spectroscopy of individual cobalt nanoparticles using photoemission electron microscopy. J Magn Magn Mater 316:426–428
161. Xin HL, Alayoglu S, Tao R et al (2014) Revealing the atomic restructuring of Pt–Co nanoparticles. Nano Lett 14:3203–3207
162. Vendelbo SB, Elkjær CF, Falsig H et al (2014) Visualization of oscillatory behaviour of Pt nanoparticles catalysing CO oxidation. Nat Mater 13:884–890
163. Billinge SJL, Levin I (2007) The problem with determining atomic structure at the nanoscale. Science 316:561–565
164. Zhao S, Li Y, Zakharov D et al Operando characterization of catalysts with a portable microreactor

Chapter 20
XAS Techniques to Determine Catalytically Active Sites in Zeolites: The Case of Cu-Zeolites

Jeroen A. van Bokhoven and Carlo Lamberti

20.1 Introduction

Oxide materials find widespread application in industry, for example as semiconductor, solar cell, catalyst, and sensor. New materials and applications continue to be reported, which is a main driver for technological development and slowly makes our society more sustainable. The function of these materials strongly depends on their structure, which is why their structural characterization receives much attention.

Zeolites are an important class of microporous crystalline oxides and they find widespread application as catalyst and catalyst support. [1–3] Within the refinery, they are the dominant catalysts, because of their unique structure, guaranteeing shape-selectivity, and thermal stability. Zeolites are crystalline alumina-silicates. They are micro-porous and therefore have very large surface areas. Silicon and aluminum atoms are tetrahedrally coordinated by bridging oxygen atoms. [4, 5] Because there is a charge imbalance for every framework aluminum, cations are located in the zeolite pores, for each aluminum one cationic charge [6]. These cations give zeolites their catalytic function, such as a Brønsted acid in case of proton-exchanged zeolites and Lewis or redox function in case of cations [7], such as iron [8] and copper. These extra-framework species catalyze a wide range of redox reactions, notably oxidation. Unique features are their stability, induced by

J.A. van Bokhoven (✉)
Institute for Chemical and Bioengineering, ETH Zürich, CH8093 Zurich, Switzerland

Swiss Light Source, Paul Scherrer Institute, CH-5232 Villigen PSI, Switzerland
e-mail: j.a.vanbokhoven@chem.ethz.ch; jeroen.vanbokhoven@psi.ch

C. Lamberti
Department of Chemistry, CrisDi Centre for Crystallography, University of Torino, I10125 Torino, Italy

IRC "Smart Materials", Southern Federal University, 344090 Rostov-on-Don, Russia

Y. Iwasawa et al. (eds.), *XAFS Techniques for Catalysts, Nanomaterials, and Surfaces*, DOI 10.1007/978-3-319-43866-5_20

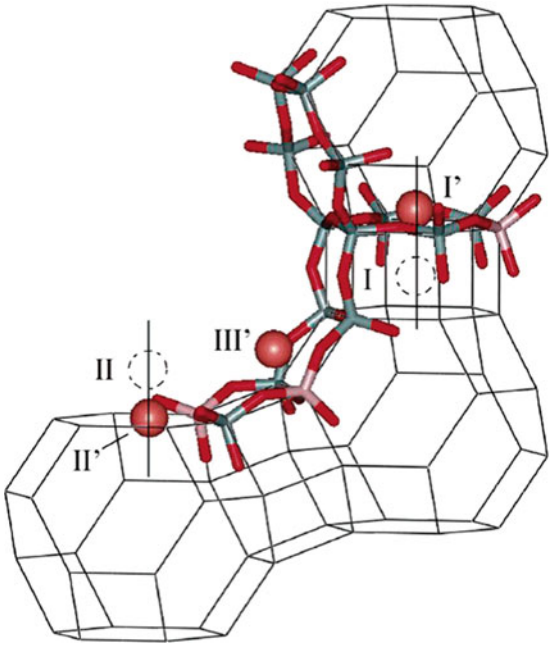

Fig. 20.1 Schematic picture of zeolite Y. *Gray* and *pink* identify the location of silicon and aluminum atoms, respectively, which are connected by bridging atoms, forming the crystalline framework. The *red* and *dashed spheres* illustrate possible and preferred locations for extra-framework ions. The faujasite structure is composed of sodalite cages, of which three are shown here. They are connected by double six-rings. The maximal pore size in faujasite contains twelve T-atoms and has a size of 7.4 Å. The largest accessible cage has a diameter of 12 Å. Adapted with permission from ref. [81], copyright American Chemical Society (2006)

the space-restricting functionality of the pores and their ability to perform oxidation reactions selectively [9–14]. Instead of aluminum, other atoms may replace silicon, which imply different activity: redox chemistry is for example done over titanium containing Ti-silicalite [15–17]. Figure 20.1 illustrates a zeolite structure, notably zeolite Y or faujasite with its preferred extra-framework cation sites.

X-ray absorption-based methods have played an important role in determining the structure of the framework and extra-framework species in the zeolite structure, as recently summarized [17]. X-ray-based techniques are attractive, because of their versatile applicability [18–22]. They yield electronic and geometric structures and can be applied under in situ conditions. Thus, a functioning material, such as a sensor, battery [23], and catalyst [24], can be structurally characterized while it performs its function. This chapter concerns the structure of extra-framework copper species in zeolites as determined by X-ray based spectroscopic methods. The focus is on copper-based zeolites, because of their large academic and commercial interest.

Copper-exchanged zeolites enjoy large academic and industrial interest. They are active catalysts for selective catalytic reduction (SCR), which converts nitrogen oxides into di-nitrogen and water [25–30]. This reaction finds widespread application in stationary and mobile exhaust control. Diesel engines on ships, trains and automobiles contain SCR catalysts, which consist of base metal oxides, such as tungsten, vanadium, and molybdenum, of precious metals, or of transition metal ions on zeolite supports. One of the most-studied ones is copper-exchanged zeolites [31]. Contemporary research focuses on the reaction mechanism and the identification of the catalytically active sites [27–30]. Here, in situ and operando X-ray absorption measurements are reviewed to provide the state of the art in site and mechanism elucidation.

A second major research field of copper-exchanged zeolites is the selective conversion of methane to methanol. Because of the higher reactivity of methanol compared to methane, the direct conversion of methane to methanol using oxygen is restricted to low conversion, because of carbon dioxide formation [32]. For this reason, methane is commercially converted into methanol via syngas production and its subsequent conversion into methanol [33, 34]. Such process is cost intensive and not suitable for small-scale operation. Methane is abundantly available, however, often at stranded locations and therefore flared, observable from outer space by pictures of the earth by night. An equivalent to one quarter of the European energy use is put to waste. Direct conversion of methane into a liquid, such as methanol, would enable transporting it, and making its conversion into fuels or chemicals possible, representing an enormous increase in value.

20.2 Brief Historical Overview

Copper-exchanged zeolites have been widely investigated after the discovery in the early 90s by the Iwamoto group [31, 35, 36] and by Li and Hall [37, 38] that Cu-ZSM-5 are active in the direct decomposition of nitric oxide to nitrogen and oxygen [39]. The study of this catalytic process has deserved a great practical interest, as nitric oxides are known to be a major cause of air pollution [40]. Successively, other Cu-exchanged zeolites have shown to be active in the selective catalytic reduction of NOx such as MOR, X, Y, USY, and IM5. X-ray absorption spectroscopies, both XANES and EXAFS played a key role in the investigation of the coordination and oxidation state of copper species in such systems in the activated forms and under different reaction conditions [41–49].

More recently, the Cu-exchanged form of the novel SSZ-13 zeolite, with CHA framework and high Si/Al ratio, is attracting a lot of attention due to its outstanding performance in NH_3-assisted selective catalytic reduction (SCR) of NO_x gases contained in the exhaust fumes from cars and industrial plants, in terms of activity and hydrothermal stability [25–30]. In order to explain such behavior and to develop the NH_3-based SCR reaction mechanism many studies were performed by the groups all over the world involving a very broad range of characterization

techniques, such as FTIR [7, 50], UV–Vis [50], EPR [50], XRD [51], and so on, as recently reviewed by Beale et al. [52] Among them X-ray spectroscopy (both absorption [18, 53] and emission [54]) is particularly useful due to its element selectivity, since the active sites of SCR reaction in Cu-SSZ-13 are low-abundance Cu ions hosted in the cavities of the zeolite framework. Careful analysis of EXAFS, XANES, and XES spectra, often assisted by the advanced DFT calculations, yields detailed information on the local environment and oxidation state of Cu centers in different reaction conditions [28–30, 52, 55–59]. In situ and *operando* studies, possible due to the high penetration depth of the hard X-rays (around 9 keV, corresponding to the Cu K-edge), provide the means to answer "chemical questions" concerning the reactivity of the Cu species towards particular gases at given temperatures, which is crucial for determining different steps of the reaction mechanism [18–20, 53].

The structure of the Cu-CHA framework has been known since the 70s from the single crystal diffraction studies [60], that of Cu-SSZ-13 is similar, just with a lower Al and Cu content. It is composed of double six-membered rings (6-rings) connected in an AABBCC sequence, forming cavities with eight-membered windows (8-rings), see Fig. 20.2.

20.3 Determination of the Local Environment of Cu in SSZ-13 Upon Activation

Once Cu-SSZ-13 has shown its outstanding catalytic properties [25, 26], the focus of the structural investigations was gradually shifted from the framework to the location of the isolated Cu ions in the hydrated and thermally activated material, which are the active sites of the SCR reaction. One of the first studies carried out by Fickel and Lobo demonstrated that the Cu ions tend to occupy the centers of the 6-rings [51]. Since every 6-ring is likely to have one negatively charged tetrahedral unit with Al substituting Si, the authors admitted, that Cu cations are expected to be shifted towards it from the center of the ring. However, XRD refinement was always converging to central position due to the lack of structural contrast. Nonetheless, it was possible to detect that, being always "projected" on the center of the 6-ring, the Cu ions were gradually approaching its plane upon calcination. The authors suggested that this effect may take place due to the dehydration of the Cu ions.

Successively, Korhonen et al. presented Cu K-edge EXAFS data for both calcined and as-synthesized (hydrated) Cu-CHA [61] and analyzed the data using as starting model the previous theoretical structure of Cu in the 6-ring reported by Pierloot et al. [62] The fit resulted in adequate agreement with the experiment, confirming that Cu is indeed situated off-axis of the 6-ring. The very substantial shift of one of the oxygens in the 6-ring from the initial position during fitting was explained by the lower degree of deformation of the ring compared to the one

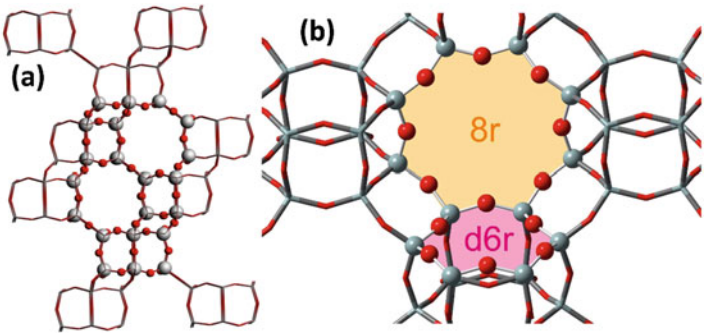

Fig. 20.2 Part (**a**): sticks representation of a fragment of CHA framework with the atoms forming the large cavity highlighted with balls. Part (**b**): zoom of the large CHA cavity showing 6- and 8-membered rings, which are reported to be the most likely hosts for Cu ions. Color code: Si—*gray*, O—*red*

predicted by DFT. First shell coordination numbers were determined as 4 for hydrated material and 3.2 for the calcined one. Presented XANES results also indicated the decrease of coordination upon dehydration due to the decrease of the white line intensity. Later the shift of the Cu ion from the center of the 6-ring was also confirmed by Deka et al. [63], by means of XANES simulations. Calculated spectrum of the model with Cu placed off-axis resulted in a much better agreement with the experimental data compared to the centered model.

Hydration issue was raised in more detail in the work of McEwen et al. [55] where it was demonstrated that Cu K-edge XANES spectrum of the as-synthesized Cu-SSZ-13 zeolite is very similar to the one of aqueous solution of Cu ions. This was further confirmed by Borfecchia et al. [59], who presented also a comparison of the EXAFS data for these two cases. High degree of similarity of both XANES and EXAFS data suggests that as long as the zeolite is exposed to air at room temperature, copper is covered by a shell of water molecules. Such shielding explains the lack of the framework contribution to the EXAFS data of the hydrated material and confirms the initial hypothesis of Fickel and Lobo [51]. At the same time, a substitution of one H_2O molecule by OH^- group cannot be excluded since these species are hardly distinguishable in EXAFS.

One of the most extensive spectroscopic studies of the Cu-SSZ-13 (Cu/Al = 0.444, Si/Al = 13.1) activation to date was carried out by Borfecchia et al. [59], who followed the activation in temperature up to 400 °C in both O_2/He and pure He flows with XANES, EXAFS, and valence-to-core XES spectroscopies. EXAFS-optimized experimental setup and rather high copper content in the sample allowed to achieve a very good data quality paving the way to a detailed quantitative analysis. XANES, EXAFS, and valence-to-core XES spectra, together with the optimized DFT models and corresponding XANES and XES simulations, are reported in Figs. 20.3 and 20.4 for O_2- and He-activated samples, respectively. Borfecchia et al. [59], tried several DFT models sitting Cu(II), or Cu(I), in the 8r or in the 6dr rings and inserting either one or two Al atoms in the T positions of the

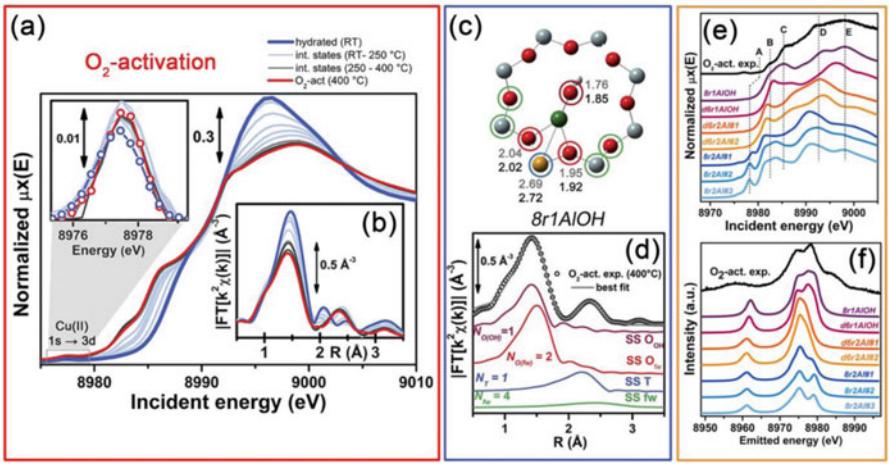

Fig. 20.3 Part (**a**): XANES spectra following the activation from room temperature (*blue curve*, hydrated material) to 400 °C (*red curve*, activated material) of Cu-SSZ-13 in 50 % O_2/He flow. The *inset* shows a magnification of the 1 s → 3d transition, typical of Cu(II) species. Part (**b**) as part (**a**) for the k^2-weighted FT of the EXAFS spectra. Part (**c**): DFT model of the dominant Cu-site in the O_2-activated material. Part (**d**): best EXAFS fit and related main individual components obtained using the model reported in part (**c**). Part (**e**): experimental HERFD XANES spectrum (*black curve*) and computed XANES spectra (colored curves) for the different optimized possible sites. Part (**f**): as pat (**e**) for the valence-to-core XES spectra. Both HERFD XANES and XES simulations support the EXAFS results. Adapted with permission from Borfecchia et al. [59], copyright Royal Society of Chemistry (2015)

ring. Structures reported in Figs. 20.3c and 20.4c, d are only those that are compatible with the experimental results.

Upon activation in O_2/He flux Cu(II) centers undergo progressive dehydration, while interacting more closely with the framework, keeping +2 oxidation state. Features typical for Cu(II) in low-symmetry environment were observed in XANES (Fig. 20.3a), while EXAFS witnesses the marked decrease of the first shell intensity due to the loss of the coordinated water molecules (Fig. 20.3b). Comparable evolution of the XANES spectra upon similar activation in oxidative environment was observed also by Kwak et al. [64] Conversely, as already observed for Cu(II)-ZSM-5 [47] and for Cu(II)-MOR [65] systems, upon activation in vacuum or in inert atmosphere (e.g., He flux) the Cu oxidation state did change to +1, as evidenced for the Cu(II)-SSZ-13 system by the disappearance of 1 s → 3d transition and by the additional redshift of the edge, see Fig. 20.4a.

Most interestingly, the high-quality EXAFS data reveal that the coordination of Cu upon He-activation was further decreased compared to the activation in O_2. Coupled with the observation that the reduction in He flow appears only at high temperature (T > 250 °C), while at lower T the evolution of the spectra is identical to the O_2-activation case, it indicates that a charged extra-ligand is still coordinated to Cu even at high temperature in case of O_2-activation. This evidence support the hypothesis of the presence of an OH^- ligand in the first coordination shell of Cu

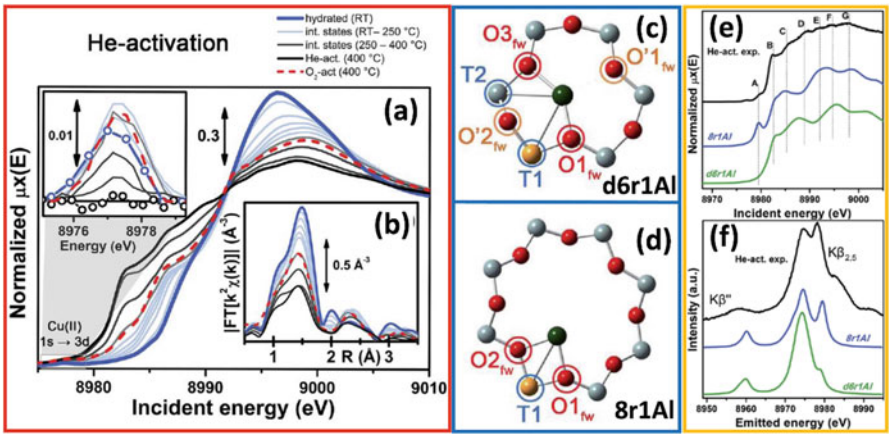

Fig. 20.4 Part (**a**): XANES spectra following the activation from room temperature (*blue curve*, hydrated material) to 400 °C (*red curve*, activated material) of Cu-SSZ-13 in inert He flow. The *inset* shows a magnification of the 1 s → 3d transition, typical of Cu(II) species and disappearing at high temperature. Part (**b**) as part (**a**) for the k^2-weighted FT of the EXAFS spectra. Parts (**c, d**): DFT model of the dominant Cu-sites in the He-activated material. Best EXAFS fit and related main individual components obtained using the model reported in part (**c**). Part (**d**): experimental HERFD XANES spectrum (*black curve*) and computed XANES spectra (*colored curves*) for the different optimized possible sites. Part (**f**): as pat (e) for the valence-to-core XES spectra. Both HERFD XANES and XES simulations support the EXAFS results. Adapted with permission from Borfecchia et al. [59], copyright Royal Society of Chemistry (2015)

(II) as advanced in the IR study of Giordanino et al. [50] to assign the ν(OH) stretching mode at 3657 cm^{-1}.

The authors have further tested this hypothesis by performing a set of DFT simulations of Cu ions in different places of the framework and using the resulting structures as input for EXAFS fits and for the simulations of the high resolution fluorescence detected (HRFD) XANES and XES spectra, see parts (e) and (f) of Figs. 20.3 and 20.4.

For the O_2-activated material, the best overall agreement with the experimental data was obtained for the models of Cu(II) in the 8-ring, in form of a Cu (OH) complex, see Fig. 20.3c confirming the first assignment of the ν(OH) stretching mode at 3657 cm^{-1} [50]. While in case of He-activation it was a bare Cu(I) cation hosted mainly in the 8r, with a minority occupancy of the d6r site.

20.4 Understanding the SCR Mechanism

A large number of studies were devoted in the understanding of the SCR reaction mechanism over Cu-SSZ-13 system. In this regard remarkable efforts were invested into measuring XAS and XES spectra in different reaction-relevant conditions. We

can divide such studies into two families The first concerns experiments in truly *operando* conditions, when the sample is exposed to the complete reaction mixture (including NO, NH_3, O_2, He, H_2O, in some studies also NO_2 and CO_2) under controlled temperature. Most often such studies are performed in plug-flow reactors, such as the one described in the work of Kispersky et al. [66], collecting XAS and XES spectra of the catalyst in different reaction-relevant conditions. The interpretation of such data is intrinsically complicated, since several different Cu species forming on the different stages of the reaction may simultaneously contribute to the signal. The common approach to analyze such data is to measure also the spectra of the relevant reference materials, and, performing linear combination analysis, determine the relative contribution of each species to the spectrum of the catalyst under SCR conditions. Such strategy was adapted in the works of McEwen et al. [55] and of Bates et al. [56], where the samples with different Cu loadings were tested. Fitting the data with the Cu(I) and Cu(II) standards allowed the authors to determine the ratio between the amounts of Cu species of these oxidation states during the reaction.

The second strategy consists in probing separately different stages of SCR reaction thus testing the independently developed hypotheses regarding the behavior of the active sites in particular conditions. Such approach allowed Janssens et al. [30] to decouple the oxidation and reduction stages of the suggested SCR cycle, see Fig. 20.5. In particular, the authors have tested the effect of different red-ox agents, namely $NO + O_2$ mixture (gray curve), O (orange curve), NH_3 (blue curve), and their mixture (red curve), see Fig. 20.5a, b. The results clearly indicate that almost complete reduction occurs only after exposure to the mixture of NO and NH_3. Resulting spectrum is characteristic for $Cu^{+}(NH_3)$ species in linear geometry [50]. Conversely, NO alone is not able to reduce Cu^{2+}. Exposure to NH_3 alone leads only to a partial reduction accompanied by the formation of a linear Cu complex, while around 75 % of Cu species remain oxidized, presumably forming a planar tetra-amino complexes [30]. This study also revealed that the interaction of Cu (I) species with NO_2 and $NO + O_2$ results in the same Cu(II) species, see Fig. 20.5c, in agreement with the suggested mechanism, see Fig. 20.5d. The obtained complex was a bidentate Cu-NO_3^{-}, as evidenced by the EXAFS and XANES analysis. The XAS and XES data reported here, supported by parallel IR, EPR, and DFT studies, confirm the proposed scheme of the SCR reaction, resulting in greatly improved understanding of its chemistry.

A similar strategy of probing particular intermediate states of the reaction was adapted by the group of Grunwaldt [29] who used valence-to-core XES and HERFD XANES for characterizing different stages of SCR reaction. It was possible to detect the formation of Cu-N bond upon coordination of NH_3 monitoring the shift of Kβ'' satellite from 8956.9 to 8958.3 eV. Notably, no such shift was observed in the cases when NH_3 was absent from the feed, indicating thus the very weak coordination of NO to Cu accompanied by minor changes in Cu local environment [29].

Summarizing, in the past six years, due to the efforts of several independent research groups, there has been a marked advance in the understanding of the

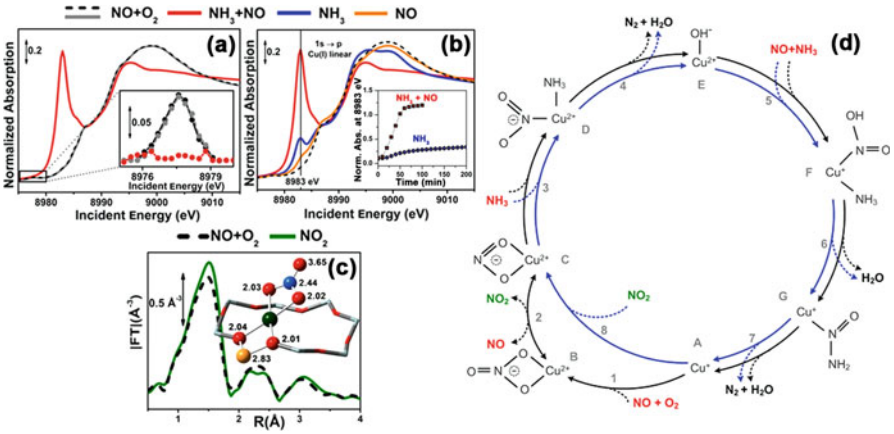

Fig. 20.5 In situ Cu K-edge XAS data collected at 200 °C under different SCR-relevant conditions. Part (**a**): XANES spectra upon initial oxidation in 1000 ppm NO + 10 % O_2 (*dashed black curve*), reduction in 1200 ppm NH_3 + 1000 ppm NO (*solid red curve*) and reoxidation in 1000 ppm NO + 10 % O_2 (*solid gray curve*). Part (**b**): XANES spectra showing the reducing capability of 1200 ppm NH_3 (*solid blue curve*), 1000 ppm NO (*solid orange curve*) and a mixture of 1200 ppm NH_3 with 1000 ppm NO (*solid red curve*) on the Cu(II) state obtained after initial oxidation in a mixture of 1000 ppm NO and 10 % O_2 (*dashed black curve*). Part (**c**): Fourier-transformed EXAFS after exposure of dehydrated Cu-SSZ-13–1000 ppm NO_2 (*solid green curves*), and to a mixture of 1000 ppm NO and 10 % O_2 (*dashed black curve*) together with the structural model of the bidentate Cu-NO_3^- species forming at these conditions. Part (**d**): catalytic SCR cycle. The fast SCR cycle is represented in the *blue* internal loop, and the NO activation cycle is represented in *black*. Reactants are indicated in *red*, reaction products are indicated in *black*, and the NO_2 intermediate is indicated in *green*. Adapted with permission from ref. [30], Copyright American Chemical Society (2015)

structure and reactivity of the active sites in Cu-SSZ-13 catalyst. As shown in this section, a significant part of the insights was gained by the element-selective XAS/XES studies, complemented by laboratory techniques and supported by DFT calculations. Several mechanisms of SCR reaction catalyzed by Cu-SSZ-13 were proposed based on the results of such multi-technique investigations [27–30]. Although there are still some contradictions in the literature regarding the stages of the reaction and the formed intermediates, there is no doubt that these issues will be eventually resolved in the coming up studies.

20.5 Methane to Methanol Over Copper-Exchanged Zeolites

As mentioned, the direct conversion of methane to methanol is very attractive; however, it is difficult. Over the years, a stepwise, chemical looping reaction has been developed over copper-exchanged zeolites [67–69]. The fundamental

principle is to stabilize any intermediate from methane, which is thus prevented from further reacting [31]. The first such system is that of Periana [70], which is based on platinum bidiazine, which reacts methane to form a methyl ester. In a subsequent step, the methanol is produced. Analogously, in the Cu-zeolite, after high temperature activation in oxygen, methane is reacted between 425 and 475 K and the thus formed intermediate remains adsorbed on the catalyst surface. Methanol can be extracted by liquid phase extraction [13] or desorbed by steam. Nature is able to selectively convert methane into methanol based on iron or on copper systems. [71, 72]. Such systems have served as inspiration for active sites in the zeolites [73]. Following the work on reduction of copper in Cu-ZSM-5 by Yamaguchi et al. [74–76], similarly to what was discussed in detail in section 20.3 for Cu-SSZ-13, Groothaert et al. [77] measured the structure of copper in ZSM-5 (over-exchanged, Si/Al = 12) during treatment in helium and in oxygen. After ion exchange, copper(II) ions were four-coordinated with oxygen atoms without evidence of copper–copper coordination (Table 20.1). Instead, a contribution of aluminum of the framework was found. Heat treatment in helium at 773 K caused the oxygen coordination number to about half its original and a copper–copper coordination of 0.5 was observed. The Cu K edge XANES showed the characteristic pre-edge of copper(I), which is indicative of copper auto-reduction. Heating in the presence of oxygen instead of inert maintained the copper oxidation state of two and the EXAFS fitting identified an oxygen coordination of four, a copper–copper coordination of one and copper–aluminum of one. Distinction between the latter two was done on the basis of combined k^0 and k^3 weighting of the fits. In the absence of a copper–copper coordination, the Debye–Waller factor of the copper–aluminum contribution decreased to unrealistic negative values, which is indicative of "making it look like a copper scatterer."

The copper–copper coordination is indicative of formation of copper dimers or of a mixture of monomers and oligomers. Based on complementary UV–Vis data, a bis(μ-oxo) dicopper core was proposed. Earlier and later proposals have suggested the formation of a mono μ-oxo core to be more likely [73, 78]. Based on theory and essentially similar EXAFS data, instead of the copper dimer, a trimer has been suggested very recently [79]. Whatever the exact nature of the oxygen-activated species, they react with methane, which, after extraction in liquid [13] or by steam [67] yields methanol.

The reaction of the oxygen-activated copper catalyst with methane has been studied by in situ quick X-ray absorption spectroscopy. Figure 20.6 shows the K-edge XANES spectra of copper-exchanged mordenite after ion exchange (1), calcination in oxygen (2), reaction with methane (3), and helium treatment at elevated temperature. The initial copper structure conforms literature and is assigned to hydrated copper(II) ions. Calcination leads to oxygenated and active copper(II) sites, indicative of the bis- respectively mono-μoxo dicopper core. Reaction of these species with methane yielded a distinct pre-edge feature at 8983.6 eV, attributed to the $1\ s \rightarrow 4p$ transition of copper(I). Quantification by linear combination fitting yielded a mixture of copper(I), copper(II) oxide, and

Table 20.1 Copper coordination over-exchanged Cu-ZSM5 (Si/Al = 12) from EXAFS fitting. Adapted with permission from ref. [77], copyright American chemical Society (2003)

	N	R (Å)	Δ_{DWF}[a] (Å^2)
After ion exchange			
Cu–O	4.0	1.96	−0.001
Cu–Al	0.7	3.18	0.008
Treated in inert at 773 K			
Cu–O	2.3	1.92	0.006
Cu–Cu	0.5	2.84	0.015
After calcination 623 K			
Cu–O	4.1	1.95	0.002
Cu–Cu	0.9	2.87	0.009
Cu–Al	0.8	3.21	0.006

[a]Debye–Waller factor, relative to the reference

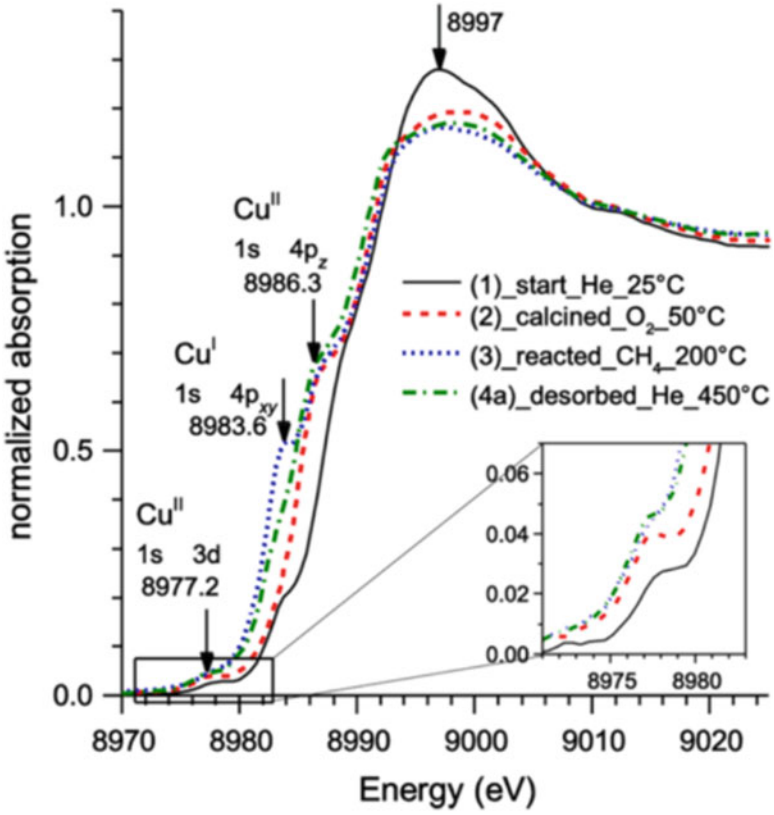

Fig. 20.6 Cu K-edge XANES of Cu-MOR (1) directly after ion exchange, (2) after high temperature calcination, (3) after reaction with methane, and (4) after high temperature desorption in inert. The temperature of measurement is given next to the sample name. The insert highlights the pre-edge region. Heating in inert causes autoreduction of copper(II); calcination yields copper (II), and subsequent reaction with methane reduction of a large fraction into copper(I). Reproduced with permission from ref. [68], copyright American Chemical Society (2014)

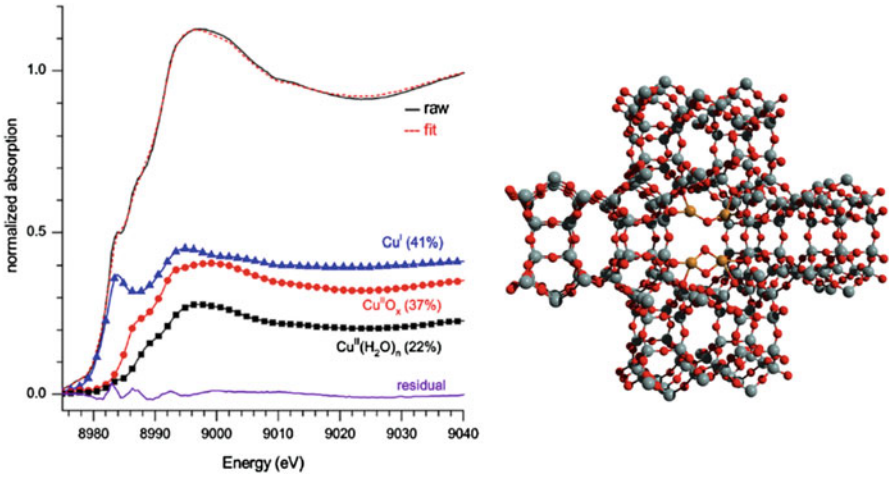

Fig. 20.7 (*left*) Measured spectrum and deconvoluted Cu K-edge XANES spectra of Cu-MOR after high temperature oxygen activation and subsequent reaction with methane. Reproduced with permission from ref. [68], copyright American Chemical Society (2014). (*right*) Depiction of the 12-membered ring in mordenite with a mono μ-oxo dicopper respectively bis μ-oxo dicopper core; the copper atoms are given in *gold*

hydrated copper(II) of 41:37:22 ratio (Fig. 20.7). Stable (Cu^{I}-OCH_3-Cu^{II}) and (Cu^{I}-OH-Cu^{II}) were identified as possible stable intermediates by DFT. [73]

During admission of steam to the methane activated sample, methanol was detected in the mass spectrometer and the concomitant formation of hydrated copper(II), some copper(II) oxide and the loss of the copper(I) were detected by XANES (Fig. 20.8). These changes in the electronic structure were paralleled by relatively minor changes in EXAFS, which identifies the absence of large structural changes and sintering. This enables performing a second cycle. The EXAFS analysis proved to be very complex and up to date no definite conclusions have been drawn from them.

Overall, oxygen activation of Cu-MOR and Cu-ZSM-5 zeolites yields small copper clusters, mostly suggested to be dimers, that contain oxygen that is reactive towards methane. The thus formed intermediate is associated to the presence of coper(I) and it can be desorbed as methanol using steam. Such step-wise process is a promising route towards direct methanol production from methane [80], even though it is currently hampered by low methanol per pass yields.

20.6 Conclusion

Cu-zeolites find commercial application in SCR and are promising catalysts for the direct methane-to-methanol conversion. X-ray absorption and emission-based techniques have played and continue to play an invaluable role in determining the

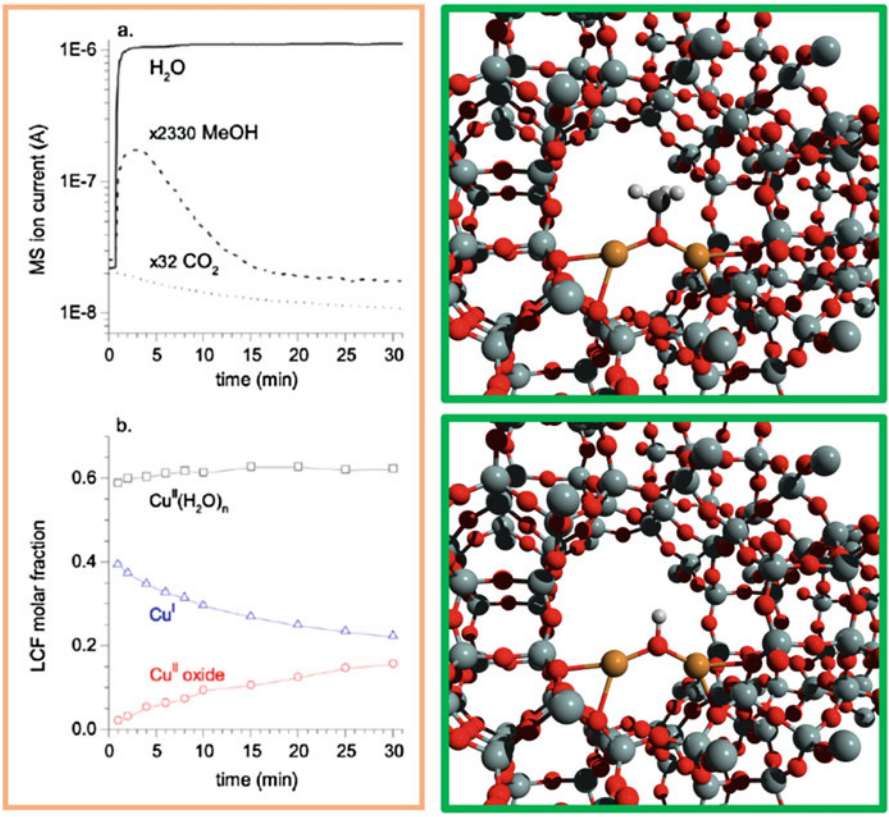

Fig. 20.8 (*left panel*) (**a**) Methanol formation identified by mass spectrometry by providing wet helium over a methane reacted Cu-mordenite catalyst after high temperature oxygen activation and (*left panel*) (**b**) linear combination fitting results of the copper species upon interaction of wet helium with a methane-reacted Cu-MOR. The two measurements were performed simultaneously. Reproduced with permission from ref. [68], copyright American Chemical Society (2014) (*right panel*) A possible dicopper core with a bridging methoxy (*top*) and hydroxyl group, calculated to be possible stable intermediates

structure of the catalytically active sites. In particular, the in situ and operando capacity in combination with element selectivity is a decisive factor in their success. In both reactions, copper undergoes a change in redox state when cycling through the reaction; in SCR NO and NH_3 and in the direct methane to methanol it is the methane that reduces copper(II) into copper(I). Despite this similarity in redox activity, the catalytically active sites have pronounced different structures, in the former reaction, single copper ions are responsible for activity, which are inactive for methane oxidation. In that case, small clusters, mostly assumed to be oxygen-bridged copper dimers and, more recently, a copper trimer, are the active species. Even though discussions about details continue, the catalytic cycle in the SCR reaction has been almost completely established. In contrast, the intermediate

that is formed upon methane interaction with the oxygen activated remains unknown and major discussions about the exact active phase continue. X-ray-based methods will continue to play a major role in further identification of active sites and catalytic cycles. Complementary experimental and theoretical characterization tools will be needed.

Both NH_3-SCR and methane to methanol reactions catalyzed by Cu-zeolites are hot topics, as testified by the fact that several relevant works appeared in the literature on in the short period between manuscript submission and proof corrections. Among them we briefly review hereafter the results obtained by four of them. The relationships among the macroscopic compositional parameters of a Cu-exchanged SSZ-13 zeolite catalyst, the types and numbers of Cu active sites, and activity NH_3-SCR has been established through combined experimental and computational analysis across the catalyst composition space by Paolucci et al. [82]. Lomachenko et al. [83] used *operando* XAS and XES to monitor the Cu-CHA catalyst in action during NH_3-SCR in the 150–400 °C range, targeting Cu oxidation state, mobility and preferential first shell N or O ligation as a function of reaction temperature. They identified two distinct regimes for the atomic-scale behavior of Cu active-sites. Low-temperature SCR (up to ca. 200 °C), characterized by balanced populations of Cu(I)/Cu(II) sites and dominated by mobile NH_3-solvated Cu-species and high-temperature SCR (from 250 °C upwards, in correspondence to the steep increase in catalytic activity) largely dominated by framework-coordinated Cu(II) sites [83]. Narsimhan et al. [84] observed the direct, catalytic oxidation of CH_4 into CH_3OH with over Cu-zeolites of different commercially available topologies at mild reaction conditions (210–225 °C and 1 bar O_2). Authors observed that the catalytic rates and the apparent activation energies are affected by the zeolite topology. Cu-SSZ-13, followed by other caged-based zeolites, showed the highest rate [84]. This study supported the previous work of Wulfers et al. who observed that small-pore Cu-zeolites (Cu-SSZ-13, Cu-SSZ-16, Cu-SSZ-39, and Cu-SAPO-34) produce more methanol per copper atom than Cu-ZSM-5 and Cu-mordenite [69]. Finally, Kulkarni et al. [85] performed DFT calculations to systematically evaluate mono-copper species as active sites for the partial methane oxidation reaction in Cu-exchanged SSZ-13. Based on kinetic and thermodynamic arguments, they suggest that $[Cu(II)OH]^+$ species in the 8r ring (see Fig. 20.2b) are responsible for the experimentally observed activity. This study was able to successfully explain the available spectroscopic data and experimental observations including (a) necessity of water for methanol extraction and (b) effect of Si/Al ratio on the catalyst activity. This model differs from the dimeric and trimeric copper species inferred to be the active sites in MOR and ZSM-5 zeolites, as reviewed in Sect. 20.5.

Acknowledgements C.L. acknowledges the Mega-grant of the Russian Federation Government to support scientific research at the Southern Federal University, no. 14.Y26.31.0001.

References

1. Weitkamp J, Puppe L (1999) Catalysis and zeolites fundamentals and applications. Springer, Berlin
2. Davis ME (2002) Ordered porous materials for emerging applications. Nature 417:813–821
3. Cejka J, Corma A, Zones S (2010) Zeolites and catalysis. Wiley VCH, Weinheim
4. Szostak RM (1989) Molecular sieves. Van Nostrand Reinhold, New York
5. Meier WM, Olson DH, Baerlocher C (1996) Atlas of zeolite structure types. Elsevier, London
6. Frising T, Leflaive P (2008) Extraframework cation distributions in X and Y faujasite zeolites: a review. Microporous Mesoporous Mater 114:27–63
7. Bordiga S, Lamberti C, Bonino F et al (2015) Probing zeolites by vibrational spectroscopies. Chem Soc Rev 44:7262–7341
8. Zecchina A, Rivallan M, Berlier G et al (2007) Structure and nuclearity of active sites in Fe-zeolites: comparison with iron sites in enzymes and homogeneous catalysts. Phys Chem Chem Phys 9:3483–3499
9. Panov GI, Sobolev VI, Kharitonov AS (1990) The role of iron in N_2O decomposition on ZSM-5 zeolite and reactivity of the surface oxygen formed. J Mol Catal 61:85–97
10. Iwamoto M, Hamada H (1991) Removal of nitrogen monoxide from exhaust gases through novel catalytic processes. Catal Today 10:57–71
11. Smits RHH, Iwasawa Y (1995) Reaction-mechanisms for the reduction of nitric-oxide by hydrocarbons on Cu-ZSM-5 and related catalysts. Appl Catal B-Environ 6:L201–L207
12. Panov GI, Uriarte AK, Rodkin MA et al (1998) Generation of active oxygen species on solid surfaces. Opportunity for novel oxidation technologies over zeolites. Catal Today 41:365–385
13. Groothaert MH, Smeets PJ, Sels BF et al (2005) Selective oxidation of methane by the bis (μ-oxo)dicopper core stabilized on ZSM-5 and mordenite zeolites. J Am Chem Soc 127:1394–1395
14. Hammond C, Dimitratos N, Lopez-Sanchez JA et al (2013) Aqueous-phase methane oxidation over Fe-MFI zeolites. Promotion through Isomorphous framework substitution. ACS Catal 3:1835–1844
15. Bordiga S, Coluccia S, Lamberti C et al (1994) XAFS study of Ti-silicalite: structure of framework Ti(IV) in presence and absence of reactive molecules (H_2O, NH_3) and comparison with ultraviolet–visible and IR results. J Phys Chem 98:4125–4132
16. Bordiga S, Bonino F, Damin A et al (2007) Reactivity of Ti(IV) species hosted in TS-1 towards H_2O_2/H_2O solutions investigated by ab initio cluster and periodic approaches combined with experimental XANES and EXAFS data: a review and new highlights. Phys Chem Chem Phys, 9:4854–4878
17. van Bokhoven JA, Lamberti C (2014) Structure of aluminum, iron, and other heteroatoms in zeolites by X-ray absorption spectroscopy. Coord Chem Rev 277:275–290
18. Bordiga S, Groppo E, Agostini G et al (2013) Reactivity of surface species in heterogeneous catalysts probed by in situ X-ray absorption techniques. Chem Rev 113:1736–1850
19. Mino L, Agostini G, Borfecchia E et al (2013) Low-dimensional systems investigated by X-ray absorption spectroscopy: a selection of 2D, 1D and 0D cases. J Phys D-Appl Phys 46:72
20. Garino C, Borfecchia E, Gobetto R et al (2014) Determination of the electronic and structural configuration of coordination compounds by synchrotron-radiation techniques. Coord Chem Rev 277:130–186
21. van Bokhoven JA, Lamberti C (2016) X-ray absorption and X-ray emission spectroscopy: theory and applications. John Wiley & Sons, Chichester
22. Iwasawa Y (2016) XAFS techniques for catalysts, nanomaterials, and surfaces. Springer, Berlin
23. Ramaker D (2016) Novel XAS techniques for probing fuel cells and batteries. In: van Bokhoven JA, Lamberti C (eds) X-ray absorption and X-ray emission spectroscopy: theory and applications. John Wiley & Sons, Chichester, pp 385–522

24. Lamberti C, van Bokhoven JA (2016) X-Ray absorption and emission spectroscopy for catalysis. In: van Bokhoven JA, Lamberti C (eds) X-ray absorption and X-ray emission spectroscopy: theory and applications. John Wiley & Sons, Chichester, pp 353–383
25. Kwak JH, Tonkyn RG, Kim DH et al (2010) Excellent activity and selectivity of Cu-SSZ-13 in the selective catalytic reduction of NO_x with NH_3. J Catal 275:187–190
26. Kwak JH, Tran D, Burton SD et al (2012) Effects of hydrothermal aging on NH_3-SCR reaction over Cu/zeolites. J Catal 287:203–209
27. Kwak JH, Lee JH, Burton SD et al (2013) A common intermediate for N_2 formation in enzymes and zeolites: side-On Cu–nitrosyl complexes. Angew Chem Int Ed 52:9985–9989
28. Paolucci C, Verma AA, Bates SA et al (2014) Isolation of the copper redox steps in the standard selective catalytic reduction on Cu-SSZ-13. Angew Chem-Int Edit 53:11828–11833
29. Günter T, Carvalho HWP, Doronkin DE et al (2015) Structural snapshots of the SCR reaction mechanism on Cu-SSZ-13. Chem Commun 51:9227–9230
30. Janssens TVW, Falsig H, Lundegaard LF et al (2015) A consistent reaction scheme for the selective catalytic reduction of nitrogen oxides with ammonia. ACS Catal 5:2832–2845
31. Iwamoto M, Yahiro H, Tanda K et al (1991) Removal of nitrogen monoxide through a novel catalytic process.1. Decomposition on excessively copper-ion exchanged ZSM-5 zeolites. J Phys Chem 95:3727–3730
32. Ahlquist M, Nielsen RJ, Periana RA et al (2009) Product protection, the Key to developing high performance methane selective oxidation catalysts. J Am Chem Soc 131:17110–17115
33. Davies P, Snopwdon FF (1967) Production of oxygenated hydrocarbons. US Patent 3,326,956 1667
34. Klier K (1982) Methanol synthesis. Adv Catal 31:243–313
35. Iwamoto M, Yahiro H, Torikai Y et al (1990) Novel preparation method of highly copper ion-exchanged ZSM-5 zeolites and their catalytic activities for NO decomposition. Chem Lett 19:1967–1970
36. Iwamoto M, Yahiro H, Mizuno N et al (1992) Removal of nitrogen monoxide through a novel catalytic process.2. Infrared study on surface-reaction of nitrogen monoxide adsorbed on copper ion-exchanged ZSM-5 zeolites. J Phys Chem 96:9360–9366
37. Li YJ, Hall WK (1990) Stoichiometric catalytic decomposition of nitric-oxide over Cu-ZSM-5 catalysts. J Phys Chem 94:6145–6148
38. Li YJ, Hall WK (1991) Catalytic decomposition of nitric-oxide over Cu-Zeolites. J Catal 129:202–215
39. Shelef M (1995) Selective catalytic reduction of NO_x with N-free reductants. Chem Rev 95:209–225
40. Li JH, Chang HZ, Ma L et al (2011) Low-temperature selective catalytic reduction of NO_x with NH_3 over metal oxide and zeolite catalysts-a review. Catal Today 175:147–156
41. Kuroda Y, Kotani A, Maeda H et al (1992) The state of excessively ion-exchanged copper in mordenite - formation of tetragonal hydroxy-bridged copper-Ion. J Chem Soc Faraday Trans 88:1583–1590
42. Grünert W, Hayes NW, Joyner RW et al (1994) Structure, chemistry, and activity of Cu-ZSM-5 catalysts for the selective reduction of NO_x in the presence of oxygen. J Phys Chem 98:10832–10846
43. Lamberti C, Bordiga S, Salvalaggio M et al (1997) XAFS, IR, and UV–vis study of the Cu^I environment in Cu^I-ZSM-5. J Phys Chem B 101:344–360
44. Lamberti C, Spoto G, Scarano D et al (1997) Cu^I-Y and Cu^{II}-Y zeolites: A XANES, EXAFS and visible-NIR study. Chem Phys Lett 269:500–508
45. Lamberti C, Bordiga S, Zecchina A et al (1998) XANES, EXAFS and FTIR characterization of copper-exchanged mordenite. J Chem Soc Faraday Trans 94:1519–1525
46. Lamberti C, Palomino GT, Bordiga S et al (2000) Structure of homoleptic $Cu^I(CO)_3$ cations in Cu^I-exchanged ZSM-5 zeolite: an X-ray absorption study. Angew Chem Int Edit 39:2138–2141

47. Turnes Palomino G, Fisicaro P, Bordiga S et al (2000) Oxidation states of copper ions in ZSM-5 zeolites. A multitechnique investigation. J Phys Chem B 104:4064–4073
48. Turnes Palomino G, Bordiga S, Zecchina A et al (2000) XRD, XAS, and IR characterization of copper-exchanged Y zeolite. J Phys Chem B 104:8641–8651
49. Prestipino C, Berlier G, Llabrés i Xamena FX et al (2002) An in situ temperature dependent IR, EPR and high resolution XANES study on the NO/Cu^{+}-ZSM-5 interaction. Chem Phys Lett 363:389–396
50. Giordanino F, Vennestrom PNR, Lundegaard LF et al (2013) Characterization of Cu-exchanged SSZ-13: a comparative FTIR, UV–vis, and EPR study with Cu-ZSM-5 and Cu-β with similar Si/Al and Cu/Al ratios. Dalton Trans 42:12741–12761
51. Fickel DW, Fedeyko JM, Lobo RF (2010) Copper coordination in Cu-SSZ-13 and Cu-SSZ-16 investigated by variable-temperature XRD. J Phys Chem C 114:1633–1640
52. Beale AM, Gao F, Lezcano-Gonzalez I et al (2015) Recent advances in automotive catalysis for NOx emission control by small-pore microporous materials. Chem Soc Rev 44:7371–7405
53. van Bohkoven JA, Lamberti C (2016) X-ray absorption and emission spectroscopy for catalysis. In: van Bokhoven JA, Lamberti C (eds) X-ray absorption and X-ray emission spectroscopy: theory and applications. John Wiley & Sons, New York, pp 354–383
54. Singh J, Lamberti C, van Bokhoven JA (2010) Advanced X-ray absorption and emission spectroscopy: in situ catalytic studies. Chem Soc Rev 39:4754–4766
55. McEwen JS, Anggara T, Schneider WF et al (2012) Integrated operando X-ray absorption and DFT characterization of Cu-SSZ-13 exchange sites during the selective catalytic reduction of NOx with NH_3. Catal Today 184:129–144
56. Bates SA, Verma AA, Paolucci C et al (2014) Identification of the active Cu site in standard selective catalytic reduction with ammonia on Cu-SSZ-13. J Catal 312:87–97
57. Doronkin DE, Casapu M, Gunter T et al (2014) Operando spatially- and time-resolved XAS study on zeolite catalysts for selective catalytic reduction of NO_x by NH_3. J Phys Chem C 118:10204–10212
58. Giordanino F, Borfecchia E, Lomachenko KA et al (2014) Interaction of NH_3 with Cu-SSZ-13 Catalyst: A Complementary FTIR, XANES, and XES Study. J Phys Chem Lett 5:1552–1559
59. Borfecchia E, Lomachenko KA, Giordanino F et al (2015) Revisiting the nature of Cu-sites in activated Cu-SSZ-13 catalyst for SCR reaction. Chem Sci 6:548–563
60. Pluth JJ, Smith JV, Mortier WJ (1977) Positions of cations and molecules in zeolites with the chabazite framework. IV Hydrated and dehydrated Cu^{2+}-exchanged chabazite. Mat Res Bull 12:1001–1007
61. Korhonen ST, Fickel DW, Lobo RF et al (2011) Isolated Cu^{2+} ions: active sites for selective catalytic reduction of NO. Chem Commun 47:800–802
62. Pierloot K, Delabie A, Groothaert MH et al (2001) A reinterpretation of the EPR spectra of Cu (II) in zeolites A, Y and ZK4, based on ab initio cluster model calculations. Phys Chem Chem Phys 3:2174–2183
63. Deka U, Juhin A, Eilertsen EA et al (2012) Confirmation of isolated Cu^{2+} Ions in SSZ-13 zeolite as active sites in NH_3-selective catalytic reduction. J Phys Chem C 116:4809–4818
64. Kwak JH, Varga T, Peden CHF et al (2014) Following the movement of Cu ions in a SSZ-13 zeolite during dehydration, reduction and adsorption: a combined in situ TP-XRD, XANES/DRIFTS study. J Catal 314:83–93
65. Llabrés i Xamena FX, Fisicaro P, Berlier G et al (2003) Thermal reduction of Cu^{2+}-mordenite and Re-oxidation upon interaction with H_2O, O_2, and NO. J Phys Chem B 107:7036–7044
66. Kispersky VF, Kropf AJ, Ribeiro FH et al (2012) Low absorption vitreous carbon reactors for operando XAS: a case study on Cu/Zeolites for selective catalytic reduction of NOx by NH_3. Phys Chem Chem Phys 14:2229–2238
67. Alayon EMC, Nachtegaal M, Ranocchiari M et al (2012) Catalytic conversion of methane to methanol using Cu-zeolites. Chimia 66:668–674
68. Alayon EMC, Nachtegaal M, Bodi A et al (2014) Reaction conditions of methane-to-methanol conversion affect the structure of active copper sites. ACS Catal 4:16–22

69. Wulfers MJ, Teketel S, Ipek B et al (2015) Conversion of methane to methanol on copper-containing small-pore zeolites and zeotypes. Chem Commun 51:4447–4450
70. Periana RA, Taube DJ, Gamble S et al (1998) Platinum catalysts for the high-yield oxidation of methane to a methanol derivative. Science 280:560–564
71. Rosenzweig AC, Frederick CA, Lippard SJ et al (1993) Crystal-structure of a bacterial nonheme iron hydroxylase that catalyzes the biological oxidation of methane. Nature 366:537–543
72. Sazinsky MH, Lippard SJ (2015) Methane monooxygenase: functionalizing methane at iron and copper. In: Kroneck PMH, Sosa Torres MA (eds) Sustaining life on planet earth: metalloenzymes mastering dioxygen and other chewy gases. Metal Ions in Life Sciences, Springer, Berlin, pp 205–256
73. Woertink JS, Smeets PJ, Groothaert MH et al (2009) A $[Cu_2O]^{2+}$ core in Cu-ZSM-5, the active site in the oxidation of methane to methanol. Proc Natl Acad Sci U S A 106:18908–18913
74. Yamaguchi A, Shido T, Inada Y et al (2000) Time-resolved DXAFS study on the reduction processes of Cu cations in ZSM-5. Catal Lett 68:139–145
75. Yamaguchi A, Inada Y, Shido T et al (2001) Time-resolved energy-dispersive XAFS study on the reduction process of Cu-ZSM-5 catalysts. J Synchrot Radiat 8:654–656
76. Yamaguchi A, Shido T, Inada Y et al (2001) In situ time-resolved energy-dispersive XAFS study on the reduction processes of Cu-ZSM-5 catalysts. Bull Chem Soc Jpn 74:801–808
77. Groothaert MH, van Bokhoven JA, Battiston AA et al (2003) Bis(μ-oxo)dicopper in Cu-ZSM-5 and its role in the decomposition of NO: a combined in situ XAFS, UV–vis-Near-IR, and kinetic study. J Am Chem Soc 125:7629–7640
78. Alayon EMC, Nachtegaal M, Bodi A et al (2015) Bis(μ-oxo) versus mono(μ-oxo)dicopper cores in a zeolite for converting methane to methanol: an in situ XAS and DFT investigation. Phys Chem Chem Phys 17:7681–7693
79. Grundner S, Markovits MAC, Li G et al (2015) Single-site trinuclear copper oxygen clusters in mordenite for selective conversion of methane to methanol. Nat Commun 6:9
80. Horn R, Schlogl R (2015) Methane activation by heterogeneous catalysis. Catal Lett 145:23–39
81. Drake IJ, Zhang Y, Briggs D et al (2006) The local environment of Cu^+ in $Cu-Y$ zeolite and Its relationship to the synthesis of dimethyl carbonate. J Phys Chem B 110:11654–11664
82. Paolucci C, Parekh AA, Khurana I et al (2016) Catalysis in a cage: condition-dependent speciation and dynamics of exchanged Cu cations in SSZ-13 Zeolites. J Am Chem Soc 138:6028–6048
83. Lomachenko KA, Borfecchia E, Negri C et al (2016) The Cu-CHA deNOx catalyst in action: temperature-dependent NH_3 selective catalytic reduction monitored by operando XAS and XES. J Am Chem Soc 139. doi: 10.1021/jacs.1026b06809
84. Narsimhan K, Iyoki K, Dinh K et al (2016) Catalytic oxidation of methane into methanol over copper-exchanged zeolites with oxygen at low temperature. ACS Central Sci 2:424–429
85. Kulkarni AR, Zhao Z-J, Siahrostami S et al (2016) Mono-copper active site for partial methane oxidation in Cu-exchanged 8MR zeolites. ACS Catal 6. doi:10.1021/acscatal.1026b01895

Chapter 21
Designed Surfaces for Active Catalysts

Satoshi Muratsugu, Mizuki Tada, and Yasuhiro Iwasawa

21.1 Introduction

Chemical design of artificial enzyme catalysts with high activity, selectivity, and molecular recognition has been a long-term challenge in catalytic materials research. Metal complexes with well-defined coordination structures around metal centers may resemble active sites/ensembles of metal enzymes in a sense, where organic and/or inorganic ligands coordinated to a metal center significantly promote and regulate not only reactivity of the metal site electronically but also reaction space around the metal center geometrically. The metal center may constitute a single metal atom or a multimetals cluster. As the result, high activity and sharp selectivity under mild reaction conditions can be achieved with metal-complex catalysts, which may be difficult to obtain on metal particles and metal single crystal surfaces. However, homogeneous metal complexes in solutions tend to gather and decompose during catalytic cycles, resulting in loss of the catalytic

S. Muratsugu
Department of Chemistry, Graduate School of Science, Nagoya University, Nagoya 464-8602, Japan

M. Tada (✉)
Department of Chemistry, Graduate School of Science, Nagoya University, Nagoya 464-8602, Japan

Research Center for Materials Science, Nagoya University, Nagoya, Aichi 464-8602, Japan

Element Visualization Team, Materials Visualization Photon Science Group, RIKEN SPring-8 Center, Hyogo 679-5148, Japan
e-mail: mtada@chem.nagoya-u.ac.jp

Y. Iwasawa
Innovation Research Center for Fuel Cells, Graduate School of Information Engineering Science, The University of Electro-Communications, Chofu, Tokyo 182-8585, Japan
e-mail: iwasawa@pc.uec.ac.jp

Y. Iwasawa et al. (eds.), *XAFS Techniques for Catalysts, Nanomaterials, and Surfaces*, DOI 10.1007/978-3-319-43866-5_21

properties. Hence, the transformation of homogeneous catalysts to a new class of heterogeneous catalysts with active structures and compositions in a molecular level has been accomplished by supporting metal complexes on oxide surfaces [1–10]. The supported metal complexes may be further transformed chemically at the surfaces to provide unique structures and compositions that are different from their homogeneous analogues and often remarkable catalytic properties. Molecular-level characterization of catalyst surfaces thus fabricated is the key issue for evidence of the design of new catalysts, which also leads to further development of new catalytic materials [1–10]. Unfortunately, most of these supported catalysts have no long-range ordered structures and distributed at surfaces or on pore walls of porous supports, which makes molecular-level characterization of their structures and electronic states very difficult. XAFS can provide the molecular-level structural and electronic information on the active metal sites and ensembles of designed catalysts under catalytic reaction conditions [11]. However, it is to be noted that molecular-level characterization of conventional supported metal catalysts, which are generally heterogeneous and complicated, is difficult particularly under catalytic reaction conditions.

The new and distinct materials and chemistry prepared stepwise in a controllable manner by using organometallic and inorganic complexes as precursors provide an opportunity for the development of efficient catalytic molecularly organized surfaces. The key factors of chemical design of supported catalyst surfaces are composition, structure, oxidation state, and spatial distribution, which are associated with in situ XAFS characterization [1–30]. Nevertheless, these issues are still a serious challenge in catalysis and materials research. In this chapter, we attempt to summarize typical examples of chemical design of active structures by supporting metal complexes on oxide surfaces and subsequent structural transformations based on in situ XAFS techniques.

21.2 In Situ XAFS Characterization of Designed Supported Metal Catalysts

21.2.1 Catalytic Ethanol Oxidation on Mo Dimers on SiO_2

With supported molybdenum dimers on SiO_2 and Al_2O_3, Iwasawa et al. have set in place a foundation for chemical design of active catalyst surfaces since 1982, presenting numerous examples with different structures and oxidation states on the basis of XAFS characterization [1–3, 12–14]. These are evidently the first supported metal catalysts having molecularly defined structures. Iwasawa et al. were the first to use in situ XAFS for direct observation of the dynamic structural change of catalytic intermediates on SiO_2 by characterizing the Mo-Mo, Mo = O, and Mo-O bond distances and coordination numbers of the designed Mo dimer sites during the course of the catalytic oxidation of ethanol as shown in

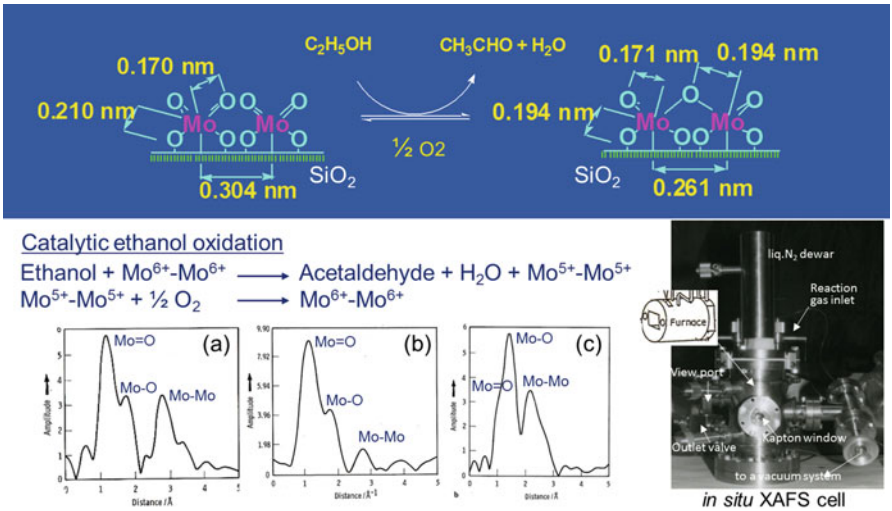

Fig. 21.1 Dynamic structural transformation of Mo dimer site on SiO_2 in catalytic ethanol oxidation characterized by in situ XAFS. Fourier transforms (**a**): Mo^{6+}-Mo^{6+} measured at 80 K, (**b**): ethanol-adsorbed intermediate measured at 200 K, (**c**): Mo^{5+}-Mo^{5+} measured at 298 K [2, 14]

Fig. 21.1 [2, 14]. The catalytic ethanol oxidation proceeds in conjunction with the reversible change of the oxidation states and local structures of Mo dimers on a SiO_2 surface, where the Mo-Mo separation changes largely by 0.04 nm between the Mo^{6+}-Mo^{6+} dimer (monomer pair at 0.304 nm) and the Mo^{5+}-Mo^{5+} dimer bridged with μ-oxygen (0.261 nm), probably involving restructuring of a part of the interface. The Mo-Mo bond in the Mo^{6+} dimer without any bridging oxygen was hard to observe at 423 K (reaction temperature), but it was observed at 0.304 nm at 80 K due to minimizing thermal vibration. The reaction intermediate in the oxidative ethanol dehydrogenation step (first step) was also identified to be a Mo^{6+} dimer with a Mo-Mo bond at 0.292 nm, which was observed by quenching the ethanol reaction at the early stage of the reaction by cooling rapidly from 423 to 200 K (Fig. 21.1). The Mo^{5+}-Mo^{5+} dimer species could be measured in situ under the ethanol reaction conditions at 423 K, but the more accurate EXAFS analysis was conducted at 298 K by cooling the XAFS cell from the reaction temperature (Fig. 21.1). The rate determining step was concluded to be the reoxidation of the Mo^{5+}-Mo^{5+} dimer to the Mo^{6+}-Mo^{6+} in the second step in Fig. 21.1 [2, 14].

21.2.2 Nb Monomer, Dimer and Monolayer on SiO_2

XAFS was used to present a new concept for acid–base reactivity control by molecular design of novel Nb monomers, dimers, and monolayers on SiO_2 surfaces [3]. The SiO_2-supported Nb monomer catalyst $\{SiO\}_2Nb(=O)_2$ was prepared by

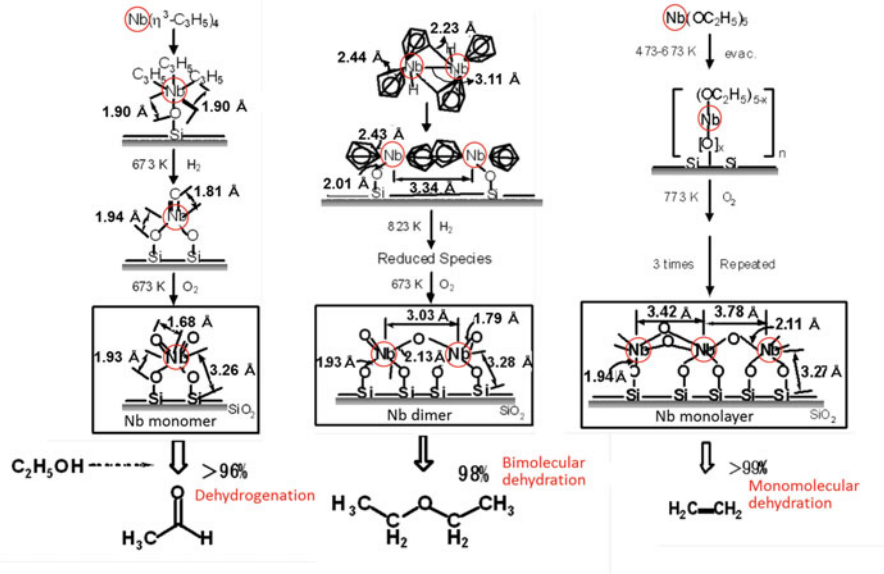

Fig. 21.2 Chemical design of Nb monomer, Nb dimer, and Nb monolayer structures at SiO_2 surfaces by using mononuclear Nb complex, dinuclear Nb complex, and Nb ethoxide as precursors, followed by chemical treatments [3, 4]

supporting $Nb(\eta^3\text{-}C_3H_5)_4$ on SiO_2, followed by chemical treatments with H_2 and O_2 as shown in Fig. 21.2. The Nb monomer catalyst exhibited high activity and selectivity (>96 %) for the dehydrogenation of ethanol to acetaldehyde and H_2 at 423–523 K. The supporting and transformation processes were characterized by XAFS. The XANES and EXAFS analysis evidenced the tetrahedral Nb-dioxo monomer structure (Nb = O: 1.68 Å) that was chemically bound to the SiO_2 surface via Nb-O-Si bonds in a bidentate form (Nb-O: 1.93 Å; Nb-Si: 3.26 Å in Fig. 21.2; their coordination number: around 2). Adsorbed ethanol on the Nb monomer decomposed to ethane and water under temperature desorption in vacuum, which indicates an acidic character (γ-hydrogen abstraction) of the Nb site. However, in the catalytic reaction in the presence of ambient ethanol (molecular adsorbed ethanol) the ethanol reaction was switched over to the dehydrogenation of ethanol to acetaldehyde and H_2, which indicates a basic character (β-hydrogen abstraction) of Nb site. It predicts new catalysis involving β-elimination of the CH bond by coordinatively unsaturated tetrahedral Nb monomers chemically attached to the SiO_2 surface [3, 4].

Nb dimers on SiO_2 were prepared by using Nb dimer complex $Nb_2(H)_2(C_5H_5)_2(C_5H_4)_2$ as precursor, which was interacted with SiO_2 surface, followed by chemical treatments with H_2 and O_2 to form the Nb-oxo dimer structure on the SiO_2 surface as shown in Fig. 21.2 [3]. The Nb-Nb separation was decided to be 3.11 Å for the Nb dimer precursor with hydride ligands, 3.34 Å for the supported Nb dimer without hydride ligands but instead bonded to surface

oxygen in a monodentate form (Nb-O: 2.01 Å), and 3.03 Å for the supported oxygen-bridging Nb-oxo dimer (Nb = O: 1.79 Å) chemically bound to surface oxygen atoms in a bidentate form (Nb-O: 1.93 Å; Nb-Si: 3.28 Å; their coordination number (CN): around 2). The local structure around Nb sites is similar to that for the supported Nb monomer, where the Nb dimer catalyst promoted the bimolecular dehydration of ethanol to diethyl ether selectively (98 %), indicating an acidic character of the Nb sites. The acidic catalysis was generated by the Nb monolayer catalyst, which was prepared by using $Nb(OC_2H_5)_5$ precursor as shown in Fig. 21.2. The obtained Nb monolayer structure on SiO_2 was characterized by XAFS, which revealed the absence of Nb = O double bond and only Nb-O single bonds were observed. The Nb monolayer was attached to the SiO_2 surface in a bidentate form (Nb-O: 1.94 Å; Nb-Si: 3.27 Å; their CN: around 2). The Nb monolayer catalyst promoted the monomolecular dehydration of ethanol to ethylene selectively (>99 %). Thus, it is obvious that the XAFS technique is a powerful tool for deeper understanding not only catalyst fabrication processes but also catalysis mechanisms in the molecular level [3, 11].

21.2.3 Metal-Coordination Assisted Hydroformylation Catalysis of a Supported Rh-dimer Catalyst

A fascinating mechanism for the ethylene (ethene) hydroformylation catalyzed by a rhodium dimer/SiO_2 catalyst, which is much more selective (88.9 % selectivity) than a conventional SiO_2-supported Rh-particle catalyst (5.6 % selectivity) under a reduced pressure at 413 K, was suggested by the detailed EXAFS analysis as illustrated in Fig. 21.3 [16, 17]. The Rh-Rh-COC_2H_5 acyl intermediate species for the ethene hydroformylation was employed as a catalyst by exposing a mixture of ethane, CO, and H_2 at 423 K. The Rh-Rh bond at 2.70 Å was cleaved by adsorption of *germ* CO ligands, forming propanal (C_2H_5CHO) hydroformylation product. The Rh-germinal CO species without direct Rh-Rh bonding was transformed back to the Rh-acyl species with Rh-Rh bond at 2.70 Å. In case of homogeneous Rh monomer complexes, CO can insert to Rh-C_2H_5 bond to form the Rh-acyl under high CO pressure or in the presence of excess PPh_3, in which CO or PPh_3 coordinates to the Rh center to assist the CO insertion as shown in Fig. 21.3 (inserted scheme). In contrast to the Rh monomer catalysis, the CO insertion proceeded by assist of rebonding of the two adjacent Rh atoms without any additional ligand at reduced pressures. It was demonstrated that the catalytic hydroformylation reaction proceeds in conjunction with a cycle of cleavage reformation of the Rh-Rh bond as proved by in situ EXAFS [16, 17].

Hydroformylation reaction of alkenes is known to proceed on mono-metal sites like mononuclear metal complexes in homogeneous systems. However, mono-metal sites are generally disadvantageous because of necessity to eliminate a part of intimate ligands to form an unsaturated site on the metal atom. On the other hand,

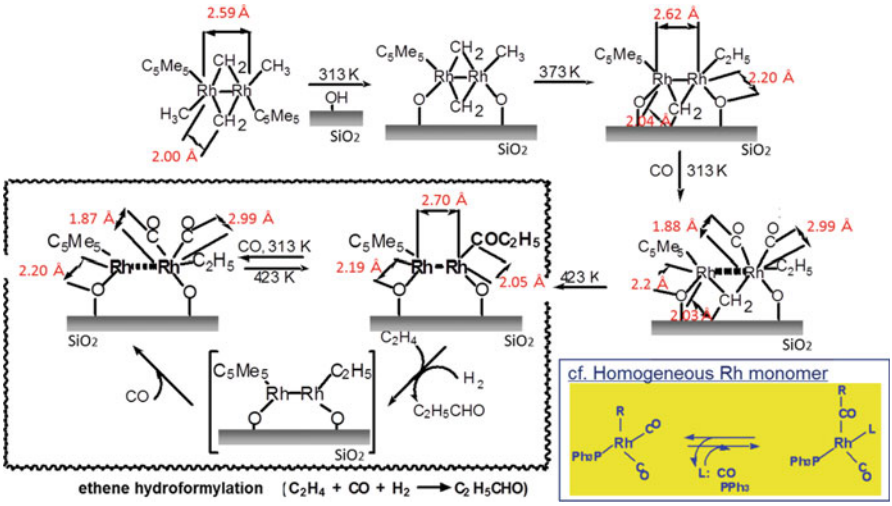

Fig. 21.3 Metal-assisted ethane hydroformylation on a designed Rh dimer/SiO_2 [16, 17]

on the attached Rh dimer, it is not necessary to dissociate any ligands during the catalytic cycle, and hence the Rh dimer acts as an effective catalytic site on SiO_2. Chemistry of the Rh dimer on the surface is different from chemistry of the homogeneous Rh monomer in a homogeneous system. The catalytic ethene hydroformylation on the Rh dimer/SiO_2 is referred to metal-coordination assisted catalysis by the two adjacent Rh atoms [6, 28].

21.2.4 Molecular Imprinting Rh-dimer Catalysts at a SiO_2 Surface

To synthesize artificial enzymatic systems with high activity, selectivity, and molecular recognition, molecular imprinting methods that can create template-shape cavities with memory of the template molecules in organic and inorganic polymer matrices have been developed thus far [5, 6, 20, 21, 28]. Artificial enzymatic materials synthesized by molecular imprinting techniques using a variety of template molecules provide promising molecular recognition catalysis for a variety of catalytic reactions where natural enzymes cannot be employed [6, 28].

Metal-complex imprinting constitutes a state of the arts currently, where ligands of the complexes are used as template molecules, which aims to create cavity near the metal site. Molecular imprinting of metal complexes enables realizing several features to note, (1) attachment of metal complex on robust supports, (2) surrounding of the metal complex by polymer matrix, and (3) production of shape selective cavity on the metal site. Metal complexes thus imprinted have been applied to molecular recognition, reactive complex stabilization, ligand exchange reaction,

and catalysis [6, 20, 21, 28]. Most of the imprinted metal-complex catalysts have been prepared by imprinting in a bulk polymer. However, active sites prepared by bulk imprinting may often be located inside the bulk polymer matrices, where access of substrate molecules to the sites is difficult. Further, such organic polymers tend to be not durable in organic solvents or under severe catalytic conditions such as in the presence of oxidants, at high temperatures, etc. However, oxide-supported metal complexes often exhibit unique property and remarkable reactivity so that molecular imprinting of metal complexes at oxide surfaces has many possibilities to produce new excellent catalysts similar to enzymatic systems. Tada et al. succeeded in preparing imprinted rhodium-dimer complexes at Ox.50 (SiO_2) surface for catalytic shape-selective hydrogenation of simple alkenes without any functional group [28]. Recognition of simple alkenes without any functional group is generally difficult.

Since a template with the same shape as the transition state of a rate-determining step is most appropriate for catalyst design, but it is hard to estimate its accurate structure. Reaction intermediates before and after the rate-determining step may be considered to have similar shapes to the early and late transition states, respectively, and those reaction intermediates can be used as templates for molecular imprinting catalysts. Tada et al. used a ligand of metal complexes as template at a SiO_2 surface for the first time, choosing a ligand of the supported metal complex with the similar shape to a reaction intermediate of alkene hydrogenation as a template molecule as shown in Fig. 21.4. $P(OCH_3)_3$ ligand has a similar shape to one of the half-hydrogenated species of 3-ethyl-2-pentene, which can produce the intermediate-shape cavity by removal of the ligand. An active and selective imprinted Rh dimer catalyst was designed by the following strategy for regulation, (1) conformation of ligands coordinated to Rh atom, (2) orientation of vacant site on Rh, (3) cavity with the template molecular shape for reaction space produced behind template removal, (4) architecture of the cavity wall, and (5) micropore in inorganic polymer-matrix overlayers stabilizing the active species at the surface. In the shape-selective hydrogenation of alkenes with H_2 on the imprinted Rh dimer catalyst, the alkenes in the template cavity coordinate to a Rh atom, and the two adjacent Rh atoms cooperate to dissociate H_2 to form a hydride on each Rh atom, and then the coordinated alkene and hydride react to form a half-hydrogenated (alkyl) intermediate in the template cavity.

The preparation steps in Fig. 21.4 were characterized by EXAFS [20, 21]. In order to create a Rh dimer structure with a template cavity on a SiO_2 (Ox.50) surface, a $Rh_2Cl_2(CO)_4$ and $P(OCH_3)_3$ were used as a Rh dimer precursor and a template ligand, respectively. The template $P(OCH_3)_3$ is regarded as an analogue to a half-hydrogenated alkyl intermediate of hydrogenation of 3-ethyl-2-pentene. $Rh_2Cl_2(CO)_4$ was attached on the Ox.50 surface retaining its dimer structure monitored by FT-IR. By exposing to $P(OCH_3)_3$, the surface-attached Rh carbonyl dimer was converted to Rh monomer pair with two $P(OCH_3)_3$ ligands on Rh accompanied with Rh-Rh bond breaking (Rh-P: 2.24 Å (CN: 2.3); no Rh-Rh bond by EXAFS), which was attached on the surface via Rh-O bond at 2.03 Å in

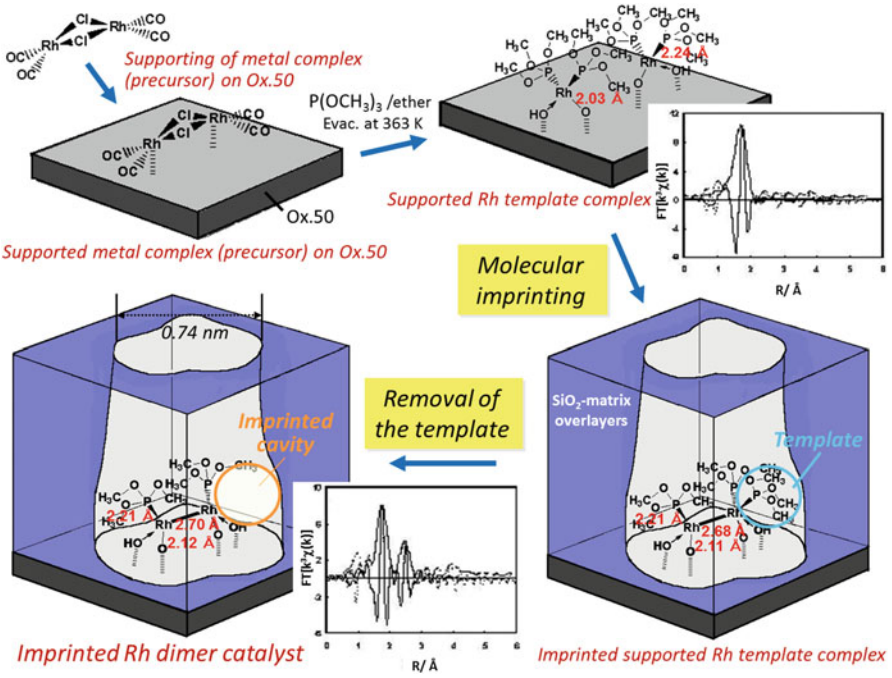

Fig. 21.4 Design of an imprinted Rh dimer catalyst with a template cavity on SiO_2 [20, 21]

a bidentate form (Fig. 21.4). After the $P(OCH_3)_3$ coordination the supported Rh template complexes were covered by SiO_2 matrix overlayers by a hydrolysis-polymerization of $Si(OCH_3)_4$. Then, a template was removed by evacuation at 363 K to produce the imprinted Rh dimer catalyst. By the imprinting procedure, Rh 3d XPS intensity reduced remarkably, indicating that the Rh species were embedded in the polymerized silica matrix overlayers that were characterized by ^{29}Si solid-state MAS NMR.

The structures around Rh atoms in the imprinted Rh dimer catalyst were also investigated by EXAFS. Note that the surface imprinting caused redimerization of the Rh-monomer pair to produce the imprinted Rh template dimer with a direct Rh-Rh bond at 2.68 Å (CN: 1.3) at the surface. The removal of the template ligand left the template cavity on a Rh atom in the pore of 7.4 Å dimension in the SiO_2-matrix overlayers to form the imprinted Rh dimer catalyst with a Rh-Rh bond at 2.70 Å (CN: 1.2), Rh-P bonds at 2.21 Å (CN: 1.1), and Rh-O (surface) bonds at 2.12 Å (CN: 2.2). The EXAFS analysis indicated the removal of a phosphite ligand per Rh by the molecular imprinting procedure, where the CN of the Rh-P bond reduced from 2.3 to 1.1. This change in the Rh structures in the imprinting processes was also explained by DFT calculation [20, 21]. It is to be noted that during the transformation of the imprinted supported Rh template complex to the

imprinted Rh dimer catalyst there was a stable structure of $Rh_2(P(OCH_3)_3)_3$ with one phosphite ligand on a Rh atom and with two phosphite ligands on another Rh atom as shown in Fig. 21.4.

21.2.5 *Designed Al_2O_3-Supported Ir Dimers for Surface-Assisted Transfer Hydrogenation*

An oxide-supported Ir dimer catalyst was prepared on an Al_2O_3 surface from an Ir dimer complex $[Ir_2\{\eta^5\text{-}C_5(CH_3)_5\}_2(\mu\text{-}CH_2)_2]$ (Ir_2) with an Ir = Ir bond. The obtained surface Ir dimer was found to be active for transfer hydrogenation of aromatic ketones. In situ Ir L_{III}-edge XAFS analysis revealed a structural transformation at the interface of the Ir dimer and the Al_2O_3 surface, which assists the transfer hydrogenation catalysis via the formation of an Ir_2–hydride species on the Al_2O_3 surface as a key intermediate in the transfer hydrogenation as shown in Fig. 21.5 [31].

When the Ir_2 complex with an Ir-Ir bond at 2.438 Å was interacted with the γ-Al_2O_3 surface, one of the two μ-CH_2 ligands reacted with the two surface Al-OH groups to release CH_4, while two $C_5(CH_3)_5$ ligands remained on the Ir_2/Al_2O_3. The EXAFS analysis of the supported Ir_2/Al_2O_3 revealed Ir-Ir bonds at 2.69 Å with CN (Ir-Ir) of 1.2 ($\pm$0.2), indicating the retention of the Ir_2 dimer unit, and Ir--Al bonds at 3.19 Å with CN(Ir--Al) of 1.9 ($\pm$0.2), suggesting chemical attachment of the Ir_2 dimer to the Al_2O_3 surface through two Al–O bonds per Ir. The corresponding Ir-O/C bonds were observed at 2.12 Å, but its CN was 3.2 ($\pm$0.2), which implies that the CN(Ir-O/C) constitutes two Ir-O(Al) bonds and one Ir-CH_2. As a consequence, it is concluded that the Ir_2 dimer was chemically bound to the Al_2O_3 surface forming the bridged dimeric structure (Ir–$(OAl)_2$–Ir) as shown in Fig. 21.5. DFT calculation was performed to model a plausible structure of Ir dimer on the γ-Al_2O_3 surface. The experimentally obtained structural parameters were used to model a supported Ir_2 dimer on a small AlOx cluster ($Al_{13}O_{34}H_{37}$) by DFT calculations. From the DFT calculations the singlet state of the bridged-attaching structure [Ir–$(OAl)_2$–Ir] (Ir_2/γ-Al_2O_3-DFT in Fig. 21.5) was obtained as a plausible structure for Ir_2/Al_2O_3 (Fig. 21.5) [31].

When the Ir_2/Al_2O_3 was exposed to isopropanol, the quantitative amount of acetone was produced, leaving the Ir_2 hydride species (Ir_2–H_2/Al_2O_3). When the obtained Ir_2–H_2/Al_2O_3 was reacted with an excess of acetophenone in toluene in the absence of i-PrOH at 343 K, the 0.9 equivalent amount of 1-phenylethanol to the Ir_2-H_2 quantity was produced in the solution by GC, suggesting that the Ir_2-H_2 structure contributes to the hydrogen transfer as an intermediate for the hydrogen transfer catalysis. Ir L_{III}-edge EXAFS for the Ir_2–H_2/Al_2O_3 revealed an Ir_2 dimeric structure involving an Ir–Ir bond at 2.67 Å (CN = 0.9 $\pm$ 0.1). It is to be noted that the CN(Ir--Al) dropped from 1.9 ($\pm$0.2) at 3.19 Å to 1.2 ($\pm$0.2) at 3.21 Å and the CN(Ir–O/C) also reduced from 3.2 ($\pm$0.2) to 2.3 ($\pm$0.2), which indicates that the

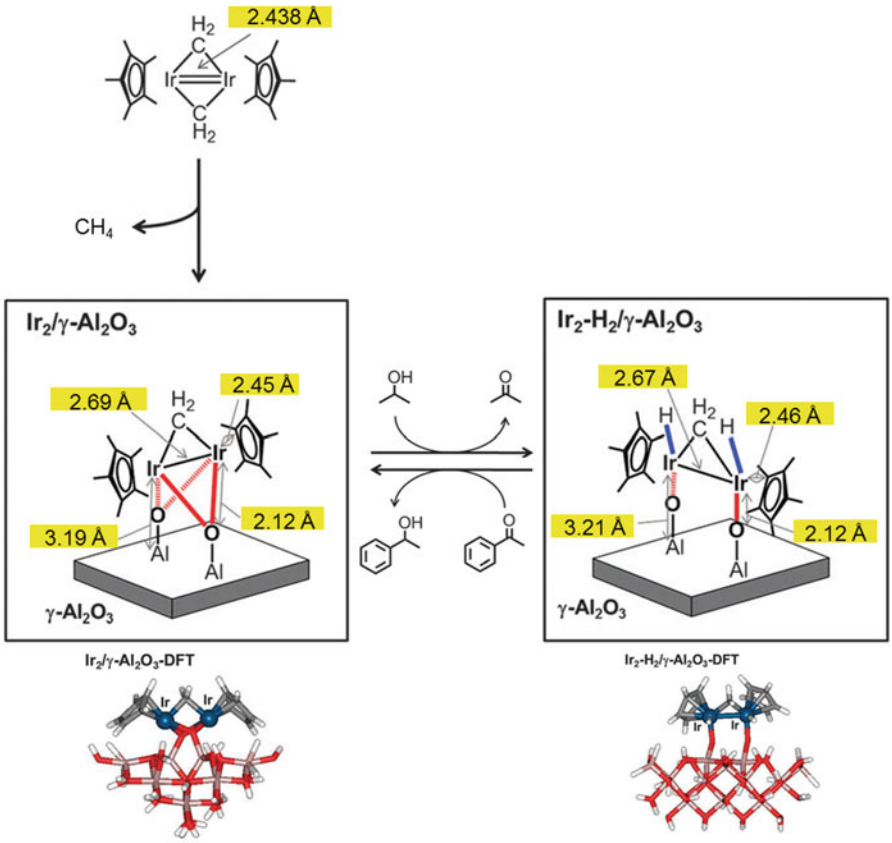

Fig. 21.5 Preparation and surface structure of the γ-Al_2O_3-supported Ir dimer (Ir_2/Al_2O_3) and Ir_2-hydride structure (Ir_2-H_2/Al_2O_3) produced by the transfer hydrogenation of acetophenone, determined by XAFS and DFT [31]

CN of Ir–O(Al) reduced from 2 to 1 under the consideration of the Ir–CH_2 contribution (CN = 1). These results suggest that the Ir–$(OAl)_2$–Ir interaction in the Ir_2/Al_2O_3 became a monodentate interaction with an Ir–O(Al) bond on each Ir atom in the Ir_2–H_2/Al_2O_3 (Fig. 21.5). The direction of the Ir-Ir bond in the Ir_2-H_2/Al_2O_3 is perpendicular to the Ir-Ir bond direction in the Ir_2/Al_2O_3. The structure of Ir_2–H_2/γ-Al_2O_3 was modeled by DFT calculations on the small $Al_{13}O_{34}H_{37}$ cluster using the experimentally determined structural parameters. The singlet state of the Ir-dimer structure with an Ir-Ir bond, two Ir-H bonds, and two Ir–O(Al) bonds was obtained as a plausible structure as shown in Fig. 21.5 [31].

While the catalytic transfer hydrogenation from isopropanol to acetophenone at 343 K slowly proceeded on the homogeneous Ir-dimer precursor (Ir_2), the Ir_2/Al_2O_3 catalyst promoted the catalytic transfer hydrogenation much more than the homogeneous catalyst. It was proposed that the interfacial bond rearrangement in

the Ir_2/Al_2O_3 assisted the formation of $Ir_2–H_2/Al_2O_3$, where the catalytic hydrogen transfer reaction may proceed in conjunction with the dynamic structure transformation with the 90° rotation of the Ir-Ir bond direction.

21.2.6 Single-Site Zeolite-Supported Ir Carbonyl Complexes

A family of HY zeolite-supported cationic organoiridium carbonyl complexes was formed by reaction of Ir-$(CO)_2$(acac) to form supported $Ir(CO)_2$ complexes, which were treated at 298 K and 1 atm with flowing gas-phase reactants, including C_2H_4, H_2, CO, and D_2O. Mass spectrometry was used to identify effluent gases, and FT-IR and XAFS were used to characterize the supported species, with the results bolstered by DFT calculations [32]. The supported species include $Ir(CO)_2$, $Ir(CO)(C_2H_4)_2$, $Ir(CO)(C_2H_4)$, $Ir(CO)(C_2H_5)$, etc. EXAFS spectra at Ir L_{III}-edge demonstrated that each Ir atom was bonded, on average, to two support oxygen atoms; thus, the support acted as a bidentate ligand. When the zeolite-supported Ir dicarbonyl was exposed to flowing ethylene at 298 K, changes in the EXAFS spectra were observed. The EXAFS data show that the Ir-C_{CO} and Ir-O_{CO} coordination numbers decreased from nearly 2 to nearly 1, indicating the removal of one of the two initially present CO ligands of the Ir complex. At the same time, the coordination number of the EXAFS contribution characterizing the sum of Ir-$O_{zeolite}$ + Ir-$C_{ethylene}$ contributions increased from nearly 2 to nearly 4.5. These data indicate replacement of carbonyl ligands by ethylene, and the noninteger value of the combined Ir-$O_{zeolite}$ + Ir-$C_{ethylene}$ contribution indicates a mixture of species, consistent with the IR spectra pointing to both $Ir(CO)(C_2H_4)$ and $Ir(CO)(C_2H_4)_2$ species [32].

21.2.7 Single-Site d^0-Zr Heterogeneous Arene Hydrogenation Catalysts

Structural characterization of the active sites on solid catalyst surfaces is frequently tenuous because their fraction among all sites typically is quite low. This problem has been overcome by supporting appropriate metal complexes on suitable support surfaces followed by chemical treatments in a controlled manner [1–10, 13–18, 20, 21, 27–29, 31, 32]. It was found that the surface Zr complexes produced by supporting $Cp^*Zr(CH_3)_3$ on Brønsted super acidic sulfated alumina (AlS) are exceptionally active for benzene hydrogenation, with ~100 % of the Zr sites catalytically significant as determined by kinetic poisoning experiments [33].

Zr K-edge XAFS data for neat $Cp_2Zr(H)_2$ and $Cp^*Zr(CH_3)_3$/AIS were measured under strictly anhydrous/anaerobic conditions, but attempts to fit the $Cp^*Zr(CH_3)_3$/AlS EXAFS spectrum with models involving four scattering shells,

Zr–C(Cp*), Zr–CH_3(Cp*), Zr–CH_3, and Zr–O, were complicated by the overlap of the scatterers arising from the insignificant differences in both bond distances and phase shift and amplitude functions. Hence, the EXAFS spectra were analyzed by fitting the difference spectra of the Zr complexes before and after the immobilization on AlS, after exposure to benzene, and after benzene hydrogenation, thus extracting the structural changes while eliminating invariant contributions [33]. In this way, the $Cp_2Zr(H)_2$ spectrum was used to isolate the scattering contributions of the Cp_2Zr fragment. The spectrum of $Cp_2Zr(H)_2$ and the curve-fitting are shown in Fig. 21.6a. The decided coordination number of 10.1 is associated with the two η^5-C_5H_5 ligands, whereas the estimated average Zr–C distance of 2.52 Å

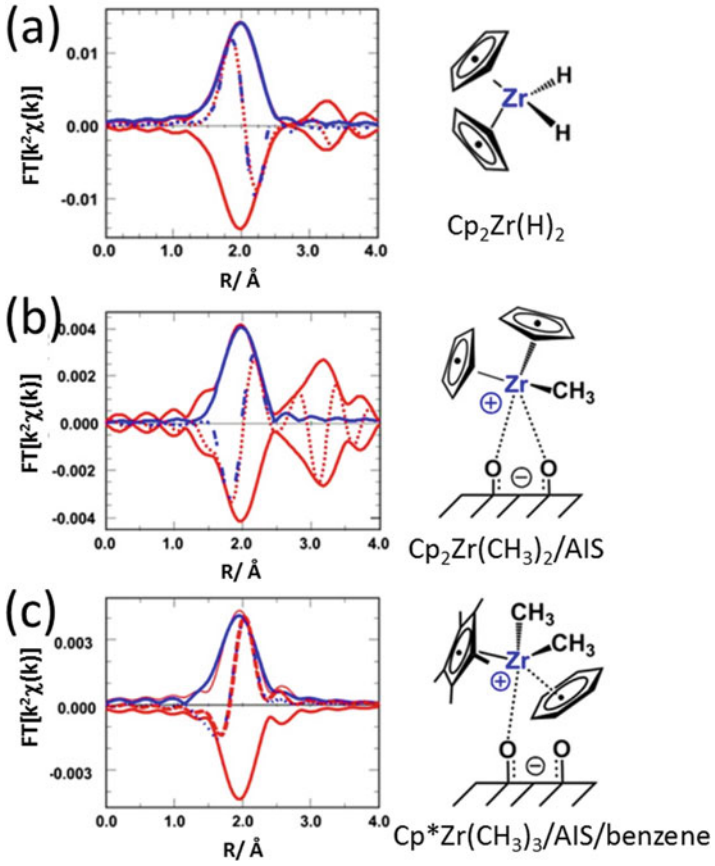

Fig. 21.6 k^2-weighted Fourier transforms (FT) of Zr K-edge EXAFS for Zr complexes. (**a**) $Cp_2Zr(H)_2$ complex. *Red*, $\Delta k = 2.5$–10.0 $Å^{-1}$ data; *blue*, fitting for $\Delta R = 1.4$–2.6 Å; *solid line*, FT magnitude; *dotted line*, FT imaginary part. (**b**) $Cp_2Zr(CH_3)_2$/AIS. *Red*, $\Delta k = 2.5$–10.2 $Å^{-1}$ data; *blue*, fitting for $\Delta R = 1.5$–2.6 Å; *solid line*, FT magnitude; *dotted line*, FT imaginary part. (**c**) $Cp^*Zr(CH_3)_3$/AIS/benzene. *Red*, $\Delta k = 2.7$–10.6 $Å^{-1}$ data; *blue*, fitting for $\Delta R = 1.6$–2.3 Å; *solid line*, FT magnitude; *dotted line*, FT imaginary part [33]

falls within the 2.39–2.58 Å Zr–C(Cp) bond distance range. Curve-fitting of the difference EXAFS spectrum of $Cp_2Zr(CH_3)_2$/AlS (Fig. 21.6b) revealed that the CN of Zr–O bonds in the supported catalyst $Cp_2Zr(CH_3)_2$/AlS was 2.1 at an average Zr–O distance of 2.37 Å, significantly longer than in typical covalent Zr–O bonds,. There are no direct Zr-Zr bonds, which may exclude a dimeric species. These results are in good agreement with the aforementioned DFT models of $Cp_2Zr(CH_3)_2$/AlS (Fig. 6b).

XAFS monitored catalytic reaction species for $Cp^*Zr(CH_3)_3$/AlS exposed to benzene, then to H_2 298 K. Fitting of the $Cp^*Zr(CH_3)_3$/AlS/benzene difference EXAFS spectrum revealed ~ 3.0 additional carbon neighbors around each Zr center at 2.35 Å (Fig. 21.6c). In principle, this coordination might correspond to (1) ~ 50 % of the organozirconium centers are coordinated to benzene in an η^6-coordination fashion or (2) ~ 100 % of the active sites are coordinated to benzene in an η^3 mode. Although η^3 coordination is relatively uncommon for π-complexed arenes, the present results are consistent with the solid-state NMR results and DFT calculations, considering the overlap of four scattering shells (Fig. 21.6c). Following the benzene hydrogenation, curve-fitting of the ($Cp^*Zr(CH_3)_3$/AlS/benzene + H_2)—$Cp^*Zr(CH_3)_3$/AlS/benzene) EXAFS difference spectrum revealed that about 50 % of the Zr sites retain a coordinated benzene molecule (CN = 1.6; Zr–C(benzene) = 2.36 Å), in good agreement with the aforementioned ^{13}C-CP MAS NMR results and kinetic data showing that benzene irreversibly adsorbed on $Cp^*Zr(CH_3)_3$/AIS, that the established rate law is zero-order to benzene, and that the first H_2 addition is rate-limiting [33]. The long $Zr^+ \cdots OAlS-$ distances indicate loose ion pairing, which finds surprisingly close analogy to homogeneous ion-paired early-transition metal polymerization catalysts, where the nature of the ion pairing strongly modulates the barrier to olefin activation and enchainment. The initial activation of the incoming olefinic molecules by the electrophilic metal center requires geometrical loosening of the ion pairing. It also suggests the intriguing possibility that such electron-deficient surfaces may be the long-sought, ultimate "weakly coordinating" anions [33].

21.2.8 Ethylene Polymerization on Isolated Chromium(III) Silicates

Mononuclear Cr(III) surface sites were synthesized from supporting [Cr(OSi(O*t*Bu)$_3$)$_3$(tetrahydrofurano)$_2$] on silica partially dehydroxylated at 973 K, followed by a thermal treatment under vacuum, and characterized by XAFS together with FT-IR, UV–vis, ESR, and DFT. The grafted sites were highly active for ethylene polymerization to yield polyethylene with a broad molecular weight distribution, similar to that typically obtained from the Phillips catalyst. XANES spectra for grafted species 1, 2, and 3 in Fig. 21.7 possessed nearly identical edge energy, suggesting the retention of the +3 oxidation state throughout the grafting and the

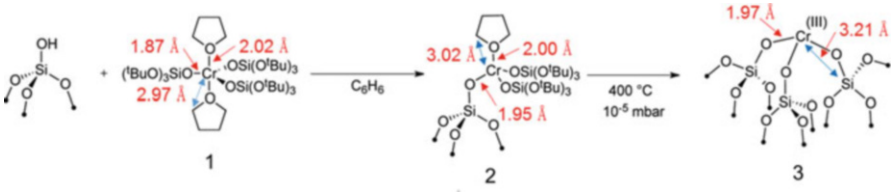

Fig. 21.7 Grafting of $[Cr(OSi(OtBu)_3)_3(THF)_2]$ (1) on 700 °C-treated SiO_2 to form $[(\equiv SiO)Cr(OSi(OtBu)_3)_2(THF)]$ (2) and thermal treatment of 2 to yield $[(\equiv SiO)_3Cr]$ (3) [34]

thermal treatment process. EXAFS data for the species 1, 2, and 3 were analyzed with Cr-O, Cr-C, and Cr-Si bonds, fixing CNs at their assumed CNs. With ~ 1.96 Å, the Cr–O bonds (~1.96 Å) for the three siloxide ligands in the species 2 and 3 are longer than the corresponding Cr–O bonds (1.87 Å) in species 1. It was suggested by poisoning effects with 4-picoline that two different types of Cr(III) sites in the species 3 are present on the surface, one of which is active in polymerization. DFT calculations using cluster models showed that the active species are tricoordinated Cr(III) and the tricoordinated Cr(III) sites initiate and regulate the polymer chain length via unique proton transfer steps in polymerization catalysis [34].

21.3 Prospect

Attaching metal complexes on oxide surfaces provides a new class of catalytic systems with advantages of both heterogeneous and homogeneous catalysts. The catalytic properties of surface site-isolated metal monomers, dimers, clusters, and even monolayers are different from those of metals and metal oxides, and also metal complexes in solution. Combination of the metal-complex attaching with structural transformations, molecular imprinting, etc. on oxide surfaces can design advanced catalytic materials. In situ XAFS characterizations including time-resolved XAFS [22, 23, 26, 30, 35–40] and spatially resolved XAFS [41–46] provide excellent opportunities for fundamental understanding of the origin and mechanism of the tremendous catalysis by the designed surfaces and for more precisely controlled synthesis of catalyst surfaces, which are needed for the higher class of research.

References

1. Iwasawa Y (ed) (1986) Tailored metal catalysts. Reidel, Dordrecht
2. Iwasawa Y (1987) Chemical design surfaces for active solid catalysts. Adv Catal 35:187–264
3. Iwasawa Y (1996) Characterization and chemical design of oxide surfaces. Stud Surf Sci Catal 101:21–34, 11th Int. Congr. Catal., Baltimore

4. Iwasawa Y (1997) Surface catalytic reactions assisted by gas phase molecules. Acc Chem Res 30:103–109
5. Tada M, Iwasawa Y (2006) Advanced catalyst design with supported metal complexes for selective catalysis. Chem Commun 21:2833–2844
6. Tada M, Iwasawa Y (2005) Chemical design and in situ characterization of active surfaces for selective catalysis. Annu Rev Mater Res 35:397–426
7. Psaro R, Recchia S (1998) Supported metals derived from organometallics. Catal Today 41:139–147
8. Gates BC (2000) Models of metal catalysts: beyond single crystals. Topics in Catal 14:173–180
9. Zecchina A, Aréan CO (1993) Structure and reactivity of surface species obtained by interaction of organometallic compounds with oxidic surfaces: IR studies. Catal Rev Sci Eng 35:261–317
10. Basset JM, Lefebvre F, Santini C (1998) Surface organometallic chemistry: some fundamental features including the coordination effects of the support. Coord Chem Rev 178–180:1703–1723
11. Iwasawa Y (ed) (1996) X-ray absorption fine structure for catalysts and surfaces. World Scientific, Singapore
12. Sato Y, Iwasawa Y, Kuroda H (1982) EXAFS study of highly active Mo_2 catalyst. Chem Lett 11:1101–1104
13. Iwasawa Y, Sato Y, Kuroda H (1983) Surface design and characterization of new Al_2O_3-attached Mo-pair catalysts. J Catal 82:289–298
14. Iwasawa Y, Asakura K, Ishii H, Kuroda H (1985) Dynamic behavior of active sites of a SiO_2-attached Mo(VI)-dimer catalyst during ethanol oxidation observed by means of EXAFS. Z Phys Chem N F 144:105–115
15. Asakura K, Iwasawa Y (1989) Extended X-ray absorption fine structure studies on the structure change of the Al_2O_3-attached $[CoII]_4$ catalyst during a CO oxidation reaction. J Phys Chem 93:4213–4218
16. Asakura K, -Bando KK, Iwasawa Y, Arakawa H, Isobe K (1990) Metal-assisted hydroformylation on a SiO_2-attached Rh dimer. In situ EXAFS and FT-IR observations of the dynamic behaviors of the dimer site. J Am Chem Soc 112:9096–9104
17. Asakura K, -Bando KK, Isobe K, Arakawa H, Iwasawa Y (1990) Metal-assisted CO insertion reaction on a new surface rhodium dimer catalyst observed by an in situ extended X-ray absorption fine structure technique. J Am Chem Soc 112:3242–3244
18. Izumi Y, Chihara T, Yamazaki H, Iwasawa Y (1994) CO-breathing structure change and catalysis for oxygenate synthesis from CO/H_2 on supported $[Ru_6C]$ clusters: structural and chemical controls by interstitial carbido carbon. J Phys Chem 98:594–602
19. Yamaguchi A, Suzuki A, Shido T, Inada Y, Asakura K, Nomura M, Iwasawa Y (2002) In situ time-resolved energy-dispersive X-ray absorption fine structure study on the decarbonylation processes of $Mo(CO)_6$ entrapped in NaY and HY zeolites. J Phys Chem B 106:2415–2422
20. Tada M, Sasaki T, Iwasawa Y (2002) Performance and kinetic behavior of a New SiO_2-attached molecular-imprinting Rh-dimer catalyst in size- and shape-selective hydrogenation of alkenes. J Catal 211:496–510
21. Tada M, Sasaki T, Shido T, Iwasawa Y (2002) Design, characterization and performance of a molecular imprinting Rh-dimer hydrogenation catalyst on a SiO_2 surface. Phys Chem Chem Phys 4:5899–5909
22. Iwasawa Y (2003) In situ characterization of supported metal catalysts and model surfaces by time-resolved and three-dimensional XAFS techniques. J Catal 216:165–177
23. Suzuki A, Inada Y, Yamaguchi A, Chihara T, Yuasa M, Nomura M, Iwasawa Y (2003) Time scale and elementary steps of CO-induced disintegration of surface rhodium clusters. Angew Chem Int Ed 42:4795–4799

24. Tada M, Taniike T, Kantam LM, Iwasawa Y (2004) Chiral self-dimerization of vanadium complexes on a SiO_2 surface: the first heterogeneous catalyst for asymmetric 2-naphthol coupling. Chem Commun 22:2542–2543
25. Bal R, Tada M, Sasaki T, Iwasawa Y (2006) Direct phenol synthesis by selective oxidation of benzene with molecular oxygen on an interstitial-N/Re cluster/zeolite catalyst. Angew Chem Int Ed 45:448–452
26. Tada M, Bal R, Sasaki T, Uemura Y, Inada Y, Tanaka S, Nomura M, Iwasawa Y (2007) Novel Re-cluster/HZSM-5 catalyst for highly selective phenol synthesis from benzene and O_2: performance and reaction mechanism. J Phys Chem C 111:10095–10104
27. Tada M, Coquet R, Yoshida J, Kinoshita M, Iwasawa Y (2007) Selective formation of a coordinatively unsaturated metal complex at a surface: a SiO_2-immobilized, three-coordinate ruthenium catalyst for alkene epoxidation. Angew Chem Int Ed 46:7220–7223
28. Tada M, Iwasawa Y (2007) Advanced design of catalytically active reaction space at surfaces for selective catalysis. Coord Chem Rev 251:2702–2716
29. Tada M, Muratsugu S, Kinoshita M, Sasaki T, Iwasawa Y (2010) Alternative selective oxidation pathways for aldehyde oxidation and alkene epoxidation on a SiO_2-supported Ru-monomer complex catalyst. J Am Chem Soc 132:713–724
30. Tada M, Uemura Y, Bal R, Inada Y, Nomura M, Iwasawa Y (2010) In situ time-resolved DXAFS for the determination of kinetics of structural changes of H-ZSM-5-supported active Re-cluster catalyst in the direct phenol synthesis from benzene and O_2. Phys Chem Chem Phys 12:5701–5706
31. Muratsugu S, Weng Z, Nakai H, Isobe K, Kushida Y, Sasaki T, Tada M (2012) Surface-assisted transfer hydrogenation catalysis on a gamma-Al_2O_3-supported Ir dimer. Phys Chem Chem Phys 14:16023–16031
32. -Macias CM, Chen M, Dixon DA, Gates BC (2015) Single-site zeolite-anchored organoiridium carbonyl complexes: characterization of structure and reactivity by spectroscopy and computational chemistry. Chemistry 21:11825–11835
33. Williams LA, Guo N, Motta A, Delferro M, Fragalà IL, Miller JT, Marks TJ (2013) Surface structural-chemical characterization of a single-site d^0 heterogeneous arene hydrogenation catalyst having 100% active sites. Proc Natl Acad Sci 110:413–418
34. Delley MF, -Zarur FN, Conley MP, Vives AC, Siddiqi G, Norsic S, Monteil V, Safonova OV, Copéret C (2014) Proton transfers are key elementary steps in ethylene polymerization on isolated chromium(III) silicates. Proc Natl Acad Sci 111:11624–11629
35. Tada M, Murata S, Asaoka T, Hiroshima K, Okumura K, Tanida H, Uruga T, Nakanishi H, Matsumoto S, Inada Y, Nomura M, Iwasawa Y (2007) In situ time-resolved dynamic surface events on the Pt/C cathode in a fuel cell under operando conditions. Angew Chem Int Ed 46:4310–4315
36. Yamamoto T, Suzuki A, Nagai Y, Tanabe T, Dong F, Inada Y, Nomura M, Tada M, Iwasawa Y (2007) Origin and dynamics of oxygen storage/release in a Pt/ordered CeO_2-ZrO_2 catalyst studied by time-resolved XAFS analysis. Angew Chem Int Ed 46:9253–9256
37. Uemura Y, Inada Y, Bando KK, Sasaki T, Kamiuchi N, Eguchi K, Yagishita A, Nomura M, Tada M, Iwasawa Y (2011) Core-shell phase separation and structural transformation of Pt_3Sn alloy nanoparticles supported on γ-Al_2O_3 in the reduction and oxidation processes characterized by in situ time-resolved XAFS. J Phys Chem C 115:5823–5833
38. Ishiguro N, Saida T, Uruga T, Nagamatsu S, Sekizawa O, Nitta K, Yamamoto T, Ohkoshi S, Iwasawa Y, Yokoyama T, Tada M (2012) Operando time-resolved X-ray absorption fine structure study for surface events on a Pt_3Co/C cathode catalyst in a polymer electrolyte fuel cell during voltage-operating processes. ACS Catal 2:1319–1330
39. Ishiguro N, Saida T, Uruga T, Sekizawa O, Nagasawa K, Nitta K, Yamamoto T, Ohkoshi S, Yokoyama T, Tada M (2013) Structural kinetics of a Pt/C cathode catalyst with practical catalyst loading in an MEA for PEFC operating conditions studied by in situ time-resolved XAFS. Phys Chem Chem Phys 15:18827–18834

40. Ishiguro N, Kityakarn S, Sekizawa O, Uruga T, Sasabe T, Nagasawa K, Yokoyama T, Tada M (2014) Rate enhancements in structural transformations of Pt-Co and Pt-Ni bimetallic cathode catalysts in polymer electrolyte fuel cells studied by in situ time-resolved X-ray absorption fine structure. J Phys Chem C 118:15874–15883
41. Tada M, Ishiguro N, Uruga T, Tanida H, Terada Y, Nagamatsu S, Iwasawa Y, Ohkoshi S (2011) μ-XAFS of a single particle of a practical $NiO_x/Ce_2Zr_2O_y$ catalyst. Phys Chem Chem Phys 13:14910–14913
42. Saida T, Sekizawa O, Ishiguro N, Hoshino M, Uesugi K, Uruga T, Ohkoshi S, Yokoyama T, Tada M (2012) 4D visualization of a cathode catalyst layer in a polymer electrolyte fuel cell by 3D-laminography-XAFS. Angew Chem Int Ed 51:10311–10314
43. Ishiguro N, Uruga T, Sekizawa O, Tsuji T, Suzuki M, Kawamura N, Mizumaki M, Nitta K, Yokoyama T, Tada M (2014) Visualization of the heterogeneity of cerium oxidation states in single $Pt/Ce_2Zr_2O_x$ Catalyst particles by nano-XAFS. ChemPhysChem 15:1563–1568
44. Takao S, Sekizawa O, Nagamatsu S, Kaneko T, Yamamoto T, Samjeské G, Higashi K, Nagasawa K, Tsuji T, Suzuki M, Kawamura N, Mizumaki M, Uruga T, Iwasawa Y (2014) Mapping platinum species in polymer electrolyte fuel cells by spatially resolved XAFS techniques. Angew Chem Int Ed 53:14110–14114
45. Takao S, Sekizawa O, Samjeské G, Nagamatsu S, Kaneko T, Yamamoto T, Higashi K, Nagasawa K, Uruga T, Iwasawa Y (2015) Same-view nano-XAFS/STEM-EDS imagings of Pt chemical species in Pt/C cathode catalyst layers of a polymer electrolyte fuel cell. J Phys Chem Lett 6:2121–2126
46. Tada M, Uruga T, Iwasawa Y (2015) Key factors affecting the performance and durability of cathode electrocatalysts in polymer electrolyte fuel cells characterized by in situ real time and spatially resolved XAFS techniques. Catal Lett 145:58–70

Chapter 22
Fuel Cells by Advanced XAFS Techniques

Mizuki Tada and Yasuhiro Iwasawa

22.1 Introduction

Fuel cell is one of the most efficient clean energy systems and several types of fuel cells have been developed. For example, polymer electrolyte fuel cells (PEFCs) are composed of proton exchange membranes with electrocatalysts and work under mild reaction conditions consuming hydrogen, alcohol etc. as fuels. Pt nanoparticles are widely used as electrocatalysts for both anode and cathode though other transition metals have been studied to apply electrocatalysts for PEFCs. Hydrogen-PEFC is considered to be suitable for automotive applications due to high power density at low temperatures. PEFC vehicle, TOYOTA MIRAI, was commercialized in Dec. 2014 for the first time, and HONDA has also announced to launch CRARITY FCV in March, 2016, and other car companies are also going to produce PEFC automobiles. This is an epoch-making technology, but for widely spread commercialization of PEFC vehicles including cars for business use, further improvements of the performance and durability of cathode electrocatalysts, reducing the cost of PEFC stacking, are indispensable. PEFCs use polymer electrolyte as proton exchange membranes, while solid oxide fuel cells (SOFCs) use ceramics

M. Tada (✉)
Research Center for Materials Science, Nagoya University, Nagoya, Aichi 464-8602, Japan

Department of Chemistry, Graduate School of Science, Nagoya University, Nagoya 464-8602, Japan

Element Visualization Team, Materials Visualization, Photon Science Group, RIKEN SPring-8 Center, Hyogo 679-5148, Japan
e-mail: mtada@chem.nagoya-u.ac.jp

Y. Iwasawa
Innovation Research Center for Fuel Cells, Graduate School of Information Engineering Science, The University of Electro-Communications, Chofu, Tokyo 182-8585, Japan
e-mail: iwasawa@pc.uec.ac.jp

Y. Iwasawa et al. (eds.), *XAFS Techniques for Catalysts, Nanomaterials, and Surfaces*, DOI 10.1007/978-3-319-43866-5_22

with O^{2-} conductivity as solid electrolytes and work at high temperatures (700–1000 °C) with high energy efficiency. In this section, the recent applications of advanced XAFS techniques, such as in situ, time-resolved and 2D/3D spatially resolved (imaging) XAFS techniques, to mainly electrocatalysts in PEFCs are summarized.

22.2 Recent XAFS Applications to Fuel Cell Electrocatalysts

XAFS is a powerful tool to characterize these fuel cell components and various studies have been reported. Recent typical examples of XAFS applications to fuel cell electrocatalysts are listed below with references in brackets. Significant XAFS applications for fuel cells are also described in Chapters 1, Chapter 4.1.1, Chapter 4.2.1, Chapter 4.2.2, and Chapter 4.3.

- In situ Pt L_{III}- and L_{II}-edge and Sn K-edge XAFS analysis of Pt/C and Pt-Sn/C catalysts for methanol oxidation reaction [1]
- XANES and XRD analyses of Pt/C, PtRu/C, and PtMo/C electrocatalysts to enhance CO tolerance [2]
- In situ PEFC cell for XAFS for H_2 and CH_3OH operation [3]
- In situ structural analysis of Pt_3Mo/C catalyst for methanol oxidation [4]
- Local structures of PtRu electrocatalysts and alloy formation [5]
- In situ XAFS analysis of Pt-M (M = Co, Cr, Ni, and Fe) bimetallic electrocatalysts in $HClO_4$ solution at different potentials [6]
- In situ XAFS for methanol electrooxidation process on Pt/C and PtRu/C electrocatalysts at different potentials [7]
- Atomic XAFS analysis for OH and CO coverage estimation on PtRu electrocatalysts in PEFC [8]
- Methanol electrooxidation on Pt/C mixed with organic complexes [9]
- XANES and EXAFS analyses for Pt-Ru nanoparticle formation process [10]
- In situ XAFS of phase-segregated nanostructured PtRu anode catalysts for DMFC [11]
- In situ time-resolved XAFS of Pt/C cathode catalysts for PEFC voltage operations [12]
- In situ XAFS analysis of Pt, Ru, and Pt-Ru/C electrocatalysts under various atmospheres [13]
- CO poisoning kinetics on PtRu electrocatalysts by operando XAFS [14]
- Activity-structure relationship on PtCo/C catalyst for oxygen reduction process [15]
- Structural difference on commercial and prepared PtRu electrocatalysts for DMFC [16]
- SK-edge XAFS for SOFC anodes [17]

- Structural changes in Pt cathode electrocatalyst for temperature and potential variations [18]
- Application of low Pt content PEFC catalysts [19]
- Co electronic structure in Pt_3Co/C cathode catalyst by Co 2p XAFS [20]
- Atomic AXAFS and Delta mu XANES for electrocatalysts [21]
- Operando XAFS for structural changes in ethanol oxidation reaction on Pt/C, PtRu/C, and PtSn/C anode electrocatalysts [22]
- Understanding of catalysts activity and stability for PtVFe/C cathode electrocatalysts in PEFC [23]
- Core-shell structure of IrNi/C anode catalyst [24]
- In situ XAFS cell design for oxygen reduction electrocatalysis with high oxygen flux [25]
- In situ electrochemical EXAFS for Pt-dendrimer-encapsulated nanoparticles [26]
- In situ anode and cathode investigation at different positions in PEFC XAFS cell [27]
- Nanostructure of Pt monolayer model catalysts by in situ fluorescent XAFS [28]
- Local structure and chemical disorder by potential cycling processes in PEFC [29]
- Local structures of Pt – Pd/C bimetallic fuel cell catalysts in acid media [30]
- Structure of Fe-Pt-Ru nanocrystals for methanol oxidation reaction [31]
- Time-resolved XAFS analysis for surface events on Pt_3Co/C cathode catalyst under voltage cycling processes [32]
- Structural strain of dealloyed bimetallic $PtCo_3$ and $PtCu_3$ catalysts for PEFC [33]
- High-energy-resolution fluorescence-detected XAFS for size-selected Pt nanoparticles for electro-oxidation [34]
- 3D visualization of MEA before and after the degradation by X-ray Laminography-XAFS [35]
- Structural kinetics of Pt/C cathode catalysts with practical catalyst loading in MEA [36]
- Surface transformation of Au-Pt/C and Pd-Pt/C electrocatalysts at different potentials [37]
- Mechanism of methanol electrooxidation on PtRu anode electrocatalysts [38]
- Electronic properties and CO and CO_2 tolerance behavior on Pt-bimetallic catalysts [39]
- Operando XAFS for mechanism observation of Pt oxide growth on PEFC electrocatalysts [40]
- In situ characterization of Pt electrocatalysts on different carbon supports using rotating disc electrodes (RDE) and membrane electrode assembly (MEA) [41]
- Characterization of carbon incorporating FeNx electrocatalysts [42]
- Characterization of PtAu core-shell electrocatalysts [43]
- In situ time-resolved XAFS analysis of transient states of Pt/C electrocatalysts for loading processes [44]
- Rate enhancement and structural kinetics of Pt-M (Co and Ni) cathode electrocatalysts for voltage cycling processes [45]

- Characterization of PtNi nanoparticle catalyst on carbon nanotubes for methanol oxidation [46]
- Structural differences on durable $PtCo_x$ electrocatalysts for voltage cycling stages [47]
- Operando XAFS analysis of Ni, NiZn, and Co hydrazine electrooxidation catalysts for anion exchange membrane fuel cells [48]
- Key factors affecting the performance and durability of cathode electrocatalysts in PEFC [49]
- Mapping Pt species in PEFC MEA [50]
- Imagings of Pt chemical species in Pt/C cathode catalyst layers of PEFC [51]
- Effects of gas exchange cycles on deterioration of Pt/C cathode catalysts in PEFCs [52]
- Potential-dependent surface structures of Pt/C, Pd@Pt(1 ML)/C, and Pd@Pt (2 ML)/C [53]
- Nano SnO_2-decorated Pt_3Co/C catalyst prepared by electrochemical Sn deposition [54]

22.3 Time-Resolved XAFS Applications to PEFCs

In situ/*operando* time-resolved XAFS spectra of Pt/C, Pt_3Co/C, and Pt_3Ni/C cathode electrocatalysts in PEFC MEAs were measured every 100 ms for voltage cycling processes between 0.4 and 1.0 V or 1.4 V vs. RHE, while measuring electrochemical evens (current and charge) at the same time [36, 45, 49]. The NEA sizes were 3.0×3.0 cm^2, and the catalyst loadings were 0.5 $mg_{metal/Pd}$ cm^{-2}. The MEA was sandwiched into an in-situ XAFS cell with Teflon gaskets at both cathode and anode sides. Flows of H_2 to the anode and N_2 or air to the cathode were regulated using mass-flow controllers. The gases were bubbled through humidifiers at 351 K and the humidified gases were supplied to the in-situ XAFS cell at 353 K. The cell voltage between the anode and the cathode was controlled using a P/G stat (VSP, BioLogic Science Instruments Co.) with a current amplifier (VMP 3B-20, BioLogic Science Instruments). View of the SPring-8 BL36XU experimental hutch for in situ time-resolved and 2D/3D imaging XAFS measurements is shown in Fig. 22.1a. Setup of in situ time-resolved XAFS experiments is also shown in Fig. 22.1b.

Systematic analysis of in situ/*operando* time-resolved XAFS spectra for Pt/C, Pt_3Co/C, and Pt_3Ni/C cathode catalysts in the transient response processes of the potential jump from 0.4 to 1.0 V or 1.4 V and from 1.0 V or 1.4 to 0.4 V can provide the structural kinetics of the cathode catalysts, where six elementary reaction steps involving Pt valence change, Pt − O bond formation and breaking, and Pt − Pt bond breaking and reformation can be observed and their rate constants can be decided. It is, in general, difficult to observe elementary reaction steps and mechanisms in the steady state conditions. In the transient response processes the reaction sequences and hence mechanism for the dynamic cathode catalysis can be grasped by in situ

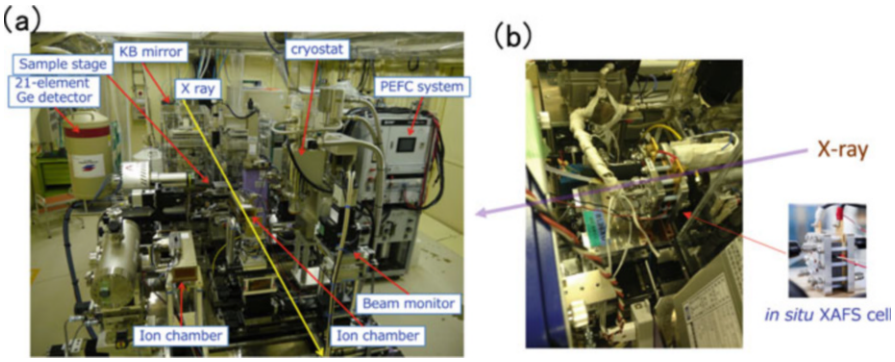

Fig. 22.1 (**a**) View of the SPring-8 BL36XU experimental hutch for in situ time-resolved and 2D/3D imaging XAFS measurements. (**b**) Setup of in situ time-resolved XAFS experiments

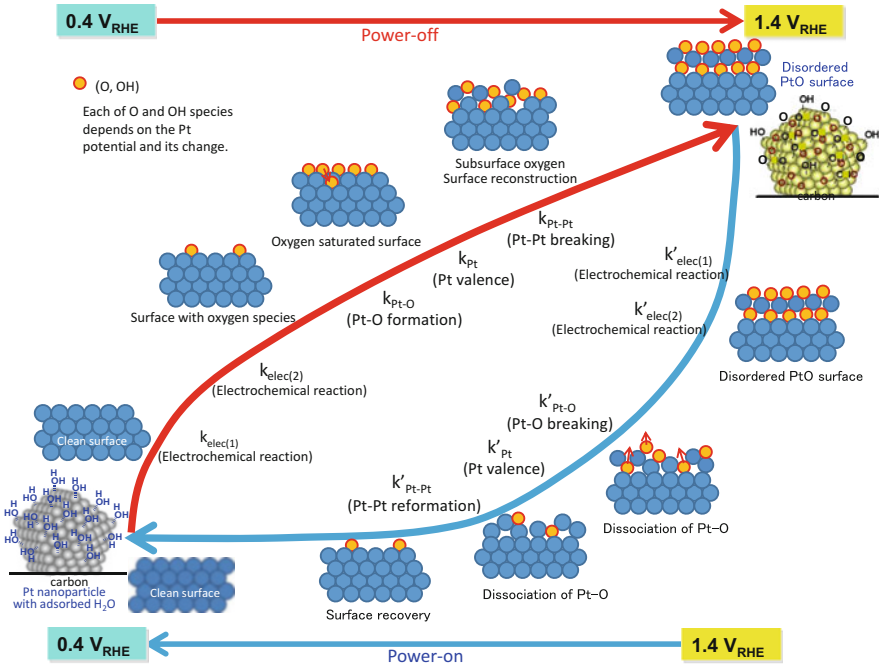

Fig. 22.2 Reaction mechanism and structural kinetics of the Pt/C cathode events in the potential-transient cycling processes by means of in situ real-time XAFS [49]

time-resolved XAFS. The typical results on the MEA Pt/C catalysis in the voltage cycling processes between 0.4 V and 1.4 V are summarized in Fig. 22.2 [36, 49].

The changes in the white line peak intensities of in situ time-resolved QXANES spectra for the voltage cycling processes were significantly different in both variation range and absolute value between the Pt/C, Pt_3Co/C, and Pt_3Ni/C. The

valence level of the Pt/C electrocatalyst at 0.4 V was metallic. The white line peak heights of Pt_3Co/C and Pt_3Ni/C at 0.4 V were less than that for Pt/C, indicating electron transfer from Co or Ni to Pt. The bond distances and coordination numbers for Pt-O, Pt-Pt, and Pt-M (M: Co or Ni) in the potential-jump process from 0.4 to 1.0 V were determined by the EXAFS curve fitting analysis. The formation of Pt – O bonds proceeds accompanied with partial dissociation of the Pt – Pt bonds, while the changes in CNs of Pt – Co and Pt – Ni were negligible in the Pt_3Co/C, and Pt_3Ni/C. These results agree with the structural model of Pt-enriched surface and Pt-M (M: Co or Ni) bimetallic core. The time profiles of the electronic and structural parameters in the voltage cycling processes of 0.4 V → 1.0 V and 1.0 V → 0.4 V were fitted with single or two exponential functions to estimate the rate constants (k and k′ in Fig. 22.2) for each elementary step. The electrochemical processes immediately proceeded and then the electronic and structural changes of the Pt electrocatalysts (Pt charging/discharging, Pt – O bond formation/breaking, and Pt – Pt bond breaking/reformation) proceeded. The aspects of the rate constants for the three electrocatalysts are similar to each other, indicating the similar reaction mechanisms at the cathode electrocatalyst surfaces. The enhancements of the rate constants by the Co and Ni addition to Pt/C are shown in Fig. 22.3 [45]. The increments compared to Pt/C were larger for the potential-jump process of 1.0 V → 0.4 V than the 0.4 V → 1.0 V jump process. Fig. 22.3 reveals that the rate enhancement of the structural kinetics of the Pt electrocatalysts has a positive correlation with the surface specific activity. The in situ time-resolved XAFS analysis demonstrates a nearly linear relationship between the increase of the rate constants $k'_{Pt\text{-}O}$ and k'_{Pt} and the improvement of PEFC activities. The rate constant ($k'_{Pt\text{-}Pt}$) for Pt-Pt reformation was also promoted by the Co and Ni addition, but the difference in the enhancement between Co and Ni was much smaller than those for $k'_{Pt\text{-}O}$ and k'_{Pt} due to the similar Pt-enriched surfaces.

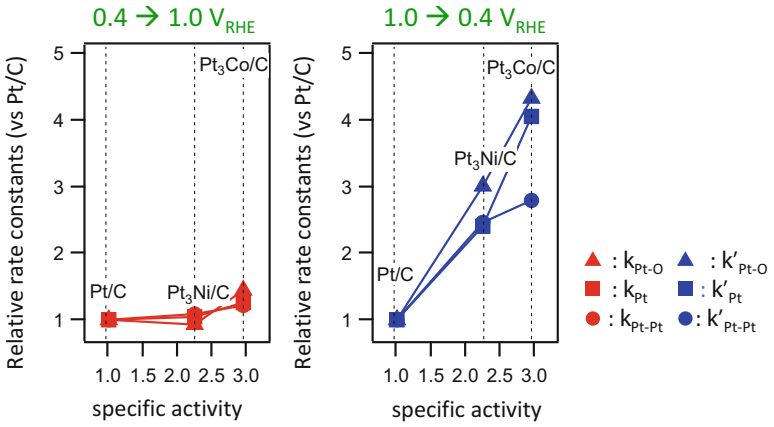

Fig. 22.3 The relationship between rate constants and surface specific activities in the potential cycling processes, 0.4 →1.0 V and 1.0 V→ 0.4 V [45]

22.4 Combined Techniques of XAFS with Other Analysis Methods for Fuel Cells

Spatially resolved XAFS imaging techniques gained new insights into the metallic and oxidized metal species of a single nanoparticle and the two-dimensional distribution of metal species and oxidation states inside a single nanoparticle relevant to mixed oxide catalysis [55, 56]. The imaging nano XAFS technique was applied to ex-situ spatially resolved XAFS measurements for a degraded MEA Pt/C cathode catalyst under humid N_2 atmosphere to examine the site-preferential mechanism for Pt oxidation and dissolution to form the Pt^{2+} monomeric species with a Pt-O_4 coordination structure in the degradation process (see Chapter 4.2.1) [50]. The 3D X-ray computed Laminography (XCL)–XAFS technique also provided a new way of the four-dimensional visualization of the structure/morphology, Pt distribution, and chemical states of the cathode electrocatalyst layer in PEFC MEA in a nondestructive manner (see Chapter 4.2.2) [35, 57].

Combined techniques of XAFS with other physical techniques, such as time-resolved XRD, in situ HAXPES (hard x-ray photoelectron spectroscopy), x-ray computed Laminography, x-ray CT (computed tomography), STEM-EDS, etc., may also provide excellent opportunities for deeper and unprecedented understanding of key issues and mechanisms for the performance and degradation of fuel cell electrocatalyst layers. In this section, the application of the same-view nano XAFS/STEM-EDS technique to polymer electrolyte fuel cells is briefly summarized. Spatially nonuniform degradation of Pt/C cathode catalysts in PEFC was successfully imaged by a combination of nano XAFS and STEM-EDS techniques in the same-view mode under humid N_2 ambient equivalent to in situ MEA conditions [51, 58].

Pt L_{III}-edge nano XAFS spectra were measured at Spring-8 BL36XU by using a Si(111) double crystal monochromator. X-ray beam at 11.39–12.17 keV was focused on 335×338 nm and 228 x 225 nm via a pair of elliptically bent KB mirrors. Nano XAFS spectra were measured in a fluorescence mode, inclining the sample to the X-ray nano-beam by 30°. In the scanning nano XAFS method, a XAFS spectrum was obtained from 206 maps in total corresponding to 206 energy points. To avoid sample damage with synchrotron X-ray irradiation, the beam stay time at each pixel in the XAFS imaging was shortened to only 6–12 μs. For the same-view nano-XAFS/STEM-EDS observations sliced MEA pieces with 100 nm thickness were used. The 100 nm thick sample was put on a SiN membrane (100 nm thick) with 0.5×0.5 mm window and with 100 μm thick Si flame. For the position calibration of nano-XAFS map and STEM image we used the orthogonal distance regression for the estimation of fitting parameters p_0, p_1, and p_2 to give a minimum residual; $A(x, y)$—$p_0 * B(x\text{-}p_1, y\text{-}p_2)$ ($A(x, y)$: absorbance of nano-XAFS map and $B(x, y)$: contrast of the STEM image for coordinate point (x, y)). Thus, the positions were calibrated by using the calculated p_1 and p_2 [51].

Figure 22.4A exhibits the nano-XAFS μ(11.600 keV) mapping, which corresponds to a map of the Pt quantity, for the Pt/C cathode catalyst layer in the

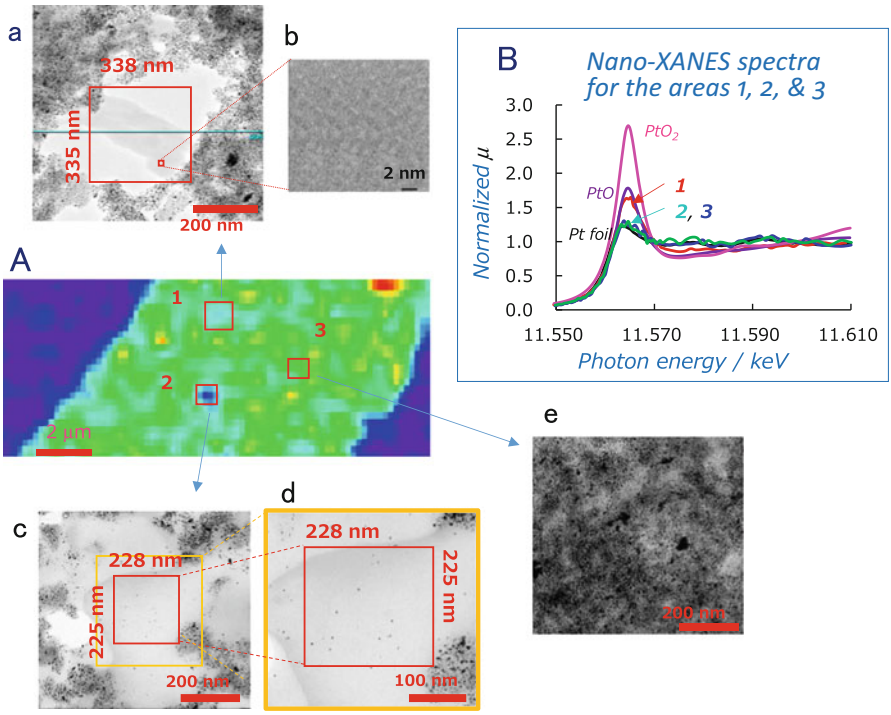

Fig. 22.4 Same view of the nano-XAFS (*A*) and STEM/TEM (**a–e**) under humid N_2 atmosphere and normalized nano-XANES spectra (*B*) for the 335 × 338 nm area **1** (*red*), the 225 × 228 nm area **2** (*green*), and the 225 × 228 nm area **3** (*blue*) and reference XANES spectra of Pt-foil (*black*), PtO (*purple*), and PtO_2 (*pink*) [50, 51]

degraded PEFC MEA (membrane-electrode assembly) after the anode-gas exchange cycles. After the nano-XAFS measurements, TEM/STEM-EDS in the same region was imaged by using the same-view cell. The same-view nano-XAFS/STEM-EDS imaging for the degraded MEA evidenced the presence of two sorts of Nafion ionomer-filled nano-holes (red squares **1** and **2**) and the normal area **3** without holes in the cathode layer as shown in Fig. 22.4A. The Pt amounts (Pt L_{III}-edge jump) in the carbon-corrosion nano-hole areas **1** and **2** were estimated to be 22 % and 18 %, respectively, of that in the area **3** without carbon corrosion. The Pt oxidation states in the areas **1–3** were estimated from a linear relationship between the Pt valence and the white line peak area of the normalized XANES spectra [37, 41]. The Pt oxidation state in the nano-hole area **1** was estimated as +1.9 (±0.15) from Fig. 22.4B, which indicates that the majority of Pt species in the nano-hole area **1** is situated in a Pt^{2+} state, leaching from the carbon support. In the nano-hole area **1**, neither nano size nor subnano size particles were observed (Fig. 22.4a, b), while certain amounts of Pt species and Nafion ionomers existed as proved by the STEM-EDS for the Pt, C, F, and S line profiles along the blue line in Fig. 22.4a [51]. The nano-EXAFS analysis for the nano-hole area **1** revealed no

Pt-Pt bonds, indicating monomeric Pt^{2+} ions. In contrast, Pt nanoparticles detached from the carbon support by carbon corrosion were distributed in the nano-hole area **2** (Fig. 22.4c, d) and their Pt valence was estimated to be zero (Fig. 22.4B). The metallic Pt nanoparticles in the area **2** were also confirmed by the nano-EXAFS analysis, which exhibited only Pt-Pt bonds with the coordination number of 11.7 (±1.7) at 0.277 nm (±0.001 nm) and no Pt-O bonds were observed [51]. The EDS line profiles in the nano-hole area **2** showed much lower F content (F element originates from the Nafion ionomers) than that in the nano-hole area **1**, while the Pt contents in both nano-hole areas were similar to each other. The Pt/ionomer ratios (wt/wt) were estimated as 0.02 and 0.12 for the areas **1** and **2**, respectively, whereas that in the normal catalyst area **3** was calculated as 1.07 (similar to the original value) by the EDS. Thus, it is to be noted that the Pt/ionomer ratio caused the different types of degradation of the Pt/C catalysts in the MEA cathode layer; leaching as Pt^{2+} ions and detaching as metallic Pt nanoparticles from the carbon support upon carbon corrosion. The normalized nano-XANES spectra in Fig. 22.4B showed an isosbestic point at 11.570 keV among them, which indicates the direct transformation of Pt^0–Pt^{2+} species during the AGEX treatments [51].

Figure 22.5 shows the scanning nano Pt L_{III}-edge XANES mapping for MEA Pt/C cathode layers in the depth direction before (a–d) and after (A–E) the accelerated durability test (ADT) 5000 load cycles using an x-ray nano beam size of 228 × 225 nm; a and A: STEM images, b and B: Pt quantity maps, c and C: the superposition of a and b and A and B, respectively, d and D: calculated Pt valence (oxidation state) maps, and E: Pt/Ionomer ratio map calculated from the EDS maps for Pt and F(originated from Nafion ionomer) elements [58]. In the aging MEA

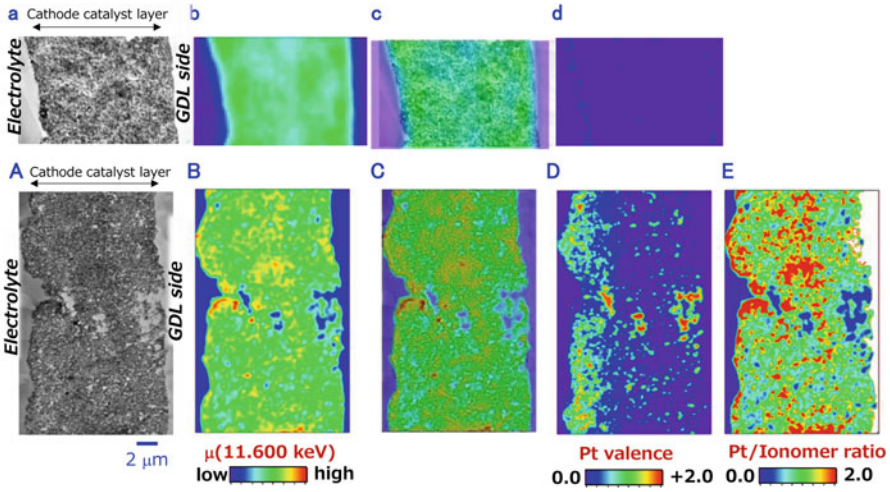

Fig. 22.5 (**a**) *A*: STEM-images, (**b**) *B*: Pt quantity maps, (**c**), *C*: the superposition of **a** and **b** and *A* and *B*, respectively, and (**d**) *D*: calculated Pt valence maps, for the MEAs after aging (**a**-**d**) and ADT cycles (*A*–*D*). *E*: Pt/Ionomer ratio map for the degraded MEA after the ADT cycles [58]

before the ADT cycles there were no significant cracks/voids (a–d), whereas in the degraded MEA after the ADT 5000 cycles many nano-cracks/voids were formed due to carbon corrosion (A–E). The nano-crack/void areas were calculated as 11.9 % of the flat cathode layer area. The Pt valence of the Pt/C cathode layer in the aging MEA was zero (metallic) as shown in Fig. 22.5d, whereas the calculated Pt valence map for the Pt/C cathode layer in the degraded MEA in Fig. 22.5D revealed the localized distribution of Pt oxidized species in the nano-micro cracks/voids as well as the cathode catalyst boundary region (about 3 μm) close to the electrolyte layer.

Figure 22.6 shows the variation of the Pt/ionomer ratio with the nano-crack.void size and the number of each crack/void size, and the effect of Pt/Ionomer ratio on the Pt valence in the degraded MEA. The mean crack/void size and average Pt/ionomer ratio were 154 (±130) nm and 0.14, respectively. The smaller nano-crack/void sizes than 200 nm were predominant in the degraded MEA after the ADT 5000 cycles, and the Pt species of ~98 % among the Pt species observed in the nano-cracks/voids existed in the nano-cracks smaller than 500 nm. The Pt valences of Pt nanoparticles in the nano-cracks/voids larger than 250 nm were 1.3–1.8+. Pt/Ionomer ratios became lower with increasing crack sizes. The tendency of easier Pt oxidation in the larger nano-cracks/voids may be caused by an increase of electric resistance and/or heterogeneous over-loaded potentials around the nano-

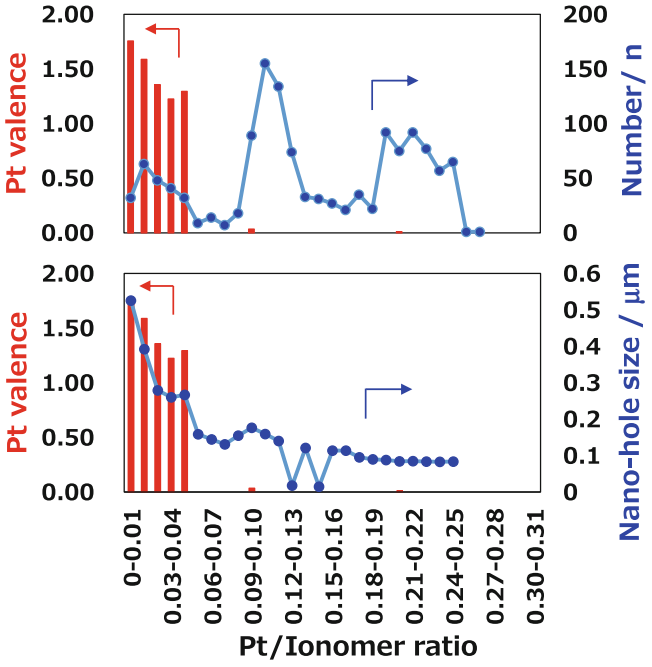

Fig. 22.6 The effect of the Pt/Ionomer ratio on the Pt valence and the variation of the nano-hole number and size with the Pt/ionomer ratio in a degraded MEA [58]

cracks. The ionomer content also plays a role in the decision of Pt oxidation states for the Pt nanoparticles detached and dissoluted from the carbon support. The number ratio of 80 % and area ratio of 35 % in the nano-cracks/voids contained Pt and ionomers at the Pt/ionomer ratios of 0.09–0.24. The nano-cracks/voids with the lower Pt/ionomer ratios than 0.05 included oxidized Pt species whose valences were 1.3–1.8+. On the other hand, Pt valences in the nano-cracks/voids with the Pt/ionomer ratios higher than 0.05 were calculated almost zero (metallic). These results suggest that the high content of ionomers in the nano-cracks/voids facilitates the oxidative dissolution of Pt and stabilizes the oxidized Pt species via the coordination of Nafion-SO_3 to the cationic Pt species, whereas the low content of ionomers in the nano-cracks/voids promotes the detachment of metallic Pt nanoparticles/clusters from the carbon support [58]. The same-view nano-XAFS/STEM-EDS imaging allowed finding the unprecedented aspect of the formations of the leached Pt^{2+} oxidation species and detached metallic Pt nanoparticles in the Nafion ionomer-filled nano-hole areas of the degraded Pt/C cathode layers.

22.5 Prospect

In situ, time-resolved and spatially resolved (imaging) XAFS techniques may provide key issues and mechanisms affecting the performance and durability of cathode electrocatalysts in fuel cells, which cannot be addressed definitely and directly by other techniques. The advanced XAFS techniques are promising tools to present real-time structural kinetics/dynamics of potential-dependent surface reactions on cathode electrocatalysts and spatial mapping of time-dependent chemical changes of Pt nanoparticles under various electrochemical conditions in a nondestructive manner. The XAFS techniques can be consorted with other new techniques such as in-situ 3D X-ray Laminography, 3D XCT, ambient-pressure HAXPES, etc. (see Chapters 1, Chapter 10, Chapter 11, and Chapter 12) [35, 59].

References

1. Mukerjee S, McBreen J (1999) An in situ X-ray absorption spectroscopy investigation of the effect of Sn additions to carbon-supported Pt electrocatalysts - Part1. J Electrochem Soc 146:600–606
2. Russell AE, Maniguet S, Mathew RJ, Yao J, Roberts MA, Thompsett D (2001) In situ X-ray absorption spectroscopy and X-ray diffraction of fuel cell electrocatalysts. J Power Sources 96:226–232
3. Roth C, Martz N, Buhrmester T, Scherer J, Fuess H (2002) In-situ XAFS fuel cell measurements of a carbon-supported Pt-Ru anode electrocatalyst in hydrogen and direct methanol operation. Phys Chem Chem Phys 4:3555–3557
4. Mukerjee S, Urian RC (2002) Bifunctionality in Pt alloy nanocluster electrocatalysts for enhanced methanol oxidation and CO tolerance in PEM fuel cells: electrochemical and in situ synchrotron spectroscopy. Electrochim Acta 47:3219–3231

5. Roth C, Martz N, Morlang A, Theissmann R, Fuess H (2004) X-ray absorption studies on alloy formation in different carbon-supported Pt-Ru electrocatalysts. Phys Chem Chem Phys 6:3557–3562
6. Teliska M, Murthi VS, Mukerjee S, Ramaker DE (2005) Correlation of water activation, surface properties, and oxygen reduction reactivity of supported Pt-M/C bimetallic electrocatalysts using XAS. J Electrochem Soc 152:A2159–A2169
7. Holstein WL, Rosenfeld HD (2005) In-situ x-ray absorption spectroscopy study of Pt and Ru chemistry during methanol electrooxidationt. J Phys Chem B 109:2176–2186
8. Roth C, Benker N, Buhrmester T, Mazurek M, Loster M, Fuess H, Koningsberger DC, Ramaker DE (2005) Determination of O[H] and CO coverage and adsorption sites on PtRu electrodes in an operating PEM fuel cell. J Am Chem Soc 127:14607–14615
9. Saito M, Shiroishi H, Ono C, Tsuzuki S, Okada T, Uchimoto Y (2006) Influence of ligand structures on methanol electro-oxidation by mixed catalysts based on platinum and organic metal complexes for DMFC. J Mol Catal A Chem 248:99–108
10. Hwang BJ, Chen CH, Sarma LS, Chen JM, Wang GR, Tang MT, Liu DC, Lee JF (2006) Probing the formation mechanism and chemical states of carbon-supported Pt-Ru nanoparticles by in situ X-ray absorption spectroscopy. J Phys Chem B 110:6475–6482
11. Stoupin S, Chung EH, Chattopadhyay S, Segre CU, Smotkin ES (2006) Pt and Ru X-ray absorption spectroscopy of PtRu anode catalysts in operating direct methanol fuel cells. J Phys Chem B 110:9932–9938
12. Tada M, Murata S, Asakoka T, Hiroshima K, Okumura K, Tanida H, Uruga T, Nakanishi H, Matsumoto S, Inada Y, Nomura M, Iwasawa Y (2007) In situ time-resolved dynamic surface events on the Pt/C cathode in a fuel cell under operando conditions. Angew Chem Int Ed 46:4310–4315
13. Roth C, Benker N, Mazurek M, Scheiba F, Fuess H (2007) Pt-Ru fuel cell catalysts subjected to H-2, CO, N-2 and air atmosphere: An X-ray absorption study. App Catal A Gen 319:81–90
14. Scott FJ, Roth C, Ramaker DE (2007) Kinetics of CO poisoning in simulated reformate and effect of Ru island morphology on PtRu fuel cell catalysts as determined by operando X-ray absorption near edge spectroscopy. J Phys Chem C 111:11403–11413
15. Hwang BJ, Kumar SMS, Chen CH, Cheng MY, Liu DG, Lee JF (2007) An investigation of structure-catalytic activity relationship for Pt-Co/C bimetallic nanoparticles toward the oxygen reduction reaction. J Phys Chem C 111:15267–15276
16. Stoupin S, Rivera H, Li ZR, Segre CU, Korzeniewski C, Casadonte DJ, Inoue H, Smotkin ES (2008) Structural analysis of sonochemically prepared PtRu versus Johnson Matthey PtRu in operating direct methanol fuel cells. Phys Chem Chem Phys 10:6430–6437
17. Braun A, Janousch M, Sfeir J, Kiviaho J, Noponen M, Huggins FE, Smith MJ, Steinberger-Wilckens R, Holtappels P, Graule T (2008) Molecular speciation of sulfur in solid oxide fuel cell anodes with X-ray absorption spectroscopy. J Power Sources 183:564–570
18. Witkowska A, Principi E, Di Cicco A, Dsoke S, Marassi R, Olivi L, Centazzo M, Albertini VR (2008) Temperature and potential-dependent structural changes in a Pt cathode electrocatalyst viewed by in situ XAFS. J Non-Cryst Solids 354:4227–4232
19. Principi E, Witkowska A, Dsoke S, Marassi R, Di Cicco A (2009) An XAS experimental approach to study low Pt content electrocatalysts operating in PEM fuel cells. Phys Chem Chem Phys 11:9987–9995
20. Kobayashi M, Hidai S, Niwa H, Harada Y, Oshima M, Horikawa Y, Tokushima T, Shin S, Nagamori Y, Aoki T (2009) Co oxidation accompanied by degradation of Pt-Co alloy cathode catalysts in polymer electrolyte fuel cells. Phys Chem Chem Phys 11:8226–8230
21. Ramaker DE, Koningsberger DC (2010) The atomic AXAFS and Delta mu XANES techniques as applied to heterogeneous catalysis and electrocatalysis. Phys Chem Chem Phys 12:5514–5534
22. Melke J, Schoekel A, Dixon D, Cremers C, Ramaker DE, Roth C (2010) Ethanol oxidation on carbon-supported Pt, PtRu, and PtSn catalysts studied by operando X-ray absorption spectroscopy. J Phys Chem C 114:5914–5925

23. Fang B, Luo J, Chen YS, Wanjala BN, Loukrakpam R, Hong JA, Yin J, Hu XA, Hu PP, Zhong CJ (2011) Nanoengineered PtVFe/C cathode electrocatalysts in PEM fuel cells: catalyst activity and stability. Chemcatchem 3:583–593
24. Sasaki K, Kuttiyiel KA, Barrio L, Su D, Frenkel AI, Marinkovic N, Mahajan D, Adzic RR (2011) Carbon-supported IrNi core-shell nanoparticles: synthesis, characterization, and catalytic activity. J Phys Chem C 115:9894–9902
25. Erickson EM, Thorum MS, Vasic R, Marinkovic NS, Frenkel AI, Gewirth AA, Nuzzo RG (2012) In situ electrochemical X-ray absorption spectroscopy of oxygen reduction electrocatalysts with high oxygen Flux. J Am Chem Soc 134:197–200
26. Myers VS, Frenkel AI, Crooks RM (2012) In situ structural characterization of platinum dendrimer-encapsulated oxygen reduction electrocatalysts. Langmuir 28:1596–1603
27. Dixon D, Habereder A, Farmand M, Kaserer S, Roth C, Ramaker DE (2012) Space resolved, in operand X-ray absorption spectroscopy: investigations on both the anode and cathode in a direct methanol fuel cell. J Phys Chem C 116:7587–7595
28. Friebel D, Viswanathan V, Miller DJ, Anniyev T, Ogasawara H, Larsen AH, Grady CPO', Norskov JK, Nilsson A (2012) Balance of nanostructure and bimetallic interactions in Pt model fuel cell catalysts: in situ XAS and DFT study. J Am Chem Soc 134:9664–9671
29. Greco G, Witkowska A, Minicucci M, Oivi L, Principi E, Dsoke S, Moretti A, Marassi R, Di Cicco A (2012) Local ordering changes in Pt-Co nanocatalyst induced by fuel cell working conditions. J Phys Chem C 116:12791–12802
30. Liu L, Samjeske G, Nagamatsu S, Sekizawa O, Nagasawa K, Takao S, Imaizumi Y, Yamamoto T, Uruga T, Iwasawa Y (2012) Enhanced oxygen reduction reaction activity and characterization of Pt – Pd/C bimetallic fuel cell catalysts with Pt-enriched surfaces in acid media. J Phys Chem C 116:23453–23464
31. Wang DY, Chou HL, Lin YC, Lai FJ, Chen CH, Lee JF, Hwang BJ, Chen CC (2012) Simple replacement reaction for the preparation of ternary $Fe_{1-x}PtRu_x$ nanocrystals with superior catalytic activity in methanol oxidation reaction. J Am Chem Soc 134:10011–10020
32. Ishiguro N, Saida T, Uruga T, Nagamatsu S, Sekizawa O, Nitta K, Yamamoto T, Ohkoshi S, Iwasawa Y, Yokoyama T, Tada M (2012) Operand time-resolved X-ray absorption fine structure study for surface events on a Pt_3Co/C cathode catalyst in a polymer electrolyte fuel cell during voltage-operating processes. ACS Catal 2:1319–1330
33. Yu ZQ, Zhang JL, Liu ZY, Ziegelbauer JM, Xin HL, Dutta I, Muller DA, Wagner FT (2012) Comparison between dealloyed $PtCo_3$ and $PtCu_3$ cathode catalysts for proton exchange membrane fuel cells. J Phys Chem C 116:19877–19885
34. Merte LR, Behafarid F, Miller DJ, Friebel D, Cho S, Mbuga F, Sokaras D, Alonso-Mori R, Weng TC, Nordlund D, Nilsson A, Cuenya BR (2012) Electrochemical oxidation of size-selected Pt nanoparticles studied using in situ high-energy-resolution X-ray absorption spectroscopy. ACS Catal 2:2371–2376
35. Saida T, Sekizawa O, Ishiguro N, Uesugi K, Hoshina M, Uruga T, Ohkoshi S, Yokoyama T, Tada M (2012) Visualization of a cathode catalyst layer in a polymer electrolyte fuel cell by 3D-laminography-XAFS. Angew Chem Int Ed 51:10311–10314
36. Ishiguro N, Saida T, Uruga T, Sekizawa O, Nagasawa K, Nitta K, Yamamoto T, Ohkoshi S, Yokoyama T, Tada M (2013) Structural kinetics of a Pt/C cathode catalyst with practical catalyst loading in an MEA for PEFC operating conditions studied by in situ time-resolved XAFS. Phys Chem Chem Phys 15:18827–18834
37. Nagamatsu S, Arai T, Yamamoto M, Ohkura T, Oyanagi H, Ishizaka T, Kawanami H, Uruga T, Tada M, Iwasawa Y (2013) Potential-dependent restructuring and hysteresis in the structural and electronic transformations of Pt/C, Au(Core)-Pt(Shell)/C, and Pd(Core)-Pt (Shell)/C cathode catalysts in polymer electrolyte fuel cells characterized by in situ X-ray absorption fine structure. J Phys Chem C 117:13094–13107
38. Pelliccione CJ, Timofeeva EV, Katsoudas JP, Segre CU (2013) In situ Ru K-Edge X-ray absorption spectroscopy study of methanol oxidation Mechanisms on model submonolayer Ru on Pt nanoparticle electrocatalyst. J Phys Chem C 117:18904–18912

39. Ehteshami SMM, Jia QY, Halder A, Chan SH, Mukerjee S (2013) The role of electronic properties of Pt and Pt alloys for enhanced reformate electro-oxidation in polymer electrolyte membrane fuel cells. Electrochim Acta 107:155–163
40. Redmond EL, Setzler BP, Alamgir FM, Fuller TF (2014) Elucidating the oxide growth mechanism on platinum at the cathode in PEM fuel cells. Phys Chem Chem Phys 16:5301–5311
41. Nagasawa K, Takao S, Higashi K, Nagamatsu S, Samjeske G, Imaizumi Y, Sekizawa O, Yamamoto T, Uruga T, Iwasawa Y (2014) Performance and durability of Pt/C cathode catalysts with different kinds of carbons for polymer electrolyte fuel cells characterized by electrochemical and in situ XAFS techniques. Phys Chem Chem Phys 16:10075–10087
42. Liu SH, Wu JR, Pan CJ, Hwang BJ (2014) Synthesis and characterization of carbon incorporated Fe-N/carbons for methanol-tolerant oxygen reduction reaction of polymer electrolyte fuel cells. J Power Sources 250:279–285
43. Kaito T, Mitsumoto H, Sugawara S, Shinohara K, Uehara H, Ariga H, Takakusagi S, Hatakeyama Y, Nishikawa K, Asakura K (2014) K-edge X-ray absorption fine structure analysis of Pt/Au Core-Shell electrocatalyst: evidence for short Pt-Pt distance. J Phys Chem C 118:8481–8490
44. Kityakarn S, Saida T, Sobe A, Ishiguro N, Sekizawa O, Uruga T, Nagasawa K, Yamamoto T, Yokoyama T, Tada M (2014) In situ time-resolved XAFS of transitional states of Pt/C cathode electrocatalyst in an MEA during PEFC loading with transient voltages. Top Catal 57:903–910
45. Ishiguro N, Kityakarn S, Sekizawa O, Uruga T, Sasabe T, Nagasawa K, Yokoyama T, Tada M (2014) Rate enhancements in structural transformations of Pt-Co and Pt-Ni bimetallic cathode catalysts in polymer electrolyte fuel cells studied by in situ time-resolved X-ray absorption fine structure. J Phys Chem C 118:15874–15883
46. Nassr AAA, Sinev I, Pohl MM, Grunert W, Bron M (2014) Rapid microwave-assisted polyol reduction for the preparation of highly active PtNi/CNT electrocatalysts for methanol oxidation. ACS Catal 4:2449–2462
47. Jia QY, Caldwell K, Strickland K, Ziegelbauer JM, Liu ZY, Yu ZQ, Ramaker DE, Mukerjee S (2015) Improved oxygen reduction activity and durability of dealloyed PtCox catalysts for proton exchange membrane fuel cells: strain, ligand, and particle size effects. ACS Catal 5:176–186
48. Sakamoto T, Matsumura D, Asazawa K, Martinez U, Serov A, Artyushkova K, Atanassov P, Tamura K, Nishihata Y, Tanaka H (2015) Operand XAFS study of carbon supported Ni, NiZn, and Co catalysts for hydrazine electrooxidation for use in anion exchange membrane fuel cells. Electrochim Acta 163:116–122
49. Tada M, Uruga T, Iwasawa Y (2015) Key factors affecting the performance and durability of cathode electrocatalysts in polymer electrolyte fuel cells characterized by in-situ real time and spatially resolved XAFS techniques. Catal Lett 145:58–70
50. Takao S, Sekizawa O, Nagamatsu S, Kaneko T, Yamamoto T, Samjeské G, Higashi K, Nagasawa K, Tsuji T, Suzuki M, Kawamura N, Mizumaki M, Uruga T, Iwasawa Y (2014) Mapping platinum species in polymer electrolyte fuel cells by spatially resolved XAFS techniques. Angew Chem Int Ed 53:14110–14114
51. Takao S, Sekizawa O, Samjeské G, Nagamatsu S, Kaneko T, Yamamoto T, Higashi K, Nagasawa K, Uruga T, Iwasawa Y (2015) Same-view nano-XAFS/STEM-EDS imagings of Pt chemical species in Pt/C cathode catalyst layers of a polymer electrolyte fuel cell. J Phys Chem Lett 6:2121–2126
52. Samjeské G, Higashi K, Takao S, Nagamatsu S, Nagasawa K, Sekizawa O, Kaneko T, Uruga T, Iwasawa Y (2015) Effects of anode or cathode gas exchange cycles on deterioration of Pt/C cathode catalysts in PEFCs characterized by in-situ time-resolved XAFS, TEM, and electrochemical techniques. ChemElectroChem 2:1595–1606
53. Nagamatsu S, Takao S, Samjeské G, Nagasawa K, Sekizawa O, Kaneko T, Higashi K, Uruga T, Gayen S, Velaga S, Saniyal MK, Iwasawa Y (2016) Structural and electronic transformations of Pt/C, Pd@Pt(1 ML)/C and Pd@Pt(2 ML)/C cathode catalysts in polymer

electrolyte fuel cells during potential-step operating processes characterized by in-situ time-resolved XAFS. Surf Sci 648:100–113. doi:10.1016/j.susc.2015.10.053
54. Nagasawa K, Takao S, Nagamatsu S, Samjeske G, Sekizawa O, Kaneko T, Higashi K, Yamamoto T, Uruga T, Iwasawa Y (2015) J Am Chem Soc 137:12856–12864
55. Tada M, Ishiguro N, Uruga T, Tanida H, Terada Y, Nagamatsu S, Iwasawa Y, Ohkoshi S (2011) μ-XAFS of a single particle of a practical $NiO_x/Ce_2Zr_2O_y$ catalyst. Phys Chem Chem Phys 13:14910–14913
56. Ishiguro N, Uruga T, Sekizawa O, Tsuji T, Suzuki M, Kawamura N, Mizumaki M, Nitta K, Yokoyama T, Mizuki T (2014) Visualizstion of the heterogeneity of cerrium oxidation states in single $Pt/Ce_2Zr_2O_x$ catalyst particles by nano-XAFS. ChemPhysChem 15:1563–1568
57. Tada M (2013) Hard X-ray time-resolved/space-resolved X-ray absorption fine structure analysis for heterogeneous metal catalysts. J Phys Soc Jpn 82:021013–021020
58. Takao S, Sekizawa O, Samjeské G, Namagatsu S, Kaneko T, Higashi K, Yamamoto T, Nagasawa K, Uruga T, Iwasawa Y (2016) Spatially non-uniform degradation of Pt/C cathode catalysts in polymer electrolyte fuel cells imaged by combination of nano XAFS and STEM-EDS techniques. Topics Catal in press doi:10.1007/s11244-016-0691-y
59. Takagi Y, Wang H, Uemura Y, Ikenaga E, Sekizawa O, Uruga T, Ohashi H, Senba Y, Yumoto H, Yamazaki H, Goto S, Tada M, Iwasawa Y, Yokoyama T (2014) In situ investigation of an oxidation reaction on a Pt/C electrode using ambient pressure hard X-ray photoelectron spectroscopy. Appl Phys Lett 105:131602

Chapter 23
Secondary Batteries

Toshiaki Ohta

23.1 Introduction

The advent of Li ion batteries (LIBs) changed the world of secondary batteries. With their excellent performance, the LIBs are widely used as electric energy storages for mobile phones, laptop computer, etc. New types of LIBs have been developed one after another and now it is a worldwide challenge to develop a large-scale battery with high capacity for hybrid and/or full electric vehicles [1]. Battery is, in principle, composed of cathode, separator, anode, and electrolyte, as shown in Fig. 23.1. It has two phases, charge and discharge, in which Li ions move from cathode to anode, and vice versa, respectively. It has several important key factors: high capacity, high cyclability, high charging rate, low cost, ease of preparation, and safety. To realize a battery with such high performances, a number of difficult subjects should be overcome. Since the battery is a very complicated target, many analytical techniques have been applied to elucidate the structures, electrochemical reactions of batteries, such as XRD (X-ray diffraction), neutron diffraction, Raman scattering, NMR, etc., as well as theoretical simulations. Especially, X-ray Absorption Fine Structure (XAFS) is a powerful tool and numerous studies with XAFS have been reported for secondary batteries. Due to the limit of page, however, this review is focused on the XAFS methodologies and how they are applied for characterization of the secondary batteries.

T. Ohta (✉)
Synchrotron Radiation Center, Ritsumeikan University, Kusatsu, Shiga 525-8577, Japan
e-mail: ohta@fc.ritsumei.ac.jp

Y. Iwasawa et al. (eds.), *XAFS Techniques for Catalysts, Nanomaterials, and Surfaces*, DOI 10.1007/978-3-319-43866-5_23

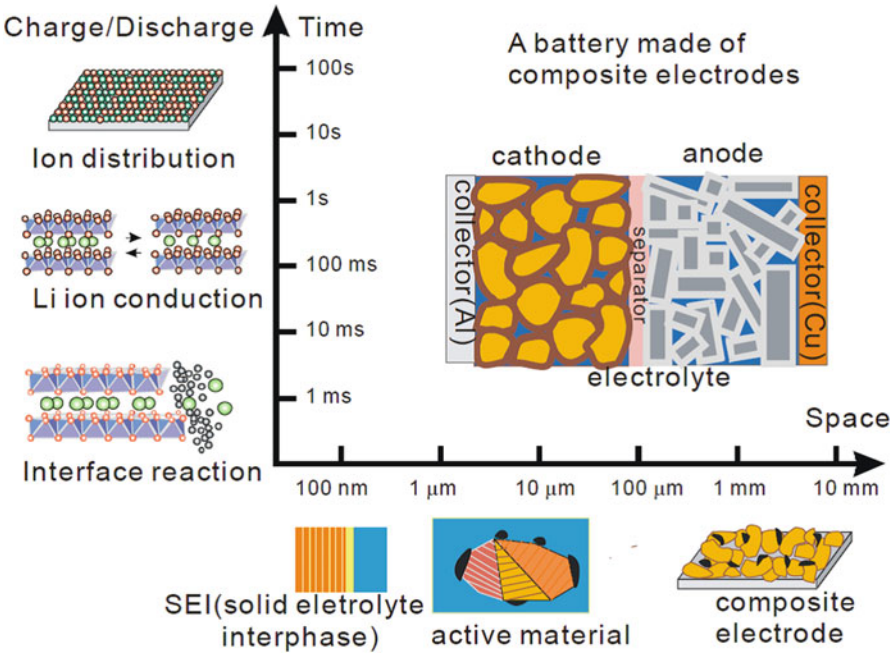

Fig. 23.1 A schematic of a secondary battery and its spatial and temporal hierarchy

23.2 Experimental Methodology

Since hard X-rays are highly penetrative, one can easily perform in situ XAFS experiments in the hard X-ray region during charge and discharge with the transmission mode. The oxidation states and the local structures of transition metals, such as Mn, Co, Ni, are revealed by the conventional XAFS technique, by using an aluminum-coated laminate pack or a home-made electrochemical cell. This in situ XAFS method has been actively used for the analysis of a variety of new electrodes [2–4].

Combining a highly brilliant X-ray beam with a 2D detector, one can get the depth-profile information. Figure 23.2 shows an experimental setup for the depth-resolved XAFS for a cathode/electrolyte interface [5]. When the X-rays irradiate a sample, fluorescent X-rays emitted in the normal direction from the sample surface come from both surface and bulk, while those emitted in the grazing direction come predominantly from surface. Thus, with a proper setup of a 2D detector relative to the sample surface (see Fig. 23.2), the depth-resolved XAFS can be performed.

The reflective index of the X-ray is slightly less than unity. Thus, if a highly collimated X-ray beam is incident to a flat surface at an angle less than the critical angle, it is totally reflected with a very shallow penetration in the sample. Since the penetration depth is as small as a few nanometers, one can probe only the surface information of the electrode under the condition. This total reflection XAFS has

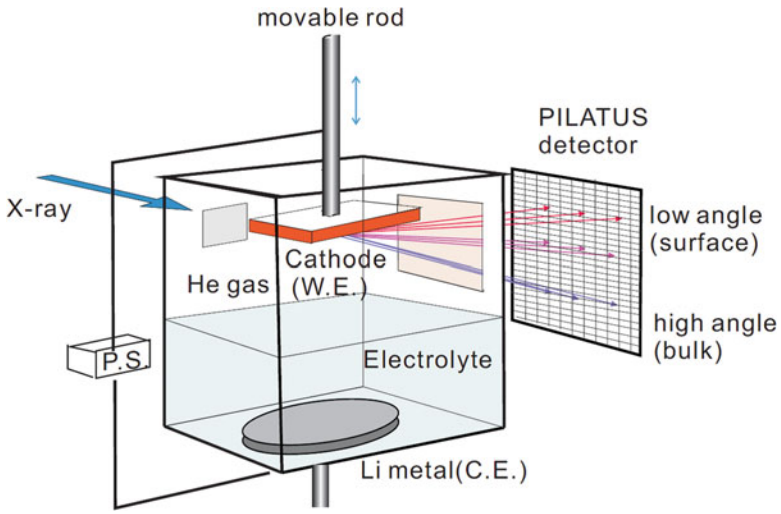

Fig. 23.2 Experimental setup for the depth-resolved XAFS for a cathode/electrolyte interface. For Li deintercalation, the cathode was dipped in the electrolyte. Then the wet cathode was pulled up for the XAFS experiment [5]

been used to study how the top surface of electrode changes by soaking in electrolyte and by charge/discharge [6, 7].

Combining a broad X-ray beam with a 2D detector, in situ 2D imaging XAFS can be realized for the battery analysis [8, 9]. With this technique, one can obtain the spatial distribution of a specific element, and also that of a specific oxidation state. Delithiation/lithiation upon charge/discharge causes the charge compensation of the elements contained in electrodes. Imaging XAFS is a useful technique to monitor how the charge/discharge proceeds.

Electrochemical reaction dynamics is one of the important issues of batteries. Quick scanning XAFS spectroscopy has been applied to study high rate delithiation behavior of an electrode [10, 11]. However, the ion diffusion upon charge/discharge proceeds sometimes inhomogeneously. It is desirable to get the fast time evolution of imaging XAFS for such cases. Recently, Katayama et al. developed a new type of dispersive XAFS by using the vertical dispersion of synchrotron white light, instead of conventional horizontal dispersion, as shown in Fig. 23.3. This vertically dispersive XAFS provides a time-resolved spatial distribution of the electrode reaction [12].

Charge and discharge processes sometimes cause structural change, phase transformation, or cation mixing in the Li and 3d transition metal layers. Combined use of XAFS and XRD is effective to study such a complicated case. However, in general, XRD and XAFS experiments are performed independently at different beamlines. Recently, Tokuda et al. constructed a beamline in SPring-8 which enables us to perform XRD and XAFS simultaneously, as shown in Fig. 23.4 [13]. Thanks to the high beam stability, the irradiated area in the sample stays

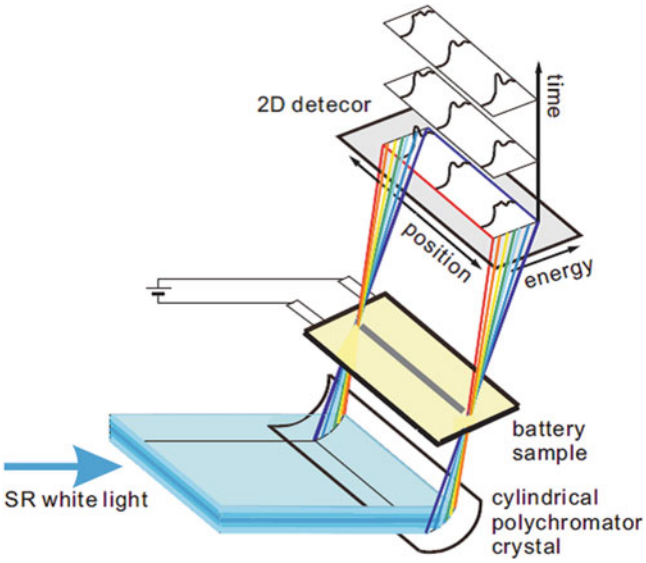

Fig. 23.3 A schematic view of the vertically dispersive XAFS method [12]

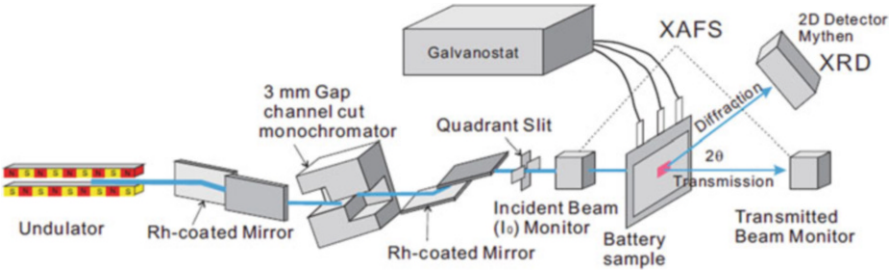

Fig. 23.4 A beamline for simultaneous use of XAFS and XRD in the SPring-8 [13]

within 1 μm upon energy scanning with a channel-cut Si(111) monochromator. The same experimental setup can be used for the experiment of the diffraction anomalous fine structure (DAFS) method. DAFS is known to be a spectroscopic analysis method coupling XAFS and XRD [14] and enables us to determine the valence state and local structure of a selected element at a specific crystalline site and/or phase. So far, it had been applied exclusively for a single crystal, not for a practical material. Recently, this DAFS was revisited as a powerful method by using a logarithmic dispersion relation, applicable to a practical polycrystalline material [15]. The improved DAFS will be an especially powerful technique for the structure analysis of a complicated system, such as a multielement intermixing composite battery [16].

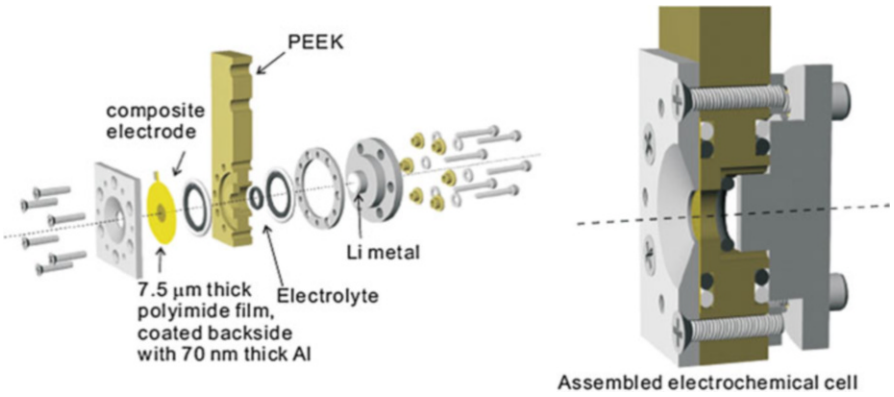

Fig. 23.5 A typical electrochemical cell for operand XAFS experiment in the soft X-ray region. Reprinted with permission from Ref. [20]. Copyright [2014], AIP Publishing LLC

On the other hand, XAFS experiments in the soft X-ray region are not straightforward. Penetration depth is shallow and, in general, the transmission mode is not available. Instead, one adopts the fluorescent yield (FY) by using a silicon drift detector (SDD) and the electron yield modes to obtain XAFS spectra. For the electron yield mode, one usually uses two types of modes: partial electron yield (PEY) mode by using a microchannel plate (MCP) electron multiplier covered with a retarding grid and total electron yield (TEY) by monitoring the sample leak current, in which the former is more surface sensitive since it rejects low energy secondary electrons. It is desirable to make use of these three modes simultaneously, which provides depth profiles of XAFS. In the soft X-ray region, there are Li, O, F, S, Si, P *K*-edges, which are important elements contained in electrodes, electrolytes, and additives. There are also 3d transition metal L-edges. Since these L-edge XAFS spectra are associated with $2p \rightarrow 3d$ transitions, they are rather complicated due to 3d spin multiplicity, but they provide information about spin state as well as valency [17]. Combined use of *K*- and *L*-edge XAFS is useful for full understanding of 3d transition metals in batteries [18, 19].

Due to the low penetration depth soft X-rays, in situ XAFS is challenging. We have to develop a special cell for the operando analysis of XAFS. Here, the key factor is to find a thin and vacuum-tight X-ray window. A typical electrochemical cell is shown in Fig. 23.5, which has worked successfully for the operando P and S K-XAFS experiments in the SR center, Ritsumeikan University [20].

23.3 Typical Applications of XAFS to Batteries

23.3.1 Depth-Resolved XAFS

Takamatsu et al. studied local structures of a $LiCoO_2$ thin film at the solid electrode/electrolyte solution interface by the depth-resolved XAFS, described in the previous section [5]. They designed a unique He gas filled spectro-electrochemical cell,

as shown in Fig. 23.2. During the charge process, the cathode was immersed in the electrolyte solution with Li metal as a counter electrode, and a constant voltage was applied by a potentiostat to charge the electrode. For each XAFS experiment, the cathode was pulled up from the electrolyte and was irradiated by the grazing incident SR beam coming through a kapton window. Fluorescent X-rays were detected by a 2D pixel array detector, PILATUS 100 K, located 0.45 m apart from the sample. XAFS spectra were taken before charge (3.2 V versus Li/Li+), charged to 4.2 V, and overcharged to 4.4 V. Figure 23.6a, b show Co *K*-edge depth-resolved XAFS spectra of the $LiCoO_2$ film before charge and their Fourier transformations, respectively. From the bulk to the interface, the edge shifts toward lower energy, indicating the surface Co was reduced by soaking. In the Fourier spectra, the first peak at 1.5 A is associated with the Co-O bond. Its peak height decreases from bulk to interface, keeping the bond distance same, indicating that the DW (Debye-Waller) factor of the surface Co-O bond was more enhanced than the bulk ones.

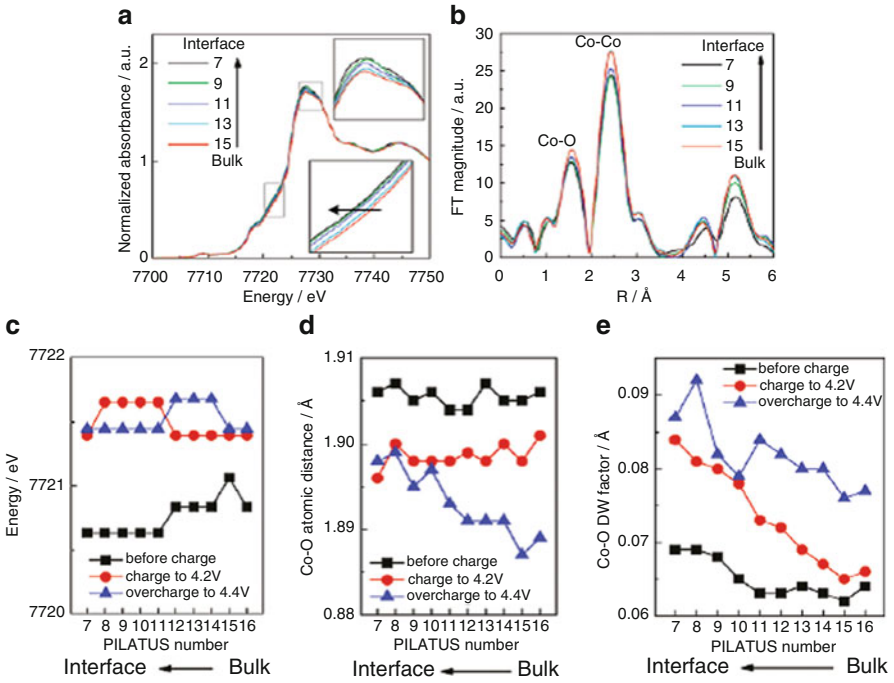

Fig. 23.6 Depth-resolved Co *K*-XAFS spectra of the $LiCoO_2$ electrode. (**a**, **b**) are the XAFS spectra before charge and their Fourier transforms, respectively. (**c**–**e**) are the depth profiles of the Co *K*-edge energies, Co-O atomic distances, and Co-O DW factors obtained from the spectra before charge, after charged to 4.2 V and after overcharged to 4.4 V, respectively. Reprinted with permission from Ref. [5] Copyright [2011] American Chemical Society

Figure 23.6c–e are, respectively, the edge energy, the C-O bond distance, and the C-O DW factor of the electrode before charge, after charged to 4.2 V and after overcharged to 4.4 V. As shown in Fig. 23.6c, the edge shifts to higher energy by charge, indicating the Co oxidation by delithiation. Figure 23.6d, e shows that upon charge to 4.2 V, the Co-O distance decreases and the DW factor increases significantly toward the surface.

When overcharged to 4.4 V, the Co-O distance decreases only in the bulk and the DW factor increases considerably, suggesting that a tremendous distortion occurs by overcharge. This distortion might be the main cause of deterioration of the electrode. These results show that the depth-resolved in situ XAFS experiments provide useful information about the structural change at the solid electrode/electrolyte interface in the nanoscale spatial resolution.

23.3.2 XAFS in the Soft X-ray Region with Three Detection Modes

As described in the previous section, simultaneous use of PEY, TEY, and PFY modes in the soft X-ray region can probe both surface and bulk structures of batteries. Since deterioration of an electrode usually starts from the surface, XAFS experiment with these three modes provides useful information. Yogi et al. studied the effect of adding lithium bis(oxalate) borate (LiBOB) to the electrolyte on the cyclability of the $LiCoO_2$ electrode [21]. Figure 23.7 shows O K-XANES spectra of $LiCoO_2$ just after soaked and after 20 cycles of charge/discharge with three detection modes. Just after soaked, the surface is covered with Li_2CO_3, though the bulk is predominantly $LiCoO_2$. After 20 cycles, the surface structure does not change in the case with LiBOB, while it changes drastically without LiBOB. From the spectral similarity, we can deduce that the $LiCoO_2$ in the surface region decomposed to CoO.

Recently, a series of Li-rich Mn-layered oxides, $yLi_2MnO_3 \cdot (1\text{-}y)LiMO_2$ (M = Ni, Co, Mn) have been paid special attention as high capacity positive electrodes in the next-generation Li ion batteries [22]. Since such a high capacity cannot be explained only by the redox reaction of transition metals, oxygen must commit the charge compensation to some extent. Oishi et al. studied O *K*-edge XANES as well as Ni, Co, and Mn *L*-edge XANES for the $Li_{1.16}Ni_{0.15}Co_{0.19}Mn_{0.50}O_2$ electrode, focusing on the reversible cycles after the initial high irreversible process [23]. Figure 23.8a shows O *K*-edge XANES spectra after first and second fully charged (4.8 V) and discharged (2.0 V) states. The spectra consists of a preedge structure (527–534 eV) and a broad structure above 534 eV. The former is associated with the transitions from O 1 s to hybridized states of O2p and metal 3d, while the latter with those from O 1 s to metal 4 s,p and O 2p hybridized states. Upon discharge, double bands at 536 and 540 eV appear. This is a typical feature of the octahedrally-coordinated metal oxides. The peak shift of the

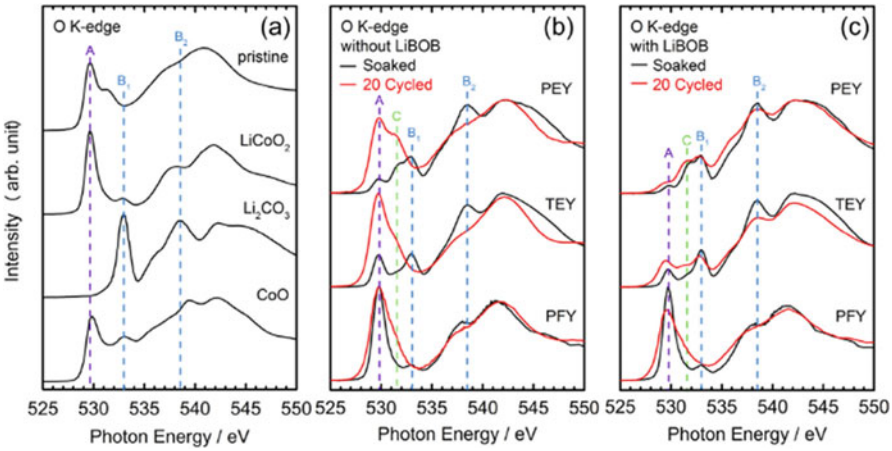

Fig. 23.7 O *K*-edge XANES spectra of the reference compounds: pristine $LiCoO_2$, Li_2CO_3, CoO powders (**a**), the soaked and 20 cycled $LiCoO_2$ electrode without (**b**) and with 0.1 wt% LiBOB (**c**). A, B(B_1,B_2), C are characteristic peaks of $LiCoO_2$, Li_2CO_3, and organic carbonyl, respectively. Reprinted from Ref. [21] with permission from Elsevier

main band toward lower energy reflects the metal-O bond lengthening by Li intercalation. Upon charge, the preedge peak is enhanced in both the first and second cycles.

Figure 23.8b shows the difference spectra between the charged and discharged states in the preedge region for first and second cycles. Peak A1 is due to the formation of the hole state at the charged state [24], while a newly appeared peak A2 might be associated with peroxide species, whose peak energy coincides with that of Li_2O_2 [25]. Although the presence of the peroxide species was proposed by XPS and ESR [26], the present experiment is the first direct observation of the peroxide species by O *K*-XAFS.

23.3.3 Combined Use of XAFS and XRD

XRD is a method for structural analysis, while XAFS provides information of valence and local structure around X-ray absorbing atoms. Thus, the combined use of XRD and XAFS is a powerful technique to study the atomic and electronic structures of the electrode, especially their changes during charge/discharge. Lithium iron phosphate ($LiFePO_4$) is an olivine-structured material and is known to be a promising cathode because of its high thermal and chemical stabilities, high charging rate, and low cost. Many research works have been focused on the elucidation of high rate performance, but its electronic and structural changes are very unique. Charge and discharge reactions proceed in a two phase manner between $LiFePO_4$(LFP) and $FePO_4$(FP) [9]. Leriche et al. [27] and Wang et al. [28] investigated the structural

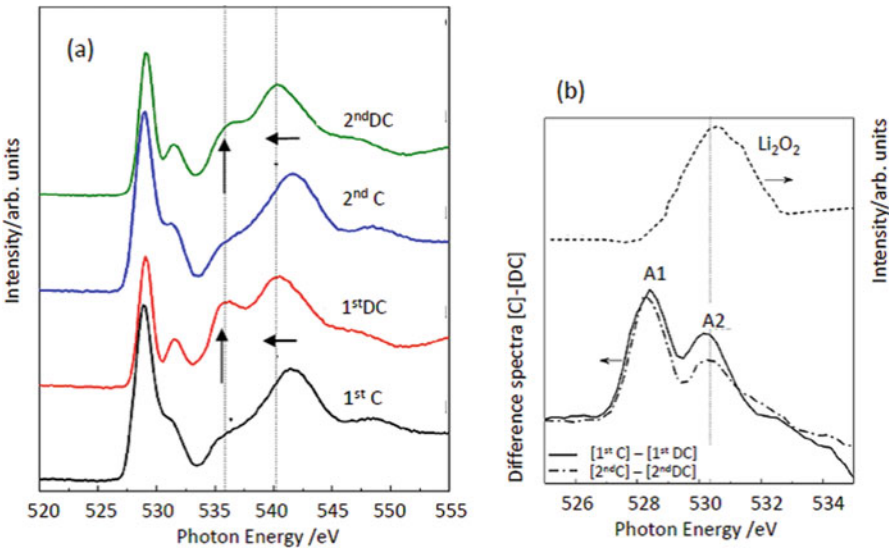

Fig. 23.8 O *K*-edge XAFS spectra during the first and second cycles with the TEY mode, in the wide range (**a**), and the difference spectra between charged and discharged states in the preedge region (**b**). C and DC stand for fully charged and discharged states, respectively. Reprinted from Ref. [23] with permission from Elsevier

changes of LFP upon charge by the combined use of in situ XRD and XAFS. However, these experiments are, in general, performed separately. To get full understanding of the changes for such a complicated electrode, simultaneous experiment of XRD and XAFS is desirable. By use of the beamline, described in the experimental section, Tokuda et al. studied the details of the correlation between the valence and structure upon charge [13].

With a rate of 1C, a XRD profile was taken at 7100 eV, just below the Fe *K*-edge, and Fe *K*-XANES spectrum was taken subsequently at each step. In situ XRD profiles and Fe *K*-XANES spectra are shown in Fig. 23.9a, b, respectively. Volume fractions of Fe(II) and Fe(III) were obtained from the XANES spectral analysis. Those of LFP and FP were also obtained from the LFP (020,211) and FP(211) and (020) in the XRD pattern, respectively. These volume fractions are plotted as a function of time, as shown in Fig.23.9c. Interestingly, there is some discrepancy between valence and structural changes, suggesting that the phase separation of LFP to FP is suppressed at the beginning of delithiation, while it is accelerated at the latter stage. This detailed information can be obtained since XRD and XAFS measurements are carried out at the same time in the same area of the sample.

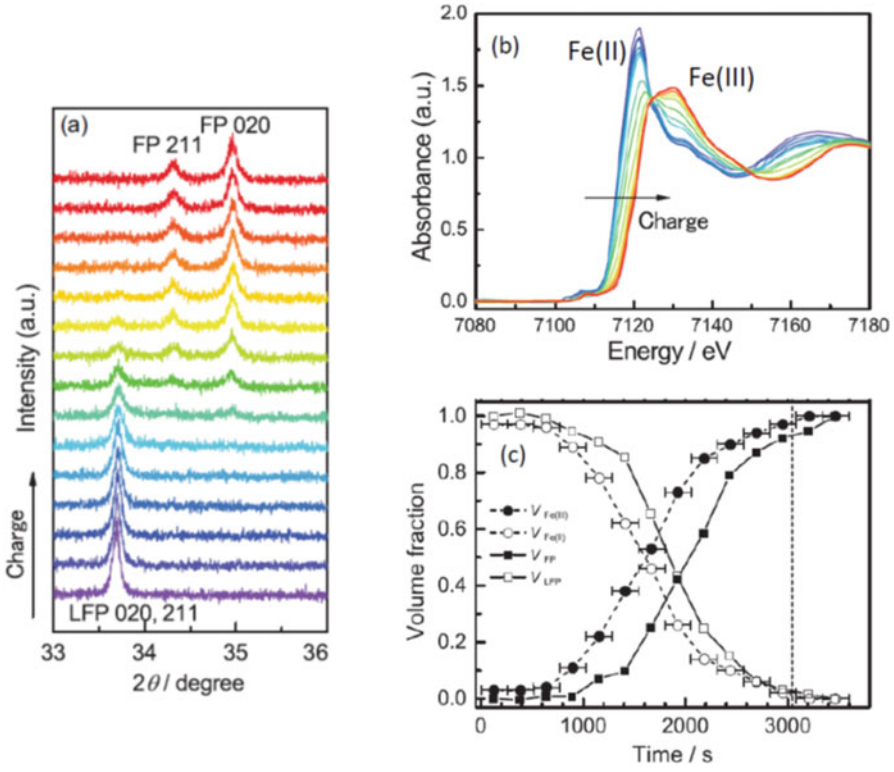

Fig. 23.9 In situ XRD profiles (**a**) and Fe *K*-XANES spectra (**b**) during the charge process of LFP. (**c**) The time evolution of the volume fractions of $V_{Fe(II)}$, $V_{Fe(III)}$, V_{LFP}, and V_{FP}. Reprinted from Ref. [13]. Copyright [2014], AIP Publishing LLC

23.3.4 Imaging XAFS

Imaging is a very impressive and effective technique and has been adopted in various methods, such as X-ray fluorescence analysis, photoelectron spectroscopy, X-ray diffraction, etc. In particular, imaging XAFS is a unique technique for the spatial analysis of a different oxidation state of transition metal species. Katayama et al. applied this technique to trace how charge/discharge of the LFP electrode proceeds [29]. With delithiation, LFP turns to FP, as described in the previous section. Fe(II) and Fe(III) can be easily discriminated by Fe *K*-XANES, as shown in Fig. 23.9b, and the distribution of Fe(III) can be regarded as the distribution of delithiation. Figure 23.10 shows the changes of the Fe(III) and Fe(II) distributions during two successive charge/discharge cycles. The charge/discharge proceeds inhomogeneously and, interestingly, the electrode reaction starts at the same spots in both the charge and discharge processes, and the redox reactions of the Fe species occur reversibly.

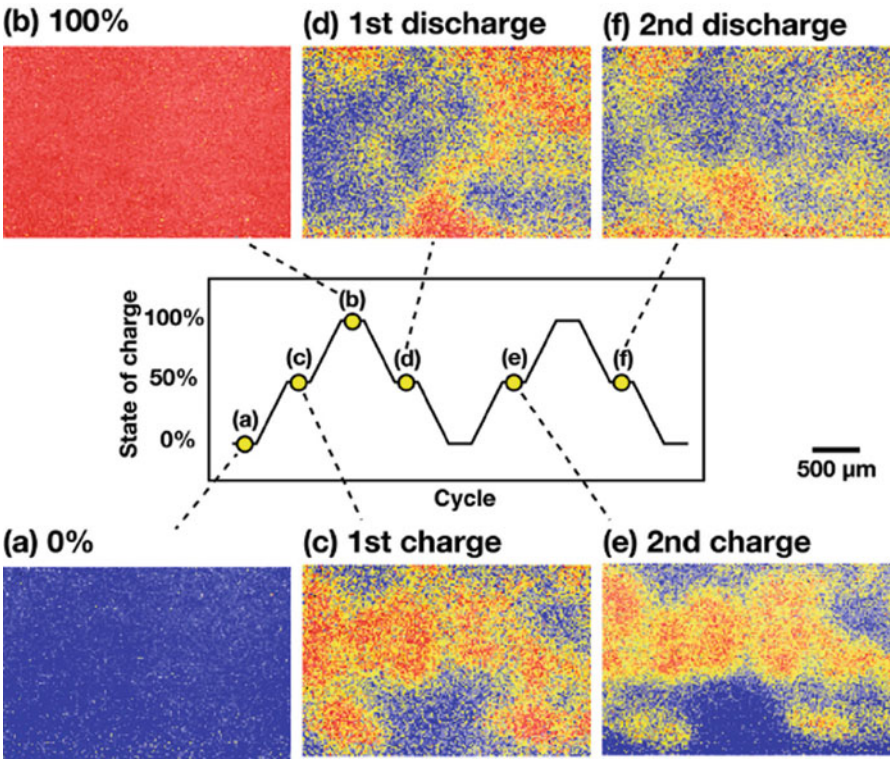

Fig. 23.10 Chemical state mapping obtained by the in situ XAFS imaging measurements during two successive LFP:FP charge/discharge cycles [29]. 100 % Fe(III) and 100 % Fe(II) are shown as *red* and *blue* colors, respectively

The maps of the first and second charge/discharge are similar to each other, indicating high reproducibility and reversibility of the inhomogeneous electrode reaction. Note that such inhomogeneous reactions are specific to the LFP electrode. Other electrodes exhibit other types of reactions, which must be related to local ion and electron conductions. This is a typical example to demonstrate how complicated the battery reactions are.

Acknowledgements Most of the works introduced in this review are those obtained in the RISING (Research & Development Initiative for Scientific Innovation of New Generation Batteries) project of NEDO (New Energy Development Organization) of Ministry of International Trade and Industry, Japan. The author appreciates great contributions by the members of the project, conducted by Profs. Z. Ogumi and Y. Uchimoto.

References

1. Tarascon J-M, Armand M (2001) Issues and challenges facing rechargeable lithium batteries. Nature 414:359–367
2. Yoon W-S et al (2003) In situ X-ray absorption spectroscopic study on $LiNi_{0.5}Mn_{0.5}O_2$ cathode material during electrochemical cycling. Chem Mater 15:3161–3169
3. Yabuuchi N et al (2011) Detailed studies of a high-capacity electrode materials for rechargeable batteries, Li_2MnO_3-$LiCo_{1/3}Ni_{1/3}Mn_{1/3}O_2$. J Am Chem Soc 133:4404–4419
4. Ito A et al (2011) In situ X-ray absorption spectroscopic study of Li-rich layered cathode material $Li[Ni_{0.17}Li_{0.2}Co_{0.07}Mn_{0.56}]O_2$. J Power Sources 196:6828–6834
5. Takamatsu D et al (2011) Nanoscale observation of the electronic and local structures of $LiCoO_2$ thin film electrode by depth-resolved X-ray absorption spectroscopy. J Phys Chem Lett 2:2511–2514
6. Takamatsu D et al (2012) First in situ observation of $LiCoO_2$ electrode/electrolyte interface by total-reflection x-ray absorption spectroscopy. Angew Chem Int Ed 51:11797–11601
7. Yamamoto K et al (2014) Improved cyclic performance of lithium-ion batteries: an investigation of cathode/electrolyte interface via in situ total reflection fluorescence X-ray absorption spectroscopy. J Phys Chem C 118:9538–9543
8. Tanida H et al (2011) In situ two-dimensional imaging quick-scanning XAFS with pixel array detector. J Synchrotron Rad 18:919–922
9. Katayama M et al (2012) Development of a two-dimensional imaging system of X-Ray absorption fine structure. J Synchrotron Radiat 19:717–721
10. Yu X et al (2012) High rate delithiolation behavior of $LiFePO_4$ studied by quick X-ray absorption spectroscopy. Chem Comm 48:11537–11539
11. Orikasa Y et al (2013) Phase transition analysis between $LiFePO_4$ and$FePO_4$ by *in situ* time-resolved X-ray absorption and X-ray diffraction. J Electrochem Soc 160:A3061–A3065
12. Katayama M et al (2015) New design of dispersive XAFS system for analysis of time-resolved spatial distribution of electrode reaction. J Synchrotron Radiat 22:1227–1232
13. Tokuda K et al (2014) Research update: retardation and acceleration of phase separation evaluated from observation of imbalance between structure and valence on $LiFePO_4$/$FePO_4$ electrode. App Phys Lett Materials 2:070701/1–070701/9
14. Stragier H et al (1992) Diffraction anomalous fine structure: a new X-ray structural technique. Phys Rev Lett 69:3064–3067
15. Kawaguchi T et al (2014) Revisit to diffraction anomalous fine structure. J Synchrotron Radiat 21:1247–1251
16. Kawaguchi T et al (2015) Roles of transition metals interchanging with lithium in electrode materials. Phys Chem Chem Phys 17:14064–14070
17. de Groot FMF (1994) X-ray absorption and dichroism of transition metals and their compounds. J Electron Spectrosc Relat Phenom 67:529–622
18. Yoon W-S et al (2005) Investigation of the charge compensation mechanism on the electrochemically Li-ion deintercalated $Li_{1-x}Co_{1/3}Ni_{1/3}Mn_{1/3}O_2$ electrode by combination of soft and hard X-ray absorption spectroscopy. J Am Chem Soc 127:17480–17487
19. Oishi M et al (2013) Charge compensation mechanisms in $Li_{1.16}Ni_{0.15}Co_{0.19}Mn_{0.50}O_2$ positive electrode material for Li-ion batteries analyzed by a combination of hard and soft X-ray absorption near edge structure. J Power Sources 222:45–51
20. Nakanishi K et al (2014) Novel spectro-electrochemical cell for in situ/operando observation of common composite electrode with liquid electrolyte by X-ray absorption spectroscopy in the tender X-ray region. Rev Sci Instrum 85:084103/1–084103/7
21. Yogi C et al (2014) Soft X-ray absorption spectroscopic studies with different probing depths: Effect of an electrolyte additive on electrode surfaces. J Power Sources 248:994–999
22. Lu Z, Dahn JR (2002) Understanding the anomalous capacity of Li / Li[NixLi (1/3-2x/3) Mn (2/3-x/3)] O2 cells using in situ X-ray diffraction and electrochemical studies. J Electrochem Soc 149:A815–A822

23. Oishi M et al (2015) Direct observation of reversible charge compensation by oxygen ion in Li-rich manganese layered oxide positive electrode material, $Li_{1.16}Ni_{0.15}Co_{0.19}Mn_{0.50}O_2$. J Power Sources 276:89–94
24. Mizokawa T et al (2013) Role of oxygen holes in Li_xCoO_2 revealed by soft X-ray spectroscopy. Phys Rev Lett 111:056404
25. Yilmaz E et al (2013) Promoting formation of non-crystalline Li_2O_2 in the Li-O_2 battery with RuO_2 nanoparticles. Nano Lett 13:4679–4684
26. Sathiya M et al (2013) Reversible anionic redox chemistry in high-capacity layered-oxide electrodes. Nat Mater 12:827
27. Leriche JB et al (2010) An electrochemical cell for *operando* study of lithium batteries using synchrotron radiation. J Electrochem Soc 157:A606–A610
28. Wang X-J et al (2011) Investigation of the structural changes in $Li_{1-x}FePO_4$ upon charging by synchrotron radiation techniques. J Mater Chem 21:11406–11411
29. Katayama M et al (2014) X-ray absorption fine structure imaging of inhomogeneous electrode reaction in $LiFePO_4$ lithium-ion battery cathode. J Power Sources 269:994–999

Chapter 24
Surfaces

Hiroshi Kondoh

24.1 Introduction

The XAFS spectroscopy has been applied to studies on local geometric and electronic structures of chemical species at surfaces. In this chapter, the contribution of the XAFS spectroscopy to surface science studies are described particularly paying attention to elucidation of the static structures of adsorbates and in-situ observation of surface dynamic processes.

In order to obtain surface-specific information, the electron-yield method is often used in many cases, which includes the total-electron-yield (TEY) method, the partial-electron-yield (PEY) method, and the Auger-electron-yield (AEY) method. Based on the dispersive mode the AEY method has been further upgraded so that the data acquisition time is reduced to be short enough to trace reaction kinetics at surfaces [2]. The electron-yield methods are also used for NEXAFS measurements of surface species under near ambient pressure conditions, which allow us to study surface processes exclusively taking place under near ambient pressure conditions such as catalytic reactions under near realistic conditions [3].

In the case where a specific element is segregated at a surface, the fluorescence-yield (FY) method is also used for collecting surface-specific information [4]. In particular, XAFS spectra for elements heavier than the second period of the periodic table are often measured by the FY method due to the higher probability for the fluorescence decay. The FY method is useful to study surface species under ambient pressure conditions via the photon-in-photon-out measurement. It has been applied to NEXAFS measurements for surface reactants under high-pressure conditions including light-element reactants like CO adsorbed on a model catalyst [5]. Recently, the photon-in-photon-out measurement is further used in

H. Kondoh (✉)
Department of Chemistry, Keio University, Yokohama 223-8522, Japan
e-mail: kondoh@chem.keio.ac.jp

Y. Iwasawa et al. (eds.), *XAFS Techniques for Catalysts, Nanomaterials, and Surfaces*, DOI 10.1007/978-3-319-43866-5_24

operando XAFS measurements together with X-ray emission spectroscopy measurements under working conditions [6].

Having an overview of the previous application studies of XAFS to surfaces, they can be divided into two categories: elucidation of the static structures of adsorbates and in-situ observation of surface dynamic processes. Therefore, this section is organized as follows: in the former half part (Sects. 24.2–24.4), the XAFS studies on the static structures of adsorbates are introduced from the following three viewpoints; (1) surface geometric structures, (2) surface electronic structures, and (3) characterization of surface-specific species. While in the latter half part (Sects. 24.5–24.7) the in-situ observations of surface dynamic processes are mentioned from the following three viewpoints; (1) dispersive-NEXAFS, (2) ambient-pressure NEXAFS, and (3) future perspective.

24.2 Surface Geometric Structures

The XAFS spectroscopy has the capability to determine structural parameters around the X-ray absorbing atom such as coordination distance, coordination number, and Debye-Waller factor. In addition to that, if polarization dependence is measured for a well-ordered surface system, we can obtain further information on bond angles from the absorbing atom to the surrounding atoms and thus on the adsorption site on the surface. This kind of structural information is quite useful to understand geometrical structures of adsorbates particularly with complicated structures as seen in the following example.

The self-assembled monolayer (SAM) of alkanethiolate molecules on Au(111) surfaces is one of prototypical SAMs of organic molecules on metal surfaces. Since the lattices formed by organic molecules are usually largely different from those of metal surfaces, they have to reconcile the large lattice mismatch between the metal surface and the organic layer to achieve self-assembly. In order to understand how organic molecules reduce strain caused by the lattice mismatch, the structure of hexanethiolate ($C_6H_{13}S$) SAMs on a Cu(100) surface has been studied in detail by combination of C K-edge and S K-edge XAFS spectroscopies [7]. STM observations for the hexanethiolate monolayer on Cu(100) revealed that the self-assembling process at the $C_6H_{13}S$-Cu interface takes a prolonged time (>10 h). Fourier transforms of S-K EXAFS oscillations for the hexanethiolate monolayer taken before and after self-assembly are shown in Fig. 24.1. Quantitative analyses for the S-Cu_n shells ($n = 1$–3) indicated that the sulfur atom of the thiolate is located at the four-fold hollow site of the unreconstructed Cu(100) surface irrespective of self-assembly as illustrated in the structure model (insets). Although no drastic change is observed between before (top) and after (bottom) self-assembly, it is discernible that a new peak appears at around 3.2 Å in the normal incidence after self-assembly, which is attributed to contribution from the nearest-neighbor (NN) sulfur atoms. Curve-fitting analyses for this peak reveal that the NN sulfur

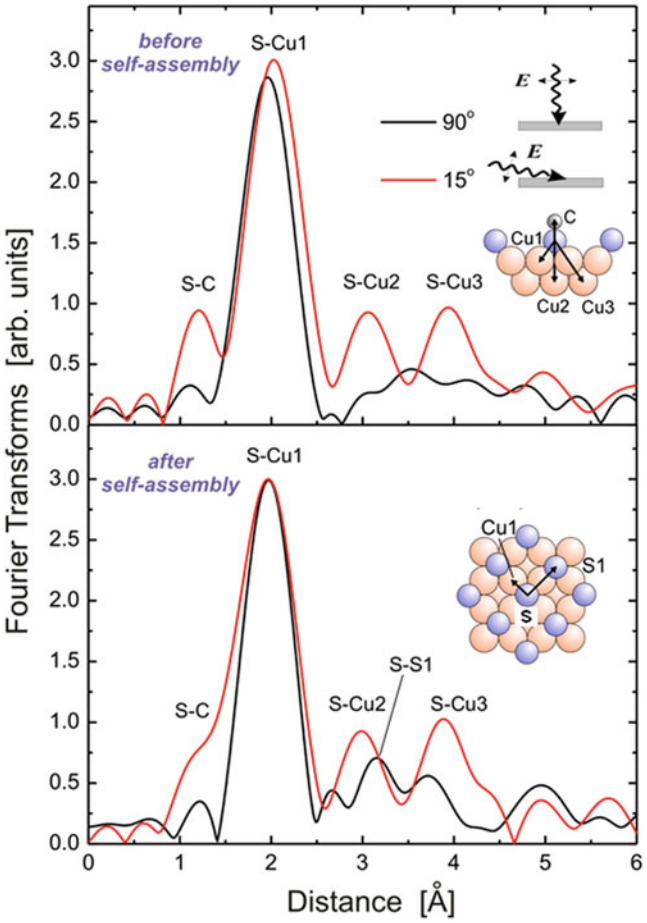

Fig. 24.1 Fourier transforms of S-K EXAFS oscillation for a hexanethiolate monolayer on Cu (100) before (*top*) and after (*bottom*) self-assembly. Adapted with permission from Ref. [7]. Copyright 2001, American Chemical Society

atoms are located at a distance of c(2 × 2) lattice (S1 in the inset). The absence of the 3.2 Å peak before self-assembly implies disordering of the S atoms on the Cu surface, though the polarization dependence of C-K NEXAFS spectra indicated that the molecular axes of hexanethiolates are well aligned along the direction tilted by 30° on average from the surface normal before self-assembly. Therefore, the hexanethiolates rapidly form a well-aligned but 2D-disordered monolayer with randomly occupying the hollow sites. This rapid process is followed by slow evolution of the 2D-ordered structure via surface diffusion. Combination of the EXAFS results and force field calculations revealed that a large lattice mismatch between the sulfur layer and the alkyl-chain layer (31 % max) is effectively reduced (7 % max) by tilting half of the S-C bonds that bridges the two layers (37° from the

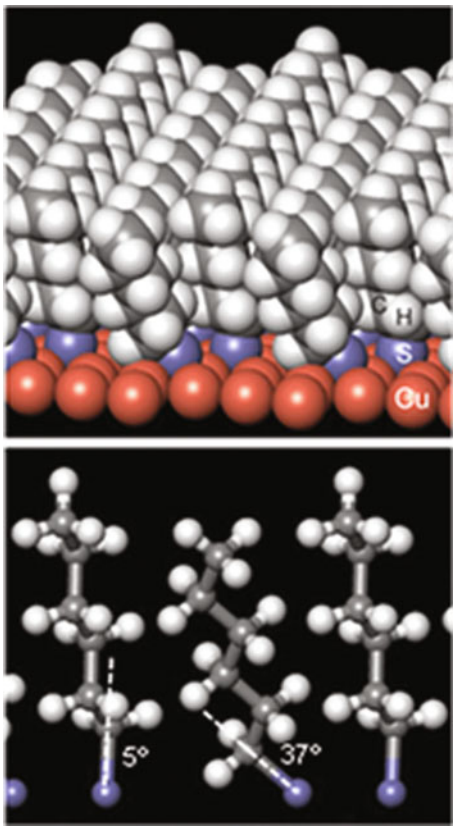

Fig. 24.2 Structure model of the hexanethiolate self-assembled monolayer on Cu (100) determined by combination of the XAFS results and the molecular force-filed calculation. (*top*) bird's-eye view. (*bottom*) side view. Adapted with permission from Ref. [7]. Copyright 2001, American Chemical Society

surface normal), as shown in Fig. 24.2. The S-C bond tilting is observable as a decrease in polarization dependence of the S-C shell in the S-K XAFS spectra after self-assembly. Thus, the XAFS spectroscopy measurements provide detailed structural information that evidences that the lattice mismatch of the molecule/metal system is effectively accommodated by the internal degree of freedom of the molecule, resulting in self-assembly of the molecules.

24.3 Surface Electronic Structures

In XAFS measurements core electrons of a particular element are excited to unoccupied states. Since the core electrons are localized near atomic nuclei of the element, the XAFS spectra provide information on local density of states of unoccupied states around the photon-absorbing atoms. Thus, the XAFS spectroscopy enables us to detect unoccupied states localized specifically at surfaces, if the photon-absorbing atoms are segregated at the surfaces.

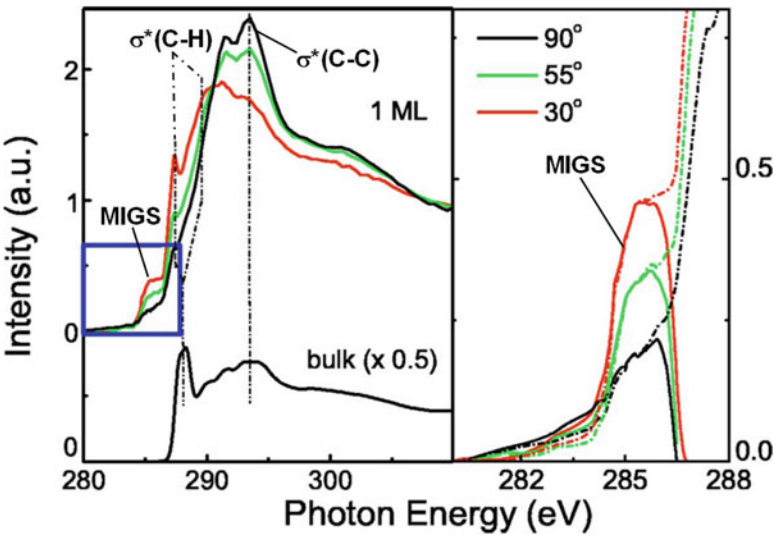

Fig. 24.3 C K-edge NEXAFS spectra for 1 ML $C_{44}H_{90}$ (TTC) films grown on Cu(100) taken with different incidence angles together with the result for a multilayer TTC on Cu(100). All the spectra are normalized by their edge jump. *Right-hand* panel shows the pre-peaks on a magnified scale, obtained by subtracting the bulk multilayer spectrum that has no structures at the edge onset. Adapted with permission from Ref. [8]. Copyright 2005, American Physical Society

On the basis of this approach, an unoccupied state localized at one-monolayer-thick films of saturated hydrocarbon molecules ($C_{44}H_{90}$) adsorbed on a Cu metal surface was identified by C K-edge NEXAFS spectroscopy as shown in Fig. 24.3 [8]. The NEXAFS spectrum of $C_{44}H_{90}$ bulk exhibits two prominent peaks associated with excitations of C 1s electrons to σ*(C-H) and σ*(C-C) unoccupied states (see Fig. 24.3, left bottom). In the case of the monolayer, however, the σ*(C-H) transition appears as two split shoulders as seen in Fig. 24.3 (left bottom). This splitting was attributed to a difference in interaction of the C-H bonds with the metal surface [9]. Since the saturated hydrocarbons are adsorbed with a flat-lying configuration with the –C-C- backbone plane being parallel to the surface, the C-H bonds of the hydrocarbons are classified into two, i.e., directing upward and downward, resulting in different interactions of the σ*(C-H) states with the surface. The flat-lying configuration in the present system $C_{44}H_{90}$/Cu(100) is supported by the incidence angle dependence of the NEXAFS spectra; the σ*(C-C) peak is most enhanced in the normal incidence (90°), while the σ*(C-H) features become most intense in the grazing incidence (30°). This polarization dependence is consistent with the flat-lying configuration with the backbone plane parallel to the surface as illustrated in Fig. 24.4 (top left). It should be noted that the monolayer spectra in Fig. 24.3 exhibit a pre-peak at 285.5 eV, which is absent in the bulk spectrum. This feature is attributed to a metal-insulator gap state (MIGS) that is spatially localized at the hydrocarbon monolayer on the Cu(100) surface, as shown in Fig. 24.4 (bottom left) [8].

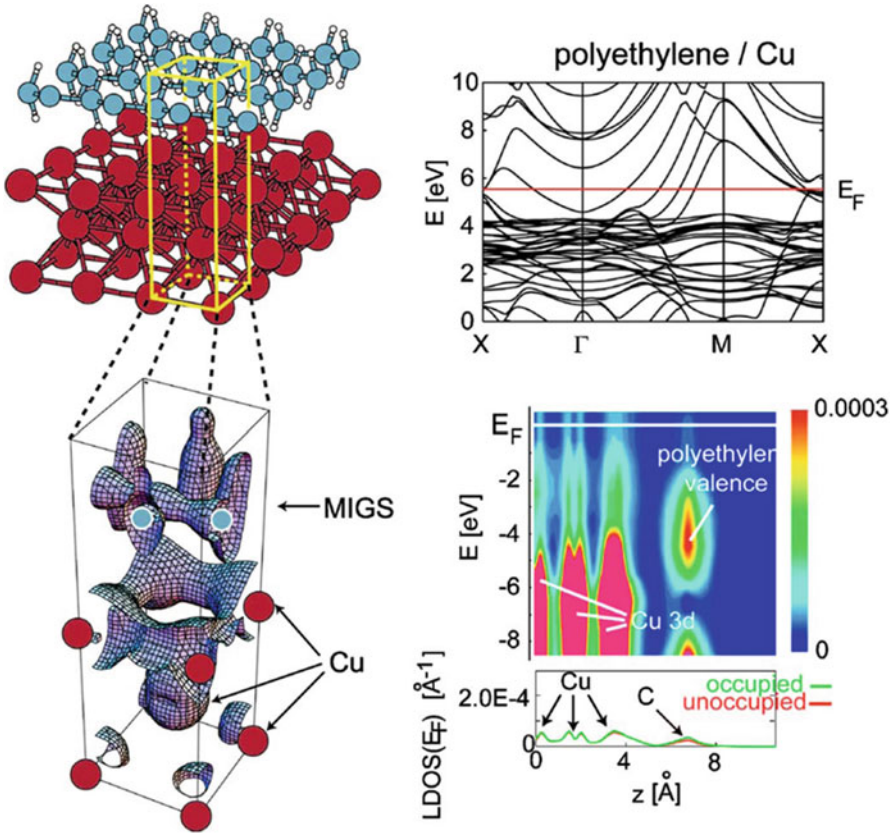

Fig. 24.4 DFT calculation results for the band structure of 1 ML polyethylene/Cu(100). Top *left-hand inset* is the atomic configuration considered here, where Cu is in *red*, C is in *gray*, and H is in *white*. *Bottom left-hand* side is a contour plot of the wave function at E_f. *Bottom right-hand inset* shows local density of states (LDOS) as a function of z and energy and the LDOS at $E_F = -0.125$ eV (occupied) and $E_F = +0.125$ eV (unoccupied) integrated over the xy plane, as a function of z. Reproduced with permission from Ref. [8]. Copyright 2005, American Physical Society

The density-functional theory (DFT) calculations for polyethylene/Cu(100) indicate that the wave function of the MIGS is distributed perpendicularly to the surface at the hydrocarbon layer as seen in Fig. 24.4 (bottom left), which is consistent with the polarization dependence of the pre-peak shown in Fig. 24.3 (left). The DFT calculations further indicate that the local density of state (LDOS) at the Fermi level shows a clear peak at the hydrocarbon level as shown in Fig. 24.4 (bottom right), although the saturated hydrocarbon (polyethylene) is a wide band-gap insulator and has no LDOS at the Fermi level. This newly appearing LDOS at the hydrocarbon-insulator/metal interface is explained by penetration of Cu 4s free-electron-like wave functions to the hydrocarbon layer and hence the pre-peak is

attributed to the MIGS [8]. The MIGS has been found also for LiCl-insulator/metal interfaces using Cl K-edge NEXFAS spectra [10]. Thus, the XAFS spectroscopy can reveal unoccupied LDOS localized at surfaces, when the photon-absorbing atoms are located exclusively at the surfaces.

24.4 Surface-Specific Species

The XAFS spectroscopy is used for characterization of surface-specific species that are formed exclusively at surfaces. Novel species with unusual chemical bonds could be formed at surfaces via interactions with surface atoms. Although identification of such species is not straightforward, surface vibrational spectroscopies like infrared reflection absorption spectroscopy (IRAS) and high-resolution electron energy loss spectroscopy (HREELS) sometimes play a role in understanding the structures of the surface species. The XAFS spectroscopy is another powerful probe to obtain chemical information of the surface species via probing unoccupied states. Excitations to π^* and σ^* orbitals of diatomic molecules such as O_2, for instance, provide information about interactions of the molecules with the surfaces; O K-edge NEXAFS spectra for O_2-adsorbed metal surfaces at 100 K revealed that O_2 molecules are adsorbed in the form of a peroxo species on Ag(110) and a superoxo species on Pt(111) [11]. Particularly unusual molecular adsorbates can be identified by comparison with theoretical simulations. For example, heteroaromatic molecules such as thiophene (C_4H_4S) adsorbed on Pt and Pd metal surfaces could form metallacycle species where the hetero atom (sulfur) is replaced by a metal atom resulting in the formation of an aromatic ring including the metal atom as a ring member (C_4H_4M, M = Pt, Pd). This surface species has been identified by a good agreement between the observed C-K NEXAFS spectra and simulated ones based on the Xα multiple-scattering calculation [1].

Solid surfaces sometimes stabilize unstable species. The NO dimer, $(NO)_2$ with a planer *cis*-O = N-N = O geometry, is one of examples for such unstable species due to the weak N–N bond (dissociation energy: 2.0 kcal/mol). The NO dimer has been observed on inert surfaces such as Cu, Ag, graphite, and NO/Rh(111) at low temperatures. For the last surface (NO/Rh(111)), the NO dimer layers were grown on a NO monomer layer formed on Rh(111). Based on a core-excited state molecular orbital calculation, peaks in the pre-edge regions of N K-edge and O K-edge NEXAFS spectra for $(NO)_2$/NO/Rh(111) were assigned and the molecular orientations of the second layer and multilayers of the NO dimer were deduced from the polarization dependence and the peak assignments [12].

Figure 24.5a shows N K-edge NEXAFS spectra for the monolayer of NO adsorbed on Rh(111) with different incidence angles from the surface parallel. The π^* peak is the most enhanced at the normal incidence (90°), while the σ^* peak appears the most intense at the grazing incidence (15°), which clearly indicates that the NO molecules are vertically adsorbed. The NEXAFS spectra for the multilayers of NO exhibit totally different curves in the pre-edge region due to the formation of

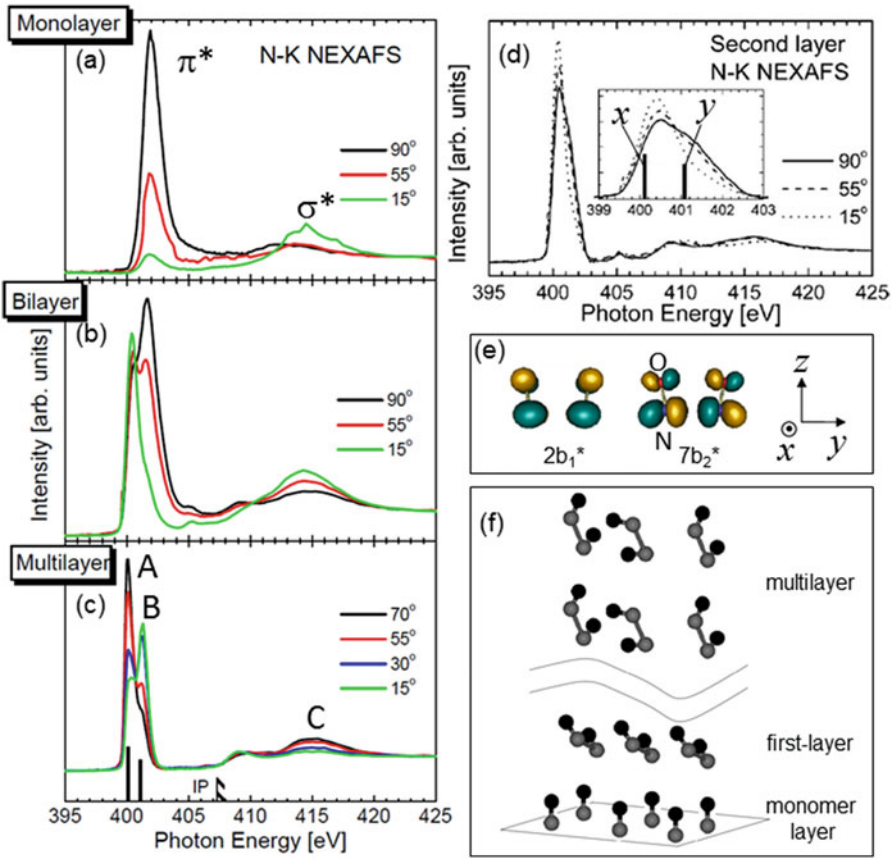

Fig. 24.5 N K-edge NEXAFS spectra taken for the monolayer (**a**), bilayer (**b**), and multilayers (**c**) of NO adsorbed on Rh(111). At the bottom of (**c**), calculated results for the pre-edge region and the ionization potential of the gas-phase *cis*-$(NO)_2$ are indicated by vertical lines. (**d**) the second-layer spectra obtained by subtraction of the monolayer spectra (**a**) from the bilayer ones (**b**). *Inset*: observed and calculated spectra in the pre-edge region on a magnified scale. (**e**) Unoccupied molecular orbitals with large oscillator strengths for the N 1s core excitation. (**f**) Structure model for the NO dimer layers formed on the NO monomer layer. The molecular orientation of the multilayers of NO dimer resembles that of a two-dimensional layer in the bulk crystal of the NO dimer, while the first layer of the NO dimer exhibits a largely different orientation probably due to interaction with the NO monomer (see the text). Adapted with permission from Ref. [12]. Copyright 2007, American Institute of Physics

the NO dimer as shown in Fig. 24.5c. From the molecular orbital calculations, the prominent peaks A and B can be attributed to excitations to $2b_1^*$ (π^*(N-O)) and $7b_2^*$ (σ^*(N-N)) unoccupied orbitals, respectively, which have the transition moments lying along the *x* and *y* directions, respectively, as shown in Fig. 24.5e. Figure 24.5d shows NEXAFS spectra for the second layer obtained by subtraction of the first

monomer layer spectra from the bilayer spectra. Two components with different polarization dependence in the pre-edge region can be associated with the two unoccupied orbitals of the NO dimer $2b_1^*$ (x) and $7b_2^*$ (y) as shown in the inset. Interestingly, there are clear differences in the polarization dependence between the second layer and multilayers of the NO dimer. From the detailed analyses for the polarization dependence, it was found that the N–N bonds in the multilayers are aligned near vertically (tilted by $37 \pm 5°$ from the surface normal), while those in the second layer are more tilted from the surface normal ($66 \pm 5°$) [12]. The molecular plane in the second layer is also more inclined to the surface parallel compared to that in the multilayers. The molecular orientation in the multilayers is similar to that in a two-dimensional layer of the bulk crystal of the NO dimer where both the N–N bond and the molecular plane are aligned perpendicularly to the layer. The inclined geometry of the N–N bond and the molecular plane to the surface in the second layer is caused by interactions with the NO monomer layer; since the LUMO ($2b_1^*$) is aligned along the out-of-plane direction of the NO dimer and has a strong electrophilic character [13], the interaction with the HOMO (π^*) of the NO monomer layer could be maximized by the inclined geometry.

24.5 Observation of Surface Dynamic Processes by Dispersive-NEXAFS

The NEXAFS measurements usually require a fairly long data acquisition time, typically several hundreds seconds per spectrum, due to scanning of the monochromator. This prevented from applying the NEXAFS technique to tracing of the progress of surface dynamic processes such as catalytic surface reaction and film growth. However, by the use of wavelength-dispersed X rays and a spatially resolved electron energy analyzer, auger-electron-yield NEXAFS spectra can be obtained in one shot without scanning of the monochromator as illustrated in Fig. 24.6. This approach enabled recording NEXAFS spectra with a data acquisition time of 30 sec/spectrum at the first stage of development [2] and approximately 10 years later it has reached 33 ms/spectrum [14]. With this technique (dispersive-NEXAFS), the kinetics of catalytic surface reaction can be traced continuously in the real-time manner if the time scale of the kinetics is of the order of second or subsecond. The dispersive-NEXAFS has been applied to elucidation of the mechanisms of prototypical catalytic reactions on metal surfaces such as CO oxidation on Pt(111) [15, 16], H_2O formation on Pt(111), and NO reduction on Rh(111) [17, 18].

Figure 24.7a, b shows time evolution of O K-edge dispersive-NEXAFS spectra taken for O-precovered Pt(111) surfaces under CO oxidation conditions at different temperatures (252 and 350 K) [15, 16]. Each spectrum was curve-fitted to estimate the O and CO coverages and the resultant coverage changes are plotted as a function of time as shown in Fig. 24.7c, d. The reaction proceeds obviously faster at the

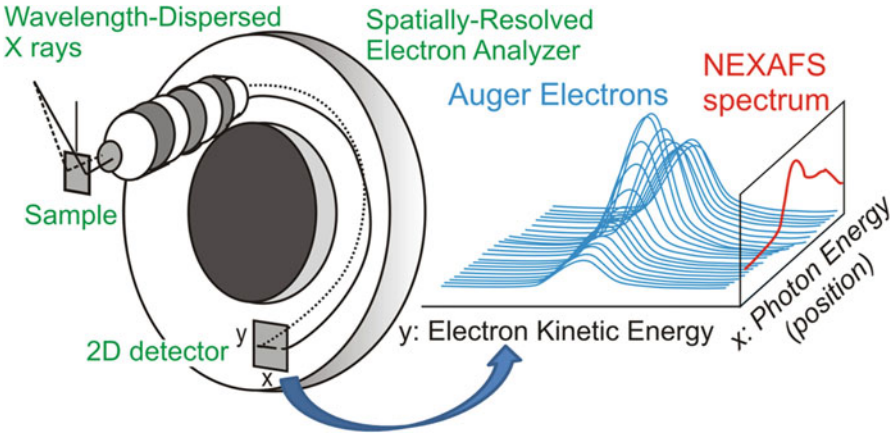

Fig. 24.6 Schematics for the principle of the wavelength-dispersed NEXAFS. Adapted with permission from Ref. [2]. Copyright 2002, Elsevier

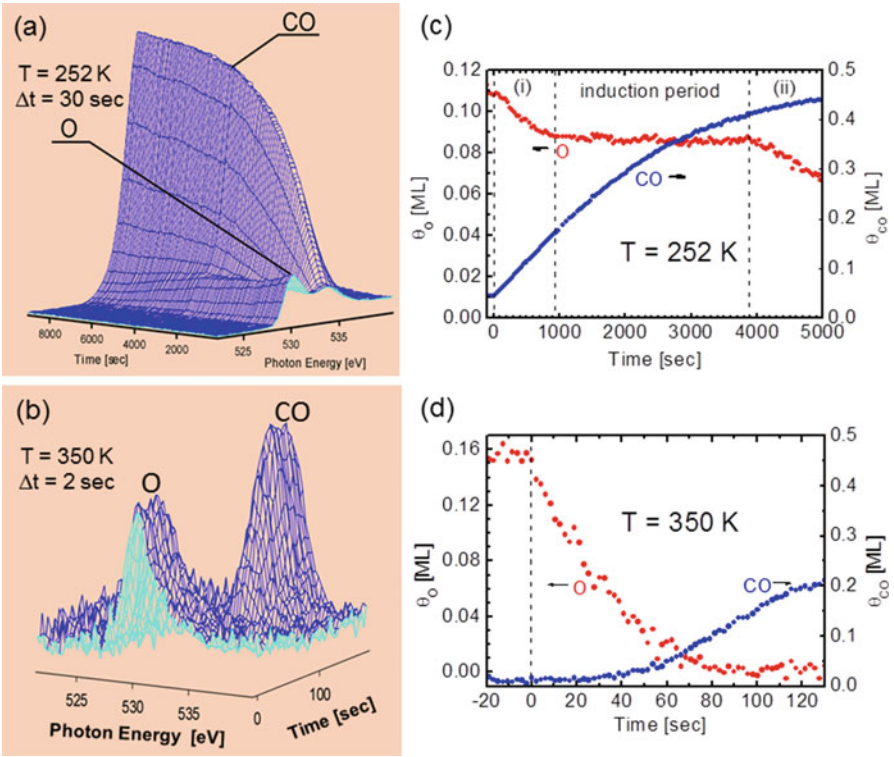

Fig. 24.7 Dispersive-NEXAFS spectra taken for O-precovered Pt(111) surfaces under CO oxidation reaction conditions at 252 K (**a**) and 350 K (**b**) with a data acquisition time for each spectrum of 30 s and 2 s, respectively. The O and CO coverages under the reaction conditions estimated from (**a**) to (**b**) with *curve fitting* analyses are shown in (**c**) and (**d**), respectively. Adapted with permission from ref. [15, 16]. Copyright 2004 and 2005, American Institute of Physics

higher temperature and interestingly the reaction kinetics is largely different between the two temperatures; at 252 K an induction period is clearly observed from 1000 to 4000 s, where no surface oxygen atoms are consumed by the CO oxidation reaction. As a consequence, the time course of the reaction at 252 K can be divided into three periods, (i), induction period and (ii) as indicated by the vertical dashed lines. Furthermore, reaction-order analyses revealed that the reaction at period (i) obeys the first-order reaction kinetics with respect to the available O coverage, while that at period (ii) exhibits the half-order kinetics for the O coverage. The reaction at 350 K appears a single process with the first-order kinetics. The first-order and the half-order kinetics can be attributed to CO oxidation by isolated (diffusing) oxygen atoms and peripheral atoms of oxygen islands, respectively [15, 16]. Thus, the dispersive-NEXAFS enables us to trace the progress of the surface reaction with respect to time evolution of the reactant coverages and hence to analyze the reaction kinetics quantitatively, which provides important kinetic parameters such as activation energy, prefactor, and reaction order.

Since the dispersive-NEXAFS measurements are performed in an in-situ manner under reaction conditions, it provides an opportunity to find a reaction intermediate if it is a stable and long-lived species. Such a case was found for N + NO reaction on Rh(111). Figure 24.8a shows N K-edge dispersive-NEXAFS spectra for an N-precovered Rh(111) surface under NO exposure at 70 K and Fig. 24.8b depicts peak deconvolution of a dispersive-NEAXFS spectrum [18]. During the course of the NO exposure, a new component starts to appear concomitantly with the ignition of the N + NO reaction. The new component can be attributed to a NO dimer species from the spectral resemblance. The NO dimer species could be formed as the second-layer species as mentioned in Sect. 24.4. According to the density functional theory calculations for the NO dimer on N-precovered Rh(111) surfaces, it can attack surface N due to an electrophilic character of the LUMO and yield N_2O into the gas-phase with remaining NO on the surface as illustrated in Fig. 24.8c [18]. The NO dimer may play a role of a reaction precursor, although it cannot be completely excluded that it exists as a spectator. Isotope-controlled experiments and results of reaction kinetics analyses support the contribution of the NO dimer as a precursor. Therefore, as demonstrated by this example, the in-situ observations with the dispersive-NEXAFS spectroscopy opened an avenue to access reaction intermediates at surfaces formed under reaction conditions.

24.6 In-Situ Ambient-Pressure NEXAFS Observation of Surfaces

The NEXAFS spectroscopy using the electron-yield methods is surface-sensitive due to detection of electrons emitted from the surfaces. However, the emitted electrons undergo inelastic scattering by gas-phase species and the electron-detecting devices such as channeltron and microchannel plate cannot work under

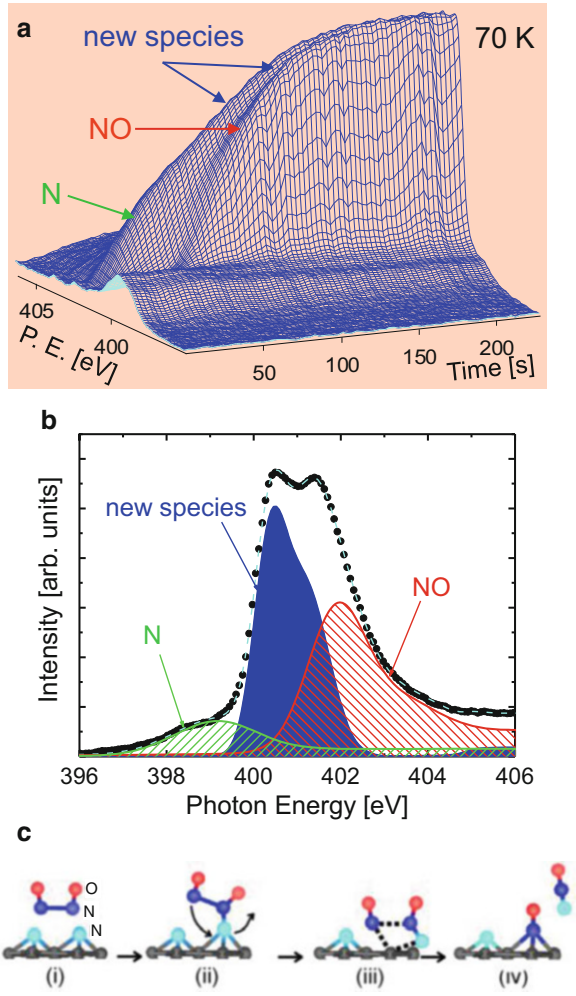

Fig. 24.8 (**a**) Dispersive-NEXAFS spectra taken for N-precovered Rh(111) surfaces under NO exposure at 70 K. (**b**) Deconvolution of a dispersive-NEXAFS spectrum into three components. (**c**) Reaction model for NO reaction with surface N via a $(NO)_2$ precursor. Adapted with permission from Ref. [18]. Copyright 2009, American Chemical Society

high-pressure conditions. The upper limit of pressure allowed for gas dose during measurements of the electron-yield NEXAFS spectra is typically of the 10^{-5} Torr order. This is obviously much lower than the ambient pressure, even though practical devices such as butteries and industrial catalysts are usually working under ambient-pressure and even higher pressure conditions, which is regarded as a problem of pressure gap. To bridge this gap, much effort has been dedicated to develop an ambient-pressure-compatible NEXAFS spectroscopy (AP-NEXAFS) [19–22].

Figure 24.9 (up right) shows an illustration for the experimental setup for the AP-NEXAFS technique using two TEY collection electrodes with a thin polyimide X-ray window [21]. The first electrode with a grid is biased at zero or negatively (> -15 V) and used for collection of auger electrons from gas-phase species (I_{gas}),

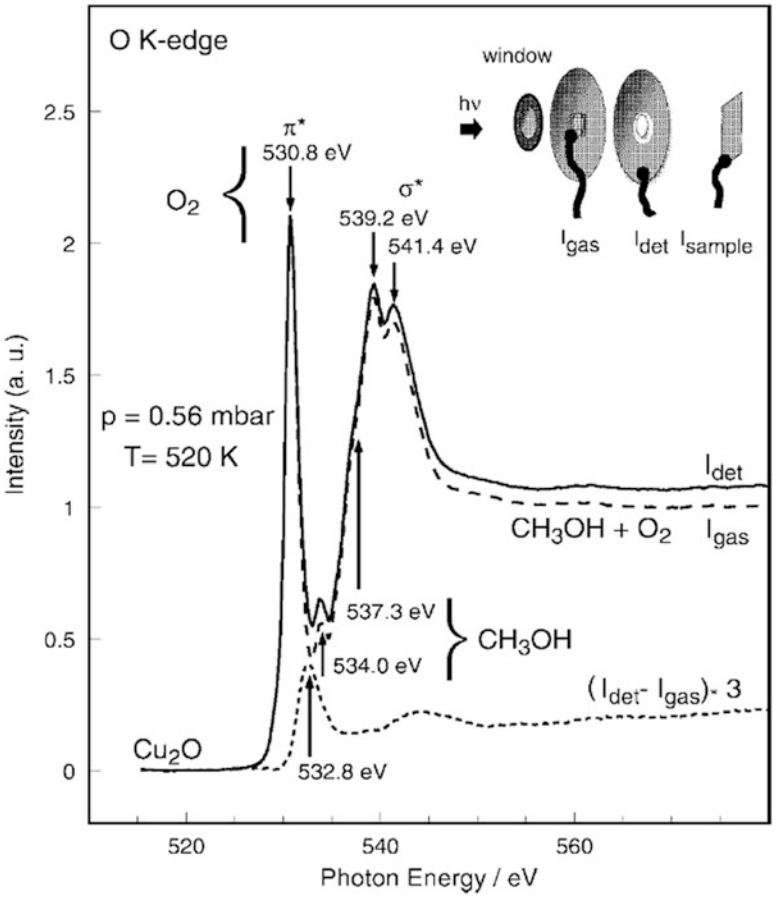

Fig. 24.9 Schematics for the TEY AP- NEXAFS setup (*up right*) and actual signals collected with I_{gas} and I_{det} electrodes (*middle*) and a difference spectrum (*bottom*) under a methanol oxidation condition (0.56 mbar, 520 K) on a Cu catalyst. Reproduced with permission from Ref. [21]. Copyright 2001, Elsevier

while the second electrode with a hole is positively biased (< +40 V) and detects electrons from both the gas-phase species and the sample surface (I_{det}) [19]. The photo-induced current of the sample was measured without applying bias voltage as a sample current (I_{sample}), which exhibited a photon-energy-dependent curve similar to that for I_{det} [19]. With this setup I_{det} and I_{gas} were measured for a Cu catalyst at 520 K under exposure to O_2/CH_3OH mixed gas at 0.56 mbar as a function of photon energy as shown in Fig. 24.9 (middle). Subtraction of I_{gas} from I_{det} after intensity normalization at the energy of the π* resonance of O_2 gas yields an O K-edge NEXAFS spectrum from the Cu catalyst surface under the reaction condition, as shown in Fig. 24.9 (bottom) [21]. Since the contribution from the gas-phase

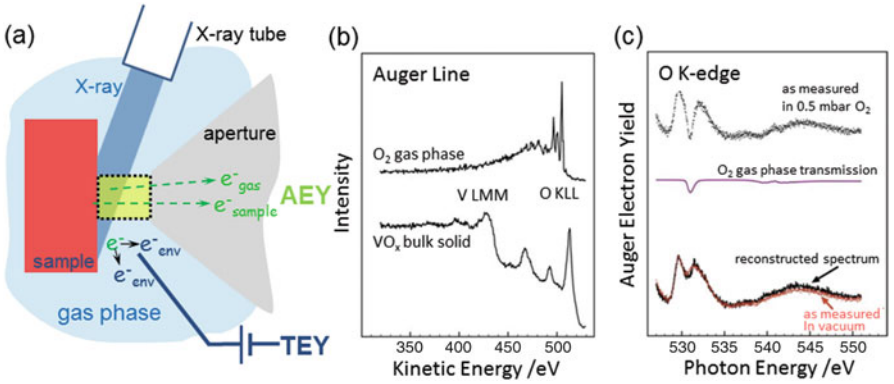

Fig. 24.10 (**a**) Schematics for the AEY AP-NEXAFS setup using a near-ambient-pressure compatible analyzer with a X-ray tube and a TEY collection electrode. (**b**) Actual auger electron spectra taken for O_2 gas phase (*upper*) and VO_x bulk solid (*lower*). (**c**) Raw O K-edge AEY AP-NEXAFS spectrum for the VO_x solid measured in 0.5 mbar O_2 (*top*), O_2 gas phase transmission (*middle*), and reconstructed NEXAFS spectrum together with spectrum measured in vacuum. Adapted with permission from Ref. [22]. Copyright 2009, Springer

species to the signals recorded with the TEY collection electrodes is dominant, the subtraction is indispensable to extract the contribution from the sample surface.

To avoid the gas-phase contribution the use of the electron-energy analyzer is sometimes effective, because the Auger electron spectra from the gas phase and the sample surface exhibit different kinetic-energy dependence and hence allow us to distinguish the contributions from the two phases. Furthermore, the electron-energy analyzer has been upgraded so that XPS spectra can be measured under near ambient pressure conditions by using a differential pumping system with electrostatic lenses [23]. This type of analyzer has been applied to measurements of AP-NEXAFS spectra with the AEY mode [22]. Schematics for the AEY AP-NEXAFS setup and actual auger electron spectra from sample exhibits a step-like increase in background intensity at the lower kinetic energies from the primary Auger peak due to multiple inelastic scattering in the solid, while the O_2 gas phase shows a more concentrated intensity at around the primary Auger peak. This enables us to enhance the sample surface-related signal more than the gas-phase-related one by choosing the kinetic energy window properly. A resultant surface-sensitive AEY AP-NEXAFS spectrum from the VO_x sample measured in 0.5 mbar O_2 is depicted in Fig. 24.10c (top). Apparently several dips are seen in the spectrum, which is caused by absorption of X-rays by O_2 gas phase as confirmed by the O_2 gas phase transmission spectrum taken with the TEY collection electrode shown in Fig. 24.10c (middle). A NEXAFS spectrum reconstructed by the transmission spectrum is shown in Fig. 24.10c (bottom) and is in good agreement with a spectrum measured in vacuum. These experimental results demonstrate that the AEY AP-NEXAFS technique has the capability to obtain nondistorted NEXAFS spectra from sample surfaces under the presence of near ambient pressure gas(es).

24.7 Future Perspective

Time-resolved experiments using the dispersive-NEXAFS technique will contribute to elucidation of molecular-level mechanisms of surface dynamic processes. In 2011, NEXAFS spectra from submonolayer adsorbates could be obtained every 33 ms continuously [14] and recently the data acquisition time has been further reduced to 333 μs/spectrum. Irreversible surface processes such as adsorption and desorption can be monitored at a submillisecond timescale continuously. If the dispersive-NEAXFS data acquisition is conducted for a repeatable surface process and synchronized with a single X-ray pulse from a single-electron bunch, the time resolution of NEXAFS reaches the X-ray pulse width, i.e., several tens picosecond. Photo-induced surface phenomena such as photo-stimulated desorption and photocatalytic surface reaction are possible targets to be studied with the time-resolved NEXAFS spectroscopy.

Spatially resolved NEXAFS experiments have been performed by a micro- or nano-beam focused with a KB mirror or a zone plate. Beam damages induced by the focused beam prevent further improvement of spatial resolution. The X-ray photoemission electron microscope technique is also suitable to NEXAFS microscopy for surface species. To improve the spatial resolution the scanning probe microscopy technique has been combined, where the scanning probe is used as a detector of X-ray absorption-induced responses. Since it requires a prolonged time to take a NEXAFS microscopy image, application to surface dynamic processes needs a breakthrough to achieve a much higher efficiency to detect position and energy-dependent responses to irradiation of X rays.

The in-situ NEAFS spectroscopy for surfaces is still under upgrading and expanding the expected application area. Particularly in the fields of catalysts and power devices, in operando observations of surfaces of functional materials under working conditions are becoming more important to understand the mechanism and improve their performances. In this sense, the emerging in-situ NEAFS spectroscopy for surfaces is expected to play a crucial role in studies on such materials. Near future operando observation with XPS and NEXAFS will be a powerful approach to analyze geometric structures and occupied and unoccupied electronic structures at surfaces of a wide variety of functional materials under working conditions.

References

1. Stöhr J (1992) NEXAFS spectroscopy. Springer, Berlin, New York
2. Amemiya K, Kondoh H, Yokoyama T, Ohta T (2002) J Electron Spectrosc Relat Phenom 124:151–164
3. Knop-Gericke A, Hävecker M, Neisius T, Schedel-Niedrig T (1998) Nucl Instrum Methods Phys Res A 406:311–322
4. Fischer DA, Döbler U, Arvantis D, Wenzel L, Baberschke K, Stöhr J (1986) Carbon K-edge structure of chemisorbed molecules by means of fluorescence detection. Surf Sci 177:114–120

5. Zaera F, Fisher DA, Shen S, Gland JL (1988) Fluorescence yield near-edge X-ray absorption spectroscopy under atmospheric conditions: CO and H_a coadsorption on Ni(100) at pressures between 10^{-9} and 0.1 Torr. Surf Sci 194:205–216
6. Niwa H, Kiuchi H, Miyawaki J, Harada Y, Oshima M, Nabae Y, Aoki T (2013) Operando soft X-ray emission spectroscopy of iron phthalocyanine-based oxygen reduction catalysts. Electrochem Commun 35:57–60
7. Kondoh H, Saito N, Matsui F, Yokoyama T, Ohta T, Kuroda H (2001) Structure of alkanethiolate monolayers on Cu(100): self-assembly on the four-fold-symmetry surface. J Phys Chem B 105:12870–12878
8. Kiguchi M, Arita R, Yoshikawa G, Tanida Y, Ikeda S, Entani S, Nakai I, Kondoh H, Ohta T, Saiki K, Aoki H (2005) Metal-induced gap states in epitaxial organic-insulator/metal interfaces. Phys Rev B 72:075446(1)–075446(5)
9. Kondoh H, Matsui F, Ehara Y, Yokoyama T, Ohta T (2001) Surface-monolayer-controlled molecular orientation in short N-alkane multilayers. Langmuir 17:8178–8183
10. Kiguchi M, Arita R, Yoshikawa G, Tanida Y, Katayama M, Saiki K, Koma A, Aoki H (2003) Metal-induced gap states at well defined alkali-halide/metal interfaces. Phys Rev Lett 90:196803(1)–196803(4)
11. Outka DA, Stöhr J, Jark W, Stevens P, Solomon J, Madix RJ (1987) Orientation and bond length of molecular oxygen on Ag(110) and Pt(111): a near-edge x-ray-absorption fine-structure study. Phys Rev B 35:4119–4122
12. Nakai I, Kondoh H, Shimada T, Yokota R, Katayama T, Ohta T, Kosugi N (2007) Geometric and electronic structures of NO dimer layers on Rh(111) studied with NEXAFS spectroscopy : experiment and theory. J Chem Phys 127:024701(1)–024701(6)
13. Zhao YL, Bartberger MD, Goto K, Shimada K, Kawashima T, Houk KN (2005) Theoretical evidence for enhanced NO dimerization in aromatic hosts: implications for the role of the electrophile $(NO)_2$ in nitric oxide chemistry. J Am Chem Soc 127:7964–7965
14. Amemiya K, Kousa Y, Nakamoto S, Harada T, Kozai S, Yoshida M, Abe H, Sumii R, Sakamaki M, Kondoh H (2011) Real-time observation of CO oxidation reaction on Ir(111) surface at 33 ms resolution by means of wavelength-dispersive near-edge x-ray absorption fine structure spectroscopy. Appl Phys Lett 99:074104(1)–074104(3)
15. Nakai I, Kondoh H, Amemiya K, Nagasaka M, Nambu A, Shimada T, Ohta T (2004) Reaction-path switching induced by spatial-distribution change of reactants: CO oxidation on Pt(111). J Chem Phys 121:5035–5038
16. Nakai I, Kondoh H, Amemiya K, Nagasaka M, Nambu A, Shimada T, Ohta T (2005) The mechanism of CO oxidation on O-precovered Pt(111) surfaces studied by energy-dispersive near-edge x-ray absorption fine structure spectroscopy. J Chem Phys 122:134709(1)–134709(10)
17. Nagasaka M, Kondoh H, Ohta T (2005) Water formation reaction on Pt(111): role of the proton transfer. J Chem Phys 122:204704(1)–204704(6)
18. Nakai I, Kondoh H, Shimada T, Nagasaka M, Yokota R, Katayama T, Amemiya K, Orita H, Ohta T (2009) Mechanism of N + NO reaction on Rh(111) surfaces: a precursor-mediated reaction. J Phys Chem C 113:13257–13265
19. Knop-Gericke A, Hävecker M, Neisius T, Schedel-Niedrig T (1998) New experimental technique: X-ray absorption spectroscopy detector for in situ studies in the soft X-ray range (250 eV $< h\nu <$ 1000 eV) under reaction conditions. Nucl Instrum Methods Phys Res A 406:311–322
20. Knop-Gericke A, Hävecker M, Schedel-Niedrig T, Schlögl R (2000) High-pressure low-energy XAS: a new tool for probing reacting surfaces of Heterogeneous catalysts. Top Catal 10:187–198
21. Knop-Gericke A, Hävecker M, Schedel-Niedrig T, Schlögl R (2001) Characterisation of active phases of a copper catalyst for methanol oxidation under reaction conditions: an in situ X-ray absorption spectroscopy study in the soft energy range. Top Catal 15:27–34

22. Hävecker M, Cavalleri M, Herbert R, Follath R, Knop-Gericke A, Hess C, Hermann K, Schlögl R (2009) Methodology for the structural characterisation of V_xO_y species supported on silica under reaction conditions by means of in situ O K-edge X-ray absorption spectroscopy. Phys Status Solidi B 246:1459–1469
23. Ogletree D, Bluhm H, Lebedev G, Hussain Z, Fadley C, Salmeron M (2002) A differentially pumped electrostatic lens system for photoemission studies in the millibar range. Rev Sci Inst 73:3872–3877

Chapter 25
Sensors

Hudson W.P. Carvalho, David Degler, Nicolae Barsan, and Jan-Dierk Grunwaldt

25.1 Introduction

Knowledge on structural properties is essential to understand the working principle of gas sensing devices based on Semiconducting Metal OXides (SMOX). For sensors, like for many other functional materials, nano-sized structures as well as the nature of surfaces and interfaces define the materials' properties. As will be shown in this chapter, X-ray absorption spectroscopy (XAS) in terms of X-ray absorption near edge structure (XANES) and extended X-ray absorption fine structure (EXAFS) was first used to analyze ex situ the powders used to prepare the sensing layers. Later, XAS was employed to explore model sensors containing high dopant loading and exposed to elevated gas concentrations. The current trend seeks to investigate real sensor devices. This implies studies on porous oxide layers with low dopant loading, at elevated temperatures (100–400 °C) and realistic reaction conditions such as low analyte gas concentrations (ppm) in oxygen (20–21 vol%) and interfering components such as water (10–60 % relative

H.W.P. Carvalho
Centro de Energia Nuclear na Agricultura, 13400-970 Piracicaba - São Paulo, Brasil

Institute for Chemical Technology and Polymer Chemistry (ITCP) and Institute of Catalysis Research and Technology (IKFT), Karlsruhe Institute of Technology, 76131 Karlsruhe, Germany

D. Degler • N. Barsan
Institute of Physical and Theoretical Chemistry, University of Tübingen, 72076 Tübingen, Germany

J.-D. Grunwaldt (✉)
Institute for Chemical Technology and Polymer Chemistry (ITCP) and Institute of Catalysis Research and Technology (IKFT), Karlsruhe Institute of Technology, 76131 Karlsruhe, Germany
e-mail: grunwaldt@kit.edu

Y. Iwasawa et al. (eds.), *XAFS Techniques for Catalysts, Nanomaterials, and Surfaces*, DOI 10.1007/978-3-319-43866-5_25

humidity). As the fundamentals of XAS and related photon-in/photon-out techniques (HERFD-XANES, XES) have been previously discussed in this book, this chapter focuses mainly on the potential and limitations using the techniques in the field of chemical gas sensors. This includes a brief introduction to the current state of the art and proposed mechanisms of gas sensing. Special focus is laid on the main advantages and some of the smart approaches presented in the literature when XAS is applied to the characterization of gas sensors. Hence, both experimental aspects and selected examples are described.

25.2 Approach to Characterize Gas Sensors

Besides common material characterization techniques such as transmission or scanning electron microscopy (TEM or SEM), X-ray photoelectron spectroscopy (XPS), and X-ray diffraction (XRD), gas sensing materials are studied by various *operando* techniques, probing the materials' electronic or chemical properties. DC resistance measurements, impedance spectroscopy (AC resistance), Hall effect measurements, and work function measurements (Kelvin Probe) are common techniques for determining the electronic properties of SMOX sensors under operation conditions [1–4]. In addition to these techniques, *operando* spectroscopic methods such as IR emission spectroscopy [5, 6], diffuse reflectance infrared Fourier transform spectroscopy (DRIFTS) [7, 8], and Raman spectroscopy [9, 10] are used to study the surface chemistry of gas sensors in various gas atmospheres. Moreover, several in situ and ex situ techniques have been applied on SMOX powders, such as EPR, UV/vis, or CEMS [11]. An overview of *operando* techniques for gas sensor research, which has tremendously increased over the past years (cf. ref. [1]), is given in Fig. 25.1. The approach has become very similar to the characterization of catalysts [12].

However, some of common material characterization techniques are not suitable or are very demanding for *operando* research since they require vacuum conditions (TEM, SEM, XPS) or long-range ordered materials (XRD); the latter one is not suited for low concentrated dopant structures or unlikely for changes caused by ppm concentrations of analyte gases. In contrast, XAS in terms of XANES and EXAFS provides detailed information on the local structure of both semiconductor materials and also of dopants when they are present. As detailed later, the technique can be used to ex situ study the sensing powder or sensor devices. Furthermore, XAS can also be employed to investigate the local chemical structure of sensors under real *operando* conditions. This latter approach is of major relevance, since the local structure might change according to the temperature, atmosphere, and electrical polarization.

Like X-ray photoelectron spectroscopy the analysis of XANES spectra (e.g., by linear combination fitting) can be used to determine the oxidation states of elements. In addition, EXAFS gives direct structural information, but in contrast to XRD not only on long-range ordered materials. For studying gas sensing materials

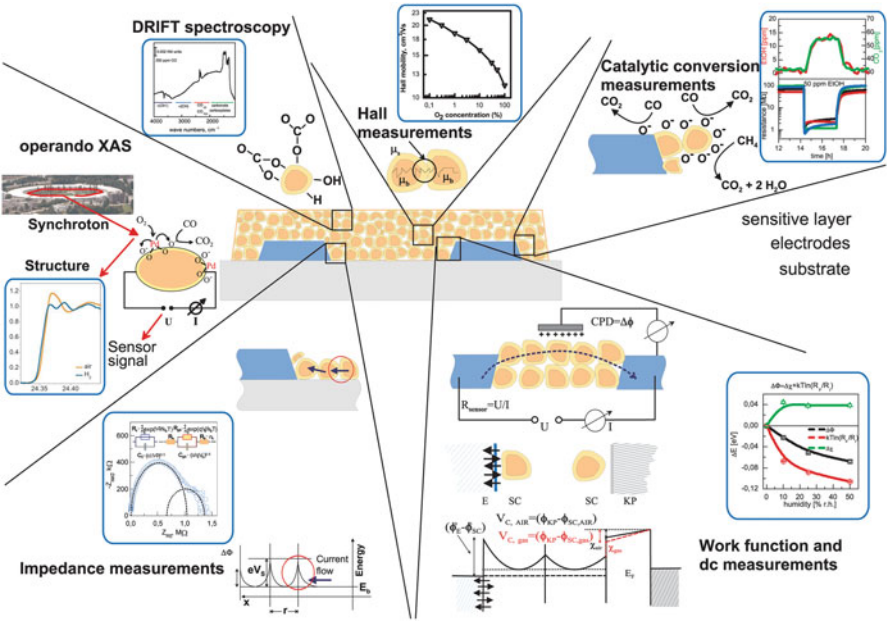

Fig. 25.1 Overview of *operando* investigation techniques for gas sensor research, including electronic (impedance, Hall effect, and work function measurements), spectroscopic (DRIFTS and X-ray techniques such as XAS and XES), and phenomenological (e.g., catalytic conversion) techniques, centered around a schematic cross-section of a SMOX gas sensor; substrate (*gray*), electrodes (*blue*), porous SMOX layer (*orange/yellow*). Adapted from ref. [1], Copyright (2007), with permission from Elsevier

one of the most important benefits of XAS is the possibility of performing experiments under in situ or *operando* conditions, since the oxidation state and structure depend on temperature and atmospheric composition, or with respect to vacuum techniques the presence of an atmosphere at all.

Two major phenomena that take place at the sensor need to be considered: (1) the chemical reaction between the analyte gas and the sensing layer, which is intrinsically a surface process and (2) the charge transfer between the grains, which depends on both grain bulk structure and grain-grain interface. Thus, the response of the sensing layer strongly depends on its structure. To understand the chemical reaction during sensing the XAS experiment has to be designed to mainly probe the local chemical environment of the atoms on the surface. To investigate the charge carrier transfer process, one may easily address the bulk structure by conventional XAS.

25.3 A Brief State-of-the-Art of Gas Sensors

In the 1950s, the pioneering works of Heiland [13] and Bielanski [14] showed that the resistance of SMOX depends on the composition of the surrounding atmosphere. In the 1960s, a SMOX-based sensor device was introduced as a detector for gas chromatography, followed by the first commercial gas sensors developed by Tagushi in the 1970s [15]. Today, SMOX-based gas sensors play an important role in the detection of ppm or lower concentrations of toxic or flammable gases, such as CO, NO_x, CH_4, and H_2 [16, 17]. Increasing demands on the gas sensing performance lead to new developments and the strong need of understanding the gas sensing process on various levels and scales [1].

25.3.1 Sensing Mechanism: Oxides, Role of Ions and Nanoparticles as Dopants

Typical SMOX used for gas sensing are WO_3, In_2O_3 (ITO), or ZnO, etc., but none of these materials are in both academia and industry as common as SnO_2 [16, 17]. The working principle of SnO_2 and other n-type SMOX, operated at temperatures around 300 °C, is based on two processes that are linked to the concentration of ionosorbed surface oxygen [18]. The first process is the reception, which is based on the interaction of an analyte gas with the SMOX surface. In case of a reducing gas such as CO this process is the oxidation of CO, reaction with ionosorbed surface oxygen, to CO_2 (Fig. 25.2a). The consumption of ionosorbed surface oxygen releases electrons to the material, which by the second process called transduction decreases the sensor's resistance, i.e., creating a sensor signal. In the porous sensing layers, which consist of small crystallite grains, the charge transport is limited by the intergrain resistance controlled by back-to-back Schottky contacts, or Schottky barriers (Fig. 25.2b). The level of the barriers depends on the surface band bending that describes the surface concentration of free charge carriers and is determined by the ionosorption of oxygen [18]. Since the concentration of ionosorbed oxygen is controlled by adsorption of atmospheric oxygen, desorption, and the reaction with reducing gases, the resistance is directly linked to the composition of the surrounding atmosphere [17, 18].

Besides the advantages of SMOX like SnO_2 such as low cost, robustness, and sensitivity they have some disadvantages, such as a poor selectivity, strong cross interferences, and lack of long-term stability. To overcome these disadvantages, i.e., improve the sensitivity, selectivity, and stability of SMOX-based gas sensors, low concentrations (0.1–5 wt%) of noble metals (e.g., Pd, Pt, Au, or various other metals/transition metals) are introduced into the sensing materials, a method that is commonly referred to as doping or sensitization of the sensing layer [17]. Depending on their distribution, structure, and oxidation state these dopants influence the chemical (reception) and/or electronic (transduction) properties of the

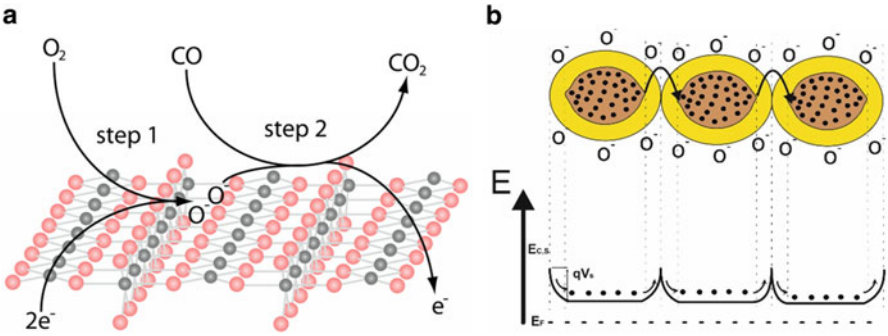

Fig. 25.2 Working principle of SnO_2 gas sensing materials: (**a**) surface chemistry of SnO_2 involving the ionosorption of oxygen (*step 1*) and the reaction of ionosorbed oxygen with CO (*step 2*), (**b**) schematic drawing of SnO_2 grains between the measurement electrodes (*top*) and the back-to-back Schottky barriers (*bottom*). The electron depletion layer of the SnO_2 grains is indicated by a paler color, cf. ref. [19]

material: Metallic clusters presented at the surface are assumed to mainly change the surface chemistry, while oxide clusters are expected to have an impact on the chemistry and the electronic properties of the material [20–22]. Like oxide clusters, atomically dispersed dopants influence the chemical and electronic properties; if they are present in the bulk their electronic effect is considerable, especially when they show oxidation states different from the sensing material itself [23]. This demonstrates the importance of structural information to understand the effect of the noble metals introduced into the sensing layer.

25.4 Experimental Aspects of X-ray Absorption Spectroscopy Experiments

25.4.1 Ex Situ Studies on Gas Sensors

The majority of the XAS studies has been focused on the structure of the semiconductor layer. Since SnO_2 is the most widely used material, there is plenty of information on the local structure of Sn oxide-based materials prepared by different methods such sol-gel, precipitation, sputtering, etc. [24–26]. For example, XAS has been used complementary to XRD to investigate the disorder (mean square deviation of interatomic distances) and the particle size (based on the number of neighbors at higher shells). XAS is complementary to XRD as it is not restricted to crystalline phases; moreover, it provides information on the local disorder instead of on the long-range one. Other semiconductors such as ZnO [27, 28] have also been reported. In addition, dopants such as Pt [29–31], Pd [32–34], Au [22], Cu [35, 36], Fe [35–37] have been in the focus of XAS investigations. Although ex situ studies pioneered the use of XAS for the characterization of

sensors and set the bases for further accomplishments, we will see in the next sections that chemical environment probed in a pellet is not necessarily the same as the one found under *operando* conditions.

XAS has been mostly used to characterize the powders used to prepare the sensitive layers; in this case, the samples are usually measured as pressed pellets diluted in cellulose, boron nitride [38], or polyethylene [39]. Similarly, although less frequently, the measurements can be carried out directly on the sensor device, i.e., recording XAS spectra for the sensing layers after the deposition on the top of the electrodes. The technique has been employed to characterize the local chemical environment of the metal species composing the semiconducting layer, dopants [30, 32], and in some cases multiple edge approach is used to investigate both [39]. More details on the impact of these studies are given in Sect. 25.5.

Regarding the detection mode, the choice follows the traditional experimental conditions. In case of powders, if the concentration of the noble metal dopant allows, the transmission detection mode has been preferred. If the noble metal dopant concentration is too low to acquire a reasonable transmission XAS spectrum, or if the experimentalist intends to study the sensing layer, which is usually deposited on the top of a thick substrate (silicon, Al_2O_3, etc.), other detection modes such as X-ray fluorescence or electron yield might be considered. Total electron yield was successfully used to study nondoped SnO_2 sensing layers [25]. Since the probability of escape of photoelectrons coming from beneath the surface exponentially decreases as a function of depth, this detection mode presents some surface sensitivity ranging from tens to hundreds of nanometers. Despite of that, this detection mode is not ideal for *operando* measurements since the ejected photoelectrons may not reach the detector due to inelastic collisions with the gas atmosphere.

X-ray fluorescence detection mode can be easily implemented to study sensors, this mode has two important advantages: (1) *operando* measurements under reaction conditions can be performed since hard X-rays are not significantly absorbed by the atmosphere and (2) depending on the roughness of the surface grazing incidence detection mode results in surface sensitivity.

25.4.2 In Situ Studies on Chemical Sensors

Although the conditions faced by in situ studies are much more challenging than those for ex situ measurements, in situ studies are carried out with model sensors. It means that the dopants and gas concentrations are much higher than those found for real sensor devices. For example, in the called model sensors, the wt% of dopants may reach two digits of magnitude and gases are also in the order of v/v%, whereas in real devices these values may be smaller than 1 wt% and gases in the order of few ppm (v/v).

The degree of complexity of the experiments also depends on the state of the art of the X-ray sources and detectors. As brighter sources and detectors with lower

detection limits have been developed more realistic sensor devices and conditions can be explored. Hence, the results of in situ studies might be carefully interpreted since they might give a flavor of the sensing mechanism but not the actual mechanism.

Once chosen the detection mode and conditions of the experiments (e.g., gases, humidity, or temperature) one has to decide what kind of cell/test house should be employed to address the raised questions. In situ studies have proved to be especially important when one seeks to investigate the role of dopants. From historical perspective XAS was first used to investigate the influence of the gas atmosphere on the chemical environment of sensor materials such as dopants and semiconductors, this we have called in situ studies. Later then XAS was combined to electrical measurements that allowed investigating the local order of atoms and simultaneously recording the electrical response of the sensor; these are the *operando* studies.

In situ measurements can be carried out exposing the sensor powders or devices to an atmosphere containing the analyte gas, such as CO or H_2. An example of such a type of study was reported by Davis et al. [36] in which the powders were diluted in fumed silica pressed and exposed to CO at high temperatures.

25.4.3 Operando *Studies on Chemical Sensors*

As stated before, *operando* studies seek to investigate the sensor devices as close as possible of its real working conditions, i.e., very low dopant and probe gas concentrations. In commercial devices dopants are usually noble metals such as Pt, Pd, or Au; thus they are employed in the minimum required concentration. One of the major challenges for in situ and *operando* measurements consists in the development of a reaction cell that would allow recording XAS spectra and at the same time controlling the atmosphere (cf. Chap. 6), temperature and ideally registering the electrical response given by the sensor device. An example of a successful design is presented in Fig. 25.3. This in situ cell was developed by some of the authors of this book chapter and used in several published studies [22, 29, 33]. It consists of a stainless steel body and sealed Kapton™ window. Due to its compact design it can be adapted to virtually any beamline.

XAS experimentalists must also be aware that the X-ray beam may heat the sensor or change the semiconductor electronic transport properties. Luckily, the parallel recorded resistance allows one to assess to which extent the beam exposure affects the sensor performance. In some cases recording XAS for sensor devices can be very challenging. Let us consider the example of a sensitive layer doped with Pt. The electrodes shown in Fig. 25.1 are usually made of Pt and the heaters are also made of Pt. As previously mentioned, Pt is one of the widest used dopants. Thus if all these three components are made of Pt, it would be impossible to study only Pt present in the sensing layer since the XAS signal would be an average of the Pt coming from sensing layer, heater, and electrodes. To surmount this obstacle our

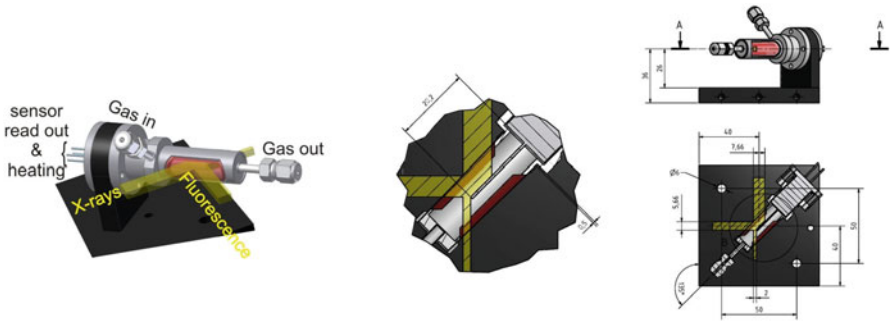

Fig. 25.3 XAS cell for *operando* measurements developed by Koziej et al. [33]. Reproduced by permission of the PCCP Owner Societies

group developed a device in which the electrodes were made of Au and the heaters made of PdAg alloy. On top of these a real sensing layer was deposited.

Pt L_3 edge is located at 11,564 eV while Au L_3 edge appears at 11,919 eV. Therefore, using a conventional energy-dispersive X-ray fluorescence (resolution $\Delta E/E \approx 0.01–0.03$, c.a. 100–300 eV) detector is impossible to record a 1000 eV EXAFS spectrum for Pt without detecting the Au edge appearing in the middle of the spectrum of Pt. One way to circumvent this inconvenient consists in recording the EXAFS spectrum in High Energy Resolution Fluorescence Detection (HERFD) mode [40–42]. Employing this detection mode allows recording the fluorescence yield within an energy window ranging at few electrons volts, e.g., 2–5 eV. Other important advantages of HERFD detection mode consist in the circumvention of the XAS spectral core-hole lifetime broadening, the result is a spectrum with sharper and clearer features. Additionally, the sensitivity to the oxidation state dramatically increases. Outstanding examples of the application of HERFD XAS to the study of sensors can be found in references [16, 23, 24].

25.5 Selected Examples

25.5.1 Ex Situ Studies: Doped Oxides, Sensor Devices or Sensor Powders

A typical example of ex situ analysis of powders used to produce sensors was given by Kanai et al. [39]. Several α-Fe_2O_3-SnO_2 composites oxides, varying the molar fraction of SnO_2, were prepared by thermal treatment of co-precipitated Fe^{3+} sulfate and Sn^{2+} chlorides. The powders were tested as CH_4 sensing materials, it was found that the sensitivity was dependent on the amount of SnO_2 in α-Fe_2O_3, the maximum sensing activity was given by the 15–20 mol% SnO_2 in α-Fe_2O_3. The Sn K and Fe K XAS analyses showed that SnO_2 can be incorporated in the lattice of α-Fe_2O_3, but only up to 15 mol% of SnO_2. Above this threshold phase segregation

occurs and the α-Fe_2O_3 becomes irregular. Thus, the sensing activity was attributed to the solid solution formed between SnO_2 and α-Fe_2O_3.

Complementary to the powder approach, the ex situ analysis of the sensor device may also provide important structural information. It can capture any structural changes that might have occurred during the deposition of the powders on the electrodes. A very instructive case was presented by Serrini et al. [25]. The local structure of several SnO_2 prepared by sputtering was thoroughly evaluated. The authors prepared thin films sensing layers with thickness ranging from 200 to 480 nm; moreover, the O_2/Ar ratio was varied during the deposition and also the effect of temperature on the substrate was investigated. Besides XAS the sensors were complementarily characterized by XRD and XPS. The sensing activity was tested against CO and NO_2. The authors pointed out the advantage of XAS over XRD in the determination of very small grain sizes, e.g., < 2 nm, for SnO_2 and most oxides the experimentalist can derive grain/crystallite size from the coordination numbers of outer shells such as second and third. Furthermore, XAS showed the presence of a contaminant β-Sn phase that might have contributed to decrease the sensor response to the analyte; this content was not detected by XRD. Finally, the combination of XAS and XRD showed that, after the thin film deposition, thermal treatment does not increase the grain size; however, the mean-square deviation of interatomic distances (EXAFS Debye-Waller factor) decreased. The results showed that the sensor performance is dependent on a combination of factors such as abundance of oxygen species on the surface (determined by XPS), small crystallites in the range of 3–4 nm, and low structural disorder. Altogether it allowed inferring that at the same time the particles must be as small as possible to have a large surface area for the analyte; however, particle itself and the boundary between grains must allow the electron conduction.

25.5.2 Examples for In Situ and Operando *Studies*

One of the first investigations for in situ measurements was carried out by Gaidi et al. [43]. They approached the role of Pt dopant in SnO_2-based sensor for CO detection [20, 21]. Pt-doped SnO_2 (3 at%, 6 at%, and 12 at% Pt) was prepared by co-deposition of precursors on oxidized Si substrate by the aerosol pyrolysis method. The procedure resulted in 3–5 nm Pt particles within SnO_2 and the influence of the atmosphere on the Pt chemical environment was investigated. A special cell was developed in which the temperature and atmosphere could be controlled; however, details on the in situ cell were not found. In this specific case the XANES measurements were carried out at Pt L_3 edge between 25 and 350 °C. Under air at 350 °C the 3 at% Pt sensor was more oxidized than the 12 at% Pt, this result highlights the important structural difference caused by the Pt loading and most likely Pt particle size. The authors also observed that CO was able to reduce the Pt dopant; however, the kinetics were temperature dependent. Pt was reduced faster at low temperatures. XAS combined to nonsimultaneous electrical

measurements led the researchers to conclude that PtO_2 is reduced by CO forming Pt. Then Pt reacts with chemisorbed O_2 regenerating the PtO_2. This interplay between oxidized and reduced Pt was appointed the responsible for electrical response of the sensor.

Simultaneous XANES and electrical measurements on similar Pt-doped SnO_2 samples were later reported by the same group [31]. The authors showed a very interesting correlation between the electrical conductance of Pt-doped SnO_2 and the oxidation state of Pt. The highest conductance was achieved when Pt species were reduced. This electrical response was attributed to the donation of electrons from metallic Pt to the conduction band of SnO_2. However, as described later, in real sensors with low concentration of Pt one could not detect the formation of a metallic phase.

Further *operando* studies using even harsher conditions were more recently reported for Pt, Au, and Pd-doped SnO_2. One should keep in mind that real sensors might present very low concentration of noble metal dopants, i.e., significantly lower than 1 wt%. Moreover, the sensing layer is porous and thin, c.a. 50 μm as shown in Fig. 25.1. Altogether it means that total loading of the analyte for XAS is extremely low. To record XAS for 0.2 wt% Pt in SnO_2 real sensor under working conditions (250 ppm CO and 50 ppm H_2), Hübner et al. [29] replaced the Pt electrodes by Au and Pt heaters by Ag/Pd alloy. EXAFS analysis showed that Pt atoms were coordinated by oxygen and located in the lattice of SnO_2. Interestingly, the HERFD-XANES showed that Pt within SnO_2 structure is even more electron deficient than PtO_2 reference compound. HERFD-XANES registered under working conditions simultaneously to the electrical resistance measurements showed that only a very small change in Pt electronic structure is observed under *operando* conditions. Therefore, the hypothesis of spillover of H_2 or O_2 promoted by Pt metallic cluster as responsible for the improvement in sensing properties had to be reassessed. In its turn, the authors suggested that the Pt insertion in the lattice of SnO_2 changes the semiconductor properties, for example Pt atoms might donate electrons to SnO_2 changing its Fermi level.

Au-doped SnO_2 was also investigated using HERFD-XANES [22]. However Au, even at low concentrations such as 0.2 wt%, is not incorporated into the lattice of SnO_2. In this case Au is found as small metallic clusters, and it showed virtually no spectral changes in the presence of 50 ppm CO and H_2 ppm H_2, while important changes in the resistance were observed. Therefore, this result ruled out the conjecture of CO or H_2 chemical bond with Au surface atoms. The authors have concluded that Au spills oxygen atoms over the surface of SnO_2, and the oxidation of CO and H_2 takes place on SnO_2.

Finally, one of the most recent *operando* XAS studies on sensor reported by our group dealt with 0.2 and 1 wt% Pd-doped SnO_2 prepared by flame spray pyrolysis (FSP) and powder impregnation (PI) methods [44]. EXAFS analysis helped to understand the initial state of the Pd, it showed that in PI prepared sensors Pd atoms presented second and third shells, although the curve fitting to theoretical data showed that the number of neighbors was smaller than the one found for PdO bulk oxide. Such higher shells were absent for FSP made sensors. The XANES data

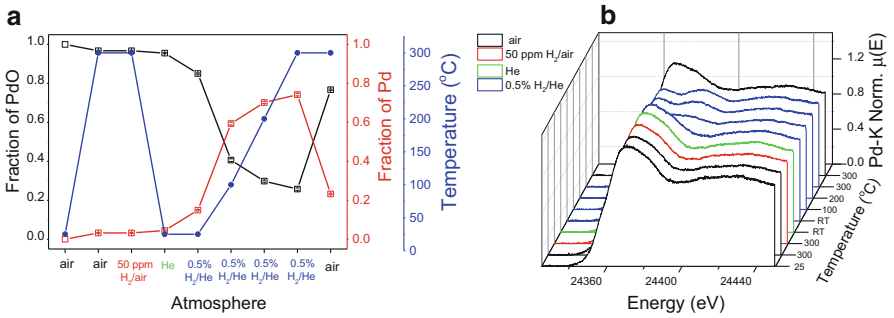

Fig. 25.4 (**a**) Linear combination analysis used to determine the ratio between oxidized and reduced fractions of Pd in 1 wt% Pd-doped SnO_2 under different atmospheres and temperatures, (**b**) respective Pd-K edge XAS edge spectra recorded in fluorescence mode using the cell shown in Fig. 25.3

recorded under working (50 ppm H_2/air) and reducing (5000 ppm H_2/He) conditions was subjected to linear combination analysis. The ratio between oxidized and reduced Pd species was determined. Figure 25.4a presents the linear combination results obtained for 1 wt% Pd-doped SnO_2 prepared by FSP and deposited by the screen printed method and Fig. 25.4b shows the spectra recorded in different conditions.

Besides the method employed to obtain the Pd-SnO_2 powder, the procedure used to make the sensing layer plays a major role in sensing properties and chemical environment of Pd under working conditions. Directly deposited FSP layers are more porous than screen-printed ones; thus Pd atoms were partially reduced under 50 ppm H_2. FSP and PI layers deposited by the screen-printed method resulted in modest reduction (<10 %) of Pd under working conditions. Under reducing conditions PI samples were almost completely reduced whereas in FSP a fraction of Pd (nearly 20 %) persisted oxidized. This was interpreted as an indication that part of the Pd atoms obtained by the FSP method was incorporated within the SnO_2 lattice, the absence of higher shells in EXAFS also pointed out that Pd atoms are well dispersed on the surface, and those incorporated by SnO_2 might be in highly disordered environment.

25.6 Present Trends and Outlook

One of the key parts for *operando* studies in the field of sensing but also related fields, such as catalysis, is the design of in situ cells (cf. Chap. 6). As it is always aiming at the best compromise to study the structure and the sensor performance, new *operando* studies need to be constructed depending on the system of interest. Additionally, the combination of XAS with further spectroscopic techniques, e.g., IR, Raman, or UV/vis, will be of great interest. On the one hand from one

experiment more information is available, which is also a trend in catalysis. On the other hand, the X-ray exposure may influence the material and alter the results, e.g., local heating or electronic effects. Since during all *operando* spectroscopic experiments the DC resistance of the sensor is recorded, separate experiments can be compared on the basis of the DC measurements afterward. This approach avoids mutual effects of the radiation, but surely doubles the effort for the measurements. Alternated recording XAS and other techniques are still time-consuming and not favorable regarding the limited access to suitable X-ray sources.

Additionally to the atomic local chemical environment, i.e., coordination numbers, atomic distances, and mean square deviation of atomic distances probed by XAS, one can draw attention to the electronic structure, i.e., probing the valence orbitals. Typically, the structure of the electronic outer shells is explored by UPS and soft X-ray techniques, which eliminate the possibility of carrying out *operando* studies since these tools require vacuum conditions. New photon-in/photon-out techniques based on hard X-rays have, however, recently become available which allow probing the electronic structure of valence orbitals under *operando* conditions. Such methods, for example X-ray emission spectroscopy, have now also been applied on realistic samples at various synchrotron radiation facilities [45–47]. Complementary structural information can be gained, e.g., valence-to-core XES can differentiate between ligands even with similar atomic number such as O from N. In addition, it is sensitive to protonation that is hardly detected by XAS since H is a poor scatterer. Resonant inelastic X-ray scattering (RIXS) has also great potential to be employed in the study of sensors since it can capture the electronic structure of outer electrons, as previously pointed out in this chapter the electron exchange between analyte and sensing layer or between the particles forming the sensing layer is a fundamental step that generates the signal of the analyte.

25.7 Conclusion

XAS applied to gas sensors provides a good example for how this spectroscopic technique can be used to unravel structure-function relationships. The well-established procedures, e.g., sample preparation and cell design, make it easier to transfer these concepts to other fields of materials science.

References

1. Bârsan N, Koziej D, Weimar U (2007) Metal oxide-based gas sensor research: how to? Sens Actuators B Chem 121(1):18–35
2. Oprea A, Bârsan N, Weimar U (2009) Work function changes in gas sensitive materials: fundamentals and applications. Sens Actuators B Chem 142(2):470–493
3. Schierbaum KD, Weimar U, Göpel W et al (1991) Conductance, work function and catalytic activity of SnO_2-based gas sensors. Sens Actuators B Chem 3(3):205–214

4. Mizsei J, Harsányi J (1983) Resistivity and work function measurements on Pd-doped SnO_2 sensor surface. Sens Actuators 4:397–402
5. Pohle R, Fleischer M, Meixner H (2001) Infrared emission spectroscopic study of the adsorption of oxygen on gas sensors based on polycrystalline metal oxide films. Sens Actuators B Chem 78(1–3):133–137
6. Pohle R, Fleischer M, Meixner H (2000) In situ infrared emission spectroscopic study of the adsorption of H_2O and hydrogen-containing gases on Ga_2O_3 gas sensors. Sens Actuators B Chem 68(1–3):151–156
7. Emiroglu S, Bârsan N, Weimar U et al (2001) In situ diffuse reflectance infrared spectroscopy study of CO adsorption on SnO_2. Thin Solid Films 391(2):176–185
8. Harbeck S, Szatvanyi A, Bârsan N et al (2003) DRIFT studies of thick film un-doped and Pd-doped SnO_2 sensors: temperature changes effect and CO detection mechanism in the presence of water vapour. Thin Solid Films 436(1):76–83
9. Sänze S, Gurlo A, Hess C (2013) Monitoring gas sensors at work: operando Raman–FTIR study of ethanol detection by indium oxide. Angew Chem Int Ed 52(13):3607–3610
10. Sänze S, Hess C (2014) Ethanol gas sensing by indium oxide: an operando spectroscopic Raman-FTIR study. J Phys Chem C 118(44):25603–25613
11. Gurlo A, Riedel R (2007) In situ and operando spectroscopy for assessing mechanisms of gas sensing. Angew Chem Int Ed 46(21):3826–3848
12. Grunwaldt J-D (2012) In situ analysis of heterogeneous catalysts in chemical energy conversion. In: Schlögel R (ed) Chemical energy storage. de Gruyter, Boston, pp 311–328
13. Heiland G (1954) Zum Einfluß von adsorbiertem Sauerstoff auf die elektrische Leitfähigkeit von Zinkoxydkristallen. Z Physik 138(3–4):459–464
14. Bielanski A, Deren J, Haber J (1957) Electric conductivity and catalytic activity of semiconducting oxide catalysts. Nature 179(4561):668–669
15. Naoyoshi T (1971) Gas-detecting device. US Patent 3631436, July 1970
16. Fierro JLG (ed) (2006) Metal oxides - chemistry and applications. CRC Press, Boca Raton
17. Jaaniso R, Tan OK (eds) (2013) Semiconductor gas sensors. Woodhead Publishing Series in Electronic and Optical Materials. Woodhead Publishing, Cambridge
18. Bârsan N, Weimar U (2001) Conduction model of metal oxide gas sensors. J Electroceram 7 (3):143–167
19. Bârsan N, Hübner M, Weimar U (2011) Conduction mechanisms in SnO_2 based polycrystalline thick film gas sensors exposed to CO and H_2 in different oxygen backgrounds. Sens Actuators B Chem 157(2):510–517
20. Yamazoe N (1991) New approaches for improving semiconductor gas sensors. Sens Actuators B Chem 5(1–4):7–19
21. Yamazoe N, Kurokawa Y, Seiyama T (1983) Effects of additives on semiconductor gas sensors. Sens Actuators 4:283–289
22. Hübner M, Koziej D, Grunwaldt J-D, Weimar U, Barsan N (2012) An Au clusters related spillover sensitization mechanism in SnO_2-based gas sensors identified by operando HERFD-XAS, work function changes, DC resistance and catalytic conversion studies. Phys Chem Chem Phys 14(38):13249–13254
23. Hübner M, Bârsan N, Weimar U (2012) Influences of Al, Pd and Pt additives on the conduction mechanism as well as the surface and bulk properties of SnO_2 based polycrystalline thick film gas sensors. Sens Actuators B Chem 171–172:172–180
24. Chadwick AV, Savin SLP, O'Dell LA (2006) Keeping it small - restricting the growth of nanocrystals. J Phys Condens Matter 18(15):L163–L170
25. Serrini P, Briois V, Horrillo MC et al (1997) Chemical composition and crystalline structure of SnO_2 thin films used as gas sensors. Thin Solid Films 304(1–2):113–122
26. Baumann TF, Kucheyev SO, Gash AE et al (2005) Facile synthesis of a crystalline, high-surface-area SnO_2 aerogel. Adv Mater 17(12):1546–1548
27. Catto A, da Silva L, Bernardi MB et al (2014) An investigation into the influence of zinc precursor on the microstructural, photoluminescence, and gas-sensing properties of ZnO nanoparticles. J Nanopart Res 16(12):1–9

28. Chadwick AV, Russell NV, Whitham AR et al (1994) Nanocrystalline metal-oxide gas sensors. Sens Actuators B Chem 18(1–3):99–102
29. Hübner M, Koziej D, Bauer M, Barsan N, Kvashnina K, Rossell MD, Weimar U, Grunwaldt J-D (2011) The structure and behavior of platinum in Sno2-based sensors under working conditions. Angew Chem Int Ed 50:2841–2844
30. Mädler L, Sahm T, Gurlo A et al (2006) Sensing low concentrations of CO using flame-spray-made Pt/SnO_2 nanoparticles. J Nanopart Res 8(6):783–796
31. Gaidi M, Chenevier B, Labeau M et al (2006) In situ simultaneous XAS and electrical characterizations of Pt-doped tin oxide thin film deposited by pyrosol method for gas sensors application. Sens Actuators B Chem 120(1):313–315
32. Gyger F, Sackmann A, Hübner M et al (2014) Pd@SnO_2 and SnO_2@Pd Core@Shell nanocomposite sensors. Part Part Syst Charact 31(5):591–596
33. Koziej D, Hübner M, Bârsan N et al (2009) Operando X-ray absorption spectroscopy studies on Pd-SnO_2 based sensors. Phys Chem Chem Phys 11(38):8620–8625
34. Erades L, Grandjean D, Nayral C et al (2006) Organometallic approach for platinum and palladium doping of tin and tin oxide nanoparticles: structural characterisation and gas sensor investigations. New J Chem 30(7):1026–1035
35. Davis SR, Chadwick AV, Wright JD (1998) The effects of crystallite growth and dopant migration on the carbon monoxide sensing characteristics of nanocrystalline tin oxide based sensor materials. J Mater Chem 8(9):2065–2071
36. Davis SR, Chadwick AV, Wright JP (1997) A combined EXAFS and diffraction study of pure and doped nanocrystalline tin oxide. J Phys Chem B 101(48):9901–9908
37. Hwang SO, Kim CH, Myung Y et al (2008) Synthesis of vertically aligned manganese-doped Fe_3O_4 nanowire arrays and their excellent room-temperature gas sensing ability. J Phys Chem C 112(36):13911–13916
38. Grandjean D, Benfield RE, Nayral C et al (2004) EXAFS and XANES study of a pure and Pd doped novel Sn/SnO_x nanomaterial. J Phys Chem B 108(26):8876–8887
39. Kanai H, Mizutani H, Tanaka T et al (1992) X-Ray absorption study on the local structures of fine particles of α-Fe_2O_3-SnO_2 gas sensors. J Mater Chem 2(7):703–707
40. Glatzel P, Sikora M, Eeckhout SG et al (2007) Hard X-ray photon-in/photon-out spectroscopy with lifetime resolution - of XAS, XES, RIXSS and HERFD. In: Choi JY, Rah S (eds) Synchrotron radiation instrumentation, Pts 1 and 2. American Institute of Physics, Melville, pp 1731–1734
41. Glatzel P, Sikora M, Smolentsev G et al (2009) Hard X-ray photon-in/photon-out spectroscopy. Catal Today 145(3–4):294–299
42. Glatzel P, Weng T-C, Kvashnina K et al (2013) Reflections on hard X-ray photon-in/photon-out spectroscopy for electronic structure studies. J Electron Spectros Relat Phenomena 188:17–25
43. Gaidi M, Labeau M, Chenevier B et al (1998) In-situ EXAFS analysis of the local environment of Pt particles incorporated in thin films of SnO_2 semi-conductor oxide used as gas-sensors. Sens Actuators B Chem 48(1–3):277–284
44. Degler D, Pereira de Carvalho HW, Weimar U et al (2015) Structure–function relationships of conventionally and flame made Pd-doped sensors studied by X-ray absorption spectroscopy and DC-resistance. Sens Actuators B Chem 219:315–323
45. Gallo E, Glatzel P (2014) Valence to core x-ray emission spectroscopy. Adv Mater 26 (46):7730–7746
46. Boubnov A, Carvalho HWP, Doronkin DE, Guenter T, Gallo E, Atkins AJ, Jacob CR, Grunwaldt J-D (2014) Selective catalytic reduction of NO over Fe-ZSM-5: mechanistic insights by operando HERFD-XANES and valence-to-core x-ray emission spectroscopy. J Am Chem Soc 136:13006–13015
47. Günter T, Carvalho HWP, Doronkin DE, Sheppard T, Glatzel P, Atkins AJ, Rudolph J, Jacob CR, Casapu M, Grunwaldt J-D (2015) Structural snapshots of the SCR reaction mechanism on Cu-SSZ-13. Chem Commun 51:9227–9230

Chapter 26
Probing Structure and Reactivity of Metal Centers in Metal–Organic Frameworks by XAS Techniques

Elisa Borfecchia, Luca Braglia, Francesca Bonino, Silvia Bordiga, Sigurd Øien, Unni Olsbye, Karl Petter Lillerud, Jeroen A. van Bokhoven, Kirill A. Lomachenko, Alexander A. Guda, Mikhail A. Soldatov, and Carlo Lamberti

26.1 Introduction: Relevance and Flexibility of MOFs Materials

In the last decade, metal-organic frameworks (MOFs, also known as coordination polymers) represented a new emerging class of porous materials that have focused the interest of many research laboratories worldwide [1–18]. MOFs diverge from some zeolites in important aspects [19, 20]. Indeed, MOFs exhibit a much larger

E. Borfecchia • L. Braglia • F. Bonino • S. Bordiga
Department of Chemistry, NIS and INSTM Reference Centers, University of Torino, I-10135 Torino, Italy

S. Øien • U. Olsbye • K.P. Lillerud
inGAP Centre for Research Based Innovation, Department of Chemistry, University of Oslo, N-0315 Oslo, Norway

J.A. van Bokhoven
Institute for Chemical and Bioengineering, ETH Zürich, CH8093 Zurich, Switzerland

Swiss Light Source, Paul Scherrer Institute, CH-5232 Villigen PSI, Switzerland

K.A. Lomachenko
Department of Chemistry, NIS and INSTM Reference Centers, University of Torino, I-10135 Torino, Italy

IRC "Smart Materials", Southern Federal University, 344090 Rostov-on-Don, Russia

A.A. Guda • M.A. Soldatov
IRC "Smart Materials", Southern Federal University, 344090 Rostov-on-Don, Russia

C. Lamberti (✉)
IRC "Smart Materials", Southern Federal University, 344090 Rostov-on-Don, Russia

Department of Chemistry, CrisDi Centre for Crystallography, University of Torino, I-10125 Torino, Italy
e-mail: carlo.lambeti@unito.it

Y. Iwasawa et al. (eds.), *XAFS Techniques for Catalysts, Nanomaterials, and Surfaces*, DOI 10.1007/978-3-319-43866-5_26

diversity and flexibility in composition (see below Figs. 26.1 and 26.2) and have less demanding topological constraints in the formation of the porous lattices. The enormous number of new MOFs reported every year reflects this flexibility and the large interest for their potential applications [21]. Zeolites are strictly based on tetrahedral building units and their different topologies are based on the possibility to make a finite number of secondary building units [22], whereas the inorganic cornerstone in MOF topologies may be a single metal atom or a more or less complex cluster of coordinated metal atoms or extended inorganic sub-structures extending in one, two or three dimensions. According to the recent classification done by Tranchemontagne et al. [23] the coordination of the inorganic cornerstone may span the whole range from 3 up to 66.

Completely different frameworks can be obtained by keeping the same linker connectivity and changing the cornerstone geometry, see Fig. 26.1a, or by fixing the cornerstone geometry and changing the linker connectivity, see Fig. 26.1b. On top of this, cornerstones can be connected using different type of organic linkers, giving rise to the synthesis of isoreticular frameworks such as the IRMOF-1/IRMOF-16 [24] or the UiO-66/UiO-68 [25–27] series, see Fig. 26.1c.

Although the industrial application of MOFs is still limited to a few cases [29, 30], this new class of materials is foreseen to play an important role in the next future, in the fields of: (1) gas separation and purification in general [31–34], and in particular: selective adsorption of H_2 or over N_2 or CO [35], bulk separation of CO_2 under near-ambient conditions for the biogas upgrading [36–39], selective capture of CO_2 [40–42], of CH_4 [40], or of O_2 [43], for hydrocarbons separation [44], selective adsorption air purification of toxic chemicals [45, 46], enantioselective sorption of alcohols [47]; (2) liquid phase separation; [33, 48] (3) adsorption and storage of gases [49–54]; (4) materials for drug delivery [55–58]; (5) optical and luminescent materials [59–67]; (6) photoactivable materials [68]; (7) magnetic materials [69, 70]; (8) solid state ion conductors [71]; (9) proton conductors [72, 73]; (10) materials for electronic and optoelectronic devices [74]; (11) materials for sensors [67]; (12) catalysis in general [28, 75–79] and in particular for: enantioselective chiral reactions [80–84]; (13) photocatalysis [85, 86].

As deeply described in several authoritative reviews and book chapters [87–98], the functionalization of MOF materials remains one of the main challenges driving the MOF community, to make newer and newer structures, with specific functionalities. Indeed, the metal sites in most of the MOF structures show at maximum one coordination vacancy (and only after removal of the solvent, see the HKUST-1 and the CPO-27-Ni cases discussed in Sects. 26.3.3 and 26.3.5, respectively), therefore limiting their application for example in catalysis, where at least two coordination vacancies are required.

MOFs functionalization (see Fig. 26.2 for some examples) is generally performed following two main routes: (1) by using during the synthesis linkers containing functionalized groups [85, 99–103] or (2) by performing post-synthesis modification of MOFs framework. The latter approach includes incorporating arenetricarbonyl complexes $[-C_6H_4M(CO)_3-]$ (M=Cr, Mo) on the linkers by

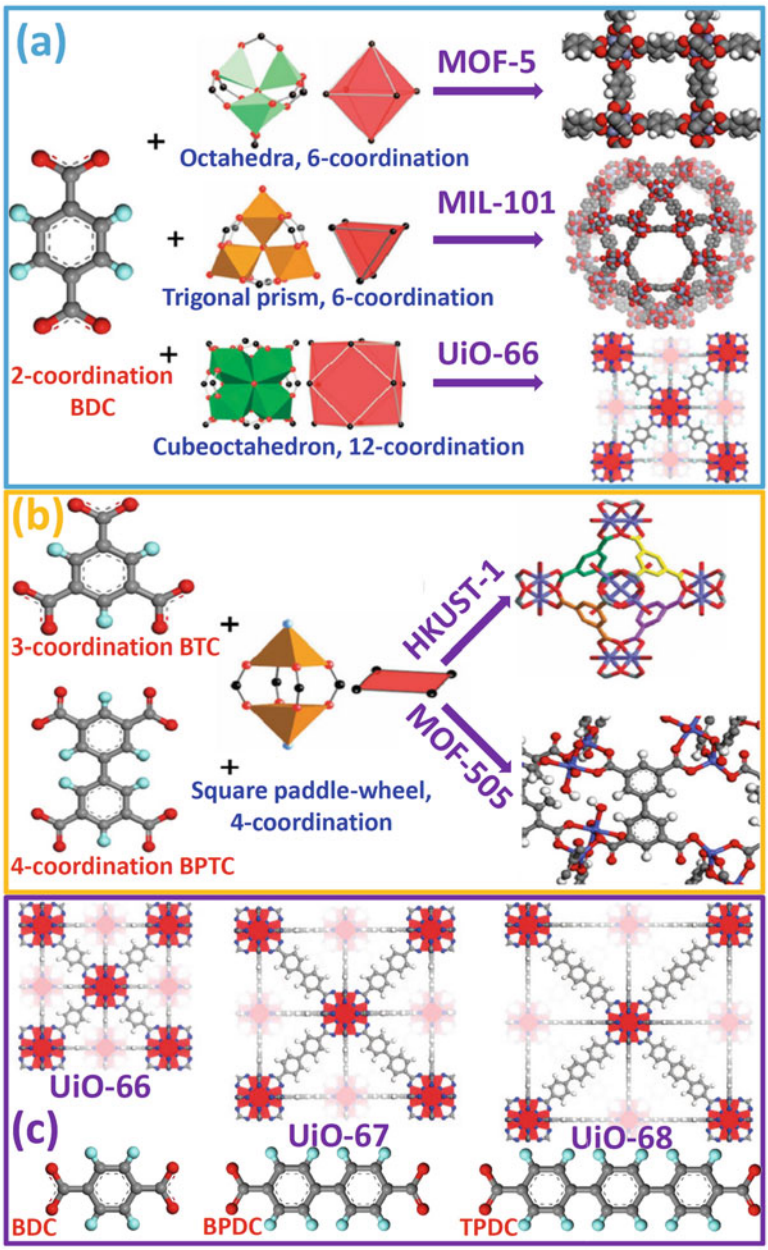

Fig. 26.1 Examples of the flexibility in the construction of MOF structures. Part (**a**): fixing the linker connectivity (twofold connected 1,4-benzene-dicarboxylate, (BDC)) and changing the cornerstone geometry. Part (**b**): fixing the cornerstone geometry and changing the linker connectivity (threefold benzene-1,3,5-tricarboxylate (BTC) and 4-fold 3,3′,5,5′-biphenyltetracarboxylate (BPTC)). Part (**c**): fixing both the linker connectivity (twofold) the cornerstone geometry (12-fold coordinated cubeoctahedron), but changing the linker length BDC, 4,4′-biphenyl-dicarboxylate (BPDC) or 4,4′-terphenyl-dicarboxylate (TPDC). Adapted by permission of Springer (copyright 2010) from Ref. [28] (parts **a**, **b**) and of the American Chemical Society (copyright 2008) from Ref. [25] (part **c**)

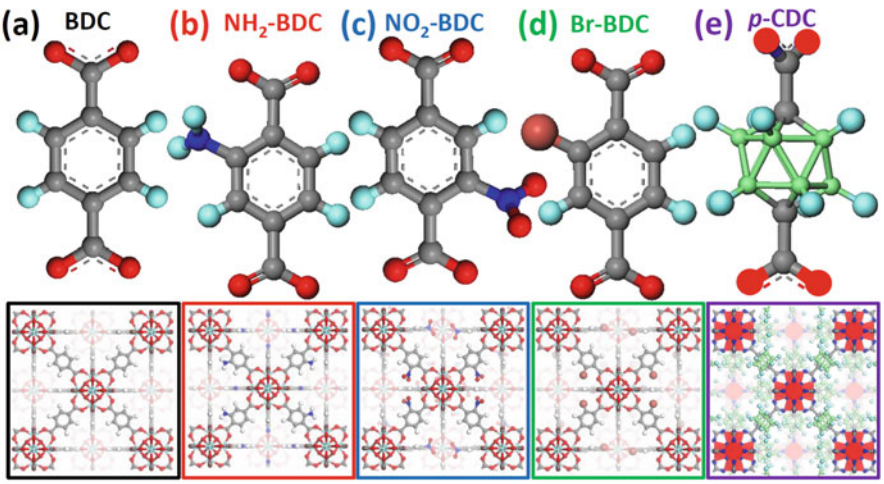

Fig. 26.2 Examples of the flexibility in the linker functionalization of MOF structures: functionalized linker (*top*) and resulting MOF structure (*bottom*). Part (**a**): BDC linker, resulting in the standard UiO-66 framework. Part (**b**): NH_2–BDC linker. Part (**c**): NO_2–BDC linker. Part (**d**): Br–BDC linker. Part (**e**): *p*-carborane–dicarboxylate (*p*-CDC) linker. *Top parts* report the linkers, *bottom parts* report the insertion of the functionalized linker in the UiO-66 framework. Previously unpublished figure inspired from Ref. [28]

interaction with M-carbonyls [104–106]; performing click reaction between the azide groups in the MOF linker network and external alkynes [107, 108]; reduction of the aldehyde functionality of imidazolate-2-carboxyaldehyde linker by $NaBH_4$, to obtain the alcohol functionality and successive conversion to imine functionality by reaction with ethanolamine [109]; insertion in the linker of $–NH_2$ groups by interaction with nicotinoyl chloride [110]; formation of $–NHCOCH_3$ or longer amide groups by interaction of $–NH_2$ groups with different acid anhydrides [102, 111, 112]; metalation reaction on N-containing organic linkers [103, 113]; carboxy-functionalization [114]; amine-functionalization [115, 116]; incapsulation of metal nanoparticles MOFs cavities [117, 118]. In this chapter, examples of functionalized MOFs characterized by XAFS techniques are reported in Sects. 26.3.2 (Pt-functionalized UiO-67) and 3.4 (phosphine-functionalized MIL-101).

26.2 Relevance of XAS-Techniques in Understanding the Structure and the Reactivity of MOFs Materials

The fact that MOFs are mainly constituted by low Z elements (C, O, N, H) implies that they are almost transparent to hard X-rays; [11, 119–121] this allows to collect, at the metal K- (for 2^{nd} and 3^{rd} row elements) or L-edges (for 4^{th} and 5^{th} row and

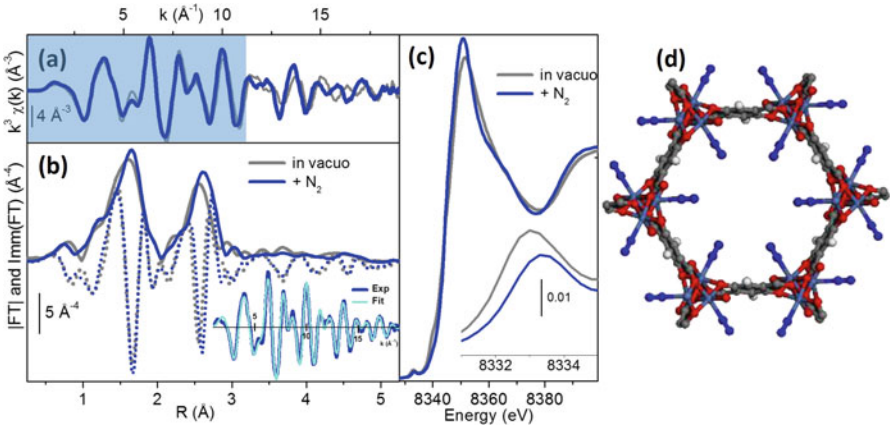

Fig. 26.3 Part (**a**): EXAFS signals of CPO-27-Ni MOF, before (*gray curve*) and after (*blue curve*) N_2 adsorption at liquid nitrogen temperature ($P_{N2} = 100$ mbar) in *k*-space. A k^3-weight has been adopted. In the low k-region (highlighted in blue), the EXAFS spectrum has been almost unaffected by N2 adsorption, that can be revealed only by the high quality data in the high k region. Part (**b**): phase uncorrected FT of the $k^3\chi(k)$ functions reported in part (**a**): modulus (*full lines*) and imaginary parts (*dotted lines*). Same color labeling as in part (**a**). The inset reports, in k-space, the comparison between the experimental spectrum collected in presence of N_2 and the best fit. Part (**c**): Normalized XANES spectra show the effect of N_2 dosage on CPO-27-Ni on the electronic levels of Ni. The inset reports a zoom on the dipole forbidden $1s \rightarrow 3d$ electronic transition. Part (**c**): Optimized periodic structures at B3LYP-D*/TZVP level of theory of CPO–27–Ni + N_2. View from the [001] direction. Parts (**a**–**c**) adapted with permission from Ref. [123], copyright Royal Society of Chemistry (2009); part (**d**) adapted with permission from Ref. [124]. Copyright Elsevier (2012)

lanthanides elements), high quality transmission X-ray absorption spectra characterized by an optimized edge jump $\Delta\mu x$ as high as 1.0–1.5, resulting in accurate data, analyzable up to 15-20 $Å^{-1}$. Figure 26.3a reports a clear example where high quality data collected up to high *k* values have been relevant in understanding fine structural details. The gray spectrum correspond to the k^3-weighted $\chi(k)$ of vacuum activated CPO-27-Ni MOF [122] (also known as MOF-74 or Ni_2(dhtp)) collected at 77 K. The blue spectrum has been recorded after N_2 dosage at 77 K [123, 124]. Up to $k \sim 11$ $Å^{-1}$ the two spectra are almost undistinguishable. The small modification induced by the weak adsorption of N_2 molecule into the coordination vacancy of Ni^{2+} (Fig. 26.3d) can be appreciated only in the 12–19 $Å^{-1}$ region. An accurate fit was performed (see inset in Fig. 26.3b) resulting in a $Ni^{2+}\cdots N_2$ distance of 2.27 ± 0.03 Å. Interesting are also the small, but well defined changes observed in the XANES region (Fig. 26.3c). See below Sect. 26.3.5 for an in depth discussion on the role of XANES simulations in understanding the adsorption geometries of CO and NO molecules on Ni^{2+} sites of CPO-27-Ni. EXAFS was used on the same CPO–27–Ni MOF system to define the coordination of CO (2.11 ± 0.02 Å) [125], H_2O (2.10 ± 0.04 Å) [126] and NO (1.87 ± 0.02 Å) [126].

The complementarity between long range order, investigated by diffraction techniques, and local range order, investigated by EXAFS, has already been recognized for complex systems, such as metalloproteins [127, 128], disordered mixed oxides [129, 130], ternary and quaternary semiconductor solid solutions [131, 132] and is here debated for MOFs. Actually, the chapter has a wider view as it deals with X-ray absorption spectroscopies, i.e., including both EXAFS [133–136] and X-ray absorption near edge structure (XANES) [137–141]. Unfortunately, due to space limitations, we do not consider X-ray emission spectroscopy (XES) [103, 142–154] that has become in the last decade a very promising technique.

26.3 Selected Recent Examples

The role of XAS and related spectroscopies in understanding the structure and the reactivity of metal centers in metal–organic framework was reviewed by some of us in 2010 [11]. In that critical review we report cases where EXAFS and XANES have been relevant in understanding the structural and electronic properties of metal clusters in MOFs. In particular, materials with cluster cornerstones (zero dimensional) and coordination four (HKUST-1, or $Cu_3(BTC)_2$) [155], six (MOF-5) [156], nine (Pt-Gd-MOF [100] and Pt-Y-MOF [99]), and twelve (UiO-66 [25, 26] and Ni-cubane [157]) as well as one example of MOF (CPO-27 [123–126]) with a one dimensional inorganic backbone were discussed.

MOFs are crystalline materials with a complex structure (see above Figs. 26.1 and 26.2), consequently, very little information can be extracted from EXAFS data alone. To perform a complete EXAFS data analysis, able to reconstruct the whole inorganic cornerstone and its binding to the organic part, i.e., to reconstruct the local environment of a metal center up to 4–5 Å, a guessed 3D structure is mandatory. Usually the 3D structure comes from a diffraction study, but it may also come from ab initio optimization [26, 27]. In review [11] it was shown that EXAFS can be successfully used for the following purposes:

1. To just confirm the structure obtained from X-ray or neutron powder diffraction refinements (hydroxylated UiO-66 [25, 26], hydrated HKUST-1 [155], Ni-cubane [157], and as prepared Pt/Gd- [100] and Pt-Y-MOF; [99] MOF)
2. To highlight that the inorganic cornerstone has a lower symmetry with respect to that of the organic framework, that escaped the powder diffraction refinement (dehydroxylated UiO-66); [25, 26]).
3. To obtain the local structure of the inorganic cluster in the desolvated material when desolvation causes a fragmentation of single crystals accompanied by a partial and reversible loss of long range ordering that causes peaks broadening, making impossible the structure solution from XRPD (dehydrated Pt/Gd-MOF) [100] or when simply the XRPD refinement (notwithstanding the quality of the collected pattern) does not reach a safe convergence (dehydrated HKUST-1); [155]).

4. To obtain the local structure of the inorganic cluster in the desolvated material after coordination of a probe (or reactant) molecule, including cluster deformation upon molecule coordination and metal-molecule binding distance (HKUST-1 [155] and CPO-27-Ni; [123–126, 158].
5. To highlight the presence of impurities in form of an amorphous extra-phase that escaped detection by diffraction methods (some MOF-5 synthesis) [156].

In review [11] it has also been underlined that, for points (3) and (4) the starting model to refine the EXAFS datum is that obtained from the refinement of the diffraction data collected on the solvated material, after removal of the solvent molecule (3), or after replacement of the solvent molecule by a probe molecule (4). In the latter case the number of coordinated probe molecules as well as the adsorption geometry may be critical to be disclosed by EXAFS alone, because the scattering contribution from the probe molecule is usually a small fraction of the overall EXAFS signal, that is still dominated by the scattering of the ordered framework atoms. In these cases any help coming from independent techniques (IR, Raman, volumetric microcalorimetry, gravimetric adsorption, etc.) is welcome to reduce the number of independent parameters optimized in the EXAFS data analysis. We show in this chapter (Sect. 26.3.5) the relevance of the use of accurate simulation of XANES to disclose the geometry and the stoichiometry of the metal site after adsorption.

On one hand it is evident that, beside point (1), EXAFS spectroscopy is a fundamental tool to disclose the local structure of the metal MOFs cornerstones. On the other hand, the existence of clear examples discussed in point (2) and (5), where diffraction methods alone resulted in a wrong solution for the structure of the inorganic clusters, makes cases listed in point (1) not a trivial exercise but an important structural check, that is recommended for all new MOFs structures.

On top of this, related XANES (and possibly XES) [119, 144, 159, 160] techniques provide complementary information on the metal electronic structure to complement standard UV–Vis, EPR measurements, and ab initio calculations. In the following we focus the attention on some relevant EXAFS and XANES results appeared in the literature in the last 5 years.

26.3.1 Zr UiO-66, 67 and Hf UiO-66 MOFs

The recently discovered UiO-66/67/68 class of isostructural MOFs [25] has attracted great interest because of its remarkable stability at high temperatures (up to 400 °C) [161], high pressures and in presence of different solvents acids and bases [26]. UiO-66 is obtained connecting $Zr_6O_4(OH)_4$ inorganic cornerstones with 1,4-benzene-dicarboxylate (BDC) as linker, while the isostructural UiO-67 material, obtained using the longer 4,4′ biphenyl-dicarboxylate (BPDC) linker [27] (Fig. 26.1c) and Hf-UiO-66 is obtained keeping the UiO-66 linker (BDC) and substituting the $Zr_6O_4(OH)_4$ blocks with $Hf_6O_4(OH)_4$ corners [162]. Due to the

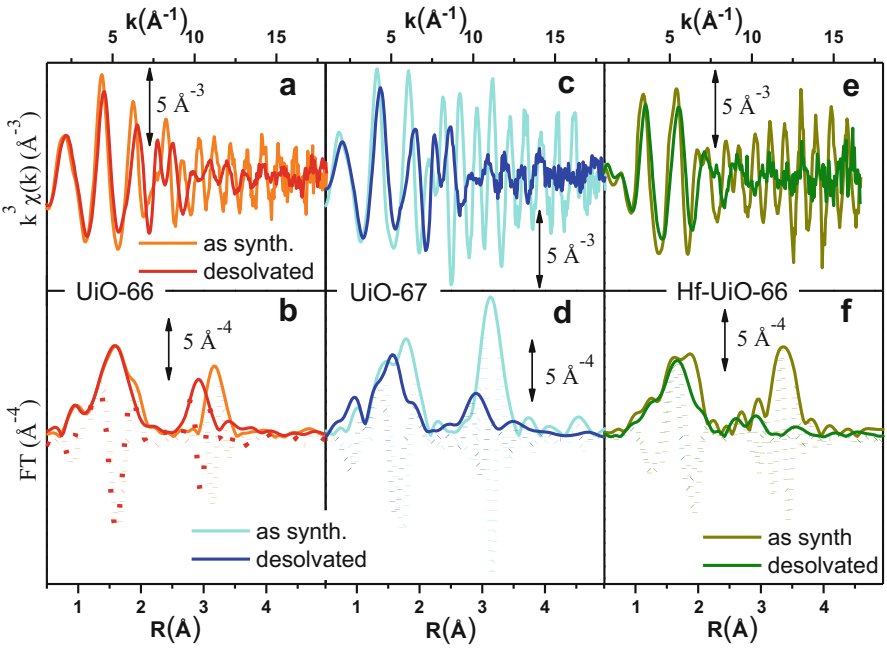

Fig. 26.4 k- (*top panels*) and R-space (*bottom panels*) EXAFS data collected on UiO-66, UiO-67 and Hf-UiO-66, parts (**a**, **b**), (**c**, **d**), and (**e**, **f**), respectively. Both as synthesized (or hydroxylated) and desolvated (or dehydroxylated) forms of the three different isostructural MOFs have been measured. With the exception of desolvated Hf–UiO–66 sample (collected at 573 K) remaining spectra were collected at 300 K. Reproduced with permission from Ref. [165]

rigidity of the framework several isostructural UiOs has been prepared and tested for the stability and gas adsorption. Kandiah et al. [102] studied the thermal and chemical stabilities of isostructural UiO-66-X ($X = NH_2$, Br, and NO_2, see Fig. 26.2c, d) and observed the lower stability of this analogue with respect to parent UiO-66. Conversely, as documented by thermogravimetric studies UiO-67 [27] and Hf-UiO-66 [162] show thermal and chemical stability similar to that of UiO-66 and exhibit the expected surface area, as determined by low temperature volumetric N_2 adsorption isotherms. Such a high stability is related to the fact that each Zr-octahedron is 12-fold connected to adjacent octahedra. This connectivity is very common for metals, resulting in the highly packed fcc structure, but it is still almost unique in MOF topologies [25].

All MOFs are synthesized in presence of a solvent, that has to be removed to make available the large pore volume for any practical applications. The desolvation process left almost unchanged the XRPD pattern of such materials: [25, 27, 162] besides a gain of intensity of the basal reflections (due to the removal of the electron density inside the pores) [163, 164] all peaks remains in almost the same 2θ position with small intensity changes. Conversely, a huge modification of the EXAFS spectra is obtained in all cases, see Fig. 26.4.

In the three hydroxylated materials, the structure determined from the Rietveld refinement of the XRPD corresponding patterns resulted in a straightforward interpretation of the complex EXAFS signals, see first three columns in Table 26.1. The dramatic modification undergone by the EXAFS spectrum upon dehydroxylation (see Fig. 26.4) makes the data analysis not so straightforward. In the case of UiO-66 (see Fig. 26.4b, but similar effects are observed in the two other cases) the changes are basically explained in terms of three main effects: (1) small contraction of the first M–O shell accompanied by a small decrease in coordination (erosion of the shoulder around 1.9 Å); (2) relevant distortion of the second shell contribution showing a maximum that moves from 3.17 to 2.91 Å, with a shoulder at 3.41 Å, thus reflecting an important splitting of the R_{M1} distances of the octahedron sides; (3) the almost complete disappearance of the weak contribution around 4.7 Å, due to the M–M SS signal of the octahedron diagonal (R_{M2}). For the three cases, differently to the hydroxylated cases, the 3D model obtained from the Rietveld refinement of XRPD data in the highly symmetric *Fm-3m* space group was inadequate to simulate the experimental datum. The origin of this failure was, obviously due to the inability of the model to account for two different R_{M1} and R_{M2} distances. For both UiO-66 [26] and UiO-67 [27] cases, the failure of the XRPD model was overcome by using the optimized geometry obtained by ab initio periodic calculations.

The inorganic cornerstones of the as synthesized materials are perfect $M_6(OH)_4O_4$ octahedron (see model in Fig. 26.5b), with 6 equivalent M at the vertex, 12 equivalent M–M1 sides and 3 equivalent and M–M2 diagonals. Upon desolvation two structural water molecules are lost per cornerstone unit (Fig. 26.5a), that evolves from $M_6(OH)_4O_4$ to M_6O_6 [26, 27, 162]. The new M_6O_6 octahedron compressed (two opposite vertexes approaching, see model in Fig. 26.5c) resulting in the shortening of 8 of the 12 edges, and the elongation of the other 4 edges. To take into account this variation the EXAFS contribution was simulated with two independently parameterized paths fixing for the degeneracy a ratio of 1/3 and 2/3 with respect to the case of the single contribution.

Summarizing, EXAFS spectroscopy allows to detect the evolution from $M_6(OH)_4O_4$ to M_6O_6 (M = Zr or Hf) of the inorganic cornerstones of UiO-66, UiO-67 and Hf-UiO-66 MOFs that escaped XRPD detection. DFT period calculations support EXAFS data. Only very recently, Øien et al. [166] succeeded in growing single crystals of UiO-66 and UiO-67 of sufficiently large size to allow synchrotron radiation single crystal data collection to be done. From such data it clearly emerges the presence of two different first shell μ_3 oxygen species, namely μ_3O and μ_3OH, which Zr−O distance agreed with the previous EXAFS studies [26, 27], see Table 26.1. These discrimination between first shell Zr neighbor escaped any previous XRPD analysis in all these class of materials, but was observed by EXAFS [26, 27, 162] and supported by IR spectroscopy.

Table 26.1 Summary of the EXAFS refinement obtained on the hydroxylated and dehydroxylated forms of UiO-66 [26], UiO-67 [27], and Hf-UiO-66 [162]

	UiO-66	UiO-67	Hf-UiO-66		UiO-66	UiO-67	Hf-UiO-66
		Hydroxylated				Dehydroxylated	
T (K)	300	300	300		300	300	537
$R_{\mu 3\text{-}O}$ (Å)	2.087 ± 0.008	2.12 ± 0.02	2.12 ± 0.01		2.06 ± 0.01	2.096 ± 0.007	2.06 ± 0.01
XRD $R_{\mu 3\text{-}O}$ (Å)	2.064 ± 0.003	2.059 ± 0.002	–		–	–	–
R_{O1} & $R_{\mu 3\text{-}OH}$ (Å)	2.235 ± 0.008	2.26 ± 0.01	2.25 ± 0.01		2.221 ± 0.007	2.249 ± 0.007	2.19 ± 0.01
XRD $R_{\mu 3\text{-}OH}$ (Å)	2.254 ± 0.005	2.256 ± 0.008	–		–	–	–
R_C (Å)	3.19 ± 0.02	3.40 ± 0.06	3.23 ± 0.06		3.17 ± 0.04	$3.15 \pm 0.04)$	3.22 ± 0.05
R_{M1} (Å)	3.511 ± 0.007	3.512 ± 0.006	3.510 ± 0.005		3.35 ± 0.01	3.365 ± 0.015	3.31 ± 0.03
R_{M1b} (Å)	–	–	–		3.74 ± 0.02	3.80 ± 0.03	3.45 ± 0.06
R_{M2} (Å)	4.99 ± 0.04	4.95 ± 0.03	4.964		$4.14 \pm 0.07)$	4.15 ± 0.07	–
R_{M2b} (Å)	–	–	–		5.30 ± 0.04	5.46 ± 0.05	–

The EXAFS refinement of the hydroxylated materials was obtained using as input model the optimized structure from Rietveld refinement of the corresponding XRPD patterns. The EXAFS refinement of the dehydroxylated materials was obtained using as input model optimized ab initio calculations for the hydroxylated of UiO-66. With this approach the coordination number (N) of each contribution is fixed by the model stoichiometry. Refinement of the experimental amplitude is done by optimizing the overall amplitude factor S_0^2 only. The fitting of the higher shells was possible only adopting the axial compressed model of the M_6O_6 octahedron represented where eight octahedron sides R_{M1} are split into eight short prismatic distances (R_{M1}, $N = 8/3$) and four long planar ones (R_{M1b}, $N = 4/3$) and where the three diagonals R_{M2} are split into a short axial diagonal and (R_{M2a}, involving two M atoms out of six; $N = 1/3$) and two long planar diagonals (R_{M2b}, involving four M atoms out of six; $N = 2/3$). For the hydroxylated forms of UiO-66 and UiO-67 also the $R_{\mu 3\text{-}O}$ and $R_{\mu 3\text{-}OH}$ distances recently obtained by single crystal XRD have been reported for comparison. Adapted with permission from Ref. [165]

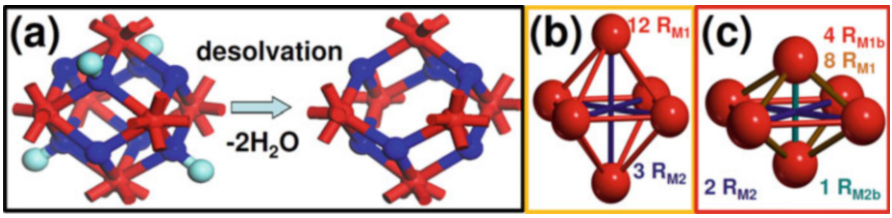

Fig. 26.5 Part (**a**): Stick and ball representation of the dehydroxylation undergone by the inorganic $M_6O_4(OH)_4$ cornerstone upon thermal treatment at 300 °C in vacuo resulting in a distorted M_6O_6 cluster (M = Zr or Hf). *Red*, *blue* and *cyan* colors refer to M, O and H atoms, respectively. Part (**b**): *Stick* and *ball* representation of the perfect M_6 octahedron, showing 12 equivalent R_{M1} sides and 3 equivalent $R_{M2} = \sqrt{2}\ R_{M1}$ diagonals. Part (**c**): *Stick* and *ball* representation of a squeezed M_6 octahedron. The 12 sides are now split into 4 in-plane long M_{M1b} sides and 8 prismatic short M_{M1a} sides, while the 3 diagonals evolve into 2 in-plane long M_{M2b} and 1 orthogonal short M_{M2a} diagonals. For clarity, O atoms are omitted in parts (**b**) and (**c**). Reproduced with permission from Ref. [165]

26.3.2 Pt-Functionalization of UiO-67 MOF

Introducing a chemically active Pt site as part of the UiO-67 framework is of great interest as platinum has rich redox chemistry, showing 0, II and IV stable oxidation states. Moreover, certain square planar Pt(II) coordination complexes are known to be active in C–H bond activation [167–171], see the scheme reported in Fig. 26.6a. In particular, the dichlorobipyrimidyl platinum(II), $PtCl_2$(BPYM), performs the catalytic oxidation in fuming or concentrated sulfuric acid, achieving high yields of methanol with selectivity higher than 90 % [172, 173]. It is consequently of potential interest to investigate the possibility to heterogenize such process anchoring the active Pt(II) complex on some high surface area material such as recently shown by the group of Schüth, for polymers first [174, 175] and for N-doped carbons [176] successively.

Øien et al. [103] have recently succeeded in functionalizing UiO-67 with $PtCl_2(H_2BPDC)$ (Fig. 26.6c) or $PtCl_4(H_2BPDC)$ units (Fig. 26.6b), substituting 10 % of the standard BPDC linkers. The authors used extended EXAFS and valence-to-core resonant inelastic X-ray scattering (RIXS) techniques to prove the insertion of Pt atoms in the expected framework position of UiO-67, see Fig. 26.6c.

Using EXAFS and XANES, the structural and oxidation state of Pt can be monitored under in situ conditions. The elimination of chlorine ligands from Pt in a continuous gas flow of H_2 have been monitored by EXAFS during temperature ramping, Fig. 26.7a. The spectrum collected at room temperature (black curve) exhibits both the first shell Pt–N and the Pt–Cl contributions centered around 1.5 and 1.9 Å (phase uncorrected FT) highlighted by vertical blue and green dashed lines, respectively. Upon increasing the temperature both contributions decreases in intensity because of the increased Debye-Waller factors (σ^2_N and σ^2_{Cl}). Starting from about 600 K the Pt-Cl contribution shows a much more relevant decrease

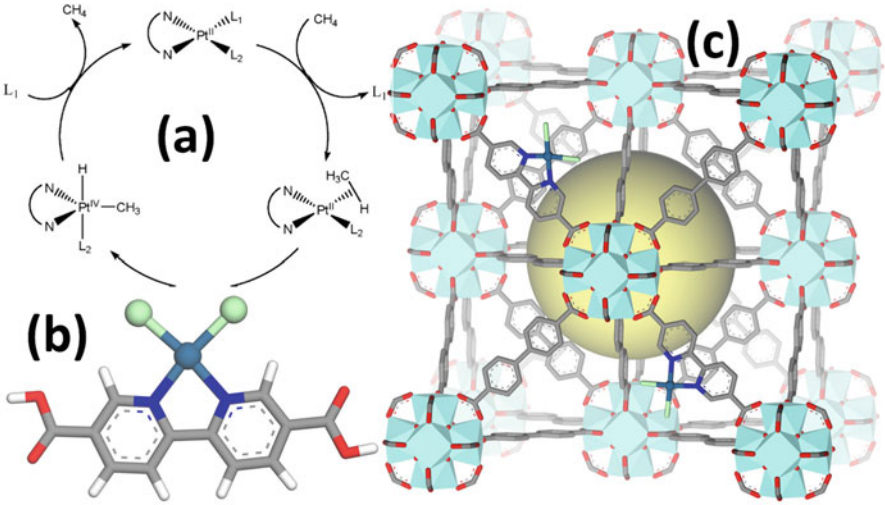

Fig. 26.6 Part (**a**): Suggested catalytic cycle of the C–H activation on square planar Pt (II) complex. L_1, L_2 = movable ligands, such as Cl, as reported in parts (**b**, **c**). Part (**b**): structure of the isolated $H_2BPDCPtCl_2$ center inserted in the MOF structure showing 2 N and 2 Cl in the first coordination shell of Pt(II) and showing the distortion induced on the two rings by Pt insertion. Part (**c**) three-dimensional representation of Pt(II)-functionalized UiO-67 MOF. Part (**a**) adapted by permission of the American Chemical Society (copyright 2006) from Ref. [99]; parts (**b**) and (**c**) adapted by permission of the American Chemical Society (copyright 2015) from Ref. [103]

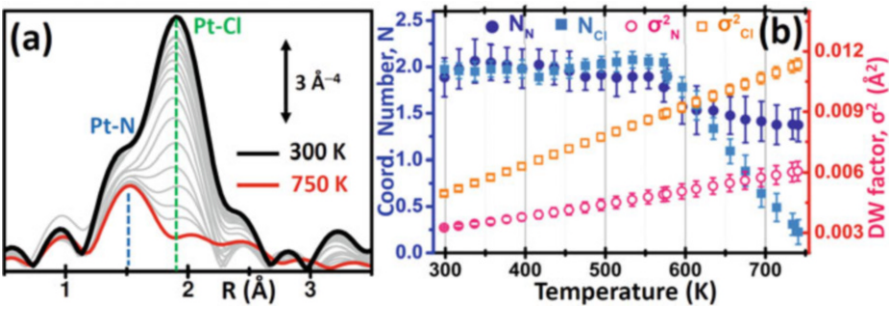

Fig. 26.7 Part (**a**): k^3-weighted, phase uncorrected, FT of Pt L_3-edge EXAFS spectra collected during the operando H_2-TPR experiments on $PtCl_2(H_2BPYDC)$ functionalized UiO-67-Pt (II) MOF in the 300 K (*black spectrum*)—750 K (*red spectrum*) range. Part (**b**): quantitative data analysis of the set of spectra shown in part (**a**) adopting a parametric refinement modeling the temperature dependence of the Debye–Waller factors (σ^2_N and σ^2_{Cl}) based on the Einstein model. Adapted by permission of the American Chemical Society (copyright 2015) from Ref. [103]

in temperature than the Pt–N one, suggesting that the system starts loosing chlorine ligands, leaving the MOF cavities as volatile HCl molecules. A standard EXAFS analysis failed because of the high correlation between the coordination numbers (N_{Pt-N}; N_{Pt-Cl}) and the thermal parameters (σ^2_N; σ^2_{Cl}) [103]. The problem was solved performing a complex data analysis briefly summarized hereafter.

First, authors worked only on the sub-set of data in the interval between RT and 473 K. In this temperature range no bond breaking occurs so that it was possible to fix $N_N = N_{Cl} = 2$. On that sub-set they performed a parametric refinement, commonly adopted in XRPD Rietveld refinements [164, 177], adopting the Einstein model for describing the temperature dependence of both σ^2_N and σ^2_{Cl} factors. The Einstein model approximates the vibrational density of states as a Dirac delta function spiked at a single frequency named Einstein frequency (ω_E). The model assumes that the pairs Pt−N (or Pt−Cl) behaves as a quantum harmonic oscillator of mass equal to the reduced mass of the atomic pair ($M = 13.070$ and 30.004 amu for the Pt−N and Pt−Cl pairs, respectively). Under such assumptions, the $\sigma^2(T)$ behavior is straightforwardly determined by the only ω_E parameter according to the Eq. (26.1): [103, 178]

$$\sigma^2(T) = \frac{h}{M\omega_E}\coth\left[\frac{h\omega_E}{2k_BT}\right] = \frac{h^2}{Mk_B\Theta_E}\coth\left[\frac{\Theta_E}{2T}\right] \tag{26.1}$$

Being Θ_E the Einstein temperature of the Pt−N (or Pt−Cl) bond, related to the Einstein frequency by the relationship: $\hbar\omega_E = k_B\Theta_E$, where $\hbar = 1.055 \times 10^{-34}$ J s is the reduced Planck constant and $k_B = 1.38 \times 10^{-23}$ J K^{-1} is the Boltzmann constant.

This approach allowed the authors to reduce the number of parameters used to optimize the thermal factors of the series from ~40 to only two, Θ_E(Pt−N) and Θ_E(Pt−Cl), with a consequent reduction of the correlation among the optimized parameters and thus a reduction of the relative error bars. Once obtained the Einstein temperatures Θ_E(Pt−N) and Θ_E(Pt−Cl), the dependence of both σ^2_N and σ^2_{Cl} vs. T was straightforwardly obtained via Eq. (26.1) and extrapolated on the whole set of data (i.e., also above 473 °C). This strategy allowed to have stable fits on the whole temperature range while optimizing both N_N and N_{Cl}, as shown in Fig. 26.7b. From this data analysis, it is evident that both N_N and N_{Cl} are stable to the stoichiometric values of 2.0 up to 575 K, when they start to decrease together. However, while N_{Cl} decreases almost linearly to 0.4 at 750 K, N_N undergoes a fast decrease to 1.6 at 610 K and then remains almost stable, reaching the value of 1.4 at 750 K. This means that a prolonged activation in H_2 of the UiO-67-Pt(II) MOF in the 610–640 K interval will result in a minimal loss of Pt(II), that will lose the Pt−N connection with the framework, but in the break of an important fraction of the Pt−Cl bonds. The experiment reported in Fig. 26.7 proved that this activation temperature interval is ideal to obtain a material where most of the functionalized Pt(II) species are still linked to the MOF framework, exhibiting the coordination vacancies needed to make the UiO-67-Pt(II) material a potential heterogeneous catalyst [103]. The presence of coordination vacancies at platinum sites was directly testified by IR spectroscopy of adsorbed CO.

EXAFS also provided evidence of the liquid phase ligand exchange with toluene-3,4-dithiol (H_2tdt) and of the liquid phase oxidative addition of Br_2 to Pt, see

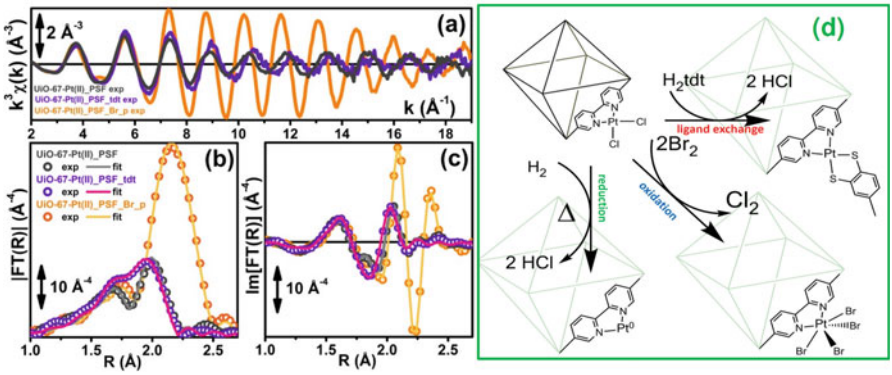

Fig. 26.8 Part (**a**): experimental Pt L_3-edge $k^3\chi(k)$ spectra of UiO-67-Pt(II) before (*black line*) and after interaction with H_2tdt (*violet line*) and Br_2 (*orange line*). Part (**b**): modulus of the k^3-weighted, phase uncorrected FT of the experimental EXAFS spectra reported in part (**a**), *open symbols*, same color code as in part (**a**). Also reported, as *continuous lines* of similar color, are the corresponding best fits. Part (**c**): as part (**b**) for the imaginary parts of the k^3-weighted, phase uncorrected FT. Part (**d**): Schematic representation of the reactivity of Pt^{II} species in functionalized UiO-67-Pt MOFs that has been *highlighted* in the EXAFS and XANES study reported in Fig. 26.7 and in parts (**a**–**c**) of this figure. The sketched *square bi-pyramid* represents the octahedral large cavity of UiO-67, measuring about 16 Å in diagonal [25, 27]. Adapted by permission of the American Chemical Society (copyright 2015) from Ref. [103]

Fig. 26.8. All observed reactions take place without any degradation of the framework, as testified by parallel XRPD experiments.

Also the XANES part of the XAS spectrum Fig. 26.9a is sensitive to the changes undergone by the local environment of Pt(II) along the chemical reactions reported in Fig. 26.8d. Indeed, upon change in the Pt oxidation state, Pt L_3-edge XANES will show a very small edge shift while exhibit a noticeable variation of the intensity of the "white-line" peak [103, 179, 180]. Indeed, the XANES part of the Pt L_3-edge mainly promotes core $2p_{3/2}$ electrons into empty $5d_{3/2}$, $5d_{5/2}$, and 6s valence states, so mainly probing the unoccupied density of 5d-states and partially 6s-states. The formal electronic configuration of platinum depends on its oxidation state as follows: Pt^0 ($6s^15d^9$), Pt^{II} ($6s^05d^8$), and Pt^{IV} ($6s^05d^6$); consequently an increase of the Pt oxidation states results in an higher density of unoccupied 5d states (and 6s) that is directly measured by an increase in the intensity of Pt L_3-edge. The XANES spectra reported in Fig. 26.9a for UiO-67-Pt(II) MOF before (red line) and after interaction with H_2tdt (blue line) and Br_2 (green line) clearly follow this quantitative, phenomenological guiding line. Interaction with H_2tdt (blue spectrum in Fig. 26.9a) does not change the white line intensity, affecting only the post edge and EXAFS region of the spectrum; on these basis it was concluded that a ligand exchange reaction occurred. Conversely interaction with Br_2 (green spectrum in Fig. 26.9a) results in a significant increase in the white line intensity, testifying an oxidation process from Pt(II) to Pt(IV) [103].

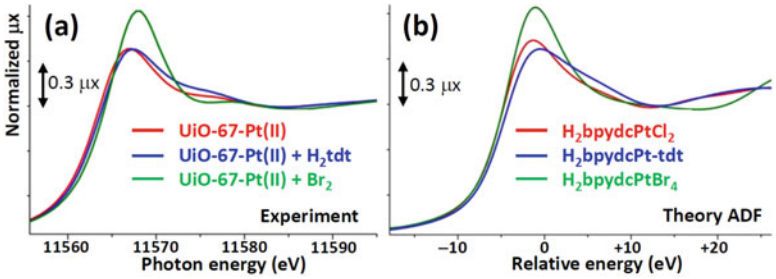

Fig. 26.9 Part (**a**): experimental Pt L_3-edge XANES spectra of UiO-67-Pt(II) before (*red line*) and after interaction with H_2tdt (*blue line*) and Br_2 (*green line*). Part (**b**): As part (**a**) for the theoretical spectra computed with ADF code. Reproduced with permission from Ref. [181]

On a more quantitative ground, the simulation of the XANES spectra, performed with quantum chemistry molecular orbital approach implemented in ADF code on the H_2bpydcPtCl_2, H_2bpydcPt-tdt, and H_2bpydcPtBr_4 molecular fragments (Fig. 26.9b), was able to reproduce correctly the variation of the white line intensity, and post edge features [181].

26.3.3 *Interaction of NH_3 with Cu^{2+} Sites in HKUST-1*

HKUST-1, also known as $Cu_3(BTC)_2$, is a Cu(II) based fcc-MOF characterized by a 3D system of square-shaped pores (9 Å × 9 Å) [182]. In $Cu_3(BTC)_2$ Cu^{2+} ions form dimers, where each copper atom is coordinated to four oxygen atoms, coming from the benzene-1,3,5 tricarboxylate (BTC) linkers ($[Cu_2C_4O_8]$ cage) and one water molecule adsorbed on each Cu^{2+} site [55, 155, 183]. A schematic representation of the $Cu_3(BTC)_2$ buildings blocks and how they are connected to give rise to the three-dimensional structure is reported in Fig. 26.10a (see also Fig. 26.1b). The EXAFS study of Prestipino et al. [155] showed that water molecules can be removed from the first coordination shell of Cu^{2+} without loss of crystallinity and porosity. This property is extremely important, as it implies the formation of coordinatively unsaturated Cu^{2+} sites that become consequently available for additional ligands such as molecules dosed from the gas phase (Fig. 26.10b). EXAFS analysis revealed that water removal from the first coordination shell of Cu^{2+} causes an important modification of the $[Cu_2C_4O_8]$ cage resulting in a decrease of the Cu^{2+}–Cu^{2+} distance from (2.64 ± 0.02) Å down to (2.50 ± 0.02) Å [155]. Successively, Borfecchia et al. [158] repeated the experiment and confirmed the shrinking of the Cu^{2+}–Cu^{2+} distance upon dehydration previously observed by Prestipino et al., but to a smaller extent: from (2.65 ± 0.02) Å down to (2.58 ± 0.02) Å, see Table 26.2.

Borfecchia et al. [158] also investigated by EXAFS the coordination of NH_3 on the dehydrated material, observing that ammonia binds to Cu^{2+} at a distance of

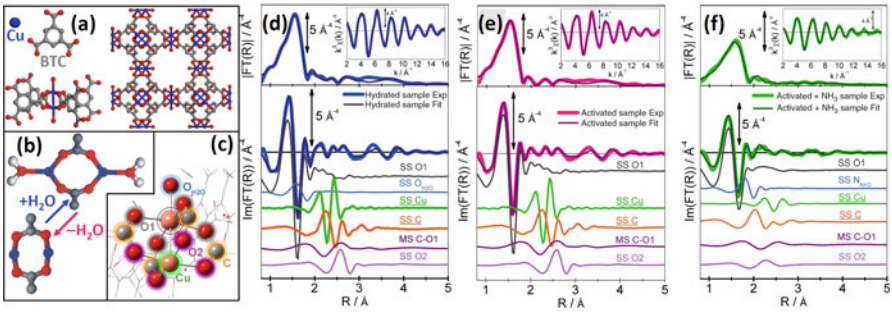

Fig. 26.10 Part (**a**): Schematic representation of the building blocks of HKUST-1. Two Cu^{2+} ions, and four benzene-1,3,5 tricarboxylate (BTC) linkers are bounded to give rise the final 3D structure. The picture shows the typical paddle wheel coordination of Cu^{2+} sites. Water molecules directly bounded to Cu^{2+} are represented by an oxygen atom only. Part (**b**) *top*: hydrated $[Cu_2C_4O_8](H_2O)_2$ cluster. Part (**b**) *bottom*: dehydrated $[Cu_2C_4O_8]$ cage. Color code: Cu^{2+} (*blue*); O (*red*); C (*gray*) H (*white*). Part (**c**): cluster used as starting point for the fitting procedure of EXAFS data. Atoms color code is the following: Cu *pale pink*, C *gray*, O *red*. The groups of atoms involved in the principal paths contributing to EXAFS signal are labeled and highlighted by different colored halos (oxygen atoms of the BTC carboxyl groups directly coordinated to the Cu_{abs}, O1, *gray*; oxygen of the water molecule directly coordinated to the Cu absorber, O_{H2O}, *light blue*; second copper atom of the dimer in front of the absorber, Cu, *green*; the four carbon atoms of the BTC carboxyl groups, C, *orange*; oxygen atoms coordinated to the not absorber copper site, O_2, *purple*). Parts (**d**), (**e**), and (**f**): Comparison between experimental and corresponding best fits for the hydrated (**d**), dehydrated (**e**), and dehydrated + NH_3 (**f**) sample. *Top panels* report the modulus of the FT, while *bottom panels* show the imaginary parts of the FT, and the principal paths contributions to the total signal. Parts (**a**, **b**) adapted with permission from Ref. [183], copyright RSC 2007; parts (**c**–**f**) adapted with permission from Ref. [158]. Copyright ACS (2012)

Table 26.2 Summary of the Cu–Cu and Cu–L (L = H_2O or NH_3) bond distances in HKUST-1 MOF obtained by single crystal (SC) XRD and EXAFS. Previously unpublished table, reporting data published in the references quoted in the last column

Ligand (L)	Technique	Cu–Cu distance (Å)	Cu–L distance (Å)	References
H_2O	SC XRD	2.628(2)	2.165(8)	[182]
H_2O	EXAFS	2.64(2)	2.19(2)	[155]
H_2O	EXAFS	2.65(2)	2.24(2)	[158]
–	EXAFS	2.50(2)	–	[155]
–	EXAFS	2.58(2)	–	[158]
NH_3	EXAFS	2.80(3)	2.31(1)	[158]

(2.31 ± 0.01) Å (while water coordinates at (2.24 ± 0.03) Å) and causes an impressive expansion of the Cu^{2+}–Cu^{2+} distance up to (2.80 ± 0.03) Å, see Table 26.2.

Of interest is also the XANES study reported by Borfecchia et al. [158] and here summarized in Fig. 26.11. Part (a) reports the experimental XANES spectra of HKUST-1 as-prepared (hydrated sample, blue solid line), after activation at 453 K (dehydrated sample, pink solid line) and upon contact with 60 mbar of ammonia at room temperature (green solid line). The XANES spectra of the as prepared and

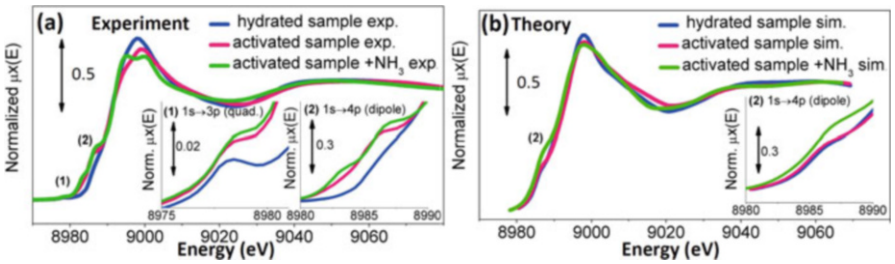

Fig. 26.11 Part (**a**): Experimental XANES spectra of HKUST-1 in its hydrated (*blue line*) and dehydrated (*pink line*) forms and after successive interaction with NH_3 (*green line*). The *insets* report magnifications of the $1s \rightarrow 3d$ quadrupolar transition (**1**) and of the shakedown $1s \rightarrow 4p$ transition (**2**). Part (**b**): as part (**a**) for the simulated spectra. Adapted with permission from Ref. [158]. Copyright ACS (2012)

dehydrated sample are typical of Cu(II) species, showing the edge jump at 8990 eV and two characteristic pre-edge peaks at ca. 8976 eV and ca. 8986 eV, labeled as (**1**) and (**2**), respectively, in Fig. 26.11a, and separately reported in the insets of the same part. Feature (**1**) is assigned to the very weak $1s \rightarrow 3d$ quadrupolar transition, while the shoulder (**2**) appearing along the white line profile is related to the dipolar shakedown $1s \rightarrow 4p$ transition.

XANES spectra reported in Fig. 26.11b were simulated using FEFF8.4 code [133]. For the hydrated version of HKUST-1 (blue spectrum) the authors adopted as input geometry the structure optimized in the single crystal XRD study of Chui et al. [182] and cutting a cluster centered on one of the Cu atoms with a radius of 6 Å around it. For a further improvement of the simulations, an optimization of geometrical parameters was performed exploiting FitIt software [184] and optimizing five structural parameters: (1) the Cu–Cu and (2) Cu–H_2O bond length, the distance between the Cu atom and the BTC carboxyl groups with a separate optimization of (3) Cu–O1 and of (4) Cu–C and Cu–O_2 distances (optimized in a correlated way to use only one free parameter) and (5) a general overall contraction or elongation of all the other distances ($R_{XANES} = \alpha\ R_{XRD}$) [126, 185]. See Fig. 26.10c for the atom notation. It has been observed that a variation of Cu–Cu distance reflected in very slight changes in the XANES features, the Cu–H_2O distance influences the intensity and partially the position in energy of the pre-edge feature (**2**), the carbonyl groups distances and a possible overall contraction or expansion strongly influence both the intensity and the position of the white line and the shape of the multiple scattering features at higher energies [158].

The simulation of the dehydrated sample was obtained removing the water molecules from the previous cluster, while for the sample in interaction with ammonia the H_2O molecules were substituted by two NH_3 ones [158]. In the case of the hydrated sample, the best agreement between the simulated curve and experimental data was obtained with a slight shortening of Cu–H_2O distance, an elongation of 0.05 Å of both Cu–O1 and the constrained Cu–C and Cu–O_2 distances, corresponding to a shift along the bond axis of the carbonyl groups and a

slight general contraction of all other distances. Upon water removal, no shift in the absorption edge is observed, providing an evidence that no change in oxidation state of the Cu center occurs. However, the XANES spectrum of the dehydrated sample shows: (1) a decrease of the white line intensity, and (2) an increase in the intensity of feature (**2**), that appears more as a well separated band than as a white line shoulder. The simulation of the XANES spectrum for the activated sample was performed with the same method previously described for the hydrated sample removing the atoms of the two water molecules, resulting in an optimization with four parameters only. Even without a structural optimization, in the simulated spectra it has been observed the same trend noticed on the experimental curves where the decrease of the white line intensity is correlated to the lower coordination number, and the increase of the intensity of feature (**2**) is ascribable to a lower symmetry of the Cu(II) species. The authors concluded that in the simulated curves this trend is less evident probably because a full description of the asymmetric distortion undergone by the Cu species in the activated sample would require a too high number of parameters to be optimized. The optimization of the bond distances resulted in a slight contraction of the distances between the absorbing Cu atom and carbonyl groups and all other distances, in agreement with the results found by EXAFS study (see Fig. 26.10 and Table 26.2). The XANES spectrum of the activated sample after the interaction with NH_3 evidences an additional increase in the intensity and a slight blue-shift of the dipole band (**2**) assigned to the $1s \rightarrow 4p$ transition [158]. Moreover, a new pre-edge peak is observed at ca. 8983 eV. Despite the edge position is not modified respect to the as prepared and activated samples (no change in oxidation state of the metal), the white line is modified towards a more structured appearance, and seems to return towards the shape observed in the case of the hydrated sample. The simulation of the spectrum for the sample after interaction with NH_3 was performed following the same method adopted for the hydrated material and substituting the water molecules with two NH_3 molecules. After the optimization of the geometrical parameters it has been observed that an increasing of the intensity of the pre-edge feature (**2**) is proportional to the Cu–NH_3 distance which was optimized at 2.3 Å with a considerable elongation with respect to the previous position of the water molecules. Moreover a splitting of the white line feature, even if less evident with respect to the experimental spectra, has been observed after a distortion of carbonyl groups simulated by a slight elongation of Cu–O1 distances but a severe shortening of both Cu–C and Cu–O_2 and all other distances. The authors concluded that that the deformation introduced to simulate the XANES spectra is in agreement with the results of the EXAFS fit [158].

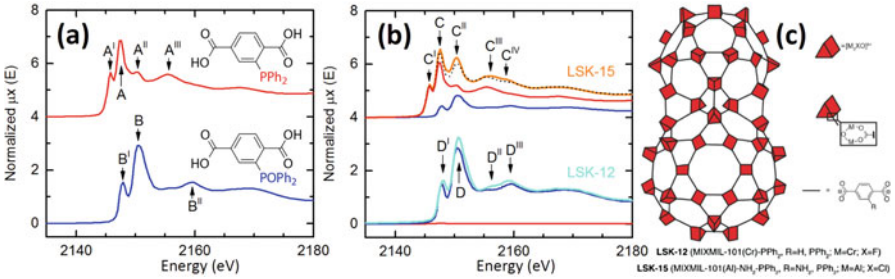

Fig. 26.12 Part (**a**): P K-edge XANES spectra of the PPh_2–BDC (*red curve*) and $POPh_2$–BDC (*blue curve*) organic linkers. Also reported are the linker structure and the peak labeling. Part (**b**): P K-edge XANES spectra of LSK-15 (*orange curve*) and LSK-12 (*cyan curve*) P-MOFs with MIL-101 topology. The *red* and *blue* spectra represent the weighted fraction of the linker spectra, see part (**a**), used to reproduce the XANES spectra of the P-MOFs with a linear combination approach (*dotted spectrum*). Part (**c**): Schematic representation of P-MOFs with MIL-101 topology. Adapted with permission from Ref. [191]. Copyright Royal Society of Chemistry (2015)

26.3.4 Discrimination Between Phosphine and Phosphine Oxide Groups in P-MOFs by P K-Edge XAS

Phosphine metal–organic frameworks (P-MOFs) are crystalline porous coordination polymers that contain phosphorus functional groups within their pores [186–191]. Incorporation of phosphine functional groups inside structures with new and existing topologies is achieved using direct solvothermal synthesis, postsynthetic modification [192] or the co-crystallization of organic linkers with similar connectivity [193]. Interesting applications for this new class of materials have been foreseen in transition metal immobilization and catalysis [187, 194].

Very recently Morel et al. [191] used soft-X-ray P-K-edge XAS to determine the phosphine to phosphine oxide ratio in two P-MOFs with MIL-101 topology, whose structure is described in Fig. 26.12c. This achievement is of particular relevance as the phosphorus oxidation state is of particular interest as the phosphine to phosphine oxide ratio influences the coordination affinity of P-MOFs for transition metals. Differently to solid state NMR spectroscopy, P–K-edge XAS can determine the oxidation state of phosphorus even when the material contains paramagnetic nuclei.

The P K-edge XAS spectra of PPh_2-BDC and $POPh_2$-BDC linkers, see Fig. 26.12a red and blue spectra respectively, provide a spectral reference for the characterization of the two P-MOFs. A blue shift in the white line from 2147.3 to 2150.6 eV is observed upon oxidation of the phosphorus nuclei, compare the pre-edge resonances (A^I and B^I in Fig. 26.12a), that are attributed to the effect of phenyl groups in the higher coordination shells of the phosphorus [195]. The spectrum of PPh_2-BDC exhibits a more pronounced pre-edge feature relative to its white line, compared to that of the $POPh_2$-BDC linker. Spectral features are not affected equally by the presence of an oxygen atom, with a 2.2 eV shift for A^I to B^I

features compared to a 3.3 eV for the A to B white lines. PPh_2-BDC displayed an additional spectral feature A^{II} at an energy very close to that of the white line of $POPh_2$-BDC (2150.3 eV) and indicates partial oxidation of the sample in agreement with a parallel ^{31}P NMR investigation [191].

The P K-edge XANES spectra of LSK-15 and LSK-12 P-MOFs are reported in Fig. 26.12b, orange and cyan spectra, respectively. The former P-MOF is characterized by a complex XANES spectrum defined by five different absorption features (C to C^{IV}), which testifies the presence of multiple phosphorus oxidation states. As for PPh_2-BDC linker, LSK-15 displayed features related to the white lines of triarylphosphine (C) and triarylphosphine oxide (C^{II}) at 2145.7 and 2150.2 eV, respectively. The relative intensity of C^{II} to C ratio is higher in LSK-15 than in the corresponding A^{II} to A ratio in the organic linker PPh_2-BDC providing proof of phosphorus oxidation inside this MOF. The pre-edge feature C^{I} is attributed to the characteristic resonance of phosphine environment in PPh_2-BDC. The XANES spectrum of LSK-12 displays fewer features than LSK-15 (D to D^{III}). Comparison based solely on the absorption edge positions of the two organic linkers is difficult due to a perceived overlap between A and B^{I}, which could both be contributors to the D^{I} feature. However, the absence of the corresponding A^{I} pre-edge feature in LSK-12, and to a lesser extent the small edge shift between C and D^{I}, are indicative of phosphine oxide as the primary phosphorus species in LSK-12. The relative intensities of the white line D and the pre-edge feature D^{I} also compare well with the $POPh_2$-BDC organic linker. Finally, Morel et al. [191] reproducing the XANES spectrum of the P-MOF samples with a linear combination of the spectra of the linkers concluded that phosphine accounts for about 70 % of the total phosphorus groups in LSK-15 and that LSK-12 contains only phosphine oxide, see Fig. 26.12b.

26.3.5 Optimized Finite Difference Method for the Full-Potential XANES Simulations: Application to Molecular Adsorption Geometries in MOFs

Over the past two decades much progress has been made in the understanding the features of the XANES region of the X-ray absorption spectra [133, 134, 137–141, 196–205].

As already outlined at the end of Sect. 26.3.3 (see Fig. 26.11 and related discussion) appearance of progressively more sophisticated codes, together with the increased computational capabilities, has made XANES a spectroscopy able to quantitatively confirm or discard a structural model for the environment of the X-ray absorbing atom, forming thus a new fundamental diagnostic tool in condensed matter physics and chemistry [119, 148, 149, 206]. Besides the multiple scattering approach (used for example by FEFF [133], XKDQ [207], CONTINUUM [208, 209], MXAN [138, 139] codes), the finite difference method (FDM)

[140, 141, 205] is attractive for calculations of the photoelectron wave function up to 100−200 eV above the absorption edge avoiding, in a simple way, the muffin tin approximation used in the multiple scattering theory approaches. In the muffin tin approximation, the potential is assumed to be spherical inside the touching (or overlapping) atomic spheres and constant between them [134]. The main drawback of the XANES simulation in the FDM approach is the heavy computational time and the huge RAM required to store the computed values. Very recently, due to the use of dedicated solvers for sparse matrices, Guda et al. [141] succeeded in reducing by more than one order of magnitude the required CPU time and in halving the needed RAM required by the standard Gaussian method previously used by the FDMNES code [140]. The potentialities of this improved version of the FDMNES code are hereafter discussed using as example the Ni K-edge XANES spectra of CPO-27-Ni MOF and its modification upon molecular adsorption on the Ni site.

CPO-27-Ni MOF [122] contains one-dimensional channels which are filled with water that can be removed by a mild thermal treatment. Upon dehydration the crystalline structure is preserved and a material with a high surface area containing unsaturated metal sites organized in helicoidal chains is obtained [126], see above Fig. 26.3d. In its dehydrated form the first coordination of Ni^{2+} atoms consists into five framework oxygen atoms in a square planar pyramidal-like configuration, leaving one coordination vacancy free for adsorbate coordination adsorbate molecules such as: CO [125], H_2O [126], NO [126], N_2 [123], C_2H_4 [123], H_2S [210]. As shown above in Fig. 26.3c, the adsorption of a molecule into the coordination vacancy of Ni^{2+} causes weak, but significant, changes in the Ni K-edge XANES spectrum of CPO-27-Ni. As just outlined, the XANES simulation in the FDM approach is CPU time consuming. Indeed, a large cluster must be cut around the Ni atom that undergoes the photoelectric effect before reaching convergence of the XANES calculations. This fact is clearly shown in Figure 26.13a showing that the simulated XANES spectrum of the dehydrated form of CPO-27-Ni changes significantly moving from a cluster cut R = 3 Å to one cut at R = 5 Å. This fact is even more evident in Figure 26.13b where the difference spectra are shown: $\Delta\mu_{7,R}^{theo}(E) = \mu_7^{theo}(E) - \mu_R^{theo}(E)$. Unfortunately, the CPU needed to perform the XANES simulation scales approximatively with an exponential function of the cluster size, as shown by the scattered squares reported in the inset of Figure 26.13a, that are almost linear in a logarithmic ordinate scale. This means that the simulation on the R = 7 Å cluster is 44 times more demanding than that on the R = 4 cluster; moreover it requires 14 times more RAM memory (data not reported in the inset). The accelerated version of the FDMNES code [141] reduces significantly the requested CPU time for the same calculations; see scattered triangles in the inset of Figure 26.13a. Of particular interest is the fact that the speed-up of the calculations (defined as the ratio between the CPU time needed in to perform a given calculation in the standard code divided by the time needed for the same calculation with the accelerated version of the code) scales favorably with the increasing cluster size: with some fluctuations it moves from 14 to 38 moving from the R = 4 Å

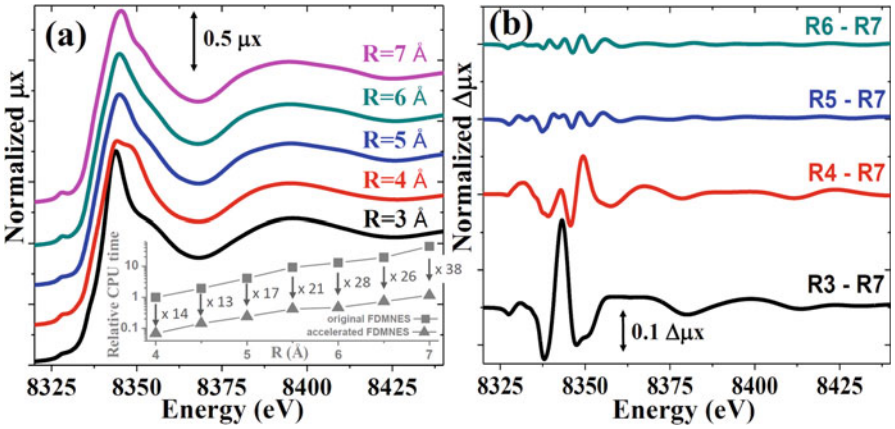

Fig. 26.13 Part (**a**): normalized theoretical Ni K-edge XANES spectra computed with the FDNMES code as a function of cluster size used in calculations for the CPO-27-Ni structure. The *inset* reports, in logarithmic scale, the relative CPU time needed to run the XANES simulation on the cluster of radius R with the original FDMNES code (*squares*) and with the new accelerated version (*triangles*), with respect to the time needed for the R = 4 Å simulation with the original version of the code. The *numbers* close to the vertical arrows represent the speed-up factor for a given cluster size defined as CPU(original)/CPU(accelerated). Part (**b**): difference XANES spectra calculated for the spectra reported in part (**a**) with respect to R = 7 Å simulation. In both panels the spectra are shifted vertically for the sake of clarity. For a view of the CPO–27–Ni structure, see Fig. 26.3. Adapted with permission from Ref. [141], copyright American Chemical Society (2015)

cluster to the R = 7 Å one (see the numbers reported close to the vertical arrows in the inset).

The gain of a factor larger than one order of magnitude (up to forty for the large clusters relevant to obtain a meaningful simulation) makes it possible to perform structural determination from a detailed XANES study. To prove this concept we show that it is possible form the simulation of the XANES spectra to determine the geometry of the molecular complex formed upon adsorption of a diatomic ligand molecule (NO or CO) on the coordination vacancy of Ni^{2+} sites in the dehydrated form of CPO-27-Ni MOF. As the spectroscopic difference between the XANES spectra collected before and after molecular adsorption are not very large (see for example the case of N_2 adsorption reported in Fig. 26.3c), they are better appreciated by reporting the difference spectra $\Delta\mu^{exp} = \mu^{exp}(+NO) - \mu^{exp}$ (dehyd), as done in the scattered dots spectrum reported in Fig. 26.14a, for the case of NO adsorption. Also reported (red curve) is the analogous difference spectrum obtained from the simulations: $\Delta\mu^{theo,\theta} = \mu^{theo,\theta}(+NO) - \mu^{theo}(dehyd)$. As shown in Fig. 26.14b, $\mu^{theo,\theta}(+NO)$, an thus $\Delta\mu^{theo,\theta}(+NO)$, depends on the

adsorption geometry of the NO molecule, in particular on the adsorption angle Ni–N–O (θ).

The simulations reported in Fig. 26.14b clearly indicate that it is possible to determine the adsorption angle θ by an appropriate comparison between the experimental Δμ and the theoretical ones computed for different θ angles. The red squares in Fig. 26.15 reports the integrated difference over all the sampled points of $|\Delta\mu^{exp}(E_i) - \Delta\mu^{theo,\theta}(E_i)|$ in the 8325–8440 eV interval plotted versus the adsorption angle θ used in the simulations. From the results it is evident that the linear geometry is not favored and that the XANES simulations predict a bent geometry for the Ni···NO adducts with a θ angle in the 90-140 ° range. Conversely, for the CO adsorption (scattered black circles in Fig. 26.15) the linear geometry (θ ~ 180°) is clearly favored. These results are in agreement with the periodic DFT calculation performed by Valenzano et al. [124] where the optimized structures were characterized by adsorption angles of Ni−N−O = 123° and of Ni−C−O = 171°, while the fitting of the EXAFS data resulted in good agreement with the experimental data by fixing the adsorption angles to Ni−N−O = 130° and of Ni−C−O = 180° [125, 126].

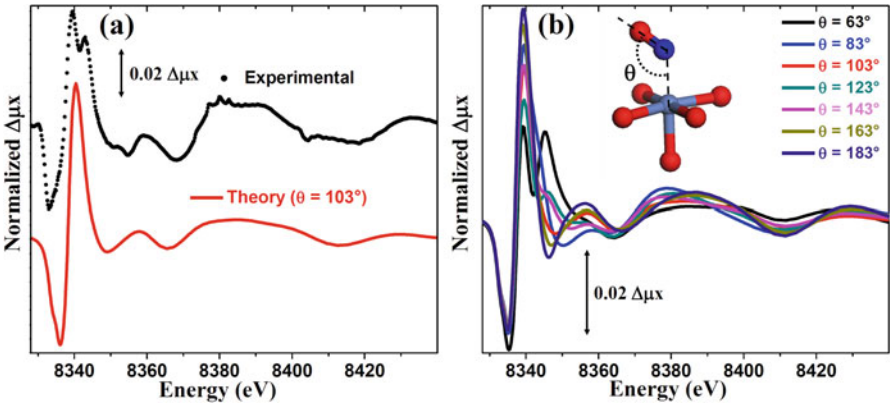

Fig. 26.14 Part (**a**): Difference XANES spectrum obtained subtracting the experimental spectrum of the dehydrated CPO-27-Ni MOF form that obtained after dosing NO on the same sample (*black scattered dots*). The *red spectrum* is the analogous difference XANES spectrum obtained from the subtracting the spectra obtained with the FDMNES simulations with a Ni–N–O angle (θ) of 103°. Part (**b**): Effect of θ in the computed difference XANES spectra. The *inset* reports, with the sticks and balls drawing, a cartoon of the first shell around Ni (*lilac*) formed by five framework O (*red*) plus the coordinated NO molecule, N (*blue*), defining the θ angle. Previously unpublished figure reporting data discussed in Ref. [141]

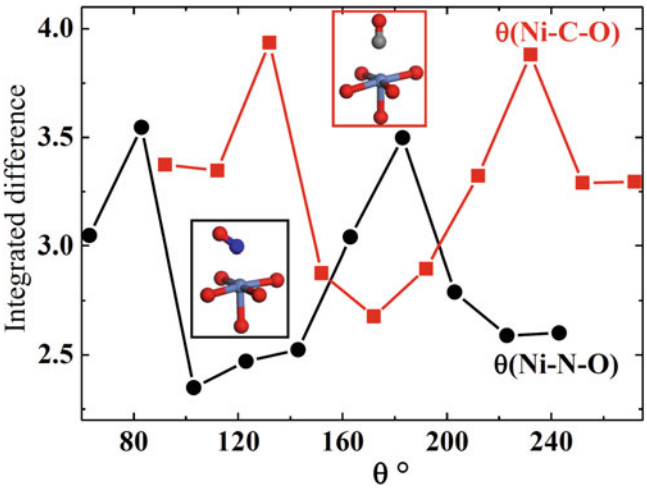

Fig. 26.15 Integrated difference over all the sampled points of $|\Delta\mu^{exp}(E_i) - \Delta\mu^{theo,\theta}(E_i)|$ in the 8325-8440 eV interval plotted versus the adsorption angle θ used in the simulations. *Red squares* and *black circles* refer to the CO and NO adsorption, respectively. The *inset* reports, with the sticks and balls drawing, a cartoon of the first shell around Ni of the carbonyl and nitisol adducts formed inside CPO–27–Ni MOF: Ni(*lilac*), O (*red*), N (*blue*), C (*gray*). Adapted with permission from Ref. [141]. Copyright American Chemical Society (2015)

26.4 Conclusions

In this chapter, we introduce MOFs as the new class of crystalline porous materials of remarkable potentialities. We underline the flexibility in the realization of different MOFs and the fact that they are ideal materials for performing X-ray absorption experiments at the metal K or L_3 edges in transmission mode. A selection of relevant results appearing in the last five years follows, underlying the relevant role of both EXAFS and XANES in determining the structural and electronic configuration of metals centers inside MOFs.

Acknowledgements We acknowledge C. Prestipino, D. Gianolio G. Agostini, S. Jakobsen, M.H. Nilsen, P.D.C. Dietzel, S. A. Guda, A. L. Bugaev, A. V. Soldatov, and F. Morel for the their contribution to some of the results reviewed here. We are indebted to F. Morel for having kindly provided a new color version of Fig. 26.12. K.A.L., A.A.G., M.A.S., and C.L. acknowledge the Mega-grant of the Russian Federation Government to support scientific research at the Southern Federal University, No. 14.Y26.31.0001. KAL acknowledges the scholarship of the President of Russia for PhD students and young scientists No. СП-2796.2016.1. AAG acknowledges the grant of the President of Russia for young scientists MK-7300.2016.2. EB acknowledges Innovation Fund Denmark (Industrial postdoc n. 5190-00018B).

References

1. Cheetham AK, Ferey G, Loiseau T (1999) Open-framework inorganic materials. Angew Chem Int Ed 38:3268–3292
2. James SL (2003) Metal-organic frameworks. Chem Soc Rev 32:276–288
3. Bradshaw D, Claridge JB, Cussen EJ et al (2005) Design, chirality, and flexibility in nanoporous molecule-based materials. Accounts Chem Res 38:273–282
4. Ferey G (2008) Hybrid porous solids: past, present, future. Chem Soc Rev 37:191–214
5. O'Keeffe M (2009) Design of MOF and intellectual content in reticular chemistry: a personal view. Chem Soc Rev 38:1215–1217
6. Perry JJ IV, Perman JA, Zaworotko MJ (2009) Design and synthesis of metal-organic frameworks using metal-organic polyhedra as supramolecular building blocks. Chem Soc Rev 38:1400–1417
7. Morris RE, Bu XH (2010) Induction of chiral porous solids containing only achiral building blocks. Nat Chem 2:353–361
8. Furukawa H, Ko N, Go YB et al (2010) Ultrahigh porosity in metal-organic frameworks. Science 329:424–428
9. Farha OK, Hupp JT (2010) Rational design, synthesis, purification, and activation of metal-organic framework materials. Accounts Chem Res 43:1166–1175
10. Seeber G, Cooper GJT, Newton GN et al (2010) Following the self assembly of supramolecular MOFs using X-ray crystallography and cryospray mass spectrometry. Chem Sci 1:62–67
11. Bordiga S, Bonino F, Lillerud KP et al (2010) X-ray absorption spectroscopies: useful tools to understand metallorganic frameworks structure and reactivity. Chem Soc Rev 39:4885–4927
12. Zhou HC, Long JR, Yaghi OM (2012) Introduction to metal-organic frameworks. Chem Rev 112:673–674
13. Furukawa H, Cordova KE, O'Keeffe M et al (2013) The chemistry and applications of metal-organic frameworks. Science 341:1230444–1230444
14. Llabrés i Xamena F, Gascon J (2013) Metal organic frameworks as heterogeneous catalysts. The Royal Society of Chemistry, Cambridge
15. Colon YJ, Snurr RQ (2014) High-throughput computational screening of metal-organic frameworks. Chem Soc Rev 43:5735–5749
16. Schneemann A, Bon V, Schwedler I et al (2014) Flexible metal-organic frameworks. Chem Soc Rev 43:6062–6096
17. Zhu QL, Xu Q (2014) Metal-organic framework composites. Chem Soc Rev 43:5468–5512
18. Butova VV, Soldatov MA, Guda A et al. (2016) Metal-organic frameworks: structure, properties, synthesis, and characterization. Russ Chem Rev 85: 280-307
19. Ferey G (2001) Microporous solids: from organically templated inorganic skeletons to hybrid frameworks ... ecumenism in chemistry. Chem Mater 13:3084–3098
20. Eddaoudi M, Moler DB, Li HL et al (2001) Modular chemistry: secondary building units as a basis for the design of highly porous and robust metal-organic carboxylate frameworks. Accounts Chem Res 34:319–330
21. Long JR, Yaghi OM (2009) The pervasive chemistry of metal-organic frameworks. Chem Soc Rev 38:1213–1214
22. Baerlocher C, Meier WM, Olson DH (2001) Atlas of zeolite frameworks types. Elsevier, Amsterdam
23. Tranchemontagne DJ, Mendoza-Cortes JL, O'Keeffe M et al (2009) Secondary building units, nets and bonding in the chemistry of metal-organic frameworks. Chem Soc Rev 38:1257–1283
24. Eddaoudi M, Kim J, Rosi N et al (2002) Systematic design of pore size and functionality in isoreticular MOFs and their application in methane storage. Science 295:469–472

25. Cavka JH, Jakobsen S, Olsbye U et al (2008) A new zirconium inorganic building brick forming metal organic frameworks with exceptional stability. J Am Chem Soc 130:13850–13851
26. Valenzano L, Civalleri B, Bordiga S et al (2011) Disclosing the complex structure of UiO-66 MOF: a synergic combination of experiment and theory. Chem Mater 23:1700–1718
27. Chavan S, Vitillo JG, Gianolio D et al (2012) H_2 storage in isostructural UiO-67 and UiO-66 MOFs. Phys Chem Chem Phys 14:1614–1626
28. Lillerud K, Olsbye U, Tilset M (2010) Designing heterogeneous catalysts by incorporating enzyme-like functionalities into MOFs. Top Catal 53:859–868
29. Müller U, Schubert M, Teich F et al (2006) Metal-organic frameworks – prospective industrial applications. J Mater Chem 16:626–636
30. Czaja A, Trukhan T, Müller U (2009) Industrial applications of metal-organic frameworks. Chem Soc Rev 38:1284–1293
31. Li J-R, Luppler RJ, Zhou HC (2009) Selective gas adsorption and separation in metal-organic frameworks. Chem Soc Rev 38:1477–1504
32. Shimomura S, Higuchi M, Matsuda R et al (2010) Selective sorption of oxygen and nitric oxide by an electron-donating flexible porous coordination polymer. Nat Chem 2:633–637
33. Li JR, Sculley J, Zhou HC (2012) Metal-organic frameworks for separations. Chem Rev 112:869–932
34. Qiu SL, Xue M, Zhu GS (2014) Metal-organic framework membranes: from synthesis to separation application. Chem Soc Rev 43:6116–6140
35. Dinca M, Long JR (2005) Strong H_2 binding and selective gas adsorption within the microporous coordination solid $Mg_3(O_2C\text{-}C_{10}H_6\text{-}CO_2)_3$. J Am Chem Soc 127:9376–9377
36. Vitillo JG, Savonnet M, Ricchiardi G et al (2011) Tailoring metal-organic frameworks for CO_2 capture: the amino effect. ChemSusChem 4:1281–1290
37. Chaemchuen S, Kabir NA, Zhou K et al (2013) Metal-organic frameworks for upgrading biogas via CO_2 adsorption to biogas green energy. Chem Soc Rev 42:9304–9332
38. Cabello CP, Berlier G, Magnacca G et al (2015) Enhanced CO_2 adsorption capacity of amine-functionalized MIL-100(Cr) metal-organic frameworks. CrystEngComm 17:430–437
39. Rodenas T, Luz I, Prieto G et al (2015) Metal–organic framework nanosheets in polymer composite materials for gas separation. Nat Mater 14:48–55
40. Ferey G, Serre C, Devic T et al (2011) Why hybrid porous solids capture greenhouse gases? Chem Soc Rev 40:550–562
41. Sumida K, Rogow DL, Mason JA et al (2012) Carbon dioxide capture in metal-organic frameworks. Chem Rev 112:724–781
42. McDonald TM, Mason JA, Kong XQ et al (2015) Cooperative insertion of CO_2 in diamine-appended metal-organic frameworks. Nature 519:303–308
43. Matsuda R, Tsujino T, Sato H et al (2010) Temperature responsive channel uniformity impacts on highly guest-selective adsorption in a porous coordination polymer. Chem Sci 1:315–321
44. Pan L, Olson DH, Ciemnolonski LR et al (2006) Separation of hydrocarbons with a microporous metal-organic framework. Angew Chem Int Edit 45:616–619
45. Barea E, Montoro C, Navarro JAR (2014) Toxic gas removal – metal-organic frameworks for the capture and degradation of toxic gases and vapours. Chem Soc Rev 43:5419–5430
46. DeCoste JB, Peterson GW (2014) Metal-organic frameworks for air purification of toxic chemicals. Chem Rev 114:5695–5727
47. Suh K, Yutkin MP, Dybtsev DN et al (2012) Enantioselective sorption of alcohols in a homochiral metal-organic framework. Chem Commun 48:513–515
48. Van de Voorde B, Bueken B, Denayer J et al (2014) Adsorptive separation on metal-organic frameworks in the liquid phase. Chem Soc Rev 43:5766–5788
49. Getman RB, Bae YS, Wilmer CE et al (2012) Review and analysis of molecular simulations of methane, hydrogen, and acetylene storage in metal-organic frameworks. Chem Rev 112:703–723

50. Wu HH, Gong QH, Olson DH et al (2012) Commensurate adsorption of hydrocarbons and alcohols in microporous metal organic frameworks. Chem Rev 112:836–868
51. Vitillo JG, Regli L, Chavan S et al (2008) Role of exposed metal sites in the hydrogen storage in MOFs. J Am Chem Soc 130:8386–8396
52. Murray LJ, Dinca M, Long JR (2009) Hydrogen storage in metal-organic frameworks. Chem Soc Rev 38:1294–1314
53. Han SS, Mendoza-Cortes JL, Goddard WA (2009) Recent advances on simulation and theory of hydrogen storage in metal-organic frameworks and covalent organic frameworks. Chem Soc Rev 38:1460–1476
54. Rossin A, Di Credico B, Giambastiani G et al (2012) Synthesis, characterization and CO_2 uptake of a chiral Co(II) metal-organic framework containing a thiazolidine-based spacer. J Mater Chem 22:10335–10344
55. Xiao B, Wheatley PS, Zhao XB et al (2007) High-capacity hydrogen and nitric oxide adsorption and storage in a metal-organic framework. J Am Chem Soc 129:1203–1209
56. Horcajada P, Chalati T, Serre C et al (2010) Porous metal-organic-framework nanoscale carriers as a potential platform for drug delivery and imaging. Nat Mater 9:172–178
57. Horcajada P, Gref R, Baati T et al (2012) Metal-organic frameworks in biomedicine. Chem Rev 112:1232–1268
58. Bloch ED, Queen WL, Chavan S et al (2015) Gradual release of strongly bound nitric oxide from $Fe_2(NO)_2$(dobdc). J Am Chem Soc 137:3466–3469
59. Bunzli JCG, Piguet C (2002) Lanthanide-containing molecular and supramolecular polymetallic functional assemblies. Chem Rev 102:1897–1928
60. Bordiga S, Lamberti C, Ricchiardi G et al (2004) Electronic and vibrational properties of a MOF-5 metal-organic framework: ZnO quantum dot behaviour. Chem Commun 20:2300–2301
61. Allendorf MD, Bauer CA, Bhakta RK et al (2009) Luminescent metal-organic frameworks. Chem Soc Rev 38:1330–1352
62. Kovalenko KA, Dybtsev DN, Lebedkin SF et al (2010) Luminescence properties of mesoporous chromium(III) terephthalate and inclusion compounds of cluster complexes. Russ Chem Bull 59:741–744
63. Wang C, Zhang T, Lin WB (2012) Rational synthesis of noncentrosymmetric metal-organic frameworks for second-order nonlinear optics. Chem Rev 112:1084–1104
64. Cui YJ, Yue YF, Qian GD et al (2012) Luminescent functional metal-organic frameworks. Chem Rev 112:1126–1162
65. Heine J, Muller-Buschbaum K (2013) Engineering metal-based luminescence in coordination polymers and metal-organic frameworks. Chem Soc Rev 42:9232–9242
66. Cui YJ, Chen BL, Qian GD (2014) Lanthanide metal-organic frameworks for luminescent sensing and light-emitting applications. Coord Chem Rev 273:76–86
67. Hu ZC, Deibert BJ, Li J (2014) Luminescent metal-organic frameworks for chemical sensing and explosive detection. Chem Soc Rev 43:5815–5840
68. Sato H, Matsuda R, Sugimoto K et al (2010) Photoactivation of a nanoporous crystal for on-demand guest trapping and conversion. Nat Mater 9:661–666
69. Kurmoo M (2009) Magnetic metal-organic frameworks. Chem Soc Rev 38:1353–1379
70. Zhang W, Xiong RG (2012) Ferroelectric metal-organic frameworks. Chem Rev 112:1163–1195
71. Horike S, Umeyama D, Kitagawa S (2013) Ion conductivity and transport by porous coordination polymers and metal-organic frameworks. Accounts Chem Res 46:2376–2384
72. Yamada T, Otsubo K, Makiura R et al (2013) Designer coordination polymers: dimensional crossover architectures and proton conduction. Chem Soc Rev 42:6655–6669
73. Canivet J, Fateeva A, Guo YM et al (2014) Water adsorption in MOFs: fundamentals and applications. Chem Soc Rev 43:5594–5617
74. Stavila V, Talin AA, Allendorf MD (2014) MOF-based electronic and optoelectronic devices. Chem Soc Rev 43:5994–6010

75. Lee J, Farha OK, Roberts J et al (2009) Metal-organic framework materials as catalysts. Chem Soc Rev 38:1450–1459
76. Corma A, Garcıa H, Llabres i Xamena FX (2010) Engineering metal organic frameworks for heterogeneous catalysis. Chem Rev 110:4606–4655
77. Ranocchiari M, van Bokhoven JA (2011) Catalysis by metal-organic frameworks: fundamentals and opportunities. Phys Chem Chem Phys 13:6388–6396
78. Llabres i Xamena FX, Gascon J (2013) Towards future MOF catalytic applications. In: Llabrés i Xamena F, Gascon J (eds) Metal organic frameworks as heterogeneous catalysts. The Royal Society of Chemistry, Cambridge, pp 406–424
79. Vermoortele F, Valvekens P, De Vos D (2013) Catalysis at the metallic nodes of MOFs. In: Llabrés i Xamena F, Gascon J (eds) F. Metal organic frameworks as heterogeneous catalysts. The Royal Society of Chemistry, Cambridge, pp 268–288
80. Kesanli B, Lin WB (2003) Chiral porous coordination networks: rational design and applications in enantioselective processes. Coord Chem Rev 246:305–326
81. Ma L, Abney C, Lin W (2009) Enantioselective catalysis with homochiral metal-organic frameworks. Chem Soc Rev 38:1248–1256
82. Yoon M, Srirambalaji R, Kim K (2012) Homochiral metal-organic frameworks for asymmetric heterogeneous catalysis. Chem Rev 112:1196–1231
83. Falkowski JM, Liu S, Lin W (2013) Asymmetric catalysis with chiral metal organic frameworks. In: Llabrés i Xamena F, Gascon J (eds) Metal organic frameworks as heterogeneous catalysts. The Royal Society of Chemistry, Cambridge, pp 344–364
84. Leus K, Liu YY, Van Der Voort P (2014) Metal-organic frameworks as selective or chiral oxidation catalysts. Catal Rev Sci Eng 56:1–56
85. Silva CG, Luz I, Llabres i Xamena FX et al (2010) Water stable Zr-benzenedicarboxylate metal-organic frameworks as photocatalysts for hydrogen generation. Chem Eur J 16:11133–11138
86. Garcia H, Ferrer B (2013) Photocatalysis by MOFs. In: Llabrés i Xamena F, Gascon J (eds) Metal organic frameworks as heterogeneous catalysts. The Royal Society of Chemistry, Cambridge, pp 365–383
87. Qiu SL, Zhu GS (2009) Molecular engineering for synthesizing novel structures of metal-organic frameworks with multifunctional properties. Coord Chem Rev 253:2891–2911
88. Wang Z, Cohen SM (2009) Postsynthetic modification of metal-organic-frameworks. Chem Soc Rev 38:1315–1329
89. Deng HX, Doonan CJ, Furukawa H et al (2010) Multiple functional groups of varying ratios in metal-organic frameworks. Science 327:846–850
90. Chen BL, Xiang SC, Qian GD (2010) Metal-organic frameworks with functional pores for recognition of small molecules. Accounts Chem Res 43:1115–1124
91. Tanabe KK, Cohen SM (2011) Postsynthetic modification of metal-organic frameworks-a progress report. Chem Soc Rev 40:498–519
92. Cohen SM (2012) Postsynthetic methods for the functionalization of metal-organic frameworks. Chem Rev 112:970–1000
93. Llabres i Xamena FX, Luz I, Cirujano FG (2013) Strategies for creating active sites in MOFs. In: Llabrés i Xamena F, Gascon J (eds) Metal organic frameworks as heterogeneous catalysts. The Royal Society of Chemistry, Cambridge, pp 237–267
94. Mondloch JE, Farha OK, Hupp JT (2013) Catalysis at the organic ligands. In: Llabrés i Xamena F, Gascon J (eds) Metal organic frameworks as heterogeneous catalysts. The Royal Society of Chemistry, Cambridge, pp 289–309
95. Burrows AD (2013) Post-synthetic modification of MOFs. In: Llabrés i Xamena F, Gascon J (eds) Metal organic frameworks as heterogeneous catalysts. The Royal Society of Chemistry, Cambridge, pp 31–75
96. Deria P, Mondloch JE, Karagiaridi O et al (2014) Beyond post-synthesis modification: evolution of metal-organic frameworks via building block replacement. Chem Soc Rev 43:5896–5912

97. Evans JD, Sumby CJ, Doonan CJ (2014) Post-synthetic metalation of metal-organic frameworks. Chem Soc Rev 43:5933–5951
98. Lu WG, Wei ZW, Gu ZY et al (2014) Tuning the structure and function of metal-organic frameworks via linker design. Chem Soc Rev 43:5561–5593
99. Szeto KC, Lillerud KP, Tilset M et al (2006) A thermally stable Pt/Y-based metal-organic framework: exploring the accessibility of the metal Centers with spectroscopic methods using H_2O, CH_3OH, and CH_3CN as probes. J Phys Chem B 110:21509–21520
100. Szeto KC, Prestipino C, Lamberti C et al (2007) Characterization of a new porous Pt-containing metal-organic framework containing potentially catalytically active sites: local electronic structure at the metal centers. Chem Mater 19:211–220
101. Szeto KC, Kongshaug KO, Jakobsen S et al (2008) Design, synthesis and characterization of a Pt-Gd metal-organic framework containing potentially catalytically active sites. Dalton Trans 15:2054–2060
102. Kandiah M, Usseglio S, Svelle S et al (2010) Post-synthetic modification of the metal-organic framework compound UiO-66. J Mater Chem 20:9848–9851
103. Øien S, Agostini G, Svelle S et al (2015) Probing reactive platinum sites in UiO-67 zirconium metal-organic frameworks. Chem Mat 27:1042–1056
104. Kamegawa T, Sakai T, Matsuoka M et al (2005) Preparation and characterization of unique inorganic-organic hybrid mesoporous materials incorporating arenetricarbonyl complexes [-$C_6H_4M(CO)_3$-] (M = Cr, Mo). J Am Chem Soc 127:16784–16785
105. Kaye SS, Long JR (2008) Matrix isolation chemistry in a porous metal-organic framework: photochemical substitutions of N_2 and H_2 in $Zn_4O[(\eta^6$-1,4-benzenedicarboxylate)$Cr(CO)_3]_3$. J Am Chem Soc 130:806–807
106. Chavan S, Vitillo JG, Uddin MJ et al (2010) Functionalization of UiO-66 metal−organic framework and highly cross-linked polystyrene with $Cr(CO)_3$: in situ formation, stability, and photoreactivity. Chem Mater 22:4602–4611
107. Goto Y, Sato H, Shinkai S et al (2008) "Clickable" metal-organic framework. J Am Chem Soc 130:14354–14355
108. Gadzikwa T, Farha OK, Malliakas CD et al (2009) Selective bifunctional modification of a non-catenated metal-organic framework material via "Click" chemistry. J Am Chem Soc 131:13613–13615
109. Morris W, Doonan CJ, Furukawa H et al (2008) Crystals as molecules: postsynthesis covalent functionalization of zeolitic imidazolate frameworks. J Am Chem Soc 130:12626–12627
110. Savonnet M, Aguado S, Ravon U et al (2009) Solvent free base catalysis and transesterifiation over basic functionalised metal-organic frameworks. Green Chem 11:1729–1732
111. Tanabe KK, Wang ZQ, Cohen SM (2008) Systematic functionalization of a metal-organic framework via a postsynthetic modification approach. J Am Chem Soc 130:8508–8517
112. Garibay SJ, Cohen SM (2010) Isoreticular synthesis and modification of frameworks with the UiO-66 topology. Chem Commun 46:7700–7702
113. Doonan CJ, Morris W, Furukawa H et al (2009) Isoreticular metalation of metal-organic frameworks. J Am Chem Soc 131:9492–9493
114. Gadzikwa T, Farha OK, Mulfort KL et al (2009) A Zn-based, pillared paddlewheel MOF containing free carboxylic acids via covalent post-synthesis elaboration. Chem Commun 25:3720–3722
115. Ingleson MJ, Barrio JP, Guilbaud JB et al (2008) Framework functionalisation triggers metal complex binding. Chem Commun 23:2680–2682
116. Hong DY, Hwang YK, Serre C et al (2009) Porous chromium terephthalate MIL-101 with coordinatively unsaturated sites: surface functionalization, encapsulation, sorption and catalysis. Adv Funct Mater 19:1537–1552
117. Hermes S, Schröter M-K, Schmid R et al (2005) Metal@MOF: loading of highly porous coordination polymers host lattices by metal organic chemical vapor deposition. Angew Chem Int Ed 44:6237–6241

118. Zhao H, Song H, Chou L (2012) Nickel nanoparticles supported on MOF-5: synthesis and catalytic hydrogenation properties. Inorg Chem Commun 15:261–265
119. Bordiga S, Groppo E, Agostini G et al (2013) Reactivity of surface species in heterogeneous catalysts probed by in situ x-ray absorption techniques. Chem Rev 113:1736–1850
120. Bonino F, Lamberti C, Chavan S et al (2013) Characterization of MOFs. 1. Combined vibrational and electronic spectroscopies. In: Llabres i Xamena F, Gascon J (eds) Metal organic frameworks as heterogeneous catalysts. The Royal Society of Chemistry, Cambridge, pp 76–142
121. Borfecchia E, Gianolio D, Agostini G et al (2013) Characterization of MOFs. 2. Long and local range order structural determination of MOFs by combining EXAFS and diffraction techniques. In: Llabres i Xamena F, Gascon J (eds) Metal organic frameworks as heterogeneous catalysts. The Royal Society of Chemistry, Cambridge, pp 143–208
122. Dietzel PDC, Panella B, Hirscher M et al (2006) Hydrogen adsorption in a nickel based coordination polymer with open metal sites in the cylindrical cavities of the desolvated framework. Chem Commun 9:959–961
123. Chavan S, Bonino F, Vitillo JG et al (2009) Response of CPO-27-Ni towards CO, N_2 and C_2H_4. Phys Chem Chem Phys 11:9811–9822
124. Valenzano L, Vitillo JG, Chavan S et al (2012) Structure-activity relationships of simple molecules adsorbed on CPO-27-Ni metal-organic framework: in situ experiments vs. theory. Catal Today 182:67–79
125. Chavan S, Vitillo JG, Groppo E et al (2009) CO adsorption on CPO-27-Ni coordination polymer: spectroscopic features and interaction energy. J Phys Chem C 113:3292–3299
126. Bonino F, Chavan S, Vitillo JG et al (2008) Local structure of CPO-27-Ni metallorganic framework upon dehydration and coordination of NO. Chem Mater 20:4957–4968
127. Diakun GP (1990) EXAFS - a probe for metalloproteins. Nature 344:83–84
128. Strange RW, Ellis M, Hasnain SS (2005) Atomic resolution crystallography and XAFS. Coord Chem Rev 249:197–208
129. Le Toquin R, Paulus W, Cousson A et al (2006) Time-resolved in situ studies of oxygen intercalation into $SrCoO_{2.5}$, performed by neutron diffraction and X-ray absorption spectroscopy. J Am Chem Soc 128:13161–13174
130. Piovano A, Agostini G, Frenkel AI et al (2011) Time resolved in situ XAFS study of the electrochemical oxygen intercalation in $SrFeO_{2.5}$ brownmillerite structure: comparison with the homologous $SrCoO_{2.5}$ system. J Phys Chem C 115:1311–1322
131. Mikkelsen JC, Boyce JB (1982) Atomic-scale structure of random solid solutions: extended X-ray-absorption fine-structure study of $Ga_{1-x}In_xAs$. Phys Rev Lett 49:1412–1415
132. Lamberti C (2004) The use of synchrotron radiation techniques in the characterization of strained semiconductor heterostructures and thin films. Surf Sci Rep 53:1–197
133. Ankudinov AL, Ravel B, Rehr JJ et al (1998) Real-space multiple-scattering calculation and interpretation of x-ray-absorption near-edge structure. Phys Rev B 58:7565–7576
134. Rehr JJ, Albers RC (2000) Theoretical approaches to x-ray absorption fine structure. Rev Mod Phys 72:621–654
135. Filipponi A, Di Cicco A, Natoli CR (1995) X-ray-absorption spectroscopy and n-body distribution functions in condensed matter.1. Theory. Phys Rev B 52:15122–15134
136. Filipponi A, Di Cicco A (1995) X-ray-absorption spectroscopy and n-body distribution functions in condensed matter.2. Data analysis and applications. Phys Rev B 52:15135–15149
137. Rehr JJ, Ankudinov AL (2005) Progress in the theory and interpretation of XANES. Coord Chem Rev 249:131–140
138. Benfatto M, Della Longa S (2001) Geometrical fitting of experimental XANES spectra by a full multiple-scattering procedure. J Synchrotron Radiat 8:1087–1094
139. Benfatto M, Della Longa S, Natoli CR (2003) The MXAN procedure: a new method for analysing the XANES spectra of metalloproteins to obtain structural quantitative information. J Synchrotron Radiat 10:51–57

140. Joly Y (2001) X-ray absorption near-edge structure calculations beyond the muffin-tin approximation. Phys Rev B 63: art. no. 125120
141. Guda SA, Guda AA, Soldatov MA et al (2015) Optimized finite difference method for the full-potential XANES simulations: application to molecular adsorption geometries in MOFs and metal–ligand intersystem crossing transients. J Chem Theory Comput 11:4512–4521
142. Kotani A, Shin S (2001) Resonant inelastic x-ray scattering spectra for electrons in solids. Rev Mod Phys 73:203–246
143. Glatzel P, Bergmann U (2005) High resolution 1s core hole X-ray spectroscopy in 3d transition metal complexes – electronic and structural information. Coord Chem Rev 249:65–95
144. Singh J, Lamberti C, van Bokhoven JA (2010) Advanced X-ray absorption and emission spectroscopy: in situ catalytic studies. Chem Soc Rev 39:4754–4766
145. Swarbrick JC, Kvashnin Y, Schulte K et al (2010) Ligand identification in titanium complexes using x-ray valence-to-core emission spectroscopy. Inorg Chem 49:8323–8332
146. Gallo E, Lamberti C, Glatzel P (2011) Investigation of the valence electronic states of Ti (IV) in Ti silicalite-1 coupling X-ray emission spectroscopy and density functional calculations. Phys Chem Chem Phys 13:19409–19419
147. Gallo E, Bonino F, Swarbrick JC et al (2013) Preference towards five-coordination in Ti silicalite-1 upon molecular adsorption. ChemPhysChem 14:79–83
148. Mino L, Agostini G, Borfecchia E et al (2013) Low-dimensional systems investigated by x-ray absorption spectroscopy: a selection of 2D, 1D and 0D cases. J Phys D Appl Phys 46:72
149. Giordanino F, Borfecchia E, Lomachenko KA et al (2014) Interaction of NH_3 with Cu-SSZ-13 catalyst: a complementary FTIR, XANES, and XES study. J Phys Chem Lett 5:1552–1559
150. Gallo E, Piovano A, Marini C et al (2014) Architecture of the Ti(IV) sites in TiAlPO-5 determined using Ti K-edge X-ray absorption and X-ray emission spectroscopies. J Phys Chem C 118:11745–11751
151. Borfecchia E, Lomachenko KA, Giordanino F et al (2015) Revisiting the nature of Cu sites in the activated Cu-SSZ-13 catalyst for SCR reaction. Chem Sci 6:548–563
152. Groppo E, Gallo E, Seenivasan K et al (2015) XAS and XES techniques shed light on the dark side of Ziegler-Natta catalysts: active-site generation. ChemCatChem 7:1432–1437
153. Groppo E, Seenivasan K, Gallo E et al (2015) Activation and in situ ethylene polymerization on silica-supported Ziegler–Natta catalysts. ACS Catal 5:5586–5595
154. Glatzel P, Alonso-Mori R, Sokaras D (2016) Hard x-ray photon-in/photon-out spectroscopy: instrumentation, theory and applications. In: van Bokhoven JA, Lamberti C (eds) X-Ray absorption and x-ray emission spectroscopy: theory and applications. Wiley, Chichester, pp 125–153
155. Prestipino C, Regli L, Vitillo JG et al (2006) Local structure of framework Cu(II) in HKUST-1 metallorganic framework: spectroscopic characterization upon activation and interaction with adsorbates. Chem Mater 18:1337–1346
156. Hafizovic J, Bjorgen M, Olsbye U et al (2007) The inconsistency in adsorption properties and powder XRD data of MOF-5 is rationalized by framework interpenetration and the presence of organic and inorganic species in the nanocavities. J Am Chem Soc 129:3612–3620
157. Masciocchi N, Galli S, Colombo V et al (2010) Cubic octanuclear Ni(II) clusters in highly porous polypyrazolyl-based materials. J Am Chem Soc 132:7902–7904
158. Borfecchia E, Maurelli S, Gianolio D et al (2012) Insights into adsorption of NH_3 on HKUST-1 metal-organic framework: a multitechnique approach. J Phys Chem C 116:19839–19850
159. Mino L, Colombo V, Vitillo JG et al (2012) Spectroscopic and adsorptive studies of a thermally robust pyrazolato-based PCP. Dalton Trans 41:4012–4019
160. Gallo E, Lamberti C, Glatzel P (2013) dd excitations in CPO-27-Ni metal-organic framework: comparison between resonant inelastic X-ray scattering and UV-vis spectroscopy. Inorg Chem 52:5633–5635

161. Shearer GC, Chavan S, Ethiraj J et al (2014) Tuned to perfection: ironing out the defects in metal-organic framework UiO-66. Chem Mater 26:4068–4071
162. Jakobsen S, Gianolio D, Wragg DS et al (2012) Structural determination of a highly stable metal-organic framework with possible application to interim radioactive waste scavenging: Hf-UiO-66. Phys Rev B 86: Art. n. 125429
163. Milanesio M, Artioli G, Gualtieri AF et al (2003) Template burning inside TS-1 and Fe-MFI molecular sieves: an in situ XRPD study. J Am Chem Soc 125:14549–14558
164. Agostini G, Lamberti C, Palin L et al (2010) In situ XAS and XRPD parametric rietveld refinement to understand dealumination of Y Zeolite catalyst. J Am Chem Soc 132:667–678
165. Gianolio D, Vitillo JG, Civalleri B et al. (2013) Combined study of structural properties on metal-organic frameworks with same topology but different linkers or metal. J Phys Conf Ser 430: Art. n. 012134
166. Øien S, Wragg D, Reinsch H et al (2014) Detailed structure analysis of atomic positions and defects in zirconium metal-organic frameworks. Cryst Growth Des 14:5370–5372
167. Crabtree RH (1995) Aspects of methane chemistry. Chem Rev 95:987–1007
168. Arakawa H, Aresta M, Armor JN et al (2001) Catalysis research of relevance to carbon management: progress, challenges, and opportunities. Chem Rev 101:953–996
169. Shilov AE, Shul'pin GB (1997) Activation of C-H bonds by metal complexes. Chem Rev 97:2879–2932
170. Labinger JA, Bercaw JE (2002) Understanding and exploiting C-H bond activation. Nature 417:507–514
171. Lersch M, Tilset M (2005) Mechanistic aspects of C-H activation by Pt complexes. Chem Rev 105:2471–2526
172. Periana RA, Taube DJ, Gamble S et al (1998) Platinum catalysts for the high-yield oxidation of methane to a methanol derivative. Science 280:560–564
173. Wolf D (1998) High yields of methanol from methane by C-H bond activation at low temperatures. Angew Chem Int Ed 37:3351–3353
174. Palkovits R, Antonietti M, Kuhn P et al (2009) Solid catalysts for the selective low-temperature oxidation of methane to methanol. Angew Chem Int Ed 48:6909–6912
175. Palkovits R, von Malotki C, Baumgarten M et al (2010) Development of molecular and solid catalysts for the direct low-temperature oxidation of methane to methanol. ChemSusChem 3:277–282
176. Soorholtz M, White RJ, Zimmermann T et al (2013) Direct methane oxidation over Pt-modified nitrogen-doped carbons. Chem Commun 49:240–242
177. Stinton GW, Evans JSO (2007) Parametric Rietveld refinement. J Appl Crystallogr 40:87–95
178. Bunker G (2010) Introduction to XAFS A practical guide to x-ray absorption fine structure spectroscopy. Cambridge University Press, Cambridge
179. Hall MD, Foran GJ, Zhang M et al (2003) XANES determination of the platinum oxidation state distribution in cancer cells treated with platinum(IV) anticancer agents. J Am Chem Soc 125:7524–7525
180. Yoshida H, Nonoyama S, Yazawa Y et al (2005) Quantitative determination of platinum oxidation state by XANES analysis. Phys Scr T115:813–815
181. Borfecchia E, Øien D, Svelle S et al (2016) A XAS study of the local environment and reactivity of Pt-sites in functionalized UiO-67 MOFs. J Phys Conf Ser, 712: art. n. 012125
182. Chui SSY, Lo SMF, Charmant JPH et al (1999) A chemically functionalizable nanoporous material $Cu_3TMA_2(H_2O)_{3n}$. Science 283:1148–1150
183. Bordiga S, Regli L, Bonino F et al (2007) Adsorption properties of HKUST-1 toward hydrogen and other small molecules monitored by IR. Phys Chem Chem Phys 9:2676–2685
184. Smolentsev G, Soldatov A (2006) Quantitative local structure refinement from XANES: multi-dimensional interpolation approach. J Synchrotron Radiat 13:19–29
185. Groppo E, Prestipino C, Lamberti C et al (2003) Growth of NiO on Ag(001): atomic environment, strain, and interface relaxations studied by polarization dependent extended X-ray absorption fine structure. J Phys Chem B 107:4597–4606

186. Humphrey SM, Allan PK, Oungoulian SE et al (2009) Metal-organophosphine and metal-organophosphonium frameworks with layered honeycomb-like structures. Dalton Trans 13:2298–2305
187. Nunez AJ, Shear LN, Dahal N et al (2011) A coordination polymer of $(Ph_3P)AuCl$ prepared by post-synthetic modification and its application in 1-hexene/n-hexane separation. Chem Commun 47:11855–11857
188. Tan X, Li L, Zhang JY et al (2012) Three-dimensional phosphine metal-organic frameworks assembled from Cu(I) and Pyridyl diphosphine. Chem Mater 24:480–485
189. Falkowski JM, Sawano T, Zhang T et al (2014) Privileged phosphine-based metal-organic frameworks for broad-scope asymmetric catalysis. J Am Chem Soc 136:5213–5216
190. Morel FL, Ranocchiari M, van Bokhoven JA (2014) Synthesis and characterization of phosphine-functionalized metal-organic frameworks based on MOF-5 and MIL-101 topologies. Ind Eng Chem Res 53:9120–9127
191. Morel FL, Pin S, Huthwelker T et al (2015) Phosphine and phosphine oxide groups in metal-organic frameworks detected by P K-edge XAS. Phys Chem Chem Phys 17:3326–3331
192. Goesten MG, Gupta K, Ramos-Fernandez EV et al (2012) Chloromethylation as a functionalisation pathway for metal-organic frameworks. CrystEngComm 14:4109–4111
193. Ranocchiari M, van Bokhoven JA (2013) Synthesis and reactivity of zn-biphenyl metal-organic frameworks, introducing a diphenylphosphino functional group. Chimia 67:397–402
194. Vaclavik J, Servalli M, Lothschutz C et al (2013) AuI catalysis on a coordination polymer: a solid porous ligand with free phosphine sites. ChemCatChem 5:692–696
195. Engemann C, Franke R, Hormes J et al (1999) X-ray absorption near-edge spectroscopy (XANES) at the phosphorus K-edge of triorganophosphinechalcogenides. Chem Phys 243:61–75
196. Norman D (1986) X-ray absorption-spectroscopy (EXAFS and XANES) at surfaces. J Phys C Solid State Phys 19:3273–3311
197. Durham PJ (1988) Theory of XANES. In: Koningsberger DC, Prins R (eds) X-ray absorption: principles, applications, techniques of EXAFS, SEXAFS and XANES. Wiley, New York, pp 53–84
198. Bianconi A (1988) XANES spectroscopy. In: Koningsberger DC, Prins R (eds) X-Ray absorption: principles, applications, techniques of EXAFS, SEXAFS and XANES. Wiley, New York, pp 573–662
199. Bianconi A, Garcia J, Benfatto M (1988) XANES in condensed systems. Top Curr Chem 145:29–67
200. Kosugi N (1996) Theory and analysis of XANES: MO approach. In: Iwasawa Y (ed) X-ray absorption fine structure for catalysts and surfaces. World Scientific, Singapore, pp 60–76
201. Joly Y, Cabaret D, Renevier H et al (1999) Electron population analysis by full-potential X-ray absorption simulations. Phys Rev Lett 82:2398–2401
202. Rehr JJ, Ankudinov AL (2001) Progress and challenges in the theory and interpretation of X-ray spectra. J Synchrotron Radiat 8:61–65
203. Yamamoto T (2008) Assignment of pre-edge peaks in K-edge x-ray absorption spectra of 3d transition metal compounds: electric dipole or quadrupole? X-Ray Spectrom 37:572–584
204. Kas JJ, Jorissen K, Rehr JJ (2016) Real-Space Multiple-Scattering Theory of X-ray Spectra. In: van Bokhoven JA, Lamberti C (eds) X-ray absorption and x-ray emission spectroscopy: theory and applications. Wiley, Chichester, pp 51–72
205. Joly Y, Grenier S (2016) Theory of X-ray absorption near edge structure. In: van Bokhoven JA, Lamberti C (eds) X-ray absorption and x-ray emission spectroscopy: theory and applications. Wiley, Chichester, pp 73–96
206. Garino C, Borfecchia E, Gobetto R et al (2014) Determination of the electronic and structural configuration of coordination compounds by synchrotron-radiation techniques. Coord Chem Rev 277:130–186

207. Bugaev LA, Gegusin II, Datsyuk VN et al (1986) Multiple-scattering approach to the XANES theory of alkali-halide crystals. I. Crystalline potential in the X-ray absorption-spectra problem. Phys Status Solidi B-Basic Res 133:195–202
208. Bianconi A, Garcia J, Benfatto M et al (1991) Multielectron excitations in the K-edge X-ray-absorption near-edge spectra of V, Cr, and Mn $3d^0$ compounds with tetrahedral coordination. Phys Rev B 43:6885–6892
209. Tyson TA, Hodgson KO, Natoli CR et al (1992) General multiple-scattering scheme for the computation and interpretation of x-ray-absorption fine-structure in atomic clusters with applications to SF_6, $GeCl_4$, and Br_2 molecules. Phys Rev B 46:5997–6019
210. Chavan S, Bonino F, Valenzano L et al (2013) Fundamental aspects of H_2S adsorption on CPO-27-Ni. J Phys Chem C 117:15615–15622

Chapter 27
Homogeneous Catalysis: From Metal Atoms to Small Clusters

John C. Linehan, Mahalingam Balasubramanian, and John L. Fulton

27.1 Introduction

27.1.1 XAFS is the Leading Spectroscopic Method for Homogeneous Catalysts

XAFS is the quintessential technique to probe catalyst structure in homogeneous systems. Amongst all spectroscopic methods it is perhaps the most powerful technique to probe the catalyst state in these reactions. Although these systems tend to lack long-range order, the local structure about the catalyst center can be probed with very high resolution. An XAFS study of the metal center provides a comprehensive map of the electronic and structural state of the catalyst precursor and of the predominant catalyst under operando conditions (while reacting at the actual conditions of pressure and temperature).

The function (activity) of a catalyst is controlled by its chemical identity, ligand structure, and electronic state. XAFS, by elucidating the structural and electronic evolution during the reaction, provides a fundamental understanding of the structure–activity relationships of homogeneous systems. The key attributes of XAFS for the study of homogeneous systems can be summarized as follows:

J.C. Linehan
Institute for Integrated Catalysis, Pacific Northwest National Laboratory, P.O. Box 999, Richland, WA 99354, USA

M. Balasubramanian
Advanced Photon Source, Argonne National Laboratory, 9700 S. Cass Avenue, Argonne, IL 60439, USA

J.L. Fulton (✉)
Physical Sciences Division, Pacific Northwest National Laboratory, P.O. Box 999, Richland, WA 99354, USA
e-mail: john.fulton@pnnl.gov

Y. Iwasawa et al. (eds.), *XAFS Techniques for Catalysts, Nanomaterials, and Surfaces*, DOI 10.1007/978-3-319-43866-5_27

(1) XAFS provides local structural information independent of the long-range order. Consequently, evolution of the local structure of molecular complexes or clusters that actively participate in homogeneous catalysis can be monitored with ease. (2) XAFS is an element-specific technique. Tuning the X-ray energy to the absorption edge focuses solely on a particular element or metal center of interest and thereby allows study of the catalyst's unique role in the reaction. An additional advantage of this element specificity is that other structural correlations, which arise from spectator entities (e.g., passive solvents), are inherently filtered out. (3) Most catalysts have X-ray absorption edges (one or more) that can be excited using an energy-tunable X-ray source (normally using a spectroscopy beamline at a synchrotron). X-ray energies involved in these measurements are usually sufficiently high that the X-rays readily penetrate the samples and windows in the reaction cell. Most importantly, this enables the measurement to be performed operando—under true reaction conditions. A key to performing such measurements, as will be discussed later, lies in the design and use of appropriate reactors or operando cells. (4) XAFS is highly sensitive to dilute catalysts when measurements are performed using fluorescence detection. This makes it a powerful technique to probe dilute constituents that potentially play important catalytic roles. (5) Careful analysis of absorption edge position and of near edge (XANES) features provides key information on various electronic aspects, such as oxidation state and site symmetry of the probed element. (6) Detailed analysis of the extended X-ray absorption spectra (EXAFS) quantitatively probes the structural coordination chemistry by elucidating both the local- and medium-range molecular structure around the probed element. In addition, information on the ligand symmetry of the first shell or the structure of collinear chains of atoms, such as metal carbonyls, can often be extracted by a careful analysis that includes multiple scattering processes [1–7]. This is a unique trait of XAFS that allows one to extract many-body correlations. (7) XAFS allows a direct quantitative analysis of the amount of the catalyst species that is dissolved in solution. This is particularly important when a metal catalyst is thought to be precipitating during the reaction. By altering the cell position with respect to the beam, while under operando conditions, the X-ray beam can probe the catalyst-containing precipitate, thereby also giving a direct analysis of the insoluble components.

In the sections that follow, the objective is to illustrate the power of the XAFS technique and to provide examples of how it has been applied to homogeneous systems in order to gain deep insight into the function of the catalyst. The examples include metal centers having either single-atom species or metal clusters that contain up to four atoms in the core. The overall subject in this chapter deals with homogeneous catalysis, although there is not a well-defined cutoff differentiating a homogeneous cluster from a nanoparticle, rather there is a continuum of sizes that can be chemically relevant. This chapter is not an exhaustive review of the literature, but it is intended to illustrate the power of XAFS spectroscopy in the study of homogeneous catalysis. Several recent examples of homogeneous catalysis are highlighted, including themes of green chemistry, hydrogen storage, and classical hydrogenation chemistry where XAFS has been used to provide completely new understanding of the underlying mechanisms.

27.1.2 There are Limitations

The method of operando XAFS is used to track the change in the metal center environment, starting with the precursor species and following the chemical conversion to the dominant species that is present under reaction conditions. There is a common misconception that XAFS captures the "active" form of the catalyst during the chemical reaction. In special circumstances, operando methods may query the active state, but more often than not, it queries a resting catalyst state or an equilibrium of different catalyst states. Thus a short-lived transition state that is the true active catalyst might not be detected in a standard XAFS experiment. This is of course true of most spectroscopic techniques. There is also the possibility that the active species is a trace component in equilibrium with a dominant, major inactive state. This situation is exemplified by palladium catalyzed C-C bond formation reactions, such as the Mizoroki–Heck reaction [8], where the active catalyst is present at the ppm levels [9–11].

Even with these limitations, XAFS is among the best existing methods to probe the catalyst in a state as close as possible to its active state. In this regard, if at all possible, the chemistry should be formulated in a series of steps to trap or favor the intermediate states. In addition, one should not overlook the often important, complimentary information that is available from other spectroscopic methods such as NMR, IR, Raman spectroscopy, or other chemical techniques such as careful kinetics or poisoning studies. Finally, critical insights can be gained using a parallel effort involving DFT-based molecular structure calculations. An especially powerful approach is the direct computation of an XAFS spectrum (MD-XAFS) from a molecular dynamics trajectory (see Chap. 18 in this volume) that can be used to make quantitative comparisons to the experimental spectrum. Thus operando XAFS probes the catalyst state in a way that is directly relevant to molecular simulation.

27.1.3 Literature Highlights

Since the advent of modern XAFS [12–14], it has been an important tool to investigate heterogeneous catalyst systems. Several authoritative review articles dealing with XAFS and heterogeneous catalysis can be found in literature [15, 16]. In contrast to heterogeneous catalysis, the use of XAFS to understand homogeneous systems is somewhat more limited; however, studies of homogeneous catalysis can be found in the literature in addition to a few recent reviews [16–18]. We highlight a few XAFS studies of homogeneous systems as representative examples.

Some homogeneous metal catalysts function with high activity when they are present in ultra-low concentrations. Taking advantage of the sensitivity of XAFS to dilute species, Fiddy et al. [9, 19] have elucidated the structure of palladium species

involved in Mizoroki–Heck chemistry—with studies of concentrations down to industrially relevant dilute limits (50 to 2 ppm). The study revealed that at high dilution the catalyst consists largely of monomeric species but that it evolves in an equilibrium with dimeric species as the concentration or temperature is increased. In some instances the increased presence of "inactive" dimers is implicated for the low turnover rate with increasing palladium concentration.

In an early energy-dispersive XAFS (ED-XAFS) study, Bogg et al. [20] obtained time resolved spectra (time resolution: ~15 s) of a nickel catalyst used for alkene oligomerization. They showed that a rapid equilibrium develops during the reaction, which entails alkyl transfer between the promoter (Al) and the precursor metals (Ni). The study showed that reversible transmetalation processes are of central importance to the mechanism of catalysis in this system.

Using a purpose-built freeze-quench attachment in conjunction with the more conventional stopped-flow methods, Barlett et al. [21] studied a molybdenum-based catalyst to gain insight into the mechanism of selective oligomerization of alkenes. In this study, the development of a freeze-quench apparatus allowed trapping of intermediates within 1 s of mixing. Subsequent fluorescence XAFS studies of the frozen samples along with complementary quick-XAFS (QXAFS) time resolved measurements (time resolution: ~20 s) shed light on the catalytic activity and deactivation pathways of this system.

Multimodal approaches, that combine XAFS with other complementary techniques (FT-IR, Raman, UV–Vis, time resolved XRD, and so on), are increasingly being used for operando studies. A multimodal approach can potentially provide a more holistic and complete understanding of the catalytic process. In this context, an elegant combined ED-XAFS/UV–Vis study was performed by Diaz-Moreno et al. [22] to monitor the structural evolution of the inner-sphere electron transfer reaction between $[IrCl_6]^{2-}$ and $[Co(CN)_5]^{3-}$. Time resolved XAFS spectra at the Ir L_3-edge suggest that the electron transfer leads to the formation of a bridged Ir (III) intermediate in a time scale much faster than the experimental time resolution of 200 ms. Using the information obtained from the simultaneously recorded UV–Vis spectra, they also estimate that the proportion of this reaction intermediate reaches 90 % at approximately 200 ms after initiation of the reaction. Similarly, Guilera et al. [23] combined UV–Vis and ED-XAFS to obtain simultaneous structural-kinetic information on a homogeneous palladium catalyst. This study allowed the verification of the structural details of the oxidative addition (PhI onto $[(PPh_3)_2Pd(dba)]$) and the subsequent isomerization reaction. Notably, XAFS is sensitive to both the local structure and changes in oxidation state of Pd, while UV–Vis is sensitive to loss of dba ligands and the isomerization. Additionally, in both of the above studies, the kinetics of the reaction was simultaneously obtained—without the need to infer the kinetics from separately conducted studies. In another study, Tromp et al. [24] have used NMR, EPR, ED-XAFS, and UV–Vis to study the arylation reaction of imidazole, catalyzed by commercially important $[Cu(OH)(TMEDA)]_2Cl_2$ precursor. The ED-XAFS and UV–Vis studies were performed simultaneously in a multimodal fashion. Careful analysis of the time resolved XANES and the EXAFS spectra, combined with judicious use of the other

complementary spectroscopic techniques, provide detailed insights into the complex evolution of the catalyst structure and the nature of the intermediates formed during the reaction. It is clear from the above discussions that multimodal approaches can provide important insights. Even more involved approaches with simultaneous use of three different techniques (e.g., XAFS, Raman, and UV–Vis), and the use of other advanced X-ray spectroscopy methods are currently being developed [25, 26]. In the authors' opinion an important future direction would be the combination of XAFS with NMR so that both XAFS and NMR spectra could be simultaneously obtained while under operando conditions.

The role of nanoparticulate gold as an efficient catalyst in many electrocatalytic and heterogeneous catalytic systems has been widely studied using XAFS. In a recent study, Hashmi et al. [27], explored whether or not gold complexes could be used as homogeneous catalysts for oxidative reactions. Specifically, using in situ XAFS, they showed unequivocally that mononuclear gold complexes can indeed catalyze the direct conversion of aldehydes and alcohols to esters. However, deactivation of the catalyst did occur and sometimes "inactive" small gold particles were detected.

More recently, Sherborne et al. [28] have exploited the ability of XAFS to characterize a sample from multiple X-ray absorber (Ir, Cl, and K) viewpoints, to understand the activation and deactivation mechanisms of an Ir-based homogenous transfer hydrogenation catalyst, $[Cp^*IrCl_2]_2$. They observed that the active precatalyst is generated by ligand exchange, namely, exchange of one chloride ligand with an alkoxide. The exchange of an additional chloride ligand leads to the formation of complex potassium alkoxide-iridate species, which are implicated in the deactivation of the catalyst.

27.2 Experimental Methods

27.2.1 Methods of XAFS Acquisition for Homogeneous Reactions

The choice of method and mode of XAFS data collection [29] depends primarily on the kinetics of the homogeneous reaction and on the concentration of the probed metal center. Various XAFS methods can be used to probe many decades of time scales from a few picoseconds up to many hours. For systems with moderate catalyst concentrations, the most common approach is the use of conventional, transmission XAFS data collection with the monochromator scanned in a step-by-step, discrete scanning mode. In such setups, a single XAFS spectrum can be obtained in 1–20 min. The time required for a scan depends, among other things, on the choice of integration time used per energy step, total number of acquired data points, and dead times associated with monochromator movement and detector settling. This classic XAFS method allows one to study dynamics that occur in the few tens of

minutes to hours. However, if measurement of dynamics in the sub-minute to few minutes time scale is required a much faster data acquisition rate is needed. This can be accomplished using the Quick XAFS (QXAFS) method [30–33] in which the monochromator is driven in a continuous fashion (using a cam-drive or piezo tuning) along with a simultaneous (on-the-fly) read-out of the detectors. This method also allows for the measurement of absorption data during movement of the monochromator in both forward (increasing energy) or backward (decreasing energy) directions. Typical times taken per scan are in the range of seconds (0.1—few seconds). A comparable technique with similar time-resolution is the use of an energy dispersive approach (ED-XAFS) [34–36]. In this approach, non-monochromatic X-rays are diffracted—either in a Bragg (reflection) or Laue (transmission) geometry—and focused to a uniform spot on the sample, using a long, bent "polychromator" crystal. The focused beam, on transiting the sample, is allowed to diverge onto a position sensitive detector (PSD) where the beam position on the PSD is correlated to energy. This dispersive arrangement affords the collection of the entire absorption spectrum simultaneously; therefore, time resolution in the few milliseconds to sub-second range can be easily achieved. Such experiments are limited, however, to transmission mode geometry and further require highly uniform and concentrated samples. For dilute species, transmission mode methods may not provide sufficient sensitivity, and the use of fluorescence detection is often warranted [29]. A variety of fluorescence detector options can be employed such as a Lytle detector with a Stern–Heald–Soller slit assembly, a multi-element energy dispersive detector, or a crystal optics system. Both XAFS and QXAFS methods can be adapted to fluorescence detection where the time required to get a good quality scan will depend on the exact counting statistics of the experiment. Finally, although not yet widely employed in homogeneous catalysis, the coupling to the time structure of the synchrotron radiation using pump-probe methods enables studies of ultrafast phenomena in the sub-picosecond to tens of picosecond time scale [37]. Such timing modes hold great promise in studying intermediate, transitory species, and can potentially shed light on diverse processes; e.g., redox chemistry, charge transfer phenomena, and making or breaking of bonds during chemical reactions.

27.2.2 Reaction Cells

A molecularly dispersed, homogeneous catalyst in a chemical reactor that incorporates X-ray transparent windows provides nearly the ideal sample configuration and uniformity for XAFS spectroscopy. There are many aspects involved in selecting the ideal XAFS cell. Many beamlines provide reaction cells that are appropriate for certain classes of systems. However, in order to most efficiently use the allotted beamtime, it is often preferable to build a small XAFS reactor that has been optimized for a particular edge-energy, catalyst concentration, beam properties, and other aspects of the reaction system. X-ray transparent windows and reactor body materials are selected based upon their chemical

inertness, the required X-ray energies, and the pressure and temperature of the system. The most common window types include polyimide (Kapton) films (25–150 μm), polyether ether ketone (PEEK) in sheet or machined forms (0.5–5 mm), single crystal or polycrystalline diamond (15 μm–1 mm), glassy carbon (0.5–3 mm), and silicon nitride (50 nm–1 μm). At high energies even amorphous materials such as silicate glasses are appropriate. Glassy carbon is an excellent material, since the amorphous structure does not add diffraction artifacts to the XAFS spectra. Glassy carbon is appropriate for moderate pressures, high temperatures and is inert under most solvent conditions [38]. The extreme inertness of diamond makes it the favored window materials for the most chemically aggressive systems at high pressure. Thin single-crystal diamonds work well at lower energies where there are limited numbers of interfering Bragg peaks. At higher energies, polycrystalline diamond windows may be used, but they may require subtraction of a background spectrum to remove weak contributions from sets of broadened Bragg peak groupings [39]. The reactor body is selected based upon the compatibility with the reaction solution—namely, the reactor body should be of a benign material that does not interfere or poison the catalytic process and should be corrosion resistant. They are usually constructed from polymers, glasses, or a wide variety of different metal alloys including stainless steel, titanium, and precious metals.

Figure 27.1 shows three different types of reaction cells with designs that span the range from simple to complex. In Fig. 27.1a, a glass sample vial has been used to study a rhodium-based dehydrogenation catalyst [40] in which a small modification incorporates an outlet tube allowing for the monitoring of hydrogen production. At 23 keV (Rh K-edge) the beam is easily transmitted through the glass vial base, the solvent and polyseal cap of this reactor. Figure 27.1b illustrates the other extreme of a much more complex design [41, 42] that is required for high-temperature (400 °C) and high pressure water studies (600 bar). This cell has been used to study the structure of a $MnBr_2$ catalyst for the oxidation of *p*-xylene in supercritical water. Finally, Fig. 27.1c illustrates a high-pressure hydrogenation cell [43] using a slightly modified commercial pressure fitting (HIP Inc) altered to accept a set of PEEK X-ray windows. A small magnetic stir bar is used to keep the lower liquid phase saturated with H_2 during the batch hydrogenation reaction.

Perhaps most importantly, comments are given on methods to most efficiently use the expensive and precious resource, that is, the allocated beamtime. There are several strategies that help lead to the best possible outcome while studying the catalyst chemistry at a beamtime. These include: (1) Bring a full range of catalyst and reactant chemistry to the beamline. During the beamtime, as much as possible, make initial structural evaluations from the XAFS spectra as they are being acquired. This allows for adjustments to the experimental plan to accommodate unexpected findings. (2) Develop a complete and detailed test plan and review the plan with the beamline scientists beforehand. Plan more experiments than the time allows, readjusting the agenda to cover failed experiments. Test the chemistry in the XAFS cell before arrival. Make sure that your trip to the beamline is fully staffed. (3) Measure all structurally related standards (typically > 6) that play an important

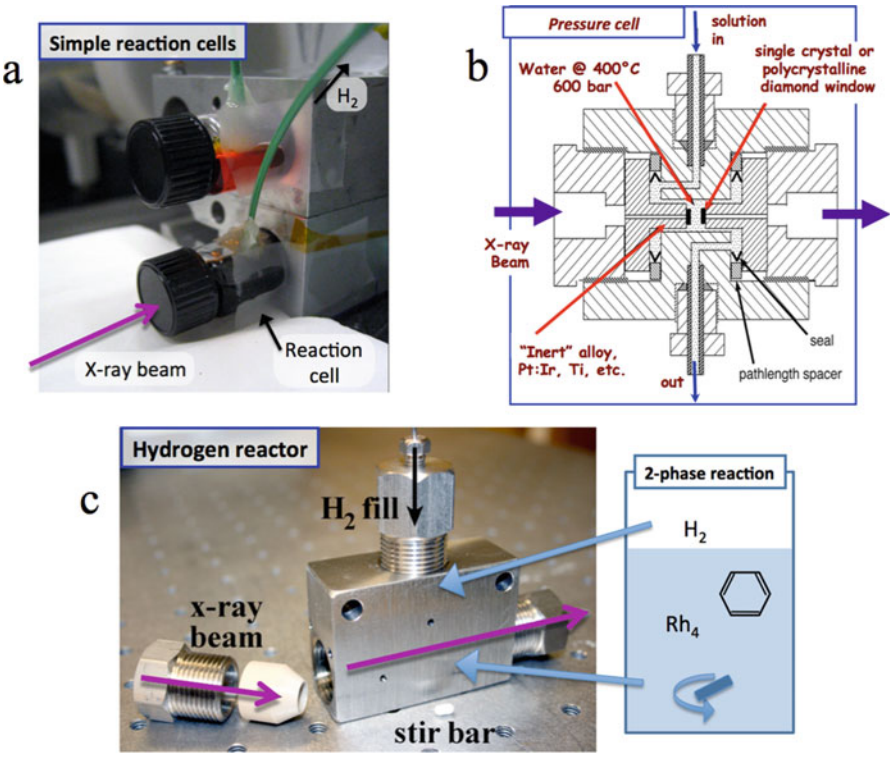

Fig. 27.1 (**a**) Photograph of a simple cell for operando studies of Rh catalyzed dehydrogenation reactions that utilizes an 8 mL standard glass vial with a polyseal cap and hole for H_2 release. (**b**) Schematic of a diamond windowed, high-pressure (600 bar), high-temperature (400 °C) cell for study of aqueous systems. (**c**) Photograph of a stainless steel operando hydrogenation cell that uses PEEK windows for pressures up to approximately 100 bar H_2 and 100 °C. Reprinted with permission from refs. [42, 43]. Copyright 2005 and 2011 American Chemical Society

role in interpretation of the XAFS spectra (4) Discuss the overall experimental plan with beamline personnel well ahead of scheduled beamtime in order to make sure that all aspects of the reaction can be operated safely under the constraints of operation in a beamline hutch and the beamline laboratory.

27.3 Examples of Homogeneous Catalytic Systems

27.3.1 $MnBr_2$ in Supercritical Water for the Oxidation of p*-xylene to Terephthalic Acid*

Terephthalic acid is the primary component in the manufacture of polyester and represents the ninth largest industrial chemical. As shown in Fig. 27.2a, the existing route to the formation of terephthalic acid involves the oxidation of *p*-xylene in

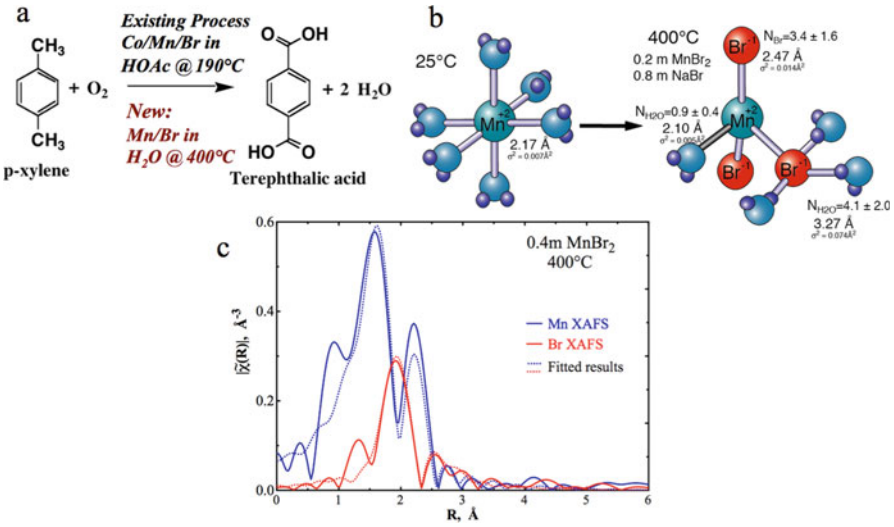

Fig. 27.2 (**a**) Reaction sequence for formation of terephthalic acid using either the conventional acetic acid solvent system or the new system involving a $MnBr_2$ catalyst in supercritical water. (**b**) Schematic of the ion pair species that forms at 400 °C and the structural parameters extracted from the simultaneous fitting of both Mn- and Br-K-edge XAFS spectra. (**c**) XAFS plots of the experimental Mn and Br XAFS to which a single, global best-fit model has been applied. Reprinted with permission from ref. [42]. Copyright 2005 American Chemical Society

acetic acid solvent at 190 °C. A new, more efficient synthesis route involves the use of high-temperature water as a green solvent [44–46]. Another primary benefit is that this approach eliminates the formation of an undesirable side product (4-carboxybenzaldehyde) that is costly to remove. An active catalyst for this reaction is $MnBr_2$, which operates in supercritical water at 400 °C and 300 bar. In situ XAFS (rather than operando in this case) has been used to probe the catalyst structure at reaction conditions to determine the mechanism of this reaction [42]. The extreme demands of this type of system, in terms of high temperature, high pressure and corrosive environment, require a specialized cell. A design similar to the one illustrated in Fig. 27.1b was employed for these studies [41]. The essential features include the use of polycrystalline diamond, X-ray windows that are affixed to a corrosion-resistant titanium alloy body.

Under ambient conditions, the Mn^{2+} is fully hydrated with six water molecules in an octahedral symmetry. In contrast, as shown in Fig. 27.2b, the local structure about Mn^{2+} undergoes a dramatic transition to the catalytic species that exists at 400 °C. The Mn^{2+} first-shell coordination structure now includes 3 Br^- anions that form a contact ion pair with the cation. As shown in Fig. 27.2c, through the acquisition of both Mn and Br K-edge XAFS spectra, a clear picture of the structural details emerge. The simultaneous refinement of these two sets of spectra imposes strong constraints on the fitted Mn-Br bond distance, disorder, and coordination numbers, as these are shared parameters in the refined fits (shown in Fig. 27.2c).

The full characterization of the Mn and Br states helps explain why this catalyst is so active under these conditions. It is suggested that the formation of contact-ion pairs aids in the Br• free radical formation process via charge transfer with Mn^{2+}/Mn^{3+} in the contact ion pair. The bromine radical, Br•, rapidly and selectively generates the benzylic radical that initiates the chain reaction with oxygen.

27.3.2 $CuCl_n^{(2-n)}$ Polyanions in Ionic Liquids for Conversion of Fructose to Hydroxymethylfurfural

Ionic liquids are of high interest because of their potential role as solvents for green chemistry. In general, ionic liquids have an extremely low vapor pressure that simplifies the recovery of the reactants and products. In addition, the unusual solvent environment may enhance certain homogeneous catalytic processes. Cu^{2+} is one of several transition metals in ionic liquids that efficiently converts fructose to hydroxymethylfurfural, an important chemical intermediate [47]. In addition, Cu^{2+} is active in the depolymerization of cellulose [48]. For these reasons, XAFS has been used [49] to measure changes in the coordination structure of Cu^{2+} in the ionic liquid, 1-ethyl-3-methylimidazolium chloride or [EMIM]Cl, a chemical system that is dominated by Cu^{2+} ion pairing with multiple Cl^- anions. The low dielectric constant of the ionic liquids and the lack of an extended water hydrogen-bonding network leads to extensive formation of Cu^{2+}-Cl^- contact ion pairs due to the lack of charge screening between the cation and anion.

Water is often an impurity or product in ionic liquid-based reactions. This is the basis for exploring the binary mixture of the [EMIM]Cl ionic liquid with water. Figure 27.3 shows the XAFS spectra for the two extremes of the fully hydrated Cu^{2+} in water and the fully ion paired species $CuCl_4^{2-}$ in the ionic liquid. The first peak in the radial structure plots of Fig. 27.3a corresponds to either full H_2O or full Cl^- first shell ligands. The coordination numbers and bond distances from XAFS for the Cu-Cl species are consistent with a tetrahedral species. In Fig. 27.3a, the multiple scattering peaks at 3.3 and 3.8 Å for the aqua and Cl^- species are due to the nearly square planar, equatorial waters and the tetrahedral chlorides, respectively (for chlorides this involves the weaker, double-return multiple scattering path). These features exemplify one of the strengths of the XAFS method, the ability to use the photoelectron multiple scattering structure to directly probe the first-shell bonding symmetry. An independent measure of symmetry is also derived from changes in the intensity of the XANES pre-edge peak (not shown) at 8978 eV that is assigned to the 1s -> 3d transition. This further confirms the symmetry changes that occur in low-dielectric constant solvent.

Figure 27.3b shows schematics of the Cu^{2+} structure at various water concentrations as they were derived from the XAFS fit results. Remarkably, the tetrahedral $CuCl_4^{2-}$ species persist up to about 80 mol% water. It is only at even higher water concentrations that the Cu^{2+} coordination with Cl- decreases and the formation of a

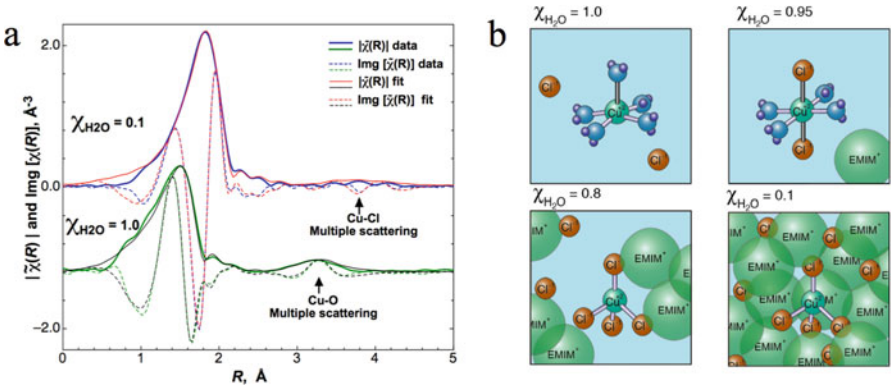

Fig. 27.3 (**a**) Cu K-edge, k^2-weighted $|\tilde{\chi}(R)|$ (*solid*) and $\mathrm{Im}[\tilde{\chi}(R)]$ (*dashed*) plots for Cu^{2+} in an [EMIM]Cl ionic liquid with 10 % water and for Cu^{2+} in pure water. (**b**) Schematic illustrations of the XAFS results for varying mole fractions of water including 0.1, 0.8, 0.95, and 1. From 0 to 80 % water, there is very little change in the structure of the tetrahedral $CuCl_4^{2-}$ species. Reprinted with permission from ref. [49]. Copyright 2010 American Chemical Society

partially hydrated Cu^{2+} occurs. This behavior is ascribed to the change in the dielectric constant of the ionic liquid/water mixture. Below 80 mol% water the dielectric constant is closer to that of a nonpolar solvent, while above 80 % the value rises rapidly to that of pure water. The types of structural transitions illustrated in Fig. 27.3b are essential starting points for an understanding of the catalyst mechanism and kinetics in such homogeneous systems.

27.4 Examples of Metal Cluster Systems

27.4.1 Rh_4 Cluster Catalyzed Dehydrogenation of Amine Boranes

There has been intense interest in the development of hydrogen storage materials and their utilization over the past 15 years. One such category of compounds is the amine boranes with the general formula NHR_2-BH_3. For these systems a catalyst is required to rapidly and quantitatively release the H_2 contained in these compounds. As shown in Fig. 27.4a, a homogeneous rhodium-based complex derived from commercially available [(1,5-cylcooctadiene)RhCl]$_2$ is an efficient catalyst for H_2 release from Me_2NHBH_3 (DMAB) at room temperature [40, 50, 51]. The starting solution is orange, but this turns black during the reaction until finally a black precipitate forms at the end of the reaction. It was initially suggested that metallic rhodium nanoparticles were the catalytic species as determined by ex situ analysis (TEM, XRD) [52]. Organometallic chemists generally believe that homogeneous

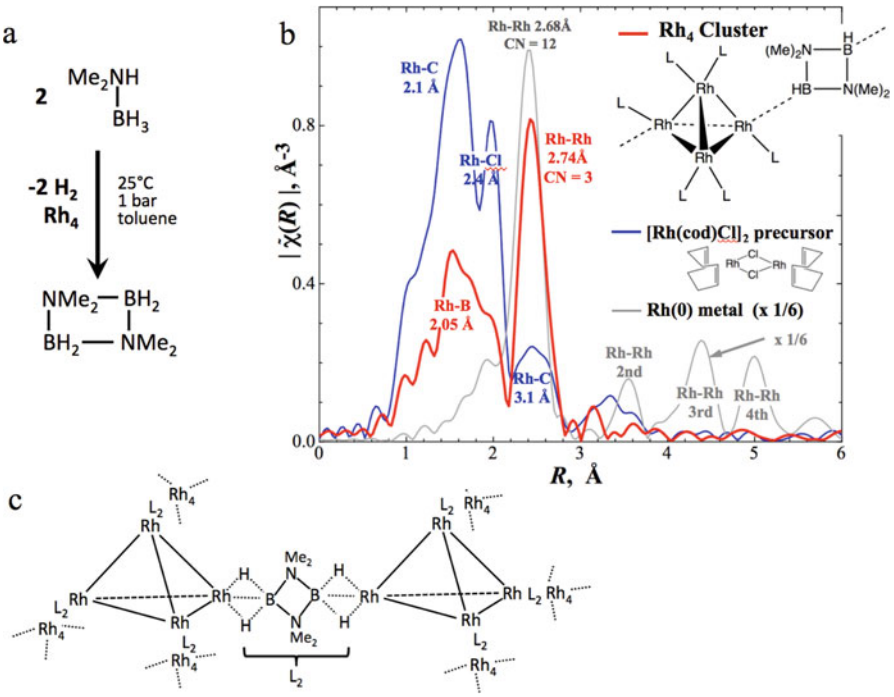

Fig. 27.4 (**a**) The dehydrogenation reaction of dimethyl ammonium borane by a Rh_4 cluster in toluene at 25 °C. (**b**) XAFS plots of the Rh precursor and the active Rh_4 cluster under operando conditions. The spectrum of Rh(0) metal that has been scaled by 1/6 is shown for comparison. (**c**) Polymeric-like chains with Rh_4 nodes that form near the endpoint of the dehydrogenation reaction. Reprinted with permission from ref. [40]. Copyright 2007 American Chemical Society

metal solutions that turn black are a sure sign that metallic particles are being formed [53].

This homogeneous catalyst reaction is an ideal system for operando XAFS. In contrast to the manganese system described above the equipment needed for this operando XAFS study is relatively simple. A small hole drilled into a standard glass vial as shown in Fig. 27.1a allows for the release of H_2 that is produced during these room temperature reactions. Figure 27.4b shows the $|\widetilde{\chi}(R)|$ plots for the starting complex and the rhodium catalyst species under operando conditions. In the region from 4 to 6 Å, there is no long-range scattering that would be expected for rhodium nanoparticles, suggesting that metal-like rhodium species are not formed during the reaction. The observed Rh–Rh distance (2.73 Å) is longer than in rhodium metal (2.68 Å) also supporting the absence of metallic rhodium. The best-fit model is a four rhodium cluster in a tetrahedral arrangement (coordination number of 3 for each rhodium to another rhodium) with light atoms (C, B, or N) directly bonded to the rhodium as ligands. Of these three light elements, the results suggest that boron is the most likely to be bonded to the rhodium [40, 51]. Spectral analysis suggests

that greater than 99 % of the rhodium in the system is present in these Rh_4 clusters. Within the accuracy of the experiments, the absence of metallic nanoparticles is confirmed. As the reaction starts to approach the endpoint, a black precipitate is observed that is concomitant with the loss of soluble rhodium signal intensity. Careful XAFS analysis of this precipitate under operando conditions (without exposing the solid to air) showed an XAFS spectrum that is almost identical to that of dissolved rhodium clusters. For this solid precipitate it is postulated that tetra-rhodium clusters are bridged by the DMAB dimer product to form extended polymer-like arrangements that are insoluble as shown in the schematic of Fig. 27.4c. This finding was supported by the observation that this black precipitate is rapidly redissolved when more of the starting DMAB compound is added to the system.

An intriguing finding from XAFS is that exposure of the reaction solution to even small amounts of oxygen (from air) either during or after the reaction led to the formation of metallic rhodium. All attempts to analyze the black precipitate spectroscopically ex situ always showed the presence of metallic rhodium due to contamination with oxygen. It was proposed the Rh_4 ligands (DMAB dimers) are extremely sensitive to oxidation and the loss of these stabilizing ligands leads immediately to the formation of metallic rhodium particles. This example demonstrates the essential role of operando XAFS spectroscopy yielding information not possible by ex situ analysis. The finding of the tetra-rhodium clusters had not previously been postulated in these systems. This new finding led to questions about whether there were other rhodium (and other metal-containing) systems that were actually catalyzed by clusters instead of metallic nanoparticles. This then led to the reinvestigation of a 30-year old chemistry question in catalysis that is described in the next section.

27.4.2 Rh_4 Cluster Catalyzed Hydrogenation of Benzene

Based upon the above results showing that tetra-rhodium clusters were important in dehydrogenation catalysis, other systems were explored in which there was uncertainty whether metallic rhodium nanoparticles or homogeneous rhodium complexes were the active species. Among these, a system described by Maitlis in 1977 for the hydrogenation of benzene stood out. Maitlis [54] proposed that a rhodium species, $[Cp^*RhCl_2]_2$ (Cp* being pentamethylcyclopentadienyl), hydrogenates benzene to cyclohexane under H_2 pressure at 100 °C (see Fig. 27.5a) through a homogeneous catalytic mechanism rather than through the presence of metallic particles. Controversy over this interpretation of the active catalyst reigned for over 30 years with more recent literature reports [55, 56] declaring that metallic rhodium nanoparticles were instead the true catalyst. As mentioned previously, a general observation in organometallic catalyst community is that the presence of a black solution or a black precipitate is evidence of metallic catalyst. In fact, the hydrogenation of benzene has come to be perceived as the “tell tale sign of heterogeneous

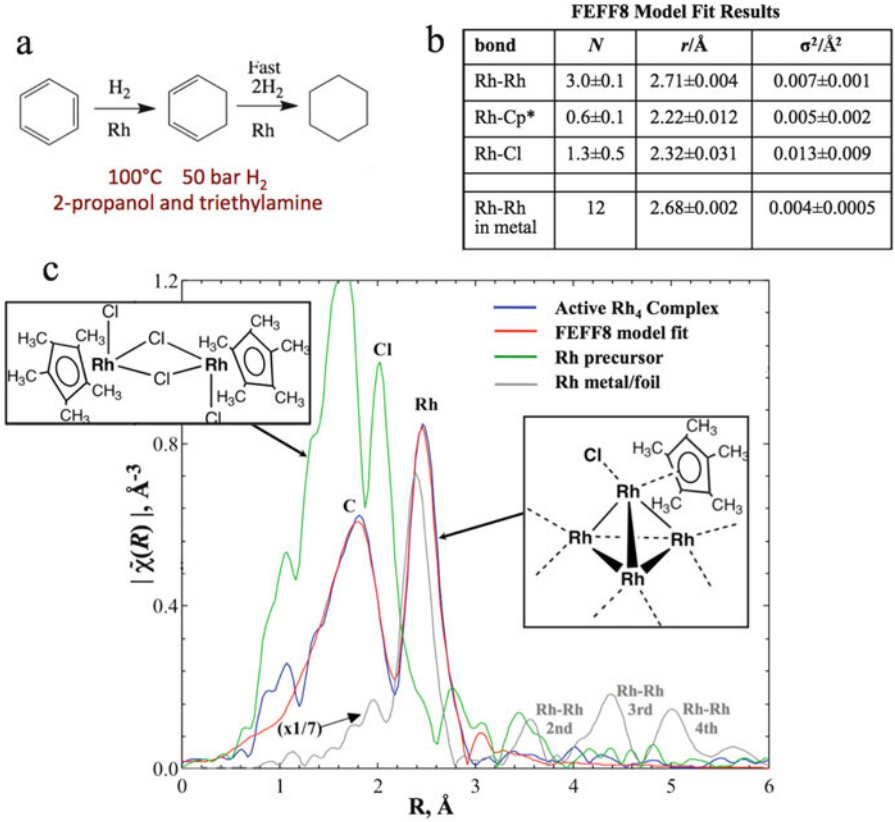

Fig. 27.5 (**a**) The reaction for the hydrogenation of benzene by a Rh_4 cluster in 2-propanol and triethylamine at 100 °C and with 50 bar H_2. (**b**) Structural parameters derived from fitting the FEFF8 model to the experimental spectra. (**c**) XAFS plots of the Rh precursor and the active Rh_4 cluster under operando conditions. The spectrum of Rh(0) metal that has been scaled by 1/7 is shown for comparison. Reprinted with permission from ref. [43]. Copyright 2011 American Chemical Society

catalysis" [53]. Further, earlier ex situ techniques [55, 56] had been used in an attempt to validate the presence of metallic rhodium and a "key" analytical test (the mercury test) was purported to demonstrate that metallic rhodium particles were the catalytic species (For a discussion of the mercury test please see references [56–59].). Operando XAFS was used to resolve this controversy [43]. The XAFS cell of choice for this system is shown in Fig. 27.1c. Built-in PEEK windows allowed operation at H_2 pressures up to 50 bar and temperatures near 100 °C.

Similar to the DMAB reaction mentioned above, no metallic rhodium was observed in this reaction system [43]. As shown in Fig. 27.5c, again tetra-rhodium clusters were the only viable fit to the XAFS spectrum, with light atoms (C and Cl) filling the outer coordination sphere of the Rh_4-cluster. The fitted structural

parameters for the Rh_4 cluster are reported in Fig. 27.5b. Indeed, even at room temperature XAFS revealed structural changes of the catalyst precursor, $[Cp^*RhCl_2]_2$, via simple dissolution in the reaction solvent. In the presence of H_2 the rhodium complex begins to form tetra-rhodium clusters as the solution slowly turns black at room temperature. At the reaction temperature of 100 °C, the transformation to the Rh_4 cluster is rapid.

In this system the rhodium-to-substrate concentration was initially four times that of the original Maitlis study. This provided an improved signal-to-noise ratio for XAFS. Reactions conducted under the original concentration and conditions also yielded the same results, showing that at least in this case, increased catalyst concentration did not affect the observed kinetics, spectroscopy, or catalyst speciation.

Later investigations [43] of the kinetics and "mercury test" for this reaction demonstrated that the mercury test also poisons the homogeneous Rh_4 clusters in a similar way that it poisons metallic nanoparticles, and it is therefore an unreliable test of whether a reaction is catalyzed by a homogeneous or a heterogeneous process. Overall, these XAFS findings completely revised the understanding of this common "textbook" example of benzene hydrogenation and raised the question of whether tetra-rhodium clusters represent a "magic" species in such catalytic reactions.

27.4.3 Rh Monomer Hydrogenation of Cyclohexene

A careful operando XAFS spectroscopic, poisoning, and kinetic reinvestigation [59] of the room temperature hydrogenation of cyclohexene earlier performed by Maitlis [54] demonstrated a different outcome for the Rh catalyst structure than for the benzene system. In this case, a black color is not obtained during the reaction and most researchers believed this to be a homogeneous (non-nanoparticle) catalyst reaction system. Yet, at much higher initial rhodium concentrations the Rh_4 clusters observed in the previous examples were again observed to form during the reaction by XAFS [59]. As previously mentioned, the structure of the initial catalyst precursor, $[Cp^*RhCl_2]_2$, immediately changes upon dissolution in the reaction medium, even before addition of H_2. As shown in Fig. 27.6, the initial rhodium dimer loses at least one chloride ligand upon dissolution in the reaction medium. Reactions under lower rhodium concentrations (near to those originally reported by Maitlis) showed far less rhodium tetramer being formed early during the reaction than at the higher concentrations. Careful kinetic and carefully redesigned catalyst poisoning experiments showed that the actual catalyst in this reaction is not a Rh_4 cluster but rather a rhodium monomer. This combined kinetic and XAFS spectroscopic study shows the high importance of operando studies to delineate the mostly likely catalytic Rh species.

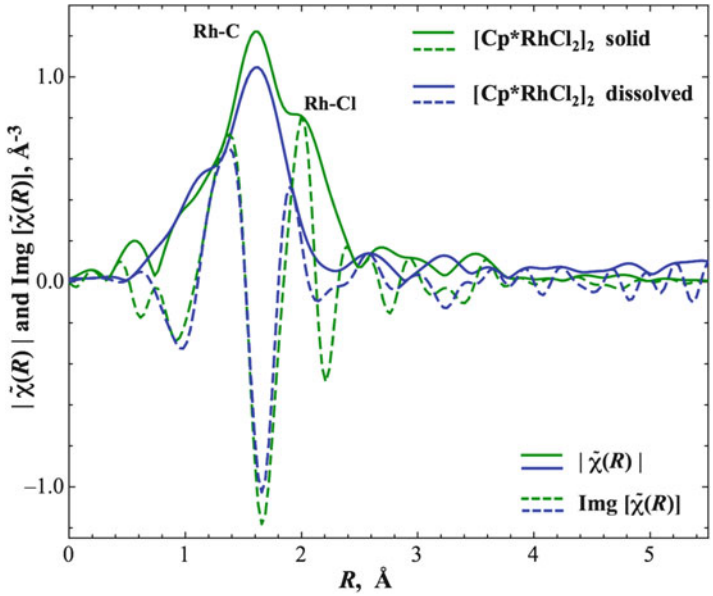

Fig. 27.6 XAFS plots for the Rh catalyst used in cyclohexene hydrogenation. The precursors from $[Cp^*RhCl_2]_2$ (Cp^* being pentamethylcyclopentadienyl) are shown for the starting pure *solid* and the species that forms when freshly dissolved in 2-propanol with triethylamine and cyclohexene. Reprinted with permission from ref. [59]. Copyright 2015 American Chemical Society

27.5 Summary

In these examples we have shown how XAFS spectroscopy probes homogeneous systems to obtain information about catalyst structure not obtainable by other methods. For instance, the unexpected discovery of tetra-rhodium organometallic clusters as the predominant species during the dehydrogenation of amine boranes and the hydrogenation of benzene was only accomplished through the use of operando XAFS. Ex situ techniques were found to yield species not relevant to the catalyst system. The knowledge that rhodium-tetramers were important for catalysis in one system led to the reinvestigation of other systems containing clusters that have not been isolable. In general, careful planning and implementation of XAFS gives a clear view of catalyst structures during the actual catalysis. While XAFS observation of a metal species during catalysis is not necessarily proof that the observed species is catalytically active, it does yield powerful information about the reaction mechanism, especially when combined with other analytical techniques. Unlike other spectroscopic techniques such as NMR and IR, there are no limitations with respect to active NMR nuclei or indirect interpretation of IR vibrational modes that typically have low extinction coefficients.

Acknowledgement We graciously acknowledge the support from our colleagues in this work including Tom Autrey, Walt Partenheimer, Greg Schenter, Roger Rousseau, Don Camaioni, Yonsheng Chen, Steve Heald, John Roberts, Tricia Smurthwaite, Nate Szymczak, Richard Finke, Jim Franz, and Ercan Bayram. This work was supported by the U.S. Department of Energy (DOE), Office of Science, Office of Basic Energy Sciences (BES), Division of Chemical Sciences, Geosciences & Biosciences. Pacific Northwest National Laboratory (PNNL) is operated for DOE by Battelle. Sector 20 facilities at the Advanced Photon Source and research at these facilities are supported by DOE-BES, the Canadian Light Source and its funding partners, the University of Washington, and the Advanced Photon Source. Use of the Advanced Photon Source, an Office of Science User Facility operated for DOE Office of Science by Argonne National Laboratory, was supported by the U.S. DOE under Contract No. DE-AC02-06CH11357.

References

1. Fulton JL, Hoffmann MM, Darab JG, Palmer BJ, Stern EA (2000) Copper(I) and copper (II) coordination structure under hydrothermal conditions at 325 degrees C: an X-ray absorption fine structure and molecular dynamics study. J Phys Chem A 104(49):11651–11663
2. Hayakawa K, Hatada K, D'Angelo P, Della Longa S, Natoli CR, Benfatto M (2004) Full quantitative multiple-scattering analysis of X-ray absorption spectra: application to potassium hexacyanoferrat(II) and -(III) complexes. J Am Chem Soc 126(47):15618–15623
3. Kuzmin A, Parent P (1994) Focusing and superfocusing effects in X-ray-absorption fine-structure at the iron K edge in Fef3. J Phys Condens Matter 6(23):4395–4404
4. Giorgetti M, Berrettoni M, Filipponi A, Kulesza PJ, Marassi R (1997) Evidence of four-body contributions in the EXAFS spectrum of Na_2Co [$Fe(CN)_6$]. Chem Phys Lett 275(1–2):108–112
5. Fulton JL, Kathmann SM, Schenter GK, Balasubramanian M (2009) Hydrated structure of Ag (I) ion from symmetry-dependent, K- and L-edge XAFS multiple scattering and molecular dynamics simulations. J Phys Chem A 113(50):13976–13984
6. Baer MD, Pham VT, Fulton JL, Schenter GK, Balasubramanian M, Mundy CJ (2011) Is iodate a strongly hydrated cation? J Phys Chem Lett 2(20):2650–2654
7. Fulton JL, Hoffmann MM, Darab JG (2000) An X-ray absorption fine structure study of copper (I) chloride coordination structure in water up to 325 degrees C. Chem Phys Lett 330 (3–4):300–308
8. Heck RF (1979) Palladium-catalyzed reactions of organic halides with olefins. Acc Chem Res 12(4):146–151
9. Fiddy SG, Evans J, Newton MA, Neisius T, Tooze RP, Oldman R (2003) Extended X-ray absorption fine structure (EXAFS) characterisation of dilute palladium homogeneous catalysts. Chem Commun 21:2682–2683
10. Hamill NA, Hardacre C, McMath SEJ (2002) In situ XAFS investigation of palladium species present during the Heck reaction in room temperature ionic liquids. Green Chem 4(2):139–142
11. Kumar A, Rao GK, Kumar S, Singh AK (2014) Formation and role of palladium chalcogenide and other species in Suzuki-Miyaura and heck C-C coupling reactions catalyzed with palladium(II) complexes of organochalcogen ligands: realities and speculations. Organometallics 33(12):2921–2943
12. Sayers DE, Stern EA, Lytle FW (1971) New technique for investigating noncrystalline structures. Fourier analysis of the extended x-ray-absorption fine structure. Phys Rev Lett 27:1204–1207
13. Stern EA (1974) Theory of extended x-ray-absorption fine-structure. Phys Rev B 10 (8):3027–3037
14. Rehr JJ, Albers RC (2000) Theoretical approaches to x-ray absorption fine structure. Rev Mod Phys 72(3):621–654

15. Bordiga S, Groppo E, Agostini G, van Bokhoven JA, Lamberti C (2013) Reactivity of surface species in heterogeneous catalysts probed by in situ x-ray absorption techniques. Chem Rev 113(3):1736–1850
16. Garino C, Borfecchia E, Gobetto R, van Bokhoven JA, Lamberti C (2014) Determination of the electronic and structural configuration of coordination compounds by synchrotron-radiation techniques. Coord Chem Rev 277:130–186
17. Nelson RC, Miller JT (2012) An introduction to X-ray absorption spectroscopy and its in situ application to organometallic compounds and homogeneous catalysts. Catal Sci Technol 2 (3):461–470
18. Sherborne GJ, Nguyen BN (2015) Recent XAS studies into homogeneous metal catalyst in fine chemical and pharmaceutical syntheses. Chem Cent J 9:37
19. Fiddy SG, Evans J, Neisius T, Newton MA, Tsoureas N, Tulloch AAD, Danopoulos AA (2007) Comparative experimental and EXAFS studies in the Mizoroki-Heck reaction with heteroatom-functionalised N-heterocyclic carbene palladium catalysts. Chem Eur J 13 (13):3652–3659
20. Bogg D, Conyngham M, Corker JM, Dent AJ, Evans J, Farrow RC, Kambhampati VL, Masters AF, McLeod DN, Ramsdale CA, Salvini G (1996) Scanning and energy dispersive EXAFS studies of ethyl transmetallation in an alkene oligomerisation catalyst. Chem Commun 5:647–648
21. Bartlett SA, Wells PP, Nachtegaal M, Dent AJ, Cibin G, Reid G, Evans J, Tromp M (2011) Insights in the mechanism of selective olefin oligomerisation catalysis using stopped-flow freeze-quench techniques: a Mo K-edge QEXAFS study. J Catal 284(2):247–258
22. Diaz-Moreno S, Bowron DT, Evans J (2005) Structural investigation of the bridged activated complex in the reaction between hexachloroiridate(IV) and pentacyanocobaltate(II). Dalton Trans 23:3814–3817
23. Guilera G, Newton MA, Polli C, Pascarelli S, Guino M, Hii KKM (2006) In situ investigation of the oxidative addition in homogeneous Pd catalysts by synchronised time resolved UV-Vis/EXAFS. Chem Commun 41:4306–4308
24. Tromp M, van Strijdonck GPF, van Berkel SS, van den Hoogenband A, Feiters MC, de Bruin B, Fiddy SG, van der Eerden AMJ, van Bokhoven JA, van Leeuwen PWNM, Koningsberger DC (2010) Multitechnique approach to reveal the mechanism of copper(II)-catalyzed arylation reactions. Organometallics 29(14):3085–3097
25. Bauer M, Kauf T, Christoffers J, Bertagnolli H (2005) Investigations into the metal species of the homogeneous iron(III) catalyzed Michael addition reactions. Phys Chem Chem Phys 7 (13):2664–2670
26. Bauer M, Gastl C (2010) X-Ray absorption in homogeneous catalysis research: the iron-catalyzed Michael addition reaction by XAS, RIXS and multi-dimensional spectroscopy. Phys Chem Chem Phys 12(21):5575–5584
27. Hashmi ASK, Lothschuetz C, Ackermann M, Doepp R, Anantharaman S, Marchetti B, Bertagnolli H, Rominger F (2010) Gold catalysis: in situ EXAFS study of homogeneous oxidative esterification. Chem Eur J 16(27):8012–8019
28. Sherborne GJ, Chapman MR, Blacker AJ, Bourne RA, Chamberlain TW, Crossley BD, Lucas SJ, McGowan PC, Newton MA, Screen TEO, Thompson P, Willans CE, Nguyen BN (2015) Activation and deactivation of a robust immobilized Cp*Ir-transfer hydrogenation catalyst: a multielement in situ x-ray absorption spectroscopy study. J Am Chem Soc 137(12):4151–4157
29. Koningsberger DC, Prins R (1988) X-ray absorption: principles, applications, techniques of EXAFS, SEXAFS and XANES. Wiley, New York
30. Frahm R (1988) Quick scanning EXAFS—First experiments. Nuc Instrum Methods Phys Res A 270(2–3):578–581
31. Richwin M, Zaeper R, Lutzenkirchen-Hecht D, Frahm R (2002) Piezo-XAFS-time-resolved x-ray absorption spectroscopy. Rev Sci Instrum 73(3):1668–1670

32. Murphy LM, Dobson BR, Neu M, Ramsdale CA, Strange RW, Hasnain SS (1995) Quick fluorescence-EXAFS: an improved method for collection of conventional XAFS data and for studying reaction intermediates in dilute systems. J Synchrotron Radiat 2:64–69
33. Dent AJ (2002) Development of time-resolved XAFS instrumentation for quick EXAFS and energy-dispersive EXAFS measurements on catalyst systems. Top Catal 18(1–2):27–35
34. Phizackerley RP, Rek ZU, Stephenson GB, Conradson SD, Hodgson KO, Matsushita T, Oyanagi H (1983) An energy-dispersive spectrometer for the rapid measurement of x-ray absorption-spectra using synchrotron radiation. J Appl Crystallogr 16:220–232
35. Dartyge E, Depautex C, Dubuisson JM, Fontaine A, Jucha A, Leboucher P, Tourillon G (1986) X-ray absorption in dispersive mode - a new spectrometer and a data acquisition-system for fast kinetics. Nuc Instrum Methods Phys Res A 246(1–3):452–460
36. Pascarelli S, Mathon O, Munoz M, Mairs T, Susini J (2006) Energy-dispersive absorption spectroscopy for hard-X-ray micro-XAS applications. J Synchrotron Radiat 13:351–358
37. Bressler C, Chergui M (2010) Molecular structural dynamics probed by ultrafast X-Ray absorption spectroscopy. Annu Rev Phys Chem 61:263–282
38. Chase ZA, Fulton JL, Camaioni DM, Mei D, Balasubramanian M, Van-Thai P, Zhao C, Weber RS, Wang Y, Lercher JA (2013) State of supported Pd during catalysis in water. J Phys Chem C 117(34):17603–17612
39. Wallen SL, Palmer BJ, Pfund DM, Fulton JL, Newville M, Ma YJ, Stern EA (1997) Hydration of bromide ion in supercritical water: an X-ray absorption fine structure and molecular dynamics study. J Phys Chem A 101(50):9632–9640
40. Fulton JL, Linehan JC, Autrey T, Balasubramanian M, Chen Y, Szymczak NK (2007) When is a nanoparticle a cluster? An operando EXAFS study of amine borane dehydrocoupling by Rh4-6 clusters. J Am Chem Soc 129(39):11936–11949
41. Fulton JL, Chen Y, Heald SM, Balasubramanian M (2004) High-pressure, high-temperature x-ray absorption fine structure transmission cell for the study of aqueous ions with low absorption-edge energies. Rev Sci Instrum 75(12):5228–5231
42. Chen YS, Fulton JL, Partenheimer W (2005) The structure of the homogeneous oxidation catalyst, Mn(II)(Br^{-1})(x), in supercritical water: an X-ray absorption fine-structure study. J Am Chem Soc 127(40):14085–14093
43. Bayram E, Linehan JC, Fulton JL, Roberts JAS, Szymczak NK, Smurthwaite TD, Ozkar S, Balasubramanian M, Finke RG (2011) Is it homogeneous or heterogeneous catalysis derived from [RhCp*Cl_2]$_2$? In operando XAFS, kinetic, and crucial kinetic poisoning evidence for subnanometer Rh-4 cluster-based benzene hydrogenation catalysis. J Am Chem Soc 133 (46):18889–18902
44. Garcia-Verdugo E, Venardou E, Thomas WB, Whiston K, Partenheimer W, Hamley PA, Poliakoff M (2004) Is it possible to achieve highly selective oxidations in supercritical water? Aerobic oxidation of methylaromatic compounds. Adv Synth Catal 346(2–3):307–316
45. Hamley PA, Ilkenhans T, Webster JM, Garcia-Verdugo E, Venardou E, Clarke MJ, Auerbach R, Thomas WB, Whiston K, Poliakoff M (2002) Selective partial oxidation in supercritical water: the continuous generation of terephthalic acid from para-xylene in high yield. Green Chem 4(3):235–238
46. Perez E, Fraga-Dubreuil J, Garcia-Verdugo E, Hamley PA, Thomas ML, Yan C, Thomas WB, Housley D, Partenheimer W, Poliakoff M (2011) Selective aerobic oxidation of para-xylene in sub- and supercritical water. Part 2. The discovery of better catalysts. Green Chem 13 (9):2397–2407
47. Zhao HB, Holladay JE, Brown H, Zhang ZC (2007) Metal chlorides in ionic liquid solvents convert sugars to 5-hydroxymethylfurfural. Science 316(5831):1597–1600
48. Yu S, Brown HM, Huang XW, Zhou XD, Amonette JE, Zhang ZC (2009) Single-step conversion of cellulose to 5-hydroxymethylfurfural (HMF), a versatile platform chemical. Appl Catal A Gen 361(1-2):117–122
49. Li GS, Camaioni DM, Amonette JE, Zhang ZC, Johnson TJ, Fulton JL (2010) [CuCln](2-n) Ion-pair species in 1-ethyl-3-methylimidazolium chloride ionic liquid-water mixtures:

ultraviolet-visible, x-ray absorption fine structure, and density functional theory characterization. J Phys Chem B 114(39):12614–12622
50. Chen YS, Fulton JL, Linehan JC, Autrey T (2005) In situ XAFS and NMR study of rhodium-catalyzed dehydrogenation of dimethylamine borane. J Am Chem Soc 127(10):3254–3255
51. Rousseau R, Schenter GK, Fulton JL, Linehan JC, Engelhard MH, Autrey T (2009) Defining active catalyst structure and reaction pathways from ab initio molecular dynamics and operando XAFS: dehydrogenation of dimethylaminoborane by rhodium clusters. J Am Chem Soc 131(30):10516–10524
52. Jaska CA, Temple K, Lough AJ, Manners I (2003) Transition metal-catalyzed formation of boron-nitrogen bonds: catalytic dehydrocoupling of amine-borane adducts to form aminoboranes and borazines. J Am Chem Soc 125:9424–9434
53. de Vries JG, Elsevier CJ (2007) Handbook of homogeneous hydrogenation. Wiley, Weinheim
54. Russell MJ, White C, Maitlis PM (1977) Stereoselective homogeneous hydrogenation of arenes to cyclohexanes catalyzed by $[Rh(C_5Me_5)Cl_2]_2$. J Chem Soc Chem Commun 13:427–428
55. Widegren JA, Finke RG (2003) A review of the problem of distinguishing true homogeneous catalysis from soluble or other metal-particle heterogeneous catalysis under reducing conditions. J Mol Catal A Chem 198(1–2):317–341
56. Hagen CM, Widegren JA, Maitlis PM, Finke RG (2005) Is it homogeneous or heterogeneous catalysis? Compelling evidence for both types of catalysts derived from $[Rh(C_5Me_5)Cl_2]_2$ as a function of temperature and hydrogen pressure. J Am Chem Soc 127(12):4423–4432
57. Widegren JA, Finke RG (2003) A review of soluble transition-metal nanoclusters as arene hydrogenation catalysts. J Mol Catal A Chem 191(2):187–207
58. Roucoux A, Schulz J, Patin H (2002) Reduced transition metal colloids: a novel family of reusable catalysts? Chem Rev 102(10):3757–3778
59. Bayram E, Linehan JC, Fulton JL, Szymczak NK, Finke RG (2015) Determination of the dominant catalyst derived from the classic $[RhCp^*Cl_2]_2$ precatalyst system: is it single-metal Rh1Cp*-based, subnanometer Rh-4 cluster-based, or Rh(0)(n) nanoparticle-based cyclohexene hydrogenation catalysis at room temperature and mild pressures? Acs Catal 5 (6):3876–3886

Chapter 28
Enzymes and Models

Junko Yano and Vittal Yachandra

28.1 Introduction

Nature uses remarkably varied systems and mechanisms to perform chemical reactions with efficiency, speed, and complexity. At the active site of many enzymes are metal centers, responsible for the rearrangement of electrons and atoms in order to carry out electron transfer and catalytic reactions. Some of the representative metal clusters, especially those that contain heterometallic clusters, that are related to important reactions in nature, are shown in Fig. 28.1 [1–4]. Many of these consist of transition metals, such as V, Mn, Fe, Co, Ni, Cu, Zn, Mo, W and others. Using the flexibility of their electronic structures that can accommodate different redox states, they catalyze multi-electron reactions in aqueous solution, under conditions of ambient temperature and pressure.

Geometric and electronic structures of metal catalytic centers have been studied with X-ray absorption spectroscopy (XAS) in numerous metalloenzymes by taking advantage of the element-specificity of X-ray spectroscopy. X-ray absorption near edge spectroscopy (XANES) has been commonly used as a probe of the metal oxidation state, while extended X-ray absorption fine structure (EXAFS) has been applied for identifying the geometric structure of the metal complexes, and the method does not require single crystals. This makes the EXAFS method a powerful tool for extracting structural information of reaction intermediates, that cannot be crystallized. While solution NMR study is another way to get structural information of non-crystalline biological samples, it is difficult to apply the method to large metalloenzymes (>100 kDa) [5] or to study paramagnetic metal centers of metalloenzymes.

J. Yano (✉) • V. Yachandra
Molecular Biophysics and Integrated Bioimaging Division, Lawrence Berkeley National Laboratory, Berkeley, CA 94720, USA
e-mail: JYano@lbl.gov

Y. Iwasawa et al. (eds.), *XAFS Techniques for Catalysts, Nanomaterials, and Surfaces*, DOI 10.1007/978-3-319-43866-5_28

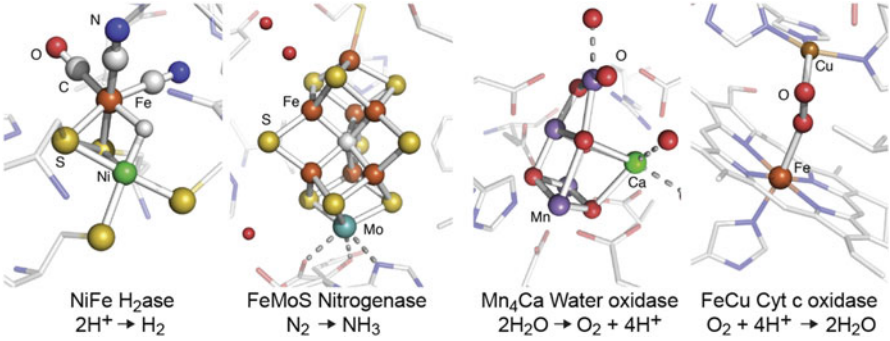

Fig. 28.1 Some examples of metalloenzymes that contain heterometallic clusters, such as NiFe hydrogenase, FeMo nitrogenase, Mn_4Ca water oxidase, and FeCu cytc oxidase, that have been studied using X-ray spectroscopic techniques

In addition to XAS, more advanced X-ray-based techniques such as RIXS (resonant inelastic X-ray scattering), XES (X-ray emission spectroscopy), and X-ray Raman spectroscopy [6], have been introduced to study biological systems, owing to the availability of bright synchrotron X-ray sources. XAS and XES data collection of biological samples have become somewhat routine. However, getting useful data often remains challenging due to several difficulties that are unique to biological systems. For example, X-ray-induced changes during data collection have been a concern. Reducing the background signal that arise from light atoms is another issue. Furthermore, interpreting X-ray spectroscopic data of biological systems often requires a set of adequate model complexes, that provide the basis for evaluating the influence of the coordination environment of the absorber elements. Study of structurally well-characterized model complexes also provides a benchmark for understanding the EXAFS from metal systems of unknown structures.

In this chapter, the X-ray spectroscopy methods that have been used for studying biological samples are described, using several examples. In addition to the synchrotron X-ray-based methods, recent introduction of XFELs (X-ray free electron lasers) have opened a new way of collecting X-ray spectroscopy of biological systems by capturing reaction intermediates under physiological conditions, and this chapter touches on some of the applications that have been demonstrated recently.

28.2 X-Ray Spectroscopy of Biological Systems

X-ray crystallography and X-ray spectroscopy of metalloenzymes provide complementary information: crystallography probes the structural changes of the cofactor and the overall protein, while XAS provides detailed information about changes in

the electronic structure of the metal of interest and its local structural information. When combined, these complementary measurements will provide a more detailed understanding of important enzymatic reactions.

In general, the advantage of EXAFS over X-ray crystallography is that the local structural information around the metal of interest can be obtained even from disordered samples such as powders and solution, and usually the metal–metal and metal–ligand distance information is much better than that can be obtained from crystallography. However, ordered samples like oriented membranes and single crystals often increase the information obtained from X-ray spectroscopy. The advantages and the limitations of XAS for the structural studies of biological systems are summarized in detail below.

1. In a metalloenzyme with multiple metal centers like cytochrome oxidase (Cu and Fe), photosystem II (Mn and Ca), or nitrogenase (Fe/V and Mo), it is possible to study the structural environment of each metal atom independently, because of the element specificity of XAS.
2. The metal of interest is never "*silent*" with respect to X-ray spectra, and one can always probe the metal site structure by X-ray spectroscopy. It could be "*silent*" with respect to EPR (electron paramagnetic resonance spectroscopy), optical, or other spectroscopic methods. However, this could become a disadvantage, if there are several metal centers going through different chemical states.
3. X-ray spectroscopy is not limited by the state of the sample, because it is sensitive only to the local metal site structure. Therefore, one can either trap intermediates in the enzymatic cycle or modify the site by the addition of inhibitors or substrate, or generate other chemical modifications or site-directed mutations. Such samples can be made as frozen solutions, avoiding the problems of trying to obtain single crystals.

It is also important to realize the intrinsic limitations of EXAFS for studying structures. A frequent problem is the inability to distinguish between scattering atoms with little difference in atomic number (C, N, O or S, Cl, or Mn, Fe). Distances are usually the most reliably determined structural parameters from EXAFS. But the range of data that can be collected, often-times due to practical reasons like the presence of the K-edge of another metal, or data collection time for dilute biological samples, limits the resolution of distance determinations to between 0.1 and 0.2 Å. Also it is difficult to determine whether a Fourier peak should be fit to one distance with a relatively large disorder parameter or to two distances, each having a small disorder parameter. Careful statistical analysis, taking into consideration the degrees of freedom in the fits, should precede any such analysis. The resolution in the distance Δr can be estimated from the relation that $\Delta r \Delta k \sim 1$ (see Sect. 4.2). Determination of coordination numbers or number of backscatterers is fraught with difficulties. The Debye-Waller factor is strongly correlated with the coordination number and one must have recourse to other information to narrow the range that is possible from curve fitting analysis alone.

It is therefore very useful to compare the spectra from the complex in the metalloenzyme to some known model complexes and then use Debye-Waller parameters obtained from the model complexes in the fits.

28.3 Radiation-Induced Changes During Data Collection

Damage to biological samples by X-rays is cause for serious concern for X-ray based experiments, in particular for the study of biological samples. However, with the right precautions one can successfully perform these experiments under the threshold of radiation damage. At synchrotron sources, most of the damage is produced by free radicals and hydrated electrons that are produced by X-rays in biological samples. The diffusion of the free radicals and hydrated electrons can be minimized by the use of low temperatures. The use of a liquid He flow cryostat or liquid He cryostream, where the samples are at atmospheric pressure in a He gas atmosphere, has greatly reduced the risk of sample damage by X-rays. XAS experiments require a lower X-ray dose than X-ray crystallography, and radiation damage can be precisely monitored and controlled, thus allowing for data collection from an intact form of metal catalytic centers.

An example of the X-ray-induced changes is shown in Fig. 28.2. Solutions of Photosystem II (PSII) that consists of the $MnCaO_5$ catalytic center were exposed to various X-ray doses at 100 K, leading to reduction of 5, 10 or 25 %, of the Mn in the sample from the native Mn(III,IV) to Mn(II) [7]. The corresponding XANES spectra are shown in Fig. 28.2a. A clear shift in the K-edge toward lower energies, due to the reduction to Mn(II) can be seen when comparing with the intact state

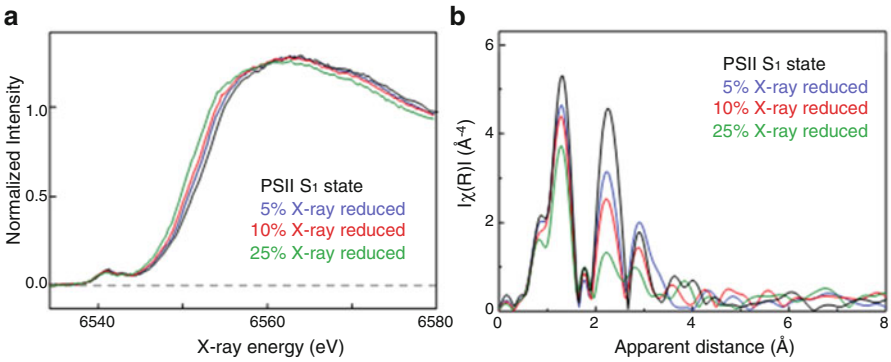

Fig. 28.2 (**a**) The Mn XANES spectrum of the oxygen-evolving complex from PS II that has been photo-reduced by X-rays to different levels between 5 and 25 %, compared to a spectrum from an intact PS II sample. (**b**) The corresponding Mn EXAFS Fourier transforms from the same PS II samples, showing the disruption of the Mn_4Ca oxo-bridged complex following X-ray radiation induced reduction. This disruption manifests itself as a decrease in the intensity of FT peaks assigned to Mn-Mn interactions at ~2.7 Å and/or Mn–Mn/Mn–Ca interactions at 3.2 Å [7]

spectrum from the native Mn(III,IV) form. In the EXAFS spectra (Fig. 28.2b), the intensities of all three peaks are decreased upon Mn reduction, with the most pronounced decrease in the second peak intensity, showing that upon Mn reduction Mn-Mn distances change and they are elongated. The reduction of the metal center by X-rays does not necessarily go through the catalytic reduction pathway, as it is likely caused by the random attack of hydroxyl radicals that are created by the interaction of X-rays and water molecules. Similar observations have been made in many Fe-containing proteins such as putidaredoxin [8], Cytochrome C peroxidase [9], and Fe/Fe and Fe/Mn ribonucleotide reductase [10], where the states generated by X-ray photoreduction are significantly different from the native catalytic state of the metal center. These studies show that radiation-induced changes are a general problem when studying metalloenzymes with X-rays. Such radiation-induced effects could potentially be turned into a tool to obtain new insights into the structural and electronic structural nature of the metal cluster.

Nevertheless, radiation-induced changes remain one of the most challenging aspects in biological X-ray spectroscopy. New approaches to overcome such effects and collect radiation-damage-free data have become possible, using XFELs which is described in Sect. 5.

28.4 Application of Various X-Ray Spectroscopy Techniques to Study Metalloenzymes

28.4.1 Polarized X-Ray Absorption Spectroscopy

As described above, the advantage of XAS is that the local structural information around the element of interest can be obtained from disordered samples such as powders and solutions. However, ordered samples like membranes and single crystals often increases the information obtained from XAS. For oriented single crystals or ordered membranes the interatomic vector orientations can be deduced from dichroism measurements.

Membrane proteins can be oriented on a substrate such that the lipid membrane planes are roughly parallel to the substrate surface. This imparts a one-dimensional order to these samples; while the z-axis for each membrane (collinear with the membrane normal) is roughly parallel to the substrate normal, the x- and y-axes remain disordered. Exploiting the plane-polarized nature of synchrotron radiation, spectra can be collected at different angles between the substrate normal and the X-ray E vector (Fig. 28.3a). The dichroism, which is the dependence of the intensity of the absorber–backscatterer pair present in the oriented samples as a function of the polarization of the X-rays, is reflected in, and can be extracted from, the resulting X-ray absorption spectra [11–13]. The EXAFS of the oriented PS II samples exhibits distinct dichroism, from which one can deduce the relative

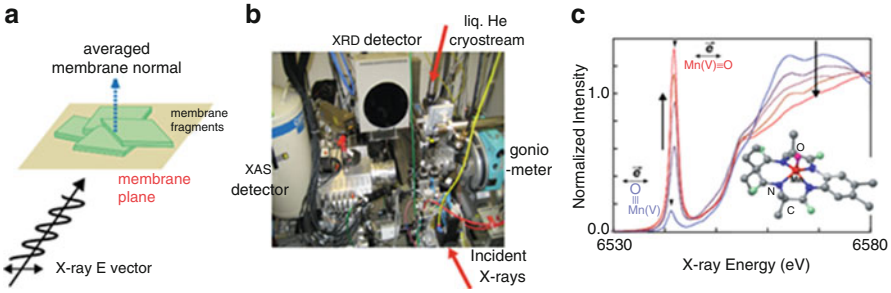

Fig. 28.3 (**a**) Experimental setup for single crystal X-ray absorption spectroscopy at the BL9-3 in SSRL. (**b**) Schematic picture of the polarized XAS data collection from 1D oriented membrane fragments. (**c**) Single crystal XAS of a Mn(V) inorganic complex, showing the pronounced dichroism of the XANES spectrum [11]

orientations of several interatomic vector directions relative to the membrane normal and derive a topological representation of the metal sites in the OEC [14].

Further refinement can be performed for samples with three-dimensional order. Figure 28.3b shows the experimental setup for collecting single crystal XAS data at the Stanford Synchrotron Radiation Lightsource, BL 9-3. It consists of a kappa goniometer, a 30-element Ge detector for collecting XAS data, and a 2D detector placed behind the sample for in situ collection of diffraction data to determine the crystal orientation. The crystals are cooled using a liquid He cryostream to minimize the radiation-induced changes of the sample. Single-crystal X-ray spectroscopy has been performed on model complexes [15] and metalloproteins [16–19]. These studies have been able to significantly expand the XAS information available for these systems over what is gleaned from studies of isotropic samples.

An example of polarized XANES spectra from a Mn(V) model complex is shown in Fig. 28.3c [11]. In this study, the orientationally resolved pre-edge peaks were correlated to DFT calculations, and the results were used for assigning the 1s to 3d transition components. The method was also applied to PSII in the dark state prior to the determination of high-resolution X-ray crystal structure, and the study improved the resolution and orientation of the metal–metal distances in EXAFS [17].

28.4.2 Range-Extended EXAFS

In the typical EXAFS measurement of biological samples, spectra are taken up to ~ 500 eV above the K-absorption edge, that provides a k-range of ~12.0 /Å. However, longer the *k*-range, the EXAFS distance resolution improves and it becomes important for some systems to resolve distance heterogeneity with similar

metal–ligand and metal–metal interactions. The distance resolution in a typical EXAFS experiment is given by

$$\Delta R = \pi / 2k_{\max} \tag{28.1}$$

where $k_{\max}$ is the maximum energy of the photoelectron of the absorber element.

Getting larger $k_{\max}$ is not always possible, in particular, for systems which contain adjacent elements in the periodic table due to the presence of the rising edge of the next element. In principle, solid-state detectors can be used for discriminating fluorescence signals from different elements, by electronically windowing the Kα fluorescence from the absorber atom and collecting XAS data as an excitation spectrum. However, the energy resolution of the detector at the transition metal absorption edges is about 150–200 eV (fwhm), and this makes it difficult to discriminate signals from adjacent transition metals. For the Mn K-edge EXAFS studies of PS II, for example, the absorption edge of the obligatory Fe in PS II (2-3Fe/PS II) limits the EXAFS energy range (Fig. 28.4). The use of a high-resolution crystal monochromator provides a method to selectively separate the fluorescence signals from adjacent metals, resulting in the collection of data to higher photoelectron energies and leading to increased distance resolution and more precise determination in the numbers of metal–metal vectors.

28.4.3 X-Ray Emission Spectroscopy

A complementary technique to XAS is XES. The photons that are emitted after the creation of a core hole in the 1s shell form the K emission spectrum. Among such emission processes, Kα lines originate from 2p to 1s transitions and Kβ lines from the 3p to 1s transitions ($K\beta_{1,3}/K\beta'$) and valence level to 1s transitions ($K\beta_{2,5}/K\beta''$)

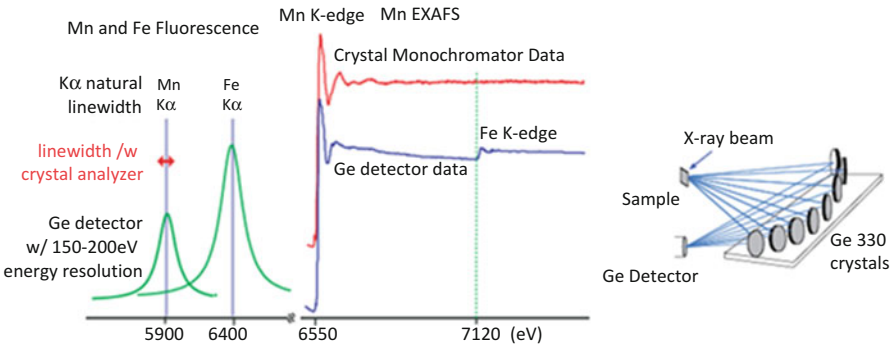

Fig. 28.4 (*left*) X-ray fluorescence of Mn and Fe. The multi-crystal monochromator with 1 eV resolution is tuned to the Mn $K\alpha_1$ peak. (*middle*) Traditional XAFS spectrum (*blue*) and using a crystal monochromator (*red*) (note the absence of Fe contribution). (*right*) The schematic for the crystal monochromator used in a backscattering configuration [14]

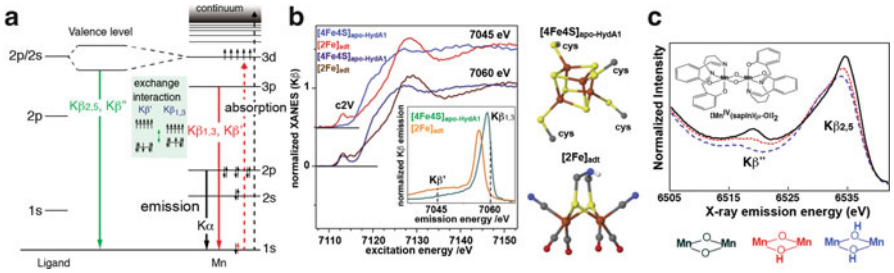

Fig. 28.5 (**a**) Energy level diagram showing the excitation and emission processes for the Kα, $K\beta_{1,3}$/Kβ′ and the $K\beta_{2,5}$/Kβ″ transitions. (**b**) Kβ-detected XAS of apo-HydA1 protein binding only the [4Fe4S] unit of the H-cluster and of a synthetic [2Fe] model complex. The *inset* shows the Kβ XES, and two detection energy for the XAS (7045 and 7060 eV) are shown as *dotted lines* in the *inset*. The figure was adapted from Ref. [20]. (**c**) The valence to core $K\beta_{2,5}$/Kβ″ emission spectra of a series of dinuclear Mn^{IV} complexes, where the bridging oxygen was protonated sequentially [21]

(Fig. 28.5a). These spectra change depending on the chemical environment of the metals of interest. In particular, Kβ spectra have been used in biological systems for probing the oxidation states and identifying the ligand environment.

$K\beta_{1,3}$/Kβ′ spectra arise predominantly from the exchange interaction between the metal 3p and the net electron spin in the metal valence shell, i.e., the effective number of unpaired metal 3d electrons. Therefore, the spectrum is sensitive to the spin state of the metals, which indirectly reflects the oxidation state and covalency of the metal site, and has often been used for determining the oxidation states of metal catalytic sites [6]. $K\beta_{1,3}$ arises from the constructive spin interactions, while Kβ′ from destructive spin interactions.

The sensitivity of the $K\beta_{1,3}$/Kβ′ spectra to the number of unpaired 3d electrons has the potential for being used for probing different metal sites in multinuclear clusters. As mentioned in Section II, there is no "silent" state in XAS. This can be a limiting factor for studying the system that contains several of the same element. For uniquely probing one particular reaction site, the use of different K-emission signals could become useful. One example is the [FeFe]-hydrogenases that contain 6 Fe in the metal catalytic center (H-cluster). Haumann et al. studied the H-cluster with site-selective XAS method, by using the $K\beta_{1,3}$ and Kβ′ signals to distinguish between the low and high spin Fe sites in the two subcomplexes (Fig. 28.5b) [20]. By using a high-resolution spectrometer, in one case the Kβ-detected XAS was collected at the Kβ′ energy and in the other case at the $K\beta_{1,3}$ energy; the former one represents the 2Fe site, while the latter one represents the 4Fe4S site. Thus the response of the two sites in different chemical states can be separately analyzed.

The higher energy emission peaks above $K\beta_{1,3}$ originate from valence-to-core transitions just below the Fermi level and can be separated into Kβ″ and the $K\beta_{2,5}$ emission (Fig. 28.5a). $K\beta_{2,5}$ emission is predominantly from ligand 2p (metal 4p) to metal 1s, and the Kβ″ emission is assigned to a ligand 2s to metal 1s; both are referred to as cross-over transitions [6]. Therefore, only direct ligands to the metal of interest are probed with $K\beta_{2,5}$/Kβ″ emission, i.e., other C, N, and O atoms in the

protein media do not contribute to the spectra. In particular, the energy of the Kβ″ transition depends on the difference between the metal 1s and ligand 2s binding energies, which reflects the environment of the ligand owing to orbital hybridization.

Detecting the chemical states of ligands is important for understanding the reaction mechanism of numerous metalloenzymes. In particular, protonation/deprotonation states of ligands moderate reaction chemistry in metal centers in biologically important processes. For example, copper oxo/hydroxo/peroxo complexes play vital roles in respiration, such as in hemocyanin [22], in biological metabolic pathways such as catechol oxidase activity or activation of aliphatic C-H bonds by dopamine β-monooxygenase [23], peptidyl-glycine α-amidating enzyme, and particulate methane monooxygenase [24]. It is also known that FeFe clusters in methane monooxygenase catalyze the hydroxylation of methane to methanol [25]. Understanding these events requires techniques that are sensitive enough to differentiate species that differ only by a single proton. Fig. 28.5c shows how the $K\beta_{2,5}$ and Kβ″ spectra change depending on the protonation state of the bridging oxygen ligands of the metal cluster [21]. Several techniques have the potential to detect such a single protonation event, that includes vibrational spectroscopy and ligand sensitive EPR techniques such as ENDOR (electron nuclear double resonance), ESEEM (electron spin echo envelope modulation), and HYSCORE (hyperfine sub-level correlation). The advantage of X-ray-based methods over EPR techniques is their element specificity and that they are unrestricted by the spin states of the compounds.

The $K\beta_{2,5}$ and Kβ″ XES was also applied for the study of nitrogenase to identify the central atom of the FeMoco cluster [26], using the element sensitivity of the Kβ″ peak position. A combination of the detailed data analysis and the theoretical calculations revealed that the central atom is a carbon.

28.4.4 Resonant Inelastic X-Ray Scattering Spectroscopy

The pre-edge region of metal K-edge XAS, that corresponds to the 1s to 3d transition, is a probe of metal oxidation state and local geometry of metal catalytic centers. However, the K pre-edge spectra are usually weak compared to the K-main edge, as they mostly arise from quadrupole transition matrix elements. In addition, it suffers from a strong background from the dipole-allowed transition of the main edge, particularly for early transition metals. Transition metal L-edge XAS are in some ways a superior chemical probe to K-edge spectra as (1) $2p \rightarrow 3d$ transitions are allowed under dipole selection rules, while only $s \rightarrow p$ transitions are allowed at the K-edge, (2) greater sensitivity to the occupancy of the 3d orbitals of metal provides a better indication of the oxidation states and symmetry of the complex involved. It is therefore anticipated that examination of the L-edge region will provide oxidation state information of the metal centers with significantly better resolution than that from K-edges. However, the disadvantage is that the energy of

these transitions requires the use of soft X-rays for direct excitation, leading to drastically increased radiation damage compared to high energy hard X-rays (100 times higher) and only surface absorption for bulk samples. These issues make soft X-ray (metal L-edge) spectroscopy less applicable to biological systems.

The above-described problems can be overcome in 1s2p RIXS (resonant inelastic X-ray scattering spectroscopy. In this method, hard X-rays tuned to the energy of the K pre-edge are used to excite a 1s electron into an unoccupied valence orbital (1s to 3d transition), and the emission due to decay of a 3p or 2p electron into the 1s shell is measured as a function of the excitation energy. In experiments, the incident energy is varied across the metal K-edge (1s to 3d) using hard X-rays, and the crystal analyzer is scanned over the Kα emission energy (2p to 1s). The energy difference between excitation and emission corresponds to the energy difference between 2p or 3p and 3d orbitals and, therefore, one can get L-edge-like XAS spectrum while taking advantage of using hard X-rays (high-excitation energy and therefore the high X-ray penetration depth and larger attenuation length) to probe these transitions indirectly. In addition, the RIXS 2D plot also makes the background separation of the pre-edge structure from the main K-edge feature easier.

As an example, the Fe site of the cytochrome c (cyt c) and its model compound was studied by Fe 1s2d RIXS [27]. The RIXS study was used to quantify the highly covalent nature of the porphyrin environment in the heme cofactor, through the analysis of the L-edge XAS-like data from RIXS, and showed the increased covalency for the Fe-S(Met) relative to Fe-N(His) axial ligand and a higher degree of covalency for the ferric states relative to the ferrous states. Namely, it suggests that the bond strengths for the Fe(II) and Fe(III) states are a critical factor for the enzymatic function.

28.5 Application of XFELs for the Study of Metalloenzymes Using X-Ray Spectroscopy

X-ray based techniques, such as X-ray spectroscopy, X-ray crystallography, as well as X-ray scattering methods, have contributed significantly to the structural and functional studies of metalloenzymes in the last decades, and have become indispensable methods. However, to minimize or eliminate radiation-induced changes during data collection has remained challenging. As described in Section II, the data collection of biological samples is usually carried out at cryogenic temperature to minimize the X-ray induced effect. However, there is an increasing effort to understand biological phenomena as the enzymes function, through studies under physiological/functional conditions. Additionally, the need to probe rare transitions, which often are superior probes of chemical states but require very high photon fluxes, , within a reasonable time, is another issue.

The recent advent of XFELs [28, 29] brought the possibility of probing labile biological systems with high dose X-rays, by outrunning the radiation damage

processes and extracting the information before manifestation of the X-ray-induced changes to the sample using fs X-ray pulses. XFELs produce high intensity X-ray pulses in the fs time regime. In practice the number of photons in a single <50 fs pulse is comparable to the number of photons available per second in a modern third generation synchrotron end station. In addition to serial femtosecond crystallography (e.g., Ref. [30]), X-ray spectroscopic techniques have been applied for the study of metalloenzymes at the XFELs, and have shown promise. Both XAS and XES methods are currently targeted at XFEL sources.

The hard X-ray XES method has a few advantages, when it is applied at the XFELs. No monochromatization is necessary and the full SASE (self-amplified spontaneous emission) bandwidth of the XFEL pulse can be used in the shot-by-shot data collection [31–33]. Kβ XES on dilute solution samples was initially demonstrated for Mn compounds [31], showing that the fs pulses used did not disturb the electronic structure of the compounds studied (Mn^{II} and $Mn^{III,IV}$). For iron(II) tris(2,2′-bipyridine) it was also possible to record time resolved XES at 50 fs to 1 ps after a laser excitation and resolve the kinetics of the light-induced spin change using 50 mM concentration in a 100 μm thick liquid jet. An XAS method was also used at XFELs for pump-probe measurements [34], providing unique insights into the evolution of the electronic structure over the reaction cycle. In addition to hard X-ray spectroscopy, XFELs provide a new opportunity to carry out biological soft X-ray spectroscopy [35] by overcoming severe radiation damage due to the high absorption cross section at the soft X-ray energy range, that has been an issue in the synchrotron X-ray sources.

Among the several X-ray spectroscopic methods, XES is well suited to be combined with other techniques. For example, XES can be collected simultaneously with X-ray crystallography by choosing the same excitation energy (Fig. 28.6). Such a method was developed and used for studying the water oxidation reaction in PS II with microcrystals [36]. In this approach, XES provides a diagnostic capability by providing the electronic structure of the highly radiation sensitive Mn_4CaO_5 cluster in PS II. Furthermore, it serves for monitoring the catalytic turn over under the experimental conditions.

28.6 Future Direction

X-ray spectroscopy, together with X-ray crystallography, has been an extremely important method for understanding the mechanism of metal catalytic reactions in metalloenzymes. The development of theoretical approaches, like density functional theory (DFT), with well-characterized model inorganic complexes has provided the necessary information for interpreting spectroscopic data. Furthermore, the recent development of bright synchrotron X-ray sources and the X-ray free electron laser further opens new horizons for data collection from biological samples under physiological conditions in a time-resolved manner. These developments altogether will provide tools for us to understand the mechanism of catalytic

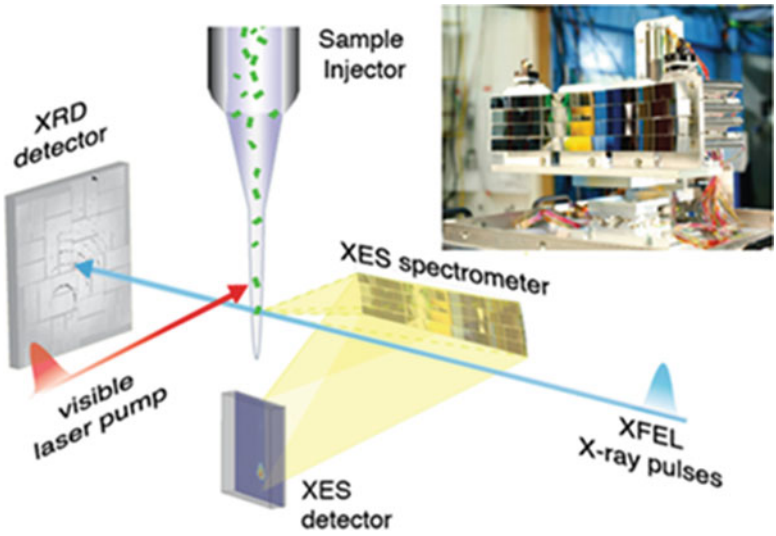

Fig. 28.6 Setup for simultaneous XES/XRD at the LCLS XFEL. The XES spectrometer is mounted at 90° to the fs X-ray pulses and the XRD is recorded in forward scattering. The sample is introduced into the interaction region using a jet as shown here, but other methods can also be used. The energy dispersive XES spectrometer is shown at *top right*. Illumination of the samples is achieved by visible laser pumps and are used for time resolved optical pump X-ray probe measurements [36]

reaction paths in metalloenzymes and the important information of how to control electron/proton flow and product/substrate transport, spatially and temporally, during catalysis using the protein framework.

References

1. Ogata H, Nishikawa K, Lubitz W (2015) Hydrogens detected by subatomic resolution protein crystallography in a [NiFe] hydrogenase. Nature 520:571
2. Kaiser JT, Hu Y, Wiig JA, Rees DC, Ribbe MW (2011) Structure of precursor-bound NifEN: a nitrogenase femo cofactor maturase/insertase. Science 331:91
3. Suga M, Akita F, Hirata K, Ueno G, Murakami H, Nakajima Y, Shimizu T, Yamashita K, Yamamoto M, Ago H, Shen J-R (2015) Native structure of photosystem II at 1.95 Å resolution viewed by femtosecond X-ray pulses. Nature 517:99
4. Tsukihara T, Aoyama H, Yamashita E, Tomizaki T, Yamaguchi H, Shinzawa-Itoh K, Nakashima R, Yaono R, Yoshikawa S (1995) Structures of metal sites of oxidized bovine heart cytochrome c oxidase at 2.8 Å. Science 269:1069
5. Tzakos AG, Grace CRR, Lukavsky PJ, Riek R (2006) NMR techniques for very large proteins and RNAs in solution. Annu Rev Biophys Biomol Struct 35:319
6. Glatzel P, Bergmann U (2005) High resolution 1s core hole X-ray spectroscopy in 3d transition metal complexes - electronic and structural information. Coord Chem Rev 249:65

7. Yano J, Kern J, Irrgang K-D, Latimer MJ, Bergmann U, Glatzel P, Pushkar Y, Biesiadka J, Loll B, Sauer K, Messinger J, Zouni A, Yachandra VK (2005) X-ray damage to the Mn4Ca complex in single crystals of photosystem II: a case study for metalloprotein crystallography. Proc Natl Acad Sci U S A 102:12047
8. Corbett MC, Latimer MJ, Poulos TL, Sevrioukova IF, Hodgson KO, Hedman B (2007) Photoreduction of the active site of the metalloprotein putidaredoxin by synchrotron radiation. Acta Cryst 63:951
9. Meharenna YT, Doukov T, Li HY, Soltis SM, Poulos TL (2010) Crystallographic and single-crystal spectral analysis of the peroxidase ferryl intermediate. Biochemistry 49:2984
10. Sigfridsson KGV, Chernev P, Leidel N, Popović-Bijelić A, Gräslund A, Haumann M (2013) Rapid X-ray photoreduction of dimetal-oxygen cofactors in ribonucleotide reductase. J Biol Chem 288:9648
11. Yano J, Robblee J, Pushkar Y, Marcus MAM, Bendix J, Workman JM, Collins TJ, Solomon EI, George SD, Yachandra VK (2007) Polarized X-ray absorption spectroscopy of single-crystal Mn(V) complexes relevant to the oxygen-evolving complex of photosystem II. J Am Chem Soc 129:12989
12. George GN, Prince RC, Frey TG, Cramer SP (1989) Oriented X-ray absorption-spectroscopy of membrane-bound metalloproteins. Physica B 158:81
13. George GN, Cramer SP, Frey TG, Prince RC (1993) X-ray-absorption spectroscopy of oriented cytochrome-oxidase. Biochim Biophys Acta 1142:240
14. Pushkar Y, Yano J, Glatzel P, Messinger J, Lewis A, Sauer K, Bergmann U, Yachandra VK (2007) Structure and orientation of the Mn Ca cluster in plant photosystem II membranes studied by polarized range-extended X-ray absorption spectroscopy. J Biol Chem 282:7198
15. Pickering IJ, George GN (1995) Polarized X-ray-absorption spectroscopy of cupric chloride dihydrate. Inorg Chem 34:3142
16. Flank AM, Weininger M, Mortenson LE, Cramer SP (1986) Single-crystal EXAFS of nitrogenase. J Am Chem Soc 108:1049
17. Yano J, Kern J, Sauer K, Latimer M, Pushkar Y, Biesiadka J, Loll B, Saenger W, Messinger J, Zouni A, Yachandra VK (2006) Where water is oxidized to dioxygen: structure of the photosynthetic Mn Ca cluster. Science 314:821
18. George GN, Hilton J, Temple C, Prince RC, Rajagopalan KV (1999) Structure of the molybdenum site of dimethyl sulfoxide reductase. J Am Chem Soc 121:1256
19. Scott RA, Hahn JE, Doniach S, Freeman HC, Hodgson KO (1982) Polarized X-ray absorption-spectra of oriented plastocyanin single-crystals - investigation of methionine copper coordination. J Am Chem Soc 104:5364
20. Chernev P, Lambertz C, Brunje A, Leidel N, Sigfridsson KG, Kositzki R, Hsieh CH, Yao S, Schiwon R, Driess M, Limberg C, Happe T, Haumann M (2014) Hydride binding to the active site of [FeFe]-hydrogenase. Inorg Chem 53:12164
21. Lassalle-Kaiser B, Boron TT 3rd, Krewald V, Kern J, Beckwith MA, Delgado-Jaime MU, Schroeder H, Alonso-Mori R, Nordlund D, Weng TC, Sokaras D, Neese F, Bergmann U, Yachandra VK, DeBeer S, Pecoraro VL, Yano J (2013) Experimental and computational X-ray emission spectroscopy as a direct probe of protonation states in Oxo-bridged Mn dimers relevant to redox-active metalloproteins. Inorg Chem 52:12915
22. Magnus KA, Tonthat H, Carpenter JE (1994) Recent structural work on the oxygen-transport protein hemocyanin. Chem Rev 94:727
23. Klinman J (2006) The copper-enzyme family of dopamine β -monooxygenase and peptidylglycine α-hydroxylating monooxygenase: resolving the chemical pathway for substrate hydroxylation. J Biol Chem 281:3013
24. Himes RA, Karlin KD (2009) Copper-dioxygen complex mediated C-H bond oxygenation: relevance for particulate methane monooxygenase (pMMO). Curr Opin Chem Biol 13:119
25. Kryatov SV, Taktak S, Korendovych IV, Rybak-Akimova EV, Kaizer J, Torelli S, Shan XP, Mandal S, MacMurdo VL, Payeras AMI, Que L (2005) Dioxygen binding to complexes with

Fe (μ-OH) cores: steric control of activation barriers and O -adduct formation. Inorg Chem 44:85
26. Lancaster KM, Roemelt M, Ettenhuber P, Hu Y, Ribbe MW, Neese F, Bergmann U, DeBeer S (2011) X-ray emission spectroscopy evidences a central carbon in the nitrogenase iron-molybdenum cofactor. Science 334:974
27. Kroll T, Hadt RG, Wilson SA, Lundberg M, Yan JJ, Weng TC, Sokaras D, Alonso-Mori R, Casa D, Upton MH, Hedman B, Hodgson KO, Solomon EI (2014) Resonant inelastic X-ray scattering on ferrous and ferric bis-imidazole porphyrin and cytochrome c: nature and role of the axial Methionine-Fe bond. J Am Chem Soc 136:18087
28. Emma P, Akre R, Arthur J, Bionta R, Bostedt C, Bozek J, Brachmann A, Bucksbaum P, Coffee R, Decker FJ, Ding Y, Dowell D, Edstrom S, Fisher A, Frisch J, Gilevich S, Hastings J, Hays G, Hering P, Huang Z, Iverson R, Loos H, Messerschmidt M, Miahnahri A, Moeller S, Nuhn HD, Pile G, Ratner D, Rzepiela J, Schultz D, Smith T, Stefan P, Tompkins H, Turner J, Welch J, White W, Wu J, Yocky G, Galayda J (2010) First lasing and operation of an Å-wavelength free-electron laser. Nat Photonics 4:641
29. Ishikawa T, Aoyagi H, Asaka T, Asano Y, Azumi N, Bizen T, Ego H, Fukami K, Fukui T, Furukawa Y, Goto S, Hanaki H, Hara T, Hasegawa T, Hatsui T, Higashiya A, Hirono T, Hosoda N, Ishii M, Inagaki T, Inubushi Y, Itoga T, Joti Y, Kago M, Kameshima T, Kimura H, Kirihara Y, Kiyomichi A, Kobayashi T, Kondo C, Kudo T, Maesaka H, Marechal XM, Masuda T, Matsubara S, Matsumoto T, Matsushita T, Matsui S, Nagasono M, Nariyama N, Ohashi H, Ohata T, Ohshima T, Ono S, Otake Y, Saji C, Sakurai T, Sato T, Sawada K, Seike T, Shirasawa K, Sugimoto T, Suzuki S, Takahashi S, Takebe H, Takeshita K, Tamasaku K, Tanaka H, Tanaka R, Tanaka T, Togashi T, Togawa K, Tokuhisa A, Tomizawa H, Tono K, Wu SK, Yabashi M, Yamaga M, Yamashita A, Yanagida K, Zhang C, Shintake T, Kitamura H, Kumagai N (2012) A compact X-ray free-electron laser emitting in the sub-Å region. NatPhotonics 6:540
30. Chapman HN, Fromme P, Barty A, White TA, Kirian RA, Aquila A, Hunter MS, Schulz J, DePonte DP, Weierstall U, Doak RB, Maia FRNC, Martin AV, Schlichting I, Lomb L, Coppola N, Shoeman RL, Epp SW, Hartmann R, Rolles D, Rudenko A, Foucar L, Kimmel N, Weidenspointner G, Holl P, Liang MN, Barthelmess M, Caleman C, Boutet S, Bogan MJ, Krzywinski J, Bostedt C, Bajt S, Gumprecht L, Rudek B, Erk B, Schmidt C, Homke A, Reich C, Pietschner D, Struder L, Hauser G, Gorke H, Ullrich J, Herrmann S, Schaller G, Schopper F, Soltau H, Kuhnel KU, Messerschmidt M, Bozek JD, Hau-Riege SP, Frank M, Hampton CY, Sierra RG, Starodub D, Williams GJ, Hajdu J, Timneanu N, Seibert MM, Andreasson J, Rocker A, Jonsson O, Svenda M, Stern S, Nass K, Andritschke R, Schroter CD, Krasniqi F, Bott M, Schmidt KE, Wang XY, Grotjohann I, Holton JM, Barends TRM, Neutze R, Marchesini S, Fromme R, Schorb S, Rupp D, Adolph M, Gorkhover T, Andersson I, Hirsemann H, Potdevin G, Graafsma H, Nilsson B, Spence JCH (2011) Femtosecond X-ray protein nanocrystallography. Nature 470:73
31. Alonso-Mori R, Kern J, Gildea RJ, Sokaras D, Weng TC, Lassalle-Kaiser B, Tran R, Hattne J, Laksmono H, Hellmich J, Glockner C, Echols N, Sierra RG, Schafer DW, Sellberg J, Kenney C, Herbst R, Pines J, Hart P, Herrmann S, Grosse-Kunstleve RW, Latimer MJ, Fry AR, Messerschmidt MM, Miahnahri A, Seibert MM, Zwart PH, White WE, Adams PD, Bogan MJ, Boutet S, Williams GJ, Zouni A, Messinger J, Glatzel P, Sauter NK, Yachandra VK, Yano J, Bergmann U (2012) Energy-dispersive X-ray emission spectroscopy using an X-ray free-electron laser in a shot-by-shot mode. Proc Natl Acad Sci U S A 109:19103
32. Zhang WK, Alonso-Mori R, Bergmann U, Bressler C, Chollet M, Galler A, Gawelda W, Hadt RG, Hartsock RW, Kroll T, Kjaer KS, Kubicek K, Lemke HT, Liang HYW, Meyer DA, Nielsen MM, Purser C, Robinson JS, Solomon EI, Sun Z, Sokaras D, van Driel TB, Vanko G, Weng TC, Zhu DL, Gaffney K (2014) Tracking excited-state charge and spin dynamics in iron coordination complexes. J Nature 509:345

33. Bertoni R, Cammarata M, Lorenc M, Matar SF, Letard JF, Lemke HT, Collet E (2015) Ultrafast light-induced spin-state trapping photophysics investigated in Fe(phen) (NCS) spin-crossover crystal. Acc Chem Res 48:774
34. Lemke HT, Bressler C, Chen LX, Fritz DM, Gaffney KJ, Galler A, Gawelda W, Haldrup K, Hartsock RW, Ihee H, Kim J, Kim KH, Lee JH, Nielsen MM, Stickrath AB, Zhang WK, Zhu DL, Cammarata M (2013) Femtosecond X-ray absorption spectroscopy at a hard X-ray free electron laser: application to spin crossover dynamics. J Phys Chem A 117:735
35. Mitzner R, Rehanek J, Kern J, Gul S, Hattne J, Taguchi T, Alonso-Mori R, Tran R, Weniger C, Schroder H, Quevedo W, Laksmono H, Sierra RG, Han G, Lassalle-Kaiser B, Koroidov S, Kubicek K, Schreck S, Kunnus K, Brzhezinskaya M, Firsov A, Minitti MP, Turner JJ, Moeller S, Sauter NK, Bogan MJ, Nordlund D, Schlotter WF, Messinger J, Borovik A, Techert S, de Groot FM, Fohlisch A, Erko A, Bergmann U, Yachandra VK, Wernet P, Yano J (2013) L-edge X-ray absorption spectroscopy of dilute systems relevant to metalloproteins using an X-ray free-electron laser. J Phys Chem Lett 4:3641
36. Kern J, Alonso-Mori R, Tran R, Hattne J, Gildea RJ, Echols N, Glockner C, Hellmich J, Laksmono H, Sierra RG, Lassalle-Kaiser B, Koroidov S, Lampe A, Han G, Gul S, Difiore D, Milathianaki D, Fry AR, Miahnahri A, Schafer DW, Messerschmidt M, Seibert MM, Koglin JE, Sokaras D, Weng TC, Sellberg J, Latimer MJ, Grosse-Kunstleve RW, Zwart PH, White WE, Glatzel P, Adams PD, Bogan MJ, Williams GJ, Boutet S, Messinger J, Zouni A, Sauter NK, Yachandra VK, Bergmann U, Yano J (2013) Simultaneous femtosecond X-ray spectroscopy and diffraction of photosystem II at room temperature. Science 340:491

Chapter 29
Green Catalysts

Adam F. Lee

29.1 Introduction

Chemoselectivity is a cornerstone of catalysis, permitting the targeted modification of specific functional groups within complex starting materials [1–5]. This ability to activate and transform only certain chemical functionalities without the use of protecting groups, and attendant improvements in atom efficiency (and waste minimisation), also underpins catalysis' green credentials [6, 7].

29.2 Selective Alcohol Oxidation

Selective alcohol oxidation (selox) represents an elegant class of atom-efficient molecular transformations for chemical valorisation catalysed by noble metals [8, 9]. The resultant aldehyde, ketone, ester and acid products are valuable intermediates for the fine chemical, pharmaceutical and agrochemical sectors, with allylic aldehydes in particular high-value components used in the perfume and flavourings industries [10]. For example, crotonaldehyde is an important agrochemical [11] and valuable precursor to the food preservative sorbic acid, while citronellyl acetate and cinnamaldehyde confer rose/fruity and cinnamon flavours and aromas, respectively with the latter a precursor to the artificial sweetener aspartame [12, 13]. The commercial synthesis of such higher oxygenates traditionally proceeded via oxidation of their alcohol analogues by toxic or hazardous stoichiometric oxidants such as chromate and permanganate salts; however, platinum group metals (PGMs), notably platinum, palladium and ruthenium, alongside

A.F. Lee (✉)
European Bioenergy Research Institute, Aston University, Birmingham B4 7ET, UK
e-mail: A.F.Lee@aston.ac.uk

Y. Iwasawa et al. (eds.), *XAFS Techniques for Catalysts, Nanomaterials, and Surfaces*, DOI 10.1007/978-3-319-43866-5_29

gold, have proven versatile heterogeneous and homogeneous catalysts for such oxidations, often employing oxygen or air as the oxidant. Recent efforts to improve the activity, selectivity and commercial implementation of heterogeneous transition metal selox catalysts have driven research into the nature of the active site, oxidation/deactivation mechanism, and the formulation of bimetallic variants, to which X-ray absorption (XAS) studies have made an invaluable contribution [12].

29.2.1 Monometallic Selox Catalysts

Quick and dispersive XAS have the capability to monitor dynamic changes in catalyst structure under reaction conditions ("operando" spectroscopy) and have been applied to alcohol selox over Pd [13–17], Pt [18, 19] and Ru [18] nanoparticles. Operando XAS measurements by Grunwaldt et al. on palladium catalysed selox [16], which mirrored an earlier original report by Lee [13], evidenced in situ reduction of oxidised palladium in a Pd/Al_2O_3 catalyst during cinnamyl alcohol oxidation within a continuous flow fixed-bed reactor, and consequently proposed a reaction mechanism in which metallic palladium was proposed the active species for benzyl alcohol selox (Scheme 29.1) [20]. Unfortunately, kinetics of cinnamyl alcohol selox were not measured in parallel with XAS to explore the impact of this palladium reduction on catalysis; however, a follow-up study of 1-phenylethanol selox employing the same reactor configuration (and oxygen-deficient conditions) demonstrated strong interplay between selox conversion/selectivity and Pd oxidation state [21]. The authors concluded that metallic Pd was the catalytically active species, an assertion re-affirmed in follow-up in situ ATR-IR/XAS measurements of benzyl [20] and cinnamyl alcohol [18] selox respectively in toluene and under supercritical CO_2.

It is interesting to note that in each of these studies the introduction of oxygen to the reactant feed improved alcohol conversion and aldehyde production, observations which the authors interpreted as due to hydrogen abstraction from the catalyst surface rather than a more plausible change in palladium oxidation state. In contrast to their liquid phase experiments, high pressure X-ray absorption near edge structure (XANES) and extended X-ray absorption fine structure (EXAFS) measurements on Pd/Al_2O_3 catalysed benzyl alcohol selox in supercritical CO_2 led Grunwaldt and Baiker to conclude that maximum activity arose from particles mainly *oxidised* in the surface/shelf-edge [22]. In parallel, Lee and co-workers systematically characterised the physicochemical properties of palladium nanoparticles as a function of size over non-reducible supports and thereby quantified fundamental structure–function relations in allylic alcohol selox [14, 15, 23–28]. The combination of XPS and XAS measurements revealed that freshly prepared carbon [14], alumina [15, 24, 27, 28] and silica [23, 25, 26] supported nanoparticles are prone to oxidation as their diameter falls below ~4 nm, with the fraction of PdO proportional to the support surface area and pore connectivity. Complementary kinetic analyses uncovered a direct correlation between the surface

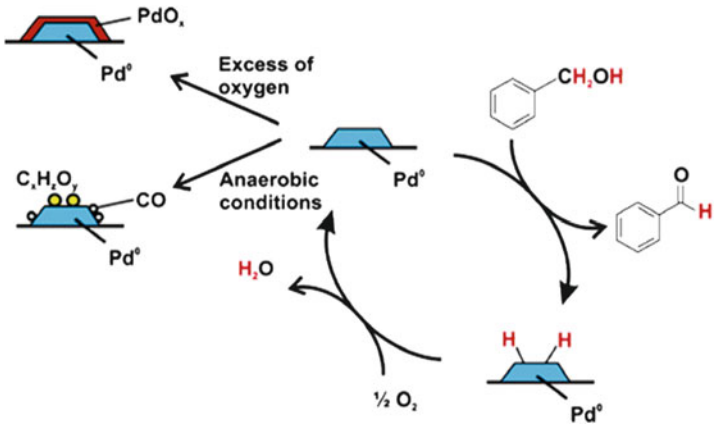

Scheme 29.1 Proposed reaction mechanism for benzyl alcohol selox over commercial Pd/Al_2O_3 catalysts [16]

PdO content and TOFs towards cinnamyl and crotyl alcohol [15, 23, 24]. Operando liquid phase XAS of Pd/C [14] and Pd/Al_2O_3-SBA-15 [27] catalysts during cinnamyl alcohol selox evidenced in situ reduction of PdO (Fig. 29.1); however, by virtue of simultaneously measuring the associated selox kinetics, Lee et al. proved unequivocally that this palladium oxide→metal transition was responsible for catalyst deactivation, the latter consistent with surface science predictions that metallic palladium favours aldehyde decarbonylation and consequent self-poisoning by CO and organic residues [29, 30]. Analogous studies of Pt catalysed alcohol selox confirmed surface PtO_2 as the active phase [31].

The nature of the active phase in alcohol selox catalysed by palladium nanoparticles was conclusively established through subsequent multi-dimensional spectroscopic investigations of vapour phase crotyl alcohol selox [32–34]. Dynamic, synchronous Diffuse Reflectance Infrared Fourier Transform Spectroscopy (DRIFTS)/mass spectrometry (MS)/XAS measurements of oxide supported and colloidal palladium were performed in a environmental cell [35] to simultaneously interrogate adsorbates on the catalyst surface, the mean oxidation state of Pd and concomitant reactivity in the absence of competitive solvent effects [36, 37]. Palladium nanoparticles were partially oxidised at low reaction temperatures, and unaffected by exposure to either alcohol or oxygen (Fig. 29.2). Oxidative hydrogenation to crotonaldehyde was facile over oxide surfaces. Higher reaction temperatures induced PdO reduction in response to crotyl alcohol exposure, mirroring the behaviour observed during liquid phase selox in Fig. 29.2, and could be reversed by subsequent oxygen exposure. Such reactant-induced restructuring was independent of the support type or catalyst synthesis method, but of a magnitude inversely proportional to particle size [34]. These dynamic measurements decoupled the relative reactivity of palladium oxide from metal, revealing that PdO favoured crotyl alcohol selox to crotonaldehyde and crotonic acid, whereas metallic palladium drove

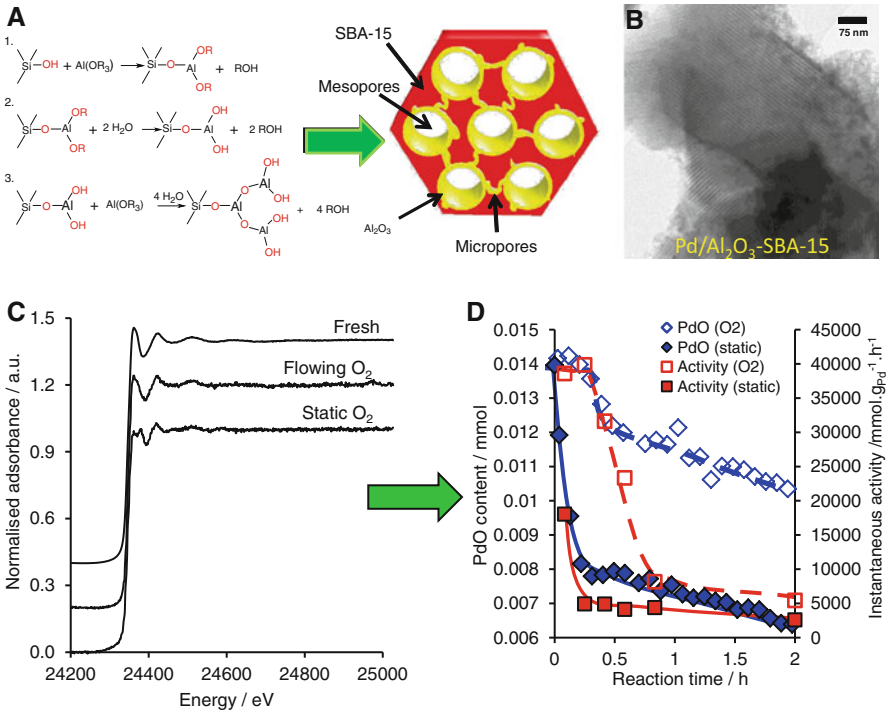

Fig. 29.1 (**a**) Synthesis of conformal alumina monolayers over SBA-15 silica. (**b**) HRTEM of Pd impregnated Al_2O_3-SBA-15 showing highly ordered pore network. (**c**) Operando Pd K-edge XAS of Pd-Al_2O_3-SBA-15 during the liquid phase aerobic selox of cinnamyl alcohol to cinnamaldehyde. (**d**) Correlation between XAS-derived PdO concentration and selox activity under static versus flowing oxygen [27]

secondary decarbonylation to propene and CO in accordance with the surface chemistry of Pd(111) model catalysts [29, 38]. Allylic alcohol selox thus depends upon a delicate balance between maximising the rate of oxidative dehydrogenation without accumulating sufficient surface hydrogen to induce reduction of catalytically active palladium surface oxide. Oxide reducibility has thus emerged as a critical factor in achieving active and selective alcohol selox catalysts.

Supported monomeric Pd complexes have also shown great promise in selox, wherein XAS has proven crucial in elucidating the active species. Mori et al. employed ex situ Pd K-edge XAS to demonstrate that hydroxyapatites treated with $PdCl_2(PhCN)_2$ afforded two types of immobilised complex with distinct coordination spheres dependent upon the Ca/P ratio of the parent hydroxyapatite (Fig. 29.3): [39, 40] a monomeric $PdCl_2$ over stoichiometric $Ca_{10}(PO_4)_6(OH)_2$ which transformed during in situ alcohol selox into 4 nm metallic Pd particles resulting in Turnover Numbers (TONs) up to 236,000; or a monomeric Pd^{II} phosphate complex at Ca-deficient sites in nonstoichiometric hydroxyapatite,

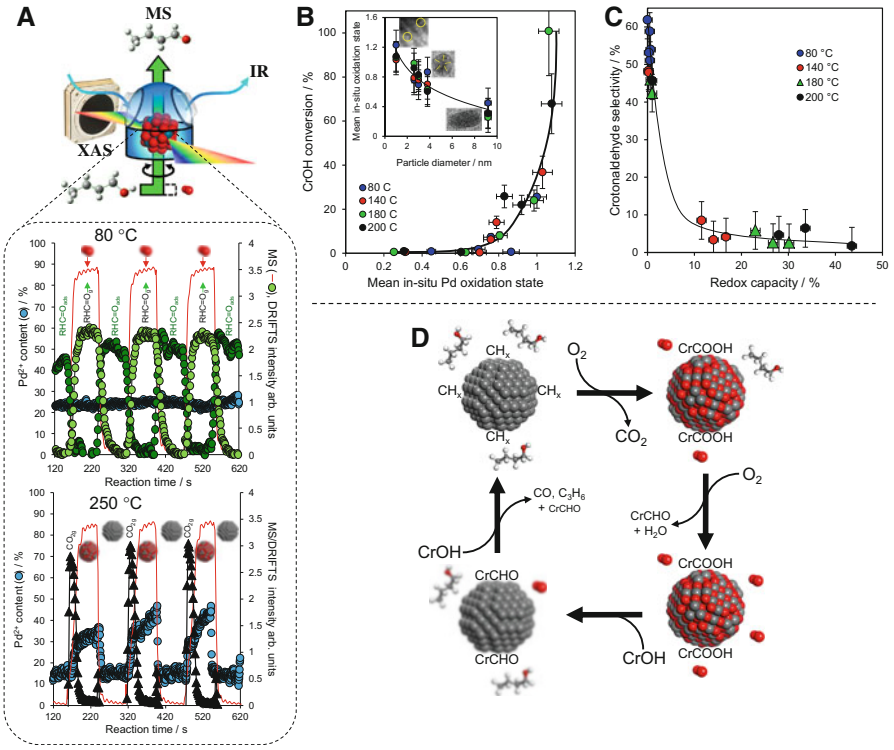

Fig. 29.2 (**a**) Dynamic, synchronous DRIFTS/MS/XAS during exposure of Pd/mesoporous Al_2O_3 catalyst to alternating crotyl alcohol/O_2 feedstreams; low temperature favours alcohol selox whereas higher temperature favours combustion. (**b**) Crotyl alcohol selox is catalysed by electron deficient palladium. (**c**) Selective oxidation to crotonaldehyde is favoured over irreducible palladium oxide. (**d**) Interdependence of Pd oxidation state and crotyl alcohol selox upon reducing or oxidising reactant environment [32, 34]

$Ca_9(HPO_4)(PO_4)_5(OH)$ (which were inactive for selox but active for Heck and Suzuki cross-couplings). Flower-like hydroxyapatite has also been employed to support Pd nanocatalysts exposing high energy (110) facets [41]. In situ XAS under solventless conditions suggest a redox mechanism in which dissociatively adsorbed molecular O_2 oxidises surface Pd atoms, which in turn abstract hydrogen atoms from chemisorbed benzylic and allylic alcohols to form the corresponding carbonyl products, and regenerate surface Pd^0 sites alongside water and oxygen. Co-promoted Ru-hydroxyapatite has also shown promise in the oxidative dehydrogenation of primary and secondary alcohols [42], in EXAFS identified an active dihydroxo-ruthenium species, which was more resistant to in situ reduction by alcohol reactants than palladium catalysts. In this instance selox was proposed to follow a Mars–van Krevelen mechanism in which reduced hydrido-ruthenium species were inactive towards alcohol dehydrogenation and the rate limiting step was either β-hydride elimination from the chemisorbed alcoholate, or reoxidation of the ruthenium-hydride intermediate.

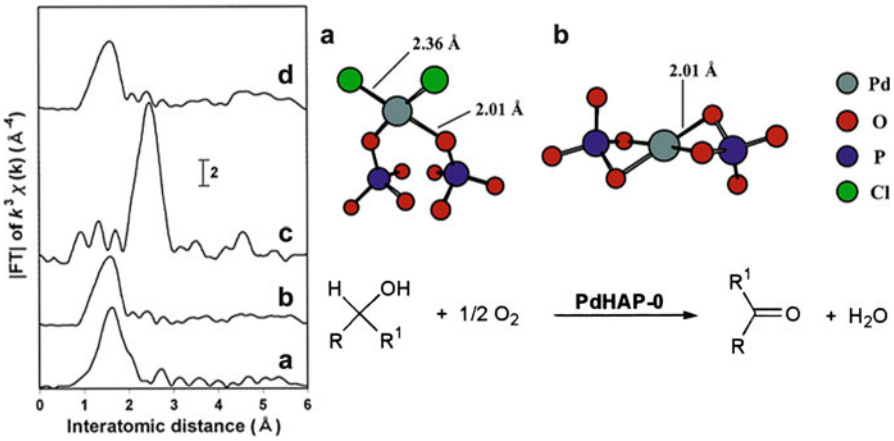

Fig. 29.3 (*left*) Fourier transforms of k^3-weighted Pd K-edge EXAFS for (**a**) PdHAP-0, (**b**) PdHAP-1, (**c**) recovered PdHAP-0, and (**d**) recovered PdHAP-1 for the oxidation of 1-phenylethanol; (*right*) proposed structures of hydroxyapatite immobilised Pd^{II} complexes, wherein (**a**) is an inert precursor to active Pd metal nanoparticles [39, 40]

29.2.2 Bimetallic Selox Catalysts

Bimetallic selox catalysts, in which a relatively inactive metal is combined with a more active component, have demonstrated significant improvements over their monometallic counterparts, with Au, Bi, Pb and Sn [17, 21, 43–45] combinations with PGMs promoting oxidation of challenging substrates such as propylene glycol [46], as well as allylic and benzylic alcohols.

Lee et al. demonstrated the efficacy of titania-supported AuPd bimetallic nanoparticles for liquid phase selective aerobic oxidation of crotyl alcohol to crotonaldehyde [47]. Ex situ EXAFS, in conjunction with powder XRD, XPS and DRIFTS evidenced spatial segregation of the two metal components in the as-synthesised catalysts, consistent with nanoparticles comprising a 5 atomic layer thick Au shell encapsulating a 20 nm Pd cores (Fig. 29.4). In situ annealing to 500 °C induced AuPd alloying, with Au–Au and Pd–Pd bond lengths intermediate between those of the respective pure bulk fcc metal phases, indicative of a homogeneous Pd-rich alloy. Pd surface segregation enhanced both activity and selectivity, with the optimum $Au_{40}Pd_{60}$ surface alloy around 85 % selective to crotonaldehyde.

Complementary research by Scott and co-workers explored the chemical, structural and electronic properties of PVP-stabilised AuPd bimetallic colloidal nanoparticles [48] by Pd K-edge and Au L_{III}-edge EXAFS and XANES for aerobic crotyl alcohol selox. In situ EXAFS of sequentially reduced bimetallic nanoparticles revealed the presence of Pd-enriched surfaces surrounding Au cores, while XANES indicated Pd atoms within the selvedge were electron deficient relative to monometallic Pd or co-reduced AuPd nanoparticles [49]. Sequentially

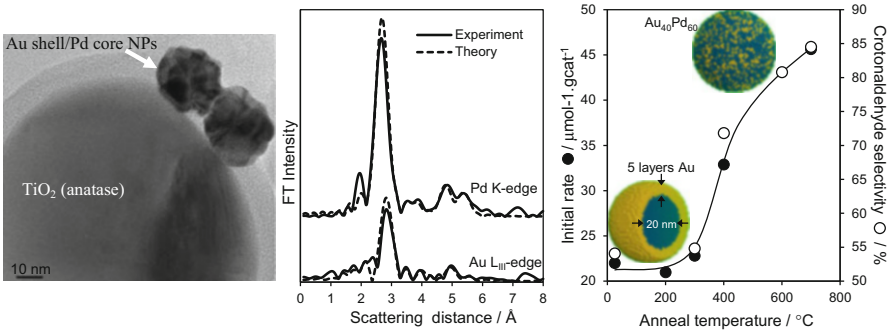

Fig. 29.4 (*left*) HRTEM and (*centre*) Fourier transforms of k^3-weighted Pd K-edge and Au L_{III}-edge EXAFS of as-synthesised Au shell-Pd core nanoparticles dispersed over TiO_2; (*right*) promotion of crotyl alcohol selox upon thermally induced AuPd surface alloying [47]

reduced (Pd rich) surfaces were extremely active for crotyl alcohol oxidation *in the absence of base* (generally considered essential for gold catalysed selox reactions [50, 51]), and exhibited excellent selectivity to crotonaldehyde, superior to co-reduced AuPd analogues wherein an induction period was observed prior to crotonaldehyde formation [52]. Scott proposed two possible selox mechanisms for the sequentially reduced AuPd bimetallic catalyst prepared from a Pd(II) salt in the presence of crotyl alcohol (Fig. 29.5) : one, a redox route in which Pd^{2+} species are stoichiometrically reduced by crotyl alcohol to deposit Pd metal on to preformed Au colloids coincident with crotonaldehyde formation, with reduced Pd surface atoms subsequently re-oxidised into solution by molecular O_2 to establish a catalytic redox pathway; second an entirely heterogeneous pathway in which electron deficient surface Pd atoms extracts a β-hydrogen from adsorbed crotyl alcohol to form crotonaldehyde and Pd-H, with dissociatively adsorbed oxygen serving as a hydride scavenger to produce water. In situ Pd L_{III}-edge XANES showed no evidence for oxidation state changes in the preformed Pd shell/Au core system following introduction of oxygen to the crotyl alcohol reaction mixture [53], suggesting that gold hinders dissolution/oxidation of catalytically active surface palladium atoms, and discounting the redox mechanism.

29.3 Selective Hydrogenation

Catalytic hydrogenation of organic compounds possessing multiple unsaturated bonds such as α,β-unsaturated aldehydes is particularly challenging [54–57], necessitating active sites able to discriminate closely related moieties, and in some instances achieve preferential activation of a more thermodynamically stable function. Noble metals are widely employed in heterogeneous catalytic hydrogenation,

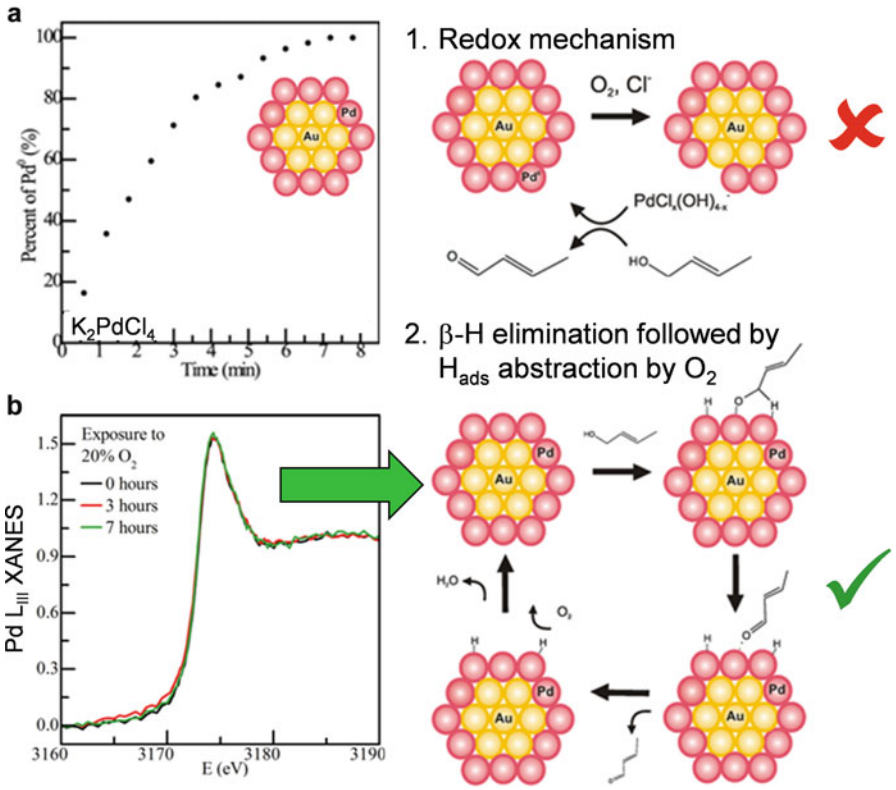

Fig. 29.5 (**a**) Reductive deposition of Pd metal over PVP-stabilised Au nanoparticles in the presence of crotyl alcohol tracked by in situ Pd K-edge XANES. (**b**) Pd L_{III}-edge XANES of in situ synthesised PVP-stabilised AuPd nanoparticles evidencing stable oxidation state during aerobic crotyl alcohol selox and hence reaction mechanism 2 involving purely heterogeneous surface chemistry [48, 53]

able to reduce a plethora of functional groups, including C=C [58], C≡C [59], C=O [60], C≡N [61], NO_2 [62] and aromatics [63] with molecular hydrogen.

The selective hydrogenation of allylic and benzylic aldehydes to unsaturated alcohols (i.e. the reverse chemistry to that described in Sect. 29.2.1) is a commercially important industrial process widely utilised within the flavour and fragrance, agrochemical and pharmaceutical sectors [55, 64]; however, the development of requisite heterogeneous catalysts has been hindered by the thermodynamic stability of C=O relative to C=C bonds and lack of insight into fundamental structure–function relations [55]. Pt L_{III}-edge and Co K-edge XANES and EXAFS studies of Pt-Co nanoparticles supported on sub-bituminous carbon for the liquid-phase hydrogenation of citral reveal strong perturbation of the Pt chemical environment and electronic properties, due to electron transfer from cobalt to platinum and the presence of alloyed bimetallic Pt–Co particles (Fig. 29.6) [65]. Bimetallic Pt-Co/C catalysts exhibited superior activity and selectivity to their monometallic Pt/C and

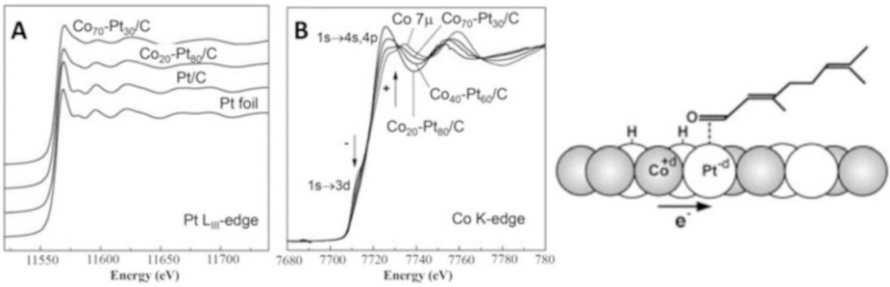

Fig. 29.6 (**a**) Pt L_{III}-edge and (**b**) Co K-edge XANES of reduced Pt-Co/C bimetallic catalysts for the selective hydrogenation of citral to geraniol/nerol via Co→Pt charge transfer and a favoured $\pi_{C=O}$ adsorption mode [65]

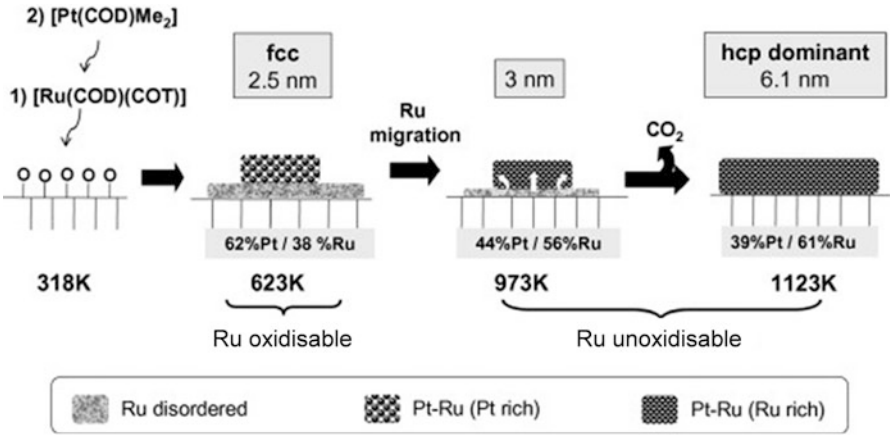

Fig. 29.7 Thermal evolution of PtRu nanoparticles supported on carbon nanotubes [66]

Co/C counterparts, attributed to strong citral binding and selective activation of the C=O function, favouring hydrogenation to geraniol/nerol versus C=C hydrogenation to citronellal, monoterpenoids widely employed in the production of flavours, fragrances, insect repellants and chemical intermediates.

XAS measurements have also proven valuable in elucidating particle size and composition effects in the selective hydrogenation of cinnamaldehyde, an aromatic allylic alcohol widely used in fragrances and flavourings over PtRu bimetallic nanoparticles dispersed on carbon nanotubes [66]. Thermal pretreatments enhanced both hydrogenation rates and selectivity towards the desired cinnamyl alcohol product, as a result of two distinct structural changes. Ex situ Pt L_{III}-edge and Ru K-edge XANES and EXAFS evidenced Pt-Ru intermixing after annealing under an inert atmosphere at 973 K to form a Ru-rich surface alloy (Fig. 29.7), delivering superior selectivity, while particle sintering >1123 K and the concomitant removal of oxygenates from the carbon nanotube surface promoted cinnamaldehyde adsorption, surface diffusion and activation over the resultant alloy. Liquid phase

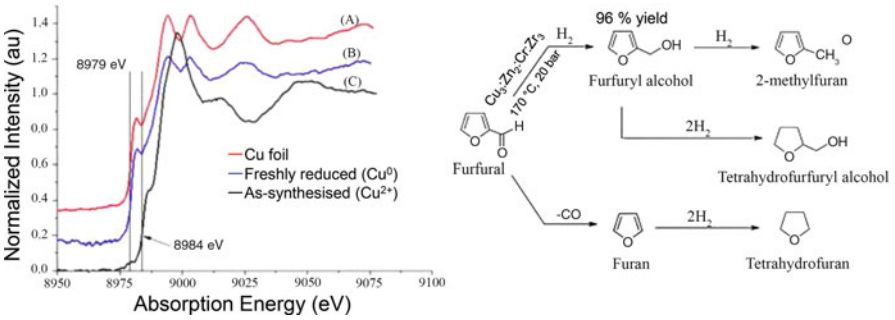

Fig. 29.8 Cu K-edge XANES of active metallic Cu species within multimetallic catalyst for the selective hydrogenation of furfural to furfuryl alcohol [36]

cinnamaldehyde hydrogenation over silica supported Co-Pt and Cu-Pt bimetallic catalysts reveals similar behaviour, with Pt L_{III}-edge XANES and EXAFS evidencing the presence of reduced platinum and the formation of bimetallic bonds respectively, resulting in higher hydrogenation activity than monometallic counterparts, with Co-Pt system offering higher selectivity to C=O hydrogenation than Cu-Pt. [67] Ex situ EXAFS has also proven useful in identifying the active species within Sn-modified SiO_2-coated Pt catalysts for hydrogenation of crotonaldehyde, an aliphatic analogue of cinnamaldehyde, to crotyl alcohol [68]. The synthetic strategy enabled Pt nanoparticles to be spatially isolated from the Sn promoter via a porous silica layer, with Sn K-edge EXAFS evidencing SnO_2 nanoparticles, which decorated the external silica and were responsible for selectively activating the carbonyl function; spillover of atomic hydrogen, remotely dissociated at separate Pt nanoparticles which are only accessible by molecular hydrogen, drives C=O hydrogenation at SnO_2. Acrolein, the simplest allylic aldehyde, has also been selectively hydrogenated over Ag/SiO_2 catalysts, in which Ag K-edge XANES and EXAFS measurements revealed a strong size dependence of the Turnover Frequency (TOF) for hydrogenation, and selectivity to allyl alcohol versus propanal: [69] larger 9 nm particles possessed a higher density of Ag(111) sites which were likely responsible for selective hydrogenation of the carbonyl.

Biomass derived chemicals are of great current academic and industrial interest due to their potential in sustainable manufacturing [70], with furfural identified as a key platform chemical for the production of both advanced biofuels and furan-based chemicals and solvents such as furfuryl alcohol and tetrahydrofuran [71]. The direct liquid phase hydrogenation of furfural to furfuryl alcohol was investigated over multimetallic Cu:Zn:Cr:Zr based catalysts prepared via co-precipitation [36]. Cu K-edge XANES (Fig. 29.8) demonstrated that the excellent activity and 96 % chemoselectivity to the desired furfuryl alcohol arose from the presence of metallic copper crystallites, whose dispersion was enhanced by the presence of Zn promoter.

5-Hydroxymethylfurfural (HMF) is another important biomass platform chemical, whose hydrogenation to 2,5-dimethylfuran (DMF) is an attractive route to high

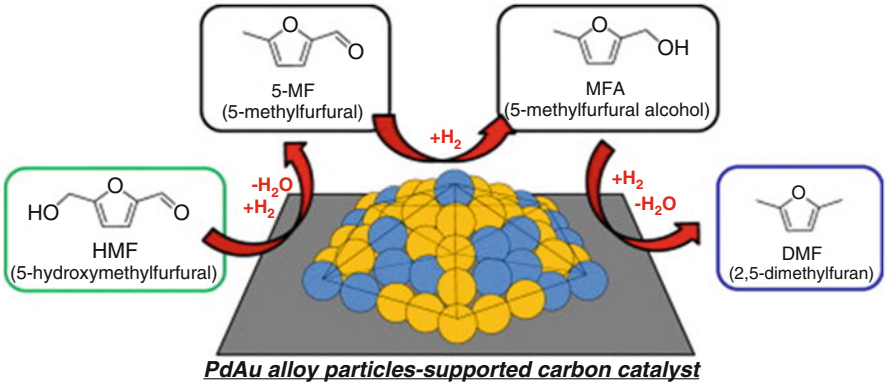

Fig. 29.9 HMF selective hydrogenation to DMF over PdAu/C bimetallic catalysts at atmospheric pressure [72]

energy density liquid transportation biofuels [37]. Bimetallic PdAu/C catalysts show promise for this reaction at atmospheric hydrogen pressure under acidic conditions, which XANES and EXAFS indicate is due to charge transfer from Pd→Au within bimetallic nanoparticles (Fig. 29.9) [72]. However, EXAFS analysis was unable to differentiate between cluster-in-cluster, Au core/Pd–shell or random homogeneous alloy nanostructures, hence it was not possible to determine whether the enhanced selectivity observed relative to monometallic counterparts reflected a purely electronic effect, or whether geometric considerations, such as different active surface ensembles and hence adsorption modes, may also have contributed to this promotion. Surprisingly there was little dependence of either HMF conversion or DMF selectivity upon bimetal composition, suggesting a common surface phase (and hence preferential surface segregation).

Partial hydrogenation of alkynes is an essential step in the petrochemical processing of alkenes for the polymer industry, in which traces of co-produced alkynes which are poisonous to downstream polymerisation catalysts must be removed via front- and/or tail-end catalytic partial hydrogenation to additional alkene [73]. Front-end hydrogenation utilises excess hydrogen and can therefore cause over hydrogenation of alkynes to alkanes [74]. Palladium is the metal of choice for such partial alkyne hydrogenations; however, the nature of the active phase is hotly debated due to possible hydrogen and carbon dissolution into the metal, and resultant hydride and carbide formation. Tew and co-workers explored the role of bulk and subsurface species in the flow partial (and total) hydrogenation of 1-pentyne in situ Pd K- and L_{III}-edge XAS under excess hydrogen [75]. Pd K-edge XANES and EXAFS of silica supported nanoparticles under H_2 evidenced a reversible 1.8 % lattice expansion at 40 °C consistent with bulk Pd-H formation. Exposure to pure 1-pentyne at 40 °C also evidenced lattice expansion and Pd-C scatterers for small Pd nanoparticles consistent with bulk Pd carbide formation, although larger nanoparticles only evidenced a carbide overlayer. Palladium hydride was unstable under simulated H_2/1-pentyne mixtures, in contrast to

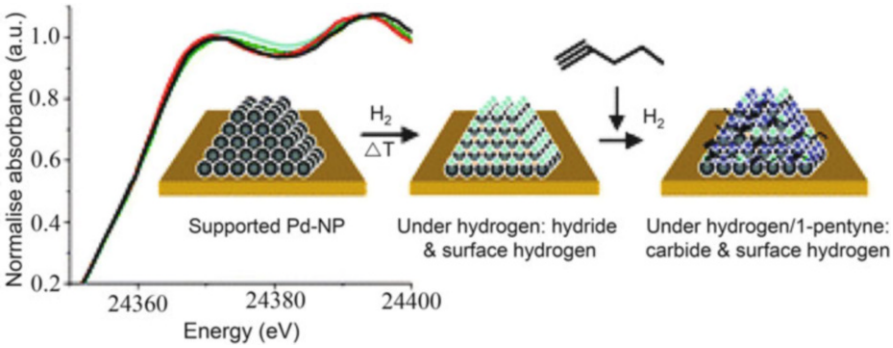

Fig. 29.10 Pd phase transitions in response to environmental composition; hydride formation under pure hydrogen, and subsequent conversion to a bulk carbide during the selective hydrogenation of 1-pentyne [75]

a carbide-like phase which was observed for all particle sizes (Fig. 29.10), albeit suppressed at 100 °C and H_2:1-pentyne = 10. This palladium carbide phase remained stable during reaction, and was only partially decomposed even under pure hydrogen [75].

Bimetallic silica supported AgPd catalysts, possessing only ppm levels of Pd, have also been developed for the selective hydrogenation of acetylene in an ethylene-rich stream [76]. Pd K-edge XANES of $AgPd_{0.01}/SiO_2$ indicated charge transfer from silver to Pd, evidencing a direct bimetal interaction, consistent with the formation of a Ag alloyed Pd single-atom system visualised by HAADF-STEM and implicated by CO DRIFTS. Microcalorimetry and XANES measurements suggest that the exceptional activity and selectivity of these catalysts arises from unique Pd single atom sites distributed within a silver surface alloy which facilitates facile acetylene hydrogenation and subsequent rapid desorption of the resulting weakly bound ethylene product (Fig. 29.11).

Aromatic amines are widely used as intermediates in the synthesis of dyes, pigments, agrochemicals, and pharmaceuticals, with the primary anilines most commonly produced via the selective reduction of nitroarenes [77] employing stoichiometric reduction procedures or homogeneous Fe based catalysts in acidic media [78], which afford poor atom efficiencies, generating significant waste and hence low E-factors. While the application of heterogeneous Au catalysts in hydrogenation is limited due to their low activity, they can offer unique hydrogenation selectivity. Cárdenas-Lizana et al. therefore investigated the catalytic gas phase hydrogenation of 1,3-dinitrobenzene (or 1,3,5-trinitrobenzene) over a Au-Ni/Al_2O_3 bimetallic catalyst, and both monometallic analogues [79]. Au L_{III}-edge XANES and EXAFS of the bimetallic system indicated either the co-existence of supported Au and Ni metal nanoparticles with significant interfacial contact, or surface decoration of Ni particles by Au. The resulting structural and electronic perturbation favoured both partial and complete $-NO_2$ reduction to 1,3-nitroaniline (or 3,5-dinitroaniline) and 1,3-phenylenediamine (or 1,3,5-triaminobenzene), in

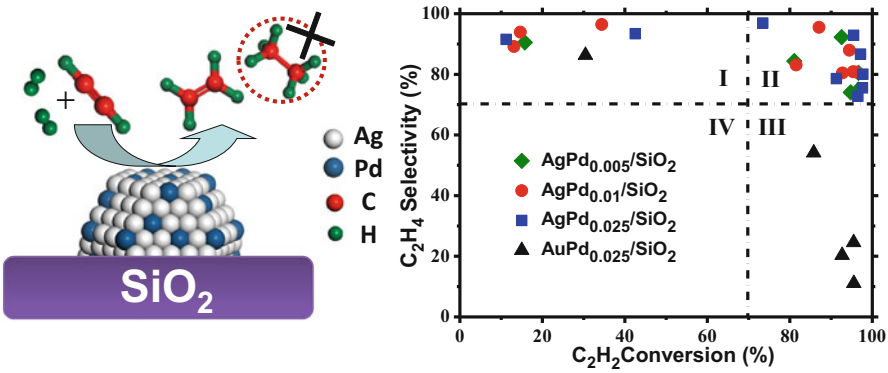

Fig. 29.11 Ag alloyed Pd single-atom catalysts offer ultraselective acetylene semi-hydrogenation in the presence of excess ethene with minimal precious metal usage [76]

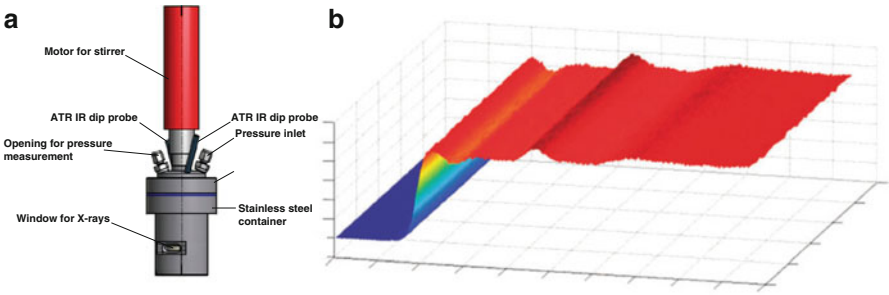

Fig. 29.12 (**a**) Schematic of HERFD XAS/ATR-FTIR autoclave. (**b**) Time-dependent revolution of Au L_{III}-edge HERFD XAS during aqueous phase nitrobenzene hydrogenation over Au/CeO_2 under 10 bar H_2 [80]

contrast to pure Au and pure Ni which promoted selective and total nitro reduction respectively. Weak Ni-O bonds observed by Ni K-edge EXAFS were attributed to the interaction of metallic nickel within small Ni particles with the alumina support.

Nitrobenzene hydrogenation was studied over Au/CeO_2 catalysts within a bespoke autoclave reactor modified for simultaneous HERFD XAS and ATR-FTIR spectroscopies (Fig. 29.12) in order to follow the evolution of electronic and geometric properties during the liquid phase reaction [80]. Since heterogeneous metal catalysts are often reduced in situ prior to their application in organic synthesis, the impact of solvent selection upon the reduction of cationic gold deposited from $HAuCl_4$ via precipitated on to a ceria support was examined via Au L_{III}-edge HERFD XAS under 10 bar H_2 at 60 °C. Reduction of Au^{3+} to Au^0 was slow in cyclohexane or tetrahydrofuran, but rapid in isopropanol or toluene, although the kinetics of this process did not correlate H_2 solubility or solvent polarity and may reflect differences in the degree of catalyst suspension. ATR-FTIR showed that nitrobenzene hydrogenation proceeded by a stepwise

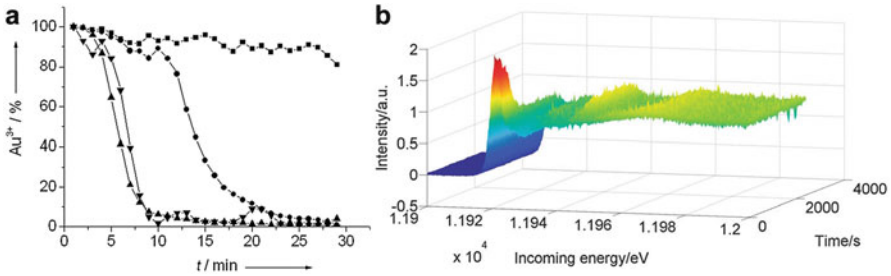

Fig. 29.13 (**a**) Time-dependent evolution of cationic gold during reduction of Au/Al_2O_3 under 10 bar of hydrogen at 60 °C (*filled rectangle*), 100 °C (*filled circle*), 150 °C (*inverted filled triangle*) and 200 °C (*filled triangle*). (**b**) Time-dependent Au L_{III}-edge HERFD XAS spectra of Au/Al_2O_3 during liquid phase nitrobenzene hydrogenation at 100 °C [81]

mechanism via an azoxybenzene intermediate, with HERFD XAS demonstrating that metallic gold was the catalytically active species throughout the hydrogenation pathway to aniline.

Particle size and support effects have also been explored in nitrobenzene hydrogenation over gold nanoparticles on alumina and titania supports employing in situ Au L_{III}-edge HERFD XAS [81]. Catalysts prepared by deposition-precipitation contained pure Au^{3+} species, which underwent rapid reduction to metallic Au nanoparticles under 10 bar H_2 at temperature >60 °C (Fig. 29.13). Hydrogen treatment of gold precursors on alumina at 60 °C lead to incomplete reduction, with the resulting cationic gold materials exhibiting poor activity for nitrobenzene hydrogenation, likely due to their inability to activate molecular hydrogen. In contrast, cationic gold reduction was rapid during nitrobenzene hydrogenation under 10 bar H_2 resulting in larger catalytically inactive gold particles; Au/Al_2O_3 activity correlated with the fraction of <2 nm metallic gold nanoparticles.

29.4 Carbon–Carbon Coupling

Aryl-aryl and heteroaryl C–C bond-forming reactions are some of the most important in modern synthetic chemistry, underpinning the construction of complex molecules from simple precursors, with applications in materials science, synthetic biology, and notably pharmaceutical drug manufacture [82]. Although transition metal homogeneous catalysts, notably palladium complexes [83], have dominated this synthetic landscape for decades, many recent studies have implicated surface reactions over nanoparticles in the catalytic cycle [84] and hence the relative contributions of homogeneous versus heterogeneous catalysed C-C couplings have been the subject of in situ XAS investigations.

Ellis et al. employed operando time-resolved Pd K-edge XAS to elucidate the catalytically active species in the Suzuki cross-coupling of iodonanisole and phenylboronic acid by size-controlled, PVP-stabilised Pd nanoparticles [85]. TOF

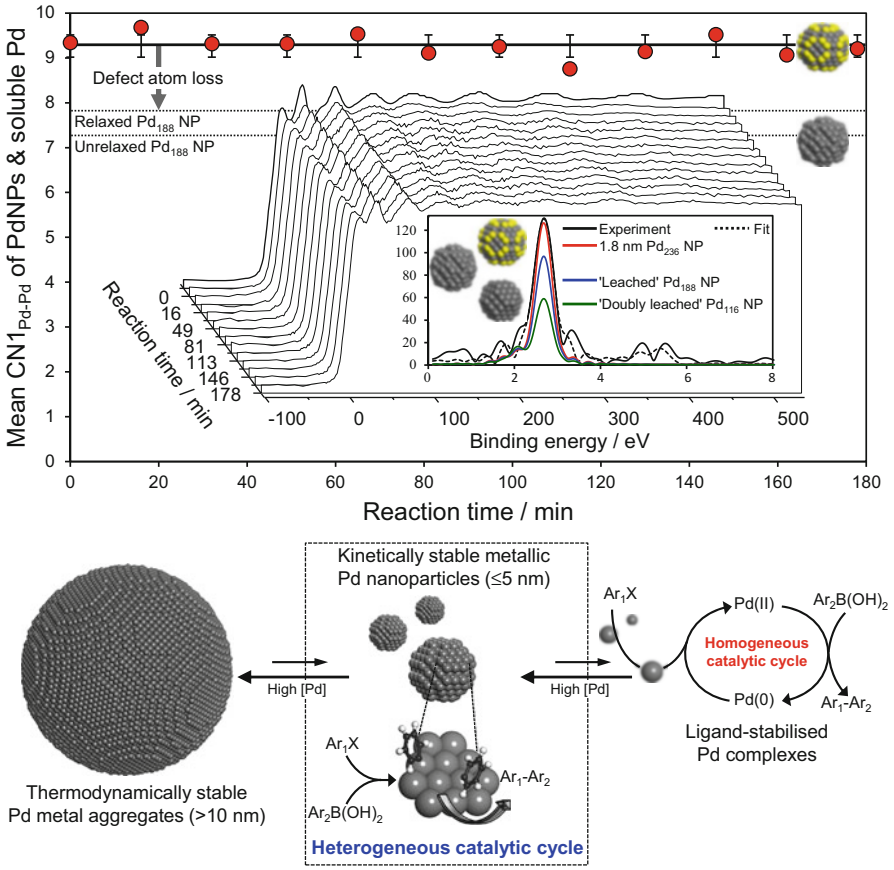

Fig. 29.14 (*top*) Operando Pd K-edge XAS spectra of Pd nanoparticles during the Suzuki coupling of iodonanisole and phenylboronic acid, and actual/simulated Fourier transforms of as-synthesised (236 atom)/leached (188 atom) Pd cubeoctahedra evidencing preservation of initial nanoparticle structure during reaction; (*bottom*) competing reaction pathways operating in Pd nanoparticle catalysed Suzuki cross-couplings [85, 86]

analysis implicated low-coordination surface defects as the active sites for cross-coupling. The time-invariant average Pd–Pd coordination number of 1.8 nm nanoparticles revealed that they were extremely stable under reaction conditions, undergoing neither sintering nor dissolution (Fig. 29.14), as confirmed by high-resolution TEM, which showed no size or shape changes between as-synthesised and post-reaction nanoparticles. Ex situ Pd K-edge XANES was also used to show that nanoporous silicas were ill-suited to the selective trapping of soluble Pd species, and that trapping protocols employing them could not therefore readily distinguish heterogeneous from homogeneous catalysis. Surface Pd defect sites were therefore directly implicated in the catalytic cycle, consistent with complementary kinetics studies which demonstrated key differences in the

reaction order between condensed and mononuclear Pd species, and in vacuo temperature programmed desorption studies of bromobenzene homo-coupling over a Pd(111) model single crystal catalyst surface [86]. Palladium speciation from $Pd(OAc)_2$, pertinent to the ligandless Suzuki–Miyaura cross-coupling of 4-chlorobromobenzene and 4-fluorophenylboronic acid, has also be studied via Pd K-edge EXAFS of the parent solid acetate, and after its dissolution in toluene or DMF. [87] Acetate monomers and $Pd_3(OAc)_6$ trimers were observed in solution, with trimer dissociation to the monomer favoured by more polar solvents, and subsequent reduction by 4-fluorophenylboronic acid inducing rapid genesis of catalytically active Pd(0) low nuclearity clusters. Spatiotemporal variations in the distribution of palladium species arising from commercial Pd/Al_2O_3 and Pd Encat™ 30NP catalysts were also explored via Pd K-edge XAS by Hii et al. during the Suzuki–Miyaura cross-coupling of 2-bromoanisole and 4-fluorophenylboronic acid within a plug-flow reactor [88]. Exposure to hot ethanol induced palladium reduction and dissolution for Pd/Al_2O_3, whereas Pd Encat™ 30NP proved more stable. Leached palladium redeposited downstream of the catalyst bed predominantly in metallic form.

Reimann et al. also used in situ Pd K-edge XANES measurements to monitor the oxidation state of palladium during the enantioselective allylic alkylation of (E)-1,3-diphenylallyl acetate over a commercial Pd/Al_2O_3 catalyst in the presence of a chiral BINAP modifier [89]. Oxidised Pd in the fresh catalyst was efficiently reduced by THF and dioxane solvents, and the sodium dimethyl malonate nucleophile, stabilising palladium against leaching. Introduction of the bulky BINAP modifier retarded initial reduction of the surface oxide, although subsequent catalyst reduction was accompanied by oxidation of BINAP. Leaching of oxidised Pd^{2+} species was suppressed under an inert atmosphere. Halogenated solvents favoured palladium leaching and the formation of soluble compounds, opening up the possibility of competing homogeneous pathways. Grunwaldt and co-workers subsequently utilised Pd K-edge Quick scanning extended X-ray absorption fine structure (QEXAFS) to gain insight into Heck coupling of bromobenzene with styrene over the same commercial Pd/Al_2O_3 catalyst. [90] XANES and EXAFS evidenced the formation of 2 nm Pd colloids (soluble, but offering heterogeneous reaction sites) during reaction, coincident with bromobenzene conversion. Deactivation coincided with pronounced changes in the EXAFS spectra attributed to the formation of mono- and dinuclear bromo-palladate complexes in the solution phase (Fig. 29.15) accompanied by sintering of the supported Pd nanoparticles.

Bimetallic Au alloyed Pd single atoms supported on an anion-exchange resin have been investigated for the Ullmann reaction of diverse (including deactivated) aryl halides to produce biphenyls in aqueous media [91]. Ex situ Pd K-Edge and Au L_{III}-edge EXAFS, in conjunction with CO DRIFTS, revealed the disruption of Pd ensembles with increasing Au:Pd molar ratios, resulting in the isolation of individual Pd atoms in a random substitutional alloy. The resulting Pd single atom alloy catalysts were extremely active in the Ulmann reaction of aryl chlorides, with TONs increasing exponentially with decreasing Pd concentration. Cu-catalysed C–C couplings have been less studied, although a recent in situ

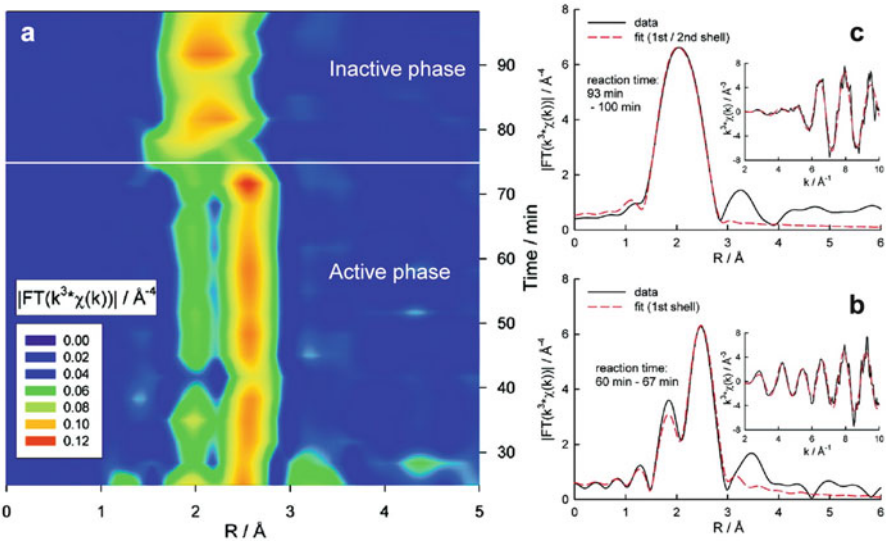

Fig. 29.15 (**a**) Time-dependent Pd K-edge Fourier transforms during the liquid phase Heck coupling of bromobenzene and styrene. (**b**) Fitted Fourier transform and k^3-weighted chi spectra of active colloidal Pd phase. (**c**) Fitted Fourier transform and k^3-weighted chi spectra of inactive bromopalladates and supported particles [90]

XAS investigation of the reaction between aryl iodide add acetylacetone catalysed by high CuI loadings identified the formation of Cu(acac)2 and metallic Cu through reaction with the β-diketone [92]. However, in the presence of PPh_3 ligands Cu K-edge in situ XANES/EXAFS evidenced a $Cu(acac)(PPh_3)_2$ complex as the active catalyst in this C−C coupling reaction, which deactivates through disproportionation to Cu^{2+}/Cu^0 spectator species.

29.5 Conclusions

X-ray absorption spectroscopy has proved an invaluable tool for catalytic scientists over many decades in characterising the structure and electronic properties of heterogeneous (and homogeneous) catalyst components. Recent advances in the design of synchrotron optics, high sensitivity and dispersive detectors, and innovative reactor cells permitting for example flow operation, multi-phase reactions and coupling to additional analytical tools for multi-dimensional experiments, in conjunction with wider access to high energy synchrotron radiation sources, now provide opportunities for investigating the nature of active species and mechanistic pathways of working catalysts for diverse green chemical transformations. However, a number of challenges remain. Further improvements in the spatial resolution of XAS methods are necessary to permit more detailed mapping of the distribution

of catalyst components across packed beds in flow reactors (micron-scale) and individual catalyst particles (1–100 nm scale); this is essential in order to better discriminate and quantify leaching of active metal components and synergies between different bimetal and/or support functions in multifunctional catalysts respectively. A shorter time resolution for spectral acquisition (1 ns–1 ms) will also help to discriminate the relative roles of spectator and active catalyst species, and identify short-lived reactive intermediates, thus providing hitherto unparalleled insight into catalyst transition states and factors influencing competing reaction pathways. Both these goals will only be possible through complementary enhancements in detector sensitivity, permitting the identification and quantification of all catalyst components at all stages of the individual catalytic cycle and overall process operation (down to ppb–ppm concentration) in order to correlate structural and kinetics measurements. In summary, XAS has to date helped shed invaluable insight into the nature of the catalytically active species participating in oxidation, hydrogenation and coupling reactions which underpin the valorisation of petrochemical and renewable chemical feedstocks, to elucidate key deactivation pathways, and to help optimise the formulation of bimetallic catalysts and reactor operating conditions.

References

1. Trost BM, Kulawiec RJ (1993) Chemoselectivity in the ruthenium-catalyzed redox isomerization of allyl alcohols. J Am Chem Soc 115:2027–2036. doi:10.1021/ja00058a059
2. Breit B, Seiche W (2001) Recent advances on chemo-, regio- and stereoselective hydroformylation. Synthesis 1:1–36
3. Fiori KW, Du Bois J (2007) Catalytic intermolecular amination of C-H bonds: method development and mechanistic insights. J Am Chem Soc 129:562–568. doi:10.1021/ja0650450
4. Magano J, Dunetz JR (2012) Large-scale carbonyl reductions in the pharmaceutical industry. Org Process Res Dev 16:1156–1184. doi:10.1021/op2003826
5. Hellal M, Falk FC, Wolf E, Dryzhakov M, Moran J (2014) Breaking the dichotomy of reactivity vs. chemoselectivity in catalytic SN1 reactions of alcohols. Org Biomol Chem 12:5990–5994. doi:10.1039/C4OB01265H
6. Sheldon RA, Arends I, Ten Brink GJ, Dijksman A (2002) Green, catalytic oxidations of alcohols. Accounts Chem Res 35:774–781. doi:10.1021/ar010075n
7. Clark JH (2002) Solid acids for green chemistry. Accounts Chem Res 35:791–797. doi:10.1021/ar010072a
8. Sheldon RA, Arends IWCE, Hanefeld U (2007) In: *Green Chemistry and Catalysis*. Wiley-VCH, Weinheim, pp 133–221
9. Vinod CP, Wilson K, Lee AF (2011) Recent advances in the heterogeneously catalyzed aerobic selective oxidation of alcohols. J Chem Technol Biotechnol 86:161–171. doi:10.1002/jctb.2504
10. Uozumi Y, Yamada YMA (2009) Development of an amphiphilic resin-dispersion of nanopalladium and nanoplatinum catalysts: design, preparation, and their use in green organic transformations. Chem Rec 9:51–65. doi:10.1002/tcr.20165
11. Cheng SS, Liu JY, Tsai KH, Chen WJ, Chang ST (2004) Chemical composition and mosquito larvicidal activity of essential oils from leaves of different Cinnamomum osmophloeum provenances. J Agric Food Chem 52:4395–4400. doi:10.1021/jf0497152

12. Lee AF (2012) Active site elucidation in heterogeneous catalysis via in situ x-ray spectroscopies. Aust J Chem 65:615–623. doi:10.1071/CH11455, http://dx.doi.org/
13. Lee AF (2001) Heterogeneous catalysts for the aerobic selective oxidation of alcohols. Abstr Pap Am Chem Soc 221:U335–U336
14. Lee AF, Wilson K (2004) Structure-reactivity correlations in the selective aerobic oxidation of cinnamyl alcohol: in situ XAFS. Green Chem 6:37–42. doi:10.1039/b310505a
15. Lee AF, Hackett SFJ, Hargreaves JSJ, Wilson K (2006) On the active site in heterogeneous palladium selox catalysts. Green Chem 8:549–555. doi:10.1039/b601984f
16. Grunwaldt JD, Keresszegi C, Mallat T, Baiker A (2003) In situ EXAFS study of Pd/Al2O3 during aerobic oxidation of cinnamyl alcohol in an organic solvent. J Catal 213:291–295. doi:10.1016/s0021-9517(02)00083-0
17. Keresszegi C, Grunwaldt JD, Mallat T, Baiker A (2003) Liquid phase oxidation of alcohols with oxygen: in situ monitoring of the oxidation state of Bi-promoted Pd/Al2O3. Chem Commun ▮:2304–2305. doi:10.1039/b304508k
18. Caravati M, Grunwaldt JD, Baliker A (2007) Comparative in situ XAS investigations during aerobic oxidation of alcohols over ruthenium, platinum and palladium catalysts in supercritical CO2. Catal Today 126:27–36. doi:10.1016/j.cattod.2006.10.005
19. Mondelli C, Grunwaldt JD, Ferri D, Baiker A (2010) Role of Bi promotion and solvent in platinum-catalyzed alcohol oxidation probed by in situ X-ray absorption and ATR-IR spectroscopy. Phys Chem Chem Phys 12:5307–5316. doi:10.1039/b926833b
20. Grunwaldt J-D, Caravati M, Baiker A (2006) Oxidic or metallic palladium: which is the active phase in Pd-catalyzed aerobic alcohol oxidation? J Phys Chem B 110:25586–25589
21. Keresszegi C, Grunwaldt JD, Mallat T, Baiker A (2004) In situ EXAFS study on the oxidation state of Pd/Al2O3 and Bi–Pd/Al2O3 during the liquid-phase oxidation of 1-phenylethanol. J Catal 222:268–280. doi:10.1016/j.jcat.2003.10.013, http://dx.doi.org/
22. Grunwaldt J-D, Caravati M, Baiker A (2006) In situ extended X-ray absorption fine structure study during selective alcohol oxidation over Pd/Al2O3 in supercritical carbon dioxide. J Phys Chem B 110:9916–9922
23. Parlett CMA, Bruce DW, Hondow NS, Lee AF, Wilson K (2011) Support-enhanced selective aerobic alcohol oxidation over Pd/Mesoporous silicas. ACS Catal 1:636–640. doi:10.1021/cs200145n
24. Hackett SFJ et al (2007) High-activity, single-site mesoporous Pd/Al2O3 catalysts for selective aerobic oxidation of allylic alcohols. Angew Chem 119:8747–8750. doi:10.1002/ange.200702534
25. Parlett CMA et al (2013) Mesoporous silicas as versatile supports to tune the palladium-catalyzed selective aerobic oxidation of allylic alcohols. ChemCatChem 5:939–950. doi:10.1002/cctc.201200301
26. Parlett CMA et al (2013) Hierarchically ordered nanoporous Pd/SBA-15 catalyst for the aerobic selective oxidation of sterically challenging allylic alcohols. ACS Catal 3:2122–2129. doi:10.1021/cs400371a
27. Parlett CMA et al (2014) Alumina-grafted SBA-15 as a high performance support for Pd-catalyzed cinnamyl alcohol selective oxidation. Catal Today 229:46–55. doi:10.1016/j.cattod.2013.11.056
28. Parlett CMA et al (2014) Selective oxidation of allylic alcohols over highly ordered Pd/meso-Al2O3 catalysts. Catal Commun 44:40–45. doi:10.1016/j.catcom.2013.07.005, http://dx.doi.org/
29. Lee AF, Chang Z, Ellis P, Hackett SFJ, Wilson K (2007) Selective oxidation of crotyl alcohol over Pd(111). J Phys Chem C 111:18844–18847. doi:10.1021/jp709944c
30. Naughton J, Lee AF, Thompson S, Vinod CP, Wilson K (2010) Reactivity of crotonaldehyde and propene over Au/Pd(111) surfaces. Phys Chem Chem Phys 12:2670–2678. doi:10.1039/B921669C
31. Durndell LJ, Parlett CMA, Hondow NS, Wilson K, Lee AF (2013) Tunable Pt nanocatalysts for the aerobic selox of cinnamyl alcohol. Nanoscale 5:5412–5419. doi:10.1039/C3NR00184A

32. Lee AF et al (2011) Reaction-driven surface restructuring and selectivity control in allylic alcohol catalytic aerobic oxidation over Pd. J Am Chem Soc 133:5724–5727. doi:10.1021/ja200684f
33. Parlett CMA et al (2013) Operando synchronous DRIFTS/MS/XAS as a powerful tool for guiding the design of Pd catalysts for the selective oxidation of alcohols. Catal Today 205:76–85. doi:10.1016/j.cattod.2012.08.022
34. Gaskell CV, Parlett CMA, Newton MA, Wilson K, Lee AF (2012) Redox-controlled crotyl alcohol selective oxidation: in situ oxidation and reduction dynamics of catalytic Pd Nanoparticles via synchronous XANES/MS. ACS Catal 2:2242–2246. doi:10.1021/cs300445y
35. Newton MA, Dent AJ, Fiddy SG, Jyoti B, Evans J (2007) Combining diffuse reflectance infrared spectroscopy (DRIFTS), dispersive EXAFS, and mass spectrometry with high time resolution: potential, limitations, and application to the study of NO interaction with supported Rh catalysts. Catal Today 126:64–72. doi:10.1016/j.cattod.2006.09.034, http://dx.doi.org
36. Sharma RV, Das U, Sammynaiken R, Dalai AK (2013) Liquid phase chemo-selective catalytic hydrogenation of furfural to furfuryl alcohol. Appl Catalysis A General 454:127–136. doi:10.1016/j.apcata.2012.12.010, http://dx.doi.org/
37. Rosatella AA, Simeonov SP, Frade RFM, Afonso CAM (2011) 5-Hydroxymethylfurfural (HMF) as a building block platform: biological properties, synthesis and synthetic applications. Green Chem 13:754–793. doi:10.1039/C0GC00401D
38. Naughton J et al (2011) Metastable de-excitation spectroscopy and density functional theory study of the selective oxidation of crotyl alcohol over Pd(111). J Phys Chem C 115:25290–25297. doi:10.1021/jp205340z
39. Mori K et al (2002) Controlled synthesis of hydroxyapatite-supported palladium complexes as highly efficient heterogeneous catalysts. J Am Chem Soc 124:11572–11573. doi:10.1021/ja020444q
40. Mori K, Hara T, Mizugaki T, Ebitani K, Kaneda K (2004) Hydroxyapatite-supported palladium nanoclusters: a highly active heterogeneous catalyst for selective oxidation of alcohols by use of molecular oxygen. J Am Chem Soc 126:10657–10666. doi:10.1021/ja0488683
41. Wang F et al (2013) Palladium nanoparticles with high energy facets as a key factor in dissociating O2 in the solvent-free selective oxidation of alcohols. Chem Commun 49:6626–6628. doi:10.1039/C3CC42674B
42. Opre Z, Grunwaldt JD, Mallat T, Baiker A (2005) Selective oxidation of alcohols with oxygen on Ru–Co-hydroxyapatite: a mechanistic study. J Mol Catal A Chem 242:224–232. doi:10.1016/j.molcata.2005.08.012, http://dx.doi.org/
43. Lee AF, Gee JJ, Theyers HJ (2000) Aspects of allylic alcohol oxidation-a bimetallic heterogeneous selective oxidation catalyst. Green Chem 2:279–282. doi:10.1039/B006528P
44. Alardin F, Delmon B, Ruiz P, Devillers M (2000) Stability of bimetallic Bi–Pd and Pb–Pd carbon-supported catalysts during their use in glyoxal oxidation. Catal Today 61:255–262. doi:10.1016/S0920-5861(00)00377-1, http://dx.doi.org/
45. Zhang HJ, Toshima N (2013) Glucose oxidation using Au-containing bimetallic and trimetallic nanoparticles. Catal Sci Technol 3:268–278. doi:10.1039/c2cy20345f
46. Pinxt HHCM, Kuster BFM, Marin GB (2000) Promoter effects in the Pt-catalyzed oxidation of propylene glycol. Appl Catal A General 191:45–54. doi:10.1016/S0926-860X(99)00304-X, http://dx.doi.org/
47. Lee AF, Ellis CV, Wilson K, Hondow NS (2010) In situ studies of titania-supported Au shell-Pd core nanoparticles for the selective aerobic oxidation of crotyl alcohol. Catal Today 157:243–249. doi:10.1016/j.cattod.2010.04.032
48. Scott RWJ (2015) Rational design and characterization of bimetallic gold-palladium nanoparticle catalysts. Can J Chem Eng 93:623–630. doi:10.1002/cjce.22159
49. Balcha T, Strobl JR, Fowler C, Dash P, Scott RWJ (2011) Selective aerobic oxidation of crotyl alcohol using AuPd core-shell nanoparticles. ACS Catal 1:425–436. doi:10.1021/cs200040a
50. Zheng N, Stucky GD (2007) Promoting gold nanocatalysts in solvent-free selective aerobic oxidation of alcohols. Chem Commun :3862–3864. doi: 10.1039/B706864F

51. Della Pina C, Falletta E, Prati L, Rossi M (2008) Selective oxidation using gold. Chem Soc Rev 37:2077–2095. doi:10.1039/B707319B
52. Hou W, Dehm NA, Scott RWJ (2008) Alcohol oxidations in aqueous solutions using Au, Pd, and bimetallic AuPd nanoparticle catalysts. J Catal 253:22–27. doi:10.1016/j.jcat.2007.10.025, http://dx.doi.org/
53. Maclennan A, Banerjee A, Hu YF, Miller JT, Scott RWJ (2013) In situ X-ray absorption spectroscopic analysis of gold-palladium bimetallic nanoparticle catalysts. ACS Catal 3:1411–1419. doi:10.1021/cs400230t
54. Blaser HU et al (2003) Selective hydrogenation for fine chemicals: recent trends and new developments. Adv Synth Catal 345:103–151. doi:10.1002/adsc.200390000
55. Gallezot P, Richard D (1998) Selective hydrogenation of α, β-unsaturated aldehydes. Catal Rev 40:81–126. doi:10.1080/01614949808007106
56. Maki-Arvela P, Hajek J, Salmi T, Murzin DY (2005) Chemoselective hydrogenation of carbonyl compounds over heterogeneous catalysts. Appl Catal A Gen 292:1–49. doi:10.1016/j.apcata.2005.05.045
57. Kliewer CJ, Bieri M, Somorjai GA (2009) Hydrogenation of the α, β-unsaturated aldehydes acrolein, crotonaldehyde, and prenal over Pt single crystals: a kinetic and sum-frequency generation vibrational spectroscopy study. J Am Chem Soc 131:9958–9966. doi:10.1021/ja8092532
58. Lee I, Delbecq F, Morales R, Albiter MA, Zaera F (2009) Tuning selectivity in catalysis by controlling particle shape. Nat Mater 8:132–138
59. Attard GA et al (2013) Semi-hydrogenation of alkynes at single crystal, nanoparticle and biogenic nanoparticle surfaces: the role of defects in Lindlar-type catalysts and the origin of their selectivity. Faraday Discuss 162:57–75. doi:10.1039/C3FD00007A
60. An K et al (2013) Preparation of mesoporous oxides and their support effects on Pt nanoparticle catalysts in catalytic hydrogenation of furfural. J Colloid Interface Sci 392:122–128. doi:10.1016/j.jcis.2012.10.029, http://dx.doi.org/
61. Poupin C, Maache R, Pirault-Roy L, Brahmi R, Williams CT (2014) Effect of Al2O3/MgO molar ratio on catalytic performance of Pt/MgO–Al2O3 catalyst in acetonitrile hydrogenation followed by Fourier transform infrared spectroscopy. Appl Catal A General 475:363–370. doi:10.1016/j.apcata.2014.01.041, http://dx.doi.org/
62. Lara P, Suárez A, Collière V, Philippot K, Chaudret B (2014) Platinum N-heterocyclic carbene nanoparticles as new and effective catalysts for the selective hydrogenation of nitroaromatics. ChemCatChem 6:87–90. doi:10.1002/cctc.201300821
63. Li S, Boucheron T, Tuel A, Farrusseng D, Meunier F (2014) Size-selective hydrogenation at the subnanometer scale over platinum nanoparticles encapsulated in silicalite-1 single crystal hollow shells. Chem Commun 50:1824–1826. doi:10.1039/C3CC48648F
64. Saudan LA (2007) Hydrogenation, processes in the synthesis of perfumery ingredients. Accounts Chem Res 40:1309–1319. doi:10.1021/ar700140m
65. Bertero NM, Trasarti AF, Moraweck B, Borgna A, Marchi AJ (2009) Selective liquid-phase hydrogenation of citral over supported bimetallic Pt-Co catalysts. Appl Catal A Gen 358:32–41. doi:10.1016/j.apcata.2009.01.036
66. Teddy J et al (2011) Influence of particles alloying on the performances of Pt-Ru/CNT catalysts for selective hydrogenation. J Catal 278:59–70. doi:10.1016/j.jcat.2010.11.016
67. Zheng RY et al (2012) Controlling hydrogenation of C=O and C=C bonds in cinnamaldehyde using silica supported Co-Pt and Cu-Pt bimetallic catalysts. Appl Catal A Gen 419:126–132. doi:10.1016/j.apcata.2012.01.019
68. Taniya K, Jinno H, Kishida M, Ichihashi Y, Nishiyama S (2012) Preparation of Sn-modified silica-coated Pt catalysts: a new Pt-Sn bimetallic model catalyst for selective hydrogenation of crotonaldehyde. J Catal 288:84–91. doi:10.1016/j.jcat.2012.01.006
69. Wei HJ et al (2013) Selective hydrogenation of acrolein on supported silver catalysts: a kinetics study of particle size effects. J Catal 298:18–26. doi:10.1016/j.jcat.2012.10.027

70. Sheldon RA (2014) Green and sustainable manufacture of chemicals from biomass: state of the art. Green Chem 16:950–963. doi:10.1039/C3GC41935E
71. Cai CM, Zhang T, Kumar R, Wyman CE (2014) Integrated furfural production as a renewable fuel and chemical platform from lignocellulosic biomass. J Chem Technol Biotechnol 89:2–10. doi:10.1002/jctb.4168
72. Nishimura S, Ikeda N, Ebitani K (2014) Selective hydrogenation of biomass-derived 5-hydroxymethylfurfural (HMF) to 2,5-dimethylfuran (DMF) under atmospheric hydrogen pressure over carbon supported PdAu bimetallic catalyst. Catal Today 232:89–98. doi:10.1016/j.cattod.2013.10.012, http://dx.doi.org/
73. McGown WT, Kemball C, Whan DA, Scurrell MS (1977) Hydrogenation of acetylene in excess ethylene on an alumina supported palladium catalyst in a static system. J Chem Soc Faraday Trans 73:632–647. doi:10.1039/F19777300632
74. Rahimpour MR et al (2012) A novel configuration for Pd/Ag/α-Al2O3 catalyst regeneration in the acetylene hydrogenation reactor of a multi feed cracker. Chem Eng J 198–199:491–502. doi:10.1016/j.cej.2012.06.005, http://dx.doi.org/
75. Tew MW, Nachtegaal M, Janousch M, Huthwelker T, van Bokhoven JA (2012) The irreversible formation of palladium carbide during hydrogenation of 1-pentyne over silica-supported palladium nanoparticles: in situ Pd K and L3 edge XAS. Phys Chem Chem Phys 14:5761–5768. doi:10.1039/C2CP24068H
76. Pei GX et al (2015) Ag alloyed Pd single-atom catalysts for efficient selective hydrogenation of acetylene to ethylene in excess ethylene. ACS Catal 5:3717–3725. doi:10.1021/acscatal.5b00700
77. Downing RS, Kunkeler PJ, Van Bekkum H (1997) Catalytic syntheses of aromatic amines. Catal Today 37:121–136. doi:10.1016/S0920-5861(97)00005-9, http://dx.doi.org/
78. Wienhöfer G et al (2011) General and selective iron-catalyzed transfer hydrogenation of nitroarenes without base. J Am Chem Soc 133:12875–12879. doi:10.1021/ja2061038
79. Cardenas-Lizana F et al (2012) Alumina supported Au-Ni: surface synergism in the gas phase hydrogenation of nitro-compounds. J Phys Chem C 116:11166–11180. doi:10.1021/jp3025528
80. Makosch M et al (2012) HERFD XAS/ATR-FTIR batch reactor cell. Phys Chem Chem Phys 14:2164–2170. doi:10.1039/C1CP21933B
81. Hartfelder U et al (2013) Particle size and support effects in hydrogenation over supported gold catalysts. Catal Sci Technol 3:454–461. doi:10.1039/c2cy20485a
82. Horton DA, Bourne GT, Smythe ML (2003) The combinatorial synthesis of bicyclic privileged structures or privileged substructures. Chem Rev 103:893–930. doi:10.1021/cr020033s
83. Johansson Seechurn CCC, Kitching MO, Colacot TJ, Snieckus V (2012) Palladium-catalyzed cross-coupling: a historical contextual perspective to the 2010 Nobel prize. Angew Chem Int Ed 51:5062–5085. doi:10.1002/anie.201107017
84. Beaumont SK (2012) Heterogeneously catalyzing C–C coupling reactions with precious metal nanoparticles. J Chem Technol Biotechnol 87:595–600. doi:10.1002/jctb.3748
85. Ellis PJ, Fairlamb IJS, Hackett SFJ, Wilson K, Lee AF (2010) Evidence for the surface-catalyzed Suzuki–Miyaura reaction over palladium nanoparticles: an Operando XAS study. Angew Chem Int Ed 49:1820–1824. doi:10.1002/anie.200906675
86. Lee AF, Ellis PJ, Fairlamb IJS, Wilson K (2010) Surface catalyzed Suzuki-Miyaura cross-coupling by Pd nanoparticles: an operando XAS study. Dalton Trans 39:10473–10482. doi:10.1039/c0dt00412j
87. Adrio LA, Nguyen BN, Guilera G, Livingston AG, Hii KK (2012) Speciation of Pd(OAc)2 in ligandless Suzuki-Miyaura reactions. Catal Sci Technol 2:316–323. doi:10.1039/C1CY00241D
88. Brazier JB et al (2014) Catalysis in flow: Operando study of Pd catalyst speciation and leaching. Catal Today 229:95–103. doi:10.1016/j.cattod.2013.10.079
89. Reimann S, Grunwaldt J-D, Mallat T, Baiker A (2010) Asymmetric C–C bond-formation reaction with Pd: how to favor heterogeneous or homogeneous catalysis? Chem Eur J 16:9658–9668. doi:10.1002/chem.201000833

90. Reimann S et al (2011) Identification of the active species generated from supported Pd catalysts in heck reactions: an in situ quick scanning EXAFS investigation. J Am Chem Soc 133:3921–3930. doi:10.1021/ja108636u
91. Zhang L et al (2014) Efficient and durable Au alloyed Pd single-atom catalyst for the Ullmann reaction of aryl chlorides in water. ACS Catal 4:1546–1553. doi:10.1021/cs500071c
92. He C et al (2013) Labile Cu(I) catalyst/spectator Cu(II) Species in copper-catalyzed C–C coupling reaction: Operando IR, in Situ XANES/EXAFS evidence and kinetic investigations. J Am Chem Soc 135:488–493. doi:10.1021/ja310111p

Chapter 30
Environmental Catalysts

Kazuhiko Dohmae

30.1 Introduction

It is well known that gasoline engines emit several pollutants as the result of fuel combustion, including carbon monoxide (CO), nitrogen oxides (NOx), and hydrocarbons (HC). These harmful gases were recognized as a serious problem for the environments beginning in the 1960s, and various laws obligating automobile manufacturers to drastically reduce pollutants in exhaust, including the Muskie Act in the United States, were enacted in many countries in the 1970s. In order to solve this problem, three-way catalysts capable of converting toxic gases into harmless compounds were put into practical use in 1977, and these systems are now employed in almost all gasoline engine vehicles. In such compounds, a monolithic honeycomb is coated with a powdered catalyst, which typically consists of precious metal particles such as platinum (Pt), rhodium (Rh), and palladium (Pd) dispersed on a metal oxide support.

To allow the practical application of three-way catalysts, it is important to maintain the air to fuel (A/F) ratio in the engine inlet gas within an ideal range, and this can be accomplished by advanced electronics and oxygen sensors. It is also vital to disperse the precious metals on the support as infinitesimal particles to achieve high catalytic performance. Analysis of the dispersion state of precious metals and measurements of particle sizes may be performed via electron microscopy, while elemental identification is accomplished by X-ray diffraction and chemical states are analyzed by X-ray photoelectron spectroscopy. X-ray absorption fine structure (XAFS) analysis of catalysts has become increasingly common as

K. Dohmae (✉)
Materials Analysis & Evaluation Dept., Toyota Central R&D Labs. Inc., 480-1192 Japan
e-mail: kdohmae@mosk.tytlabs.co.jp

Y. Iwasawa et al. (eds.), *XAFS Techniques for Catalysts, Nanomaterials, and Surfaces*, DOI 10.1007/978-3-319-43866-5_30

the use of synchrotron radiation has been more widely adopted. In recent years, XAFS has become an indispensable technique in catalyst analysis because of its ability to determine both the local structure and the chemical state of each element and to readily perform in situ analyses.

30.2 EXAFS Analysis of the Local Structure of CeO_2–ZrO_2 Oxide

Automotive three-way catalysts are able to eliminate CO, NOx, and HC from exhaust gases only under stoichiometric conditions, meaning that the A/F ratio of the gases being introduced to the engine must be approximately 14.6. Because it is difficult to accurately supply the correct amount of fuel to maintain an ideal A/F ratio, in practice the composition of the inlet gases actually fluctuates around the stoichiometric ratio. In such cases, the catalyst often does not function efficiently, depending only on the catalytic activity of the noble metals employed. For this reason, three-way catalysts contain a promoter having a suitable oxygen storage/release capacity (OSC) in order to maintain stoichiometric conditions in the vicinity of the catalyst. Ceria-based oxides are widely used as promoters due to the high OSC efficiency of these materials based on the reversible redox reaction $CeO_2 \leftrightarrow CeO_{2-x} + (x/2)O_2$ ($x = 0$ to 0.5). It has been demonstrated that the addition of ZrO_2 to CeO_2 enhances the OSC of the promoter and also improves its thermal stability [1–3], and so CeO_2–ZrO_2 has been widely utilized for many three-way catalysts. Nagai et al. clarified the relationship between the OSC and the local structure of CeO_2–ZrO_2 using XAFS analysis [4].

In their study, Ce *K*-edge (40.5 keV) extended X-ray absorption fine structure (EXAFS) has been applied to the analysis of the cation–cation (cation = Ce, Zr) network as well as the oxygen environment in CeO_2–ZrO_2. In the past, Ce L_3-edge (5.7 keV) EXAFS was utilized for CeO_2-ZrO_2 analysis [5, 6]. However, the usable electron wavenumber (k) region of Ce L_3-edge EXAFS is limited to the range of approximately 3 to 9 $Å^{-1}$ due to the presence of the Ce L_2-edge (6.2 keV), even though the Ce and Zr contributions to the EXAFS signals are significant in the high-*K* region [7].

Three types of CeO_2-ZrO_2 compounds having the same composition but different OSC efficiencies (Ce/Zr = 1; CZ55-1, CZ55-2, and CZ55-3) were prepared for this study. CZ55-1 was synthesized by precipitation with aqueous NH_3 using CeO_2 powder and an aqueous $ZrO(NO_3)_2$ solution followed by calcination in air at 500 °C for 3 h. CZ55-2 was prepared by co-precipitation with aqueous NH_3 using aqueous solutions of $Ce(NO_3)_3$ and $ZrO(NO_3)_2$ and subsequent calcination in air at 500 °C for 3 h. CZ55-3 was obtained using the same co-precipitation process as applied to CZ55-2, except that the dried powder was reduced at 1200 °C for 4 h in CO and further oxidized in air at 500 °C for 3 h. The OSC properties of these materials are summarized in Table 30.1, which shows that the OSC value increases in the order of

Table 30.1 OSC properties of CeO_2–ZrO_2 mixed oxides

Sample	OSC (μmol–O/g)[a]	Ce efficiency (%)[b]
CZ55-1	160	9.6
CZ55-2	880	51.7
CZ55-3	1500	88.6

[a]OSC (oxygen storage/release capacity) of 1 wt.% Pt-loaded Ce compounds was measured at 773 K
[b]The ratio of $Ce^{3+}/(Ce^{3+} + Ce^{4+})$ under reductive condition

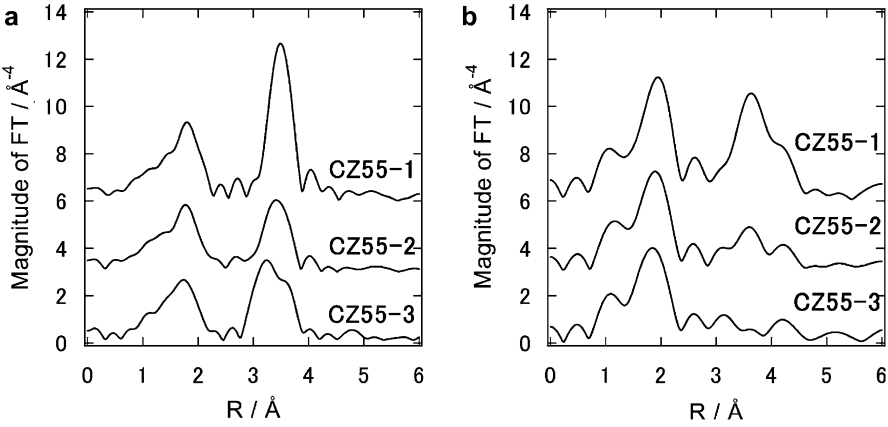

Fig. 30.1 Fourier-transformed $k^3\chi$ data from (**a**) Ce *K*-edge and (**b**) Ce L_3-edge EXAFS of CeO_2–ZrO_2 samples

CZ55-1 < CZ55-2 < CZ55-3. It is noteworthy that almost all of the Ce in the CZ55-3 contributes to the OSC.

Fourier transforms (FTs) of the 3-17 $Å^{-1}$ regions of the Ce *K*-edge EXAFS spectra are presented in Fig. 30.1a. The first and second peaks at 1.8 and 3.5 Å correspond to the Ce–O and Ce-cation (cation = Ce, Zr) bonds, respectively. The position and amplitude of the Ce–O peaks generated by the three materials are slightly different from one another: the magnitudes of the Ce-cation peaks of CZ55-2 and CZ55-3 are lower than that of CZ55-1. Additionally, the Ce-cation peak of CZ55-3 appears to be split in two, and the FTs of the Ce L_3-edge of the Ce-cation peaks of CZ55-2 and CZ55-3 almost disappear due to the lack of an EXAFS signal for heavy elements in the high-*k* part (Fig. 30.1b). These results indicate that the acquisition of *K*-edge EXAFS spectra is necessary for the precise analysis of Lanthanide elements, including Ce.

Figure 30.2 shows the X-ray absorption near edge structure (XANES) spectra at the Zr *K*-edge. A comparison of the spectra reveals differences at the rising absorption edge (region A) and at the peak top (region B); specifically, the weak shoulder in region A is more apparent in the CZ55-1 and CZ55-2 spectra than that of CZ55-3. This pre-edge can be assigned to the absorption of the 1 s to 4d transition, which is most weak when the oxygen configuration around the Zr is

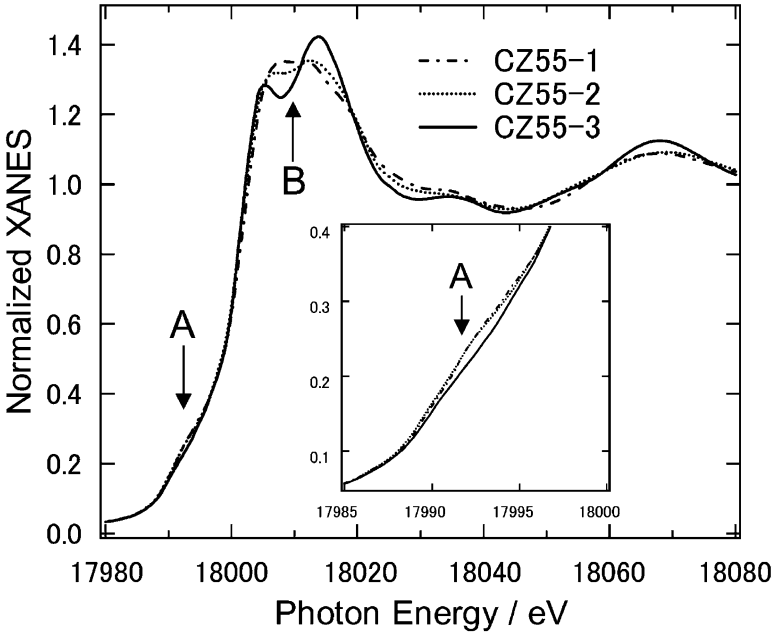

Fig. 30.2 Zr *K*-edge XANES spectra of CeO_2–ZrO_2 samples

symmetrical. In terms of this feature, the XANES spectra of CZ55-1 and CZ55-2 closely resemble that of tetragonal ZrO_2, while the CZ55-3 spectrum matches that of cubic ZrO_2 [8]. In region B, the CZ55-1 spectrum exhibits a single broad peak, whereas CZ55-2 generates a slight splitting and CZ55-3 shows clear splitting. Similar splitting has been observed for a solid solution of Y_2O_3-ZrO_2 [9]. These results suggest that the degree of Ce insertion into the ZrO_2 increases in the order CZ55-1 < CZ55-2 < CZ55-3.

The curve-fitting results for the cation–cation shells in the FTs of the Ce *K*-edge and Zr *K*-edge EXAFS spectra are summarized in Table 30.2. For CZ55-1, the Ce-cation shell was fitted with a single Ce–Ce bond, and the Zr-cation shell was also fitted with a single Zr–Zr bond. These results demonstrate that CZ55-1 is a mixture of pure CeO_2 and ZrO_2. The coordination number (CN) of the Zr–Zr bond for CZ55-1 is 6.6 while that of the Ce–Ce bond is about 12, suggesting that the average crystallite size of the ZrO_2 in the CZ55-1 was small. Both Ce–Ce (Zr–Zr) and Ce–Zr (Zr–Ce) bonds were required to obtain an appropriate fit for the cation–cation shell at the Ce (Zr) *K*-edge for CZ55-2. The CN of the Ce–Ce bond (CN = 8.0) for the Ce-cation shell is larger than that of Ce–Zr bond (CN = 3.6), while the CN of the Zr–Ce bond (CN = 4.0) is close to that of the Ce–Zr bond. Thus, it is evident that a CeO_2–ZrO_2 solid solution was formed in the case of CZ55-2, although Ce-rich and Zr-rich domains still remain. Finally, in the case of CZ55-3, both the Ce-cation and Zr-cation shells were fitted with same Ce and Zr CN value

Table 30.2 Results of curve-fitting analysis for Ce-cation shells[a]

Sample	Bond	CN	R (Å)	$\Delta\sigma^2$ (Å^2)[b]
Cubic CeO_2[c]	Ce–Ce	12	3.826	
CZ55-1	Ce–Ce	11.9(2)	3.82(0)	0.0026(1)
CZ55-2	Ce–Ce	8.0(4)	3.78(0)	0.0034(2)
	Ce–Zr	3.6(5)	3.71(0)	0.0063(13)
CZ55-3	Ce–Ce	6.0(3)	3.78(0)	0.0016(2)
	Ce–Zr	6.0(3)	3.72(0)	0.0022(3)

[a]The standard deviation is given in parentheses
[b]Relative Debye–Waller factor
[c]Standard compound

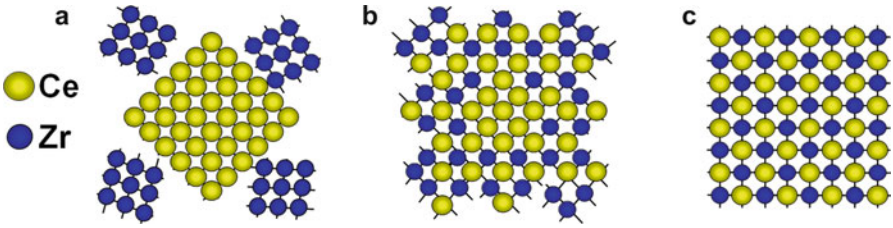

Fig. 30.3 Illustrations of cation–cation networks in various CeO_2–ZrO_2 materials: (**a**) CZ55-1 consists of pure CeO_2 and ZrO_2, (**b**) CZ55-2 consists of a CeO_2–ZrO_2 solid solution, although Ce-rich and Zr-rich domain remain, and (**c**) CZ55-3 consists of a homogeneous $Ce_{0.5}Zr_{0.5}O_2$ solid solution formed at the atomic level with an ordered arrangement of Ce and Zr ions

(CN = 6.0) for the cation, and the Ce–Ce to Ce–Zr and Zr–Zr to Zr–Ce CN ratios were simply unity. These CN ratios indicate that a homogeneous $Ce_{0.5}Zr_{0.5}O_2$ solid solution was formed in the case of CZ55-3. Figure 30.3 illustrates the cation–cation networks of the CeO_2–ZrO_2 samples proposed on the basis of these curve-fitting analyses, in which the homogeneity of the CeO_2–ZrO_2 solid solution increases in the order CZ55-1 < CZ55-2 < CZ55-3. These results lead to the conclusion that the OSC is increased by enhancing the homogeneity of the Ce and Zr atom distributions throughout the CeO_2–ZrO_2 solid solution.

30.3 XAFS Analysis of Interactions Between Supported Platinum and Support Oxides

In three-way catalysts, precious metals such as Pt, Pd and Rh are highly dispersed on the support oxides as small particles only several nanometers in diameter. Exposing the catalyst to high temperatures (~800 °C and above) agglomerates and sinters the precious metals, decreasing their active surface area. [10–13] The decreased efficiency caused by sintering of the precious metals is one factor that can degrade the effectiveness of three-way catalysts and, as such, is a crucial issue that

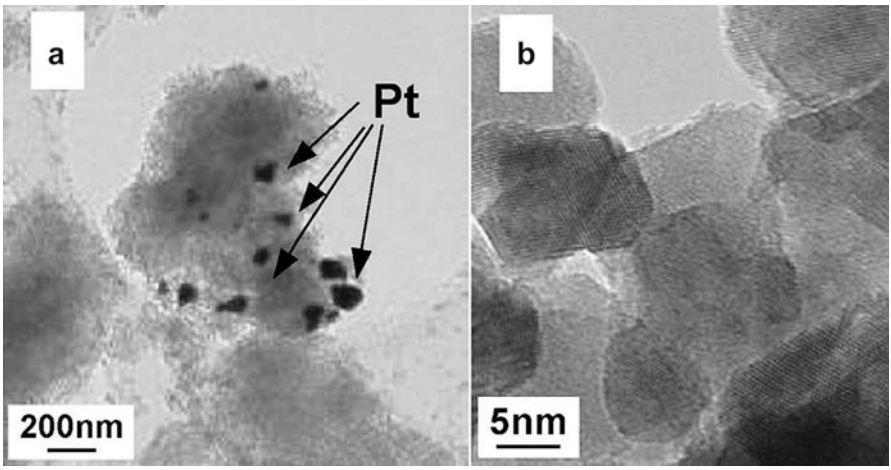

Fig. 30.4 TEM images of supported Pt catalysts after aging in air for 5 h at 800 °C: (**a**) Pt/Al_2O_3 and (**b**) Pt/CZY

must be addressed during the development of advanced catalysts. The activity of Pt-supported catalysts exhibits an especially large decrease after high temperature aging in an oxidative atmosphere, due to the sintering of Pt particles [10, 11]. The degree of sintering will vary depending on the support oxide, and ceria-based oxides are known to help stabilize precious metal dispersions based on experimental evidence [14, 15]. Nagai et al. studied the interactions between supported Pt and various oxides using primarily XAFS and also investigated the sintering mechanism of Pt particles in an oxidizing atmosphere [16].

In this study, Pt(2 wt%)/Al_2O_3 and Pt(2 wt%)/ceria-based oxide (CeO_2(50 wt%)-ZrO_2(46 wt%)-Y_2O_3(4 wt%); CZY) were prepared, and samples of these materials were heated in air at 800 °C for 5 h as a high temperature aging. Figure 30.4 shows transmission electron microscopy (TEM) images of the Pt/Al_2O_3 and Pt/CZY catalysts after this aging treatment, in which Pt particles ranging from 3 to 150 nm are observed in the Pt/Al_2O_3. In contrast, no explicit Pt particles were found on the Pt/CZY, even though Pt was detected by energy dispersive X-ray (EDX) analysis. Since no Pt particles were observed before aging of these samples, these findings indicate that Pt particles supported on the Al_2O_3 were sintered by the aging treatment at 800 °C.

Figure 30.5a shows the Pt L_3-edge XANES spectra obtained from the aged catalysts as well as those of reference samples. The absorption peak at approximately 11.57 keV is referred to as the "white line," and its intensity reflects the degree of vacancy in the 5d orbitals of the Pt atoms, such that a greater extent of Pt oxidation results in a more intense line. Here the white line intensity of the Pt/Al_2O_3 is equal to that of Pt foil, suggesting that the Pt on the Al_2O_3 was in a metallic state after aging. In contrast, the white line intensity of the Pt/CZY is similar to that of PtO_2, so that the Pt on CZY was evidently oxidized to Pt^{2+} or Pt^{4+} species.

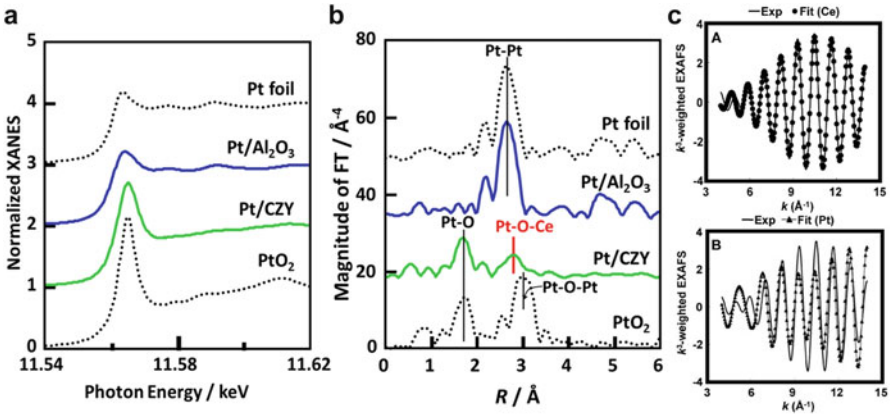

Fig. 30.5 (**a**) Pt L_3-edge XANES spectra, (**b**) Fourier-transformed k^3x data and (**c**) the results of curve-fitting analysis of the inverse Fourier-transform of the second peak of the aged Pt/CZY catalyst in (**b**). The data for standard samples of Pt foil and PtO_2 powder are also shown in (**a**) and (**b**). (**c**)-A: experimental (–) and curve-fitting for Ce atoms (●). (**c**)-B: experimental (—) and curve-fitting for Pt atoms (–▲–)

Table 30.3 Results of curve-fitting analysis for Zr-cation shells[a]

Sample	Bond	CN	R (Å)	$\Delta\sigma^2$ (Å^2)[b]
Cubic ZrO_2[c]	Zr–Zr	12	3.628	
CZ55-1	Zr–Zr	6.6(2)	3.66(0)	0.0061(1)
CZ55-2	Zr–Zr	3.0(6)	3.69(0)	0.0124(19)
	Zr–Ce	4.0(3)	3.76(0)	0.0030(3)
CZ55-3	Zr–Zr	6.0(4)	3.62(0)	0.0086(6)
	Zr–Ce	6.0(3)	3.75(0)	−0.0010(1)

[a]The standard deviation is given in parentheses
[b]Relative Debye–Waller factor
[c]8 mol% Y-doped cubic ZrO_2 as standard compound

According to its thermodynamic phase diagram, PtO_2 decomposes to metallic Pt under oxidizing conditions at 600 °C and above; [17] therefore, our finding that the Pt on Al_2O_3 was in the metallic state after aging at 800 °C is consistent with thermodynamic expectations. In contrast, the Pt on CZY was still in the oxidized state after aging, which suggests that there is some kind of interaction between the supported Pt and the CZY that stabilizes the oxidation state of Pt.

FTs of the Pt L_3-edge EXAFS spectra performed over the range 3.0–16.0 Å^{-1} are presented in Fig. 30.5b. Table 30.3 summarizes the curve fitting results from the EXAFS spectra for the inverse FTs of the Pt-oxygen and Pt-cation (cation = Pt, Ce, and Zr) shells. The FT of Pt/Al_2O_3 is seen to coincide with that of Pt foil, and the peaks at 2.76 Å in the FTs of both samples are assigned to Pt–Pt bonds. The CN of the Pt–Pt bond of Pt/Al_2O_3 was determined to be 11.5, indicating that the average diameter of the Pt particles was at least 20 nm [18]. However, the FT of the Pt/CZY

was different from those of both Pt foil and PtO_2; the first neighboring peak is found at 2.02 Å in the FT of Pt/CZY but at 2.04 Å for PtO_2. These peaks were assigned to Pt–O bonds. The second neighboring peak in the FT of Pt/CZY was found at 3.01 Å, which is below that of PtO_2. Figure 30.5c shows the curve fitting results for the second peak of Pt/CZY, based on the supposition that the second neighboring atom was Ce or Pt. It is evident that there is excellent agreement between the experimental and simulation results for Ce, although appropriate fitting could not be obtained for Pt. Curve fitting analyses for the second neighboring atoms, Zr and Y, were also conducted, but again appropriate results could not be obtained. From these results it is concluded that the second neighboring element of the Pt in Pt/CZY is Ce and that the Pt supported on CZY forms Pt–O–Ce bonds during aging at 800 °C. The CN of the Pt–Ce bond was determined to be 3.5, a relatively small value compared to that of 12.0 derived for the cubic fluorite structure. This result suggests that the Pt on the CZY support is highly dispersed and also present on the surface of the CZY.

The findings of this study indicate that the Pt supported on CZY interacts with the Ce in the same support and forms Pt–O–Ce bonds at high temperatures under an oxidizing atmosphere, resulting in less sintering of the Pt particles. Since the Pt supported on Al_2O_3 does not undergo sufficient interaction to form Pt-support bonds and is able to diffuse on the support, it undergoes aggregation into Pt particles.

30.3.1 Operando *XAFS Analysis of the Pt/Al_2O_3 Catalyst*

The *operando* spectroscopic method was recently introduced in catalysis research [19–24]. This technique allows the spectroscopic investigation of the catalyst during the actual reaction, with simultaneous assessments of activity, selectivity and stability. Since the catalytic reaction efficiency is affected by the state of the catalyst, such as the oxidation state of the supported metal, the surface structure and the surface composition, this *operando* approach is a very powerful technique for understanding the relationship between the state of the catalyst and the catalytic efficiency under working conditions. Recently, high speed XAFS has been made available as the result of the high intensity X-rays being generated in synchrotron radiation facilities [25, 26]. With these advanced techniques, it is possible to observe dynamic changes in the catalyst throughout the reaction using time-resolved XAFS experiments. This makes XAFS a very powerful tool for the analysis of automotive catalysts because reaction conditions are always transient during the operation of a motor vehicle. This section reports the results of *operando* experiments using the XAFS technique to study Pt-supported catalysts during the oxidation of C_3H_6 [19].

In order to perform *operando* XAFS analysis, both in situ XAFS instrumentation and a system to evaluate catalytic activity are required. Figure 30.6 shows a

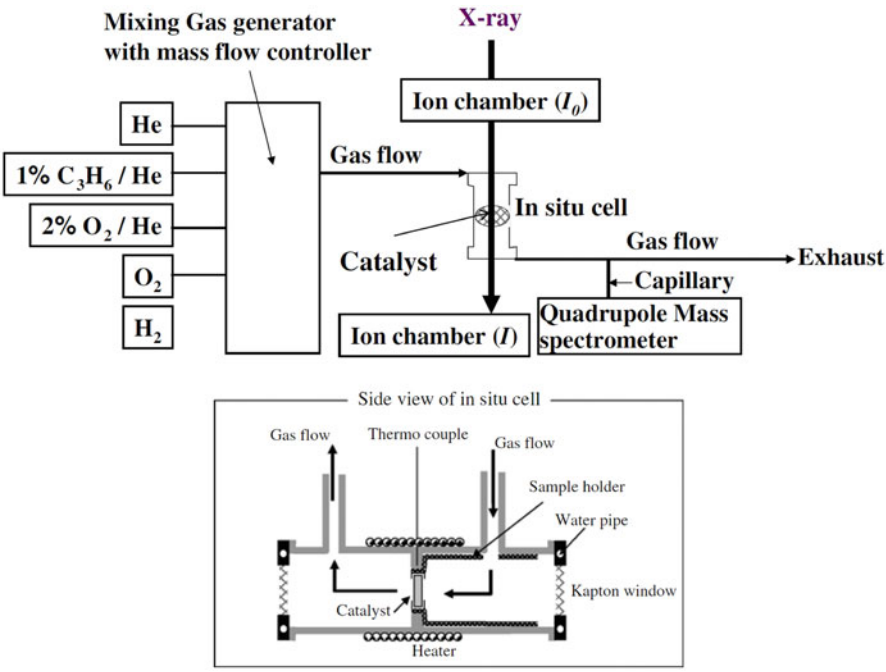

Fig. 30.6 Diagram of the experimental set up for the *operando* XAFS investigations and side view of the *operando* cell

diagram of the *operando* XAFS analysis system used by Tanabe et al., consisting of a transmission XAFS cell, a gas generator to supply reaction gases to the cell and a quadrupole mass spectrometer to evaluate the effluent gas coming from the cell. In the experiments, a catalyst composed of Pt (1 wt%) supported on Al_2O_3 was used. The catalyst sample was first formed into a disk and placed in the in situ cell, after which it was reduced in 3 % H_2 in He followed by oxidized in 20 % O_2 in He at 500 °C as a pretreatment. After the pretreatment, the flow was switched so as to supply the reaction gas (0.6 % O_2 and 0.1 % C_3H_6 in He) at room temperature and the sample was heated to 500 °C at 10 °C/min. During this temperature ramp, XANES spectra were recorded at one minute intervals and the catalytic reaction was monitored at one second intervals by measuring the concentrations of effluent gases. Figure 30.7 presents the changes in the Pt L_3-edge XANES spectra during the temperature ramp. Following the oxidizing pretreatment at 500 °C, a strong white line corresponding to oxidized Pt is observed at the beginning of the reaction. The white line intensity decreases as the temperature increases up to 200 °C, meaning that some portion of the oxidized Pt was reduced during the reaction even under oxidizing conditions. The white line intensity then begins to increase above 200 °C, indicating reoxidation of the Pt. The fraction of oxidized Pt could be estimated from the white line intensity, based on the assumption of a linear trend between the oxidation states of PtO_2 and Pt foil, representing 100 % and 0 % oxidized,

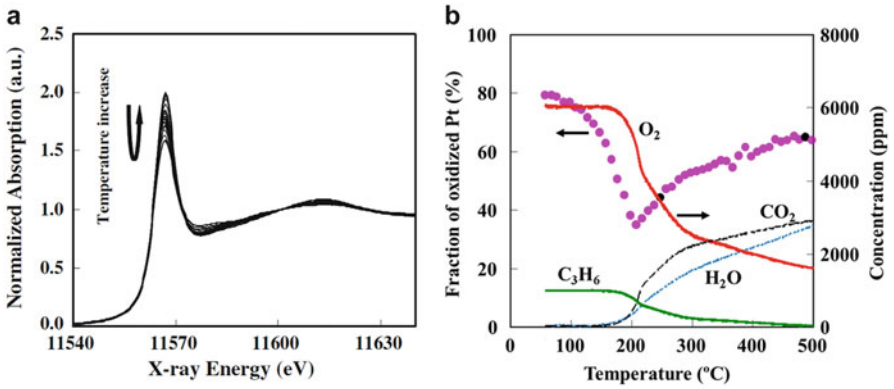

Fig. 30.7 (**a**) The Pt L_3-edge XANES spectra acquired during the C_3H_6 oxidation reaction (0.6 % O_2 and 0.1 % C_3H_6 in He, total flow of 100 mL/min) and (**b**) variations in the fraction of oxidized Pt and the concentrations of C_3H_6, O_2, CO_2, and H_2O during the reaction as functions of temperature

respectively. While the XANES spectra were being acquired, the catalytic reaction in the *operando* cell was monitored by quantifying the outlet gases using the mass spectrometer. The concentration changes in the gas species and the fraction of oxidized Pt are plotted versus reaction temperature in Fig. 30.7b. The concentrations of O_2 and C_3H_6 both decreased at a temperature of approximately 160 °C while, at the same time, CO_2 and H_2O began to form. These changes indicate that the catalytic C_3H_6 oxidation reaction started at that temperature. After the onset of the catalytic reaction, Pt reduction proceeded and the conversion increased as the temperature ramped up. The fraction of oxidized Pt began to increase above 200 °C and was increased to about 60 % at 500 °C.

Figure 30.8 shows the overall *operando* results, plotted as the fraction of metallic Pt and the C_3H_6 conversion (chosen as an indicator of the catalytic activity) vs. temperature. The temperature range can be divided into three regions, as indicted in the figure. In region I, the oxidized Pt is reduced gradually without any catalytic C_3H_6 conversion, while in region II the Pt is reduced along with increasing catalytic conversion. In region III, the Pt is reoxidized while the catalytic conversion increases as the temperature is increased. Figure 30.9 provides diagrams of the proposed mechanisms corresponding to each temperature region.

In region I, the fraction of metallic Pt increases, although no C_3H_6 conversion is observed. This suggests a self-poisoning effect during the C_3H_6–O_2 reaction over the Pt surface, through preferential adsorption of C_3H_6 instead of O_2 on the Pt surfaces. Although the adsorbed C_3H_6 is expected to reduce the oxidized Pt, no catalytic reaction is observed because the temperature is not high enough to break the C–C bonds of the adsorbed C_3H_6. In region II, some conversion of C_3H_6 is observed and the conversion rate increases as the temperature is increased. The reaction in this region is believed to be controlled by the number of the active sites, because the conversion of C_3H_6 is below 30 %. The surface area covered by

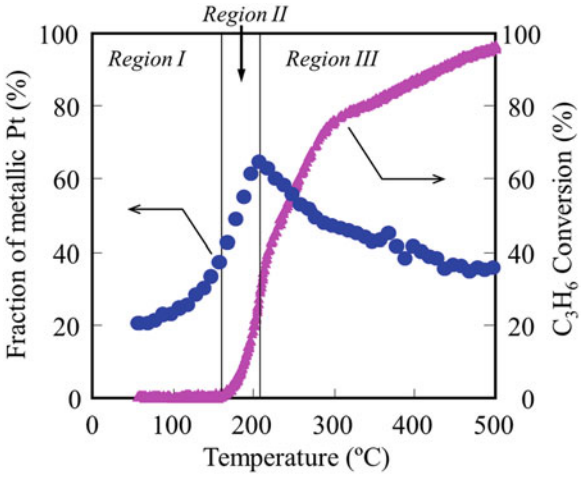

Fig. 30.8 The temperature dependencies of the metallic Pt fraction and the conversion rate during catalytic C_3H_6 oxidation over Pt/Al_2O_3. Legend: metallic Pt fraction (*filled circle*), C_3H_6 conversion (*filled triangle*)

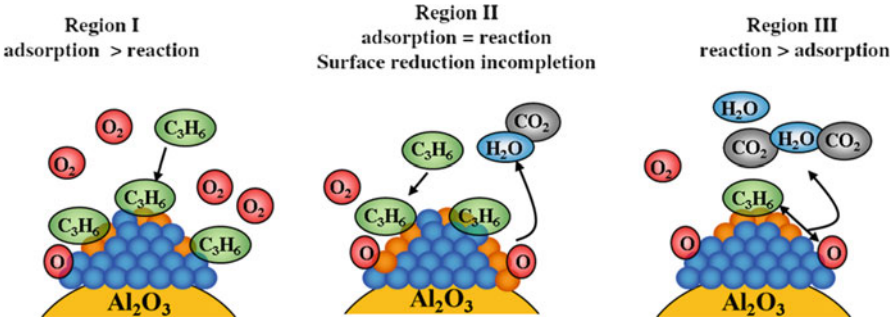

Fig. 30.9 Proposed mechanisms for catalysis in regions I, II, and III during the oxidation reaction. Legend: = oxidized Pt, = metallic Pt

metallic Pt therefore appears to be associated with the extent of the catalytic reaction. In region III, the metallic Pt fraction decreases with increasing temperature. In contrast, the conversion of C_3H_6 steadily increases to over 30 % in this region, and hence, the area covered by metallic Pt evidently does not completely correlate with the progression of the catalytic reaction. Therefore, the presence of a certain amount of the metallic Pt appears to promote the catalytic reaction, although there are apparently other factors involved. The loss of metallic Pt in region III is believed to occur through oxidation by residual oxygen following the conversion reaction, as shown in Fig. 30.9.

The *operando* analysis in this work allowed assessments of the oxidation state of Pt in the catalyst and its effect on the activation process. These studies demonstrated that the early stage of the catalytic activation consists of a combination of the creation of active sites and a catalytic reaction over these sites. This result indicates that the formation of metallic Pt sites and the activation of adsorbed

species on Pt are both important to the progression of the catalytic reaction at low temperatures. More generally, this project has also shown that *operando* spectroscopy is a very useful technique for understanding the behavior of automotive catalysts.

References

1. Matsumoto S, Miyoshi N, Kimura M (1999) Haikigasu-zyouka-you shokubai (Exhaust emission control catalyst) Japanese Patent No. 2140560
2. Matsumoto S, Miyoshi N, Kanazawa T, Kimura M, Ozawa M (1991) In: Yoshida S, Tabezawa N, Ono T (eds) Catalysis science and technology, vol 1. Kodansha/VCH, Tokyo/Weinheim, p 335
3. Ozawa M, Kimura M, Isogai A (1993) The application of Ce·Zr oxide solid solution to oxygen storage promoters in automotive catalysts. J Alloys Compd 193:73–75
4. Nagai Y, Yamamoto T, Tanaka T, Yoshida S, Nonaka Okamoto T, Suda A, Sugiura M (2002) X-ray absorption fine structure analysis of local structure of CeO_2–ZrO_2 mixed oxides with the same composition ratio (Ce/Zr = 1). Catal Today 74:225–234
5. Vlaic G, Fornasiero P, Geremia S, Kašpar J, Granziani M (1997) Relationship between the Zirconia-Promoted reduction in the Rh-loaded $Ce_{0.5}Zr_{0.5}o_2$mixed oxide and the Zr–O local structure. J Catal 168:386–392
6. Li P, Chen IW, Penner-Hahn JE (1994) Effect of dopants on zirconia stabilization—an X-ray absorption study: II, tetravalent dopants. J Am Ceram Soc 77:1281–1288
7. Teo BK (1986) EXAFS: basic principles and data analysis. Springer, Berlin
8. Li P, Chen IW, Penner-Hahn JE (1993) X-ray-absorption studies of zirconia polymorphs: I. Characteristic structures. Phys Rev B 48:10063–10073
9. Li P, Chen IW, Penner-Hahn JE (1993) X-ray-absorption studies of zirconia polymorphs: II. Effect of Y_2O_3 dopant on ZrO_2 structure. Phys Rev B 48:10074–10081
10. Harris PJF (1986) The sintering of platinum particles in an alumina-supported catalyst: further transmission electron microscopy studies. J Catal 97:527–542
11. Fiedorow RMJ, Chahar BS, Wanke SE (1978) The sintering of supported metal catalysts: II. Comparison of sintering rates of supported Pt, Ir, and Rh catalysts in hydrogen and oxygen. J Catal 51:193–202
12. Bartholomew CH (2001) Mechanisms of catalyst deactivation. Appl Catal A Gen 212:17–60
13. Birgersson H, Eriksson L, Boutonnet M, Järås SG (2004) Thermal gas treatment to regenerate spent automotive three-way exhaust gas catalysts (TWC). Appl Catal B Environ 54:193–200
14. Yao HC, Yao HF (1984) Ceria in automotive exhaust catalysts: I. Oxygen storage. J Catal 86:254–265
15. Su EC, Rothschild WG (1986) Dynamic behavior of three-way catalysts. J Catal 99:506–510
16. Nagai Y, Hirabayashi T, Dohmae K, Takagi N, Minami T, Shinjoh H, Matsumoto S (2006) Sintering inhibition mechanism of platinum supported on ceria-based oxide and Pt-oxide–support interaction. J Catal 242:103–109
17. Livingstone SE (1973) Pergamon Text Inorg Chem 25
18. Greegor RB, Lytle FW (1980) Morphology of supported metal clusters: determination by EXAFS and chemisorption. J Catal 63:476–486
19. Tanabe T, Nagai Y, Dohmae K, Takagi N, Takahashi N, Shinjoh H (2009) Operando X-ray absorption spectroscopy study of Pt/γ-Al_2O_3 during the total oxidation of C_3H_6. Top Catal 52:1433–1439
20. Tanabe T, Nagai Y, Dohmae K, Takagi N, Takahashi N, Matsumoto S, Shinjoh H (2011) Operando X-ray absorption spectroscopy study of supported Pt catalysts during NO reduction by hydrocarbons. Appl Catal B Enviorn 105:41–49

21. Nagai Y, Tanabe T, Dohmae K (2015) *Oprando* XAFS study of automotive exhaust catalysts. R&D Rev Toyota CRDL 46:11–19
22. Newton MA, Belver-Coldeira C, Martínez-Arias A, Fernández-García M (2007) Dynamic *in situ* observation of rapid size and shape change of supported Pd nanoparticles during CO/NO cycling. Nat Mater 6:528–532
23. Topsøe H (2003) In situ characterization of supported metal catalysts and model surfaces by time-resolved and three-dimensional XAFS techniques. J Catal 216:155–164
24. Guerrero S, Miller JT, Kropfc AJ, Wolf EE (2009) *In situ* EXAFS and FTIR studies of the promotion behavior of Pt–Nb_2O_5/Al_2O_3 catalysts during the preferential oxidation of CO. J Catal 262:102–110
25. Nonaka T, Dohmae K, Araki T, Hayashi Y, Hirose Y, Uruga T, Yamazaki H, Mochizuki T, Tanida H, Goto S (2012) Quick-scanning x-ray absorption spectroscopy system with a servo-motor driven channel-cut monochromator with a temporal resolution of 10 ms. Rev Sci Instrum 83:083112
26. Ferrer S, Petroff Y (2002) Surface science done at third generation synchrotron radiation facilities. Surf Sci 500:605–627

Chapter 31
Solid–Liquid Interfaces

Takuya Masuda, Toshihiro Kondo, and Kohei Uosaki

31.1 Introduction

The structural study at solid–liquid interfaces, i.e., electrode–electrolyte interfaces, is one of the key targets not only of fundamental surface science but also of various applied sciences such as fuel cells, sensors, and batteries, because many important processes, such as adsorption/desorption, solvation/desolvation, and the electrode reaction itself, take place at the electrode–electrolyte interfaces. It is essential to clarify the electronic and geometric structures at these interfaces with atomic dimensions, in situ, and in real time [1–3]. Various surface analysis methods, such as scanning electron and transmission electron microscopies (SEM and TEM, respectively), low-energy electron diffraction (LEED), and X-ray photoelectron spectroscopy (XPS), using electrons as a probe are powerful tools to determine the surface geometric structures and/or electronic states in a vacuum. Because of their vacuum requirement, however, these methods cannot be used to study electrode–electrolyte interfaces in situ.

Since the 1980s, several surface analysis methods, such as scanning probe microscopy (SPM) [4, 5], surface X-ray scattering (SXS) [6, 7], and nonlinear spectroscopy [8, 9], have been developed to investigate the geometric structures and electronic states at electrode–electrolyte interfaces with an atomic resolution under electrochemical potential control, i.e., in situ. However, these techniques still have intrinsic limitations. SPM can determine the geometric structure with a high spatial resolution, but only of the outermost surface layer. Although SXS can determine the three-dimensional structure at electrode–electrolyte interfaces with a high spatial resolution, it is essential to use a single crystal as the electrode.

T. Masuda • T. Kondo (✉) • K. Uosaki
Global Research Center for Environment and Energy based on Nanomaterials Science (GREEN), National Institute for Materials Science (NIMS), Tsukuba 305-0044, Japan
e-mail: kondo.toshihiro@ocha.ac.jp

Y. Iwasawa et al. (eds.), *XAFS Techniques for Catalysts, Nanomaterials, and Surfaces*, DOI 10.1007/978-3-319-43866-5_31

Optical spectroscopies using ultraviolet, visible, and infrared lights have a high time resolution, but not a high enough spatial resolution.

The X-ray absorption fine structure (XAFS) technique, as documented in the previous chapters, provides a lot of information about both the three-dimensional geometric and electronic structures at electrode–electrolyte interfaces with atomic dimensions, both in situ and in real time [1, 2, 6, 10]. Because X-rays transmit through the electrolyte solution without any significant interactions, X-rays are considered to be an ideal probe for the structural analysis of electrode–electrolyte interfaces. In order to obtain the signal from the electrode–electrolyte interfaces with a high signal-to-noise (S/N) ratio and to use an incident X-ray source with a continuous wavelength distribution, however, in situ XAFS measurements at the electrode–electrolyte interfaces usually require synchrotron radiation light as the X-ray source.

Moreover, XAFS has the following few advantages over SPM and SXS: (1) XAFS is applicable not only to single crystal flat surfaces but also to polycrystalline surfaces and nanoparticles because it is unnecessary for this technique to use the sample with a long range order, (2) XAFS can analyze not only the local geometric structure, but also the electronic structure of the target atom, and (3) XAFS can selectively detect the signal from the target atom. Therefore, it has been utilized for a variety of electrode–electrolyte interfaces such as single-/polycrystal surfaces, thin films, and nanoparticles.

During the early stage, research studies of the electrode–electrolyte interfaces using the in situ XAFS technique focused on the adsorbed species on the electrode surface [11–13], surface oxide [6, 14–21], and electrodeposited metal layers on the metal [22–24] and semiconductor [25–27] electrode surfaces. The targets of the in situ XAFS studies were then expanded to a wide range of applications such as polymer electrolyte membrane fuel cells (PEMFCs) [14, 28–34] and Li ion batteries (LIBs) [28, 35]. Because the studies of PEMFCs and LIBs were summarized in detail in Chapters 22 and 23, respectively, we focus on the more fundamental systems. In this section, the experimental setups for electrode–electrolyte interfaces, which are keys for the in situ XAFS measurements, are briefly described and then the recent topics of the in situ XAFS studies, especially the structural determinations of electrodeposited metal thin films on various substrate electrodes and clarifications of the mechanism of multi-electron transfer reactions of electrocatalysts, are reviewed.

31.2 Experimental Methodology

Since XAFS is not inherently surface sensitive due to the relatively long penetration depth of the X-rays, the obtained signal is often buried within information from the bulk, which is not involved in the electrochemical reactions. Thus, various in situ electrochemical cells have been developed to selectively extract the signal from the

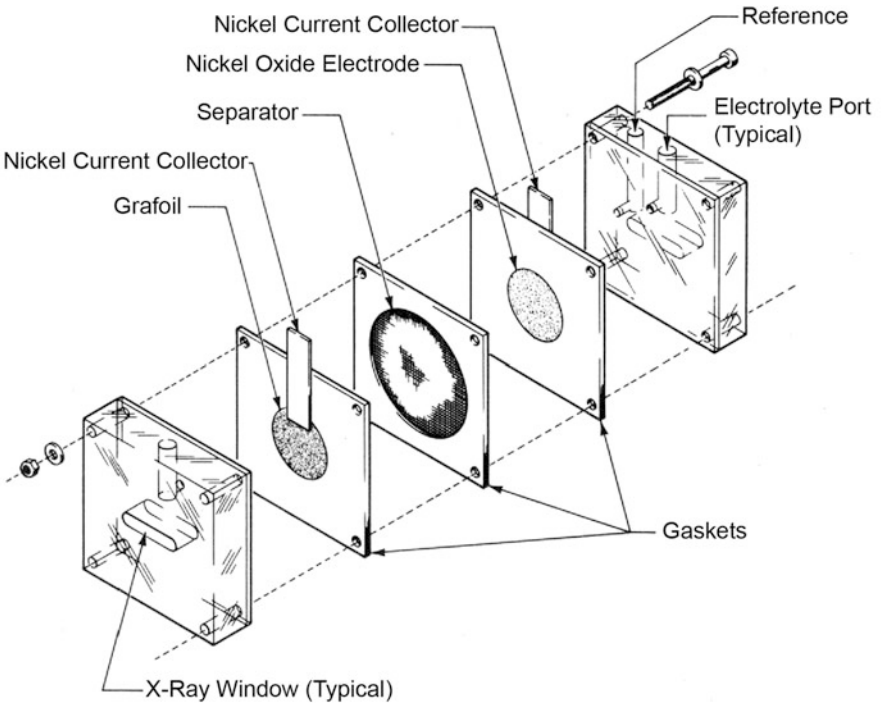

Fig. 31.1 Schematic illustration of typical in situ electrochemical cell for the transmission mode [14]

target atom at the electrode–electrolyte interfaces. The typical configuration of the electrochemical cell for the in situ XAFS measurements in the transmission mode, as shown in Fig. 31.1, was reported in the late 1980s [14, 28, 36, 37]. In this electrochemical cell, a thin metal layer, used as the working electrode, is deposited on the window (Mylar® or Kapton® film) of conventional thin layer liquid cells. This basic configuration is still widely used for various electrochemical systems [37] and these transmission cells are suitable for thin films and nanoparticlesdeposited on the electrode surface. Using a similar configuration, the membrane electrode assembly (MEA), which is constructed by binding carbon-supported catalyst layers on both sides of the electrolyte membranes, in the PEMFC was straightforwardly measured to study the reaction mechanisms [29–34].

As compared to the transmission mode, on the other hand, the fluorescence mode is more useful for in situ studies at electrode–electrolyte interfaces in the following cases: (1) the quantity of the target material is too small to detect the difference between the incident and transmitted X-ray intensities, and/or (2) the thickness of the sample is too thick for X-rays to transmit. Electrochemical cells in the thin layer configuration [11, 38–40], which are used for in situ SXS measurements, are also employed for in situ XAFS measurements in the fluorescence mode.

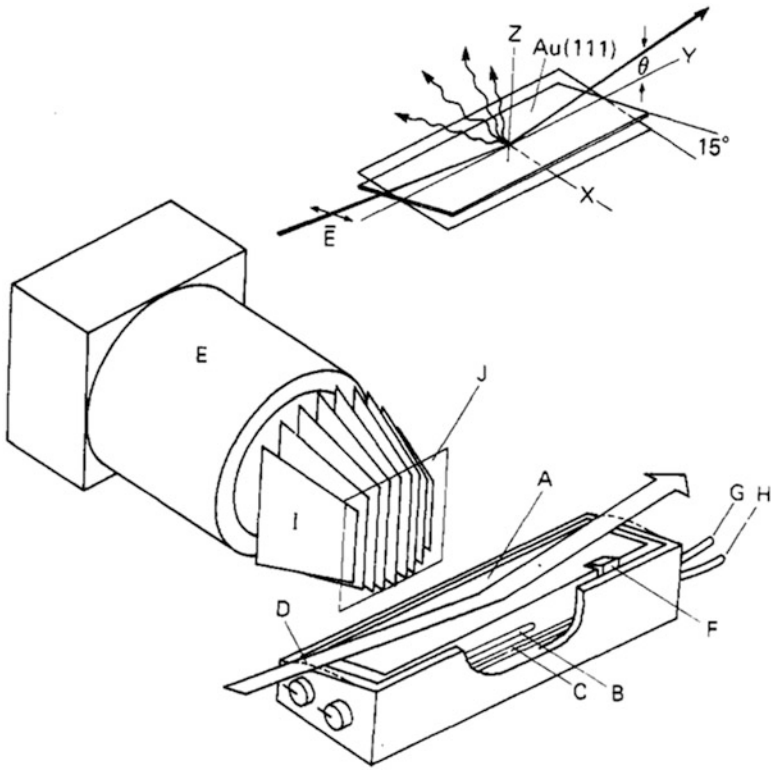

Fig. 31.2 Schematic illustration of typical in situ electrochemical cell and experimental setup for the fluorescence mode: gold(111) film on mica (*A*); Ag/AgCl reference electrode (*B*); Pt counter electrode (*C*); 13-μm polypropylene film (*D*); solid-state detector (*E*); gold wire working electrode contact (*F*); solution inlet and outlet (*G*, *H*); Soller slits (*I*); Ni filter (*J*). *Inset*: X-ray geometry and appropriate angles. The beam is incident on the sample at a grazing incidence ($\theta > 89°$), and the polarization of the *E*-vector is 15° off parallel to the surface [40]

Significant X-ray scattering from the electrolyte solution layer can be avoided when the thickness of the solution layer is less than several tens of μm, as shown in Fig. 31.2 [40].

This configuration can be used for the total reflection fluorescence mode, which enables the surface sensitive analysis, typically at a depth of several nm. Furthermore, since EXAFS oscillations are sensitive to the angle between the bond direction and polarization vector of the incident X-ray, polarization-dependent measurements can be performed by employing this configuration. A disadvantage of this thin-layer configuration is, however, suppression of the effective mass transfer due to the thin electrolyte layer. In order to obtain an effective mass transfer, the backside illumination fluorescence configuration was proposed [15, 16]. In this configuration, a thin metal layer coated on a thin film window is used as the working electrode as in the case of the transmission cells and it is

exposed to the sufficiently thick electrolyte solution layer. The backside of the working electrode (window) is irradiated by the incident X-rays and the fluorescent X-rays, which emit at the electrode–electrolyte interface, can be detected through the window. Various window materials, such as Si_3N_4 [41], polyimide [42], poly (dimethylsiloxane) (PDMS) [43], and a graphite layer peeled from highly oriented pyrolytic graphite (HOPG) [44], have recently been employed for the in situ XAFS measurements in the fluorescence mode.

31.3 Topics of In Situ XAFS at Electrode/Electrolyte Interfaces

31.3.1 Metal Deposition on Single Crystalline Metal and Semiconductor Electrodes

Since deposition of a metal monolayer and submonolayer on a foreign metal substrate can strongly modify the reactivity and electrocatalytic activity, well-defined metal layers deposited on single crystal electrode surfaces, such as an underpotentially deposited (UPD) metal monolayer, have been investigated by various in situ techniques including SPM, SXS, and XAFS. There is an advantage of in situ XAFS over SPM and SXS for investigating electrochemically deposited metal layers; in situ XAFS can selectively probe not only the local structure, but also the oxidation state of the target atoms.

Cu UPD is one of the most studied systems because Cu K-edge spectra of various Cu-based compounds are available as references. In addition, the atomic arrangement of electrodeposited Cu layers have been determined by SPM [45–48], SXS [48–51], and several optical spectroscopies [48, 52]. In situ XAFS characterization of a Cu UPD layer on the Au(111) single crystal electrode was first performed by Abruña et al. [22, 40]. Fitting of the EXAFS oscillation at the Cu K-edge showed that Cu atoms in the UPD monolayer exist at the three-fold hollow site of the Au(111)-(1×1) surface with a (1×1) structure, and an oxygen species adsorbs on the atop site of the deposited Cu atoms. Tadjeddine et al. then systematically showed that the Cu UPD monolayer is epitaxial on the Au(111) surface and the oxidation state of Cu is close to Cu^+ [23]. On the way to the formation of Cu (1×1) monolayer on Au(111), the initial stable arrangement of adsorbed Cu atoms was found to be a $(\sqrt{3} \times \sqrt{3})R30^\circ$ hexagonal honeycomb arrangement [23, 24, 53, 54]. At the potential where this Cu adatom structure forms, it was confirmed that the sulfate anion is also coadsorbed in the $(\sqrt{3} \times \sqrt{3})R30^\circ$ structure on the Au(111) surface (Fig. 31.3). This initial $(\sqrt{3} \times \sqrt{3})$ structure of a ca. 0.3 monolayer became equilibrated with a $c(5 \times 5)$ structure (Fig. 31.4) [23].

The effect of the coadsorption of a chloride anion on the structure of the Cu UPD layer on Au(111) was investigated by in situ XAFS and FEFF multiple scattering

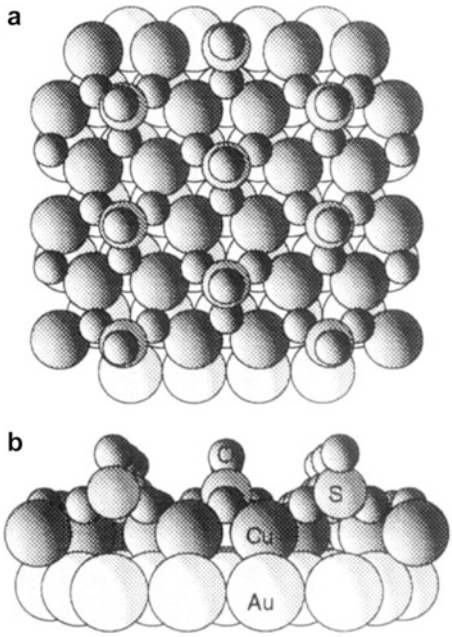

Fig. 31.3 Model for the honeycomb ($\sqrt{3} \times \sqrt{3})R30°$ structure of Cu and sulfate coadsorbed on Au(111) surface: (**a**) top view, (**b**) side view [54]

calculations by Wu et al. [55]. The in situ XAFS results showed a remarkable dichroism consistent with a bilayer in which the Cu adatoms are covered by chloride anions. Previous scanning tunneling microscopy (STM) results suggested either the (5×5) structure, which is similar to that of the (111) plane of a CuCl single crystal or a (4×4)-based structure [46, 56, 57]. From the FEEF calculations, it was concluded that there is a large degree of static disorder. An in situ XAFS study of the electrodeposited Cu monolayer and multilayer was also carried out in alkaline solution [58].

There were also many reports about the in situ XAFS analysis of electrodeposited Cu on the Pt(111) system. The effect of the halide ions on the adsorbed structure of Cu was studied by Abruña et al. [59–62]. It was concluded that at a potential of +0.1 V (vs. Ag/AgCl) corresponding to a coverage of ca. 0.75 monolayer, the electrodeposited Cu is incompletely discharged with a Cu–Cu bond length of 2.85 Å and oxygen species (from either bisulfate anion or water molecule) is present on the Cu adlayer with a Cu–O bond length of 2.16 Å in the absence of Cl^-. In the presence of Cl^-, on the other hand, the atomic arrangement of the electrodeposited Cu is the same as in the absence of Cl^-, but no Cu–O bond is formed at the Cu adlayer, indicating that Cl^- acts as a protective overlayer precluding the adsorption of oxygen species. When the fully discharged Cu is formed on the Pt(111) surface, the Cu–Cu bond distance was observed to be 2.59 Å, which is close to the bulk Cu value (2.56 Å) in the presence of Cl^-. However, they did not describe in detail the Cu–Cl interaction that may be due to a low amount of and/or random orientation of the adsorbed Cl^-.

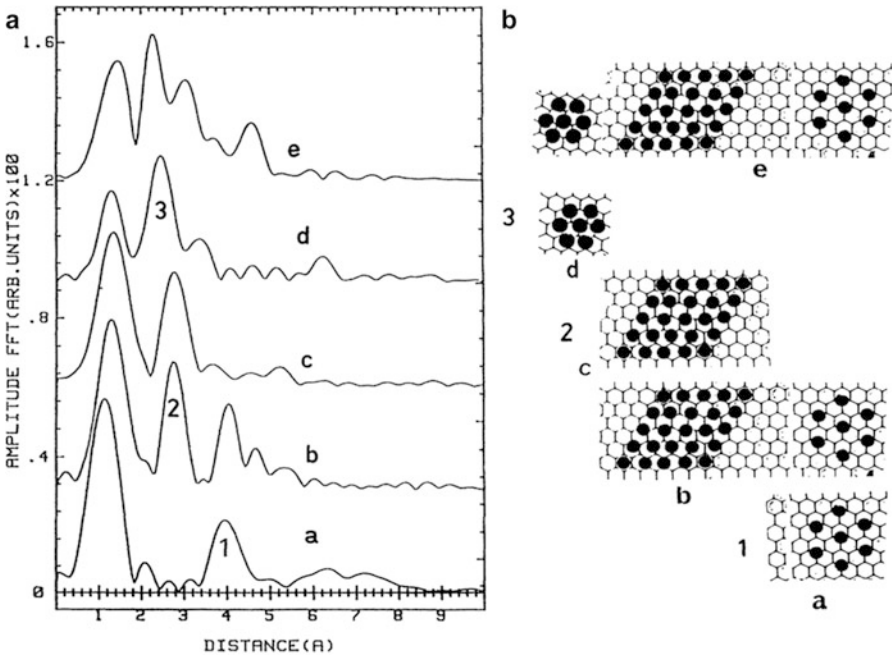

Fig. 31.4 (**a**) Fourier transforms of the Cu k^3-weighted EXAFS spectra, measured in 0.5 M Na_2SO_4 containing 0.1 mM $CuSO_4$ adjusted to a pH of 3 with H_2SO_4, and (**b**) corresponding model structures for Cu adlayers on Au(111): *a*, freshly deposited 0.3 mL; *b*, 0.3 mL after 1 h; *c*, 0.6 mL during the negative-going scan; *d*, 1 mL; and *e*, 0.6 mL during the positive-going scan. *Labels 1*, *2*, *3* refer to the $(\sqrt{3} \times \sqrt{3})R30°$, the $c(5 \times 5)$, and the (1×1), respectively, hexagonal arrangements of the Cu adlayer. In (**b**), *open* and *solid circles* represent Au and Cu atoms, respectively [24]

After the pioneering research by Abruña et al. [59–62], Soldo et al. investigated this system in detail using the fluorescence mode under grazing and normal X-ray incidence with FEFF theoretical calculations [63]. In the absence of Cl^-, there is a full monolayer of oxygen atoms at the atop site of the adsorbed Cu. The Cu–Cu bond distance is 2.68 Å, which is smaller than the Pt-Pt distance of 2.77 Å, suggesting that the Cu full monolayer is composed of bidimensional domains with (1×1) and three-fold hollow sites. In the presence of Cl^-, the position and structure of the Cu adlayer is the same as in the absence of Cl^-, but the oxygen atoms are replaced by chlorine atoms with the $(\sqrt{3} \times \sqrt{3})R30°$ superstructure. These analyzed EXAFS data in the absence and presence of Cl^- are summarized in Tables 31.1 and 31.2, respectively [63].

In addition to Cu on Au(111) and Pt(111), various UPD systems have been studied by in situ XAFS. In the late 1980s and 1990s, the geometric and electronic structures of electrodeposited Pb on Ag(111) [64], Ag on Au(111) [65], Cu on Au (100) [23, 66], and Ni on Au(100) [66] were investigated. The quality of the in situ XAFS spectra have been significantly improved by the developments of the

Table 31.1 Results of the FEFFIT analysis for a Cu monolayer on Pt(111) prepared in the absence of Cl^- at 0.2 V (vs. SCE) [63]

Scatterer	N_{deg} (FEFF)	E_0 (eV)	R (Å)	σ^2 (Å^2)	N_{deg}
Parallel polarization					
Path 1 Pt	1	2.8 ± 0.9	2.60 ± 0.01	0.008 ± 0.001	1.05 ± 0.13
Path 2 Pt	2	2.9 ± 0.9	2.60 ± 0.01	0.008 ± 0.001	2.1 ± 0.3
Path 3 Cu	2	1.0 ± 1.5	2.67 ± 0.01	0.021 ± 0.002	2.2 ± 0.4
Path 4 Cu	4	1.0 ± 1.5	2.67 ± 0.01	0.021 ± 0.002	4.4 ± 0.9
Perpendicular polarization					
Path 1 O	1	3.0 ± 1.4	1.96 ± 0.01	0.008 ± 0.002	1.02 ± 0.13
Path 2 Pt	3	2.8 ± 0.9	2.60 ± 0.01	0.008 ± 0.001	3.2 ± 0.4

Values of N_{deg} (FEFF) and N_{deg} represent number of equivalent paths obtained by the FEFF and FEFFIT calculations, respectively. Values of E_0, R, and σ^2 represent energy shift, interatomic distance, and Debye–Waller factor. In the FEFF calculation, values of reduced χ^2 of 10.7 and r-factor of 0.018 were used

Table 31.2 Results of the FEFFIT analysis for a Cu monolayer on Pt(111) prepared in the presence of Cl^- at 0.2 V (vs. SCE) [63]

Scatterer	N_{deg} (FEFF)	E_0 (eV)	R (Å)	σ^2 (Å^2)	N_{deg}
Parallel polarization					
Path 1 Pt	1	2.6 ± 1.1	2.62 ± 0.01	0.009 ± 0.0016	1.0 ± 0.2
Path 2 Pt	2	2.6 ± 1.1	2.62 ± 0.01	0.009 ± 0.0016	2.0 ± 0.35
Path 3 Cu	2	1.5 ± 1.7	2.68 ± 0.02	0.023 ± 0.003	2.0 ± 0.5
Path 4 Cu	4	1.5 ± 1.7	2.68 ± 0.02	0.023 ± 0.003	4.1 ± 0.9
Path 5 Cl	1	-1.6 ± 3.0	2.21 ± 0.02	0.008 ± 0.0037	1.1 ± 0.3
Perpendicular polarization					
Path 1 Cl	1	-1.6 ± 3.0	2.21 ± 0.02	0.008 ± 0.0037	1.1 ± 0.3
Path 2 Pt	3	2.6 ± 1.1	2.62 ± 0.01	0.009 ± 0.0016	3.0 ± 0.5

Values of N_{deg} (FEFF) and N_{deg} represent number of equivalent paths obtained by the FEFF and FEFFIT calculations, respectively. Values of E_0, R, and σ^2 represent energy shift, interatomic distance, and Debye–Waller factor. In the FEFF calculation, values of reduced χ^2 of 41.2 and r-factor of 0.023 were used

electronics, equipment, and electrochemical cells since the 2000s. For example, Prinz and Strehblow determined the structures of the Cu and Cd UPD layers on the high index surface of Pt(533) [67].

From the point of view of corrosion/inhibition, Lee et al. structurally studied the Zn UPD layer on Au(111) in the presence of the phosphate anion [68]. The in situ XAFS results showed that the structure of the Zn adatoms is the commensurate $(\sqrt{3} \times \sqrt{3})R30°$ at the coverage of 0.33 and reside within the three-fold hollow sites of the Au(111) surface. The structure of the coadsorbed phosphate anion is also the $(\sqrt{3} \times \sqrt{3})R30°$ structure where each phosphate ion bridges between three Zn adatoms and the central phosphorous atom resides above a vacant three-fold hollow site of the Au(111) surface (Fig. 31.5).

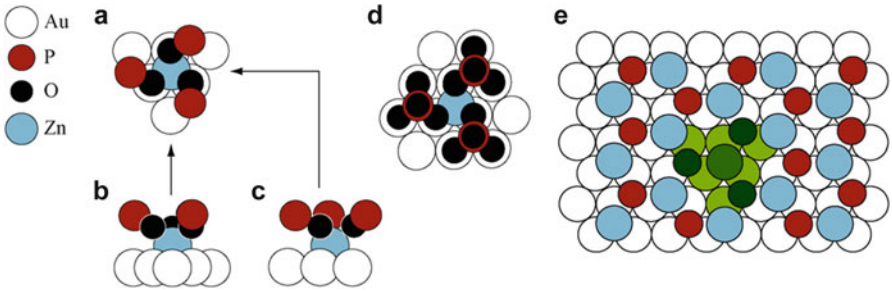

Fig. 31.5 Schematic illustrations of the local environment of Zn adatoms within the UPD adlayer on Au(111) from the phosphate supporting electrolyte. (**a**) Top view, (**b**), (**c**) side views. (**d**) A projection of the local environment displayed in (**a**). (**e**) The projection of this local environment over the Au(111) surface [68]

Lee et al. also performed in situ XAFS measurements of the Cu UPD monolayer formed on the Au(111) surface premodified with a self-assembled monolayer (SAM) of butanethiol (BT) in the total reflection mode which enables a surface-sensitive analysis and polarization-dependent measurements by using polarized X-rays [69]. Unfortunately, the S/N ratio of the spectra collected in the s-polarization was too low to allow it to be analyzed. Analysis of the p-polarization EXAFS data indicated that the Cu ions penetrate between the SAM and Au(111) surface. The Cu adatoms exist at the face-centered cubic three-fold hollow sites of the Au(111)-(1 × 1) surface. No information about Cu–Cu bond was obtained because it should be parallel to the surface and because the EXAFS oscillation at the K-edge is polarization sensitive (Fig. 31.6).

Structure analyzes of the electrodeposited metal layer on a semiconductor electrode were also reported. We investigated the local structures of electrodeposited Cu on p-GaAs(100) with various coverages by in situ XAFS [25–27]. In all the coverage ranges, fully discharged Cu nanoclusters formed on the p-GaAs(100) surface, but the length of Cu–Cu bond was dependent on the Cu nanocluster size. When the coverage is more than a 0.25 monolayer, the length of Cu–Cu bond is 2.56 Å, which is the same as that of the bulk Cu. When the coverage is less than a 0.25 monolayer, however, the bond length is shorter than that of the bulk Cu.

31.3.2 Metal Deposition on Polycrystalline Electrode and Nanoparticle Surfaces

Because XAFS can analyze the local structure not only of the single crystal electrode but also of the polycrystal, there were several structural studies of electrodeposited metal layers on polycrystal electrode and nanoparticle surfaces. Furtak et al. investigated the local environment of the electrodeposited Cu

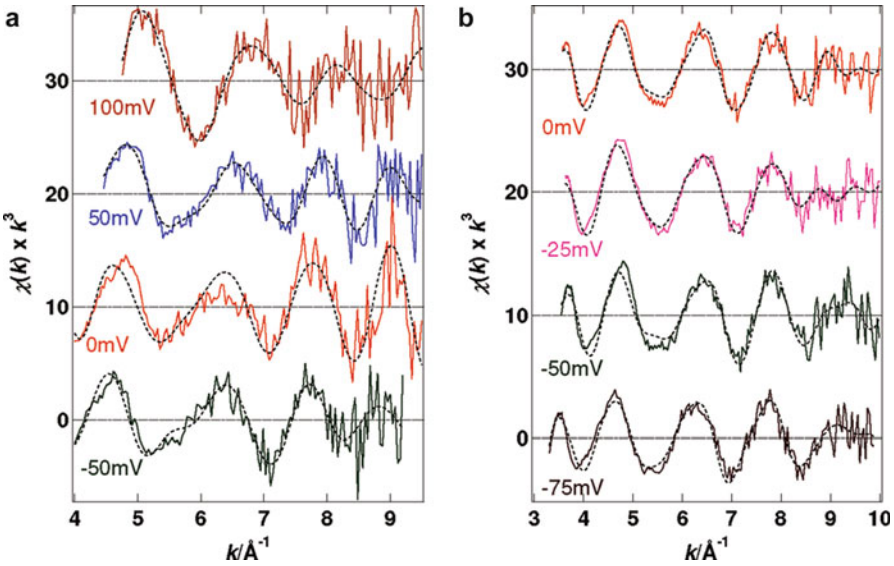

Fig. 31.6 The p-polarization Cu K-edge EXAFS spectra (*solid lines*) and theoretical models (*dashed lines*) for Cu UPD on (**a**) bare and (**b**) BT-SAM-modified Au(111) electrodes, measured in 0.1 M H_2SO_4 containing 0.5 mM $CuSO_4$ and saturated calomel electrode (SCE) was used as the reference electrode [69]

monolayer on the polycrystalline Pt electrode by in situ XAFS [70, 71]. The difference in the EXAFS spectra between the s- and p-polarizations showed that the surface has not reconstructed to the extent of eliminating the original surface plane. The distance from the Cu adatoms to oxygen, Pt, and Cu atoms are 2.06 Å, 2.58 Å, and 2.62 Å, respectively.

From the point of view of corrosion/inhibition, Seo et al. studied the structure of the electrodeposited Pb [72] and Sn [73] on Ni polycrystalline electrodes by in situ XAFS. In the case of Pb, at the potential more positive than −0.245 V (vs. SHE), which is the equilibrium potential of Pb, the XANES spectrum showed that the electrodeposited Pb is metallic, indicating the UPD Pb on the Ni surface. EXAFS data showed that the Pb–Ni bond length is 2.64 Å, which is significantly shorter than that (3.00 Å) calculated from the radii of the bulk Pb and Ni, suggesting that the Pb–Ni bond is covalent. The EXAFS results also suggested the coexistence of the surface alloy phase. In the case of Sn, electrodeposited Sn atoms are substituted at the fcc sites in the first Ni layer with the Sn-Ni bond distance of 2.55−2.57 Å and an oxygen species is adsorbed on the substituted Sn with a bond length of 2.03−2.04 Å. This structure is independent of the Ni electrode potential. A relatively short Sn-O bond suggests the formation of a strong covalent bond of Sn-Ni like a surface alloy. The adsorption of oxygen species on the Sn atoms in addition to the strong covalent bond of Sn-Ni prevents the anodic stripping of the Sn UPD layer, indicating a strong inhibition effect of Sn on the aqueous corrosion of Ni.

A significant number of in situ XAFS studies on the metal nanoparticle surfaces have been carried out because of their potential applications for electrocatalysts. Especially, metal deposited nanoparticles are the most studied system in conjunction with PEMFCs [14, 28–34].

McBreen and coworkers investigated the geometric and electronic structures of electrodeposited Cu [22] and Pb [74] on the carbon-supported Pt surface. In the case of Cu, the Cu K-edge XANES spectrum showed that the electrodeposited Cu has an oxidation state close to Cu^+ and a tetrahedral coordination for the electrodeposited Cu species. Pt L_{III}-edge XANES spectrum showed a partial filling of the d-band vacancies of Pt upon the adsorption of Cu. Electrodeposited Cu^+ species are apparently associated with the sulfate anion when used as an electrolyte, which is the same feature as Cu UPD on Pt(111) [59–63]. Recently, Jia et al. investigated the electrodeposition of Cu on carbon-supported Pt nanoparticles over the potential range of the PEMFC operation and explored the poisoning effects of Cu on both the oxygen reduction and hydrogen oxidation [75]. In the case of Pb, the XANES spectra showed that the oxidation state of the Pb UPD layers is essentially zero but the oxidation state is +2 in the potential region more positive than the main UPD peak in the cyclic voltammogram (CV). These features are the same as the Pb electrodeposited on the Ni polycrystalline electrode [72]. EXAFS oscillation was fitted on the basis of a two-shell fit (Pt–Pb and Pb–Pb) in the potential region more negative than the second UPD peak (5 UPD peaks were observed between 0.4 V and −0.3 V) in the CV, indicating the formation of Pb and Pt in this potential region. However, the EXAFS oscillation was fitted to a simple single Pb–Pt coordination shell in this potential region, indicating a high degree of lateral disorder in the electrodeposited Pb layer. There is no interaction of Pb with oxygen species in the UPD region.

In order to clarify the origin of the difference in the electrocatalytic activities for the methanol oxidation between the UPD Sn on the carbon-supported Pt and carbon-supported SnPt alloy, in situ XAFS measurements were carried out by McBreen and Mukerjee [76]. In the SnPt alloy, alloying with Sn causes partial filling of the d band vacancies of Pt and an extension of the Pt–Pt bond from 2.77 to 2.8 Å. For the UPD Sn, on the other hand, Pt is not structurally and electronically affected by the formation of the Sn UPD layer (Fig. 31.7). In the entire potential range, the surface Sn atoms are associated with oxygen species and the nature and strength of the Sn-O bonds are varied by the applied potential. They concluded that the differences in the electrocatalytic activity of the two catalysts for methanol oxidation are due to the effects of alloying on the electronic structure of Pt that inhibit the ability of the Pt to adsorb methanol and dissociate C–H bonds.

In order to study the effect of Ru modification on the carbon monoxide tolerance to the Pt catalyst for the PEMFCs, the geometric and electronic structures of Ru-modified carbon-supported Pt were investigated by in situ XAFS [77–85]. Ramaker et al. carried out a series of in situ XAFS studies on carbon-supported Pt_nRu, Pt_nMo, and PtSn electrocatalysts [79–83]. Based on the potential dependent coverages of CO, OH, and H adsorbed on Pt, which were determined by the $\Delta\mu$

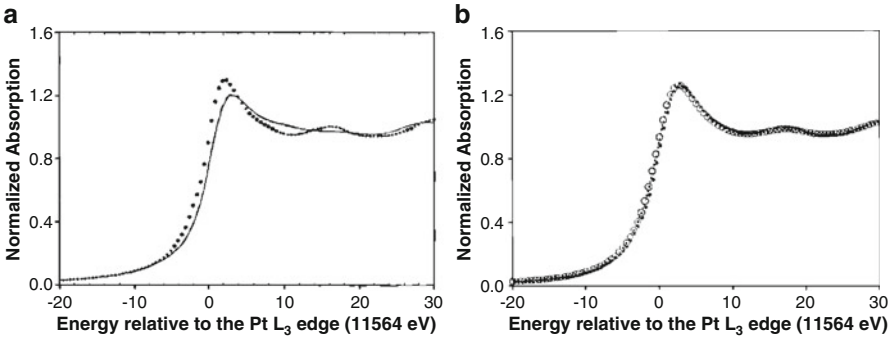

Fig. 31.7 XANES spectra at the Pt L_{III}-edge measured in 1 M $HClO_4$ for (**a**) PtSn alloy at 0.0 V (vs. RHE) (*solid line*), 0.54 V (*dotted line*), and 0.84 V (*dashed line*) and (**b**) UPD Sn on the carbon-supported Pt at 0.33 V (*open circles*) and 0.54 V (*dotted line*). Data for a Pt foil reference standard are also shown in each figure for comparison (*plus sign*) [76]

analysis of the Pt L_{II}- and L_{III}-edges XANES spectra in combination with a FEFF simulation, they discussed the metal-ligand effects on the electrocatalytic activity for CO oxidation. It was shown that Mo and Sn islands on PtMo and PtSn are fully oxidized over a wide potential region in contrast to the fact that the oxidation state of Ru on PtRu depends on the applied potential. The Pt–OH bond and Pt–CO bond strengthen and weaken, respectively, depending on the strength of the ligand effect; $Ru < MoO_n \approx SnO_n < RuO_n$. Thus, a strong ligand effect is exerted at all potentials for PtMo and PtSn although it significantly depends on the potential only for PtRu.

Pelliccione et al. structurally and electronically studied Pt nanoparticles with and without electrodeposited Ru layers [84]. A significant differences were found in the oxidation state of catalyst in the absence and presence of methanol in the electrolyte solution. In the absence of methanol, Ru was gradually oxidized from metallic to a Ru^{3+}/Ru^{4+} mixture as potential was made more positive. In the presence of methanol, however, the oxidation state of Ru remains a mixture of metallic and Ru^{3+} even as potential was made more positive. Carbon monoxide species were found to be adsorbed on the Ru atoms in the entire potential region and the OH species start to coadsorb when the potential was made more positive than 0.175 V (vs. Ag/AgCl), at which the methanol oxidation starts. They concluded that the coadsorption of carbon monoxide and OH group on the Ru atoms plays a crucial role in the methanol oxidation process. These results are consistent with the previously suggested bifunctional methanol oxidation mechanism with respect to the need for OH groups for the removal of carbon monoxide from Pt sites [85]. They also found the methanol adding effects that decreased the Ru–Ru and Ru–Pt bond lengths, increased the number of Ru–Pt near neighbors, and decreased the number of Ru–Ru near neighbors. Their results are summarized in Fig. 31.8.

Structural studies of the electrodeposited Cu layers on the iodine-treated carbon-supported Pt surface [86] and Pt nanoparticle surface [87] by in situ XAFS have also been reported.

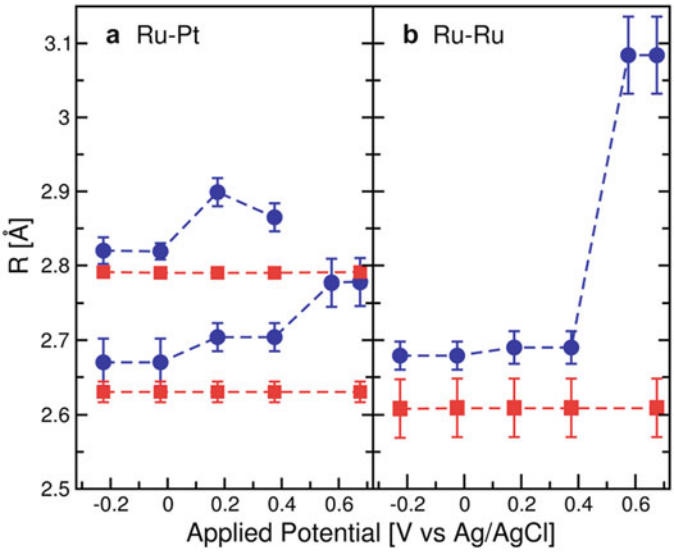

Fig. 31.8 (**a**) Ru–Pt and (**b**) Ru–Ru bond distances as a function of electrode potential without methanol (*blue circles*) and with methanol (*red squares*) [84]

Thus, in situ XAFS has been utilized for various electrochemical systems for the structural determination from a fundamental point of view.

31.3.3 Electrocatalytic Reactions

Key processes in energy conversion devices, such as fuel cells, rechargeable batteries, and photocatalysts, are usually very complicated, involving multiple reactions of electrons, protons, and solution species, and then the reaction activity, selectivity, and durability are strongly affected by the geometric and electronic structures of the active materials on the electrodes. Since XAFS can analyze both the geometric and electronic structures, as already mentioned, in situ XAFS has been applied for clarifications of the mechanism of multi-electron and proton transfer reactions associated with the development of energy conversion devices.

PEMFCs have attracted much attention because of their high theoretical efficiency [87–91]. Currently, Pt-based materials are used as electrocatalysts for both the anode and cathode because of their very high catalytic activity for the hydrogen oxidation reaction (HOR) [92, 93] and oxygen reduction reaction (ORR) [94]. However, the potential loss at the cathode caused by the slow kinetics of the ORR is a critical issue to improve the cell performances.

One of the effective approaches to improve the ORR activity and reduce the loading amount of Pt, which is a precious and high cost material, is utilization of co-catalysts in combination with Pt, and a variety of transition metals [95–99] and

metal oxides [100–105] have been used as co-catalysts to enhance the electrocatalytic activity for the ORR. Our group investigated the role of CeO_x in the enhancement of the ORR activity by in situ XAFS of the Pt-CeO_x/C catalyst [39]. Upon the incorporation of CeO_x into Pt, not only Ce^{4+} corresponding to bulk CeO_2 but also Ce^{3+} species were observed probably due to the formation of the Pt/CeO_x interface. When the oxidation/reduction cycling was performed in a 0.5 M H_2SO_4 solution, residual CeO_2 is preferentially eluted in the solution, so that the Ce^{3+} species formed at the Pt surface is dominant. Thus, in contrast to the assumption that small Pt particles (a few nm) are attached to the relatively large CeO_x particles (a few tens nm), Pt nanoparticles with a diameter of 3−5 nm are coated with a few CeO_x layers in this Pt-CeO_x/C catalyst.

Figure 31.9 shows the XANES spectra at the Pt L_{III}-edge of the conventional Pt/C catalyst and at the Pt L_{III}- and Ce L_{III}-edges of the Pt-CeO_x/C catalyst. At the Pt L_{III}-edge, the white line intensity of the Pt/C catalyst increases as the potential becomes more positive than 1.0 V (vs. Ag/AgCl), showing the formation of Pt oxide because the white line intensity reflects the *d*-band vacancies. It is clear that the Pt surface of the Pt/C catalyst is partly covered with Pt oxide at the potentials where the ORR takes place. In contrast, only a slight change was observed in the white line intensity of the Pt-CeO_x/C catalyst, showing the suppression of the Pt oxide formation. In fact, it is known that the ORR activity at the bare Pt surface is higher than that at the Pt oxide surface. Thus, the Pt-CeO_x/C catalyst shows a higher electrocatalytic activity for the ORR because the intrinsic catalytic activity of the

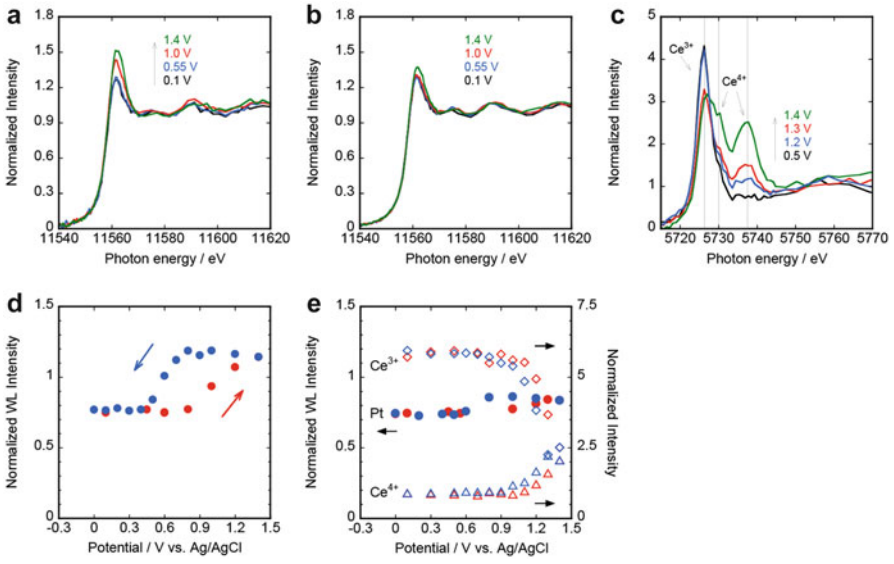

Fig. 31.9 Potential-dependent XANES spectra at the (**a**, **b**) Pt L_{III}- and (**c**) Ce L_{III}-edges of (**a**) Pt/C and (**b**, **c**) Pt-CeO_x/C in an aqueous solution of 0.5 M H_2SO_4 saturated with O_2. *White line* intensities of (**d**) Pt/C and (**e**) Pt-CeO_x/C as a function of the potential in the positive (*red*) and negative (*blue*) scan directions [39]

bare Pt surface is maintained by the suppression of the Pt oxide formation by CeO_x. At the Ce L_{III}-edge of the Pt-CeO_x/C catalyst, a singlet peak assignable to the Ce^{3+} species at the Pt/CeO_x interface turned into a doublet peak characteristic of the CeO_2 in the potential region more negative than 1.1 V. This interconversion is considered to be the origin of suppression of the Pt oxide formation.

The hydrogen evolution reaction (HER) has attracted much attention regarding the relation with artificial photosynthesis. Recently, we constructed organic molecular layers, which consist of viologen moieties as an electron transfer mediator and Pt complexes as a multi-electron transfer catalyst, on the hydrogen-terminated Si(111) surface, denoted as the Pt-V^{2+}-Si(111) surface and demonstrated high photoelectrochemical HER activity [106, 107]. Since the HER takes place at a potential much more negative than the redox potential of the Pt complexes, e.g., +0.51 V (vs. Ag/AgCl) for $PtCl_4^{2-}$ ions, we originally considered that the Pt complexes incorporated within the molecular layer were reduced to Pt metal nanoparticles and the actual catalyst for HER was the Pt metal nanoparticle. However, the formation of such nanoparticles was not observed by SEM, and the peak positions of the Pt 4f peaks in the XP spectrum of the Pt-V^{2+}-Si(111) surface after the HER was at a binding energy slightly higher than that of Pt in the metallic state. Thus, an in situ polarization-dependent total-reflection fluorescence (PTRF)—XAFS analysis of the Pt-V^{2+}-Si(111) surface was performed to identify the actual catalytic species. Figure 31.10 shows the XANES and EXAFS oscillations of the Pt-V^{2+}-Si(111) surface measured in air and in a 0.1 M Na_2SO_4 solution at various potentials, together with those for K_2PtCl_4 and Pt foil as references [38].

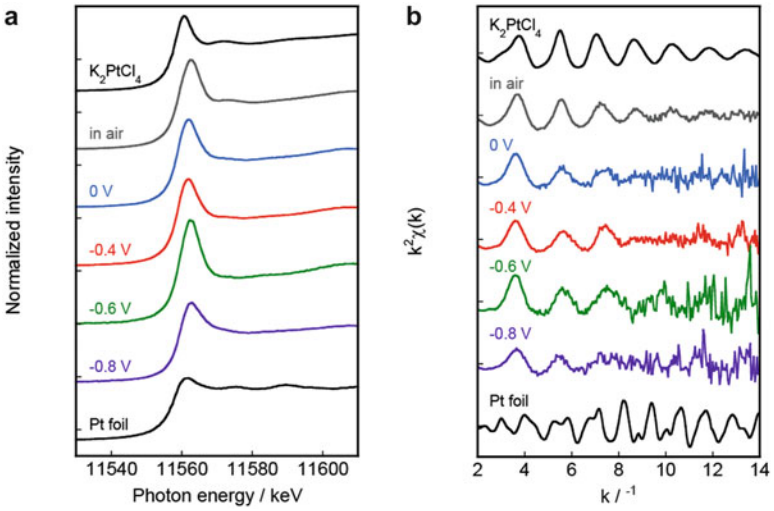

Fig. 31.10 Pt L_{III} XANES and EXAFS oscillations of the Pt-V^{2+}-Si(111) surface measured in air and in 0.1 M Na_2SO_4 solution at various potentials. Those for K_2PtCl_4 and Pt foil were also measured in air as references [38]

At the Pt-V^{2+}-Si(111) surface measured in air, the insertion of the $PtCl_4^{2-}$ was confirmed by the observation of a small shoulder characteristic of the Pt–Cl bond just above the white line peak in the XANES spectra and the shape of the EXAFS oscillations was in good agreement with that of K_2PtCl_4, indicating that Pt exists as $PtCl_4^{2-}$ in the molecular layer in air. As the potential was made more negative, the shoulder gradually decreased and finally disappeared at −0.6 V. The EXAFS oscillation in the region of k between 8 and 12 was significantly changed due to the replacement of Cl^- with oxygenated species such as water or hydroxyl groups, which was supported by a FEFF simulation. Thus, Pt complexes act as molecular catalysts confined within the organic molecular layers without being converted into metal nanoparticles. Since noble metals are generally very extensive and limited resources, the atom efficiency needs to be a maximum as long as their practical uses are concerned. Such single atomic and molecular catalysts which enable a 100 % atom efficiency are a promising concept.

References

1. Uosaki K (2015) In situ real-time monitoring of geometric, electronic, and molecular structures at solid/liquid interfaces. Jpn J Appl Phys 54:030102/1–030102/14
2. Jerkiewicz G, Soriaga MP, Uosaki K, Wieckowski A (1997) Solid-liquid electrochemical interfaces. American Chemical Society, Washington
3. Abruña HD (ed) (1991) Electrochemical interfaces: modern techniques for in-situ interface characterization. Wiley, New York
4. Gewirth AA, Niece BK (1997) Electrochemical applications of in situ scanning probe microscopy. Chem Rev 97:1129–1162
5. Szklarczyk M, Strawski M, Bienkowski K (2008) 25 Years of the scanning tunneling microscopy. Mod Aspects Electrochem 42:303–368
6. Toney MF, McBreen J (1993) In situ synchrotron X-ray techniques for determining atomic structure at electrode/electrolyte interfaces. Electrochem Soc Interface 2:22–31
7. Feidenhansl R (1989) Surface-structure determination by X-ray-diffraction. Surf Sci Rep 10:105–188
8. Tadjeddine A, Peremans A (1998) Non-linear optical spectroscopy of the electrochemical interface. Adv Spectrosc 26:159–217
9. Shen YR (1989) Surface-properties probed by 2nd-harmonic and sum-frequency generation. Nature 337:519–525
10. Melendres CA, Tadjeddine A (1994) Synchrotron techniques in interfacial electrochemistry. Springer, Dordrecht
11. Albarelli MJ, White JH et al (1988) In situ surface EXAFS at chemically modified electrodes. J Electroanal Chem 248:77–86
12. Gordon JG, Melroy OR et al (1986) Surface EXAFS of an electrochemical interface iodine on platinum (111). J Electroanal Chem 210:311–314
13. Endo O, Kiguchi M (1999) In-situ X-ray absorption studies of bromine on the Ag(100) electrode. J Electroanal Chem 473:19–24
14. McBreen J, O'Grady WE et al (1987) EXAFS study of the nickel-oxide electrode. Langmuir 3:428–433
15. Kordesch ME, Hoffman RW (1984) Electrochemical-cells for in situ EXAFS. Nucl Instrum Methods Phys Res A 222:347–350

16. Davenport AJ, Isaacs HS et al (1991) In situ X-ray absorption study of chromium valency changes in passive oxides on sputtered AlCr thin-films under electrochemical control. J Electrochem Soc 138:337–338
17. Bardwell JA, Sproule GI et al (1992) In situ XANES detection of Cr(VI) in the passive film on Fe-26Cr. J Electrochem Soc 139:371–373
18. Pandya KI, Hoffman RW et al (1990) In situ X-ray absorption spectroscopic studies of nickel-oxide electrodes. J Electrochem Soc 137:383–388
19. Pandya KI, O'Grady WE et al (1990) Extended X-ray absorption fine structure investigations of nickel hydroxides. J Phys Chem 94:21–26
20. McBreen J, O'Grady WE et al (1989) In situ time-resolved X-ray absorption near edge structure study of the nickel-oxide electrode. J Phys Chem 93:6308–6311
21. Guay D, Tourillon G et al (1991) In situ time-resolved EXAFS study of the structural modifications occurring in nickel-oxide electrodes between their fully oxidized and reduced states. J Electroanal Chem 305:83–95
22. Blum L, Abruña HD et al (1986) Study of underpotentially deposited copper on gold by fluorescence detected surface EXAFS. J Chem Phys 85:6732–6738
23. Tadjeddine A, Tourillon G, Guay D (1991) Structural and electronic characterization of underpotentially deposited copper on gold single-crystal probed by in situ X-ray absorption-spectroscopy. Electrochim Acta 36:1859–1862
24. Tadjeddine A, Guay D et al (1991) Electronic and structural characterization of underpotentially deposited submonolayers and monolayer of copper on gold (111) studied by in situ X-ray-absorption spectroscopy. Phys Rev Lett 66:2235–2238
25. Kondo T, Tamura K et al (1997) Coverage dependent structure of electrochemically deposited Cu on p-GaAs(100) in H_2SO_4 solution determined by in situ surface X-ray absorption fine structure spectra. Chem Lett 8:761–762
26. Uosaki K, Kondo T et al (1997) Structural study of electrochemically deposited copper on p-GaAs(001) by atomic force microscopy and surface X-ray absorption fine structure measurement. Appl Surf Sci 121:102–106
27. Tamura K, Oyanagi H et al (2000) Structural study of electrochemically deposited Cu on p-GaAs(100) in H_2SO_4 solution by in situ surface-sensitive X-ray absorption fine structure measurements. J Phys Chem B 104:9017–9024
28. McBreen J, O'Grady WE, Pandya KI (1988) EXAFS – a new tool for the study of battery and fuel-cell materials. J Power Sources 22:323–340
29. Tada M, Murata S et al (2007) In situ time-resolved dynamic surface events on the Pt/C cathode in a fuel cell under operando conditions. Angew Chem Int Ed 46:4310–4315
30. Uemura Y, Inada Y et al (2011) In situ time-resolved XAFS study on the structural transformation and phase separation of Pt_3Sn and PtSn alloy nanoparticles on carbon in the oxidation process. Phys Chem Chem Phys 13:15833–15844
31. Ishiguro N, Saida T et al (2012) Operando time-resolved X-ray absorption fine structure study for surface events on a Pt_3Co/C cathode catalyst in a polymer electrolyte fuel cell during voltage-operating processes. ACS Catal 2:1319–1330
32. Ishiguro N, Saida T et al (2013) Structural kinetics of a Pt/C cathode catalyst with practical catalyst loading in an MEA for PEFC operating conditions studied by in situ time-resolved XAFS. Phys Chem Chem Phys 15:18827–18834
33. Nagasawa K, Takao S et al (2014) Performance and durability of Pt/C cathode catalysts with different kinds of carbons for polymer electrolyte fuel cells characterized by electrochemical and in situ XAFS techniques. Phys Chem Chem Phys 16:10075–10087
34. Kityakarn S, Saida T et al (2014) In situ time-resolved XAFS of transitional states of Pt/C cathode electrocatalyst in an MEA during PEFC loading with transient voltages. Top Catal 57:903–910
35. McBreen J (2009) The application of synchrotron techniques to the study of lithium-ion batteries. J Solid State Electrochem 13:1051–1061

36. Dewald HD, Watkins JW et al (1986) Development of extended X-ray absorption fine-structure spectroelectrochemistry and its application to structural studies of transition-metal ions in aqueous-solution. Anal Chem 58:2968–2975
37. Kaito T, Mitsumoto H et al (2014) A new spectroelectrochemical cell for in situ measurement of Pt and Au K-edge X-ray absorption fine structure. Rev Sci Instrum 85:084104/1–084104/8
38. Masuda T, Fukumitsu H et al (2012) Molecular catalysts confined on and within molecular layers formed on a Si(111) surface with direct Si-C bonds. Adv Mater 24:268–272
39. Masuda T, Fukumitsu H et al (2012) Role of cerium oxide in the enhancement of activity for the oxygen reduction reaction at Pt-CeO_x nanocomposite electrocatalyst - an in situ electrochemical X-ray absorption fine structure study. J Phys Chem C 116:10098–10102
40. Melroy OR, Samant MG et al (1988) Inplane structure of underpotentially deposited copper on gold(111) determined by surface EXAFS. Langmuir 4:728–732
41. Gorlin Y, Lassalle-Kaiser B et al (2013) In situ X-ray absorption spectroscopy investigation of a bifunctional manganese oxide catalyst with high activity for electrochemical water oxidation and oxygen reduction. J Am Chem Soc 135:8525–8534
42. Nakanishi K, Kato D et al (2014) Novel spectro-electrochemical cell for in situ/operando observation of common composite electrode with liquid electrolyte by X-ray absorption spectroscopy in the tender X-ray region. Rev Sci Instrum 85:084103/1–084103/6
43. Erickson EM, Thorum MS et al (2012) In situ electrochemical X-ray absorption spectroscopy of oxygen reduction electrocatalysis with high oxygen flux. J Am Chem Soc 134:197–200
44. Uehara H, Uemura Y et al (2014) In situ back-side illumination fluorescence XAFS (BI-FXAFS) studies on platinum nanoparticles deposited on a HOPG surface as a model fuel cell: a new approach to the Pt-HOPG electrode/electrolyte interface. Phys Chem Chem Phys 16:13748–13754
45. Hachiya T, Honbo H et al (1991) Detailed underpotential deposition of copper on gold(111) in aqueous solution. J Electroanal Chem 315:275–291
46. Batina N, Will T et al (1992) Study of the initial stage of copper deposition by in situ scanning tunneling microscopy. Faraday Discuss 94:93–106
47. Gewirth AA (1992) Atomic resolution electrochemistry of underpotential deposition processes. AIP Conf Proc 241:253–261
48. Finnefrock AC, Buller LJ et al (1997) Time-resolved surface X-ray scattering study of surface ordering of electrodeposited layers. J Am Chem Soc 119:11703–11704
49. White JH, Abruña HD (1990) Coadsorption of copper with anions on platinum (111): the role of surface redox chemistry in determining the stability of a metal monolayer. J Phys Chem 94:894–900
50. Lucas CA, Markovic NM et al (1996) In situ X-ray scattering study of the Pt(111)-solution interface: ordered anion structures and their influence on copper underpotential deposition. Phys B Condens Matter 221:245–250
51. Cappadonia M, Robinson KM et al (1997) X-ray surface diffraction of metal deposits at metal/liquid interfaces. Part I: copper deposit on Au(100). Surf Rev Lett 4:1173–1178
52. Chang SC, Weaver MJ (1991) Influence of coadsorbed bismuth and copper on carbon monoxide adlayer structures at ordered low-index platinum-aqueous interfaces. Surf Sci 241:11–24
53. Gordon JG, Melroy OR, Toney MF (1995) Structure of metal electrolyte interfaces - copper on gold(111), water on silver(111). Electrochim Acta 40:3–8
54. Wu S, Lipkowski J et al (1995) Effect of anion adsorption on early stages of copper electrocrystallization at Au(111) surface. Prog Surf Sci 50:227–236
55. Wu S, Shi Z et al (1997) Early stages of copper electrocrystallization: electrochemical and in situ X-ray absorption fine structure studies of coadsorption of copper and chloride at the Au (111) electrode surface. J Phys Chem B 101:10310–10322
56. Hotlos J, Magnussen OM (1990) Effect of trace amounts of Cl^- in Cu underpotential deposition on Au(111) in perchlorate solutions: an in-situ scanning tunneling microscopy study. Surf Sci 335:129–144

57. Matsumoto H, Oda I (1993) Coadsorption of copper and halogens on Pt(111) and Au(111) electrode surfaces studied by scanning tunneling microscopy. J Electroanal Chem 356:275–280
58. Friebel D, Mbuga F et al (2014) Structure, redox chemistry, and interfacial alloy formation in monolayer and multilayer Cu/Au(111) model catalysts for CO_2 electroreduction. J Phys Chem C 118:7954–7961
59. Yee HS, Abruña HD (1993) In-situ X-ray-absorption spectroscopy studies of copper underpotentially deposited in the absence and presence of chloride on platinum(111). Langmuir 9:2460–2469
60. Yee HS, Abruña HD (1993) In situ X-ray studies of the underpotential deposition of copper on platinum(111). J Phys Chem 97:6278–6288
61. Yee HS, Abruña HD (1994) Ab-initio XAFS calculations and in-situ XAFS measurements of copper underpotential deposition on Pt(111) - a comparative-study. J Phys Chem 98:6552–6558
62. Gomez R, Yee HS et al (1995) Anion effects and the mechanism of Cu UPD on Pt(111) - X-ray and electrochemical studies. Surf Sci 335:101–109
63. Soldo Y, Sibert E et al (2002) In situ X-ray absorption spectroscopy study of copper under potential deposition on Pt(111): role of the anions on the Cu structural arrangement. Electrochim Acta 47:3081–3091
64. Samant MG, Borges GL et al (1987) In situ surface extended X-ray absorption fine-structure spectroscopy of a lead monolayer at a silver(111) electrode electrolyte interface. J Am Chem Soc 109:5970–5974
65. White JH, Albarelli MJ et al (1988) Surface extended X-ray absorption fine-structure of underpotentially deposited silver on Au(111) electrodes. J Phys Chem 92:4432–4436
66. Furtak TE, Wang L et al (1994) Structure of the copper-monolayer/platinum-electrode interface as measured in in situ X-ray absorption spectroscopy. J Electrochem Soc 141:2369–2373
67. Prinz H, Strehblow HH (2002) The structure of Cu- and Cd-UPD-layers on a stepped Pt(533) single crystal surface studied by grazing incidence XAFS, XRD and XPS. Electrochim Acta 47:3093–3104
68. Lee JRI, O'Malley RL et al (2010) X-ray absorption spectroscopy characterization of Zn underpotential deposition on Au(111) from phosphate supporting electrolyte. Electrochim Acta 55:8532–8538
69. Lee JRI, O'Malley RL et al (2009) X-ray absorption spectroscopy characterization of Cu underpotential deposition on Au(111) and organothiol-self-assembled-monolayer-modified Au(111) electrodes from sulfate supporting electrolyte. J Phys Chem C 113:12260–12271
70. Lurio LB, Pant L et al (1995) XAS study of the liquid/UPD Cu/Pt interfacial region. Phys B 208&209:413–414
71. McBreen J, O'Grady WE et al (1991) XANES study of underpotential deposited copper on carbon-supported platinum. J Electroanal Chem 307:229–240
72. Price SWT, Rhodes JM et al (2013) Revealing the details of the surface composition of electrochemically prepared Au@Pd core@shell nanoparticles with in situ EXAFS. J Phys Chem C 117:24858–24865
73. Seo M, Habazaki H et al (2014) In situ X-ray absorption spectroscopy study of Sn underpotential deposition on Ni from perchloric acid. J Electrochem Soc 161:H195–H202
74. McBreen J, Sansone M (1994) In situ X-ray absorption spectroscopic study of adsorbed Pb on carbon-supported Pt. J Electroanal Chem 373:227–233
75. Jia Q, Ramaker DE et al (2013) Fundamental aspects of ad-metal dissolution and contamination in low and medium temperature fuel cell electrocatalysis: a Cu based case study using in situ electrochemical X-ray absorption spectroscopy. J Phys Chem C 117:4585–4596
76. Mukerjee S, McBreen J (1999) An in situ X-ray absorption spectroscopy investigation of the effect of Sn additions to carbon-supported Pt electrocatalysts. J Electrochem Soc 146:600–606

77. Rose A, Crabb EM et al (2007) Potential dependence of segregation and surface alloy formation of a Ru modified carbon supported Pt catalyst. Electrochim Acta 52:5556–5564
78. Rose A, Bilsborrow R et al (2009) In situ Ru K-edge EXAFS of CO adsorption on a Ru modified Pt/C fuel cell catalyst. Electrochim Acta 54:5262–5266
79. Roth C, Benker N et al (2005) Determination of O[H] and CO coverage and adsorption sites on PtRu electrodes in an operating PEM fuel cell. J Am Chem Soc 127:14607–15615
80. Scott FJ, Mukerjee S, Ramaker DE (2007) CO coverage/oxidation correlated with PtRu electrocatalyst particle morphology in 0.3 M methanol by in situ XAS. J Electrochem Soc 154:A396–A406
81. Scott FJ, Roth C, Ramaker DE (2007) Kinetics of CO poisoning in simulated reformate and effect of Ru island morphology on PtRu fuel cell catalysts as determined by operando X-ray absorption near edge spectroscopy. J Phys Chem C 111:11403–11413
82. Scott FJ, Mukerjee S, Ramaker DE (2010) Contrast in metal-ligand effects on Pt_nM electrocatalysts with M equal Ru vs Mo and Sn as exhibited by in situ XANES and EXAFS measurements in methanol. J Phys Chem C 114:442–453
83. Melke J, Schoekel A et al (2010) Ethanol oxidation on carbon-supported Pt, PtRu, and PtSn catalysts studied by operando X-ray absorption spectroscopy. J Phys Chem C 114:5914–5925
84. Pelliccione CJ, Timofeeva EV et al (2013) In situ Ru K-edge X-ray absorption spectroscopy study of methanol oxidation mechanisms on model submonolayer Ru on Pt nanoparticle electrocatalyst. J Phys Chem C 117:18904–18912
85. Stoupin S, Chung E (2006) Pt and Ru X-ray absorption spectroscopy of PtRu anode catalysts in operating direct methanol fuel cells. J Phys Chem B 110:9932–9938
86. Bommarito GM, Acevedo D et al (1994) Potential-dependent structural-changes of underpotentially deposited copper on an iodine-treated platinum surface determined in-situ by surface EXAFS and its polarization dependence. J Electroanal Chem 379:135–150
87. Carino EV, Crooks RM (2011) Characterization of Pt@Cu core@shell dendrimer-encapsulated nanoparticles synthesized by Cu underpotential deposition. Langmuir 27:4227–4235
88. Kordesch KV, Simader GR (1995) Environmental-impact of fuel-cell technology. Chem Rev 95:191–207
89. Winter M, Brodd RJ (2004) What are batteries, fuel cells, and supercapacitors? Chem Rev 104:4245–4269
90. Wang CY (2004) Fundamental models for fuel cell engineering. Chem Rev 104:4727–4765
91. Borup R, Meyers J et al (2007) Scientific aspects of polymer electrolyte fuel cell durability and degradation. Chem Rev 107:3904–3951
92. Gasteiger HA, Markovic NM et al (1995) H_2 and CO electrooxidation on well-characterized Pt, Ru, and Pt-Ru. 1. Rotating disk electrode studies of the pure gases including temperature effects. J Phys Chem 99:8290–8301
93. Gasteiger HA, Markovic NM et al (1995) H_2 and CO electrooxidation on well-characterized Pt, Ru, and Pt-Ru. 2. Rotating disk electrode studies of CO/H2 mixtures at 62 °C. J Phys Chem 99:16757–16767
94. Markovic NM, Schmidt TJ et al (2001) Oxygen reduction reaction on Pt and Pt bimetallic surfaces: a selective review. Fuel Cells 1:105–116
95. Mukerjee S, Srinivasan S (1993) Enhanced electrocatalysis of oxygen reduction on platinum alloys in proton-exchange membrane fuel-cells. J Electroanal Chem 357:201–224
96. Toda T, Igarashi H et al (1999) Enhancement of the electroreduction of oxygen on Pt alloys with Fe, Ni, and Co. J Electrochem Soc 146:3750–3756
97. Paulus UA, Wokaun A et al (2002) Oxygen reduction on carbon-supported Pt-Ni and Pt-Co alloy catalysts. J Phys Chem B 106:4181–4191
98. Stamenkovic VR, Mun BS et al (2007) Trends in electrocatalysis on extended and nanoscale Pt-bimetallic alloy surfaces. Nat Mater 6:241–247
99. Stamenkovic VR, Fowler B et al (2007) Improved oxygen reduction activity on $Pt_3Ni(111)$ via increased surface site availability. Science 315:493–497

100. Ioroi T, Siroma Z et al (2005) Sub-stoichiometric titanium oxide-supported platinum electrocatalyst for polymer electrolyte fuel cells. Electrochem Commun 7:183–188
101. Lee KH, Kwon K et al (2008) Synthesis and characterization of nanostructured PtCo-CeO_x/C for oxygen reduction reaction. J Power Sources 185:871–875
102. Sasaki K, Zhang L et al (2008) Niobium oxide-supported platinum ultra-low amount electrocatalysts for oxygen reduction. Phys Chem Chem Phys 10:159–167
103. Elezovic NR, Babic BM et al (2009) Synthesis and characterization of MoO_x-Pt/C and TiO_x-Pt/C nano-catalysts for oxygen reduction. Electrochim Acta 54:2404–2409
104. Garsany Y, Epshteyn A et al (2010) High-activity, durable oxygen reduction electrocatalyst: nanoscale composite of platinum-tantalum oxyphosphate on vulcan carbon. J Phys Chem Lett 1:1977–1981
105. Fugane K, Mori T et al (2011) Activity of oxygen reduction reaction on small amount of amorphous CeO_x promoted Pt cathode for fuel cell application. Electrochim Acta 56:3874–3883
106. Masuda T, Uosaki K (2004) Construction of organic monolayers with electron transfer function on a hydrogen terminated Si(111) surface via silicon-carbon bond and their electrochemical characteristics in dark and under illumination. Chem Lett 33:788–789
107. Masuda T, Shimazu K et al (2008) Construction of mono- and multimolecular layers with electron transfer mediation function and catalytic activity for hydrogen evolution on a hydrogen-terminated Si(111) surface via Si-C bond. J Phys Chem C 112:10923–10930

Chapter 32
Three-Dimensional Structures on Oxide Single-Crystal Surfaces

Kiyotaka Asakura

32.1 Introduction

The surface structure of supported metal clusters can be finely controlled by using a well-defined metal complex and surface modifications, as described in the other chapter. The surface structures are stabilized by the interaction between the metal and support oxide. Investigation of a metal species on a single-crystal oxide surface will provide further knowledge regarding the structure of the metal species on oxide surfaces and the metal–oxide interaction. However, the investigation of a metal species on a single-crystal oxide surface is not easy because of the small amount of metal species and high penetration ability of the X-ray. As described in the other chapter, polarization-dependent total reflection fluorescence XAFS (PTRF-XAFS) will provide three-dimensional structural information of a metal species highly dispersed on flat surfaces. In this chapter, we discuss how to obtain an atomically dispersed metal species by controlling the oxide surface property and structure (mainly a TiO_2 (110) surface) and how to determine the three-dimensional structure on an atomic level using PTRF-XAFS. The structure mainly depends on the strengths of the metal–metal and metal–oxide interactions. *What is the metal–oxide interaction*?

Komiyama et al. reported that the metal–support interaction can be classified by the metal–oxide formation energies [1]. Larger metal–oxide formation energies, found from the early transition metals, give a smaller two-dimensional metal cluster or no aggregation, while the metals with smaller metal–oxide formation energies result in aggregated clusters. Komiyama et al. divided the transition metals into three domains [1]. In Domain I, the formation energy of metal–metal is larger than that of metal–oxygen, so three-dimensional growth is preferred. In Domain III,

K. Asakura (✉)
Institute for Catalysis, Hokkaido University, Sapporo 001-0021, Japan
e-mail: askr@cat.hokudai.ac.jp

Y. Iwasawa et al. (eds.), *XAFS Techniques for Catalysts, Nanomaterials, and Surfaces*, DOI 10.1007/978-3-319-43866-5_32

which is composed of many of the early transition metals, the metal–oxygen interaction is larger than that of the metal–metal interaction; two-dimensional growth is often observed. Domain II is the intermediate domain where both growth modes are observed.

32.2 Metals in Domain III

Molybdenum is located in Domain III as it has a strong interaction with the oxide surface. Actually, Mo is often observed not in the metallic state but in the hexavalent state (Mo^{6+}), when PTRF-XAFS is applied to the Mo system on the TiO_2 (110) surface. Figure 32.1 shows the ball model for the TiO_2 (110) surface. TiO_2 (110) is the most well-studied oxide surface. There are three types of surface atoms. One is the exposed Ti atom (denoted as fivefold Ti), another is the topmost oxygen (termed as bridging oxygen), and the last is the oxygen atoms in the same plane of the fivefold Ti (termed as in-plane oxygen) [2, 3].

There are two types of Ti. One is exposed Ti, known as fivefold Ti, while the other Ti is covered with bridging oxygen atoms, known as sixfold Ti [2, 3]. Fig. 32.2.

The Mo structure strongly depends on the preparation conditions even if the same precursor, $(NH_4)_6Mo_7O_{24}$, was used. The Mo dimer species, with a Mo–Mo distance (3.35 Å) parallel to the $[1\bar{1}0]$ direction, was observed when $(NH_4)_6Mo_7O_{24}$ was dissolved in ultrapure water and was deposited on the TiO_2 (110) surface [2, 3]. The Mo structure has a motif of the MoO_3 (100) plane parallel to the TiO_2 (110) surface. The Mo dimer shared the bridging oxygen atoms. However, the $(NH_4)_6Mo_7O_{24}$ in distilled water, where a small amount of metal cation should be present, was deposited on the TiO_2 (110) surface, and the Mo monomer species was stabilized with a tetrahedral structure. A small amount of K^+ and Na^+ dissolved in distilled water was deposited on the TiO_2 (110) surface, which stabilized the Mo tetrahedral species. The structure of the Mo species was controlled by the small

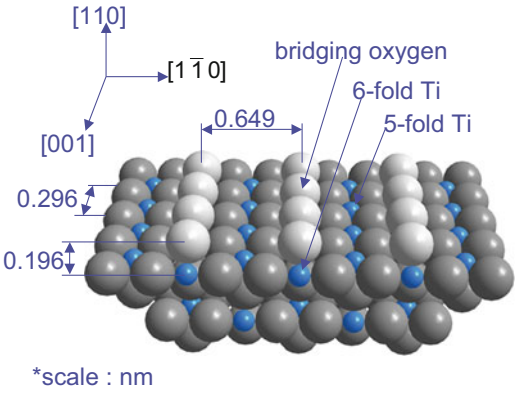

Fig. 32.1 TiO_2 (110) surface. *Large* and *small balls* are oxygen and Ti atoms, respectively

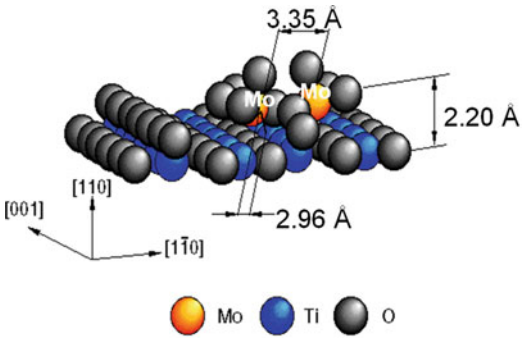

Fig. 32.2 Mo dimer structure on the TiO_2 (110) surface. The Mo dimer was located at both sides of the bridging oxygen atoms with a Mo–Mo distance of 2.96 Å [2, 3]

amount of alkaline species. It was reported that the Mo species deposited on SiO_2 using ultrapure water was MoO_3 and that more than 100 ppm Na converted the MoO_3 to Mo monomer or dimer [4–6]. Na^+ enhanced the basicity of the oxide surface and stabilized the negative charge of the surface oxygen. On a MgO (0001) surface, which had a larger basicity than TiO_2 (110), the MoO_4^{2-} monomer species was found even if it was prepared using $(NH_4)_6Mo_7O_{24}$ dissolved in ultrapure water [7]. Therefore, the metals in Domain III have a high valence state and their structures are affected by the surface acidity or basicity.

32.3 Metals in Domain II

Ni is located on the border of Domains I and II. Therefore, the Ni structures vary depending on the preparation conditions. A two-dimensional dispersion has been observed when the Ni was deposited on the TiO_2 (110) surface with a deposition amount of less than 2×10^{14} cm^{-2} [8]. At higher deposition amounts, the Ni grows three-dimensionally. When the Ni loading was decreased, atomically dispersed Ni was observed. The Ni was atomically dispersed at a density of 1×10^{13} cm^{-2} of Ni on TiO_2 (110) [9, 10]. Ni was bound to the surface by oxygen atoms with no Ni–Ti bonds observed. There were several threefold sites on the TiO_2 (110) surface [9]. The Ni structure on any sites of the terrace could not reproduce the Ni K-edge PTRF-XAFS oscillations in any direction because of the underlying Ti effects. The EXAFS oscillations could only be reproduced when the Ni was located at the step-kink site, as shown in Fig. 32.3. This site was the virtual Ti site where Ti should be located in the bulk crystal and oxygen dangling bonds directed in the Ni direction. The Ni was trapped by the oxygen dangling bonds [10].

It is often assumed that the Ni–Ti interaction on the TiO_2 (110) is important for stabilizing the metal species on the surface. We could not observe the Ni–Ti interaction on the clean TiO_2 (110) surface [8–10, 12]. To increase the possibility for Ni–Ti formation, we removed the surface oxygen atoms by gentle sputtering to create the oxygen defects [13]. We applied the PTRF-XAFS analyses on the gently

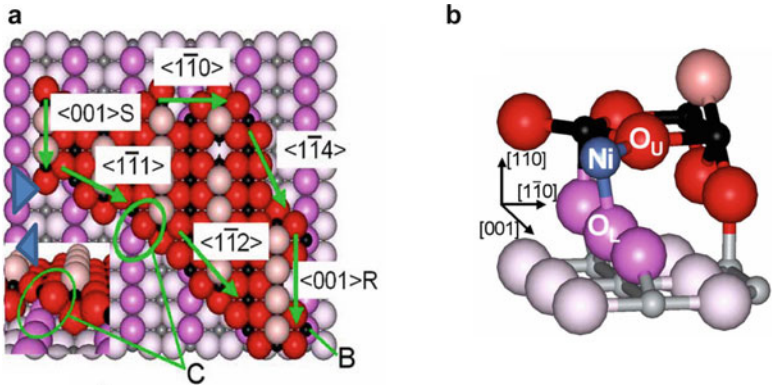

Fig. 32.3 Ball models of TiO_2 (110). (**a**) Large balls correspond to oxygen atoms and small balls correspond to Ti atoms. TiO_2 (110) with a single-height step along the $<n11>$ and $<001>$ directions. The two types of step edges along the $<001>$ direction, that is, smooth and rugged structures, are shown as $<001>S$ and $<001>R$, respectively [11]. The *green ellipse* labeled "C" indicates the proposed Ni adsorption site at the step edges along $<n11>$ direction. The *inset* shows an enlarged side view around the adsorption site "C". (**b**) The proposed local structure around Ni. (Figure is reproduced with permission from Elsevier Co. License number 3677861161206)

sputtered surface. However, we hardly observed a Ni–Ti interaction in any of the directions. We found a one-dimensional Ni trimer structure attached to the step running along the $<001>$ direction on the TiO_2 (110) surfaces, as shown in Fig. 32.4 [13]. The Ni–Ni distances were 2.60 Å, longer than those found in Ni foil (Ni–Ni = 2.48 Å) and Ni clusters on the flat TiO_2 (110) (Ni–Ni = 2.40 Å). In the $[1\bar{1}0]$ direction, we found only the Ni–O interaction. After sputtering, oxygen defects and step sites were both created. The Ni defect interaction was not as strong as the step site where the Ni linear trimer structure was stabilized [13]. We concluded again that the metals are stabilized by the surface anions (oxygen atoms) rather than by a Ni–cation interaction [12].

Similar interactions were observed on an Al_2O_3 (0001) surface. Ijima et al. studied Ni deposited on Al_2O_3 [10, 14]. They found three-dimensional growth of Ni clusters for a loading of 2×10^{14} cm^{-2} with Ni–Ni distance on the Al_2O_3 (001) surface. When the Ni loading was 3×10^{13} cm^{-2}, atomically dispersed Ni was observed. PTRF-XAFS analysis indicated that the Ni was fixed to the threefold oxygen atoms. There were three types of oxygen threefold sites at the Al_2O_3 (0001) surface, as shown in Fig. 32.5. The differences of these three sites were the positions of the underlying Al. Site 1 contained surface Al atoms which could be replaced with Ni atoms. Consequently, no underlying Al atoms were present. Sites 2 and 3 had the Al at 2.42 Å and 2.79 Å below the surface oxygen layer, respectively. The p-polarization XAFS indicated the presence of Ni–Al at 2.79 Å, indicating that the Ni was located at Site 3. Site 3 was the virtual Al site, that is, Al was removed by the formation of the surface. Thus, the oxygen dangling bonds

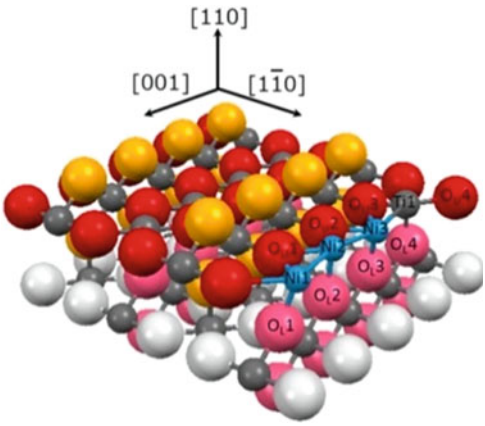

Fig. 32.4 Surface structure of the Ni trimer on TiO_2 (110). *Large balls* and *small dark balls* are oxygen atoms and Ti atoms, respectively [13]. The *small blue balls* are Ni (Figure is reproduced with permission from Elsevier, Copyright 2013. License Number 3677861161206)

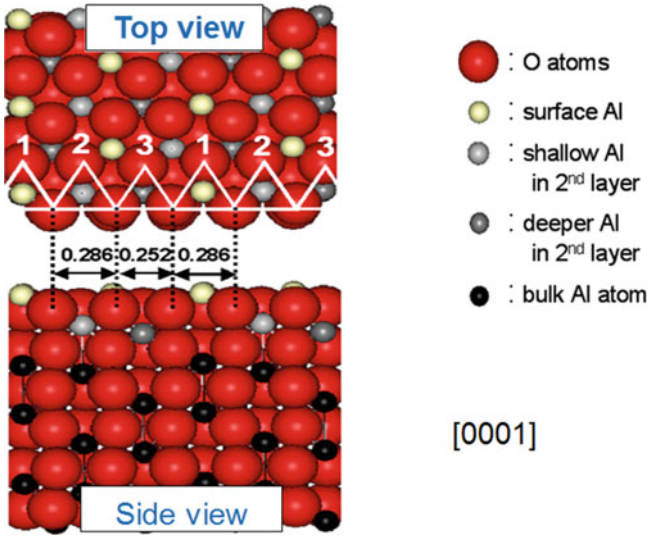

Fig. 32.5 Ni monomer on an Al_2O_3 (0001) surface. Al_2O_3 crystal (corundum structure) has a hexagonal unit cell structure. To balance the surface charge, the surface is terminated with Al (*gold small ball*) [15]. There are three hold sites, denoted as 1, 2, and 3, in the figure. Site 1 is the surface Al site and the Al can be replaced by Ni. Sites 2 and 3 have underlying Al with different depths. Site 3 has a deep Al atom (*grey small ball*) underneath. Site 3 corresponds to the Al position in the crystallography. Site 2 is an empty site where Al should not be located

were directed to this site. Ni was considered to be trapped at this position by making the Ni and oxygen through these oxygen dangling bonds similar to the Ni trapped in the step-kink on the TiO_2 (110) surface [10]. Both examples show that the anion is the interaction site with Ni and the dangling bond of the anion plays an important role in forming a bond with the metal atoms [9]. The Ni–cation interaction was not strong enough to stabilize the atomically dispersed Ni metal.

32.4 Precious Metals in Domain I and Their Atomic Distributions

Additional precious metals in Domain I, such as Au and Cu, which have more metal–metal interactions than metal–oxygen interactions, are easily aggregated on the oxide surface. Figure 32.6 shows Au on the TiO_2 (110) surface with a coverage of 1×10^{13} cm^{-2} with various polarization directions [16, 17]. The Au–Au bonds were found in all directions. The coordination number was smaller than that observed for Au foil indicating the formation of a three-dimensional nanocluster with a size of 1–2 nm. Cu similarly coalesced to create the Cu three-dimensional nanoparticle [18].

Easy aggregation of Cu and Au arises from the weak interaction with oxygen atoms on the surface of oxides, as discussed by Komiyama [1]. There are several ways to prevent the coalescence. One method is to stabilize the atomic metal species or small metal clusters using protecting ligands or polymers. The Au nanoclusters were stabilized as in the state of the protective colloid. The thiol ligand can stabilize the Au nanoclusters, and the Au nanocluster size can be controlled by adjusting the number of atoms [19]. Especially, thiolate- or triphenylphosphine-protected Au nanoclusters with the magic number were highly stabilized by their superatomic effect [20]. Peptide-stabilized Au nanoclusters were deposited on TiO_2 and studied by glancing angle XAFS [21]. Judging from the incident angle, the total reflection conditions might not be satisfied. The ratio of Au to peptide controlled the Au size, with the Au size becoming smaller as the ratio of Au to peptide decreased. Two peptides, N-(2-mercapto-propionyl) glycine (MPG) and glutathione (GSH), were investigated. GSH provided a smaller-sized Au than MPG

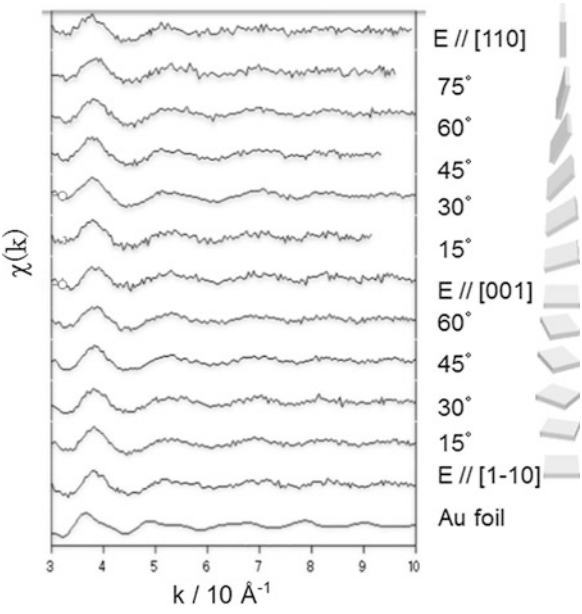

Fig. 32.6 XAFS oscillation of Au on a TiO_2 (110) surface with various polarization directions. The orientations are indicated on the right of the figure with the X-ray coming from the front to the back [16, 17]

when the same molar ratio was used. Both GSH and MPG could disperse Au species atomically when the Au to peptide ratio was 2.

An organometallic compound was used as a highly dispersed metal species on an oxide surface. When $Cu(DPM)_2$ (DPM = dipivaloylmethanate, 2,2,6,6,-tetramethyl-3,5-heptadione) was reacted with the TiO_2 (110) surface, atomically dispersed Cu species on the TiO_2 (110) were obtained [7, 22, 23]. One of the DPM ligands remained on the Cu species, and Cu complex was attached to the bridging oxygen row with a tetrahedral structure and a Cu–O bond distance of 1.94 Å [23]. The Cu species attached to the TiO_2 (110) surface could be transformed to Cu_3 (Cu trimer) or Cu_6 (Cu hexamer) by following a mild reduction treatment [7, 22, 23].

The other method to disperse the metal species is an anchoring method using a compound that has two binding sites: the metal binding site and oxide surface binding site. The TiO_2 (110) surface strongly adsorbs the organic carboxylic acid [11]. Acetic acid and formic acid formed an ordered surface structure on the TiO_2 (110) surface, such as (2×1), where the COO^- moiety was adsorbed on the exposed Ti^{4+} in a bidentate form, as shown in Fig. 32.7. The SH ligand can make a strong bond with Au. The mercaptobenzoic acid has two moieties that could be used to anchor the Au onto the TiO_2 (110) surface.

Figure 32.8 shows the XAFS oscillations of the Au on TiO_2 covered with *o*-mercaptobenzoic acid (*o*-MBA). Au was deposited on the TiO_2 (110) surface by vacuum evaporation by heating a Au wire under ultrahigh vacuum conditions. When Au was deposited on the bare TiO_2 (110) surface, Au nanoparticles were found, as shown in Fig. 32.6. However, when Au was deposited on the MBA-pre-modified surface, the oscillations were not observed up to the high k region, as shown in Fig. 32.8a, indicating no Au–Au interaction and Au was atomically dispersed. Further analysis showed that the Au species was sandwiched by the S of *o*-MBA and the bridging O of the surface [24]. The bond angle between S–Au–O was nearly 180° with a direction of 50° against the surface normal of TiO_2 (110). The bond lengths of Au–S and Au–O were 2.32 Å and 2.11 Å, respectively. This sandwiched structure stabilized the Au atomically dispersed structure. The Au–S

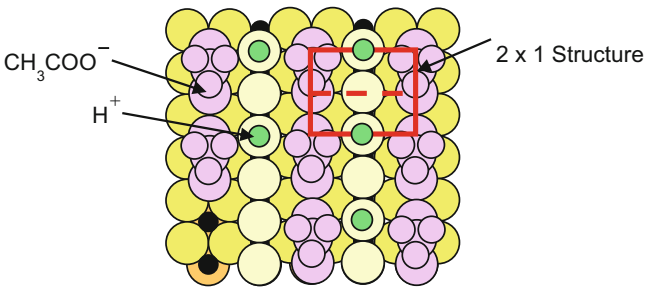

Fig. 32.7 Adsorption structure of TiO_2 (110). *Small black circles* represent Ti and *yellow larger circles* represent oxygen atoms. *Purple circles* indicate the acetate (CH_3COO^-) group. The acetates formed an ordered structure termed as (2×1). *Green circles* represent the proton dissociated from CH_3COOH

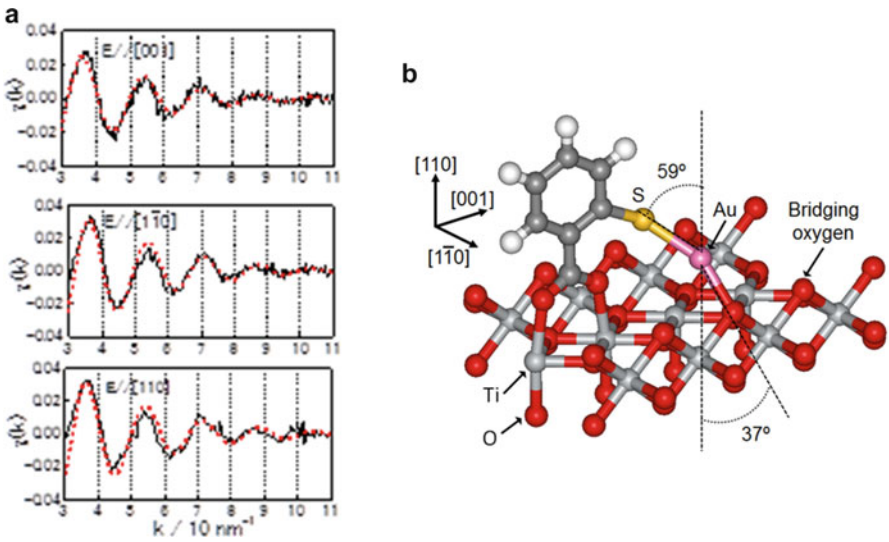

Fig. 32.8 XAFS oscillations of Au on an o-MBA covered TiO_2 (110) surface with different polarization directions (**a**) and model structures (**b**). The figure is reproduced from Figs. 6 and 7 in Ref. [24] with permission from The Royal Society of Chemistry (RSC)

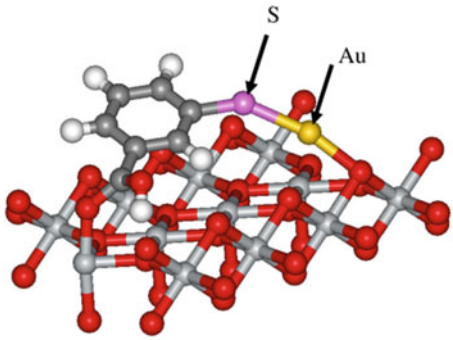

Fig. 32.9 Ball-and-stick model for Au on the *m*-MBA modified TiO_2 (110) surface. The *m*-MBA was fixed to the surface by one O-Ti bond owing to the strong S–Au bond [24]

bond was strong enough to modify the surface structure of mercaptobenzoate. In the *m*-mercaptobenzoic acid and *p*-mercaptobenzoate, S–Au–O structures were found where one Ti–O bond in the carboxylic moiety was cleaved and mercaptobenzoic acid was fixed to the surface with the other Ti–O bond, as shown in Fig. 32.9 [24].

Cu could be dispersed on the MBA-modified TiO_2 (110) surface in a similar way. Takakusagi et al. investigated the Cu structure on the three MBA isomers (*o*-, *m*-, and *p*-MBA). The atomically dispersed Cu species was stabilized on the *o*-MBA-pre-covered surface by bond formation with sulfur atoms of the MBA molecules and the bridging oxygen atoms on the TiO_2 (110) substrate surface. The Cu–S bond length was found to be 2.19 Å, while the distance

associated with the Cu–O interaction was 1.85 Å. The Cu–S and Cu–O bond angles to the surface normal were 45° and 43°, respectively. The S–Cu–O was nearly 180°. When the TiO_2 (110) surface was pre-covered with *m*-MBA and *p*-MBA (regio-isomers of *o*-MBA), a similar S–Cu–O structure was observed. The Cu–S and Cu–O bond distances were 2.19 Å and 1.85 Å, respectively, on the *m*-MBA pre-covered surface. The S–Cu–O had a collinear structure with a 44° tilt against the surface normal. However, the S–Cu–O on the *p*-MBA was found to have a different structure. The Cu–S and Cu–O distances were 2.23 Å and 1.90 Å, respectively, which were longer than those in the S–Cu–O complexes on the *o*-MBA and *m*-MBA pre-covered surfaces. Another difference observed in the S–Cu–O complexes was the tilt angle against the surface normal. The tilt angle between the surface normal and S–Cu–O complex on the *p*-MBA pre-covered surface was approximately 60°. The S–Cu–O was more parallel to the surface in *p*-MBA than *m*- and *o*-MBA. The regio-isomers of MBA could tune the surface structure.

In the case of Cu, thiophene carboxylic acid (TCA) also dispersed Cu atomically, making a sandwich structure between the S of TCA and surface oxygen atoms with bond distances of 2.19 Å and 1.89 Å, respectively [18, 25, 26]. However, TCA could not disperse Au atomically, owing to the different bond strengths of thiophene's S–Au and thiolate's S–Au bonds [24]. The former was a weak bond. Actually, as far as the author knows, no compounds have been found with the thiophene's S–Au bond though there are many examples of compounds binding with mercapto's S–Au bond [24].

When the TiO_2 (110) surface was modified with benzoic acid and acetic acid, the atomically dispersed Cu species on the surface was not obtained because of the weak interactions between Cu and the benzoic ring or methyl species. Interestingly, Cu was atomically dispersed when the surface was covered with acetic anhydride $(CH_3CO)_2O$ [27]. Cu has a sandwich structure composed of the O from the acetate and the bridging O. The two Cu–O distances were 1.96 Å and the O–Cu–O angle was 166°. The O–Cu–O linear structure was tilted by 47° from the surface normal. The structure was quite similar to those found in the thiophene and MBA molecules' pre-covered surfaces. The $(CH_3CO)_2O$ was adsorbed on the TiO_2 (110) surface dissociatively. Ashima et al. investigated the surface using X-ray photoelectron spectroscopy (XPS), low-energy electron diffraction (LEED), and high-resolution electron energy loss (HREELS) [28]. They found that the typical acetic acid adsorption LEED pattern was the $p(2 \times 1)$ structure. The adsorption amount was 0.55 ML larger than the saturation coverage (0.5 ML) in XPS. Considering the $(CH_3CO_2)_2O$ composition, the dissociation reaction provided two types of acetate, as shown in Fig. 32.10.

One acetate (A) adsorbed on the TiO_2 surface in a bidentate structure and the other acetate (B) was bound to the bridging oxygen of TiO_2 (110) with its molecular plane perpendicular to the surface [28]. If these two structures fully covered the surface, a maximum of 0.75 ML coverage was achievable. The observed coverage was 0.55 ML. Because a $p(2 \times 1)$ structure was observed where only acetate A was present, some acetate B was converted to acetate A with the creation of oxygen

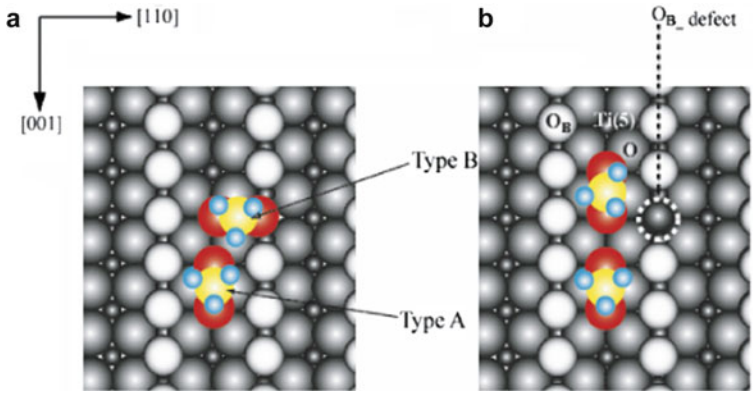

Fig. 32.10 Acetic anhydride absorption structure. (**a**) Acetate A is the normal acetate and Acetate B is the acetate whose oxygen in the carboxyl group arises from the bridging oxygen on the TiO_2 (110) surface. (**b**) The acetate B is converted to acetate A with the creation of a defect site [28]

defects, as shown in Fig. 32.10b. Kinoshita et al. demonstrated two types of acetate structures in their STM [29]. The Cu was assumed to diffuse along the channel on the bridging oxygen atoms. Acetate B or the oxygen defect blocked the Cu diffusion and consequently the Cu diffusion was hindered. The Cu species reacted with the acetate species to form the O–Cu–O sandwich structure [27]. The atomically dispersed Cu requires two ligands for stabilization and formation of the sandwich structure.

32.5 Summary

Total reflection fluorescence XAFS is a unique method that reveals atomically dispersed metal on a single crystal or flat surface. Basically, dispersion of the metal is determined by the strength of the metal–anion interaction. Control of the metal–anion interaction enables us to control the fine structure of the metal species on the surface.

References

1. Hu M, Noda S, Komiyama H (2002) A new insight into the growth mode of metals on TiO2 (1 1 0). Surf Sci 513:530
2. Chun WJ, Asakura K, Iwasawa Y (1998) Anisotropic structure analysis for Mo oxide on TiO2 (110) single crystal surface by polarization-dependent total reflection fluorescence EXAFS. Chem Phys Lett 288(May):868–872

3. Chun W-J, Asakura K, Iwasawa Y (1998) Polarization-dependent total-reflection fluorescence XAFS study of Mo oxides on a rutile TiO_2(110) single crystal surface. J Phys Chem 102 (Nov):9006–9014
4. Chun WJ, Asakura K, Ishii H, Liu T, Iwasawa Y (2002) The effect of ppm-level Na Impurity on the structure of SiO2-supported Mo catalysts prepared in a clean room. Top Catal 20:89–95
5. Takenaka S, Tanaka T, Funabiki T, Yoshida S (1998) Effect of alkali-metal ion addition to SiO2-Supported Mo oxide on photocatalysis photooxidation of propane and propene, and photo-assisted metathesis of propene. J Chem Soc Faraday Trans 94:695
6. Takenaka S, Tanaka T, Funabiki T, Yoshida S (1998) Structures of Mo species in SiO2-Supported Mo oxide and alkali-ion mdified SiO2-Mo oxide. J Phys Chem B 102:2960
7. Tanizawa Y, Chun WJ, Shido T, Asakura K, Iwasawa Y (2001) Three-dimensional analysis of the local structure of Cu on TiO2(110) by in-situ polarization dependent total reflection fluorescence XAFS. J Synchro Rad 8:508–510
8. Koike Y, Fujikawa K, Suzuki S, Chun WJ, Ijima K, Nomura M, Iwasawa Y, Asakura K (2008) Origin of self-regulated cluster growth on the TiO2(110) surface studied using polarization-dependent total reflection fluorescence XAFS. J Phys Chem C 112(12):4667–4675. doi:10.1021/jp711028w
9. Koike Y, Ijima K, Chun WJ, Ashima H, Yamamoto T, Fujikawa K, Suzuki S, Iwasawa Y, Nomura M, Asakura K (2006) Structure of low coverage Ni atoms on the TiO2(110) surface - polarization dependent total-reflection fluorescence EXAFS study. Chem Phys Lett 421 (1-3):27–30. doi:10.1016/j.cplett.2006.01.045
10. Koike Y, Chun WJ, Ijima K, Suzuki S, Asakura K (2009) What is the interaction between atomically dispersed Ni and oxide surfaces? Mater Trans 50(3):509–515
11. Diebold U (2003) The surface science of titanium dioxide. Surf Sci Rep 48(5-8):53
12. Asakura K (2012) Polarization-dependent total reflection fluorescence extended X-ray absorption fine structure and its application to supported catalysis. In: Catalysis: Volume 24. The Royal Society of Chemistry, pp 281–322. doi:10.1039/9781849734776-00281
13. Uehara H, Bin Hanaffi MH, Koike Y, Fujikawa K, Suzuki S, Ariga H, Takakusagi S, Chun WJ, Iwasawa Y, Asakura K (2013) Anisotropic growth of a nickel trimer formed on a highly-stepped TiO2(110) surface. Chem Phys Lett 570:64–69. doi:10.1016/j.cplett.2013.02.053
14. Ijima K, Koike Y, Chun W-J, Satio Y, Tanizawa Y, Shido T, Iwasawa Y, Nomura M, Asakura K (2004) A local structure of low coverage Ni species on the a-Al2O3(0001) surface- a polarization dependent XAFS studies. Chem Phys Lett 384:134–138
15. Walters CF, McCarty KF, Soares EA, Van Hove MA (2000) The surface structure of a-Al2O3 determined by LEED Al termination and evidence for anomolous large thermal vibrations. Surf Sci 464:L732
16. Chun WJ, Miyazaki K, Watanabe N, Koike Y, Takakusagi S, Fujikawa K, Nomura M, Asakura K (2011) Angle resolved total reflection fluorescence XAFS and its application to Au clusters on TiO 2 (110) (1 × 1). J Ceram Soc Jpn 119:890–893. doi:10.2109/jcersj2.119.890
17. Chun W-J, Miyazaki K, Watanabe N, Koike Y, Takakusagi S, Fujikawa K, Nomura M, Iwasawa Y, Asakura K (2013) Au clusters on TiO2(110) (1 × 1) and (1 × 2) surfaces examined by polarization-dependent total reflection fluorescence XAFS. J Phys Chem C 117 (1):252–257. doi:10.1021/jp308567e
18. Chun WJ, Koike Y, Ijima K, Fujikawa K, Ashima H, Nomura M, Iwasawa Y, Asakura K (2007) Preparation of atomically dispersed Cu species on a TiO2(110) surface premodified with an organic compound. Chem Phys Lett 433:345–349
19. Tsukuda T (2012) Toward an atomic-level understanding of size-specific properties of protected and stabilized gold clusters. Bull Chem Soc Jpn 85(2):151–168
20. Walter M, Akola J, Lopez-Acevedo O, Jadzinsky PD, Calero G, Ackerson CJ, Whetten RL, Grönbeck H, Häkkinen H (2008) A unified view of ligand-protected gold clusters as superatom complexes. Proc Natl Acad Sci 105(27):9157–9162. doi:10.1073/pnas.0801001105

21. Christensen SL, Chatt A, Zhang P (2013) Peptide-directed preparation and x-ray structural study of Au nanoparticles on titanium surfaces. Langmuir 29(15):4894–4900. doi:10.1021/la4003466
22. Tanizawa Y, Chun WJ, Shido T, Asakura K, Iwasawa Y (2001) Three dimensional analysis of the local structure of Cu on TiO2(110) by in-situ polarization-dependent total reflection fluorescence XAFS Studies. Surf Sci Catal 132:757–760
23. Tanizawa Y, Shido T, Iwasawa Y, Nomura M, Chun W-J, Asakura K (2003) Three-dimensional local structure analysis of Cu species on TiO2(110) surface studied by polarization-dependent total reflection fluorescence X-ray absorption fine structure(PTRF-XAFS). J Phys Chem 107:12917–12929
24. Asakura K, Takakusagi S, Ariga H, Chun W-J, Suzuki S, Koike Y, Uehara H, Miyazaki K, Iwasawa Y (2013) Preparation and structure of a single Au atom on the TiO2(110) surface: control of the Au-metal oxide surface interaction. Faraday Discuss 162:165–177. doi:10.1039/c2fd20131c
25. Takakusagi S, Chun W-J, Uehara H, Asakura K, Iwasawa Y (2013) Polarization-dependent total-reflection fluorescence x-ray absorption fine structure for 3D structural determination and surface fine tuning. Top Catal 56:1–11. doi:10.1007/s11244-013-0134-y
26. Takakusagi S, Nojima H, Ariga H, Uehara H, Miyazaki K, Chun W-J, Iwasawa Y, Asakura K (2013) Fine tuning and orientation control of surface Cu complexes on TiO2(110) premodified with mercapto compounds: the effect of different mercapto group positions. Phys Chem Chem Phys 14:14080–14088. doi:10.1039/c3cp51425k
27. Chun WJ, Koike Y, Ashima H, Kinoshita K, Ijima K, Fujikawa K, Suzuki S, Nomura M, Iwasawa Y, Asakura K (2009) Atomically dispersed Cu species on a TiO(2)(110) surface precovered with acetic anhydride. Chem Phys Lett 470(1-3):99–102. doi:10.1016/j.cplett.2009.01.030
28. Ashima H, Chun WJ, Asakura K (2007) Room-temperature-adsorption behavior of acetic anhydride on a TiO2(110) surface. Surf Sci 601(8):1822–1830. doi:10.1016/j.susc.2007.02.008
29. Kinoshita K, Suzuki S, Chun WJ, Takakusagi S, Asakura K (2009) Adsorption structure of acetic anhydride on a TiO(2)(110) surface observed by scanning tunneling microscopy. Surf Sci 603(3):552–557. doi:10.1016/j.susc.2008.12.019

Index

Y. Iwasawa et al. (eds.), *XAFS Techniques for Catalysts, Nanomaterials, and Surfaces*, DOI 10.1007/978-3-319-43866-5